UNIWERSYTET IM. ADAMA MICKIEWICZA W POZNANIU

Wydział Nauk Geograficznych i Geologicznych

Kierunek studiów: Geologia

Nr albumu: 396913

mgr inż. Bartosz Pieterek

Rekonstrukcja systemów magmowych wielkiej prowincji wulkanicznej Tharsis w kontekście przyszłych badań nad dystrybucją mineralizacji rudnej na Marsie

Reconstruction of magmatic plumbing systems of the Tharsis Volcanic Province in the context of future research on the distribution of ore mineralization on Mars

Praca doktorska napisana
w Instytucie Geologii
Uniwersytetu im. Adama Mickiewicza w Poznaniu
pod kierunkiem
prof. dr hab. Andrzeja Muszyńskiego
oraz
dr Jakuba Ciążeli

Poznań 2023

Spis treści

Załączniki

Publikacja nr 1

Pieterek, B., Ciazela, J., Lagain, A., Ciazela, M. (2022). Late Amazonian dike-fed parasitic volcanism in the Tharsis volcanic province on Mars. *Icarus*, *vol. 386, 115151.* https://doi.org/10.1016/j.icarus.2022.115151

Publikacja nr 2

Pieterek, B., Laban, M., Ciazela, J., Muszyński, A. (2022). Explosive volcanism in Noctis Fossae region on Mars. *Icarus, vol. 375, 114851*. https://doi.org/10.1016/j.icarus.2021.114851

Publikacja nr 3

Ciążela, J., Bakala, J., Kowalinski, M., Plocieniak, S., Zalewska, N., **Pieterek, B.,** Mrozek, T., Ciążela, M., Paslawski, G., Steslicki, M., Szaforz, Z., Barylak, J., Kuzaj, M., Maturilli, A., Helbert, J., Muszyński, A., Rataj, M., Gburek, S., Józefowicz, M., Marciniak, D. (2022). Concept and design of Martian far-IR ORE Spectrometer (MIRORES). *Remote Sensing, 14, 2799.* https://doi.org/10.3390/rs14122799

Podziękowania

Przygotowanie przedłożonej rozprawy doktorskiej było możliwe dzięki funduszom pozyskanym w ramach projektu GEO-INTER-APLIKACJE (projekt POWR.03.02.00-00- I027/17), współfinansowanemu przez Unię Europejską ze środków Europejskiego Funduszu Społecznego w ramach Programu Operacyjnego Wiedza Edukacja Rozwój. Serdecznie dziękuję kierownikowi projektu Panu Profesorowi Jackowi Michniewiczowi oraz pozostałym osobom Pani Katarzynie Piotrowskiej, Marcie Mitrędze, Joannie Zdebko-Okońskiej, Magdalenie Walczak, które stanowiły wsparcie podczas realizacji projektu.

Praca doktorska nie powstałaby bez udziału Mateusza Józefowicza, który reprezentując przedsiębiorstwo ABM Space Sp. z o.o. oraz Europejską Fundację Kosmiczną, które stanowią Interesariuszy realizowanej pracy doktorskiej, wspierał realizację moich badań oraz zawsze służył dobrym słowem i pomocą.

Pragnę wyrazić głęboką wdzięczność wobec moich promotorów:

Panu Profesorowi Andrzejowi Muszyńskiemu dziękuję za niekończącą się motywację do działania, wskazanie odpowiedniej ścieżki naukowej, a także życiowej oraz wielogodzinne dyskusje. Dziękuję za ogromne wsparcie, pomoc w realizacji badań, założeń naukowych, niezawodność w każdym momencie, i wyrozumiałość oraz motywację do krytycznego spojrzenia na problematykę badawczą. Szczególne podziękowania pragnę złożyć Panu Profesorowi za pomoc w jasnym formułowaniu myśli, nie tylko naukowej, oraz inspirację do zgłębiania otaczającego nas świata i ludzi.

Chciałam wyrazić głęboką wdzięczność Panu Doktorowi Jakubowi Ciążeli, bez którego moja praca doktorska nie mogłaby powstać. Dziękuję za inspirację do badań, pomoc w planowaniu badań oraz kreatywne podejście w poszukiwaniu rozwiązań problemów geologicznych. Pragnę również podziękować za pomoc w redagowaniu pracy oraz motywację do opracowania samodzielnych koncepcji na tle istniejącej literatury naukowej.

Szczególne wyrazy wdzięczności składam pracownikom Instytutu Geologii Uniwersytetu im. Adama Mickiewicza w Poznaniu za wprowadzenie mnie w świat nauk geologicznych, przekazaną wiedzę i wsparcie, które zawsze otrzymywałem. W szczególności pragnę podziękować Panu prof. Witoldowi Szczucińskiemu oraz Panu dr Robertowi Jagodzińskiemu za pomoc i życzliwość. Chciałbym również podziękować Pani Annie Langner, która obdarzyła mnie niezwykłą cierpliwością oraz zawsze wspierała w finansowych 'sprawach beznadziejnych'.

Chciałabym również podziękować Rodzinie oraz Przyjaciołom, za nieustanne wsparcie oraz motywację. W szczególności dziękuję moim Rodzicom za wspieranie mnie w wyborze drogi zawodowej oraz nigdy niegasnącą wiarę w moje decyzje i poczynania. Dziękuję Dobrochnie za ogromną wyrozumiałość, cierpliwość, dbanie o moje zdrowie oraz niekończące się wsparcie, które stale pozwala Nam się wspólnie rozwijać.

Streszczenie

W dzisiejszych czasach, środowisko badaczy planetarnych stoi u progu nowego zadania jakim jest dokładne poznanie oraz zrozumienie procesów kształtujących powierzchnię Marsa. Kluczowe wydaje się także poznanie zasobów planety, rozważanej jako przyszły cel załogowych misji marsjańskich. Jednym z głównych wyzwań przyszłej eksploracji Marsa będzie dostęp do lokalnych surowców metalicznych i energetycznych. Zrozumienie procesów magmowych i wulkanicznych będzie mieć kluczowe znaczenie w poszukiwaniu perspektywicznych nagromadzeń minerałów rudnych na Marsie. Młoda aktywność wulkaniczna może odgrywać kluczową rolę w rozwoju lokalnych systemów magmowo-hydrotermalnych odpowiadających za powstawanie siarczków i tlenków, które będą stanowić przyszły cel poszukiwań. W pracy doktorskiej podjąłem się zbadania największego na Marsie systemu magmowego Tharsis w kontekście aktywności wulkanicznej, która prawdopodobnie kontrolowała pomagmową aktywność hydrotermalną oraz stowarzyszoną z nią mineralizację. Badania procesów magmowych w obszarze Tharsis, w połączeniu z koncepcją spektrometru badającego powierzchnię Marsa pod kątem występowania minerałów rudnych, stanowi nowatorskie i interdyscyplinarne podejście naukowe. Może ono znaleźć zastosowanie w przemyśle kosmicznym, a zwłaszcza w dynamicznie rozwijającym się górnictwie kosmicznym.

Przygotowana rozprawa doktorska składa się z trzech artykułów naukowych recenzowanych i opublikowanych w czasopismach z listy JCR, które zostały poświęcone: 1) regionalnej rekonstrukcji systemu magmowego Tharsis w oparciu o wulkanizm rozproszony, 2) udokumentowaniu eksplozywnego pola wulkanicznego piroklastycznych stożków scoria w obszarze Noctis Fossae (południowa część obszaru Tharsis), oraz 3) opracowaniu koncepcji i projektu spektrometru MIRORES do poszukiwań minerałów rudnych na powierzchni Marsa. Badania opisane w dwóch pierwszych artykułach zostały przeprowadzone przy użyciu ogólnodostępnych obrazów satelitarnych powierzchni oraz numerycznych modeli terenu Marsa. Wykorzystano je do kartowania form wulkanicznych, datowania ich ostatniej aktywności za pomocą metody zliczania kraterów, obliczania parametrów morfometrycznych oraz tworzenia trójwymiarowych modeli terenu badanych form wulkanicznych. W procesie tworzenia koncepcji spektrometru MIRORES zostały wykorzystane opublikowane dane spektralne oraz wykonane pomiary emisyjności pirytu. Posłużyły one do kalibracji układu detektorów oraz przeprowadzenia modelowania wykrywalności siarczków przez spektrometr. Zaprojektowano też zintegrowany układ optyczny, elektroniczny i mechaniczny przyrządu.

Na podstawie uzyskanych wyników w pierwszym artykule udało się dowieść, że rozproszony wulkanizm w obszarze Tharsis jest najprawdopodobniej stowarzyszony (czasowo i przestrzennie) z aktywnością sąsiadujących, wulkanów centralnych oraz, że magma zasilająca rozproszony wulkanizm, migruje w skorupie marsjańskiej tworząc system dajek radialnych i pierścieniowych. W niniejszym artykule zostały przedstawione hipotezy świadczące o tym, że magma tworząc podpowierzchniowe dajki, może migrować z komór magmowych zlokalizowanych pod głównymi wulkanami Tharsis lub ze stref częściowego topienia występujących na granicy skorupy i płaszcza na Marsie. Przeprowadzona rekonstrukcja pozwoliła wyróżnić sześć oddzielnych systemów magmowych, które mogły pozostawać aktywne po ustaniu wulkanizmu w obrębie głównego wulkanu. Udokumentowanie obecności stosunkowo młodych potoków lawowych (<40 milionów lat) tworzących stoki kartowanych form wulkanicznych wskazuje, że wulkanizm w obszarze Tharsis nie jest całkowicie wygasły. Datowania sugerują, że wulkanizm obecnie pozostaje nieaktywny, ale w przeszłości był on też przeplatany takimi okresami uśpienia, wskazując na powtarzające się impulsy wzmożonej aktywności magmowej.

Na Ziemi, odpowiednikiem prowincji wulkanicznej Tharsis są wielkie prowincje magmowe, z którymi zazwyczaj stowarzyszony jest wulkanizm eksplozywny, tworzący lokalne pola wulkaniczne. W ramach kontynuowania prac kartograficznych w rejonie Tharsis, w drugim artykule, udało się udokumentować i scharakteryzować pole wulkaniczne składające się z niewielkich (<4 km średnicy) stożków scoria, których obecność świadczy o obecności lokalnego wulkanizmu eksplozywnego. Przeprowadzone badania morfometryczne wraz z datowaniami potwierdziły, że w obrębie badanego pola wulkanicznego, stożki ujawniają zróżnicowany wiek aktywności, wskazując na długotrwałe procesy magmowe w obszarze Noctis Fossae. Udokumentowanie wulkanizmu o charakterze eksplozywnym na starej (>2 mld lat), pociętej uskokami skorupie wskazuje, że wyniesione obszary, które nie uległy odmłodzeniu przez rozległe potoki lawowe mogą stanowić nowy wgląd w ewolucję wulkanizmu na Marsie. Eksplozywny typ erupcji może być związany z utworzeniem się okresowej komory magmowej pod obszarem Noctis Fossae. Stagnująca w komorze magma mogła ulec: 1) dyferencjacji do składu chemicznego o większej zawartości krzemionki, 2) stratyfikacji z większą zawartością gazów w górnej jej części, 3) zasymilować uwodnione minerały budujące przypowierzchniową część skorupy marsjańskiej lub/oraz 4) wejść w interakcje z wodą/zmarzliną skutkując eksplozywnym typem erupcji. Zaproponowane procesy związane z asymilacją uwodnionych minerałów oraz interakcją magmy z wodą/zmarzliną, mogły odegrać kluczową rolę w zapoczątkowaniu migracji roztworów hydrotermalnych. We wcześniejszych badaniach dotyczących eksplozywnych stożków scoria w rejonie Coprates Chasma na Marsie, potwierdzono już obecność siarczanów, przestrzennie stowarzyszonych z wulkanizmem, które sugerują powstanie w procesach hydrotermalnych. Jednakże, aby w pełni zrozumieć charakter oraz typ mineralizacji w obszarze Noctis Fossae konieczne są satelitarne badania widmowe w bliskiej, i docelowo także dalekiej podczerwieni.

Przedstawione w pracy doktorskiej wyniki mają znaczenie nie tylko regionalne, ale również globalne dla Marsa. Zaobserwowane zależności oraz zdobyta wiedza dają podstawy sądzić, że podobne procesy mogły/mogą także występować w pozostałych obszarach wulkanicznych na Marsie. Na Ziemi systemom wulkanicznym często towarzyszy aktywność hydrotermalna prowadząca do powstania mineralizacji rudnej zawierającej siarczki. Obecnie używane spektrometry, badające skład mineralny powierzchni Marsa w bliskiej podczerwieni, nie wykrywają siarczków, będących głównym nośnikiem metali. Aby umożliwić prowadzenie szczegółowych badań nad mineralizacją rudną na powierzchni Marsa, opracowana została koncepcja spektrometru MIRORES działającego w dalekiej podczerwieni. Jego zadaniem będzie identyfikacja występujących na Marsie siarczków o genezie hydrotermalnej lub magmowej (piryt, chalkopiryt i markasyt) (Artykuł 3), zarówno w opisanych powyżej prowincjach wulkanicznych (Artykuł 1 i 2) jak i strefach impaktowych analogicznych do tej z krateru Sudbury w Kanadzie.

W ramach przygotowanej rozprawy doktorskiej zostały opublikowane dwa powiązane tematycznie pierwszoautorskie recenzowane artykuły naukowe w czasopismach z listy JCR, dotyczące procesów wulkanicznych na Marsie. Przyrząd MIRORES przedstawiony w trzecim artykule, stanowi ważny element aplikacyjności dla wyników badań uzyskanych w pracy doktorskiej.

Wykonane analizy oraz interpretacje obrazów satelitarnych pozwoliły dostarczyć nowych informacji na temat systemu magmowego wielkiej prowincji wulkanicznej Tharsis. Uzyskane dane mogą być kluczowe w aspekcie badań satelitarnych przy wykorzystaniu zaprojektowanego spektrometru MIRORES. Cykl przygotowanych artykułów stanowi zarys badań, które mogą być kontynuowane dzięki wynikom uzyskanym w pracy. Jest to wkład naukowy w dalsze zrozumienie procesów wulkanicznych i obszarów potencjalnej aktywności hydrotermalnej na Marsie, w kontekście kontynuacji badań orbitalnych oraz planowanej eksploracji Marsa.

Streszczenie w języku angielskim - Summary

Nowadays, the planetary research community is on the verge of a new task that assumes a thorough understanding of the processes that have shaped the surface of Mars. Also, it seems crucial to identify the planet's resources, which are considered a future target for human-operated Martian missions. One of the main challenges of the future exploration of Mars will be access to local resources of metals and energy. Understanding the igneous and volcanic processes will be crucial in searching for ore mineralization on Mars. Relatively young Martian volcanic activity may play a vital role in developing local magmatic-hydrothermal systems responsible for the formation of sulfides and oxides, which will constitute a future target for exploration and *in-situ* utilization. In my Ph.D. thesis, I investigated the most extensive magmatic system on Mars, Tharsis, to understand the evolution of volcanic activity, which probably controlled the post-magmatic hydrothermal activity and associated ore mineralization. The study of volcano-magmatic processes in Tharsis, combined with the designed concept of a spectrometer examining the surface of Mars in terms of the identification of ore minerals, is an innovative and interdisciplinary scientific approach. It can be successfully used in the space industry, especially in the dynamically developing branch of space mining.

The doctoral dissertation comprises three peer-reviewed and published scientific articles in journals from the JCR list, which are devoted to 1) regional reconstruction of the Tharsis magmatic plumbing system based on distributed volcanism, 2) documenting the explosive-origin volcanic field of pyroclastic scoria cones in the Noctis Fossae region (southern part of Tharsis), and 3) developing the concept of the MIRORES spectrometer devoted for the identifying ore minerals on the Martian surface. The results presented in the first two articles were obtained using public-domain satellite images of the surface and digital elevation models of Mars. These data were used to map volcanic landforms, determine the ages of the latest volcanic activity using the crater counting method, calculate morphometric parameters, and create three-dimensional terrain models of the studied volcanic landforms. In designing the MIRORES spectrometer, the available published spectral data have been used to determine and calibrate the detectors’ positions. In addition, the pyrite emissivity measurements were conducted to model the sulfide detection accuracy of the designed spectrometer. An integrated optical, electronic and mechanical systems of the instrument was also designed by the MIRORES team for the purposes of this project.

Based on the regional study of Tharsis, in the first paper, it has been proven that the distributed volcanism is most likely geologically associated (temporally and spatially) with the

activity of the central volcanoes and that the magma feeding the distributed volcanism has migrated in the Martian crust using radial and circumferential dikes. The authors proposed that magma may migrate using subsurface dikes from magma chambers beneath the central Tharsis volcanoes or from magmatic underplating zones at the crust-mantle boundary. The conducted reconstruction of the volcanic activity allowed us to distinguish six separate magmatic plumbing systems that may have remained active after the volcanic activity had been stopped within the adjacent central volcano. The presence of relatively young lava flows on Tharsis (<40 million years old) forming the slopes of mapped volcanic features indicates that volcanism in the studied province is not wholly extinct. The obtained ages suggest that the volcanism remains inactive. However, in the past, it was probably interrupted by periods of dormancy that indicate the repeated pulses of increased magmatic activity.

On Earth, large igneous provinces are often associated with explosive volcanism forming local volcanic fields and might constitute a terrestrial analog for the Tharsis volcanic province. Continuing the mapping of Tharsis, a local volcanic field comprising small scoria cones (<4 km in diameter) indicates the occurrence of putative explosive volcanism. Detailed morphometrical studies and age determinations confirmed that the Noctis Fossae volcanic field hosts volcanic edifices that reveal a varied age of their last activity, indicating long-term magmatic evolution. The documentation of explosive volcanism on an old (>2 billion years old), fractured crust indicates that old and elevated terrains that escaped resurfacing by younger basaltic lava flows might provide fruitful insights into the evolution of Martian volcanism. The explosive eruptive style might be related to the formation of a temporary magma chamber beneath the Noctis Fossae region. The magma stagnating in the chamber could have undergone: 1) chemical differentiation to a composition with a higher silica content, 2) stratification resulted in a higher content of gases in its upper part, 3) assimilation of hydrated minerals, and/or 4) interaction with subsurface water /permafrost deposits resulting in an explosive-type eruption. The proposed processes related to the assimilation of hydrated minerals and the interaction of magma with water/permafrost could have played a vital role in the generation of hydrothermal fluids. Previous studies of explosive-origin scoria cones in the Coprates Chasma region of Mars have confirmed the presence of sulfates spatially associated with volcanic edifices that suggest their hydrothermal origin. However, near- and, ultimately, far-infrared orbital spectral studies are required to understand the volcanic-associated mineralization in Noctis Fossae fully.

The presented results are not only of regional but also global importance. The observed relationships give grounds to believe that similar processes could/may also occur in other volcanic regions on Mars. On Earth, volcanic systems are often associated with hydrothermal activity leading to the formation of sulfide-containing ore mineralization. The current using near-infrared spectrometers that investigate Martian mineralization cannot identify sulfides, which are the primary source of precious metals. To enable sulfide identification and their future prospecting, the concept of the MIRORES spectrometer operating in the far-infrared was developed. The designed spectrometer will be able to identify commonly occurring on Mars sulfides, including pyrite, chalcopyrite, and marcasite (Article 3), both in the volcanic provinces described above (Articles 1 and 2) and the impact crater zones, which are analogous to that in Sudbury, Canada.

The doctoral dissertation comprises two first-author peer-reviewed scientific published articles in journals from the JCR list and constitutes a collection of thematically related papers focused on magmatic and volcanic processes on Mars. The concept of the MIRORES spectrometer presented in the third article attached to this dissertation is a crucial element showing an interdisciplinary approach and applicability for the research results obtained in this thesis.

The analyses and interpretations of satellite images allowed us to provide insight into the magmatic systems of the volcanic province of Tharsis. The obtained data may be crucial regarding satellite missions using the designed MIRORES spectrometer. The published articles might constitute an introduction to the more in-depth research that can be continued thanks to the obtained in this work results. This thesis might constitute an essential contribution to further understanding volcanic processes on Mars and the usage of surficial observation for designing orbital-working cameras and instruments.

Lista publikacji wchodzących w skład rozprawy doktorskiej

Przedstawiona rozprawa doktorska stanowi zbiór powiązanych tematycznie artykułów opublikowanych w międzynarodowych czasopismach naukowych posiadających współczynnik wpływu (ang. *Impact Factor*; IF). Sumaryczny IF (zgodny z rokiem publikacji artykułów) przedstawionego zbioru artykułów naukowych wynosi 12.663, zaś suma punktów MEiN wynosi 380.

W skład rozprawy wchodzą następujące publikacje:

1. **Pieterek, B.**, Ciazela, J., Lagain, A., Ciazela, M. (2022). Late Amazonian dike-fed parasitic volcanism in the Tharsis volcanic province on Mars. *Icarus*, *vol. 386, 115151.* https://doi.org/10.1016/j.icarus.2022.115151
   (IF_{2022} = **3.657**, pkt. MEiN = **140**)

2. **Pieterek, B.**, Laban, M., Ciazela, J., Muszyński, A. (2022). Explosive volcanism in Noctis Fossae region on Mars. *Icarus, vol. 375, 114851.* https://doi.org/10.1016/j.icarus.2021.114851
   (IF_{2022} = **3.657**, pkt. MEiN = **140**)

3. Ciążela, J., Bakala, J., Kowalinski, M., Plocieniak, S., Zalewska, N., **Pieterek, B.,** Mrozek, T., Ciążela, M., Paslawski, G., Steslicki, M., Szaforz, Z., Barylak, J., Kuzaj, M., Maturilli, A., Helbert, J., Muszyński, A., Rataj, M., Gburek, S., Józefowicz, M., Marciniak, D. (2022). Concept and design of Martian far-IR ORE Spectrometer (MIRORES). *Remote Sensing, 14, 2799.* https://doi.org/10.3390/rs14122799
   (IF_{2022} = **5.349,** pkt. MEiN **= 100**)

STRESZCZENIE ROZPRAWY DOKTORSKIEJ

Rekonstrukcja systemów magmowych wielkiej prowincji wulkanicznej Tharsis w kontekście przyszłych badań nad dystrybucją mineralizacji rudnej na Marsie

Reconstruction of magmatic plumbing systems of the Tharsis Volcanic Province in the context of future research on the distribution of ore mineralization on Mars

1. Wprowadzenie

Procesy endogeniczne odgrywają kluczową rolę w kształtowaniu budowy geologicznej i ewolucji planet w Układzie Słonecznym. Prowadzone obserwacje satelitarne od dziesięcioleci wskazują, że powierzchnia Marsa w znaczący sposób została ukształtowana przez procesy wulkaniczne. Doprowadziły one do powstania dwóch głównych jednostek wulkanicznych nazywanych prowincjami Tharsis i Elysium, gdzie wulkany centralne (Wilson i in., 2001; Plescia, 2004) stowarzyszone są z formami wulkanizmu rozproszonego (Bleacher i in., 2009, 2010; Hauber i in., 2009; Richardson i in., 2021). Wczesne modele dotyczące termalno-magmowej ewolucji Marsa sugerowały, że wulkanizm, po wzmożonej aktywności we wczesnym okresie historii planety, uległ znacznemu ograniczeniu i prawdopodobnie ustał kilkaset milionów lat temu (Weizman i in., 2001; Hauck i Phillips, 2002; Breuer i Spohn, 2003). Jednakże, wraz z rozwojem badań i ciągłym dostarczaniem nowych zdjęć o wyższej rozdzielczości, predykcje te okazały się nie w pełni prawdziwe. Obecne obserwacje wskazują, że wulkanizm na Marsie był aktywny przez cały okres późnego Amazonu (<300 mln lat) (Neukum i in., 2004; Hauber i in., 2011; Robbins i in., 2011; Mouginis-Mark i Wilson, 2019; Krishnan i Kumar, 2022), a najmłodsze dotychczas udokumentowane osady piroklastyczne wskazują, że ostatnia odnotowana erupcja wulkaniczna prawdopodobnie miała miejsce od około 222 do 46 tys. lat temu (Horvath i in., 2021). Natomiast najmłodszy potok lawowy na Marsie został udokumentowany na zboczach Olympus Mons ujawniając wiek 2.4 mln lat (Neukum i in., 2004). Najnowsze dane sejsmiczne z łazika *InSight* wskazują na obecność płynnego jądra planety oraz aktywność sejsmiczną (Clinton i in., 2021; Khan i in., 2021; Stähler i in., 2021), która może sugerować obecność współczesnych procesów magmowych w płaszczu i skorupie. Najnowsze modele dotyczące procesów zachodzących w marsjańskim płaszczu oraz wiedza dotycząca budowy skorupy Marsa, wskazują na aktywne strefy topienia płaszcza, które zlokalizowane pod prowincjami wulkanicznymi, odpowiadają za generowanie stopów magmowych (Plesa i in., 2018, 2023). Możemy stąd przypuszczać, że aktywność wulkaniczna na Marsie nie jest całkowicie wygasła, a jedynie obecnie uśpiona, przez co nie obserwuje się żadnych powierzchniowych przejawów wulkanizmu w postaci współczesnych erupcji.

Eksploracja Marsa trwa już od kilkudziesięciu lat, jednak momentem przełomowym w rozwoju badań było potwierdzenie obecności wody na jego powierzchni (Martín-Torres i in., 2015). Wskazuje to, że w przeszłości mogły panować tam warunki sprzyjające rozwojowi życia na powierzchni, przez co Mars stał się, zaraz po Księżycu, jednym z głównych celów planowania załogowych misji oraz stworzenia tam samowystarczalnych baz (Levchenko i in., 2019; Starr i Muscatello, 2020). Europejska Agencja Kosmiczna (ESA) w swoim raporcie (ESA, 2019) wskazała, że dostęp do zasobów kosmicznych umożliwi zrównoważoną eksplorację Księżyca, a następnie Układu Słonecznego. Działania na Księżycu powinny przygotować drogę dla rozwoju przyszłej eksploracji Marsa i asteroid. Wyzwania związane z zasobami kosmicznymi mogą być również sposobem na rozwój innowacji na Ziemi, które sprostają globalnym wyzwaniom. Z tego względu, według ESA, zasoby kosmiczne będą głównym międzynarodowym tematem w następnych dekadach, a kluczowe sektory rozwoju dotyczą górnictwa kosmicznego, metalurgii, energii, robotyki i automatyki (ESA, 2019). Patrząc z perspektywy kilku dekad na rozwój eksploracji kosmosu, kluczowe wydaje się pełne zrozumienie procesów geologicznych na Marsie, które mogą kontrolować i warunkować przyszłe działania skupiające się na rozpoznaniu zasobów mineralnych.

W oparciu o stan wiedzy oraz dane obserwacyjne dotyczące procesów magmowych i wulkanicznych na Marsie dostępnych w momencie rozpoczęcia doktoratu (rok 2018), została postawiona hipoteza badawcza zakładająca związek pomiędzy aktywnością centralnych wulkanów, a rozproszonym wulkanizmem w rejonie Tharsis. Zważywszy na stosunkowo młodą aktywność wulkaniczną uważałem, że badania systemów magmowych mogą dostarczyć nowych informacji na temat potencjalnych obszarów mineralizacji hydrotermalnej stowarzyszonej z wulkanizmem. Procesy magmowe prawdopodobnie mogą odpowiadać za metalogenezę oraz kontrolować rozmieszczenie mineralizacji rudnej na Marsie. Z tego względu, niniejsza rozprawa doktorska poświęcona jest problematyce występowania aktywności wulkanicznej i rekonstrukcji systemów magmowych w wielkiej prowincji wulkanicznej Tharsis na Marsie. Pozyskane dane oraz oparte na nich wnioski dotyczące przestrzenno-czasowej ewolucji wulkanizmu posłużyły w zaproponowaniu potencjalnych obszarów zainteresowań dla koncepcji spektrometru MIRORES, będącego instrumentem do poszukiwania mineralizacji siarczkowej na powierzchni Marsa. Badania procesów wulkanicznych w obszarze Tharsis, w połączeniu z koncepcją spektrometru MIRORES, stanowią nowatorskie i interdyscyplinarne podejście naukowe. Może ono znaleźć praktyczne zastosowanie w przemyśle kosmicznym, a zwłaszcza w dynamicznie rozwijającym się górnictwie kosmicznym.

Praca badawcza, przeprowadzona w ramach przedstawionej rozprawy doktorskiej, obejmuje badania kartograficzne powierzchni Marsa, interpretację zdjęć satelitarnych oraz analizy w zakresie występowania aktywności wulkanicznej w skali regionalnej i lokalnej. Otrzymane wyniki mogą posłużyć do badań globalnych przy użyciu instrumentu działającego na orbicie Marsa. Obszarem badawczym była prowincja wulkaniczna Tharsis, która na podstawie danych literaturowych wykazywała największe zróżnicowanie form wulkanicznych oraz wskazywała na występowanie stosunkowo młodej aktywności wulkanicznej w kontekście ewolucji całej planety. Przedmiot badań obejmował zagadnienia związane z rozwojem i rekonstrukcją systemów magmowych na Marsie oraz współudział w stworzeniu koncepcji spektrometru badającego mineralizację siarczkową, ze szczególnym uwzględnieniem obszarów wulkanicznych. W rozprawie doktorskiej poruszono następujące problemy badawcze:

1. **Określenie związku pomiędzy aktywnością centralnych wulkanów Tharsis, a rozproszonym wulkanizmem**, uwzględniając:
    a. aspekt rozmieszczenia i relacji przestrzennych, w tym orientacji struktur wulkanicznych,
    b. relacje czasowe pomiędzy ostatnią aktywnością wulkanizmu centralnego i rozproszonego,
    c. rekonstrukcję systemów magmowych oraz źródła magm zasilających wulkanizm.
2. **Zróżnicowanie cech morfologicznych różnych stylów erupcji w prowincji Tharsis,** w tym:
    a. scharakteryzowanie pola wulkanicznego piroklastycznych stożków scoria, wskazujących na obecność wulkanizmu eksplozywnego,
    b. określenie ewolucji czasowej wulkanizmu eksplozywnego w rejonie Noctis Fossae;
    c. wyznaczenie obszarów źródłowych dla magm zasilających wulkanizm eksplozywny.
3. **Określenie perspektywicznych obszarów wulkanicznych, o których wiedza została wykorzystana w opracowaniu koncepcji instrumentu do prowadzenia badań satelitarnych w kontekście identyfikacji mineralizacji siarczkowej na Marsie.**

Dążąc do rozwiązania problemów badawczych, w rozprawie doktorskiej wyróżniono następujące cele:

1. **Regionalne prace kartograficzne** skupiające się na określeniu **rozmieszczenia wulkanizmu rozproszonego** w prowincji Tharsis, ze szczególnym **uwzględnieniem parametrów morfometrycznych** oraz **datowania ostatniej aktywności wulkanicznej** dla skartowanych form wulkanicznych.
2. **Lokalne badania eksplozywnego pola wulkanicznego** w rejonie Noctis Fossae przy szczególnym uwzględnieniu **parametrów morfometrycznych** badanych form wulkanicznych oraz ich **relacji przestrzenno-czasowych**.
3. **Wskazanie perspektywicznych obszarów wulkanicznych, których analizy spektralne mogą dostarczyć wglądu w rozwój mineralizacji pomagmowej na Marsie.**

Rozprawa składa się z zestawu trzech powiązanych tematycznie, recenzowanych artykułów naukowych opublikowanych w indeksowanych czasopismach naukowych (zob. Lista publikacji wchodzących w skład rozprawy) i opatrzonych wspólnym streszczeniem. Opublikowane wersje artykułów dołączono w dalszej części niniejszej rozprawy doktorskiej (zob. załączniki Artykuły 1-3) wraz z ich materiałami uzupełniającymi. Wszystkie artykuły są wieloautorskie, z których w dwóch Autor niniejszej rozprawy jest pierwszym autorem i korespondencyjnym, a wkład kluczowych współautorów został udokumentowany stosownymi oświadczeniami (zob. Oświadczenia autorów). Metodologia przeprowadzonych obserwacji oraz analiz w ramach niniejszej rozprawy doktorskiej została opracowana samodzielnie na podstawie literatury oraz odbytych szkoleń i staży przy konsultacji z Promotorami (prof. dr hab. Andrzejem Muszyńskim oraz dr Jakubem Ciążelą). W ramach prac nad dwoma pierwszoautorskimi publikacjami, byłem zaangażowany w cały proces badawczy tj. opracowanie koncepcji badań, przeprowadzenie wszystkich analiz oraz proces przygotowania publikacji, pełniąc także funkcję autora korespondencyjnego. Natomiast w ramach prac nad artykułem wieloautorskim, uczestniczyłem w procesie badawczo-publikacyjnym wykonując powierzone mi zadania i elementy pracy badawczej.

- W ramach pracy nad publikacją nr 1 (***Pieterek, B.,*** *Ciążela, J., Lagain, A., Ciążela, M. (2022). Late Amazonian dike-fed parasitic volcanism in the Tharsis volcanic province on Mars)*, byłem odpowiedzialny za kartowanie form wulkanicznych w prowincji Tharsis, określenie wieku ich ostatniej aktywności wulkanicznej, przygotowanie wszystkich elementów graficznych oraz przeprowadzenie interpretacji i rekonstrukcji systemów magmowych. Jako pierwszy i korespondencyjny autor odpowiadałem za przygotowanie manuskryptu oraz odpowiedzi na otrzymane recenzje.

- W ramach pracy nad publikacją nr 2 (***Pieterek, B.,*** *Laban, M., Ciążela, J., Muszyński, A. (2022). Explosive volcanism in Noctis Fossae region on Mars)*, byłem odpowiedzialny za koncepcję oraz metodologię prowadzonych badań, wspólnie z współautorką artykułu (*Magdaleną Laban*) przeprowadziłem proces kartowania oraz analizę strukturalną wraz z datowaniami powierzchni wyznaczonych obszarów. Jako pierwszy i korespondencyjny autor odpowiadałem za przygotowanie manuskryptu (wraz z *Magdaleną Laban*) oraz odpowiedzi na otrzymane recenzje.
- W ramach pracy nad publikacją nr 3 (*Ciążela, J., Bakala, J., Kowalinski, M., Plocieniak, S., Zalewska, N.,* **Pieterek, B.,** *Mrozek, T., Ciążela, M., Paslawski, G., Steslicki, M., Szaforz, Z., Barylak, J., Kuzaj, M., Maturilli, A., Helbert, J., Muszyński, A., Rataj, M., Gburek, S., Józefowicz, M., Marciniak, D. (2022). Concept and design of Martian far-IR ORE Spectrometer (MIRORES))*, byłem odpowiedzialny za wskazanie perspektywicznych obszarów wulkanicznych do przyszłych badań za pomocą spektrometru MIRORES, opracowanie oraz przygotowanie zestawień graficznych dotyczących charakterystyki spektralnej krzemianów i siarczków, przygotowanie dużej części rycin (11 z 16) oraz wniosłem wkład w edycję manuskryptu.

2. Słownik terminów

MRO – (ang. *Mars Reconnaissance Orbiter*) marsjańska sonda, obecnie prowadząca obserwacje, na której pokładzie zamontowane są kamery, których zdjęcia posłużyły w prowadzonych badaniach.

MOLA – (ang. *Mars Orbiter Laser Altimeter*) instrument zbierający informację na temat topografii Marsa, zamontowany na pokładzie sondy Mars Global Surveyor, która zakończyła misję w listopadzie 2006 roku (instrument zbierał dane do czerwca 2001 roku).

HRSC – (ang. *High Resolution Stereo Camera*) kamera zamontowana na pokładzie sondy *Mars Express*, której zadaniem jest wykonywanie zdjęć powierzchni Marsa w celu poszukiwania dowodów na obecność wody i życia.

THEMIS – (ang. *Thermal Emission Imaging System*) kamera zamontowana na pokładzie satelity *Mars Odyssey*, która wykonuje zdjęcia powierzchni Marsa w zakresie widma widzialnego i podczerwieni. Jej głównym zadaniem jest zbadanie dystrybucji minerałów i ich związku z formami morfologicznymi na powierzchni.

CTX – (ang. *Context Camera*) kamera zamontowana na pokładzie sondy MRO, której zadaniem jest wykonywanie zdjęć w skali szarości o rozdzielczości ~6 m/piksel, które obecnie stanowią podstawowe zdjęcia dla prowadzonych badań, pokrywając >99% powierzchni Marsa. Wykorzystując dwa pokrywające się zdjęcia CTX można wyliczyć topografię terenu tworząc numeryczny model terenu (ang. *digital terrain model (DTM)*).

HiRISE – (ang. *High Resolution Imaging Science Experiment*) kamera zamontowana na pokładzie satelity MRO, której zadaniem jest wykonywanie wysoko rozdzielczych zdjęć satelitarnych o rozdzielczości dochodzącej do ~25 cm/piksel (głównie ~50 cm/piksel). Podobnie jak w przypadku zdjęć CTX, posiadając pokrywające się zdjęcia HiRISE można obliczyć DTM.

Przedstawiony podział okresów geologicznych Marsa został oparty na pracy Hartmanna (2005):

Amazon (okres amazoński) – (ang. *Amazonian*) to najmłodszy okres (<3 mld lat) w historii geologicznej Marsa charakteryzujący się niskimi wskaźnikami uderzeń meteorytów. Był on zdominowany przez powstawanie kraterów impaktowych, procesy eoliczne, a w prowincjach Tharsis i Elysium także przez wulkanizm. Granice pomiędzy okresami/podokresami nie są dokładnie określone, a stanowią przedziały czasu, które są różnie definiowane z zależności od przyjętego systemu chronologicznego. Okres ten jest podzielony na wczesny (>2000–1000), środkowy (<2000–1000) i późny (<600–200 mln lat).

Hesperian (okres hesperiański) – (ang. *Hesperian*) to okres geologiczny na Marsie charakteryzujący się powszechnie występującą aktywnością wulkaniczną i wysoko energetycznymi procesami fluwialnymi, które wyrzeźbiły ogromne kanały odpływowe na jego powierzchni. Początek tego okresu nastąpił po zakończeniu wzmożonej aktywności impaktowej powierzchni Marsa ok. 3700–3500 milionów lat temu i trwał do początku Amazonu. Okres ten jest podzielony na wczesny (>3600–3200) i późny (<3600–3200 mln lat).

Noachian (okres noachiański) – (ang. *Noachian*) to wczesny okres geologiczny na Marsie charakteryzujący się wysokim wskaźnikiem impaktów meteorytów oraz intensywną aktywnością wulkaniczną, zwłaszcza w regionie Tharsis. Bezwzględny wiek okresu trwał od początku ewolucji planety do ok. 3500 milionów lat temu i jest podzielony na wczesny (>4100–3800), środkowy (<4100–3800) i późny (<3900–3600 mln lat).

3. Charakterystyka obszaru badań

Mars jest czwartą od Słońca planetą skalistą Układu Słonecznego, która krąży pomiędzy orbitą Ziemi, a pasem planetoid, oddzielającym go od orbity Jowisza. Promień Marsa jest prawie o połowę mniejszy od promienia Ziemi, co skutkuje, że jego objętość stanowi ~15% objętości Ziemi i tylko ~11% jej masy. Wskazuje to na mniejszą średnią gęstość Marsa (~3933 kg/m^3) niż Ziemi (5513 kg/m^3). Najnowsze dane dotyczące budowy wewnętrznej Marsa, w oparciu o dane sejsmiczne (sejsmometr *ang. Seismic Experiment for Interior Structure; SEIS*) z lądownika *InSight*, wskazują, że jądro Marsa zbudowane jest głównie z Fe i S oraz lekkich pierwiastków i ma średnicę 1830 ± 40 km (Stähler i in., 2021; Sun i Tkalčić, 2022). Strefa przejściowa pomiędzy jądrem, a dolnym płaszczem, w której prawdopodobnie dochodzi do przetapiania i generowania stopów magmowych może występować pomiędzy ~800, a ~1600 km (Lagain i in., 2021).

Skorupa marsjańska charakteryzuje się zróżnicowaną miąższością. Typowa miąższość skorupy Marsa wynosi od ~30-40 do ~70 km (Knapmeyer-Endrun i in., 2021; Wieczorek i in., 2022). Pod obszarami wulkanicznymi, jej miąższość może być zwiększona i sięgać nawet ~100 km (Tenzer i in., 2015; Plesa i in., 2023). Dodatkowo, praca Bonnet Gibet i in. (2022) wykazała, że granica dychotomii Marsa oddzielająca północne obszary nizinne od południowych wyżynnych, znajduje odzwierciedlenie w grubości skorupy marsjańskiej. Obecne mapy grubości skorupy Marsa, stworzone na podstawie danych topograficznych i grawitacyjnych uzyskanych z łazika *InSight* ukazują, że skorupa budująca południowe obszary wyżynne jest o 18 nawet do 28 km grubsza od skorupy budującej obszary północne (Bonnet Gibet i in., 2022). Powstanie granicy dychotomii Marsa wiązane było z gigantycznym impaktem (Marinova i in., 2008; Golabek i in., 2011; Leone i in., 2014) lub kilkoma zdarzeniami impaktowymi (Frey i Schultz, 1988), które nastąpiły w późnym etapie formowania się planety, powodując intensywne procesy magmowe oraz prowadząc do uformowania się południowych obszarów wyżynnych. Najnowsze badania Bonnet Gibet i in. (2022), w oparciu o dane, że skorupa marsjańska jest wzbogacona w pierwiastki generujące ciepło (ang. *heat-producing elements*) (Ojha i in., 2019; Knapmeyer-Endrun i in., 2021), wskazują, że zróżnicowany zespół procesów cienienia skorupy i topienia płaszcza, mogły doprowadzić do powstania globalnej granicy dychotomii w okresie Hesperianu (Ryc. 1a).

Na podstawie początkowych obserwacji satelitarnych dla powierzchni Marsa zaobserwowano, że rozmieszczenie form wulkanicznych jest nierównomierne i istnieją obszary, w których nagromadzenie wulkanów jest większe, nazywając te obszary prowincjami wulkanicznymi (Zimbelman i in., 2015). Niedaleko od granicy dychotomii Marsa, zlokalizowane są dwie wielkie prowincje wulkano-tektoniczne (ang. *volcano-tectonic provinces*) Tharsis i Elysium (Werner, 2009; Baratoux i in., 2011; Bouley i in., 2018; Mouginis-Mark i in., 2021a, 2021b), które zawierają w swoim obrębie największe (nazywane także centralnymi) wulkany na Marsie (Ryc. 1). W przedstawionej rozprawie doktorskiej, badania nad rekonstrukcją systemów magmowych zostały przeprowadzone w prowincji Tharsis, która charakteryzuje się największą koncentracją form wulkanicznych. Znajdują się one na wyniesionym obszarze rejonu Tharsis (ang. *Tharsis bulge*) o średnicy około ~4000 km, którego centrum zlokalizowane jest na przecięciu równika i południka 110°W (Carr, 2007; Zimbelman i in., 2015).

Ze względu na fakt, że w początkowej fazie badań marsjańskich, rozdzielczość otrzymywanych zdjęć pozwalała w głównej mierze na badania dominujących struktur na Marsie, większość badaczy planetarnych skupiała się na zrozumieniu genezy prowincji wulkanicznych i globalnych procesów tektonicznych. Obecnie istnieje konsensus, że ruch płyt tektonicznych mógł być obecny we wczesnej fazie ewolucji Marsa (Breuer i Spohn, 2003; Lenardic i in., 2004; Connerney i in., 2005). Jednak w trakcie powstawania południowych obszarów wyżynnych (Noachian/Hesperian), gdy większość skorupy Marsa została uformowana, musiało dojść do ustania tektoniki płyt. Dzięki temu mogły powstawać ogromne struktury wulkaniczne, które nie ulegały przemieszczeniu w stosunku do źródła magmy, tak jak odbywa się to na Ziemi (np. Hawaje). Po ustaniu przypuszczalnego ruchu płyt, procesy tektoniczne były kontynuowane na mniejszą skalę (Mège i Masson, 1996; Bouley i in., 2018) i występują prawdopodobnie aż do dzisiaj, co zostało zarejestrowane przez sejsmometr SEIS (Giardini i in., 2020; Jacob i in., 2022; Kim i in., 2023). Dla większości zarejestrowanych trzęsień marsjańskich (ang. *Marsquakes*) lokalizacja epicentrum interpretowana jest w rejonie Cerberus Fossae w pobliżu prowincji Elysium i wiązana jest aktywnością magmową (Drilleau i in., 2022; Jacob i in., 2022; Sita i van der Lee, 2022; Stähler i in., 2022), jednak epicentrum wstrząsu zarejestrowanego 18 września 2021 o magnitudzie (M_w>4.0) przypisywane jest nawet rejonowi Tharsis (np. Ceraunius Fossae) (Krishnan i Kumar, 2022). Część zarejestrowanych wstrząsów generowana jest również przez obecnie występujące zdarzenia impaktowe (Garcia i in., 2022).

Na przestrzeni dekad, zaproponowano wiele modeli próbujących wyjaśnić genezę prowincji Tharsis, np. poprzez 1) obciążenie skorupy przez formy wulkaniczne (ang. *volcanic construction*) (Solomon i Head, 1982; Williams i in., 2008); 2) pióropusze płaszcza (Mège i Masson, 1996; Wilson i Head, 2002; Anderson i in., 2004; Zhong, 2009); 3) połączenie wulkanizmu i pióropuszy płaszcz (Zhong, 2002); 4) pióropuszy płaszcza generowanych przez impakty (Reese i in., 2004); 5) wyniesieniem i częściowym topieniem płaszcza (Johnson i Phillips, 2005). Część naukowców przyjmuje, że wyniesienie Tharsis stanowi wyjątkowy przykład obecności super pióropusza płaszcza, który zasila pojedyncze systemy magmowe głównych wulkanów (Dohm i in., 2007; Lagain i in., 2021). Obecnie, Lagain i in. (2021) wykazali, że aktywność wulkaniczna w Tharsis w okresie amazońskim (od 2 400 mln lat temu do 330 mln lat temu) była zasilana przez głęboko zakorzeniony w płaszczu (~1600 km) superpióropusz, który był prawdopodobnie aktywny od samego początku formowania się obszaru wulkanicznego Tharsis. Przypuszcza się, że proces formowania się Tharsis związany był z intensywnym epizodem magmowym zasilanym poprzez plamy gorąca (ang. *hotspots*) w środkowym noachianie wraz z późniejszymi dostawami magmy do ogromnych systemów magmowych (Mège i Masson, 1996; Wilson i Head, 2002; Anderson i in., 2004).

Na podstawie datowań, badacze zauważyli globalne rozpoczęcie wzmożonej aktywności wulkanicznej na Marsie w okresie noachiańskim (>3.7 mld lat temu; Anderson i in., 2001; Bouley i in., 2016), która następnie skoncentrowała się do regionów wulkanicznych (np. Tharsis, Elysium, Circum-Hellas), a w końcowym etapie była kontynuowana tylko w obrębie prowincji wulkanicznych Tharsis i Elysium (Werner, 2009; Robbins i in., 2011). Zapis najstarszej aktywności wulkanicznej jest prawdopodobnie związany z wulkanem Tharsis

Tholus (>3.9 mld lat; Platz i in., 2011) lub kalderą wulkanu Uranius Tholus, której wiek oszacowany jest na ~3.9 – 3.6 mld lat (Werner, 2009; Robbins i in., 2011). Szczegółowe badania kalder szczytowych centralnych wulkanów Tharsis oraz ich stoków wykazały, że aktywność wulkaniczna występowała przez cały okres ewolucji Tharsis, od momentu uformowania się pierwszych form wulkanicznych, aż prawie do 'dzisiaj' (Neukum i in., 2004; Werner, 2009; Robbins i in., 2011). Potwierdzeniem tych danych są datowania obszarów wulkanicznych w pobliżu Olympus Mons (Neukum i in., 2004; Krishnan i Kumar, 2022) oraz Cerberus Fossae w pobliżu prowincji Elysium (Horvath i in., 2021), które ujawniają bardzo młody wiek erupcji wulkanicznych (<10 mln lat; nawet do 46 tys. lat temu). Badania tektoniczne wskazują na przedłużający się proces formowania obszaru Tharsis podczas pierwszego kwartału ewolucji Marsa (>3 mld lat), a następnie zmniejszenie intensywności procesów od ~ 3 mld lat temu (Bouley i in., 2018).

Obszar prowincji wulkanicznej Tharsis reprezentuje skorupę, która jest wyniesiona ~10 km powyżej marsjańskiego punktu odniesienia (ang. *Martian datum*) mieszcząc w swoim obrębie 12 wulkanów centralnych, w tym największy wulkan w Układzie Słonecznym, Olympus Mons. Wulkany te mają zróżnicowaną wielkość i wiek ostatniej aktywności wulkanicznej zapisanej w kalderze szczytowej (Plescia, 2004; Werner, 2009; Robbins i in., 2011; Ciazela i in., 2019). Do grona gigantycznych wulkanów (średnica podstawy stożka wulkanicznego ma setki kilometrów), których aktywność wulkaniczna występowała stosunkowo niedawno < 200 Ma, należą Olympus Mons, Alba Mons oraz trzy wulkany wchodzące w skład Tharsis Montes (od południa Arsia Mons, Pavonis Mons i Ascraeus Mons). Pozostałe wulkany Tharsis charakteryzują się mniejszymi rozmiarami i wykazują dowody na wcześniej zakończoną (starszą) aktywność wulkaniczną (Werner, 2009; Robbins i in., 2011; Ciazela i in., 2019). Oprócz głównych wulkanów, w centralnym obszarze Tharsis występują setki (>600) mniejszych form wulkanicznych, które są nierównomiernie rozmieszczone w obrębie prowincji wulkanicznej, koncentrując się głównie w pobliżu centralnych wulkanów (Bleacher i in., 2007, 2009; Hauber i in., 2009, 2011; Richardson i in., 2020, 2021).

Szeroko rozprzestrzenione potoki lawowe, pochodzące z erupcji wulkanicznych stowarzyszonych z systemami magmowymi centralnych wulkanów oraz rozproszonym wulkanizmem, są dominującym elementem budującym obecną powierzchnię prowincji Tharsis. Na podstawie globalnej mapy geologicznej Marsa, Tanaka i in. (2014) wykazali, że jednostki wulkaniczne wieku amazońsko-hesperiańskiego tworzą dominującą (~60%) część centralnego rejonu Tharsis (Ryc. 1b). W obrębie tej regionalnej jednostki występują lokalne obszary/pola wulkaniczne chrakteryzujące się nagromadzeniem form wulkanicznych wieku amazońskiego (Brož, 2010; Hauber i in., 2011; Tanaka i in., 2014). Jednakże oprócz młodego wulkanizmu, udokumentowano również obszary charakteryzujące się starszą aktywnością. Należą do nich region Ulysses Fossae, Tempre Terra, czy region Fortuna Fossae (Tanaka i in., 2014). Brož i Hauber (2011) wskazali, że wyniesione obszary spękanej skorupy wieku hesperiańskiego w obszarze Tharsis mogą stanowić miejsca poszukiwań form wulkanicznych kluczowych dla zrozumienia wczesnej ewolucji systemów magmowych Tharsis. Na podstawie swoich założeń zbadali obszar Ulysses Fossae, gdzie udokumentowali obecność piroklastycznych stożków scoria i oszacowali prawdopodobny wiek ich powstania w przedziale czasowym od 1500 do 400 mln lat temu (Brož i Hauber, 2012). Badania pola wulkanicznego Ulysses Fossae wskazują, że wcześniej w historii Marsa, wulkanizm o charakterze eksplozywnym mógł być bardziej powszechny, co jest zgodne z założeniami zaproponowanymi przez Wilsona i Heada (1994). Autorzy ci zasugerowali, że szeroko rozprzestrzeniony wulkanizm wieku amazońskiego prawdopodobnie przykrył wcześniejsze formy wulkaniczne, uniemożliwiając wgląd w ewolucję starszej aktywności wulkanicznej i zakrywając związane z nim mniejsze formy (Brož i Hauber, 2011). Warto zaznaczyć, że wśród rozproszonych wulkanów w obszarze Tharsis opisywane są formy wulkaniczne wskazujące na bardziej energetyczne erupcje wulkaniczne w porównaniu do relatywnie nisko energetycznych erupcji efuzywnych (Hauber i in., 2009; Brož i in., 2021).

Stosunkowo młoda, centralna część prowincji Tharsis graniczy z dwoma zewnętrznymi obszarami wulkanicznymi Syria Planum i Tempe Terra, które również zaliczane są w obręb tej prowincji (Tanaka i in., 2014; Richardson i in., 2021). Obszar wulkaniczny Syria Planum zlokalizowany jest w południowym obszarze Tharsis i jest odgraniczony od amazońskich potoków lawowych przez spękaną skorupę wieku hesperiańskiego obszarów Noctis Labyrinthus i Noctis Fossae (Tanaka i in., 2014). Syria Planum zawiera w sobie >250 form wulkanicznych (Bleacher i in., 2010; Richardson i in., 2020; Pozzobon i in., 2023). Podobnie jak w obszarze Tharsis aktywność wulkaniczna prawdopodobnie rozpoczęła się na początku okresu noachiańskiego (>4.0 mld lat temu; Xiao i in., 2012) i trwała >1000 mln lat do wczesnego okresu amazońskiego (Richardson i in., 2012). Hipoteza zakładająca dawną aktywność wulkaniczną (>2.7 mld lat) nie jest w pełni potwierdzona, ponieważ datowania wulkanów w centralnej części Syria Planum ujawniają wieki późnego Amazonu, wskazując na długotrwałą aktywność wulkaniczną (Brož, 2010; Hauber i in., 2011) konieczną do zweryfikowania. Podobną charakterystykę geologiczną wykazuje obszar Tempe Terra, który zlokalizowany jest w północno-wschodniej części prowincji Tharsis (Hauber i Kronberg, 2001). W jego obrębie również skartowano formy wulkaniczne, starsze od tych z centralnej części Tharsis (Brož, 2010; Hauber i in., 2011).

Na podstawie pierwszych zdjęć satelitarnych, stoki centralnych wulkanów wydawały się być pozbawione mniejszych struktur wulkanicznych, jednak wraz z rozwojem kamer i otrzymywaniem zdjęć powierzchni Marsa o wyższej rozdzielczości, ujawniły one niezwykłą różnorodność morfologicznych form wulkanicznych takich jak: kanały lawowe, tunele lawowe, szczeliny wulkaniczne, czy rozproszone pasożytnicze stożki wulkaniczne (Keszthelyi i in., 2008; Zimbelman i in., 2015). Morfologia centralnych wulkanów przypomina budowę ziemskich wulkanów tarczowych, jednakże w znacznie większej skali. Charakteryzuje się m.in. dużą średnicą podstawy wulkanu, która przy nawet ogromnych wysokościach względnych skutkuje niskim nachyleniem stoków (Plescia, 1994, 2004; Ivanov i Head, 2006). Jednakże, najnowsza praca Leone i in. (2022) wskazuje, że trzy wulkany Tharsis Montes nie są typowymi wulkanami tarczowymi, a powinny zostać zaklasyfikowane jako stratowulkany (ang. *low-composite volcanoes*). Dlatego nowo zaproponowana graniczna wartość nachylenia stoków oddzielająca wulkany tarczowe od stratowulkanów na Marsie może wynosić 1,5°, a nie 12° jak na Ziemi. Pomimo nowo zaproponowanego podziału, w literaturze powszechnie definiuje się te formy wulkaniczne jako wulkany tarczowe (Baratoux i in., 2009; Hauber i in., 2009; Richardson i in., 2021). Formy tworzące rozproszony wulkanizm Tharsis, który stowarzyszony jest z centralnymi wulkanami, również w większości zaliczane są do wulkanów tarczowych, powstających w wyniku efuzywnych erupcji (Bleacher i in., 2007; Hauber i in., 2009, 2011; Richardson i in., 2021) magm o składzie bazaltowym (Hauber i in., 2009; Mangold i in., 2010). Badania kraterów impaktowych, które na swoich stokach odsłaniają świeże wychodnie skał nie pokrytych luźnymi osadami wskazują, że skały wulkaniczne budujące prowincje Tharsis są bogate w piroksen o dużej zawartości wapnia (ang. *high-Ca pyroxene; HCP*), czyli głównie klinopiroksen oraz dodatkowo oliwin. Skał mineralny wskazuje, że skały wieku amazońskiego są podobne do skał hesperiańskich (Viviano i in., 2019), ale w znaczący sposób różnią się od skał noachianu, które są zdominowane przez oliwin i pirokseny o niskiej zawartości wapnia (ang. *low-Ca pyroxene; LCP*), czyli głównie ortopirokseny (Poulet i in., 2009; Baratoux i in., 2013).

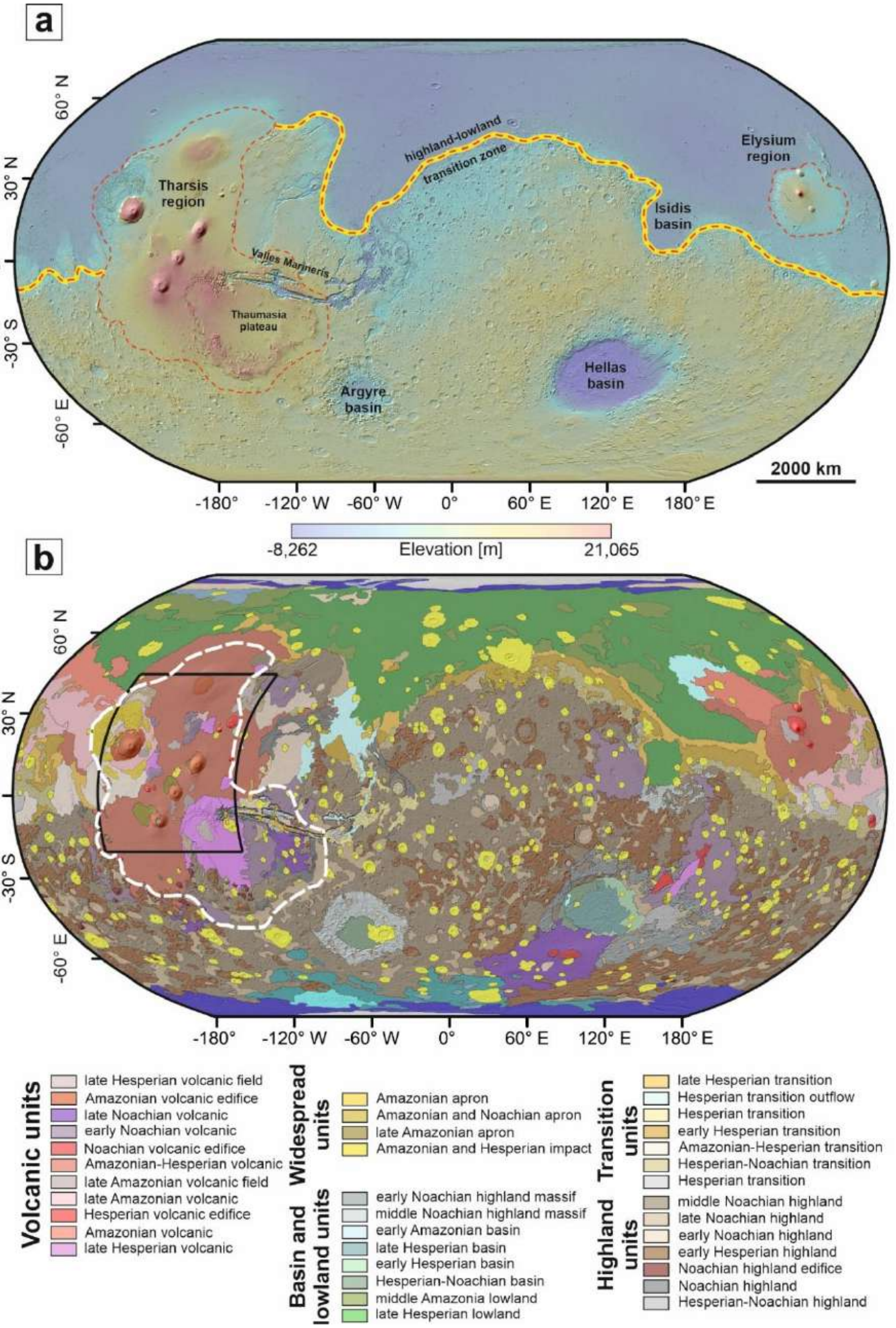

Rycina 1. (a) Globalna mapa topograficzna Marsa ukazująca granicę dychotomii oraz rozmieszczenie wielkich prowincji wulkanicznych. Tło stanowi cieniowana mapa stworzona na podstawie danych uzyskanych z Mars Orbiter Laser Altimeter (MOLA; Smith i in., 2001) o rozdzielczości 463 m/pixel, na którą zostały nałożone dane dotyczące numerycznego modelu

terenu powstałe w wyniku połączenia danych z MOLA i HRSC (Gwinner i in., 2016) tworząc globalną mapę o rozdzielczości 200 m/pixel (Fergason i in., 2018). **(b)** Uproszczona mapa geologiczna Marsa (Tanaka i in., 2014), która ukazuje budowę prowincji wulkanicznych. Są one w dominującym stopniu pokryte przez jednostki wulkaniczne wieku amazońsko-hesperiańskiego. Szczegółowa mapa geologiczna centralnej części prowincji Tharsis (czarna ramka na mapie geologicznej) wraz z naniesioną lokalizacją rozproszonego wulkanizmu została przedstawiona w Artykule nr 1. Czerwona (a) oraz biała (b) przerywana linia wyznacza zasięg prowincji Tharsis.

Stratygrafia Marsa

Metoda określania wieku powierzchni na podstawie gęstości kraterów impaktowych na powierzchni planet skalistych opiera się na matematycznej analizie, która została opracowana przez grupę ang. *Crater Analysis Techniques Working Group* (1979). Założeniem tej metody jest zależność między rozkładem częstości występowania i wielkości kraterów (ang. *Crater-Size Frequency Distribution; CSFD*), a względnymi wiekami powierzchni planet. Metoda ta została pierwotnie opracowana dla Księżyca, skąd zostały pozyskane próbki geologiczne przez misję Apollo oraz inne sondy kosmiczne. Okazy z Księżyca datowano metodami radioizotopowymi i skorelowano uzyskany wiek z gęstością kraterów impaktowych w miejscach pobrania próbek. W ten sposób osiągnięto możliwość skorelowania gęstości kraterów impaktowych i bezwzględnego wieku jednostek geologicznych bombardowanych przez bolidy. Wynikiem tej analizy była skumulowana krzywa produkcji (ang. *cumulative production function*) przedstawiająca stosunek kraterów impaktowych do badanej powierzchni. Krzywa dla Księżyca została później skalibrowana dla warunków marsjańskich (Ivanov, 2001). Było to możliwe, biorąc pod uwagę podobne warunki we wczesnym etapie formowania się wewnętrznego Układu Słonecznego (Neukum i in., 2001). Najważniejszym parametrem, który w kluczowy sposób wpływa na kształt izochrony jest współczynnik impaktowy (ang. *Mars/Moon cratering ratio*), który różni się od przyjętego systemu chronologicznego od 1.6 (Hartmann i in., 1999), 2.0 (Ivanov, 2001) do 3.15 (Hartmann, 2005).

Na podstawie obserwacji zdjęć satelitarnych i kartowania kraterów impaktowych na powierzchni Marsa, powierzchnia planety została podzielona na trzy główne jednostki stratygraficzne (Scott i Carr, 1978; Tanaka, 1986) (Ryc. 1a). Zmienna gęstość kraterów impaktowych na odmiennych jednostkach geologicznych pozwoliła wyznaczyć względną stratygrafię, nawet dla obszarów nie kontaktujących się ze sobą (w oparciu o relacje strukturalne). Obecny stan wiedzy pozwala wyznaczyć wiek absolutny badanych jednostek na podstawie dopasowania gęstości kraterów do modelowej krzywej wieku (Hartmann i Neukum, 2001; Ivanov, 2001; Hartmann, 2005; Werner i Tanaka, 2011). Najstarszą jednostką stratygraficzną jest Noachian, który obejmuje utwory powstałe od początku uformowania się planety do ~3.7-3.5 mld lat temu (Hartmann i Neukum, 2001; Zimbelman i in., 2015). Okres noachiańskim może zostać podzielony jeszcze na trzy podokresy, wczesny, środkowy i późny, charakteryzujące się różną gęstością dla największych kraterów impaktowych >16 km średnicy (Tanaka, 1986). Kolejną jednostką stratygraficzną jest okres hesperiański (3.7–3.0 mld lat temu), który w historii geologicznej Marsa charakteryzował się obecnością wody. Ten okres również został podzielony na wczesny i późny. Okres przejściowy pomiędzy Amazonem, a Hesperianem obejmuje zakres czasowy od 3.3 do 2.9 mld lat temu (Hartmann i Neukum, 2001). Amazon stanowi najmłodszą jednostkę stratygraficzną Marsa obejmując prawie 3 mld lat. Okres ten został podzielony na wczesny, środkowy i późny, a obszary o wieku amazońskim różnią się od siebie gęstością kraterów impaktowych o średnicy 2 km (Tanaka, 1986).

Neukum i in. (2001) oraz Ivanov (2001) użyli metody zliczeń kraterów w celu oszacowania wieku powierzchni Marsa i połączyli te wyniki z datowaniami meteorytów (większość meteorytów marsjańskich jest stosunkowo młoda; Ryc. 2b) marsjańskich, aby ustalić przybliżoną chronologię historii Marsa. Dodatkowo, Hartmann i Neukum (2001) wykorzystali liczbę kraterów do datowania epok marsjańskich zdefiniowanych wcześniej przez Tanakę (1986) (Ryc. 2b). Następnie krzywa chronologiczna została zmodyfikowana przez Hartmanna (2005) oraz Hartmanna i Daubara (2017). Należy jednak podkreślić, że metoda zliczeń kraterów ma pewne ograniczenia, które należy rozważyć przy interpretacji wyników. Pierwsze ograniczenie związane jest z procesem interpretowania kraterów impaktowych przez osobę wykonującą kartowanie, które jest subiektywne (np. kratery wtórne, zapadliska wulkaniczne). Metoda ta opiera się również na założeniu, że kartowaniu podlega jednowiekowa jednostka, której granice są również wyznaczane przez osobę prowadzącą kartowanie. Wyznaczenie zasięgu jednowiekowej jednostki (powierzchni) opiera się na subiektywnej ocenie osoby prowadzącej datowanie, co wpływa na otrzymywany wynik. Ostanie ograniczenie związane jest z założeniem, że prowadząc badania tą metodą określamy wiek tylko ostatniej aktywności jakiej została poddana powierzchnia (np. najmłodszy potok lawowy). Jako, że metoda zliczeń kraterów jest metodą statystyczną, to wymaga ona, aby obszar kartowany był stosunkowo duży w celu uzyskania wiarygodnych wyników (odpowiednia ilość kraterów impaktowych użytych do dopasowania krzywej wieku). Wszystkie ww. ograniczenia wpływają na końcowy wynik uzyskany podczas datowania, który może być obarczony niepewnością (ang. *uncertainty*) od 5 do 40% (Hartmann i Neukum, 2001; Hartmann, 2005).

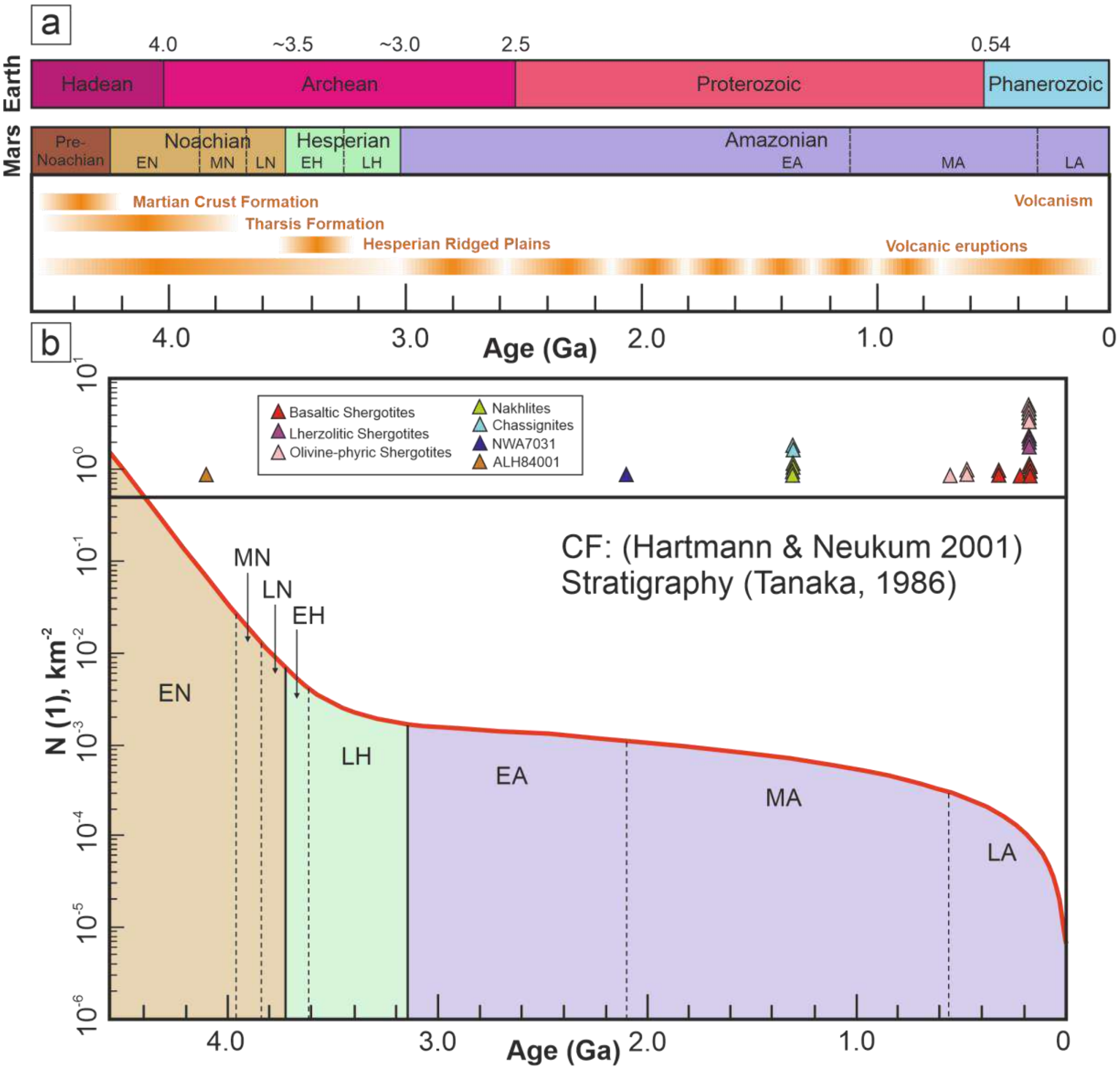

Rycina 2. (a) Porównanie stratygrafii Ziemi i Marsa z głównymi jednostkami stratygraficznymi wyznaczonymi dla poszczególnych planet (zmienione za Grady (2020)). Należy zwrócić uwagę na wydzielenie okresu przed noachiańskiego, którego nie używa się dla systemów chronologicznych. Dla głównych jednostek stratygraficznych Marsa zostały wyszczególnione podokresy np. *EN – Early Noachian; MN – Middle Noachian; LN – Late Noachian*. Dolny panel przedstawia zestawienie głównych zdarzeń wulkanicznych związanych z obszarem Tharsis. Model wiekowy dla zdarzeń wulkanicznych został oparty na pracach Grady (2020), Ehlmann i Edwardsa (2014) oraz badaniach własnych, szczególnie dla okresu środkowego i późnego Amazonu. **(b)** Krzywa chronologiczna (CF; ang. *chronology function*) określona przez Neukuma i Ivanova (Neukum i in., 2001) z zastosowaniem podziału stratygraficznego zaproponowanego przez Tanakę (1986). Zestawienie datowań meteorytów marsjańskich zaadoptowano z Grady (2020).

4. Dane i metodologia badań

4.1. Pozyskiwanie danych i proces kartowania

W rozprawie użyto danych satelitarnych pozyskiwanych z różnych instrumentów zainstalowanych na sondach badających powierzchnię Marsa: *Mars Global Surveyor; Mars Express, Mars Odyssey* oraz *Mars Reconnaissance Orbiter*. Dane pozyskiwane przez satelity są przesyłane na Ziemię, przetwarzane oraz udostępniane w dostępie otwartym (publicznym), umożliwiając ich pobieranie np. w systemie PDS (ang. *Planetary Data System*) co pozwala na wykonywanie analiz (Ryc. 3). Analizując procesy wulkaniczne i powstałe formy w wyniku ich aktywności, konieczne jest wykorzystanie zarówno danych topograficznych, jak i zdjęć satelitarnych powierzchni Marsa. Każdy z zestawów danych charakteryzuje się różną rozdzielczością, umożliwiając prowadzenie badań w odmiennych skalach (Ryc. 4). Pierwsze zdjęcia Marsa charakteryzowały się niską rozdzielczością i nie pozwalały na rozróżnienie małych form terenu. Od 2006 roku, dane o wysokiej rozdzielczości (kamery zainstalowane na satelicie MRO) w świetle widzialnym, podczerwonym i ultrafioletowym, dają szansę na dokładniejsze obserwacje (Ryc. 4). W celu zbadania wulkanizmu rozproszonego w prowincji Tharsis, w pracy głównie użyto zdjęć o rozdzielczości kilku metrów na piksel, które stanowią kompromis umożliwiający pokrycie większych obszarów (np. prowincji Tharsis) z rozdzielczością wystarczającą do rozpoznania małych kraterów impaktowych powyżej średnicy kilkudziesięciu metrów używanych do datowania.

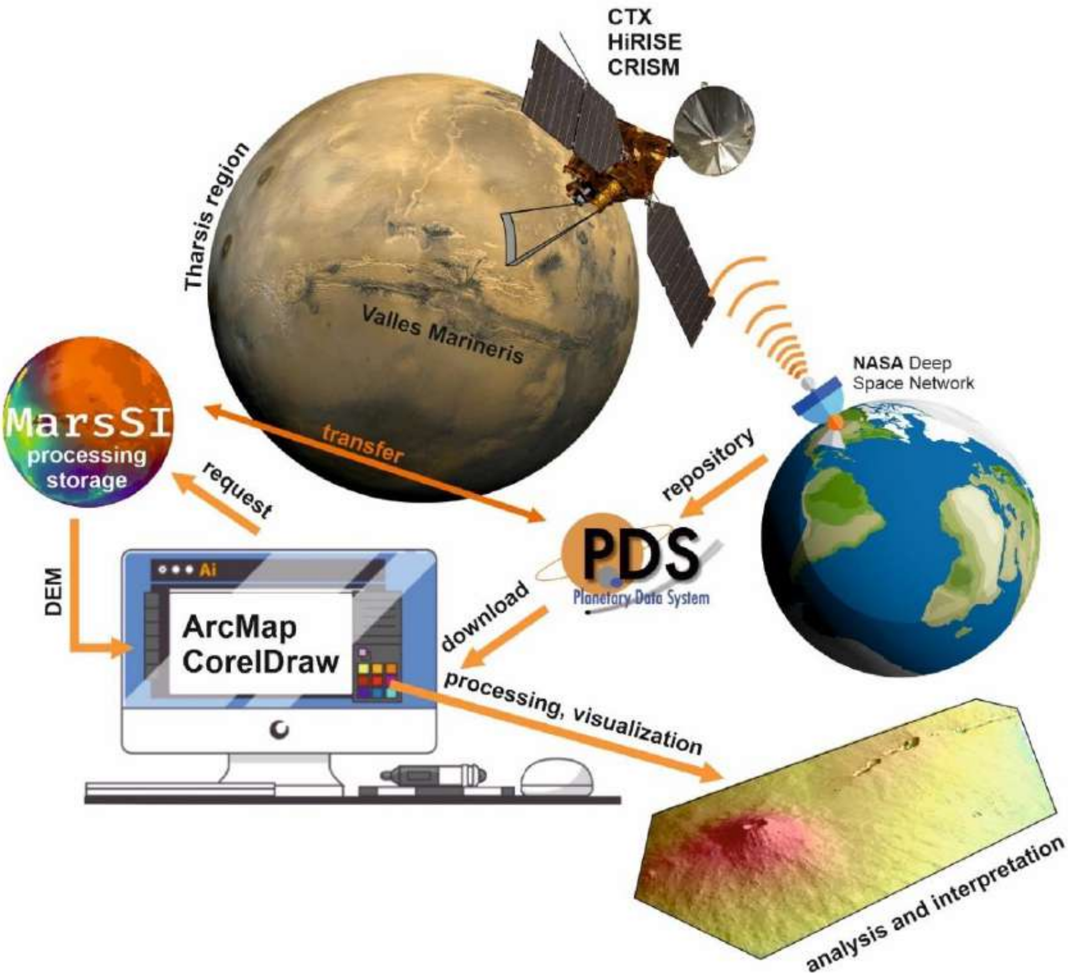

Rycina 3. Schemat metodologiczny ukazujący proces od pozyskiwania danych satelitarnych, ich przesyłania, a następnie przetwarzania i prowadzenia własnych analiz za pomocą programów geoinformatycznych i graficznych. W końcowym etapie, dane były wizualizowane w postaci map i przekrojów, na podstawie których została przeprowadzona rekonstrukcja systemów magmowych.

Prowadząc kartowanie form wulkanicznych w prowincji wulkanicznej Tharsis, korzystałem z globalnej mozaiki wykonanej przez kamerę THEMIS, która charakteryzuje się rozdzielczością ~100 m/piksel (Edwards i in., 2011). Po wstępnym wyznaczeniu ich lokalizacji, w celu szczegółowego kartowania zasięgu przestrzennego badanych form wulkanicznych, korzystałem zarówno z pojedynczych zdjęć CTX o rozdzielczości ~6 m/piksel (Malin i in., 2007) jak i globalnej mozaiki tych zdjęć (5–6 m/piksel) (Dickson i in., 2018, 2023), która umożliwia prowadzenie kompleksowego kartowania. Zastosowanie zdjęć CTX pozwala na dokładniejsze wyznaczenie granicy zasięgu potoków lawowych związanych z badaną formą wulkaniczną. Z kolei połączenie zdjęć z kamery THEMIS oraz CTX idealnie nadaje się do identyfikacji rozmieszczenia wulkanicznych form terenu podczas prowadzenia badań regionalnych. Rozdzielczość zdjęć CTX umożliwia prowadzenie obserwacji oraz wykonywania pomiarów struktur wulkanicznych (m.in. wydłużonych szczelin i szczytowych kraterów wulkanicznych). Prowadząc bardziej szczegółowe obserwacje powierzchni form wulkanicznych wykorzystałem również zdjęcia HiRISE (McEwen i in., 2007), które umożliwiły kartowanie stożków wulkanicznych o średnicy <1 km. Zestawienie zdjęć i danych pochodzących z różnych kamer i instrumentów satelitarnych, które obrazuje zakres zastosowania poszczególnych zestawów danych zostało przestawione na Rycinie 4.

Niezbędnym uzupełnieniem dla obserwacji zdjęć satelitarnych, zarówno podczas badań regionalnych jak i lokalnych, są dane dotyczące topografii Marsa uzyskane dla globalnego zestawu danych poprzez połączenie numerycznych modeli terenu z instrumentów MOLA oraz HRSC (Fergason i in., 2018). W obu artykułach dotyczących wulkanizmu Tharsis zaprezentowanych w tej rozprawie, dane topograficzne MOLA-HRSC posłużyły do wykonania pomiarów morfometrycznych dla badanych wulkanów według metodologii zaproponowanej przez Grosse i in. (2012). Jednakże, prowadząc lokalne badania w obszarze Noctis Fossae (Artykuł 2), dla mniejszych form wulkanicznych, konieczne było użycie danych topograficznych o wyższej rozdzielczości. Jest to możliwe dzięki tworzeniu numerycznych modeli terenu w oparciu o nakładające się na siebie zdjęcia CTX, czy HiRISE (ang. *stereo-pair images*). W celu uzyskania DTM pozyskanych w oparciu o zdjęcia CTX, użyłem systemu MarsSI (MARS Système d'Information), który umożliwia przetwarzanie danych satelitarnych (Quantin-Nataf i in., 2018). Jest to internetowa aplikacja Systemu Informacji Geograficznej, która umożliwia wyszukiwanie, przetwarzanie i pobieranie danych z sond marsjańskich. Algorytm zastosowany w systemie MarsSI oparty jest na sekwencjach wyspecjalizowanych modułów do kalibracji i projekcji (Laura i in., 2021) oraz przetwarzania danych w oparciu o NASA Ames Stereo Pipeline (ASP) (Beyer i in., 2018).

Wszystkie dane satelitarne użyte w rozprawie doktorskiej opracowano przy użyciu oprogramowania ArcGIS, w szczególności programów ArcMap oraz ArcScene (wersja 10.5). Dodatkowo, w celu przeprowadzenia analiz orientacji struktur linijnych (wydłużenia szczelin oraz kraterów wulkanicznych) zostało wykorzystane oprogramowanie Stereonet (wersja 10.2). Charakterystykę użytych danych (numery referencyjne dla poszczególnych zdjęć oraz ich charakterystyka orbitalna) przedstawiono w artykułach stanowiących rozprawę doktorską.

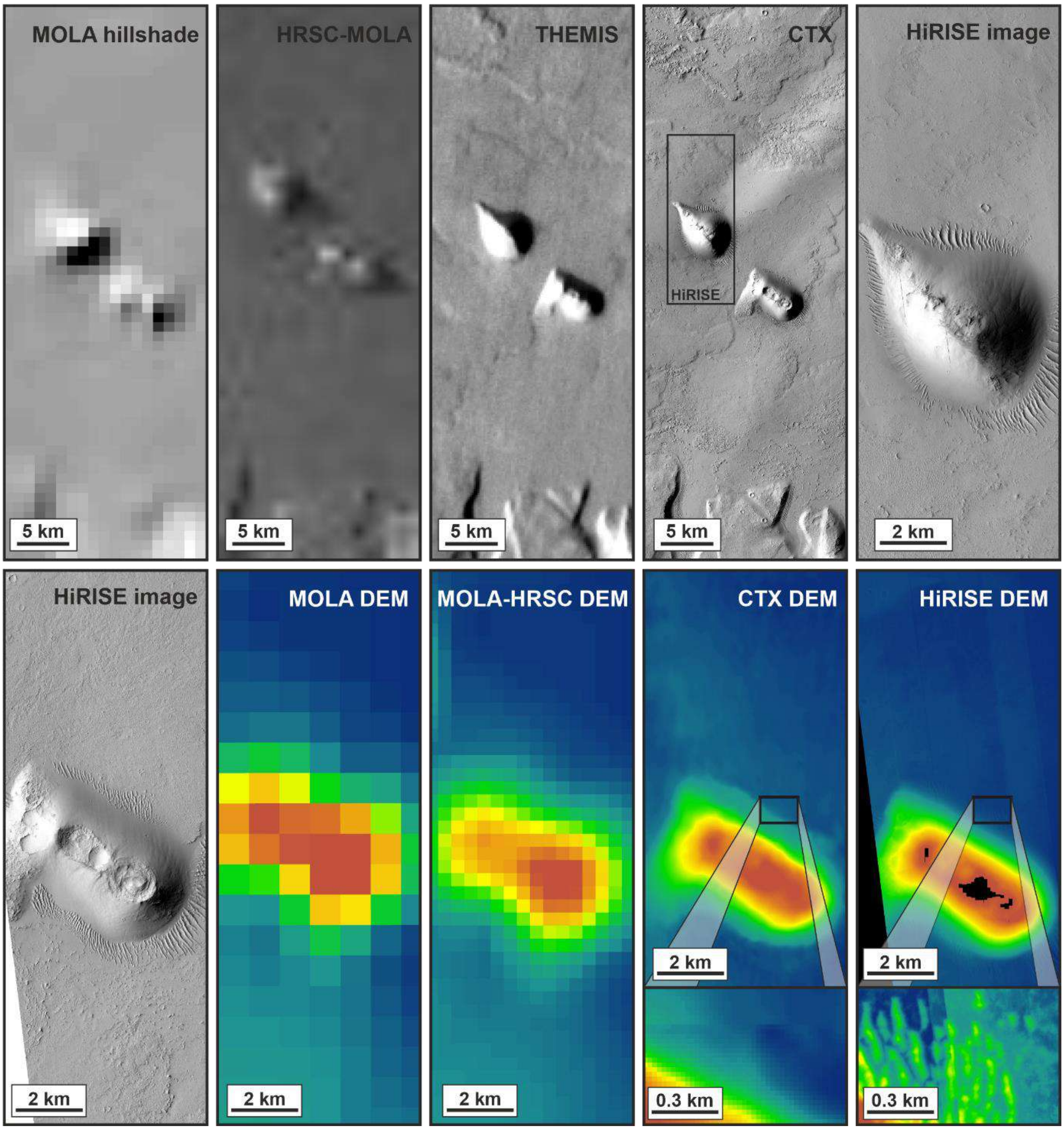

Rycina 4. Zestawienie dostępnych danych i zdjęć satelitarnych wykonanych przez różne instrumenty zainstalowane na sondach pracujących na orbitach Marsa. Górny zestaw zdjęć prezentuje różne obrazowania danych, które pozwalają na obserwację powierzchni Marsa, natomiast dolny zestaw danych przedstawia numeryczne modele terenu dostępne dla badanego stożka wulkanicznego w Noctis Fossae (Artykuł 2). Ze względu na wysoką rozdzielczość zestawów danych CTX i HiRISE, różnice w skali całej obrazowanej formy wulkanicznej nie są dobrze widoczne. Dla tych zestawów danych zostały przedstawione powiększenia, które prezentują różnicę rozdzielczości, umożliwiając dokładne obserwacje topograficzne.

4.2. Datowanie powierzchni Marsa

W badaniach planetarnych powszechnie stosowaną metodą określania wieku powierzchni powstałych w wyniku jednoczasowego zdarzenia, jest metoda zliczania kraterów impaktowych. W przedłożonej rozprawie doktorskiej datowanie powierzchni stożków wulkanicznych oraz potoków lawowych było kluczowe w celu przeprowadzenia czasowej rekonstrukcji zdarzeń wulkanicznych dla badanych obszarów. Wyznaczając obszary odpowiednie do przeprowadzenia zliczeń kraterów, ich zasięg przestrzenny był określany na podstawie dostępnych zdjęć CTX, które z dużą dokładnością pozwalały na wyznaczenie zasięgu powierzchni powstałej w wyniku jednoczasowego zdarzenia wulkanicznego. W artykułach przedłożonych do rozprawy doktorskiej została wykorzystana metodyka określania wieku powierzchni oparta na kartowaniu kraterów impaktowych przy użyciu programu CraterTools 2.1 (Kneissl i in., 2011), który jest dodatkowym narzędziem instalowanym w systemie ArcGIS. Przy jego użyciu prowadziłem kartowanie datowanych powierzchni oraz kraterów impaktowych, których charakterystyki były następnie eksportowane do pliku zbiorczego. Dalsza analiza dotycząca statystyki kraterów oraz określenie wieku bezwzględnego datowanej powierzchni w oparciu o dopasowanie izochrony (modelowej krzywej wskazującej dystrybucję kraterów impaktowych na jednowiekowej powierzchni; ang. *isochrone*) była przeprowadzona w programie CraterStats (Michael i Neukum, 2010).

Obecnie trwa debata na temat minimalnej średnicy kraterów impaktowych przydatnych do datowania (m.in. ograniczenia związane z ich kartowaniem za pomocą dostępnych zdjęć) (McEwen i in., 2005; Werner, 2009; Lagain i in., 2021). W przedstawionych artykułach udało się wykazać, że zastosowanie kraterów o średnicy >50 metrów jest niezbędne w celu określenia wieku dla obszarów wulkanicznych o ograniczonym zasięgu przestrzennym. Przy datowaniu stosunkowo niewielkich obszarów mała ilość kraterów impaktowych w znaczącym stopniu wpływa na reprezentatywność otrzymanych wyników. Szczegółowy opis wykorzystanych systemów chronologicznych wraz z dyskusją dotyczącą zastosowania kraterów impaktowych o średnicy >50 metrów do datowań powierzchni zostały przedstawione w artykułach stanowiących rozprawę doktorską (Artykuły 1 i 2).

5. Problematyka i wyniki badań

Procesy endogeniczne (wewnętrzne) odgrywają kluczową rolę w kształtowaniu budowy geologicznej planet skalistych w Układzie Słonecznym. Procesy magmowe bezpośrednio odpowiadają za aktywność wulkaniczną, cyrkulację hydrotermalną, procesy złożowe i dystrybucję metali. W ostatnich dwóch dekadach, Europejska Agencja Kosmiczna (*ang. ESA*) poczyniła intensywne starania w dziedzinie górnictwa kosmicznego i opracowała strategię dotyczącą zasobów kosmicznych, wdrożyła badania, technologie i działania w zakresie prospekcji i eksploatacji potencjalnych zasobów energetycznych i metali na innych planetach skalistych i księżycach (ESA, 2019).

Rozprawa doktorska została poświęcona zbadaniu aktywności wulkanicznej w prowincji Tharsis na Marsie, aby określić jej ewolucję czasową i przestrzenną i uzyskać wgląd w rozwój systemów magmowych. Pierwszy artykuł naukowy wchodzący w skład rozprawy doktorskiej stanowi pracę o charakterze regionalnym, w której podejmuję się zrekonstruowania systemów magmowych w prowincji Tharsis w oparciu o rozproszony wulkanizm (Artykuł 1). W drugim artykule, na podstawie przeprowadzonych badań regionalnych udało się udokumentować i opisać lokalne pole wulkaniczne w rejonie Noctis Fossae, które charakteryzuje się eksplozywnym stylem erupcji odmiennym od efuzywnego w innych obszarach (Artykuł 2), ukazując złożony charakter wulkanizmu w obszarze Tharsis. Przeprowadzone badania nad przestrzenną i czasową ewolucją systemów wulkanicznych Tharsis posłużyły do wytypowania potencjalnych obszarów zainteresowania dla wykorzystania spektrometru MIRORES. Celem użycia tego spektrometru jest poszukiwanie wystąpień minerałów rudnych na powierzchni Marsa (Artykuł 3). Badania procesów wulkanicznych w obszarze Tharsis, w połączeniu z koncepcją spektrometru badającego powierzchnię Marsa pod kątem występowania minerałów rudnych, stanowi nowatorskie i interdyscyplinarne podejście naukowe. Może ono znaleźć zastosowanie w przemyśle kosmicznym, a zwłaszcza w dynamicznie rozwijającym się górnictwie kosmicznym.

Artykuł 1

Pieterek, B., *Ciążela, J., Lagain, A., Ciążela, M. (2022). Late Amazonian dike-fed parasitic volcanism in the Tharsis volcanic province on Mars. Icarus, vol. 386, 115151*

Pierwsza publikacja ze zbioru artykułów wchodzących w skład rozprawy doktorskiej dotyczy rekonstrukcji systemów magmowych wielkiej prowincji wulkanicznej Tharsis na Marsie. Przeprowadzona interpretacja została opracowana w oparciu o szczegółowe badania związane z przestrzennym rozmieszczeniem oraz czasową rekonstrukcją rozproszonej aktywności wulkanicznej, która towarzyszy centralnym wulkanom Tharsis. Motywacją dla podjęcia tych badań był związek przestrzenno-czasowy pomiędzy ostatnią aktywnością centralnych wulkanów, a rozproszonym wulkanizmem. W ostatnich 20 latach, wraz z dostarczaniem nowych zdjęć powierzchni Marsa, podjęto się nowego kartowania jednostek wulkanicznych i określenia wieku ich powstania. W ten sposób dostarczono nowych hipotez dotyczących rozwoju systemów magmowych w obszarze Tharsis (Bleacher i in., 2007; Hauber i in., 2009, 2011; Brož, 2010; Christoph i Garry, 2017; Richardson i in., 2017, 2020, 2021). Jednakże, żadna z dotychczasowych prac nie łączyła szczegółowych danych kartograficznych i wieku aktywności rozproszonych wulkanów z wiekiem ostatniej aktywności wulkanicznej pobliskich wulkanów centralnych Tharsis. W szczególności nie było wiadomo czy rozproszona aktywność wulkaniczna związana jest z systemami magmowymi wulkanów centralnych. Ile systemów magmowych było/jest aktywnych w Tharsis i w jaki sposób magma jest transportowana do form wulkanicznych zasilających rozporoszony wulkanizm.

Dzięki użyciu dostępnych zdjęć satelitarnych THEMIS oraz CTX przeprowadziłem regionalne prace kartograficzne, mające na celu wyznaczenie lokalizacji oraz zasięgu przestrzennego form wulkanicznych w centralnej części prowincji Tharsis (dokładny opis kartowania znajduje się Artykule 1). By zrozumieć procesy kontrolujące ich rozmieszczenie, określiłem orientację wydłużenia kraterów szczytowych lub szczelin skartowanych form wulkanicznych. W wyniku tych prac udało się skartować 659 form wulkanicznych, z których 379 wykazywało określoną orientację. Rozmieszczenie form wulkanicznych oraz pomiary ich orientacji pozwoliły na wyznaczenie pięciu subprowincji stowarzyszonych z jednym z centralnych wulkanów Tharsis (Ryciny 1 oraz 4; Artykuł 1). Na podstawie obserwacji strukturalnych większość form udało się zakwalifikować do systemów stowarzyszonych z aktywnością następujących wulkanów: 1) Olympus Mons; 2) Alba Mons; 3) Ascraeus Mons; 4) Pavonis Mons; oraz 5) Arsia Mons.

Jednakże, aby przeprowadzić pełną rekonstrukcję systemów magmowych w oparciu o zależność pomiędzy centralnymi wulkanami a rozproszonym wulkanizmem, kluczowe było określenie ich wzajemnych relacji czasowych. Wykorzystując metodę zliczeń kraterów impaktowych przeprowadziłem datowania jednowiekowych powierzchni, którymi były stoki wcześniej skartowanych form wulkanicznych. Z zestawu wszystkich skartowanych form, wybrałem 94, których powierzchnie były odpowiednie do przeprowadzenia datowania. By zapewnić reprezentatywność otrzymanych wyników, starałem się wyznaczyć podobną ilość wulkanów dla każdej z wcześniej wyznaczonych subprowincji (Tabela 3; Artykuł 1). Pomimo niewielu udokumentowanych form wulkanicznych, ze względu na pogrzebanie większości z nich przez rozległe wylewy law bazaltowych, które miały miejsce w późnym Amazonie, otrzymane wyniki analizy czasowej pozwoliły mi na wyróżnienie szóstej subprowincji, Uranius Mons. Udało się potwierdzić, że pięć wyodrębnionych systemów magmowych stowarzyszonych z wulkanami Olympus Mons, Alba Mons, Ascraeus Mons, Pavonis Mons oraz Arsia Mons, wykazuje stosunkowo młody wiek <250 mln lat. Natomiast system magmowy wulkanu Uranius Mons musiał być aktywny wcześniej, wykazując aktywność rzędu ~ 1 mld lat temu.

We wszystkich sześciu wyodrębnionych systemach magmowych (Ryc. 5), wulkanizm rozproszony był prawdopodobnie zasilany przez magmy wykorzystujące dajki radialne i pierścieniowe. Magmy migrowały z komór magmowych zlokalizowanych pod centralnymi wulkanami lub bezpośrednio ze stref topienia umiejscowionych na granicy płaszcza i skorupy Marsa (Rycina 10; Artykuł 1). Dla wulkanów, których nie udało się przypisać do żadnego systemu magmowego został zaproponowany scenariusz zakładający migrację magmy z głębokich stref topienia zlokalizowanych na granicy skorupy i płaszcza.

Otrzymane wyniki sugerują, że wulkanizm rozproszony mógł/może być również aktywny po ustaniu głównej aktywności wulkanicznej, zapisanej przez kaldery szczytowe centralnych wulkanów. Zaproponowana w Artykule 1 rekonstrukcja systemów magmowych (Ryc. 5) zakłada obecność istnienia super pióropusza płaszcza obecnego przez większość historii Marsa (Lagain i in., 2021). Super pióropusz rozdzielający się na pojedyncze pióropusze zasilał systemy magmowe centralnych wulkanów i związanego z nimi wulkanizmu rozproszonego (Rycina 10; Artykuł 1). Pełna rekonstrukcja systemów magmowych Tharsis, oparta na pozyskanych danych oraz przeglądzie literaturowym, pozwoliła wykazać, że wulkanizm w badanej prowincji był aktywny od początku jej powstania niemal do dziś. Zapis czasowej ewolucji magmowej w formach wulkanicznych wykazuje powtarzające się cyklicznie epizody wzmożonej aktywności. Zależność czasowa pomiędzy wulkanami centralnymi, a rozproszonym wulkanizmem sugeruje, że systemy magmowe głównych wulkanów Tharsis nie są całkowicie wygasłe, ale mogą być obecnie uśpione i w przyszłości może dojść do ich reaktywacji.

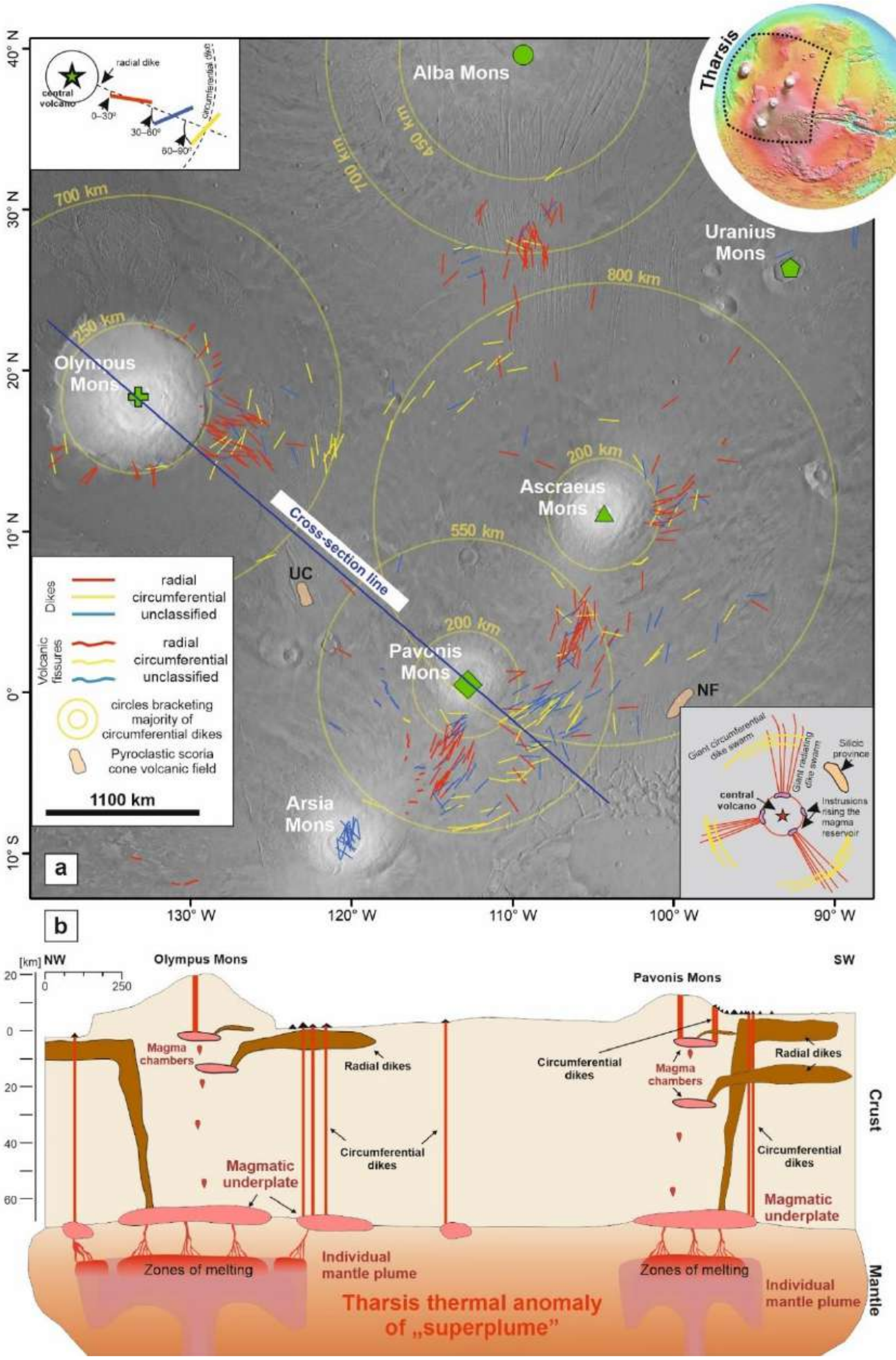

Rycina 5. Rekonstrukcja systemu magmowego prowincji Tharsis w oparciu o przestrzenno-czasowe badania wulkanizmu rozporoszonego. **(a)** Dystrybucja form wulkanicznych wskazująca na przypuszczalny przebieg dajek radialnych i pierścieniowych oraz **(b)** uproszczony przekrój geologiczny ukazujący rozwój systemów magmowych Tharsis w okresie późnego Amazonu.

Artykuł 2

***Pieterek, B.**, Laban, M., Ciążela, J., Muszyński, A. (2022). Explosive volcanism in Noctis Fossae region on Mars. Icarus, vol. 375, 114851*

Druga publikacja wchodząca w skład rozprawy doktorskiej jest bezpośrednio powiązana z artykułem pierwszym, ponieważ w tej publikacji podejmuję się wykonania dokładniejszej charakterystyki jednego z pól wulkanicznych prowincji Tharsis: Noctis Fossae. Obszar ten został wytypowany podczas regionalnych prac kartograficznych, ze względu na fakt, że udokumentowane w tym rejonie formy wulkaniczne wykazywały odmienną charakterystykę morfologiczną (Rycina 3; Artykuł 1). Wilson i Head (1994) przewidzieli, że eksplozywny wulkanizm powinien być bardziej powszechny, niż wskazywałyby na to istniejące dotychczas dane. Do momentu rozpoczęcia tych badań, w obszarze Tharsis zostało udokumentowane jedno pole wulkaniczne stożków scoria (Brož i Hauber, 2012) oraz pojedyncze, nierównomiernie rozproszone wulkany o charakterystyce morfologicznej wskazującej na eksplozywne erupcje (Brož i in., 2021 oraz cytowania w pracy). W ostatnich latach erupcje eksplozywne stały się ważnym tematem w badaniach wulkanizmu Marsa, ponieważ skartowanie i identyfikacja pól wulkanicznych o charakterystyce erupcji eksplozywnych jest kluczowa w kontekście pełnego zrozumienia systemów magmowych, szczególnie dla prowincji wulkanicznej Tharsis.

Przy zastosowaniu dostępnych zdjęć satelitarnych CTX oraz HiRISE, a także numerycznych modeli terenu opartych o dane pozyskane z instrumentów MOLA, HRSC i CTX, przeprowadziłem lokalne prace kartograficzne mające na celu charakterystykę morfologiczną i interpretację geologiczną badanych form. W obszarze Noctis Fossae zostało skartowanych 25 stożków wulkanicznych, których wydłużenie ujawnia dominujący kierunek NNW-SSE. Ich rozmieszczenie wskazuje, że większość (23) z udokumentowanych form wulkanicznych występuje na hesperiańskim obszarze poprzecinanym rowami tektonicznymi o przebiegu N-S. Natomiast dwa najlepiej zachowane stożki znajdują się w północnej części badanego pola na obszarze pokrytym amazońskimi potokami lawowymi, związanymi z aktywnością wulkaniczną prowincji Tharsis (Rycina 2; Artykuł 2). Na podstawie wykonanej analizy porównawczej badanych form (Rycina 3; Artykuł 2) z marsjańskimi stożkami wulkanicznymi scoria (Brož i in., 2015) wykazałem, że obszar Noctis Fossae stanowi przykład pola wulkanicznego charakteryzującego się erupcjami eksplozywnymi. Udokumentowane stożki scoria charakteryzują się niewielką objętością oraz stromym nachyleniem stoków

(Tabela 2; Artkuł 2), w porównaniu do dominujących w prowincji Tharsis wulkanów tarczowych (Rycina 5; Artykuł 2).

Dodatkowo, w celu wykonania pogłębionej analizy systemu magmowego wraz z określeniem potencjalnego obszaru źródłowego dla migrujących magm, konieczna była informacja na temat wieku aktywności wulkanicznej w obrębie Noctis Fossae. Jednym z dowodów, które mogły świadczyć o różnym wieku badanych stożków, był ich odmienny stopień zachowania. Zaobserwowano różnicę pomiędzy stożkami północnymi, a tymi zlokalizowanymi na południu w obrębie spękanej hesperiańskiej skorupy (Rycina 2; Artykuł 2). Obserwacje morfologiczne zostały potwierdzone poprzez wykonane datowania powierzchni potoków lawowych, które były w bezpośredniej relacji ze stożkami (Rycina 7; Artykuł 2). Otrzymane wyniki wskazują, że powstanie stożków występujących w południowej i centralnej części pola musiało nastąpić przed 300 mln lat temu, natomiast północne stożki prawdopodobnie powstały w przedziale czasowym pomiędzy 126, a 55 mln lat temu (Tabela 4; Artykuł 2).

W wyniku przeprowadzonych analiz zostały rozważone trzy obszary mogące stanowić źródło magmy: Tharsis Montes, Syria Planum oraz Valles Marineris. Żaden z trzech obszarów nie może być całkowicie odrzucony ze względu na to, że w ich obrębie występują dowody na intensywne procesy wulkaniczne i tektoniczne o zbliżonym wieku do badanego obszaru Noctis Fossae (Tabela 5; Artykuł 2). Jednakże z pośród nich najbardziej perspektywiczny wydaje się obszar Tharsis Montes (zbadany w Artykule 1). Magmy zasilające wulkanizm w Noctis Fossae najprawdopodobniej pochodziły z systemu magmowego znajdującego się na południe od Tharsis Montes. Magma migrując systemem dajek mogła zgromadzić się komorze pod obszarem Noctis Fossae. W trakcie stagnacji magma mogła dyferencjonować w magmę wzbogaconą w substancje lotne lub magmę o podwyższonej zawartości krzemionki, co mogło doprowadzić do erupcji eksplozywnej. Należy również rozważyć możliwość asymilacji uwodnionych minerałów budujących przypowierzchniową część skorupy marsjańskiej lub prawdopodobne interakcje magmy z wodą w postaci wiecznej zmarzliny, które dodatkowo mogły skutkować wysoko energetyczną erupcją.

Przeprowadzone badania w obszarze Noctis Fossae pozwoliły udokumentować drugie w prowincji Tharsis, po Ulysses Fossae (Brož i Hauber, 2012), pole wulkanicznych stożków scoria, które mogły powstać w wyniku erupcji eksplozywnych. Odmienny stan zachowania stożków, wynikający z różnego wieku ich powstawania (który został potwierdzony datowaniami), sugeruje aktywność wulkaniczną wydłużoną w czasie. Aktywność wulkaniczna prawdopodobnie rozpoczęła się >300 mln lat temu, a ostatni jej zapis reprezentują północne, najlepiej zachowane stożki o wieku 122 a 55 mln lat. Relacje strukturalne (formy wulkaniczne są nałożone na skarpy uskokowe) pomiędzy badanymi formami wulkanicznymi, a rowami tektonicznymi obszaru Noctis Fossae wskazują, że procesy wulkaniczne nastąpiły po głównym zdarzeniu tektonicznym. Rozmieszczenie przestrzenne oraz orientacja (wydłużenie) form wulkanicznych (N015W) wskazuje, że pole wulkaniczne w Noctis Fossae było kontrolowane przez regionalny reżim tektoniczny (Bistacchi i in., 2004). Musiał ulec on zmianie od momentu powstania rowów tektonicznych (N015E), ponieważ przeprowadzone obserwacje wskazują, że wulkanizm jest młodszy niż efekty głównych procesów tektonicznych. Pole wulkaniczne Noctis Fossae stanowi obecnie najmłodszy zapis wulkanizmu eksplozywnego w obszarze Tharsis.

Udokumentowanie nowego pola wulkanicznego o charakterze eksplozywnym dostarcza dowodów na różnorodność marsjańskiego wulkanizmu. Obserwacje te potwierdzają hipotezy, że eksplozywny wulkanizm w prowincji Tharsis był bardziej powszechny niż wcześniej sądzono i wskazują na potrzebę dalszych prac kartograficznych dla pełnej rekonstrukcji aktywności wulkanicznej na Marsie. Wykrycie form wulkanicznych pochodzenia eksplozywnego może również pomóc w wykrywaniu mineralizacji hydrotermalnej (np. uwodniona krzemionka, jarosyt, ałunit). Dane o stowarzyszonej z wulkanizmem mineralizacji dostarczyłaby więcej informacji o ewolucji systemów magmowych na Marsie i rozwoju potencjalnych systemów hydrotermalnych.

Uzupełnienie Najnowsze wyniki modelowania marsjańskiego płaszcza (Plesa i in., 2018, 2023), w oparciu o dane geofizyczne z łazika *InSight*, wskazują na prawdopodobną obecność wysokich ilości stopów magmowych w rejonach prowincji Tharsis i Elysium. Plesa i in (2023) rozważając trzy scenariusze budowy skorupy Marsa, wskazali na istnienie stopów (ang. *present-day high melt fraction zones*) pod obszarem na południe of Tharsis Montes włączając w to rejon Syria Planum i Claritas Fossae (Ryc. 6). Zasięg występowania stopów obejmuje również badany rejon Noctis Fossae. Powstanie stopów wiązane jest ze strefami konwekcji płaszcza, które powodują częściowe topienie i generowanie stopów magmowych. Wskazuje to, że nasze rozważania dotyczące potencjalnych obszarów źródłowych dla magm zasilających wulkanizm w Noctis Fossae oraz Tharsis są zgodne z obecnymi danymi dotyczącymi modelowania procesów wewnętrznych planety (Ryc. 6). Badania wykonane przez zespół Plesa i in. (2023) wskazują również na to, że konkluzje dotyczące młodego wieku aktywności wulkanicznej w obszarze Noctis Fossae i w centralnej części Tharsis (Artykuł 1) mogą być powiązane z obecnym procesem generowania stopów dla młodej aktywności wulkanicznej na Marsie (Ryc. 6).

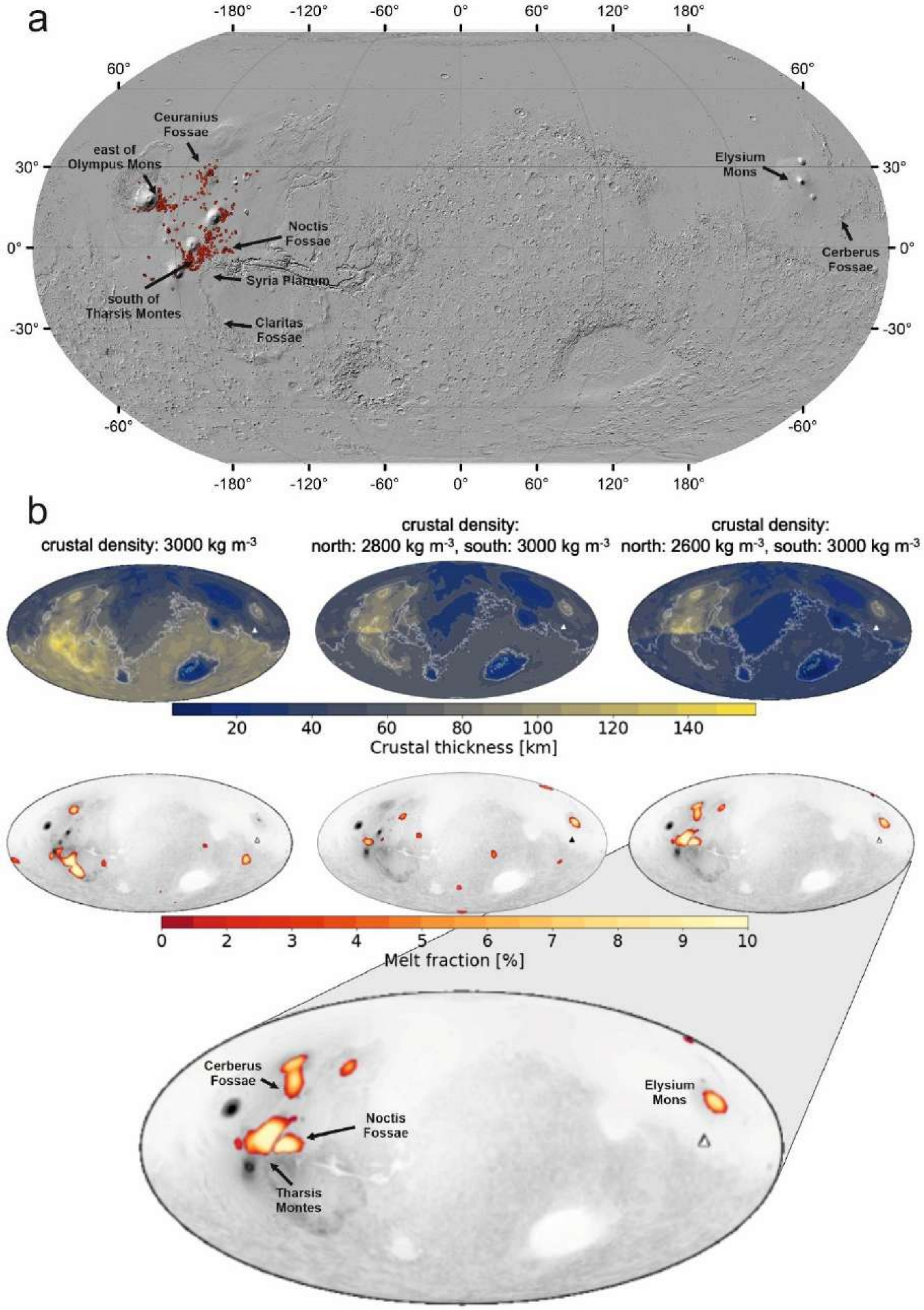

Rycina 6. Zestawienie otrzymanych wyników dotyczących obserwacji wulkanizmu na powierzchni (Artykuł 1 oraz 2) oraz najnowszych danych dotyczących modelowania budowy wewnętrznej Marsa (Plesa i in., 2023). **(a)** Globalna mapa Marsa w oparciu o cieniowane zdjęcia MOLA (Tanaka i in., 2014) z naniesionym rozmieszczeniem skartowanych form wulkanicznych (czerwone kropki). **(b)** Modelowanie miąższości skorupy Marsa oraz obecnych stref bogatych w stopy magmowe przy założeniu trzech scenariuszy średniej gęstości skorupy marsjańskiej (Plesa i in., 2023). W trzecim scenariuszu zakładającym odmienną gęstość skorupy w części północnej i południowej, strefy bogate w stop magmowy zlokalizowane są w prowincji Tharsis i Elysium (powiększenie). Korelują się one w znacznym stopniu z przeprowadzonym kartowaniem i datowaniem aktywności wulkanicznej w prowincji Tharsis przedstawionych w Artykule 1 i 2.

Artykuł 3

Ciążela, J., Bakala, J., Kowalinski, M., Plocieniak, S., Zalewska, N., ***Pieterek, B.,*** *Mrozek, T., Ciążela, M., Paslawski, G., Steslicki, M., Szaforz, Z., Barylak, J., Kuzaj, M., Maturilli, A., Helbert, J., Muszyński, A., Rataj, M., Gburek, S., Józefowicz, M., Marciniak, D. (2022). Concept and design of Martian far-IR ORE Spectrometer (MIRORES). Remote Sensing, 14, 2799*

Trzecia publikacja wchodząca w skład rozprawy doktorskiej stanowi ważny element interdyscyplinarności i aplikacyjności prowadzonych badań, które skupiały się na lepszym zrozumieniu, a następnie rekonstrukcji systemów magmowych na Marsie. Na Ziemi, procesy magmowe w dominującym stopniu odpowiadają za dystrybucję metali oraz rozwój systemów hydrotermalnych. Obecność siarczków została już potwierdzona w meteorytach marsjańskich (Lorand i in., 2005, 2018) oraz zinterpretowana na podstawie danych z łazików w kraterach Gusev i Gale (Morris i in., 2008; Vaniman i in., 2014). Dotychczas w pobliżu pojedynczych form wulkanicznych na Marsie zostały rozpoznane minerały hydrotermalne (Skok i in., 2010; Brož i in., 2017), co wskazuje na konieczność dalszego rozwoju tego kierunku badań. Znaczącym wpływem na ograniczenie badań nad mineralizacją Marsa jest brak wysoko rozdzielczych danych spektralnych (Rycina 2; Artykuł 3) oraz brak wyraźnych cech widmowych siarczków w dotychczasowych danych orbitalnych. W zakresie bliskiej podczerwieni powszechnie występujące krzemiany (np. klinopirokseny) wykazują podobną charakterystykę widmową do siarczków (np. piryt; Rycina 1; Artykuł 3). Z tego względu, korzystając z obecnie pracujących instrumentów spektralnych na orbitach Marsa w zakresie bliskiej podczerwieni, naukowcy nie mają możliwości zinterpretowania przypuszczalnej mineralizacji siarczkowej na jego powierzchni. Aby umożliwić prowadzenie szczegółowych badań nad mineralizacją siarczkową na powierzchni Marsa, opracowano koncepcję spektrometru MIRORES działającego w dalekiej podczerwieni. Umożliwi to jednoznaczne wykrycie siarczków wykazujących w dalekiej podczerwieni silne cechy widmowe, w odróżnieniu od powszechnie występujących piroksenów, dostarczając przy tym ważnych informacji o mineralizacji rudnej.

Zadaniem spektrometru MIRORES będzie identyfikacja występujących na Marsie siarczków o genezie magmowo-hydrotermalnej (piryt, chalkopiryt i markasyt), których szczegółowa charakterystyka widmowa w dalekiej podczerwieni ujawnia obecność silnych cech widmowych w zakresie 23–28 µm (Rycina 5; Artykuł 3). Działanie spektrometru z zakresie dalekiej podczerwieni pozwala uniknąć nakładania się cech widmowych siarczków z dominującymi na powierzchni Marsa piroksenami. Projekt spektrometru MIRORES zakłada prowadzenie pomiarów charakterystyki widmowej powierzchni Marsa przy użyciu trzech wąskopasmowych detektorów piroelektrycznych, z których każdy jednocześnie bada określony referencyjny zakres widmowy dla siarczka (23.2, 24.3 oraz 27.6 µm), oraz jednego detektora badającego zakres dla klinopiroksenu (29.0 µm) i dwóch detektorów referencyjnych (21.5 oraz 26.1 µm). Kluczowym do rozwiązania aspektem związanym z badaniem mineralizacji rudnej jest jej stosunkowo niewielka procentowa zawartość w stosunku do całej skały macierzystej. Na podstawie przeprowadzonego modelowania udało się wykazać, że ~10–20 obj.% pirytu w skale umożliwia jego identyfikację za pomocą spektrometru MIRORES. Zastosowanie układu optycznego Cassegraina umożliwiło osiągnięcie wysokiej rozdzielczości (< 20 m/piksel), która przypuszczalnie jest wystarczająca do badań mineralizacji siarczkowej zarówno na Ziemi (np. złoże Rio Tinto w Hiszpanii) jak i analogicznie na Marsie. Stworzenie koncepcji spektrometru skupiającego się jedynie na poszukiwaniu siarczków, umożliwiło uzyskanie korzystnych dla ergonomii misji rozmiarów instrumentu (32 × 32 × 42 cm) i masy (<10 kg) (Rycina 8 i 9; Artykuł 3).

Korzystając ze wcześniej zdobytej wiedzy dotyczącej systemów magmowych Tharsis (Artykuły 1 i 2) oraz ziemskich analogów wydaje się, że zbadane i opisane obszary wulkaniczne w Tharsis, szczególnie związane z wulkanizmem eksplozywnym (potencjalne interakcje magmy z wodą w postaci wiecznej zmarzliny, uruchamiające procesy hydrotermalne), będą najbardziej perspektywiczne w kontekście poszukiwań mineralizacji siarczkowej na Marsie. Przedstawione w publikacjach wyniki dotyczące wulkanizmu powinny mieć znaczenie nie tylko regionalne, ale również globalne dla Marsa, ponieważ procesy mineralizacji siarczkowej związanej z wulkanizmem i aktywnością hydrotermalną mogły/mogą także występować w pozostałych obszarach wulkanicznych na Marsie. Obecność gorących roztworów pomagmowych może prowadzić do powstania mineralizacji, która będzie dostępna do identyfikacji dzięki wychodniom skał, np. na stokach wulkanów, kraterów impaktowych oraz w pobliżu szczelin wulkanicznych. Podsumowując, niniejszy artykuł jest przykładem jak łączenie badań geologicznych z innowacyjną technologią może przybliżyć nas w przyszłości do lepszego poznania procesów mineralizacji rudnej na Marsie.

Uzupełnienie W oparciu o koncepcję marsjańskiego spektrometru MIRORES zostało przyznane finansowanie na rozpoznanie rynku oraz rozwój koncepcji ziemskiego spektrometru do poszukiwań złóż metali (grant Europejskiej Agencji Kosmicznej nr ESA AO/1-10824/21/NL/RA). Grant ten, w którym doktorant jest jednym z wykonawców, realizowany jest w ramach konsorcjum w skład którego wchodzą jednostki naukowo-badawcze Instytut Nauk Geologicznych Polskiej Akademii Nauk (ING PAN) oraz Centrum Badań Kosmicznych PAN (CBK PAN), a także firmy SKA Polska Sp. z o.o. i Europejska Fundacja Kosmiczna (przedstawicielem jest Interesariusz projektu Mateusz Józefowicz). Realizacja tego grantu stanowi jedynie etap w rozwoju satelitarnej wersji spektrometru, która jest rozwijana przy wsparciu finansowym Polskiej Agencji Kosmicznej (umowa nr PAK/U/167/2022/DBI/MBC).

6. Wnioski i implikacje

Przedstawiona rozprawa doktorska została poświęcona zbadaniu aktywności wulkanicznej w prowincji Tharsis na Marsie w kontekście dynamicznie rozwijających się badań planetarnych oraz branży górnictwa kosmicznego. Czasoprzestrzenna rekonstrukcja aktywności wulkanicznej w prowincji Tharsis dostarczyła nowych informacji na temat rozwoju systemów magmowych. Uzyskane wyniki są istotne w kontekście rozwoju instrumentów satelitarnych badających powierzchnię Marsa oraz umożliwiają weryfikację modeli opisujących obecne procesy wewnętrzne planety. Poniżej zostały przedstawione najważniejsze wnioski i implikacje wynikające z przeprowadzonych badań w ramach niniejszej rozprawy doktorskiej.

- Badania regionalne prowincji Tharsis wykazały, że wulkanizm rozproszony jest przestrzennie i czasowo stowarzyszony z centralnymi wulkanami Tharsis. Szczegółowe analizy pozwoliły zidentyfikować sześć systemów magmowych, z których pięć jest stosunkowo młodych, wykazujących aktywność wulkaniczną w okresie późno amazońskim (<250 milionów lat) oraz jeden system stowarzyszony z wulkanem Uranius Mons, którego aktywność musiała występować około 1 miliarda lat temu.
- Wulkanizm rozproszony w Tharsis był zasilany przez zespoły dajek radialnych i pierścieniowych. Interpretacja geologiczna pozwoliła przeprowadzić rekonstrukcję, która

zakłada, że generowana przez pióropusze płaszcza magma tworzy rezerwuary na granicy górnego płaszcza i skorupy (ang. *magma underplating*) lub migruje do komór magmowych w obrębie skorupy marsjańskiej. W obu scenariuszach magma, w ostatnim etapie przed erupcją przemieszcza się do stref przypowierzchniowych poprzez systemy dajek.

- Regionalny charakter prowadzonych badań pozwolił wykazać związek przestrzenny oraz czasowy pomiędzy rozporoszonym wulkanizmem, a centralnymi wulkanami Tharsis. Otrzymane wyniki wskazują, że erupcje wulkanizmu rozproszonego były kontynuowane nawet po ustaniu aktywności wulkanów centralnych.
- Wyniki datowań wskazują na długotrwałą aktywność wulkaniczną w obszarze Tharsis sugerując, że systemy magmowe głównych wulkanów Tharsis nie są całkowicie wygasłe, ale mogą być obecnie uśpione i w przyszłości może dojść do ich ponownej reaktywacji.
- Przeprowadzenie szczegółowych prac kartograficznych we wschodniej części prowincji Tharsis pozwoliło udokumentować nowe pole wulkaniczne piroklastycznych stożków scoria w obszarze Noctis Fossae. Ich obecność wskazuje na eksplozywny charakter lokalnych erupcji wulkanicznych. Wyniki datowań powierzchni stożków i przestrzennie stowarzyszonych potoków lawowych wskazują, że wulkany zlokalizowane na spękanej skorupie reprezentują starszy epizod wulkaniczny (>300 milionów lat temu). Natomiast dwa najlepiej zachowane stożki w północnej części pola wulkanicznego powstały prawdopodobnie pomiędzy 126, a 55 milionów lat temu.
- Na podstawie własnych obserwacji strukturalnych i danych literaturowych, jako najbardziej perspektywiczny obszar źródłowy dla magm zasilających wulkanizm w Noctis Fossae, został wytypowany rejon Tharsis Montes. Opisanie drugiego pola wulkanicznego stożków scoria w obszarze Tharsis, po pracy Broža i Haubera (2012), dostarczyło dowodów, że wulkanizm eksplozywny mógł być bardziej powszechny w przeszłości, niż wskazujące na to dotychczasowe dane. Związek ze starą spękaną skorupą marsjańską, która nie została przykryta przez rozległe potoki lawowe sugeruje, że obszary te mogą stanowić nowy, uzupełniający wgląd w zapis ewolucji wulkanizmu w prowincji Tharsis.
- Zaprezentowane w niniejszej rozprawie doktorskiej wyniki dotyczące systemów magmowych Tharsis i ich przestrzenno-czasowej ewolucji, są zgodne z najnowszymi modelami rozmieszczenia obecnych stref bogatych w magmę (ang. *present-day melt fraction zones*) we wnętrzu Marsa (Plesa i in., 2023). Mogą one stanowić ważny element weryfikacji zaproponowanych modeli. Uzyskane dane świadczące o młodej aktywności

wulkanicznej w obszarze Tharsis mogą stanowić istotny wkład w przyszłe modele dotyczące procesów endogenicznych na Marsie.

- Interdyscyplinarne podejście do prowadzonych badań, łączących wiedzę geologiczną, inżynieryjną oraz zaaplikowanie pozyskanej wiedzy przez przemysł, znalazło swoje zastosowanie w projekcie spektrometru MIRORES. Głównym zadaniem instrumentu jest identyfikacja siarczków, jako minerałów rudnych, typowych dla środowisk magmowo-hydrotermalnych. Uzyskane wyniki badań nad rekonstrukcją systemów magmowych znajdują swoją aplikacyjność w wytypowaniu marsjańskich prowincji wulkanicznych jako najbardziej perspektywicznych obszarów dla poszukiwań mineralizacji siarczkowej na powierzchni Marsa. Jest to związane z udokumentowaniem stosunkowo młodych systemów magmowych, w których potencjalna mineralizacja rudna nie została pogrzebana pod młodszymi osadami, a urozmaicona wulkaniczna rzeźba terenu umożliwia badania wychodni skał nie pokrytych luźnymi osadami na stokach form wulkanicznych, kraterach szczytowych, czy w pobliżu szczelin wulkanicznych.

7. Bibliografia

Anderson, R.C., Dohm, J.M., Golombek, M.P., Haldemann, A.F.C., Franklin, B.J., Tanaka, K.L., Lias, J., Peer, B., 2001. Primary centers and secondary concentrations of tectonic activity through time in the western hemisphere of Mars. J. Geophys. Res. Planets 106, 20563–20585. https://doi.org/10.1029/2000JE001278

Anderson, R.C., Dohm, J.M., Haldemann, A.F.C., Hare, T.M., Baker, V.R., 2004. Tectonic histories between Alba Patera and Syria Planum, Mars. Icarus 171, 31–38. https://doi.org/10.1016/j.icarus.2004.04.018

Baratoux, D., Pinet, P., Toplis, M.J., Mangold, N., Greeley, R., Baptista, A.R., 2009. Shape, rheology and emplacement times of small martian shield volcanoes. J. Volcanol. Geotherm. Res. 185, 47–68. https://doi.org/10.1016/j.jvolgeores.2009.05.003

Baratoux, D., Toplis, M.J., Monnereau, M., Gasnault, O., 2011. Thermal history of Mars inferred from orbital geochemistry of volcanic provinces. Nature 472, 338–341. https://doi.org/10.1038/nature09903

Baratoux, D., Toplis, M.J., Monnereau, M., Sautter, V., 2013. The petrological expression of early Mars volcanism 118, 59–64. https://doi.org/10.1029/2012JE004234

Beyer, R.A., Alexandrov, O., McMichael, S., 2018. The Ames Stereo Pipeline: NASA's Open Source Software for Deriving and Processing Terrain Data. Earth Sp. Sci. 5, 537–548. https://doi.org/10.1029/2018EA000409

Bistacchi, N., Massironi, M., Baggio, P., 2004. Large-scale fault kinematic analysis in Noctis Labyrinthus (Mars). Planet. Space Sci. 52, 215–222. https://doi.org/10.1016/j.pss.2003.08.015

Bleacher, J.E., Glaze, L.S., Greeley, R., Hauber, E., Baloga, S.M., Sakimoto, S.E.H., Williams, D.A., Glotch, T.D., 2009. Spatial and alignment analyses for a field of small volcanic vents south of Pavonis Mons and implications for the Tharsis province, Mars. J. Volcanol. Geotherm. Res. 185, 96–102. https://doi.org/10.1016/j.jvolgeores.2009.04.008

Bleacher, J.E., Greeley, R., Williams, D.A., Cave, S.R., Neukum, G., 2007. Trends in effusive style at the Tharsis Montes, Mars, and implications for the development of the Tharsis province. J. Geophys. Res. Planets 112, 1–15. https://doi.org/10.1029/2006JE002873

Bleacher, J.E., Richardson, J.A., Richardson, P.W., Glaze, L.S., Baloga, S.M., Greeley, R., Hauber, E., Lillis, R.J., 2010. Updates to the Catalog of Tharsis Province Small Volcanic Vents, Mars, w: 41st Annual Lunar and Planetary Science Conference. s. 1615.

Bonnet Gibet, V., Michaut, C., Wieczorek, M., Lognonné, P., 2022. A Positive Feedback Between Crustal Thickness and Melt Extraction for the Origin of the Martian Dichotomy. J. Geophys. Res. Planets 127, e2022JE007472. https://doi.org/10.1029/2022JE007472

Bouley, S., Baratoux, D., Matsuyama, I., Forget, F., Séjourné, A., Turbet, M., Costard, F., 2016. Late Tharsis formation and implications for early Mars. Nature 531, 344–347. https://doi.org/10.1038/nature17171

Bouley, S., Baratoux, D., Paulien, N., Missenard, Y., Saint-Bézar, B., 2018. The revised tectonic history of Tharsis. Earth Planet. Sci. Lett. 488, 126–133. https://doi.org/10.1016/j.epsl.2018.02.019

Breuer, D., Spohn, T., 2003. Early plate tectonics versus single-plate tectonics on Mars: Evidence from magnetic field history and crust evolution. J. Geophys. Res. 108 (E7), 5072. https://doi.org/10.1029/2002je001999

Brož, P., 2010. Plains volcanism in Tharsis region on Mars: Ages and Rheology of Eruption Products (Master Thesis). Charles University in Prague.

Brož, P., Bernhardt, H., Conway, S.J., Parekh, R., 2021. An overview of explosive volcanism on Mars. J. Volcanol. Geotherm. Res. 409, 107125. https://doi.org/10.1016/j.jvolgeores.2020.107125

Brož, P., Čadek, O., Hauber, E., Rossi, A.P., 2015. Scoria cones on Mars: Detailed investigation of morphometry based on high-resolution digital elevation models. J. Geophys. Res. Planets 120, 1512–1527. https://doi.org/doi:10.1002/2015JE004873

Brož, P., Hauber, E., 2012. A unique volcanic field in Tharsis, Mars: Pyroclastic cones as evidence for explosive eruptions. Icarus 218, 88–99. https://doi.org/10.1016/j.icarus.2011.11.030

Brož, P., Hauber, E., 2011. Windows of old fractured crust and associated volcanism in Tharsis, Mars, w: European Planetary Science Congress. s. EPSC-DPS2011-742-1. https://doi.org/10.1029/2011GL047310

Brož, P., Hauber, E., Wray, J.J., Michael, G., 2017. Amazonian volcanism inside Valles Marineris on Mars. Earth Planet. Sci. Lett. 473, 122–130. https://doi.org/10.1016/j.epsl.2017.06.003

Carr, M.H., 2007. The surface of Mars. Cambridge University Press. https://doi.org/doi.org/10.1017/CBO9780511536007

Christoph, J.M., Garry, W.B., 2017. Spatial and Temporal Relationships Among Low Shield Volcanoes in the Ceraunius Fossae Region of Tharsis: The Last Gasp of Martian Volcanism, w: 48th Annual Lunar and Planetary Science Conference. s. 2798.

Ciazela, J., Mege, D., Pieterek, B., Ciazela, M., Gurgurewicz, J., Lagain, A., Tesson, P.-A., 2019. Largest Tharsis volcanoes keep growing and mark >4-Ga-lasting Martian hot spots, w: 49th Annual Lunar and Planetary Institute Conference Abstracts. s. 1364.

Clinton, J.F., Ceylan, S., van Driel, M., Giardini, D., Stähler, S.C., Böse, M., Charalambous, C., Dahmen, N.L., Horleston, A., Kawamura, T., Khan, A., Orhand-Mainsant, G., Scholz, J.R., Euchner, F., Banerdt, W.B., Lognonné, P., Banfield, D., Beucler, E., Garcia, R.F., Kedar, S., Panning, M.P., Perrin, C., Pike, W.T., Smrekar, S.E., Spiga, A., Stott, A.E., 2021. The Marsquake catalogue from InSight, sols 0–478. Phys. Earth Planet. Inter. 310, 106595. https://doi.org/10.1016/j.pepi.2020.106595

Connerney, J.E.P., Acuña, M.H., Ness, N.F., Kletetschka, G., Mitchell, D.L., Lin, R.P., Reme, H., 2005. Tectonic implications of Mars crustal magnetism. Proc. Natl. Acad. Sci. U. S. A. 102, 14970–14975. https://doi.org/10.1073/pnas.0507469102

Crater Analysis Techniques Working Group., 1979. Standard techniques for presentation and analysis of crater size-frequency data. Icarus 37, 467–474. https://doi.org/10.1016/0019-1035(79)90009-5

Dickson, J.L., Ehlmann, B.L., Kerber, L.H., Fassett, C.I., 2023. Release of the Global CTX Mosaic of Mars: An Experiment in Information-Preserving Image Data Processing, w:

54th Lunar Planetary Science Conference. s. 2806.

Dickson, J.L., Kerber, L.A., Fassett, C.I., Ehlmann, B.L., 2018. A global, blended CTX mosaic of Mars with vectorized seam mapping: A new mosaicking pipeline using principles of non-destructive image editing, w: 49th Lunar and Planetary Science Conference. s. 2083.

Dohm, J.M., Baker, V.R., Maruyama, S., Anderson, R.C., 2007. Traits and evolution of the Tharsis Superplume, Mars, w: Superplumes: Beyond Plate Tectonics. ss. 523–536. https://doi.org/10.1007/978-1-4020-5750-2_17

Drilleau, M., Samuel, H., Garcia, R.F., Rivoldini, A., Perrin, C., Michaut, C., Wieczorek, M., Tauzin, B., Connolly, J.A.D., Meyer, P., Lognonné, P., Banerdt, W.B., 2022. Marsquake Locations and 1-D Seismic Models for Mars From InSight Data. J. Geophys. Res. Planets 127, e2021JE007067. https://doi.org/10.1029/2021JE007067

Edwards, C.S., Nowicki, K.J., Christensen, P.R., Hill, J., Gorelick, N., Murray, K., 2011. Mosaicking of global planetary image datasets: 1. Techniques and data processing for Thermal Emission Imaging System (THEMIS) multi-spectral data. J. Geophys. Res. E Planets 116, 1–21. https://doi.org/10.1029/2010JE003755

Ehlmann, B.L., Edwards, C.S., 2014. Mineralogy of the Martian Surface. Annu. Rev. Earth Planet. Sci. 42, 291–315. https://doi.org/10.1146/annurev-earth-060313-055024

ESA, 2019. ESA Space Resources Strategy.

Fergason, R.L., Hare, T.M., Laura, J., 2018. HRSC and MOLA Blended Digital Elevation Model at 200m v2. [WWW Document]. Astrogeology PDS Annex. U.S. Geol. Surv. URL http://bit.ly/HRSC_MOLA_Blend_v0

Frey, H., Schultz, R.A., 1988. Large impact basins and the mega-impact origin for the crustal dichotomy on Mars. Geophys. Res. Lett. 15, 229–232. https://doi.org/10.1029/GL015i003p00229

Garcia, R.F., Daubar, I.J., Beucler, É., Posiolova, L. V, Collins, G.S., Lognonné, P., Rolland, L., Xu, Z., Wójcicka, N., Spiga, A., Fernando, B., Speth, G., Martire, L., Rajšić, A., Miljković, K., Sansom, E.K., Charalambous, C., Ceylan, S., Menina, S., Margerin, L., Lapeyre, R., Neidhart, T., Teanby, N.A., Schmerr, N.C., Bonnin, M., Froment, M., Clinton, J.F., Karatekin, O., Stähler, S.C., Dahmen, N.L., Durán, C., Horleston, A., Kawamura, T., Plasman, M., Zenhäusern, G., Giardini, D., Panning, M., Malin, M., Banerdt, W.B., 2022. Newly formed craters on Mars located using seismic and acoustic wave data from InSight. Nat. Geosci. 15, 774–780. https://doi.org/10.1038/s41561-022-01014-0

Giardini, D., Lognonné, P., Banerdt, W.B., Pike, W.T., Christensen, U., Ceylan, S., Clinton, J.F., van Driel, M., Stähler, S.C., Böse, M., Garcia, R.F., Khan, A., Panning, M., Perrin, C., Banfield, D., Beucler, E., Charalambous, C., Euchner, F., Horleston, A., Jacob, A., Kawamura, T., Kedar, S., Mainsant, G., Scholz, J.R., Smrekar, S.E., Spiga, A., Agard, C., Antonangeli, D., Barkaoui, S., Barrett, E., Combes, P., Conejero, V., Daubar, I., Drilleau, M., Ferrier, C., Gabsi, T., Gudkova, T., Hurst, K., Karakostas, F., King, S., Knapmeyer, M., Knapmeyer-Endrun, B., Llorca-Cejudo, R., Lucas, A., Luno, L., Margerin, L., McClean, J.B., Mimoun, D., Murdoch, N., Nimmo, F., Nonon, M., Pardo, C., Rivoldini, A., Manfredi, J.A.R., Samuel, H., Schimmel, M., Stott, A.E., Stutzmann, E., Teanby, N., Warren, T., Weber, R.C., Wieczorek, M., Yana, C., 2020. The seismicity of Mars. Nat. Geosci. 13, 205–212. https://doi.org/10.1038/s41561-020-0539-8

Golabek, G.J., Keller, T., Gerya, T. V, Zhu, G., Tackley, P.J., Connolly, J.A.D., 2011. Origin of the martian dichotomy and Tharsis from a giant impact causing massive magmatism. Icarus 215, 346–357. https://doi.org/10.1016/j.icarus.2011.06.012

Grady, M.M., 2020. Exploring Mars with Returned Samples. Space Sci. Rev. 216, 51. https://doi.org/10.1007/s11214-020-00676-9

Grosse, P., van Wyk de Vries, B., Euillades, P.A., Kervyn, M., Petrinovic, I.A., 2012. Systematic morphometric characterization of volcanic edifices using digital elevation models. Geomorphology 136, 114–131. https://doi.org/10.1016/j.geomorph.2011.06.001

Gwinner, K., Jaumann, R., Hauber, E., Hoffmann, H., Heipke, C., Oberst, J., Neukum, G., Ansan, V., Bostelmann, J., Dumke, A., Elgner, S., Erkeling, G., Fueten, F., Hiesinger, H., Hoekzema, N.M., Kersten, E., Loizeau, D., Matz, K.D., McGuire, P.C., Mertens, V., Michael, G., Pasewaldt, A., Pinet, P., Preusker, F., Reiss, D., Roatsch, T., Schmidt, R., Scholten, F., Spiegel, M., Stesky, R., Tirsch, D., Van Gasselt, S., Walter, S., Wählisch, M., Willner, K., 2016. The High Resolution Stereo Camera (HRSC) of Mars Express and its approach to science analysis and mapping for Mars and its satellites. Planet. Space Sci. 126, 93–138. https://doi.org/10.1016/j.pss.2016.02.014

Hartmann, W.K., 2005. Martian cratering 8: Isochron refinement and the chronology of Mars. Icarus 174, 294–320. https://doi.org/10.1016/j.icarus.2004.11.023

Hartmann, W.K., Daubar, I.J., 2017. Martian cratering 11. Utilizing decameter scale crater populations to study Martian history. Meteorit. Planet. Sci. 52, 493–510. https://doi.org/10.1111/maps.12807

Hartmann, W.K., Malin, M., McEwen, A., Carr, M., Soderblom, L., Thomas, P., Danielson, E., James, P., Veverka, J., 1999. Evidence for recent volcanism on mars from crater counts. Nature 397, 586–589. https://doi.org/10.1038/17545

Hartmann, W.K., Neukum, G., 2001. Cratering chronology and the evolution of Mars. Space Sci. Rev. 96, 165–194. https://doi.org/10.1023/A1011945222010

Hauber, E., Bleacher, J., Gwinner, K., Williams, D., Greeley, R., 2009. The topography and morphology of low shields and associated landforms of plains volcanism in the Tharsis region of Mars. J. Volcanol. Geotherm. Res. 185, 69–95. https://doi.org/10.1016/j.jvolgeores.2009.04.015

Hauber, E., Brož, P., Jagert, F., Jodowski, P., Platz, T., 2011. Very recent and wide-spread basaltic volcanism on Mars. Geophys. Res. Lett. 38, 1–5. https://doi.org/10.1029/2011GL047310

Hauber, E., Kronberg, P., 2001. Tempe Fossae, Mars: A planetary analogon to a terrestrial continental rift? J. Geophys. Res. 106, 20,587-20,602.

Hauck, S.A., Phillips, R.J., 2002. Thermal and crustal evolution of Mars. J. Geophys. Res. Planets 107, 5052. https://doi.org/10.1029/2001je001801

Horvath, D.G., Moitra, P., Hamilton, C.W., Craddock, R.A., Andrews-Hanna, J.C., 2021. Evidence for geologically recent explosive volcanism in Elysium. Icarus 365, 114499. https://doi.org/10.1016/j.icarus.2021.114499

Ivanov, B.A., 2001. Mars/Moon cratering rate ratio estimates. Space Sci. Rev. 96, 87–104. https://doi.org/10.1023/A:1011941121102

Ivanov, M.A., Head, J.W., 2006. Alba Patera, Mars: Topography, structure, and evolution of a unique late Hesperian-early Amazonian shield volcano. J. Geophys. Res. Planets 111, E09003. https://doi.org/10.1029/2005JE002469

Jacob, A., Plasman, M., Perrin, C., Fuji, N., Lognonné, P., Xu, Z., Drilleau, M., Brinkman, N., Stähler, S., Sainton, G., Lucas, A., Giardini, D., Kawamura, T., Clinton, J., Banerdt, W.B., 2022. Seismic sources of InSight marsquakes and seismotectonic context of Elysium Planitia, Mars. Tectonophysics 837, 229434. https://doi.org/10.1016/j.tecto.2022.229434

Johnson, C.L., Phillips, R.J., 2005. Evolution of the Tharsis region of Mars: insights from magnetic field observations. Earth Planet. Sci. Lett. 230, 241–254. https://doi.org/10.1016/j.epsl.2004.10.038

Keszthelyi, L., Jaeger, W., McEwen, A., Tornabene, L., Beyer, R.A., Dundas, C., Milazzo, M., 2008. High resolution imaging science experiment (HiRISE) images of volcanic terrains from the first 6 months of the Mars reconnaissance orbiter primary science phase. J. Geophys. Res. Planets 113, E04005. https://doi.org/10.1029/2007JE002968

Khan, A., Ceylan, S., van Driel, M., Giardini, D., Lognonné, P., Samuel, H., Schmerr, N.C., Stähler, S.C., Duran, A.C., Huang, Q., Kim, D., Broquet, A., Charalambous, C., Clinton, J.F., Davis, P.M., Drilleau, M., Karakostas, F., Lekic, V., McLennan, S.M., Maguire, R.R., Michaut, C., Panning, M.P., Pike, W.T., Pinot, B., Plasman, M., Scholz, J.-R., Widmer-Schnidrig, R., Spohn, T., Smrekar, S.E., Banerdt, W.B., 2021. Upper mantle structure of Mars from InSight seismic data. Science (80). 373, 434–438. https://doi.org/10.1126/science.abf2966

Kim, D., Clinton, J., Ceylan, S., Horleston, A., Stähler, S., Kawamura, T., Charalambous, C., Dahmen, N., Duran, C., Plasman, M., Euchner, F., Knapmeyer, M., Giardini, D., Lognonné, P., Panning, M., Banerdt, W., 2023. The Marsquake Service since the InSight mission to Mars, w: EGU General Assembly Conference Abstracts. s. EGU-14918. https://doi.org/10.5194/egusphere-egu23-14918

Knapmeyer-Endrun, B., Panning, M.P., Bissig, F., Joshi, R., Khan, A., Kim, D., Lekić, V., Tauzin, B., Tharimena, S., Plasman, M., Compaire, N., Garcia, R.F., Margerin, L., Schimmel, M., Stutzmann, É., Schmerr, N., Bozdag, E., Plesa, A.C., Wieczorek, M.A., Broquet, A., Antonangeli, D., McLennan, S.M., Samuel, H., Michaut, C., Pan, L., Smrekar, S.E., Johnson, C.L., Brinkman, N., Mittelholz, A., Rivoldini, A., Davis, P.M., Lognonné, P., Pinot, B., Scholz, J.R., Stähler, S., Knapmeyer, M., van Driel, M., Giardini, D., Banerdt, W.B., 2021. Thickness and structure of the martian crust from InSight seismic data. Science (80). 373, 438–443. https://doi.org/10.1126/science.abf8966

Kneissl, T.A., Gasselt, S. Van, Neukum, G., 2011. Map-projection-independent crater size-frequency determination in GIS environments — New software tool for ArcGIS. Planet. Space Sci. 59, 1243–1254. https://doi.org/10.1016/j.pss.2010.03.015

Krishnan, V., Kumar, P.S., 2022. Long-Lived and Continual Volcanic Eruptions, Tectonic Activity, Pit Chains Formation, and Boulder Avalanches in Northern Tharsis Region: Implications for Late Amazonian Geodynamics and Seismo-Tectonic Processes on Mars. J. Geophys. Res. Planets 128, e2022JE007511. https://doi.org/10.1029/2022JE007511

Lagain, A., Benedix, G.K., Servis, K., Baratoux, D., Doucet, L.S., 2021. The Tharsis mantle source of depleted shergottites revealed by 90 million impact craters. Nat. Commun. 12, 6352. https://doi.org/10.1038/s41467-021-26648-3

Laura, J., Acosta, A., Addair, T., Adoram-Kershner, L., Alexander, James Alexandrov, O., Alley, S., Anderson, D., Anderson, James, Anderson, Jeff, Annex, A., Archinal, B., Austin, C., Backer, J., Barrett, J., Bauers, J., Becker, K., Becker, T., Bennett, G., Berry, K., Beyer, R., Bonn, J., Boyd, M., Brownsberger, S., Chaves, P., Christensen, W., Clark, R., Combs, C., Cook, D., Covington, J., Crawforth, J., Crosby, S., Crough, J.A., Curtis, A., Cushing, N., Dahmer, L., Danton, J., Davidson, D., Davis, P., Dean, B., Drossary, P., Dunn, E., Edmundson, K., Edwards, K., Eis, M., Eliason, E., Eliason, P., Fergason, R., Gaddis, L., Gault, E., Geissler, P., George, B., Giroux, A., Giroux, T., Goins, A., Gregg, V., Hahn, M., Hare, T., Harvey, R., Herkenhoff, K., Heyer, E., Hilt, N., Howington-Kraus, E., Humphrey, I., Isbell, C., Jensen, P., Johnson, J., Jones, M., Kamp, L., Kelleher, T., Keszthelyi, L., Kieffer, H., Kirk, R., Koechle, S., Lambright, S., Lee, E.M., Lee, K., Leggett, R., Lewis, R., Licht, A., Lindelow, J., Lipkowitz, B., Lo, J., Mapel, J., Martin, M., Martinez, P., Mathews, J., Mawhinney, J., McEwin, A., McMacken, D., Mehlman, B., Milazzo, M., Miller, D., Miller-Ribelin, E., Neubauer, C., Oyama, K., Paquette, A., Parker, W., Prasad, S., Redding, B., Richie, J., Rideout, J., Robinson, M., Rodriguez, K., Rose, C., Saleh, R., Sanders, A., Scott, B., Seignovert, B., Shepard, M., Shinaman, J., Sides, K., Sides, S., Silva, V., Smythe, B., Soderblom, L., Soltesz, D.L., Stamile, A., Stapleton, J., Stapleton, S., Stebenne, A., Sucharski, R., Sucharski, T., Takir, D., Thomas, O., Thompson, T., Titus, T., Torson, J., Wallace, R., Weller, L., Williams, K., Wilson, T., Young, A., 2021. Integrated Software for Imagers and Spectrometers. https://doi.org/10.5281/zenodo.5347823

Lenardic, A., Nimmo, F., Moresi, L., 2004. Growth of the hemispheric dichotomy and the cessation of plate tectonics on Mars. J. Geophys. Res. E Planets 109, E02003. https://doi.org/10.1029/2003je002172

Leone, G., Grosse, P., Ahrens, C., Gasparri, D., 2022. Geomorphological and morphometric characteristics of the volcanic edifices along a volcanic alignment of Tharsis on Mars. Geomorphology 414, 108385. https://doi.org/10.1016/j.geomorph.2022.108385

Leone, G., Tackley, P.J., Gerya, T. V., May, D.A., Zhu, G., 2014. Three-dimensional simulations of the southern polar giant impact hypothesis.pdf. Geophys. Res. Lett. 41, 8736–8743. https://doi.org/10.1002/ 2014GL062261

Levchenko, I., Xu, S., Mazouffre, S., Keidar, M., Bazaka, K., 2019. Mars Colonization: Beyond Getting There. Glob. Challenges 3, 1800062. https://doi.org/10.1002/gch2.201800062

Lorand, J.P., Chevrier, V., Sautter, V., 2005. Sulfide mineralogy and redox conditions in some shergottites. Meteorit. Planet. Sci. 40, 1257–1272. https://doi.org/10.1111/j.1945-5100.2005.tb00187.x

Lorand, J.P., Pont, S., Chevrier, V., Luguet, A., Zanda, B., Hewins, R., 2018. Petrogenesis of martian sulfides in the Chassigny meteorite. Am. Mineral. 103, 872–885. https://doi.org/10.2138/am-2018-6334

Malin, M.C., Bell, J.F., Cantor, B.A., Caplinger, M.A., Calvin, W.M., Clancy, R.T., Edgett, K.S., Edwards, L., Haberle, R.M., James, P.B., Lee, S.W., Ravine, M.A., Thomas, P.C., Wolff, M.J., 2007. Context Camera Investigation on board the Mars Reconnaissance Orbiter. J. Geophys. Res. Planets 112, E05S04. https://doi.org/10.1029/2006JE002808

Mangold, N., Loizeau, D., Poulet, F., Ansan, V., Baratoux, D., LeMouelic, S., Bardintzeff, J.M., Platevoet, B., Toplis, M., Pinet, P., Masson, P., Bibring, J.P., Gondet, B., Langevin, Y., Neukum, G., 2010. Mineralogy of recent volcanic plains in the Tharsis region, Mars, and implications for platy-ridged flow composition. Earth Planet. Sci. Lett. 294, 440–450. https://doi.org/10.1016/j.epsl.2009.07.036

Marinova, M.M., Aharonson, O., Asphaug, E., 2008. Mega-impact formation of the Mars hemispheric dichotomy. Nature 453, 1216–1219. https://doi.org/10.1038/nature07070

Martín-Torres, J.F., Zorzano, M.P., Valentín-Serrano, P., Harri, A.M., Genzer, M., Kemppinen, O., Rivera-Valentin, E.G., Jun, I., Wray, J., Bo Madsen, M., Goetz, W., McEwen, A.S., Hardgrove, C., Renno, N., Chevrier, V.F., Mischna, M., Navarro-González, R., Martínez-Frías, J., Conrad, P., McConnochie, T., Cockell, C., Berger, G., Vasavada, A.R., Sumner, D., Vaniman, D., 2015. Transient liquid water and water activity at Gale crater on Mars. Nat. Geosci. 8, 357–361. https://doi.org/10.1038/ngeo2412

McEwen, A.S., Eliason, E.M., Bergstrom, J.W., Bridges, N.T., Hansen, C.J., Delamere, W.A., Grant, J.A., Gulick, V.C., Herkenhoff, K.E., Keszthelyi, L., Kirk, R.L., Mellon, M.T., Squyres, S.W., Thomas, N., Weitz, C.M., 2007. Mars Reconnaissance Orbiter's High Resolution Imaging Science Experiment (HiRISE). J. Geophys. Res. 112, E05S02. https://doi.org/10.1029/2005JE002605

McEwen, A.S., Preblich, B.S., Turtle, E.P., Artemieva, N.A., Golombek, M.P., Hurst, M., Kirk, R.L., Burr, D.M., Christensen, P.R., 2005. The rayed crater Zunil and interpretations of small impact craters on Mars. Icarus 176, 351–381. https://doi.org/10.1016/j.icarus.2005.02.009

Mège, D., Masson, P., 1996. A plume tectonics model for the Tharsis province, Mars. Planet. Space Sci. 44, 1499–1546. https://doi.org/10.1016/S0032-0633(96)00113-4

Michael, G.G., Neukum, G., 2010. Planetary surface dating from crater size – frequency distribution measurements : Partial resurfacing events and statistical age uncertainty. Earth Planet. Sci. Lett. 294, 223–229. https://doi.org/10.1016/j.epsl.2009.12.041

Morris, R. V., Klingelhöfer, G., Schröer, C., Fleischer, I., Ming, D.W., Yen, A.S., Gellert, R., Arvidson, R.E., Rodionov, D.S., Crumpler, L.S., Clark, B.C., Cohen, B.A., McCoy, T.J., Mittlefehldt, D.W., Schmidt, M.E., De Souza, J.A., Squyres, S.W., 2008. Iron mineralogy and aqueous alteration from Husband Hill through Home Plate at Gusev Crater, Mars: Results from the Mössbauer instrument on the Spirit Mars Exploration Rover. J. Geophys. Res. 113, E12S42. https://doi.org/10.1029/2008JE003201

Mouginis-Mark, P.J., Crown, D.A., Zimbelman, J.R., Williams, D.A., 2021a. 3 - The Tharsis Province, w: Zimbelman, J.R., Crown, D.A., Mouginis-Mark, P.J., Gregg, T.K.P. (Red.), . Elsevier, ss. 36–68. https://doi.org/10.1016/B978-0-12-822876-0.00013-8

Mouginis-Mark, P.J., Wilson, L., 2019. Late-stage intrusive activity at Olympus Mons, Mars: Summit inflation and giant dike formation. Icarus 319, 459–469. https://doi.org/10.1016/j.icarus.2018.09.038

Mouginis-Mark, P.J., Zimbelman, J.R., Crown, D.A., Garry, W.B., 2021b. 4 - The Elysium Province, w: Zimbelman, J.R., Crown, D.A., Mouginis-Mark, P.J., Gregg, T.K.P. (Red.), . Elsevier, ss. 70–91. https://doi.org/10.1016/B978-0-12-822876-0.00008-4

Neukum, G., Ivanov, B.A., Hartmann, W.K., 2001. Cratering Records in the Inner Solar System in Relation to the Lunar Reference System. Sp. Sci. Rev. Chronol. Evol. Mars 96, 55–86. https://doi.org/10.1023/A:1011989004263

Neukum, G., Jaumann, R., Hoffmann, H., Hauber, E., Head, J.W., Basilevsky, A.T., Ivanov, B.A., Werner, S.C., Van Gasselt, S., Murray, J.B., McCord, T., 2004. Recent and episodic volcanic and glacial activity on Mars revealed by the High Resolution Stereo Camera. Nature 432, 971–979. https://doi.org/10.1038/nature03231

Ojha, L., Karimi, S., Lewis, K.W., Smrekar, S.E., Siegler, M., 2019. Depletion of Heat Producing Elements in the Martian Mantle. Geophys. Res. Lett. 46, 12756–12763. https://doi.org/10.1029/2019GL085234

Platz, T., Münn, S., Walter, T.R., Procter, J.N., McGuire, P.C., Dumke, A., Neukum, G., 2011. Vertical and lateral collapse of Tharsis Tholus, Mars. Earth Planet. Sci. Lett. 305, 445–455. https://doi.org/10.1016/j.epsl.2011.03.012

Plesa, A.C., Padovan, S., Tosi, N., Breuer, D., Grott, M., Wieczorek, M.A., Spohn, T., Smrekar, S.E., Banerdt, W.B., 2018. The Thermal State and Interior Structure of Mars. Geophys. Res. Lett. 45, 12,198-12,209. https://doi.org/10.1029/2018GL080728

Plesa, A.C., Wieczorek, M., Knapmeyer, M., Rivoldini, A., Bozdag, E., Walterova, M., Knapmeyer-Endrun, B., Kim, D., Broquet, A., Stähler, S., Mittelholtz, A., Breuer, D., Johnson, C.L., Hauber, E., Panning, M., Spohn, T., Lognonné, P., Smrekar, S.E., Banerdt, W.B., InSight Science Team, 2023. Insight’s constraints on the interior of Mars: Geodynamical models and observations, w: 54th Lunar Planetary Science Conference. s. 2212.

Plescia, J.B., 2004. Morphometric properties of Martian volcanoes. J. Geophys. Res. Planets 109, E03003. https://doi.org/10.1029/2002je002031

Plescia, J.B., 1994. Geology of the Small Tharsis Volcanoes: Jovis Tholus, Ulysses Patera, BibIls Patera, Mars. Icarus 111, 246–269. https://doi.org/https://doi.org/10.1006/icar.1994.1144

Poulet, F., Mangold, N., Platevoet, B., Bardintzeff, J.M., Sautter, V., Mustard, J.F., Bibring, J.P., Pinet, P., Langevin, Y., Gondet, B., Aléon-Toppani, A., 2009. Quantitative compositional analysis of martian mafic regions using the MEx/OMEGA reflectance data. 2. Petrological implications. Icarus 201, 84–101. https://doi.org/10.1016/j.icarus.2008.12.042

Pozzobon, R., Mazzarini, F., Isola, I., 2023. Syria Planum volcanic province , an example of diffuse volcanism on Mars : insights from vents distribution analysis and spatial clustering, w: EGU General Assembly Conference Abstracts. s. 15312.

Quantin-Nataf, C., Lozac, L., Thollot, P., Loizeau, D., Bultel, B., Fernando, J., Allemand, P., Dubuffet, F., Poulet, F., Ody, A., Clenet, H., Leyrat, C., Harrisson, S., 2018. MarsSI: Martian surface data processing information system. Planet. Space Sci. 150, 157–170. https://doi.org/10.1016/j.pss.2017.09.014

Reese, C.C., Solomatov, V.S., Baumgardner, J.R., Stegman, D.R., Vezolainen, A. V, 2004. Magmatic evolution of impact-induced Martian mantle plumes and the origin of Tharsis 109, E08009. https://doi.org/10.1029/2003JE002222

Richardson, J.A., Bleacher, J.E., Connor, C.B., Glaze, L.S., 2021. Small Volcanic Vents of the Tharsis Volcanic Province, Mars. J. Geophys. Res. Planets 126, e2020JE006620. https://doi.org/10.1029/2020JE006620

Richardson, J.A., Bleacher, J.E., Connor, C.B., Glaze, L.S., 2020. Tharis volcanic vents enhanced database. https://doi.org/doi: 10.5281/zenodo.4275144

Richardson, J.A., Bleacher, J.E., Glaze, L.S., 2012. The volcanic history of Syria Planum, Mars. J. Volcanol. Geotherm. Res. 252, 1–13. https://doi.org/10.1016/j.jvolgeores.2012.11.007

Richardson, J.A., Wilson, J.A., Connor, C.B., Bleacher, J.E., Kiyosugi, K., 2017. Recurrence rate and magma effusion rate for the latest volcanism on Arsia Mons, Mars. Earth Planet. Sci. Lett. 458, 170–178. https://doi.org/10.1016/j.epsl.2016.10.040

Robbins, S.J., Di Achille, G., Hynek, B.M., 2011. The volcanic history of Mars: High-resolution crater-based studies of the calderas of 20 volcanoes. Icarus 211, 1179–1203. https://doi.org/10.1016/j.icarus.2010.11.012

Scott, D.H., Carr, M.H., 1978. Geologic map of Mars. U.S. Geol. Surv. Misc. Invest. Ser. Map I-1083, scale 1 25,000,000.

Sita, M., van der Lee, S., 2022. Potential Volcano-Tectonic Origins and Faulting Mechanisms of Three Low-Frequency Marsquakes Detected by a Single InSight Seismometer. J. Geophys. Res. Planets 127, e2022JE007309. https://doi.org/doi.org/10.1029/2022JE007309

Skok, J.R., Mustard, J.F., Ehlmann, B.L., Milliken, R.E., Murchie, S.L., 2010. Silica deposits in the Nili Patera caldera on the Syrtis Major volcanic complex on Mars. Nat. Geosci. 3, 838–841. https://doi.org/10.1038/ngeo990

Smith, D.E., Zuber, M.T., Frey, H. V., Garvin, J.B., Head, J.W., Muhleman, D.O., Pettengill, G.H., Phillips, R.J., Solomon, S.C., Zwally, H.J., Banerdt, W.B., Duxbury, T.C., Golombek, M.P., Lemoine, F.G., Neumann, G.A., Rowlands, D.D., Aharonson, O., Ford, P.G., Ivanov, A.B., Johnson, C.L., McGovern, P.J., Abshire, J.B., Afzal, R.S., Sun, X., 2001. Mars Orbiter Laser Altimeter: Experiment summary after the first year of global mapping of Mars. J. Geophys. Res. Planets 106, 23,689-23,722. https://doi.org/10.1029/2000JE001364

Solomon, S.C., Head, J.W., 1982. Evolution of the Tharsis Province of Mars: The Importance of Heterogeneous Lithospheric Thickness. J. Geophys. Res. 87, 9755–9774.

Stähler, S.C., Khan, A., Bruce Banerdt, W., Lognonné, P., Giardini, D., Ceylan, S., Drilleau, M., Al., E., 2021. Seismic detection of the martian core. Science (80). 373, 443–448. https://doi.org/10.1126/science.abi7730

Stähler, S.C., Mittelholz, A., Perrin, C., Kawamura, T., Kim, D., Knapmeyer, M., Zenhäusern, G., Clinton, J., Giardini, D., Lognonné, P., Banerdt, W.B., 2022. Tectonics of Cerberus Fossae unveiled by marsquakes. Nat. Astron. 6, 1376–1386. https://doi.org/10.1038/s41550-022-01803-y

Starr, S.O., Muscatello, A.C., 2020. Mars in situ resource utilization: a review. Planet. Space Sci. 182, 104824. https://doi.org/10.1016/j.pss.2019.104824

Sun, W., Tkalčić, H., 2022. Repetitive marsquakes in Martian upper mantle. Nat. Commun. 13, 1695. https://doi.org/10.1038/s41467-022-29329-x

Tanaka, K.L., 1986. The Stratigraphy of Mars. Lunar Planet. Sci. Conf. Proc. 91, 139-E158.

Tanaka, K.L., Robbins, S.J., Fortezzo, C.M., Skinner, J.A., Hare, T.M., 2014. The digital global geologic map of Mars: Chronostratigraphic ages, topographic and crater morphologic characteristics, and updated resurfacing history. Planet. Space Sci. 95, 11–24. https://doi.org/10.1016/j.pss.2013.03.006

Tenzer, R., Eshagh, M., Jin, S., 2015. Martian sub-crustal stress from gravity and topographic models. Earth Planet. Sci. Lett. 425, 84–92. https://doi.org/10.1016/j.epsl.2015.05.049

Vaniman, D.T., Bish, D.L., Ming, D.W., Bristow, T.F., Morris, R. V., Blake, D.F., Chipera, S.J., Morrison, S.M., Treiman, A.H., Rampe, E.B., Rice, M., Achilles, C.N., Grotzinger, J.P., McLennan, S.M., Williams, J., Bell, J.F., Newsom, H.E., Downs, R.T., Maurice, S., Sarrazin, P., Yen, A.S., Morookian, J.M., Farmer, J.D., Stack, K., Milliken, R.E., Ehlmann, B.L., Sumner, D.Y., Berger, G., Crisp, J.A., Hurowitz, J.A., Anderson, R., Des Marais, D.J., Stolper, E.M., Edgett, K.S., Gupta, S., Spanovich, N., 2014. Mineralogy of a mudstone at Yellowknife Bay, Gale crater, Mars. Science (80). 343. https://doi.org/10.1126/science.1243480

Viviano, C.E., Murchie, S.L., Daubar, I.J., Morgan, M.F., Seelos, F.P., Plescia, J.B., 2019. Composition of Amazonian volcanic materials in Tharsis and Elysium, Mars, from MRO/CRISM reflectance spectra. Icarus 328, 274–286. https://doi.org/10.1016/j.icarus.2019.03.001

Weizman, A., Stevenson, D.J., Prialnik, D., Podolak, M., 2001. Modeling the Volcanism on Mars. Icarus 150, 195–205. https://doi.org/10.1006/icar.2000.6572

Werner, S.C., 2009. The global martian volcanic evolutionary history. Icarus 201, 44–68. https://doi.org/10.1016/j.icarus.2008.12.019

Werner, S.C., Tanaka, K.L., 2011. Redefinition of the crater-density and absolute-age boundaries for the chronostratigraphic system of Mars. Icarus 215, 603–607. https://doi.org/10.1016/j.icarus.2011.07.024

Wieczorek, M.A., Broquet, A., McLennan, S.M., Rivoldini, A., Golombek, M., Antonangeli, D., Beghein, C., Giardini, D., Gudkova, T., Gyalay, S., Johnson, C.L., Joshi, R., Kim, D., King, S.D., Knapmeyer-Endrun, B., Lognonné, P., Michaut, C., Mittelholz, A., Nimmo, F., Ojha, L., Panning, M.P., Plesa, A.C., Siegler, M.A., Smrekar, S.E., Spohn, T., Banerdt, W.B., 2022. InSight Constraints on the Global Character of the Martian Crust. J. Geophys. Res. Planets 127, e2022JE007298. https://doi.org/10.1029/2022JE007298

Williams, J.-P., Nimmo, F., Moore, W.B., Paige, D.A., 2008. The formation of Tharsis on Mars: What the line-of-sight gravity is telling us. J. Geophys. Res. 113, E10011. https://doi.org/10.1029/2007JE003050

Wilson, L., Head, J.W., 2002. Tharsis-radial graben systems as the surface manifestation of plume-related dike intrusion complexes: Models and implications. J. Geophys. Res. 107. https://doi.org/10.1029/2001JE001593

Wilson, L., Head, J.W., 1994. Review and analysis and of volcanic eruption to theory relationships landforms. Rev. Geophys. 32, 221–263. https://doi.org/10.1029/94RG01113

Wilson, L., Scott, E.D., Head III, J.W., 2001. Evidence for episodicity in the magma supply to the large Tharsis volcanoes. J. Geophys. Res. 106, 1423–1433. https://doi.org/10.1029/2000JE001280

Xiao, L., Huang, J., Christensen, P.R., Greeley, R., Williams, D.A., Zhao, J., He, Q., 2012. Ancient volcanism and its implication for thermal evolution of Mars. Earth Planet. Sci. Lett. 323–324, 9–18. https://doi.org/10.1016/j.epsl.2012.01.027

Zhong, S., 2009. Migration of Tharsis volcanism on Mars caused by differential rotation of the lithosphere. Nat. Geosci. 2, 19–23. https://doi.org/10.1038/ngeo392

Zhong, S., 2002. Effects of lithosphere on the long-wavelength gravity anomalies and their implications for the formation of the Tharsis rise on Mars. J. Geophys. Res. 107, 5054. https://doi.org/10.1029/2001JE001589

Zimbelman, J.R., Garry, W.B., Bleacher, J.E., Crown, D.A., 2015. Chapter 41 - Volcanism on Mars, Second Edi. ed, The Encyclopedia of Volcanoes. Elsevier. https://doi.org/10.1016/B978-0-12-385938-9.00041-9

OŚWIADCZENIA AUTORÓW

Artykuł 1

Pieterek, B., Ciazela, J., Lagain, A., Ciazela, M. (2022) Late Amazonian dike-fed parasitic volcanism in the Tharsis volcanic province on Mars. *Icarus*, *vol. 386, 115151.* https://doi.org/10.1016/j.icarus.2022.115151 (IF$_{2022}$ = **3.657**, pkt. MEiN = **140**)

Pan Bartosz Pieterek uczestniczył w każdym etapie badawczym oraz był odpowiedzialny za przeprowadzenie wszystkich badań zawartych w publikacji, tj. proces kartowania prowincji Tharsis i wykonywania pomiarów morfometrycznych zmapowanych form wulkanicznych, datowania powierzchni wulkanów za pomocą metody zliczania kraterów impaktowych (otrzymane wyniki zweryfikowane zostały przez dr Anthony'ego Lagain) oraz interpretacji i rekonstrukcji przebiegu podpowierzchniowych dajek, w tym systemów magmowych.

Pan Bartosz Pieterek przygotował wszystkie zawarte w publikacji mapy wraz z materiałami uzupełniającymi. Istotne elementy interpretacji uzyskanych wyników zostały zaproponowane przez Doktoranta.

Pan Bartosz Pieterek był odpowiedzialny za przygotowanie pierwotnej wersji manuskryptu oraz przygotował wszystkie ilustracje (ryciny, tabele, załączniki) zawarte w publikacji. Pan Bartosz Pieterek uczestniczył we wszystkich etapach procesu publikacyjnego, w tym pełniąc funkcję autora korespondencyjnego i udzielając odpowiedzi recenzentom.

Autor	Podpis	Data
Bartosz Pieterek	B. Pieterek	29.03.2023
Jakub Ciążela		14.04.2023
Anthony Lagain		30.03.2023
Marta Ciążela		13.04.2023

Publication no. 1:

Pieterek, B., Ciazela, J., Lagain, A., Ciazela, M. (2022). Late Amazonian dike-fed parasitic volcanism in the Tharsis volcanic province on Mars. *Icarus*, *vol. 386, 115151.* https://doi.org/10.1016/j.icarus.2022.115151 (IF_{2022} = **3.657**, pkt. MEiN = **140**)

Mr. Bartosz Pieterek participated in each stage of the research and was responsible for conducting all research tasks and objectives, i.e., mapping of volcanic edifices located within the Tharsis volcanic, conducting morphometric measurements of the mapped volcanic edifices, age determination of the volcanoes' surfaces using the crater counting method (the obtained results were checked and discussed with Dr. Anthony Lagain), and the interpretation and reconstruction of subsurface magmatic plumbing systems of Tharsis.

Mr. Bartosz Pieterek prepared all maps included in the publication along with supplementary materials. The Ph.D. student proposed significant elements of the interpretation of the obtained results.

Mr. Bartosz Pieterek was responsible for preparing the original draft of the manuscript and preparing all the graphics (figures, tables, appendices) included in the publication. Mr. Bartosz Pieterek participated in all stages of the publication process, including serving as the corresponding author and responding to reviewers.

Autor	Podpis	Data
Bartosz Pieterek	B. Pieterek	29.03.2023
Jakub Ciążela		14.04.2023
Anthony Lagain		30.03.2023
Marta Ciążela		13.04.2023

Artykuł 2

Pieterek, B., Laban, M., Ciazela, J., Muszyński, A. (2022). Explosive volcanism in Noctis Fossae region on Mars. *Icarus, vol. 375, 114851.* https://doi.org/10.1016/j.icarus.2021.114851 (IF$_{2022}$ = **3.657**, pkt. MEiN = **140**)

Pan Bartosz Pieterek był koordynatorem i współwykonawcą wszystkich badań zawartych w publikacji (wykonywanych ze współautorką, Panią Magdaleną Laban), tj. przygotowanie map, proces kartowania, wykonywania pomiarów morfometrycznych zmapowanych form wulkanicznych, datowania powierzchni wulkanów za pomocą metody zliczania kraterów impaktowych oraz interpretacji i rekonstrukcji systemu magmowego. Koncepcja zakładająca rozważenie i przedyskutowanie różnych obszarów źródłowych stanowiących potencjalne miejsce generowania stopów magmowych była pomysłem Doktoranta.

Pan Bartosz Pieterek z Panią Magdaleną Laban byli odpowiedzialni za przygotowanie pierwotnej wersji manuskryptu. Doktorant brał udział w przygotowaniu wszystkich ilustracji (ryciny, tabele, załączniki) zawartych w publikacji. Pan Bartosz Pieterek uczestniczył we wszystkich etapach procesu publikacyjnego, w tym pełniąc funkcję autora korespondencyjnego i udzielając odpowiedzi recenzentom.

Autor	Podpis	Data
Bartosz Pieterek	B. Pieterek	29.03.2023
Magdalena Laban	Magdalena Laban	29.03.2023
Jakub Ciążela		14.04.2023
Andrzej Muszyński	A. Muszyński	29.03.2023

Artykuł 3

Ciążela, J., Bakala, J., Kowalinski, M., Płocieniak, S., Zalewska, N., **Pieterek, B.,** Mrozek, T., Ciążela, M., Paslawski, G., Steslicki, M., Szaforz, Z., Barylak, J., Kuzaj, M., Maturilli, A., Helbert, J., Muszyński, A., Rataj, M., Gburek, S., Józefowicz, M., Marciniak, D. (2022). Concept and design of Martian far-IR ORE Spectrometer (MIRORES). *Remote Sensing, 14, 2799.* https://doi.org/10.3390/rs14122799 (IF$_{2022}$ = **5.349,** pkt. MEiN = **100**)

Pan Bartosz Pieterek włączył się w prace zespołu projektującego spektrometr MIRORES latem 2019 roku. Badania Pana Bartosza Pieterka dotyczące wulkanizmu w prowincji Tharsis posłużyły w wytypowaniu perspektywicznych obszarów badawczych, w kontekście poszukiwań mineralizacji siarczkowej na Marsie. Był on również zaangażowany w opracowanie oraz przygotowanie zestawień graficznych dotyczących charakterystyki spektralnej krzemianów i siarczków. Pan Bartosz Pieterek odpowiadał również za przygotowanie próbki pirytu, dla której zostały przeprowadzone pomiary emisyjności. Doktorant odpowiadał lub uczestniczył w przygotowaniu dużej części rycin (11 z 16) zawartych w publikacji oraz abstraktu graficznego. Niezwykle cenne były również jego uwagi merytoryczne i komentarze podczas edycji tekstu. Przez cały okres realizacji projektu Pan Bartosz Pieterek aktywnie uczestniczył oraz realizował wszystkie powierzone mu zadania w ramach tworzenia i rozwijania spektrometru MIRORES.

Uzupełnienie Projekt MIRORES jest obecnie kontynuowany w ramach grantu Europejskiej Agencji Kosmicznej nr ESA AO/1-10824/21/NL/RA, przyznanego w celu rozpoznania rynku oraz rozwoju ziemskiej wersji spektrometru. Dodatkowo, realizacja grantu ESA stanowi jedynie etap w rozwoju satelitarnej wersji spektrometru, która jest rozwijana przy wsparciu finansowym Polskiej Agencji Kosmicznej (umowa nr PAK/U/167/2022/DBI/MBC). Pan Bartosz Pieterek jest aktywnym członkiem obu zespołów.

Autor	Podpis	Data
Jakub Ciążela		14.04.2023
Jarosław Bąkała		14.04.2023
Mirosław Kowaliński	Kowalinski	14.04.2023
Stefan Płocieniak	Stefan Płocieniak	13.04.2023
Natalia Zalewska	Natalia Zalewska	13.04.2023
Bartosz Pieterek	B. Pieterek	29.03.2023

ZAŁĄCZNIKI

Publikacja 1

Pieterek, B., Ciazela, J., Lagain, A., Ciazela, M. (2022). Late Amazonian dike-fed parasitic volcanism in the Tharsis volcanic province on Mars. *Icarus*, *vol. 386, 115151.* https://doi.org/10.1016/j.icarus.2022.115151 (IF$_{2022}$ = **3.657**, pkt. MEiN = **140**)

Icarus 386 (2022) 115151

Contents lists available at ScienceDirect

Icarus

journal homepage: www.elsevier.com/locate/icarus

Late Amazonian dike-fed distributed volcanism in the Tharsis volcanic province on Mars

Bartosz Pieterek[a,*], Jakub Ciazela[b], Anthony Lagain[c], Marta Ciazela[b]

[a] Institute of Geology, Adam Mickiewicz University, ul. Bogumiła Krygowskiego 12, 60-680 Poznań, Poland
[b] Institute of Geological Sciences, Polish Academy of Sciences, ul. Podwale 75, 50-449 Wrocław, Poland
[c] Space Science and Technology Centre, School of Earth and Planetary Sciences, Curtin University, Perth, Western Australia, Australia

ARTICLE INFO

Keywords:
Martian volcanism
Tharsis
Magmatic plumbing system
Dikes
Mapping

ABSTRACT

Tharsis is the largest volcanic province on Mars and in the solar system. This region includes major volcanoes (Olympus Mons, Alba Mons, Arsia Mons, Pavonis Mons, and Ascraeus Montes) and hundreds of small volcanic cones and vents, whose origin is not yet fully understood. Although the main Tharsis' edifices plumbing system has been extensively studied, smaller volcanoes' origin remains unknown. The formation of those minor volcanic landforms may be related to the large volcanic edifices' evolution, and/or controlled by the fault systems through which magma migrates towards the Martian surface. In this study, we analyzed the central part of the Tharsis volcanic province using satellite images with a resolution of ~6 m/px from the Context Camera onboard the Mars Reconnaissance Orbiter (CTX/MRO). We identified and mapped 659 volcanic edifices >1 km in diameter. We analyzed (1) their spatial distribution, (2) alignment of summit craters, and (3) surface model ages derived from crater counting. We found that volcanic edifices are unevenly distributed across the Tharsis province and proposed that their formation is controlled by at least six individual magma-plumbing systems associated with major edifices: Olympus Mons, Alba Mons, Arsia Mons, Pavonis Mons, Ascraeus Mons, and Uranius Mons. Their summit alignment orientations indicate they were controlled by radial and circumferential dikes originated from magma sources beneath the six central volcanoes, either magma chambers in the crust or other magmatic underplates at the base of the crust. Volcano flanks of distributed volcanoes are of similar age or younger than the summit calderas of the associated central volcano indicating a common magmatic system. Magma migration and eruptions from distributed volcanoes may thus extend beyond the magma waxing periods when magma supply was high enough to sustain summit eruptions. The relatively young age of documented volcanic activity within the Tharsis province may imply recently active hydrothermal systems triggered by magma-water interaction.

1. Introduction

Early thermal-magmatic models of Martian crust evolution indicate that volcanism considerably diminished after 4 Ga, and most likely stopped a few hundreds of millions of years ago (Weizman et al., 2001; Hauck and Phillips, 2002; Breuer and Spohn, 2003). Recent data suggest, however, that Mars was volcanically active throughout the Late Amazonian until <10 Ma (Neukum et al., 2004; Werner, 2009; Platz and Michael, 2011; Robbins et al., 2011; Xiao et al., 2012). Thus, volcanic processes played a major role in shaping the surface of Mars. Young terrains related to volcanic activity have been found in many locations on Mars, including the second largest volcanic province, Elysium Planitia with Cerberus Fossae (Neukum et al., 2004; Horvath et al., 2021; Krishnan and Kumar, 2021). In addition, the newest seismic data retrieved from the *Insight* lander indicate a liquid core (Stähler et al., 2021), and suggests a relatively deep source of seismic activity (Clinton et al., 2021). These interpretations imply the possibility of current mantle activity, and consequently, the possibility of magmatic activity in the Martian crust, which could give rise to recent or future volcanic eruptions. Khan et al. (2021) claimed that the Martian crust is highly enriched in heat-producing (radioactive) elements resulting in higher temperatures of the crust compared to the Martian interior. Thus, volcanic activity on Mars might not have vanished but is currently dormant. The activity of major volcanoes in the Tharsis region has been known to cease <100 Ma (Neukum et al., 2004; Werner, 2009; Robbins et al., 2011; Richardson et al., 2017; Ciazela et al., 2019). Moreover, the

---

* Corresponding author.
E-mail address: barpie@amu.edu.pl (B. Pieterek).

https://doi.org/10.1016/j.icarus.2022.115151
Received 5 October 2021; Received in revised form 13 June 2022; Accepted 23 June 2022

volcanism on the flanks of the Tharsis Montes, Olympus Mons, and Alba Mons even postdates the summit caldera activity of the central volcanoes (Crumpler and Aubele, 1978; Neukum et al., 2004; Hauber et al., 2011; Pieterek et al., 2019; Krishnan and Kumar, 2021).

Tharsis (15°S to 45°N, 90 to 140°W) hosts hundreds of small volcanic edifices and vents in addition to twelve major volcanoes (Fig. 1). This large set of volcanic edifices consists of various geomorphological types including low shields and scoria cones volcanoes. While low shield morphology indicates effusive eruptions (Bleacher et al., 2007, 2009; Hauber et al., 2009), scoria cones suggest explosive-style volcanism in Tharsis (Brož, 2010; Brož and Hauber, 2012, 2013; Brož et al., 2015, 2021; Pieterek et al., 2022a). Although Tharsis is characterized by the thickest crust on Mars (>80 km in some places; Tenzer et al., 2015), there is a regional variability of a crustal thickness (Genova et al., 2016). Younger shields, such as Olympus Mons, show crustal thinning (Zuber, 2000). The thickened lithosphere of Tharsis implies an important role of crustal loading, supported by recent gravity and topography data (Zuber, 2000, 2001; Zhong and Roberts, 2003; Wieczorek and Zuber, 2004; Beuthe et al., 2012). The Tharsis volcanic activity could also have been sustained by long-standing mantle plumes or a superplume (Kiefer, 2003; Zhong, 2009; Breuer and Moore, 2015; Plesa et al., 2018; Lagain et al., 2021).

Considering various hypotheses of Tharsis origin along with a long-term magmatic activity lasting from Early Noachian (Bouley et al., 2016) up to the Late Amazonian (Fig. 1), there is still a gap of knowledge about the magma sources feeding major Tharsis volcanoes and adjacent distributed volcanoes. The distributed volcanoes are located in the summit calderas or on the flanks of the central edifices, or often further away (Fig. 1). On Earth, the volcanic activity of central volcanoes is often accompanied by eruptions fed by lateral dikes forming smaller volcanic edifices (Nakamura, 1977; Carr and Pontier, 1981; Corazzato and Tibaldi, 2006; Yokoyama, 2015). Thus, it seems necessary to verify whether and how the Martian distributed volcanism is geologically linked to the volcanism of major volcanoes.

To date, several studies aimed at the detailed mapping of volcanic and tectonic features in Tharsis (Bleacher et al., 2007, 2009; Hauber et al., 2009; Bouley et al., 2018; Richardson et al., 2020, 2021), and their surface dating (Brož, 2010; Hauber et al., 2011; Christoph and Garry, 2017; Pieterek et al., 2019). None of the studies, however, combined detailed mapping data and ages of distributed volcanoes with the ages of the latest volcanic activity of the nearby central Tharsis volcanoes. In addition, it seems that the investigation of morphology and summit alignments of volcanic edifices may be crucial in reconstructing the volcano-tectonic regime and magma plumbing system beneath the Tharsis dome. This study attempts to fill this gap by characterizing the system of small volcanic edifices in both space and time.

To test the affinity between the distributed and the central Tharsis volcanoes, we investigate the spatial distribution of volcanic edifices along with orientations of their summit craters or fissures, and their surface ages. These efforts have the overall goal of deciphering the geological origin of distributed volcanism and the volcanic processes involved in its formation. Here, we use geomorphological features of volcanic edifices along with their surface ages to reveal their relationship with the major Tharsis volcanoes. Besides, we propose that magma chambers or underplates beneath Olympus Mons, Tharsis Montes, and Alba Mons may still be active.

2. Geological settings

Tharsis, which is the largest volcanic province in the solar system (Bouley et al., 2018), hosts the twelve central volcanic edifices (Fig. 1). The 21.3-km-high Olympus Mons is accompanied by other giant volcanoes such as Alba Mons and three Tharsis Montes including Arsia Mons, Pavonis Mons, and Ascraeus Mons. In addition, there are seven large volcanoes including Uranius Mons, Tharsis Tholus, Biblis Tholus, Ceraunius Tholus, Ulysses Tholus, Uranius Tholus, and Jovis Tholus (Fig. 1). In this study, we consider the central part of the Tharsis region focusing on the surroundings of the twelve major volcanoes that exhibit a complex evolutional history of their summit caldera activity (Werner, 2009; Robbins et al., 2011). We mapped and investigated the region limited by the hemispheric dichotomy boundary on the northern and western part of Tharsis but including the flanks of Olympus Mons north of the boundary. Elsewhere, the study area is limited by Tempe Terra on the northeast, Lunae Planum on the east, Syria Planum on the southeast, and Terra Cimmeria-Sirenum on the south and southwest, which are all not considered here (Fig. 1). The five largest volcanoes are interpreted to be Amazonian in age (Tanaka et al., 2014), whereas the latest volcanic activity of other volcanic edifices is mostly Hesperian. These major volcanoes are surrounded by numerous smaller volcanic edifices concentrated in several clusters unevenly distributed within Tharsis (Richardson et al., 2021). The vast lobate flows covering the majority of the Tharsis dome, especially in the surroundings of Tharsis Montes, Alba Mons, and Uranius group volcanoes, are interpreted as Amazonian and Hesperian volcanic unit (AHv; Fig. 1). Within this large volcanic unit, Tanaka et al. (2014) distinguished several smaller units, various in age, emplaced mostly in the vicinity of Tharsis Montes, Olympus Mons, and Ceraunius Fossae. These terrains host clusters of distributed volcanic edifices that have been previously investigated within the Tharsis Montes region (Bleacher et al., 2007, 2009; Hauber et al., 2011), near Olympus Mons (Bleacher et al., 2007; Peters and Christensen, 2017; Mouginis-Mark and Wilson, 2019), and within the Ceraunius Fossae (Hauber et al., 2009; Christoph and Garry, 2017; Krishnan and Kumar, 2021).

The earliest volcanic activity of Tharsis is recorded mostly by the growth events of the Uranius Tholus shield volcano (>4.0 Ga) followed by its summit caldera emplacement (~3.9 Ga; Werner, 2009). Age estimations of the most recent summit calderas for the twelve major Tharsis volcanoes (Ciazela et al., 2019) show a decreasing but relatively continuous magmatic activity through Amazonian. Recently, Lagain et al. (2021) suggested that Amazonian volcanism in Tharsis (from at least 2.4 Gyr until at least 330 Myr ago) was likely sourced by a continuously active superplume that is deep-seated in the mantle, since the beginning of the Tharsis formation. The Tharsis superplume is likely emplaced underneath the entire volcanic province embracing individual mantle plumes that might be still active and generate magma ascending through central volcano magma chambers and dikes to the distributed volcanoes. The youngest volcanic activity within Tharsis, dated to 2.4 Ma was documented by Neukum et al. (2004) for lava flows on the Olympus Mons flanks. In addition, Krishnan and Kumar (2021) found young lava flows of 8.1 Ma in the Ceraunius Fossae region, south of Alba Mons (Fig. 1). Despite many hypotheses on the genesis of Tharsis, there is a consensus that the Tharsis construction began early in Martian history, most likely in the Noachian period continued until Amazonian (Phillips et al., 2001; Johnson and Phillips, 2005; Werner, 2009; Bouley et al., 2016, 2018; Lagain et al., 2021).

3. Methods

3.1. Volcanic edifices and summit alignments mapping

The volcanic edifices and fissures are identified using the Thermal Emission Imaging System (THEMIS) daytime infrared mosaic (Edwards et al., 2011) onboard Mars Odyssey (MO) (spatial resolution of ~100 m/pixel) and mapped using the high-resolution mosaic (6 m/pixel) of the Context Camera (CTX) dataset onboard of the Mars Reconnaissance Orbiter (MRO) (Dickson et al., 2018). The combination of the THEMIS and CTX imagery is well suited to identify the distribution of volcanic landforms over the wide Tharsis region (Fig. 2). In the vicinity of Olympus Mons and Arsia Mons, we analyzed images from the High-Resolution Imaging Science Experiment (HiRISE; 25–32 cm/pixel). The HiRISE and CTX images allowed distinguishing small volcanic edifices (1–2 km in diameter) and verifying whether fissures consisting of

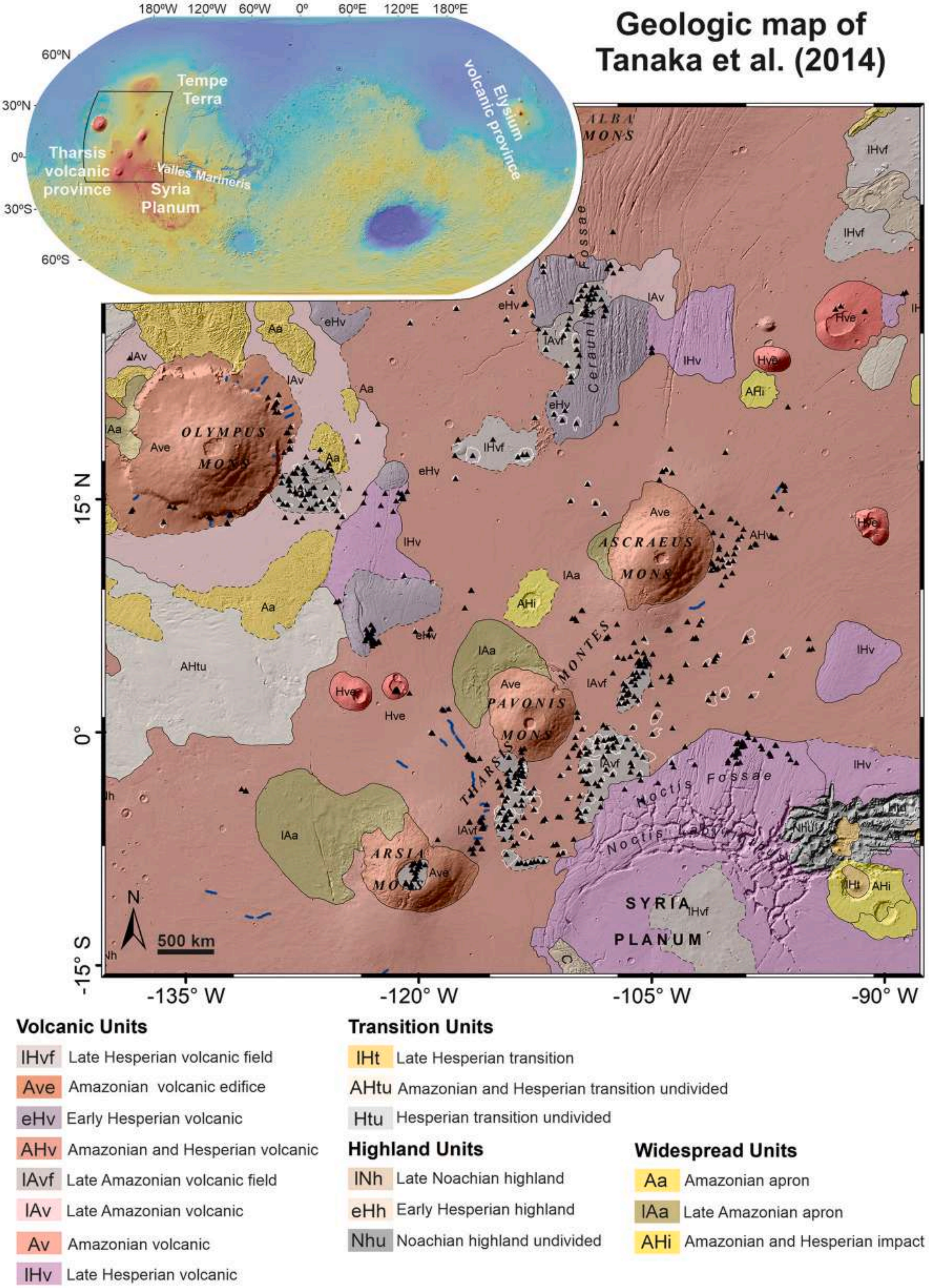

Fig. 1. Geologic map of the Tharsis province adapted from Tanaka et al. (2014). The 12 major volcanoes are accompanied by 659 distributed volcanoes >1 km (black triangles; the contour is marked in white) as well as volcanic fissures (in blue lines). For more details, the reader is referred to Supplementary Data 2. The study area covers the small volcanic edifice clusters in the three major regions associated with Olympus Mons, Tharsis Montes, and (most likely) Alba Mons. In most cases studied herein, volcanic landforms are located on the Amazonian and Hesperian volcanic (AHv) as well as Late Amazonian volcanic field (lAvf) units. The inset indicates the position of the Tharsis province with respect to the Valles Marineris and is based on the MOLA shaded relief basemap (128 pixels/degree) adapted from Tanaka et al. (2014) and digital elevation model (DEM) from MOLA/MGS (128 pixels/degree). (For interpretation of the references to colour in this figure legend, the reader is referred to the web version of this article.)

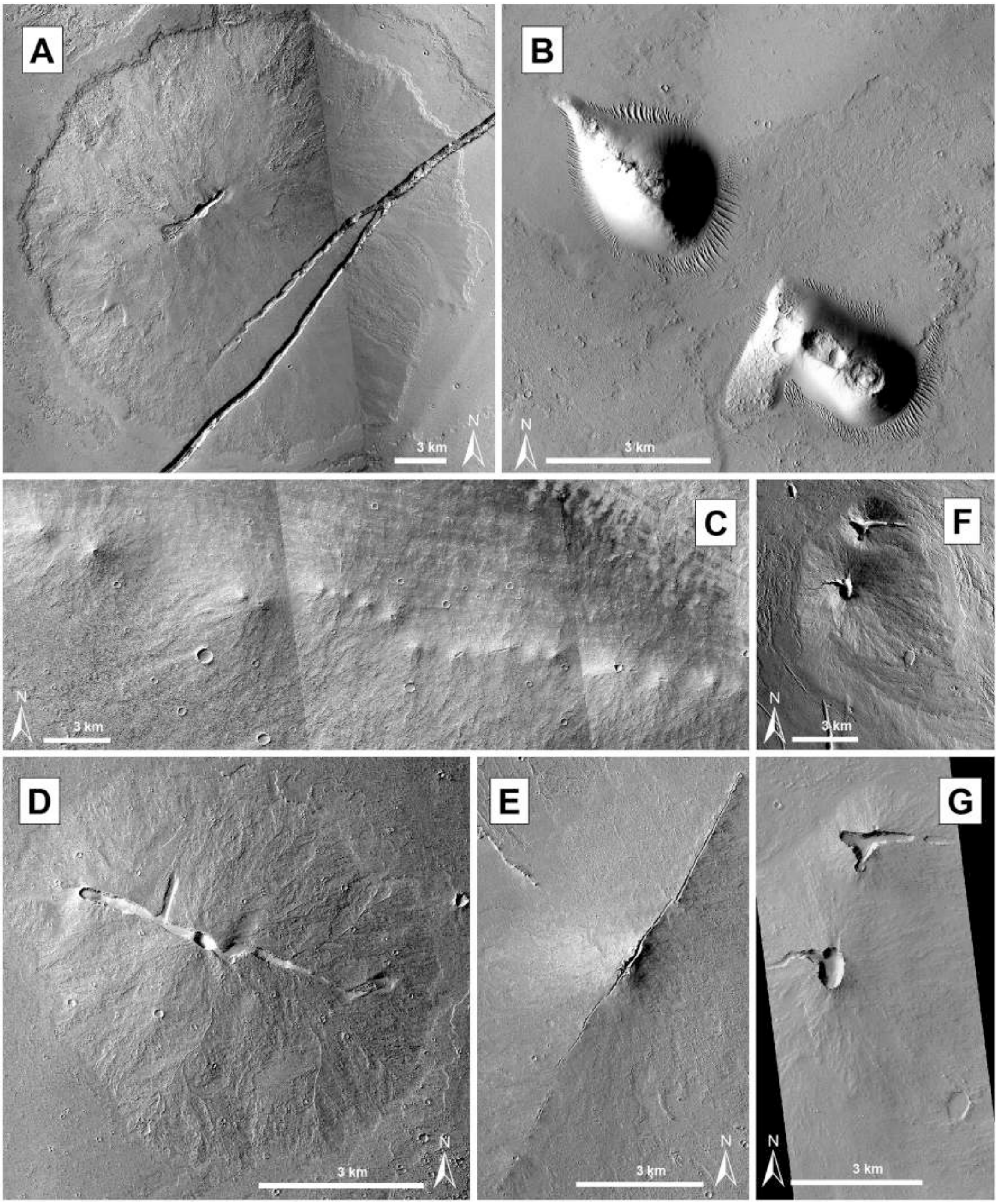

Fig. 2. (A) Conical volcanic edifice (low-shield volcano) with elongated summit caldera. The southwestern flank of the volcanic edifice has been later cut by a lava channel. CTX images P21_008237_1800 and P07_003752_1796. (B) Two individual volcanic cones with relatively steep flank suggest likely explosive origin in the vicinity of the Noctis Fossae region. CTX image F04_037508_1798. (C) Volcanic fissure composed of several <1-km-large edifices. CTX mosaic from the P19_008447_1697, G23_027146_1697, and P22_009449_1698 images. (D) Low-shield volcano with a well-developed summit fissure. CTX image P22_009686_1954. (E) Fissure-sourced volcanic edifice in the vicinity of Olympus Mons CTX image P22_009680_1954. (F and G) The CTX (F02_036427_1847) and HiRISE (ESP_036427_1850) images showing two volcanic edifices that overlapped by their lava aprons.

several individual cones with overlapping flanks are of volcanic origin. Mapping of the volcanic edifices was conducted using ArcGIS software.

In this study, we defined the volcanic landforms as topographic features associated with lava flows or pyroclastic deposits, mostly elevated compared to the surrounding area, often revealing a central volcanic vent (Fig. 2). Some of the volcanic landforms in Tharsis do not exhibit intact volcanic vents. However, their morphological characteristics such as size, shape, and elevation are similar to other mapped edifices of volcanic origin (Fig. 3). Similar mapping was earlier provided by Bleacher et al. (2010) and completed by Richardson et al. (2020) (Fig. S1 in Supplementary Data 1), who mapped volcanic vents locations in Tharsis that were distinguished as topographic depressions associated with lava flows or pyroclastic deposits. Here, we completed the previous catalogs by mapping the contours of the topographic base of each volcano edifice or the youngest lava flow extending from the summit that is recognizable on the CTX images (Supplementary Data 2). Such detailed information will be critical for future quantitative studies on the rate of magma supply in the Tharsis region. The entire study area was carefully

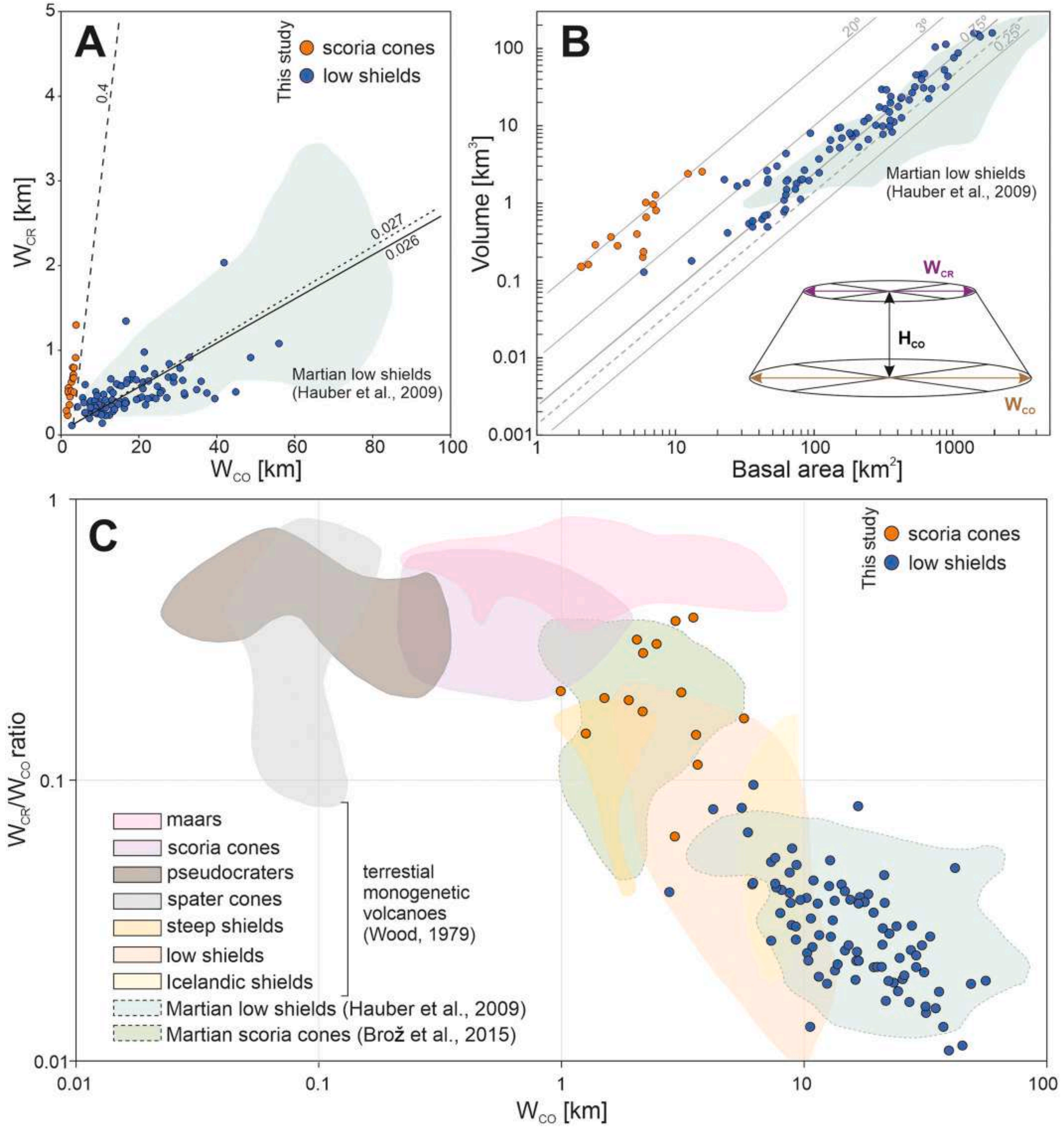

Fig. 3. Morphometric parameters of studied volcanic edifices within Tharsis. (A) Basal width of the volcanic edifice (W_{CO}) versus the width of the summit crater (W_{CR}) was measured perpendicular to the elongation (data from Table 4). The solid line represents the best fit (linear regression) of W_{CR}/W_{CO} ratio of 0.026 obtained by Hauber et al. (2009). The dotted and dashed lines have been adapted from Hauber et al. (2009) and mark trends for terrestrial composite volcanoes determined by Wood (1978) of 0.027 and terrestrial cinder cones of 0.4 (W_{CR}/W_{CO} ratios) (Wood, 1980). (B) Volume of the edifices versus their basal area. For any given basal area, a lower flank slope results in a smaller volume. The lines on the plot are adapted from Hauber et al. (2009) who has shown that the best fit for the low shield flank slopes in Tharsis is 0.43° (dashed line). Moreover, we included volcanic edifices described by Brož and Hauber (2012) as scoria cones and also similar cones found within Tharsis that are significantly different than typical low shields. (C) W_{CR}/W_{CO} ratio versus W_{CO} of the studied Martian edifices (data from Table 4) along with various types of terrestrial monogenetic volcanoes (Wood, 1979). There is clear evidence that most of the studied volcanoes represent Martian low shields that are partially overlapping with terrestrial low shields. We also found a distinct morphological set of edifices (likely scoria cones) indicating the different styles of volcanism within Tharsis that is plotted between the terrestrial low shield or steep shield and scoria cones or maars.

mapped and further compared to the catalogs provided by Bleacher et al. (2010) and Richardson et al. (2020) (see Fig. S1 for more details). In Tharsis, there are many depressions on the flanks and in the vicinity of major volcanoes, similar to volcanic vents, showing common morphological characteristics. However, in this study, without any evidence of the eruptive activity, they cannot be unambiguously classified as volcanic landforms (Richardson et al., 2021). Although most of the volcanic landforms have been interpreted and mapped the same in all the three studies, we documented some volcanic landforms that have not been included in the previous catalogs provided by Bleacher et al. (2010) and Richardson et al. (2020) (see Fig. S1 for more details). In some cases, we used different terminology. For example, Richardson et al. (2021) mapped a significant number of small vents in the vicinity of Arsia Mons, whereas we classified these landforms as volcanic fissures consisting of an array of adjacent or superimposed volcanic edifices (Fig. 2C). Summit alignments and edifice basements contours of individual cones are difficult to determine in plan view but volcanic fissures that control them likely indicate directions of subsurface dikes, which resemble those of terrestrial volcanic fissure systems such as Laki (Thordarson and Self, 1993) and Krafla fissure eruptions (Hjartardóttir et al., 2012). The difference in the number of mapped features (>1100 vents mapped by Richardson et al., 2020) is also caused by differences in the defined study areas. In contrast to Richardson et al. (2021), we focused only on the Tharsis region, which is dominated by late Amazonian volcanism. We excluded the regions of Tempe Terra and Syria Planum because they are significantly older than Tharsis (majority between 800 and 400 Ma and 1600–800 Ma, respectively, according to Hauber et al. (2011)). In addition, we excluded from the mapping the volcanic vents on the flanks of Olympus Mons as we believe they represent the surface manifestation of the effusive eruptions forming lava flows, sometimes with no evident vents, that cover the flanks of Olympus Mons (Mouginis-Mark and Christensen, 2005; Mouginis-Mark and Wilson, 2019) and do not construct typical volcanic edifices. Shapefiles of the mapped volcano areas have been attached to this manuscript as Supplementary Data 2.

We determined the orientations of summit crater alignments for the whole set of distinguished landforms (Fig. 4). These orientations have been measured either along the elongated summit craters or central fissure vents (Figs. 2A, D, E). Using these orientations, we classified these volcanic structures into radial or circumferential sets. This classification was based on the angle measurements between the potential

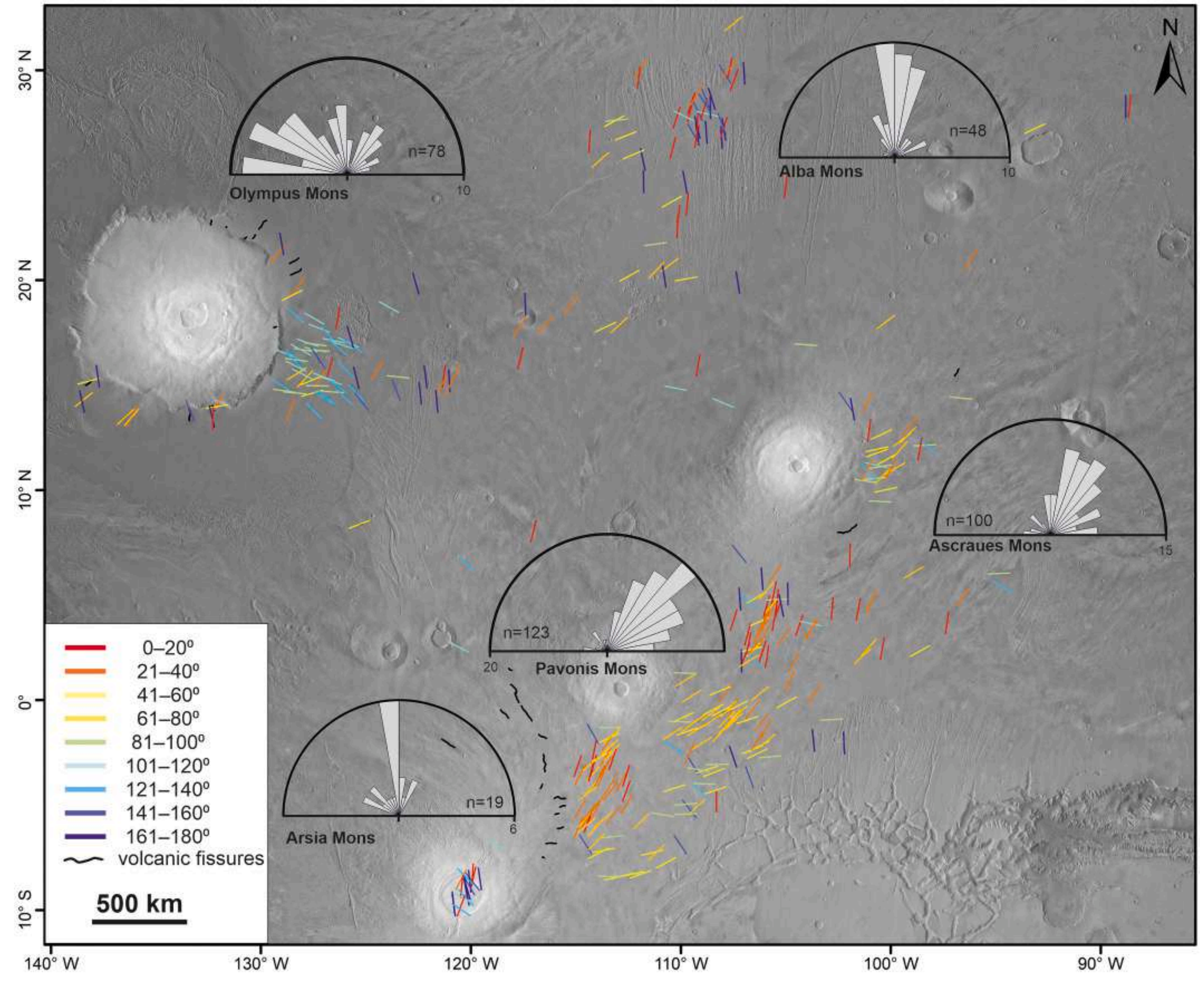

Fig. 4. Distribution map of summit crater alignments clustered into 20° classes in Tharsis. Rose diagrams showing the summit alignment orientations of the measured structures (n – number of measurements) within the distinguished subprovinces associated with the major Tharsis volcanoes (Alba Mons, Arsia Mons, Ascraeus Mons, Olympus Montes, Pavonis Mons, and Ascraeus Mons). Using this dataset, we interpreted the course of radial and circumferential dikes on the Martian surface. (For interpretation of the references to colour in this figure legend, the reader is referred to the web version of this article.)

dike in plan view, migrating outwards the central volcano and the measured summit alignment for individual structures. The structures were classified into radial (0–30°) and circumferential (60–90°) sets, whereas all remaining structures (30–60°) have been marked as non-classified (Fig. 5). The rose diagrams were plotted using Stereonet 10.2. For edifices exhibiting elongated summit craters, we measured both the basal width of the edifices and the width of the summit craters in two directions: parallel and perpendicular to the summit crater elongation (Table 4 and Fig. 3) using the CTX global mosaic base map (Dickson et al., 2018).

3.2. Model age determination

We determined the surface ages of areas representing one volcanic event, for example, one lava flow (Figs. 6 and S2–S97 in Supplementary Data 1). The outlines of the dated areas were determined based on the morphology of the lava flows visualized on the CTX images (Supplementary Data 3). Although in some cases, there is clear morphological evidence of the multiple eruption events from the same volcano edifice (e.g., superposition of lava flows), we dated only the youngest surface that we distinguished on the image. For age-dating, we used the most representative set of volcanic edifices unevenly distributed throughout

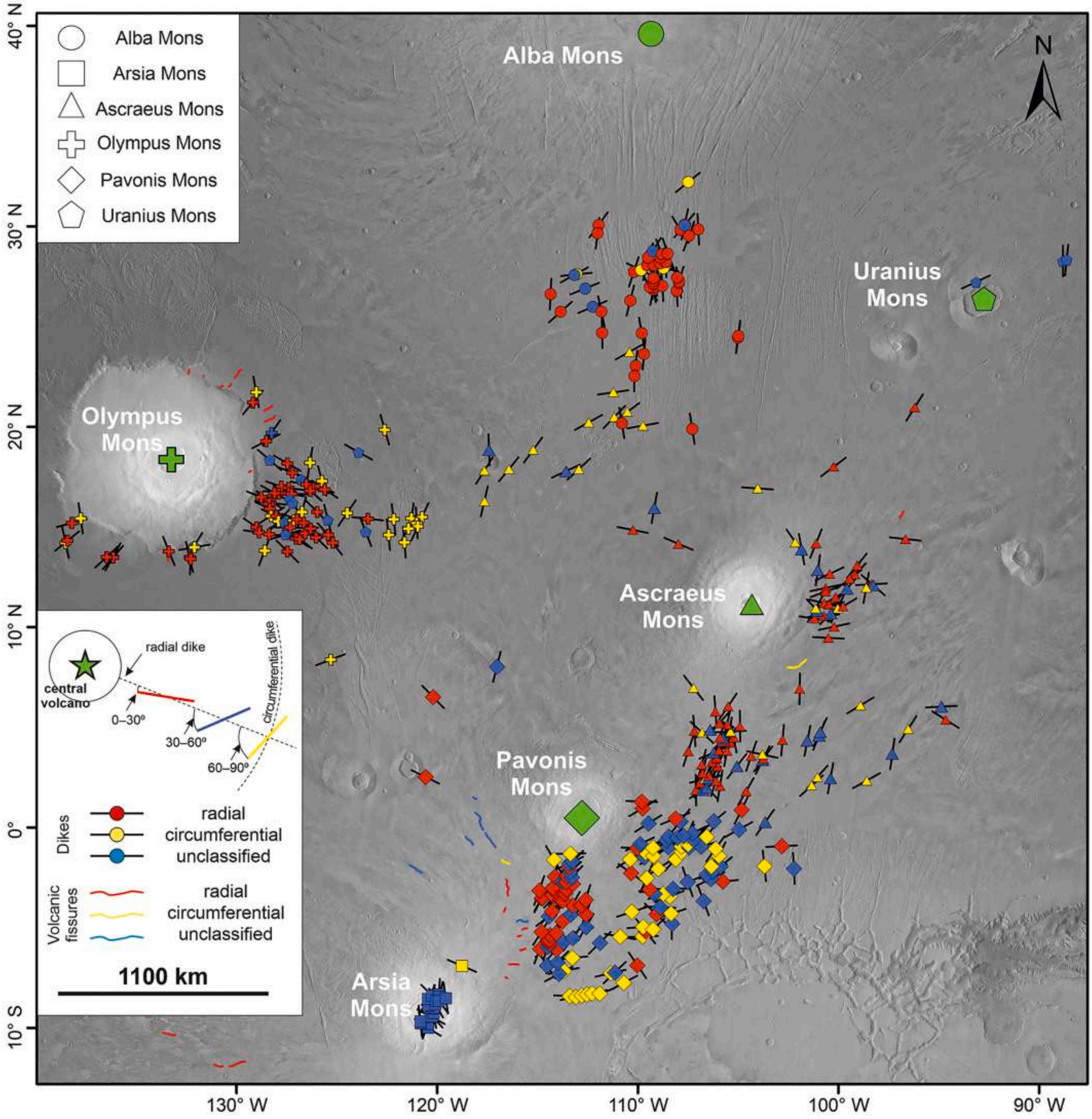

Fig. 5. Proposed distribution of radial and circumferential dikes around central Tharsis volcanoes based on the orientations of summit craters and fissures in small distributed volcanoes. The left insert shows the methodology applied in this study to classify volcanic structures. (For interpretation of the references to colour in this figure legend, the reader is referred to the web version of this article.)

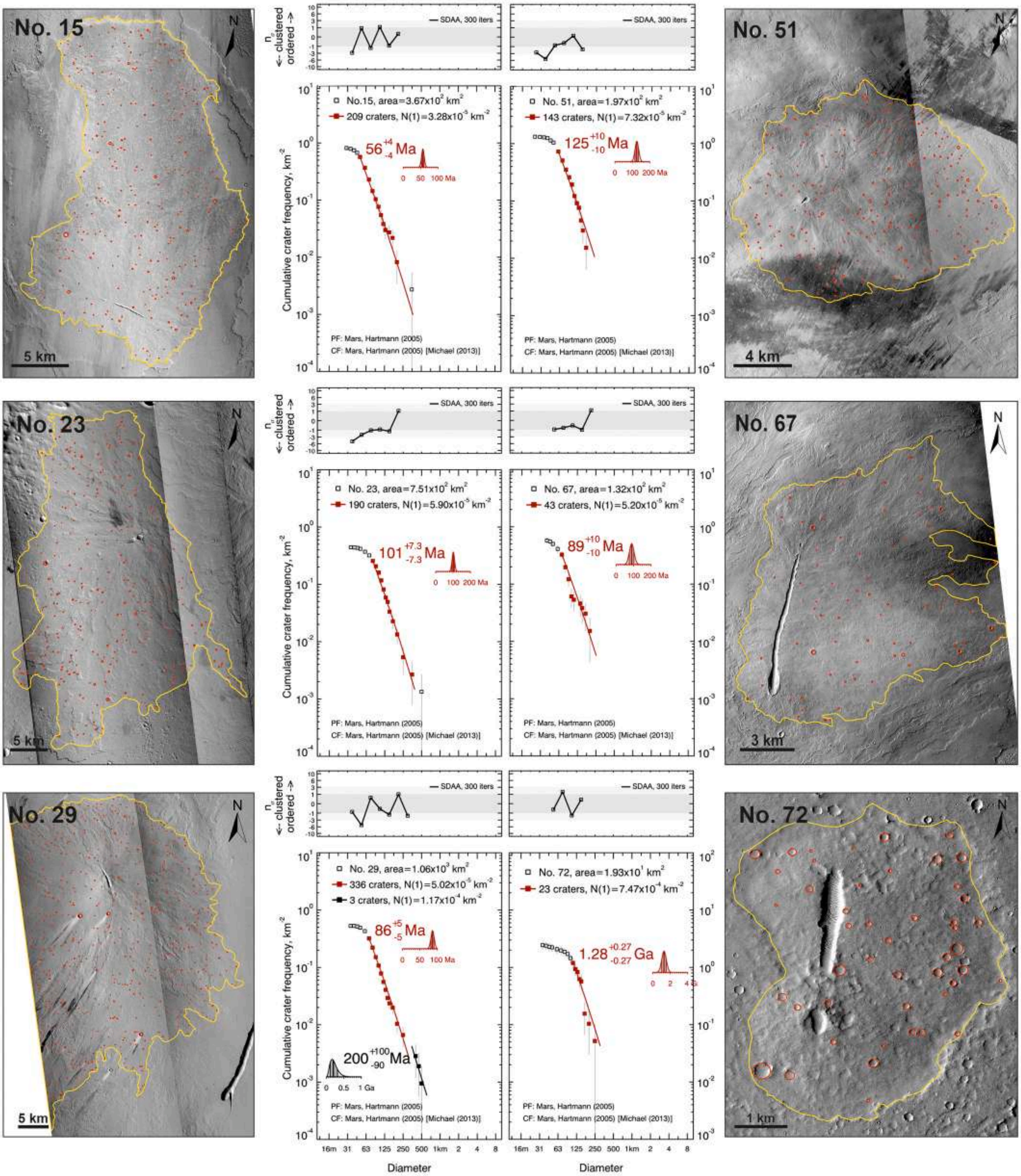

Fig. 6. Example of crater counts and associated Crater Size-Frequency Distributions (CSFD) and absolute model ages (± is 1σ as age uncertainty based on the number of craters fitted) measured on six vents located on each province considered in this study (for more details see Table 2). The dated areas (outlined in yellow) together with the mapped impact craters (red circles) are shown on CTX images downloaded from the ASU website: (http://viewer.mars.asu.edu/viewer/ctx#T=0; available on 10.02.2022). The upper panels of CSFD plots are results of randomness analyses using the (inversed) standard deviation of the adjacent area (SDAA) parameter (Michael et al., 2012; see Section 3.2). For more details, the reader is referred to Table 2 and Supplementary Data 3. (For interpretation of the references to colour in this figure legend, the reader is referred to the web version of this article.)

the Tharsis region (Figs. 7 and S2). The dated areas range from 8 to 2850 km^2 with a median value of 185 km^2 (Table 2). Although we used a wide range of dated area sizes, we did not observe any bias in obtained ages related to area size (Fig. S98A in Supplementary Data 1).

The age of the latest volcanic activity of the individual volcanic edifices is estimated by counting craters with diameters $> \sim 50$ m (varies to some extent depending on the volcanoes' diameter; see Table 2) using the ArcGIS extension CraterTools2.1 (Kneissl et al., 2011) on the CTX mosaic base map (Dickson et al., 2018). Although there is still ongoing discussion about the crater sizes usable for dating (e.g., McEwen et al., 2005; Werner, 2009; Fassett, 2016; Williams, 2018), the advances in the quality of remote observations and image processing techniques allow scientists to conduct regional or even local studies that require using smaller craters for dating (<50 m). For example, Brož (2010) and Hauber et al. (2011) have used craters down to 30 m for isochrons fitting based on CTX images of low shield volcanoes in Tharsis.

Here, we mapped a total of ~15,000 impact craters for the entire set of 94 volcanic edifices. The number of impact craters for individual areas ranges from 15 to 746. The number of craters used for fitting Crater Size-Frequency Distributions (CSFDs) with isochrons varies from 5 to 463 (for more details, see Table 2 and Figs. S3–S96). Although we used a small number of craters for some model age determinations, we did not observe any correlation between the obtained ages and the number of fitted craters (Table 2, Fig. S98B). Such correlation could be interpreted as a bias due to crater obliteration by erosion processes (Lagain et al., 2020). Crater statistics and derivation of crater model ages, including errors, were carried out using CraterStats II (Michael and Neukum, 2010). We fitted the CSFD using the Hartmann (2005) chronology model and the Poisson timing analysis, allowing us to avoid any bias related to the crater size binning (Michael et al., 2016). In addition, we compared our results using two other chronology systems: Ivanov (2001) and Hartmann and Neukum (2001) (Table 2). The shapefiles including dated area, mapped impact craters, and CraterStats files for the entire set of dated volcanic edifices are attached to this manuscript as Supplementary Data 3.

To evaluate the potential contamination of secondary craters in our counting, the degree of clustering was measured at various crater diameter bins using the Randomness Analysis tool (Michael et al., 2012). The standard deviation of the adjacent area (SDAA) was determined for each size bin using $\sqrt{2}$ intervals. This technique divides the count areas into several subareas, separated by boundaries defined by mid-distances between the craters. The inversed SDAA values (n_σ) are displayed above the chronology curves for each dated volcanic edifice (Figs. S3–S96). The higher are clustering of defined subarea sizes and related standard deviation values (Michael et al., 2012; Williams, 2018; see SDAA plot above chronology curves where clustering increases downward; Fig. S3–S96) the higher is the probability of surface contamination by secondary craters or spatially heterogeneous resurfacing processes. The non-random diameter ranges are excluded from the fitted crater population (i.e. $n_\sigma \geq \pm 3$).

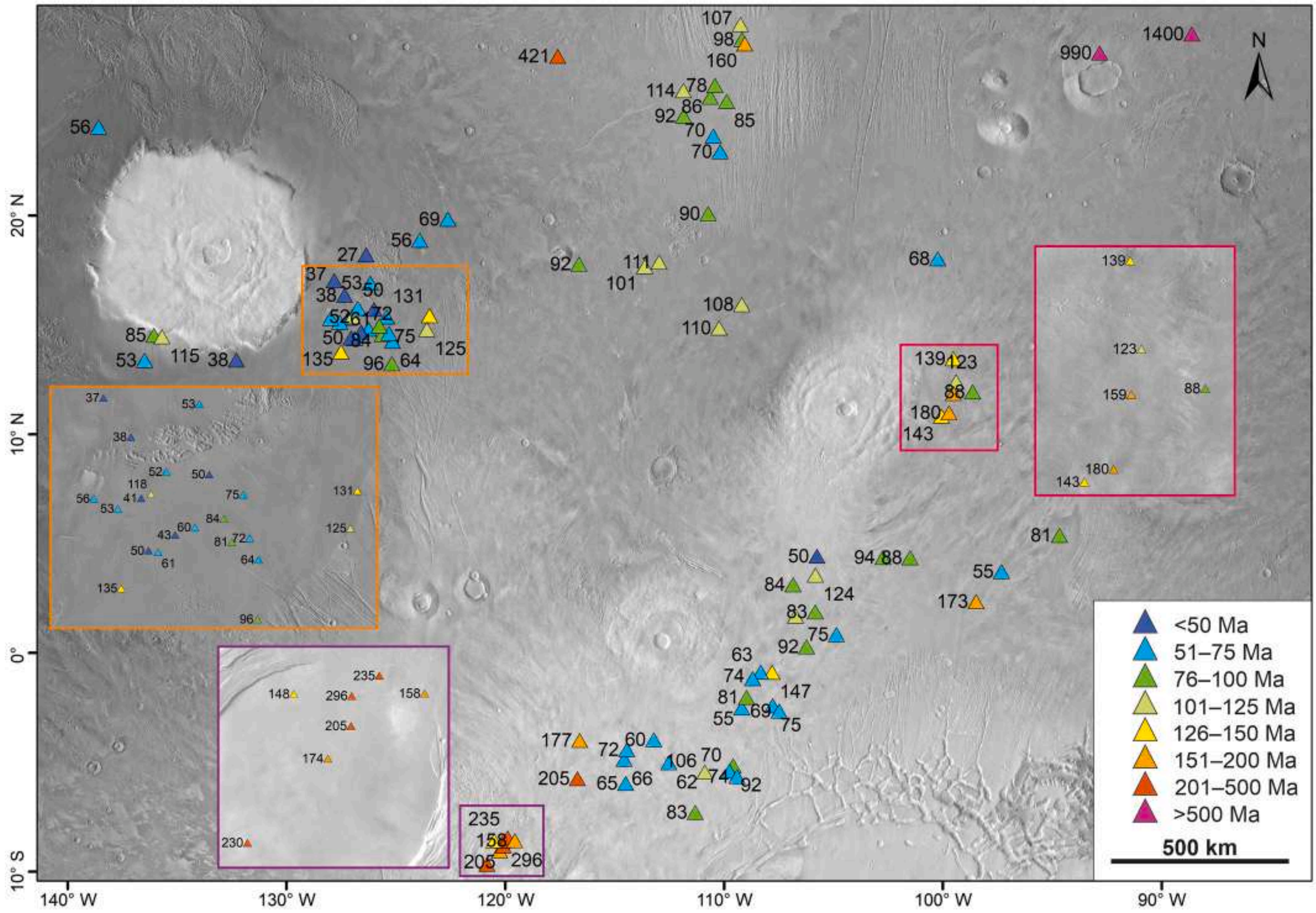

Fig. 7. The Tharsis region with 94 dated landforms (triangles). The numbers adjacent to the symbols represent the ages of the latest volcanic activity. To derive the ages, we used the Poisson fitting technique developed by Michael et al., (2016) together with the Hartmann (2005) production and chronology functions. Background image: MGS MOLA–MEX HRSC Blended DEM Global 200 m v2 (Fergason et al., 2018) and THEMIS-IR Day Global Mosaic 100 m (Edwards et al., 2011). (For interpretation of the references to colour in this figure legend, the reader is referred to the web version of this article.)

4. Results

4.1. *Spatial distribution of volcanic edifices and orientation of summit alignments*

Except for the twelve well-known main volcanoes, Tharsis volcanic province hosts at least 659 smaller volcanic landforms (>1 km in diameter) (Fig. 1). Using the combination of THEMIS and CTX imageries, we divided and grouped the set of 659 volcanic landforms into the five major subprovinces using their locations with respect to the central volcanoes and orientations of summit alignments. The five subprovinces are composed of several dozens of either multi-cone clusters or isolated volcanic edifices (Table 1). To obtain the volcano-tectonic context of the mapped landforms, the orientations of the summit alignments have been measured for 379 volcanic edifices that exhibited the elongated volcanic summit craters or central fissure vents (Fig. 4).

Based on the spatial distribution and orientations of volcanic summit alignments, we distinguished five major subprovinces associated with the major Tharsis volcanoes: (1) Olympus Mons – 101 edifices, (2) Alba Mons – 51 edifices, (3) Arsia Mons – 98 edifices, (4) Pavonis Mons – 160 edifices, and (5) Ascraeus Mons – 165 edifices (Table 1 and Fig. 1). In addition, we mapped 5 volcanic edifices in the vicinity of Uranius Mons, 11 edifices within the Ulysses Tholus caldera, 63 scoria cones in Ulysses Colles and Noctis Fossae (Brož and Hauber, 2012; Brož et al., 2015; Pieterek et al., 2022a, 2022b), whereas 5 edifices are isolated elsewhere. Assuming geological affinity between the subprovinces of volcanic edifices and the nearby-located major Tharsis volcano, each subprovince has been analyzed separately to identify potential magma supplying sources.

4.1.1. *Olympus Mons*

The giant Olympus Mons volcano is accompanied by a set of 101 much smaller volcanic edifices of various sizes (1–70 km in the longest axis including lava flows; Table 1). Although most of the volcanic edifices are clustered in the eastern set, we found several isolated edifices around the outer rim on the northwestern and southwestern sides of the Olympus Mons. We measured the summit alignment orientations in 78 edifices and obtained the mean direction of ~N126E (Fig. 4), which included 1) edifices showing radial ($n = 45$), and 2) revealing concentric ($n = 22$) orientations around Olympus Mons (Fig. 5). The remaining alignments ($n = 11$) were not classified based on a cut-off test that classified them on the angle measurements between the potential dike in the plan view migrating outwards the central volcano. The structures were classified into radial (0–30°) or circumferential (60–90°) sets, whereas the remaining structures (30–60°) were not classified (Fig. 5). The radial-set of edifices shows the average summit alignments direction of ~N115E. The concentric-set is focused in two locations with directions of ~N030E and ~ N175E. Based on the above observations, especially the spatial distribution of small volcanic edifices with their summit alignment orientations, the volcanic edifices within the studied subprovince are emplaced ~750 km from the center of the summit caldera and belong to Olympus Mons magmatic system. Mouginis-Mark and Wilson (2019) found even more distant structures related to Olympus Mons volcanic systems such as Aganippe Fossa (7°00′S, 233°40′E) and a graben within Phoenicis Lacus (13°00′S, 233°40′E) located up to 1700 and 2500 km southeast from the Olympus Mons edifice.

4.1.2. *Ceraunius Fossae*

In the Ceraunius Fossae south of Alba Mons, we found 74 volcanic edifices, with 60 summit alignments measured to distinguish a feeding magma reservoir emplaced beneath either Alba or Ascraeus Mons. From this set, 39 measurements show mainly radial orientations in relation to Alba Mons, revealing the direction of ~N010E, with one volcano likely exhibiting a concentric orientation of ~N050E. In the southern part of Ceraunius Fossae, we found another group of 13 volcanic edifices characterized by summit alignments with almost perpendicular orientations to those from the radial set of Alba Mons. They show a consistent trend of ~N065E. As these volcanic edifices are located close to the triple point between Olympus Mons, Alba Mons, and Ascraeus Mons, we have considered the aforementioned potential magmatic systems. Using their spatial distribution together with summit alignment orientations, we observed that these 13 edifices are emplaced along SW-NE-trending circular curves whose center is located in Ascraeus Mons caldera. Therefore, we classified this group of 13 edifices into the Ascraeus Mons subprovince.

4.1.3. *Tharsis Montes*

In the Tharsis Montes, 423 volcanic landforms were mapped in three subclusters 1) nearby the Arsia Mons summit caldera and its northern flanks, 2) on the south and southeastern flanks of Pavonis Mons, and 3) southern and eastern flanks of Ascraeus Mons.

Arsia Mons, revealing the oldest caldera activity among the three Tharsis Montes volcanoes (Neukum et al., 2004; Werner, 2009; Richardson et al., 2017), hosts distributed volcanic edifices both inside the summit caldera and on the northeastern flank, beyond the base of the main edifice. We found 18 small edifices within the summit caldera (4–14 km large in the long axis) characterized by summit alignment orientations of ~N175E. These orientations are close to the linear trends of vent spatial density (~N015E) provided by Connor et al. (2019), which are each parallel to graben sets that cut the flanks of Arsia Mons (Fig. 4). On the northeastern Arsia's flank, we mapped 60 small edifices between 1 and 10 km in diameter and several elongated structures that comprise multiple adjacent or superimposed edifices classified as volcanic fissures. Although summit caldera orientations of individual edifices are unmeasurable, the linear arrangement of conical edifices,

Table 1
Summary of the identified volcanic landforms and their summit crater alignments (for more details see Figs. 1 and 4) within the central part of the Tharsis volcanic province. Almost all of the volcanic structures were classified into individual subprovinces that indicate their association with one of the major Tharsis volcanoes.

Subprovince/volcano type	Total volcanoes	Min. area [km^2]	Max. area [km^2]	Median area [km^2]	No. of summit alignments	Mean direction[2] [°]	1SD
Alba Mons	51	5.06	1339.4	77.0	48	4	9
Arsia Mons	98	0.5	130.1	5.2	19	164	139
Ascraeus Mons	165	0.2	2528.9	43.4	100	36	9
Olympus Mons	101	0.6	924.1	51.3	78	126	24
Pavonis Mons	160	0.6	2658.4	124.7	123	49	6
Uranius Mons	5	19.4	124.7	25.3	3	–	–
Ulysses caldera	11	0.5	3.9	1.7	0	–	–
Scoria cones[1]	63	0.7	14.0	3.7	0	–	–
Unknown	5	16.3	291.0	80.0	2	–	–

Min., Max., and Median area of the base of the mapped volcanic landforms. No. of summit alignments – number of measurements determined for summit crater alignments for the whole dataset of the identified volcanic edifices; SD – standard deviation.

[1] Scoria cones were not classified into the distinguished subprovinces due to the uncertainty of their original feeding source.

[2] Mean direction values of the summit alignments measured from the north.

similar to those of terrestrial volcanic fissures such as Laki on Iceland, indicates structural directions occurring within the Arsia Mons subprovince. On the NE side of Arsia Mons, the most distant volcanic fissures consisting of volcanic edifices are located ~600 km from the summit caldera. In addition, we documented similar fissure structures emplaced ~750 km away on the WSW side of the Arsia Mons.

Pavonis Mons is accompanied by 160 volcanic landforms, grouped into two major clusters situated on the south and southeast sides of the nearby-located major volcano (Fig. 1). Interestingly, we have not documented any of the volcanic landforms on the northern side of the Pavonis Mons edifice. These volcanic edifices together with their inherent lava flows form structures ranging from several to >50 km (in the longest axis including lava flows). Among 123 measured summit alignments, 44 are oriented radially and 36 concentrically in relation to the edifice of Pavonis Mons. The remaining summit alignments were not classified due to the cut-off test. The summit alignment trends show directions of ~N030E for the radial set and ~ N075E for the concentric set.

Ascraeus Mons is accompanied by unevenly distributed 165 volcanic landforms. Near Ascraeus Mons, two clusters consist of volcanic edifices located on the eastern ($n = 48$) and southern flanks ($n = 81$). Furthermore, we identified two additional sets of volcanic edifices, most likely fed by the Ascraeus Mons magmatic system, on the southeastern ($n = 14$) and northwestern side ($n = 25$), distant ~500 km and ~ 750 km from the center of the summit caldera, respectively. The summit alignments of the cones within the Ascraeus Mons subprovince are oriented radially ($n = 50$) or concentrically (n = 25). Similar to previous subprovinces, the remaining summit alignments (n = 25) were not classified due to the cut-off test (Table 1). The summit alignment measurements of radial-set are focused around one direction of ~N020E. The structures oriented concentrically show a mean value of ~N040E (Fig. 4). In addition, we identified the northwestern cluster of volcanic edifices partially occurring in the Ceraunius Fossae (~1000 km away from the Ascraeus Mons; Figs. 1 and 4). It reveals the summit alignment directions of ~N065E being in line with other volcanoes, in the vicinity of Jovis Tholus, that show the concentric orientations to Ascraeus Mons. We considered them as belonging to the Ascraeus Mons magmatic system (see Section 4.1.2).

4.2. *Chronology of the activity of the distributed volcanoes*

We dated 94 volcanic edifices from all the subprovinces (see Table 2 and Fig. 5) and compared their ages with the ages of central volcanoes. The ages are consistent within each subprovince. This confirms our categorization of volcanoes into subprovinces based on their summit alignments (see Section 4.1). Based on dating, we were able to distinguish one additional subprovince related to the Uranius Mons. The age deviation within the subprovince is the lowest for the youngest subprovinces (Table 2 and Fig. 5). In addition, we observed a correlation between volcanic edifices' ages determined in this study and the youngest summit caldera activity for the central Tharsis volcanoes obtained by Neukum et al. (2004), Werner (2009), Robbins et al. (2011), and Ciazela et al. (2019) (Fig. 7).

4.2.1. *Olympus Mons*

In the surroundings of Olympus Mons, we chose 30 of the most suitable volcano flanks from the set of 107 volcanic landforms mapped within this subprovince to determine the surface age model. The ages range from 27 ± 6 Ma up to 135 + 45/−37 Ma with an average value of 69 Ma with a standard deviation of 29 Myr (Table 1). There is no visible correlation between spatial distribution and the age of the volcanic landforms, however, the isolated edifices located around the Olympus Mons (e.g., on the south and northwestern side of the edifice) show ages at the same range of ~55 Ma indicating a common time of their formation and activity. We distinguished three pulses of volcanism related to the summit caldera activity of Olympus Mons that occurred either 64 ± 26 Ma (cf. Ciazela et al., 2019) or > 100 Ma (cf. Neukum et al., 2004; Werner, 2009; Robbins et al., 2011): (1) early activity >100 Ma characterized by individual volcanic edifices that are unevenly distributed around the volcano cluster's rim (5 edifices), (2) main stage 50–100 Ma consisting of the clustered cones on the SE flanks (17 edifices), and (3) post-main caldera activity <50 Ma with volcanic edifices unevenly distributed on the outer rim of the major volcano construction (8 edifices) (for more details, see Table 2 and Fig. 5).

4.2.2. *Alba Mons*

Alba Mons is located in the northernmost part of the Tharsis region accompanied by a cluster of volcanic edifices and a series of parallel faults cutting its flanks, especially in the south direction. We determined the ages of 12 volcanic edifices situated within the Ceraunius Fossae, beyond the central edifice of Alba Mons. These landforms reveal ages between 70 ± 7 Ma and 160 ± 31 Ma forming two clusters characterized by a similar age range. One volcano edifice, emplaced to the west of Ceraunius Fossae, is much older (421 ± 53 Ma; Fig. 7). The southernmost set is younger with an average value of 83 Ma and a standard deviation of 8 Myr. The northern set was likely formed in a different, earlier magmatic event (ages >100 Ma).

4.2.3. *Tharsis Montes*

Considering the high diversity of distributed volcanism nearby the Tharsis Montes volcanoes, we distinguished a representative set of the youngest volcano flanks and lava flows to determine the age models in this region (including the Arsia, Pavonis, and Ascraeus subprovinces). The Arsia Mons subprovince hosts volcanic edifices both within the summit caldera and beyond the main edifice, mainly on the northeastern flank, possibly controlled by the same magmatic events. These edifices situated within the Arsia Mons summit caldera, show ages ranging from 148 ± 37 Ma up to 296 ± 36 Ma with an average age of 202 Ma and a standard deviation of 55 Myr, which implies prolongated plutonic and volcanic activity. The volcanic edifices at the northeastern flank are in line with those in the summit caldera showing the range from 177 ± 77 Ma to 256 ± 160 Ma with an average age of 212 Ma and a standard deviation of 40 Myr (Table 2).

To determine the geological affinity between the distributed volcanoes in the vicinity of the Pavonis Mons edifice with the central volcano, we dated a set of 21 volcanic edifices. Our results range from 55 ± 6 Ma to 137 ± 22 Ma (for more details, see Table 2). Eighteen of the dated volcanic edifices exhibit ages <100 Ma. We did not observe any relationship between the spatial distribution of volcanic edifices and their ages.

Ascraeus Mons is accompanied by a set of 40 clustered volcanic landforms on the eastern side and 22 more scattered edifices on the northern and northwestern sides. On the eastern side, seven edifices together with their lava flows were dated showing ages between 69 ± 13 Ma and 180 ± 10 Ma with an average age value of 129 Ma and a standard deviation of 36 Myr. Northwestern volcanoes are slightly younger ranging from 92 ± 4 Ma to 119 ± 18 Ma with an average value of 106 Ma and a standard deviation of 10 Ma. In addition, the volcanic edifices situated on the rim of Jovis Tholus show a surface age of 92 ± 4 Ma indicating its association with other volcanic edifices on the northwestern flank of Ascraeus Mons.

Using summit crater alignments, we found that 72 volcanic edifices located to the south and southeast of Ascraeus Mons edifice may be related to the magmatic system of Ascraeus. To confirm that, we determined the age of eight volcanoes. The age-dating exhibited a wide range of values from 50 ± 14 Ma to 173 + 51/−42 Ma with an average age of 93 Ma and a standard deviation of 37 Myr. These results are similar to those obtained for volcanic edifices located on the eastern flanks of Pavonis Mons (137–55 Ma). However, we believe that these edifices belong to the Ascraeus Mons subprovince based on their summit alignment orientations.

We demonstrated that all volcanic edifices clustered nearby the Arsia Mons (296–148 Ma), Pavonis Mons (147–55 Ma), and Ascraeus Mons

Table 2

Comparison of ages obtained by slope flank dating of volcanic edifices between the six distinguished subprovinces (A-F) related to the major Tharsis volcanoes: (A) Olympus Mons (B) Alba Mons, (C) Pavonis Mons, (D) Arsia Mons, (E) Ascraeus Mons, and (F) Uranius Mons.

Subprovince	No.	Coordinates		Chronology system						Minimum crater size used for fitting (m)	Number of mapped craters	Number of craters used for fitting	Dated area (km^2)	Brož[1]	
		Longitude	Latitude	Hartmann, 2005		Ivanov, 2001		Neukum-Ivanov, 2001							
Olympus Mons (A)	1	125° 59′ 30,984″ W	15° 42′ 48,197″ N	50	±6	37	±4	31	±4	60	89	74	256	NDA	
	2	126° 15′ 15,655″ W	14° 48′ 52,580″ N	60	±6	44	±5	37	±4	90	128	95	275	59	±5
	3	125° 9′ 18,787″ W	14° 15′ 18,176″ N	64	±7	47	±5	40	±4	60	123	86	234	52	±6
	4	125° 36′ 52,753″ W	14° 33′ 53,545″ N	81	±10	60	±10	51	±9	60	59	34	71	75	±17
	5	125° 22′ 39,627″ W	14° 37′ 49,782″ N	72	±10	64	±9	54	±8	120	252	50	932	68	±5
	6	125° 25′ 1572″ W	15° 22′ 41,053″ N	75	±10	59	±8	50	±7	80	107	57	303	53	±7
	7	127° 10′ 45,163″ W	15° 17′ 27,053″ N	41	±5	29	±3	25	±3	50	104	79	192	54	±4
	8	127° 0′ 2847″ W	15° 23′ 0,479″ N	118	±17	84	±14	72	±10	50	72	48	40	111	±14
	9	127° 34′ 11,657″ W	15° 7′ 35,541″ N	53	±3	39	±2	33	±2	60	335	263	852	62	±4
	10	128° 1′ 58,761″ W	15° 17′ 6561″ N	56	±5	40	±4	34	±3	50	150	104	182	74	±8
	11	126° 35′ 2512″ W	14° 40′ 53,470″ N	43	±10	28	±8	24	±6	35	24	15	13	NDA	
	12	127° 30′ 22,618″ W	13° 46′ 14,205″ N	135	+45; −37	111	+37; −30	94	+31; −26	95	73	10	56	NDA	
	13	125° 44′ 53,127″ W	14° 58′ 9087″ N	84	±8	64	±6	54	±5	70	170	109	362	NDA	
	14	123° 27′ 14,116″ W	15° 26′ 12,647″ N	131	±22	97	±16	82	±14	60	51	34	44	93	±12
	15	123° 55′ 29,274″ W	18° 54′ 0,202″ N	56	±4	40	±3	34	±2	50	299	209	367	54	±4
	16	126° 52′ 49,632″ W	14° 23′ 3043″ N	61	±10	43	±10; −9	37	±8; −7	50	42	21	36	86	±15
	17	127° 2′ 18,487″ W	14° 25′ 13,183″ N	50	+19; −15	40	+15; −12	34	+13; −10	50	138	8	68	NDA	
	73	123° 34′ 39,461″ W	14° 47′ 55,654″ N	125	±21	88	±15	75	±12	50	82	36	31	NDA	
	80	138° 35′ 24,922″ W	24° 3′ 33,527″ N	56	±9	38	±6	32	±5	50	95	37	75	NDA	
	81	136° 29′ 39,714″ W	13° 23′ 14,561″ N	53	±4	38	±6	32	±5	50	271	152	284	NDA	
	82	136° 3′ 27,881″ W	14° 31′ 58,024″ N	85	+27; −22	61	+19; −16	51	+16; −13	50	24	11	14	NDA	
	83	135° 41′ 46,254″ W	14° 27′ 50,438″ N	115	+41; −31	83	+29; −24	70	+25; −20	50	27	9	8	NDA	
	84	132° 17′ 31,162″ W	13° 23′ 58,861″ N	38	±11; −9	26	±7; −6	22	±6; −5	40	18	14	20	NDA	
	87	122° 37′ 12,118″ W	19° 50′ 33,130″ N	69	±14	49	±10	43	±9	50	53	23	34	NDA	

Subprovince	No.	Coordinates		Chronology system						Minimum crater size used for fitting (m)	Number of mapped craters	Number of craters used for fitting	Dated area (km2)	Brož[1]	
		Longitude	Latitude	Hartmann, 2005		Ivanov, 2001		Neukum-Ivanov, 2001							
Olympus Mons (A)	88	126° 21′ 28,673″ W	18° 12′ 40,051″ N	27	±6	18	±4	16	±4	40	32	20	41	NDA	
	89	127° 48′ 40,713″ W	17° 1′ 50,972″ N	37	±3	26	±2	22	±2	45	233	183	383	NDA	
	90	127° 20′ 35,616″ W	16° 21′ 35,437″ N	38	±6	25	±4	21	±4	40	46	39	54	NDA	
	91	126° 10′ 7238″ W	16° 55′ 24,250″ N	53	±10	36	±7	31	±6	40	42	30	29	NDA	
	92	125° 10′ 33,660″ W	13° 14′ 14,455″ N	99	±10	70	±9	59	±8	50	79	58	61	NDA	
	96	126° 44′ 4450″ W	15° 45′ 51,664″ N	52	±8	35	±6	30	±5	40	58	40	40	NDA	
Alba Mons (B)	18	110° 28′ 53,402″ W	23° 39′ 33,997″ N	70	±7	52	±5	44	±5	60		93	226	58	±5
	19	110° 12′ 57,826″ W	22° 53′ 53,416″ N	70	±13	62	±12	53	±10	130	424	27	729	69	±10
	20	110° 44′ 43,226″ W	20° 6′ 36,082″ N	90	±5	69	±4	58	±3	70	453	291	871	70	±5
	21	109° 53′ 35,947″ W	25° 14′ 36,607″ N	85	±4	65	±3	55	±3	70	556	455	1440	57	±8
	22	109° 15′ 26,861″ W	28° 45′ 48,084″ N	107	±11	82	±8	70	±7	70	138	96	241	99	±10
	24	111° 49′ 44,829″ W	24° 33′ 9331″ N	59	+15; −12	53	+13; −11	45	+11; −10	130	232	18	552	83	±6
	26	111° 51′ 27,276″ W	25° 43′ 42,910″ N	114	±23	88	±18	75	±15	80	81	24	118	97	±11
	28	109° 10′ 31,850″ W	28° 4′ 3475″ N	98	+33; −27	78	+26; −21	66	+22; −18	100	115	10	170	NDA	
	29	110° 37′ 15,134″ W	25° 24′ 9701″ N	86	±5	66	±4	56	±3	70	560	336	1060	NDA	
	30	110° 28′ 40,798″ W	25° 55′ 31,074″ N	78	±14	64	±11	54	±9	90	169	33	237	NDA	
	31	109° 2′ 20,628″ W	27° 51′ 46,289″ N	160	±31	115	±22	98	±19	50	46	26	16	NDA	
	93	117° 35′ 39,249″ W	27° 17′ 55,696″ N	417	±53	375	±48	318	±40	130	211	61	263	NDA	
Arsia Mons (C)	54	120° 49′ 56,519″ W	9° 39′ 21,177″ S	230	±40	190	±30	160	±30	80	79	29	49	168	±23
	56	120° 15′ 26,482″ W	9° 2′ 58,388″ S	174	±70	143	±55	122	±50	90	48	8	28	NDA	
	57	120° 3′ 3143″ W	8° 49′ 44,849″ S	205	+73; −59	189	+67; −54	160	+57; −46	140	122	9	104	NDA	
	58	120° 5′ 6914″ W	8° 35′ 55,410″ S	296	±36	235	±28	199	±24	80	91	68	91	NDA	
	59	120° 29′ 47,098″ W	8° 35′ 5329″ S	148	±37	117	±29	99	±25	80	77	18	50	NDA	
	60	119° 53′ 40,441″ W	8° 27′ 10,399″ S	235	±43	172	±32	146	±27	60	46	29	21	135	±18
	61	119° 32′ 56,336″ W	8° 34′ 53,667″ S	158	±21	119	±16	101	±13	70	82	58	107	NDA	
	77	116° 41′ 8896″ W	5° 44′ 39,417″ S	205	±47	147	±34	124	±28	50	37	21	10	NDA	

Subprovince	No.	Coordinates		Chronology system						Minimum crater size used for fitting (m)	Number of mapped craters	Number of craters used for fitting	Dated area (km2)	Brož[1]	
		Longitude	Longitude	Hartmann, 2005		Ivanov, 2001		Neukum-Ivanov, 2001							
Arsia Mons (C)	79	116° 35′ 3598″ W	3° 59′ 32,569″ S	177	±34	141	±27	119	±23	80	44	27	61	NDA	
	32	107° 47′ 15,847″ W	0° 53′ 0,041″ S	147	±25	132	±23	112	±19	140	224	34	595	NDA	
	33	106° 12′ 24,794″ W	0° 17′ 47,605″ N	92	±19	73	±15	62	±13	80	75	24	103	NDA	
	34	107° 47′ 30,503″ W	2° 22′ 58,645″ S	75	±5	60	±4	51	±3	80	421	234	1240	59	±8
	35	107° 28′ 4833″ W	2° 39′ 7909″ S	69	±8	54	±6	46	±6	80	117	70	416	NDA	
	36	108° 21′ 5355″ W	0° 52′ 42,266″ S	63	±11	50	±9	43	±8	80	89	31	195	NDA	
	37	108° 39′ 2881″ W	1° 9′ 10,064″ S	74	±7	60	±5	51	±5	90	361	128	994	NDA	
Pavonis Mons (D)	38	109° 34′ 46,396″ W	5° 9′ 3481″ S	92	±14	73	±11	62	±9	80	81	42	187	74	±32
	39	109° 43′ 31,484″ W	5° 23′ 43,576″ S	70	±19	56	±15	47	±13	80	34	15	89	76	±31
	40	109° 22′ 35,049″ W	5° 38′ 18,184″ S	74	+17; −15	62	+14; −12	52	+12; −10	100	69	21	238	66	±22
	41	110° 52′ 17,773″ W	5° 26′ 44,568″ S	106	±37	84	±30	71	±25	80	22	9	36	NDA	
	42	109° 7′ 27,824″ W	2° 30′ 29,673″ S	55	±6	44	±4	37	±4	80	206	98	711	NDA	
	43	108° 56′ 44,311″ W	2° 0′ 26,387″ S	81	±21	65	±16	55	±14	80	44	17	86	NDA	
	44	112° 30′ 32,863″ W	5° 1′ 14,485″ S	62	±9	49	±7	42	±6	80	156	50	330	76	±16
	45	111° 18′ 52,079″ W	7° 17′ 30,620″ S	83	±12	66	±10	56	±8	80	119	46	223	NDA	
Pavonis Mons (D)	46	113° 9′ 39,688″ W	4° 1′ 24,217″ S	60	±5	48	±4	40	±3	80	227	143	956	NDA	
	47	106° 46′ 6023″ W	1° 41′ 13,029″ N	104	±7	83	±5	70	±5	80	490	236	906	NDA	
	49	104° 51′ 25,153″ W	0° 51′ 16,541″ N	75	±5	57	±4	48	±3	70	413	233	854	NDA	
	50	105° 48′ 53,026″ W	1° 52′ 54,132″ N	83	±8	65	±6	55	±5	80	238	114	580	NDA	
	94	114° 33′ 41,290″ W	4° 51′ 55,526″ S	67	±10	51	±7	43	±6	70	77	47	191	NDA	
	95	114° 25′ 58,478″ W	4° 25′ 44,655″ S	74	±10	65	±10	55	±10	120	64	28	535	NDA	
	97	114° 29′ 33,602″ W	5° 57′ 46,386″ S	65	±6	48	±4	41	±4	60	136	132	344	NDA	
E of Ascraeus Mons (E)	51	99° 22′ 23,282″ W	12° 25′ 15,740″ N	125	±10	92	±8	78	±6	60	260	143	197	NDA	
	52	99° 28′ 55,166″ W	11° 51′ 29,823″ N	159	±23	126	±20	107	±17	80	160	41	102	NDA	
	53	100° 2′ 31,662″ W	10° 49′ 58,531″ N	143	±8	106	±6	90	±5	60	391	298	355	NDA	

Subprovince	No.	Coordinates		Chronology system						Minimum crater size used for fitting (m)	Number of mapped craters	Number of craters used for fitting	Dated area (km2)	Brož[1]	
		Longitude	Longitude	Hartmann, 2005		Ivanov, 2001		Neukum-Ivanov, 2001							
E of Ascraeus Mons (E)	62	98° 28′ 19,486″ W	11° 56′ 28,116″ N	88	+28; −23	80	+25; −21	67	+21; −18	60	290	11	236	NDA	
	63	99° 34′ 41,717″ W	10° 57′ 9887″ N	180	±10	140	±7	120	±6	70	565	354	525	NDA	
	64	99° 30′ 53,509″ W	13° 27′ 53,878″ N	139	±27	100	±19	84	±16	50	35	27	19	NDA	
	99	100° 13′ 12,912″ W	18° 2′ 4836″ N	69	±13	49	±9	41	±8	50	31	27	41	NDA	
S of Ascraeus Mons (E)	48	106° 50′ 32,777″ W	3° 7′ 39,692″ N	84	+23; −19	62	+17; −14	53	+14; −12	70	39	15	62	NDA	
	65	97° 18′ 10,588″ W	3° 43′ 32,991″ N	55	±8	40	±6	34	±5	50	70	48	86	NDA	
	66	98° 25′ 59,786″ W	2° 23′ 43,866″ N	173	+51; −42	174	51; −43	148	+43; −36	200	317	13	558	NDA	
	67	101° 28′ 33,135″ W	4° 21′ 47,016″ N	88	±10	67	±10	57	±9	70	76	43	132	NDA	
	68	102° 43′ 37,861″ W	4° 22′ 14,730″ N	94	±44	79	±37	67	±32	100	15	5	50	NDA	
	69	105° 44′ 8871″ W	4° 25′ 43,952″ N	50	+15; −12	38	+11; −9	32	+9; −8	70	30	13	79	NDA	
	70	105° 48′ 52,524″ W	3° 34′ 5169″ N	124	±28	95	±22	80	±18	70	30	21	47	NDA	
	98	94° 39′ 14,207″ W	5° 22′ 54,203″ N	81	±10	55	±7	46	±6	40	72	65	42	NDA	
NW of Ascraeus Mons (E)	23	113° 37′ 6397″ W	17° 40′ 59,088″ N	101	±7	81	±6	68	±5	80	332	192	751	106	±8
	25	113° 3′ 33,193″ W	17° 53′ 34,177″ N	111	±7	93	±6	79	±5	100	657	289	203	126	±6
	27	116° 36′ 46,142″ W	17° 49′ 12,926″ N	92	±4	76	±4	64	±3	90	746	463	2850	104	±5
	85	110° 12′ 27,310″ W	14° 52′ 1556″ N	110	±18	94	±16	80	±13	110	112	37	375	NDA	
	86	109° 11′ 2143″ W	15° 56′ 24,353″ N	108	±13	86	±10	73	±9	80	108	72	264	NDA	
Uranius Mons (F)	72	88° 36′ 32,730″ W	28° 18′ 41,768″ N	1400	+330; −280	1170	+280; −240	993	+230; −200	110	47	20	19	NDA	
	76	92° 48′ 51,330″ W	27° 27′ 20,376″ N	990	±280	1000	±280	847	±240	200	115	14	105	NDA	

± is 1σ as age uncertainty based on the number of craters fitted; NDA - no data available.

[1] Comparison between ages obtained in this study and Brož, 2010. Note that Brož (2010) applied Hartmann and Neukum (2001) chronology system and Ivanov (2001) production function.

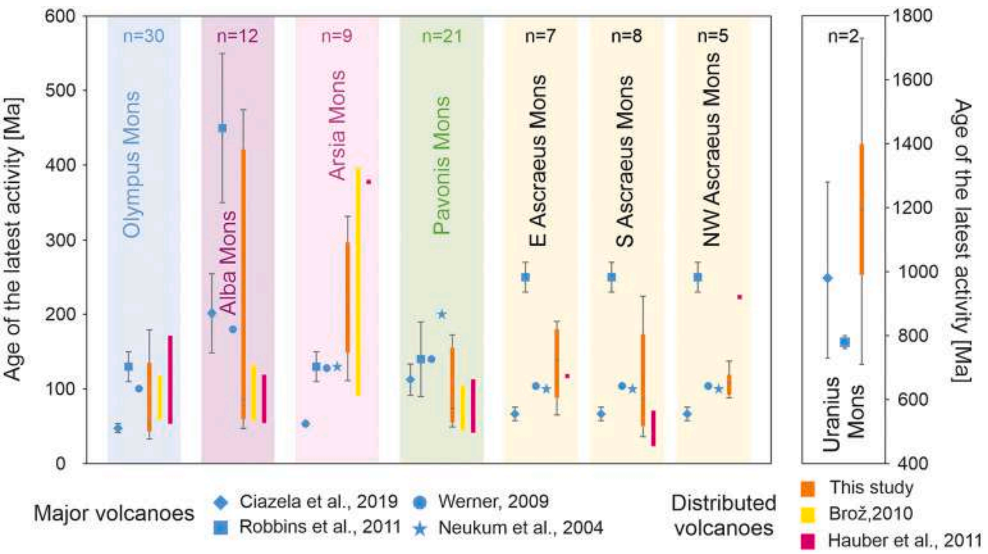

Fig. 8. Ages of the last activity in the summit calderas of major volcanoes obtained by Ciazela et al. (2019), Robbins et al. (2011), Werner (2009), and Neukum et al., (2004), and associated volcanic edifices obtained by Brož, (2010) and Hauber et al. (2011), and this study in Tharsis on Mars (see Table 3 for more details). The results of the surface age determination for volcanic edifices represent the range of values obtained for each subprovince (see Table 2 for more details on model ages). The lower and upper uncertainties are given by the uncertainty of the individual age (e.g., the lower boundary for the Olympus Mons is given by age of 43 ± 10 Ma while the upper by 135 + 45;-37 Ma). For Brož (2010) and Hauber et al. (2011), the range of ages determined for each subprovince is plotted. These authors distinguished volcanoes within the Ceraunius Fossae region, while we classified them to Alba Mons subprovince. The right section of the plot presents ages obtained for the Uranius Mons subprovince most likely showing the oldest activity associated with the formation of the distributed volcanism within Tharsis.

(180–50 Ma) exhibit similar ages within each subprovince, and these ages mostly match the ages of the summit caldera activity of the adjacent central volcano (Fig. 8). In most cases, these ages indicate prolonged distributed volcanism that was active both before and after the latest volcanic activity at the summit caldera of the major Tharsis volcano (Table 3).

4.2.4. *Uranius Mons*

From the five volcanic landforms located adjacent to the Uranius Mons, only two were suitable for dating showing surface model ages of 990 ± 280 Ma and 1400 + 330/−260 Ma (Table 2). These ages match the age of the last Uranius Mons summit caldera activity of 1020 ± 140 Ma (Ciazela et al., 2019).

5. Discussion

5.1. *The volcanic origin of the mapped edifices*

Tharsis hosts the highest concentration of volcanic landforms on Mars. Prior studies have investigated the morphology and rheological properties (i.e., viscosity and effusion rate) of the magma originated from Olympus Mons (Bleacher et al., 2007; Peters and Christensen, 2017; Mouginis-Mark and Wilson, 2019), Tharsis Montes (Bleacher et al., 2007, 2009; Hauber et al., 2011; Richardson et al., 2017, 2021), and the Ceraunius Fossae region (Hauber et al., 2009; Krishnan and Kumar, 2021; Richardson et al., 2021), however, none of the previous studies performed a complex reconstruction of the magmatic plumbing system for the entire Tharsis region. The major volcanoes are accompanied by hundreds of small volcanic structures. Their distribution,

Table 3

Model ages of the latest summit volcanic activity in the major volcanoes [ages obtained by Ciazela et al., 2019, Robbins et al., 2011, Werner, 2009, and Neukum et al., 2004] and associated Tharsis volcanic edifices (this study).

Volcano/ subprovince	Ciazela et al., 2019		Robbins et al., 2011		Werner, 2009	Neukum et al., 2004	This study						
Chronology function	Hartmann (2005)		Ivanov & Neukum (2001)		Hartmann and Neukum (2001)	Hartmann and Neukum (2001)	Hartmann (2005)						
							min. Age		max. Age		model age	SD	n
Olympus Mons	64	±26	140	±20	140	200	43	±10	135	+45; −37	58	29	30
Alba Mons	133	±42	450	±100	180	n/a	59	+15; −12	421	±53	86*	26*	12*
Arsia Mons	126	±6	130	±20	128	130	148	±37	296	±36	205	43	9
Pavonis Mons	138	±13	130	±20	82	n/a	55	±6	147	±25	74	20	21
E Ascraeus Mons							88	+28; −23	180	±10	139	36	7
S Ascraeus Mons	193	±17	250	±20	104	100	50	+15; −12	173	+51; −42	86	37	8
NW Ascraeus Mons							92	±4	111	±7	108	7	5
Uranius Mons	1020	±140	780	±20	n/a	n/a	990	±280	1400	+330; −280	1195	205	2

Model age – the median age of the surface age determinations of the volcanic edifices in a given subprovince (this study); SD – standard deviation; n – number of volcanic edifices dated within each subprovince; ± is 1σ as age uncertainty based on the number of craters fitted.

* The median age of the Alba Mons subprovince did not include the exceptional age of 421 ± 53 Ma.

Table 4

Detailed morphometric parameters of the investigated volcanic edifices through the distinguished subprovinces within the Tharsis region on Mars. The heights of the base and summit of the volcanic edifices have been determined using MOLA MEX HRSC Blended DEM Global 200 m/px (Fergason et al., 2018).

Subprovince/volcano type	Longitude[a]	Latitude[a]	A_{CO} [km^2]	W_{CO} [km]	W_{CR} [km]	H_{CO} [km]	H_{CR} [km]	H [km]	r_B [km]	avg. slope [^{0}][b]	volume [km^3][c]	W_{CR}/W_{CO}
Alba Mons	110° 44′ 3.617″ W	20° 6′ 30.679″ N	893	33.0	0.9	2.498	2.878	0.38	16.9	1.3	113.1	0.03
	110° 12′ 2.038″ W	22° 54′ 16.152″ N	872	31.8	0.5	2.901	3.082	0.18	16.7	0.6	52.6	0.01
	110° 39′ 45.211″ W	25° 31′ 28.185″ N	617	31.6	0.5	3.167	3.317	0.15	14.0	0.6	30.8	0.02
	109° 10′ 58.430″ W	28° 4′ 44.890″ N	148	15.2	0.4	3.437	3.625	0.19	6.9	1.6	9.3	0.03
	109° 44′ 37.331″ W	27° 51′ 39.140″ N	590	21.1	0.6	3.472	3.705	0.23	13.7	1.0	45.8	0.03
	109° 27′ 18.973″ W	26° 56′ 12.407″ N	533	25.8	0.5	3.543	3.721	0.18	13.0	0.8	31.6	0.02
	111° 48′ 30.425″ W	24° 38′ 6.367″ N	405	23.4	0.4	2.963	3.093	0.13	11.4	0.7	17.6	0.02
	117° 35′ 2.502″ W	27° 16′ 55.537″ N	326	21.3	1.0	2.027	2.180	0.15	10.2	0.9	16.6	0.05
	111° 51′ 27.276″ W	25° 43′ 42.910″ N	131	12.9	0.4	2.984	3.133	0.15	6.5	1.3	6.5	0.03
	108° 51′ 55.311″ W	28° 27′ 54.974″ N	85	10.7	0.3	3.496	3.590	0.09	5.2	1.0	2.7	0.03
	120° 49′ 48.471″ W	9° 39′ 26.605″ S	54	8.1	0.3	16.278	16.445	0.17	4.1	2.3	3.0	0.04
	120° 26′ 48.616″ W	9° 47′ 41.854″ S	46	7.6	0.4	16.306	16.478	0.17	3.8	2.6	2.6	0.05
	120° 15′ 13.966″ W	9° 2′ 29.720″ S	24	5.5	0.4	16.292	16.344	0.05	2.7	1.1	0.4	0.08
	120° 4′ 46.247″ W	8° 49′ 50.585″ S	62	8.9	0.5	16.289	16.329	0.04	4.4	0.5	0.8	0.06
	120° 3′ 35.676″ W	8° 37′ 34.429″ S	46	8.7	0.4	16.255	16.374	0.12	3.8	1.8	1.8	0.05
	119° 34′ 10.603″ W	8° 31′ 39.330″ S	36	9.6	0.4	16.217	16.258	0.04	3.4	0.7	0.5	0.04
Ascraeus Mons	116° 31′ 44.392″ W	17° 48′ 56.005″ N	2529	55.9	1.1	1.946	2.389	0.44	28.4	0.9	373.4	0.02
	113° 4′ 8.573″ W	17° 53′ 10.526″ N	1928	48.6	0.9	2.164	2.410	0.25	24.8	0.6	158.1	0.02
	99° 31′ 4.003″ W	13° 28′ 3.147″ N	23	6.2	0.3	3.608	3.876	0.27	2.7	5.8	2.0	0.04
	99° 22′ 25.047″ W	12° 25′ 20.308″ N	200	16.3	0.3	3.520	3.640	0.12	8.0	0.9	8.0	0.02
	99° 38′ 17.221″ W	11° 29′ 29.355″ N	109	13.3	0.5	3.488	3.556	0.07	5.9	0.7	2.5	0.04
	99° 43′ 16.082″ W	11° 0′ 39.512″ N	187	14.7	0.4	3.459	3.575	0.12	7.7	0.9	7.2	0.02
	100° 2′ 27.985″ W	10° 50′ 0.932″ N	511	27.1	0.4	3.411	3.568	0.16	12.8	0.7	26.7	0.02
	110° 12′ 15.602″ W	14° 52′ 8.171″ N	377	24.3	0.4	1.922	2.011	0.09	11.0	0.5	11.2	0.02
	108° 36′ 34.515″ W	14° 44′ 46.401″ N	672	30.5	0.8	1.627	1.727	0.10	14.6	0.4	22.4	0.03
	108° 1′ 25.941″ W	14° 4′ 52.059″ N	354	21.0	0.5	1.627	1.727	0.10	10.6	0.5	11.8	0.03
	98° 25′ 29.482″ W	2° 24′ 0.242″ N	627	34.8	0.5	4.116	4.342	0.23	14.1	0.9	47.2	0.02

Subprovince/volcano type	Longitude[a]	Latitude[a]	A_{CO} [km^2]	W_{CO} [km]	W_{CR} [km]	H_{CO} [km]	H_{CR} [km]	H [km]	r_B [km]	avg. slope [^{0}][b]	volume [km^3][c]	W_{CR}/W_{CO}
Ascraeus Mons	101° 10′ 35.932″ W	2° 6′ 11.287″ N	1528	41.8	2.0	4.680	4.978	0.30	22.1	0.8	151.8	0.05
	100° 18′ 15.329″ W	2° 29′ 41.755″ N	1421	44.8	0.5	4.391	4.723	0.33	21.3	0.9	157.3	0.01
	105° 55′ 17.079″ W	4° 29′ 12.916″ N	73	9.2	0.3	6.185	6.247	0.06	4.8	0.7	1.5	0.03
	105° 11′ 33.047″ W	4° 32′ 23.350″ N	94	10.8	0.3	5.996	6.252	0.26	5.5	2.7	8.0	0.03
	105° 43′ 49.549″ W	4° 25′ 33.505″ N	80	10.9	0.5	6.180	6.326	0.15	5.1	2.0	2.3	0.04
	105° 48′ 49.869″ W	3° 34′ 5.659″ N	47	9.3	0.5	5.952	6.083	0.13	3.9	1.9	2.0	0.05
	106° 50′ 32.960″ W	3° 7′ 34.665″ N	63	8.7	0.3	5.621	5.830	0.21	4.5	2.7	4.4	0.04
	106° 0′ 4.699″ W	2° 59′ 40.854″ N	183	13.7	0.3	5.765	5.895	0.13	7.6	1.0	7.9	0.02
	106° 38′ 51.290″ W	2° 57′ 57.648″ N	180	13.1	0.4	5.670	5.804	0.13	7.6	1.0	8.1	0.03
	106° 46′ 2.799″ W	2° 40′ 46.775″ N	108	10.3	0.2	5.657	5.760	0.10	5.9	1.0	3.7	0.02
	110° 27′ 40.809″ W	23° 39′ 25.412″ N	246	14.7	0.6	2.979	3.132	0.15	8.9	1.0	12.6	0.04
	99° 2′ 40.711″ W	13° 3′ 5.366″ N	63	8.8	0.3	3.608	3.669	0.06	4.5	0.8	1.3	0.04
	99° 10′ 51.856″ W	12° 35′ 39.835″ N	92	11.4	0.4	3.539	3.603	0.06	5.4	0.7	2.0	0.04
	109° 7′ 23.555″ W	15° 57′ 31.182″ N	350	20.7	0.4	1.891	1.975	0.08	10.6	0.5	9.8	0.02
	112° 29′ 41.866″ W	20° 14′ 46.191″ N	295	21.5	0.8	2.520	2.697	0.18	9.7	1.0	17.4	0.04
	100° 8′ 55.093″ W	11° 29′ 26.741″ N	65	10.4	0.2	3.565	3.658	0.09	4.5	1.2	2.0	0.02
	100° 42′ 48.435″ W	11° 11′ 55.188″ N	36	7.6	0.3	3.622	3.671	0.05	3.4	0.8	0.6	0.04
	105° 23′ 0.960″ W	4° 43′ 55.414″ N	33	6.2	0.6	6.130	6.298	0.17	3.2	3.0	1.8	0.10
Olympus Mons	125° 59′ 17.325″ W	15° 42′ 28.914″ N	279	17.7	0.7	1.213	1.322	0.11	9.4	0.7	10.1	0.04
	126° 43′ 58.702″ W	15° 44′ 18.222″ N	46	8.0	0.3	1.167	1.199	0.03	3.8	0.5	0.5	0.03
	126° 59′ 57.580″ W	15° 22′ 59.014″ N	42	7.7	0.3	1.116	1.160	0.04	3.7	0.7	0.6	0.04
	126° 40′ 16.372″ W	15° 13′ 8.003″ N	80	12.4	0.2	1.138	1.180	0.04	5.0	0.5	1.1	0.02
	126° 52′ 40.949″ W	14° 23′ 17.174″ N	34	6.1	0.3	1.090	1.138	0.05	3.3	0.8	0.5	0.04
	127° 9′ 59.012″ W	15° 18′ 58.796″ N	61	10.6	0.1	1.103	1.141	0.04	4.4	0.5	0.8	0.01
	127° 59′ 22.448″ W	15° 29′ 39.104″ N	75	11.5	0.2	0.912	0.984	0.07	4.9	0.8	1.8	0.02
	127° 34′ 39.875″ W	15° 16′ 51.124″ N	889	28.9	0.6	1.005	1.112	0.11	16.8	0.4	31.7	0.02
	127° 30′ 27.202″ W	13° 46′ 30.902″ N	61	10.2	0.4	0.929	0.983	0.05	4.4	0.7	1.1	0.04
	123° 27′ 14.116″ W	15° 26′ 12.647″ N	46	7.3	0.2	1.134	1.180	0.05	3.8	0.7	0.7	0.03
	125° 25′ 1.572″ W	15° 22′ 41.053″ N	314	16.8	0.4	1.235	1.309	0.07	10.0	0.4	7.7	0.02

Subprovince/volcano type	Longitude[a]	Latitude[a]	A_{CO} [km^2]	W_{CO} [km]	W_{CR} [km]	H_{CO} [km]	H_{CR} [km]	H [km]	r_B [km]	avg. slope [^{0}][b]	volume [km^3][c]	W_{CR}/W_{CO}
Olympus Mons	128° 46′ 33.805″ W	16° 27′ 52.827″ N	129	12.7	0.5	0.806	0.921	0.12	6.4	1.0	5.0	0.04
	127° 21′ 14.195″ W	16° 20′ 19.635″ N	63	7.3	0.4	1.130	1.201	0.07	4.5	0.9	1.5	0.05
	127° 11′ 50.071″ W	16° 11′ 49.082″ N	159	13.4	0.3	1.111	1.242	0.13	7.1	1.1	6.9	0.02
	127° 24′ 49.818″ W	16° 57′ 16.486″ N	44	9.2	0.3	1.066	1.113	0.05	3.7	0.7	0.7	0.03
	136° 9′ 41.256″ W	13° 28′ 2.693″ N	6	2.8	0.1	−0.128	−0.063	0.07	1.4	2.7	0.1	0.04
	125° 45′ 4.534″ W	14° 58′ 18.042″ N	366	20.0	0.4	1.213	1.281	0.07	10.8	0.4	8.3	0.02
	125° 24′ 59.397″ W	14° 38′ 34.002″ N	924	37.4	0.5	1.189	1.331	0.14	17.2	0.5	43.7	0.01
Pavonis Mons	106° 10′ 13.145″ W	0° 17′ 59.927″ N	486	24.0	0.7	5.512	5.645	0.13	12.4	0.6	21.5	0.03
	105° 45′ 9.777″ W	2° 40′ 34.967″ S	355	18.3	0.7	5.710	5.877	0.17	10.6	0.9	19.8	0.04
	107° 48′ 6.933″ W	0° 53′ 17.704″ S	597	27.8	0.8	5.772	5.971	0.20	13.8	0.8	39.6	0.03
	108° 24′ 40.076″ W	0° 23′ 11.241″ S	704	27.5	0.7	5.810	5.938	0.13	15.0	0.5	30.0	0.02
	109° 8′ 30.337″ W	2° 30′ 38.706″ S	703	28.9	0.7	6.185	8.412	2.23	15.0	8.6	521.8	0.02
	107° 28′ 8.474″ W	2° 39′ 44.985″ S	423	19.3	0.4	5.876	6.036	0.16	11.6	0.8	22.6	0.02
	108° 58′ 26.211″ W	4° 17′ 3.149″ S	1092	39.5	0.4	6.424	6.664	0.24	18.6	0.7	87.4	0.01
	109° 34′ 46.266″ W	5° 10′ 21.111″ S	229	16.5	0.4	6.604	6.752	0.15	8.5	1.0	11.3	0.02
	114° 7′ 2.389″ W	2° 30′ 54.363″ S	155	14.2	0.6	8.000	8.185	0.19	7.0	1.5	9.5	0.04
	114° 20′ 10.453″ W	2° 39′ 2.662″ S	28	5.9	0.4	7.957	8.135	0.18	3.0	3.4	1.7	0.07
	113° 27′ 24.083″ W	2° 46′ 42.505″ S	63	8.9	0.3	8.000	8.091	0.09	4.5	1.2	1.9	0.03
	113° 32′ 19.752″ W	3° 8′ 26.380″ S	308	16.7	1.3	7.686	7.974	0.29	9.9	1.7	29.6	0.08
	113° 42′ 9.746″ W	3° 42′ 0.542″ S	358	17.0	0.7	7.619	7.819	0.20	10.7	1.1	23.9	0.04
	113° 52′ 51.906″ W	3° 36′ 36.289″ S	13	4.2	0.3	7.707	7.748	0.04	2.0	1.2	0.2	0.08
	113° 11′ 55.834″ W	3° 57′ 26.982″ S	748	25.4	0.5	7.369	7.786	0.42	15.4	1.5	103.9	0.02
	112° 27′ 20.882″ W	4° 30′ 34.880″ S	1576	35.9	0.6	7.155	7.425	0.27	22.4	0.7	141.9	0.02
	112° 29′ 28.541″ W	5° 2′ 41.733″ S	333	15.5	0.6	7.107	7.369	0.26	10.3	1.5	29.0	0.04
	114° 17′ 18.444″ W	3° 20′ 25.276″ S	82	11.5	0.3	7.785	7.859	0.07	5.1	0.8	2.0	0.03
	113° 21′ 25.511″ W	4° 43′ 12.246″ S	153	12.8	0.7	7.345	7.447	0.10	7.0	0.8	5.2	0.05
	114° 12′ 45.948″ W	5° 4′ 28.596″ S	350	22.4	0.6	7.385	7.514	0.13	10.6	0.7	15.0	0.03
	114° 0′ 38.972″ W	5° 19′ 22.877″ S	544	24.7	0.6	7.264	7.514	0.25	13.2	1.1	45.4	0.02
	114° 51′ 50.279″ W	6° 7′ 18.685″ S	427	21.7	0.4	7.277	7.366	0.09	11.7	0.4	12.7	0.02

Subprovince/volcano type	Longitude[a]	Latitude[a]	A_{CO} [km^2]	W_{CO} [km]	W_{CR} [km]	H_{CO} [km]	H_{CR} [km]	H [km]	r_B [km]	avg. slope [^{0}][b]	volume [km^3][c]	W_{CR}/W_{CO}
Pavonis Mons	113° 10′ 10.256″ W	6° 32′ 46.034″ S	1018	31.2	0.6	7.088	7.311	0.22	18.0	0.7	75.7	0.02
	114° 28′ 12.168″ W	6° 1′ 54.696″ S	246	16.8	0.6	7.267	7.348	0.08	8.9	0.5	6.6	0.04
	110° 40′ 21.491″ W	7° 44′ 38.610″ S	428	22.3	0.4	6.952	7.116	0.16	11.7	0.8	23.4	0.02
	111° 19′ 14.873″ W	7° 17′ 46.458″ S	209	16.5	0.4	6.968	7.044	0.08	8.2	0.5	5.3	0.02
	114° 1′ 51.043″ W	6° 48′ 21.585″ S	312	19.3	0.7	7.140	7.235	0.10	10.0	0.5	9.9	0.03
	114° 36′ 15.779″ W	4° 54′ 52.550″ S	221	13.6	0.5	7.350	7.484	0.13	8.4	0.9	9.9	0.04
	112° 43′ 58.191″ W	6° 48′ 2.705″ S	150	11.3	0.3	7.046	7.133	0.09	6.9	0.7	4.3	0.03
Scoria cones	122° 58′ 25.240″ W	5° 34′ 43.745″ N	16	3.8	1.3	4.456	4.947	0.49	2.2	12.8	2.5	0.34
	122° 56′ 59.172″ W	5° 41′ 50.947″ N	6	2.7	0.6	4.575	5.074	0.50	1.4	21.4	1.0	0.23
	122° 59′ 19.990″ W	5° 46′ 36.916″ N	3	1.9	0.6	4.327	4.654	0.33	0.9	21.3	0.3	0.30
	122° 50′ 1.732″ W	5° 46′ 47.458″ N	7	3.2	0.7	4.506	4.924	0.42	1.5	16.6	1.0	0.23
	122° 51′ 22.092″ W	5° 49′ 53.341″ N	3	2.0	0.5	4.607	4.926	0.32	1.0	18.1	0.4	0.25
	122° 52′ 56.350″ W	5° 53′ 25.111″ N	7	3.0	0.7	4.774	5.304	0.53	1.5	21.0	1.3	0.22
	122° 33′ 50.899″ W	5° 51′ 45.029″ N	12	3.7	0.9	4.478	5.063	0.59	2.0	17.5	2.4	0.24
	123° 1′ 3.935″ W	6° 4′ 58.553″ N	4	2.3	0.5	4.586	4.806	0.22	1.1	11.6	0.3	0.20
	123° 1′ 34.246″ W	6° 21′ 44.341″ N	6	3.0	0.8	4.782	5.102	0.32	1.4	13.3	0.7	0.27
	123° 1′ 42.187″ W	6° 24′ 20.430″ N	2	1.9	0.5	4.891	5.096	0.21	0.9	13.8	0.2	0.28
	123° 4′ 1.146″ W	6° 55′ 29.462″ N	2	1.7	0.2	4.874	5.090	0.22	0.8	15.5	0.2	0.14
	105° 0′ 18.341″ W	24° 26′ 22.367″ N	3	2.1	0.4	1.957	2.002	0.05	1.0	2.5	0.0	0.17
	104° 59′ 11.610″ W	24° 31′ 21.286″ N	6	2.6	0.5	1.956	2.059	0.10	1.4	4.3	0.2	0.20
	98° 51′ 56.226″ W	0° 2′ 44.309″ S	5	3.3	0.5	4.413	4.639	0.23	1.3	10.1	0.4	0.15
	98° 48′ 39.151″ W	0° 6′ 8.210″ S	6	3.2	0.7	4.388	4.508	0.12	1.4	5.0	0.2	0.21
	99° 23′ 9.465″ W	1° 12′ 45.488″ S	7	3.3	0.8	5.585	5.917	0.33	1.5	12.7	0.8	0.24

A_{CO} – area of the volcano edifice basement; W_{CO} – the basal width of the volcanic edifice (assuming the circular shape of the edifice, we have calculated W_{CR} parameter converting perimeter using ArcMap software); W_{CR} – the summit crater width measured the same as W_{CO} using perimeter from ArcMap software; H_{CO} – basal volcano height; H_{CR} – the height of the summit crater; H – the absolute height of the volcano edifice (the difference between H_{CR} and H_{CO}).

[a] Longitudes and latitudes are based on the Geographic Coordinate System.

[b] Slope analysis has been conducted based on the MEX HRSC Blended DEM Global 200 m (Fergason et al., 2018). To calculate flank slopes, we used a simplified model of the cone as a frustum.

[c] Volume has been measured using the equation for frustum.

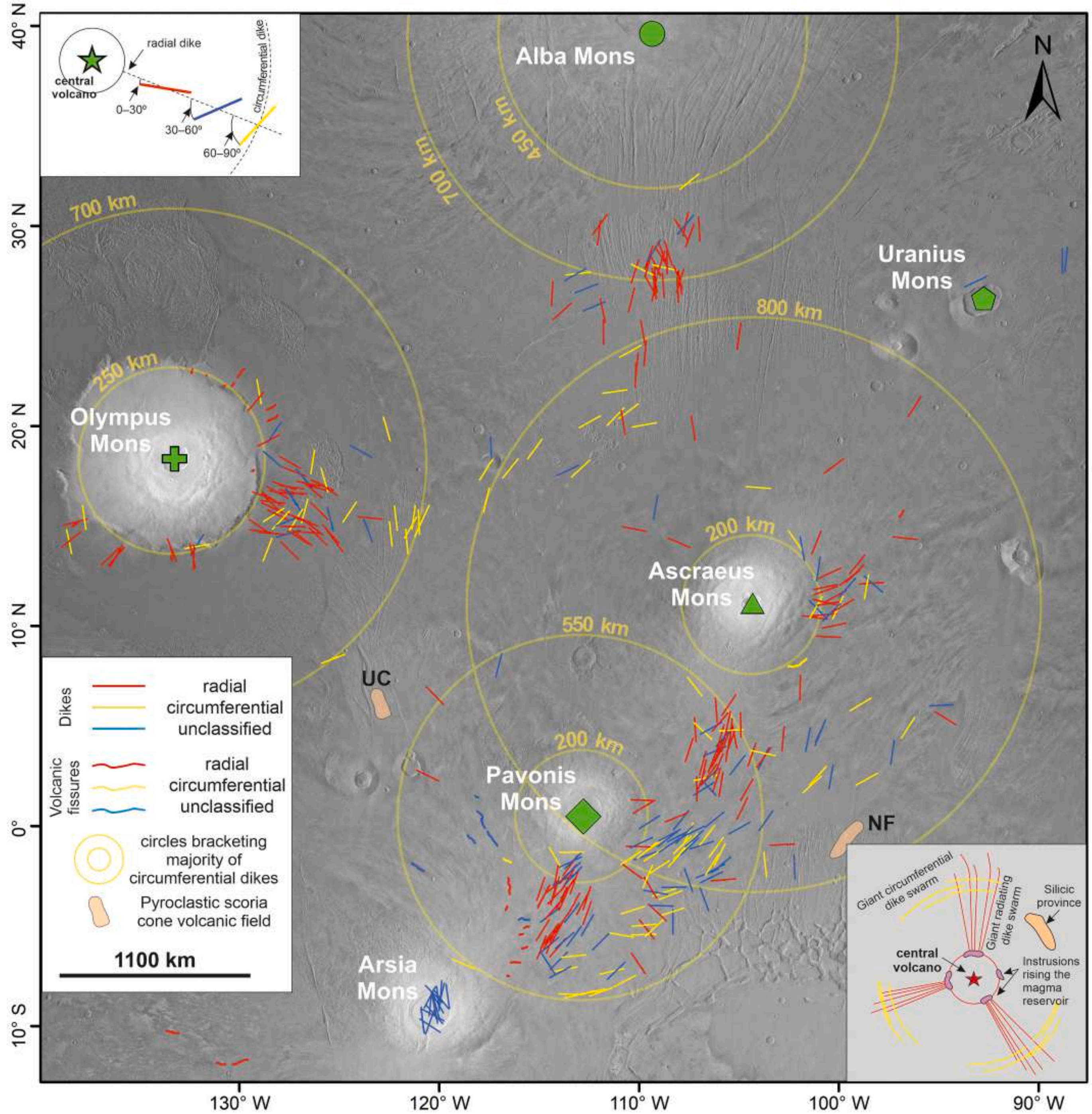

Fig. 9. Presumed stress orientations of the predicted radial and circumferential dikes around central Tharsis volcanoes. The left insert shows the methodology applied in this study to classify volcanic structures. The right insert has been adapted from Ernst et al. (2019) to visualize the simplified arrangement of radial and circumferential dikes in the plan view for the terrestrial plumbing system of a large igneous province associated with mantle plumes. To visualize this magmatic system, the reader is referred to cross section on Fig. 10. UC – Ulysses Colles; NF – Noctis Fossae volcanic fields.

evolution, and their origin have been extensively discussed (Bleacher et al., 2009; Hauber et al., 2009, 2011; Richardson et al., 2021). These edifices are common and unevenly distributed in Tharsis forming clusters in the vicinity of the major volcanoes (Hauber et al., 2009; Richardson et al., 2021). Volcanic edifices studied herein consist of various geomorphological types including the low-shields edifices, fissure constructs, as well as rounded pyroclastic scoria cones (Fig. 3A–C). Except for typical axisymmetric edifices (Fig. 2A), or multi-cone clusters with overlapping lava aprons (Fig. 2B), the volcanic landforms may form elongated edifices parallel to the local tectonic features (Fig. 2C-E) or even steep-flank edifices suggesting their explosive origin (Fig. 2B). We also observed elongated structures consisting of small edifices that are volcanic fissures (Fig. 2C). These features are hundreds of meters to several dozen kilometers wide (including their lava flows), and hundreds of meters high. Although Tharsis is the largest volcanic province on Mars, the origin of numerous small volcanic edifices in this area is not yet fully understood. Their genesis may be related to (1) the evolution of larger volcanic edifices (Hughes et al., 2005; Richardson et al., 2021) such as Olympus Mons or the Tharsis Montes, (2) magma ascend through axial crustal fractures via dikes from the

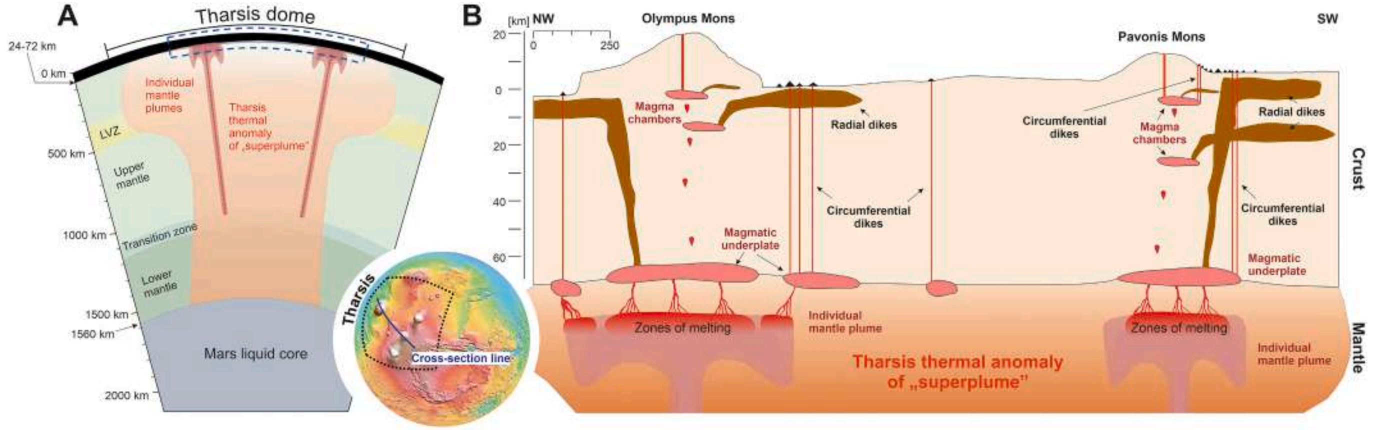

Fig. 10. Interpretation of the magmatic plumbing system of Tharsis volcanic province. (A) Schematic cross-section of Mars beneath the Tharsis dome adapted from Lagain et al. (2021). Below Tharsis, there is located a thermal anomaly of a potential single superplume within which the individual mantle plumes might have occurred. The thermal anomaly below Tharsis is proposed by Breuer and Moore (2015) who think that the extensive long-standing volcanism within Tharsis could be explained with stable and long-standing plumes that have a higher temperature than the average mantle. The insert shows the topographic map of Mars with the marked cross-section line. The blue dashed area shows the location of the cross-section. LVZ – Low Velocity Zone. (B) Cross-section of the Tharsis region based on the interpretation of the distributed volcanism associated with central volcanoes. We suppose that each central Tharsis volcano is sourced by an individual mantle plume that forms a magmatic system. The adjacent distributed volcanoes are likely sourced by radial and circumferential dikes. The radiating and circumferential swarms might be sourced either by deep-seated magmatic underplate at the crust-mantle boundary or magma chambers within the Martian crust. The cross-section profile is based on the Mars MGS MOLA - MEX HRSC digital elevation model of 200 m/px resolution (Fergason et al., 2018). (For interpretation of the references to colour in this figure legend, the reader is referred to the web version of this article.)

asthenosphere source zones (Richardson et al., 2021), (3) locally-restricted tectonic trends (Mouginis-Mark and Christensen, 2005; Hauber et al., 2009), (4) independent younger magma production events (Bleacher et al., 2007, 2009), (5) mantle plumes (Kiefer and Li, 2009; Grott and Breuer, 2010), or (6) zones of enhanced partial melting underneath a thickened crust of Tharsis (Schumacher and Breuer, 2007).

Hauber et al. (2009), who analyzed the low shield volcanoes in Tharsis, claim that their spatial distribution does not show any affinity with large-scale tectonic features. Thus, they cannot be related to the mantle plumes supplying major volcanoes. In addition, Bleacher et al. (2009) documented small volcanic vents south of Pavonis Mons and also interpreted the lack of affinity between them and the central volcano. In contrast, Richardson et al. (2021) suggested that magmas that sourced the distributed volcanism into the east of Tharsis Montes might be located beneath the eastern side of Tharsis Montes and could efficiently ascend through axial crustal fractures feeding the small volcanic structures over the last 500 Ma. Considering the spatial distribution of the edifices along with their ages, it appears that volcanic landforms in Tharsis are age-related within the subprovinces and occur mainly in the vicinity, besides the slopes, or rarely on the slopes of the major volcanoes (for example Olympus Mons or Tharsis Montes).

In the study area, clusters of edifices are mainly concentrated on the eastern or southern sides of the Olympus Mons, Alba Mons, and the three Tharsis Montes volcanoes. This contrasts to the northern and western sides which are almost devoid of volcanic edifices. In addition, we found volcanic edifices only on the eastern side of Uranius Mons both on the slopes and beside the main edifice. Based on the mapping, we found only a few mostly isolated volcanic edifices on the northern sides of Olympus Mons and Ascraeus Mons. Richardson et al. (2021) suggest that this discrepancy in the volcanic landforms arrangement is caused by the existence of ice deposits on the northwestern slopes of each volcano (e.g., Scanlon et al., 2015) or more efficient burial by rift lava aprons. They also proposed that the northwestern sides of the Tharsis Montes might not have been affected by the volcanic activity as frequently as the southeastern flanks.

The morphology and topography of volcanic features are crucial in providing information on their tectonic settings and origin. Hauber et al. (2009) provided detailed morphological information about Martian landforms such as low shields, vents, and lava flows associated with volcanism on Mars. Here, we compared a wide set of the well-preserved and well-visible summit craters of volcanic edifices to the previous studies of Martian low shields to investigate the volcanic origin and volcanism styles within the Tharsis region (Hauber et al., 2009). The comparison of these results with previously published data showed a high similarity (Fig. 3C).

Using the above morphological data, we demonstrated that the Tharsis region hosts at least two different types of volcanism. These volcanic edifices are various in size and flank slope angles (Fig. 3B). Our morphological data for low shield volcanoes of <1° for the slopes match previous measurements (cf. Sakimoto et al., 2002; Hauber et al., 2009). We also found a cluster of edifices characterized by higher values of flank slopes ranging from 3 to 21° (Fig. 3) suggesting an explosive character of eruptions in Tharsis (Brož and Hauber, 2012; Pieterek et al., 2022a). Except for explosive origin, some of these edifices (3–5°) might be also caused by repetitive, low-volume lava flows with higher viscosity around the central vent as is the case for the terrestrial small shield volcanoes of the eastern Snake River Plain (Greeley, 1982).

Based on the theoretical considerations such as lower gravity, fluid convective motions, crystal setting processes, and ascent rates of the magma through the Martian crust, explosive volcanism should be common on Mars (Wilson and Head, 1994). To date, only Brož and Hauber (2012) and Pieterek et al. (2022a, 2022b) described volcanic fields of scoria cones in Tharsis. Brož and Hauber (2012) pointed out the possibility of old, more explosive volcanism in Tharsis. This discrepancy in the number of explosive volcanic fields compared to effusive volcanism may result from common explosive eruptions in the past, and related landforms are not well preserved on the Martian surface. The lack of evidence for late Amazonian explosive eruptions prompted Brož et al. (2021) to suggest that ascending magmas in the Noachian period could have been more volatile-rich and/or that the underground magma-water interaction was more frequent. Alternatively, widespread effusive plain-style volcanism episodes over the Late Amazonian period may have buried the older explosive-origin volcanic features. This is in line with a hypothesis suggesting a change of volcanism style from explosive to effusive around the Hesperian-Amazonian proposed by Robbins et al. (2011). The hypothesis is further supported by Kremer et al. (2019) and Baratoux et al. (2013) who pointed out that planet-wide change in volcanism style may have occurred in the Hesperian period.

The different styles of volcanism may be related to various compositions of magmas changing in time and space. The most typical Martian low shield volcanoes and their lava flows are basaltic with low silica content <52.5 wt% (Zimbelman, 2000; Taylor et al., 2010). Mineralogical constraints on the late 100–50 Ma volcanic plain in Noctis Labyrinthus imply basaltic composition with plagioclase, clinopyroxene, and low olivine content (Mangold et al., 2010). The supplying magmas are characterized by low viscosity due to the high effusion rates, high-temperature eruptions, or chemical composition of erupting magmas (low Si content). Thus, the low shield volcanoes might form low-angle slope cones, which clustered together, create large volcanic fields (for example, southeast of Pavonis Mons or east of Ascraeus Mons). However, explosive volcanic eruptions appear to be more common than previously thought. They should form much smaller structures with lower basal diameters and much steeper flank slopes (7–29^0) (Brož and Hauber, 2012; Brož et al., 2015; Pieterek et al., 2022a). These observations are in line with our results showing both lower basal areas and higher slopes (in this study ranging from ~3^0 to ~21^0) for scoria cones (Fig. 3).

5.2. *The affinity of distributed volcanoes and the major Tharsis volcanoes*

Except for twelve major volcanoes, Tharsis volcanic province on Mars hosts at least 659 volcanic landforms clustered into subprovinces (Fig. 1). These clusters most likely show affinity with nearby central volcanoes. Clusters of volcanic edifices comprise either low-shield volcanoes or scoria cones associated with volcanogenic vents have been previously described in the Tharsis volcanic province by Hughes et al. (2005), Hauber et al. (2009, 2011), Bleacher et al. (2007, 2009), Brož and Hauber (2012, 2013), Brož et al. (2015), Ciazela et al. (2019), and Richardson et al. (2021). Although Richardson et al. (2021) highlighted that the distributed-style volcanism has been common throughout the Tharsis history and has been affected by large volcanoes and regional fossae, we interpreted the origin of distributed volcanic edifices in Tharsis differently based on our data set. The differences in mapping, interpretations, and conclusions compared to Richardson et al. (2021) may be caused by the exclusion of the Tempe Terra and Syria Planum regions in this study, which represent ancient volcanic activity (majority between 0.4 and 1.6 Ga; Hauber et al., 2009). Here, the spatial distribution, the orientation of volcano summit alignments (Section 4.1), and absolute surface age of the distributed volcanoes (Section 4.2) allowed us to identify six subprovinces related to the major Tharsis volcanoes (Olympus Mons, Alba Mons, Arsia Mons, Pavonis Mons, Ascraeus Mons, and Uranius Mons).

Large Igneous Provinces (LIPs) on Earth may serve as analogs (Magee et al., 2019). Buchan and Ernst (2019) pointed out that giant dike systems on Earth being an important component of terrestrial LIPs, may be similar to those on Mars (Fig. 9). By using terrestrial analogs to understand how dike swarms are expressed at the Martian surface, we can attempt to reconstruct magma plumbing systems underneath the Tharsis region (Fig. 10). In this study, we assumed that small volcanic features classified to the different subprovinces belong to large magmatic systems controlled by the migration of magmas through dikes sourced from either the magma chambers within the Martian crust or individual deep-sourced zones emplaced beneath the nearby central volcano. The concentrated arrangement of the small distributed volcanoes around the central volcanoes in Tharsis is similar to the terrestrial volcanic systems (Connor et al., 2000; Le Corvec et al., 2013; Buchan and Ernst, 2019). On Earth, we can distinguish monogenetic and polygenetic volcanic systems (Németh and Kereszturi, 2015). Considering the distributed volcanism in Tharsis, we can observe many similarities with the theoretical model for dominantly large-volume polygenetic volcanoes and small-volume, satellite volcanoes commonly inferred to be monogenetic volcanoes as proposed by Németh and Kereszturi (2015). In this model, shallow magma chamber beneath the central volcano is supplied by a deeper source zone. The volcanic edifices on the flanks of a central volcano may be sourced by dike systems rooting from the crustal magma chambers or independent deep-seated magma zones ascending through the crust. Based on the theoretical consideration of the ascent, emplacement, and eruption of magma on Mars, Wilson and Head (1994) inferred that magma chambers are expected to lie about four times deeper on Mars than on Earth. In addition, using a model for the plumbing system of terrestrial LIPs associated with mantle plumes proposed by Ernst et al. (2019), we inferred that each magmatic system of the central Tharsis volcano may be associated with distributed volcanoes sourced by radial and circumferential dikes. Magma may migrate through giant radiating dike swarms from the same sources (e.g., magmatic underplate or magma chamber) as in the Németh and Kereszturi (2015) model.

The formation of circumferential dikes can be considered in two, possibly complementary, models (Buchan and Ernst, 2019; Ernst et al., 2019). In the first model, these dikes are emplaced above the edge of the plume head which has been flattened at the base of the lithosphere. In this case, the magmas could have migrated beyond the main edifices of central volcanoes, creating giant circumferential dike swarms that erupted on the surface hundreds of kilometers away from the central uplift. Circumferential dikes of terrestrial LIPs are mostly centered around the focal point of roughly coeval radial dikes (e.g., High Arctic, Buchan and Ernst, 2018; Madagascar and Yakutsk-Vilyui, Syberia, Buchan and Ernst, 2019) and show diameters of ~450 to ~2500 km (Buchan and Ernst, 2019).

In the second model, the circumferential dikes are emplaced above the edge of the magmatic underplate (i.e., at the base of the crust) and manifest on the surface even on the flanks of the central volcano. On Mars, Montési (2001) documented concentric structures within the main edifice of Pavonis Mons and interpreted them as an underground circumferential dike swarm originated from the Tharsis Montes magma reservoir. In addition, Richardson et al. (2021) mapped and interpreted volcanic vents in the Tharsis volcanic province as individual surface eruptions that concentrated in some regions of Tharsis form volcanic fields. These volcanic landforms have been interpreted as monogenetic volcanoes fed by deep-seated systems of dikes (Hauber et al., 2009; Richardson et al., 2021). Richardson et al. (2021) suggest that the distributed volcanism beyond the central edifice (e.g., Tharsis Montes) is sourced by the individual ascending dikes through axial fractures from the asthenosphere source, whereas landforms on the flanks of the central edifice are likely sourced by focused magma radiating via fractured pathways. In this case, the summit crater alignments may reflect the orientations of the underlying dikes that sourced the volcanic activity of the edifices. However, on Earth, rift systems may be also associated with dikes that have been developed due to the magma ascent from the asthenosphere source zones (e.g., Tolbachik eruption; Koulakov et al., 2017).

On Earth, silicic magmas are often associated with LIP (Fig. 9; Ernst et al., 2019). Although silicic magmatism is typically a minor component of many terrestrial LIPs, some examples have been documented (Columbia River – 16 Ma, Parana-Etendeka – 134 Ma, and Emeishan – 260 Ma; Ernst et al., 2019 and references therein). On Mars, felsic rocks and silicic material have been already discovered, demonstrating that extreme magma differentiation has occurred (Christensen et al., 2005; Wray et al., 2013; Morris et al., 2016). These observations indicate that the Martian crust, although dominated by basalt, contains a variety of igneous rocks. Currently, only two volcanic fields of pyroclastic scoria cones potentially owed to silicic magmas have been described in Tharsis (Brož and Hauber, 2012; Pieterek et al., 2022a). In both cases, authors have considered long-lived magma chambers located beneath the study areas that allowed magma to differentiate to more silicic compositions. The presence of scoria cone volcanic fields in Tharsis (Fig. 9) suggests that the silicic type of magmatism may be considered as a part of large magmatic systems related to central volcanoes.

5.3. Reconstruction of the magmatic plumbing system of Tharsis

In this study, we linked the spatial distribution of the volcanic edifices and the summit alignment orientations with surface ages to verify if theoretical models of the magmatic plumbing system including the formation of radial and circumferential dikes are valid for Tharsis. On Earth, the occurrence of both giant circumferential and radial swarms often indicates the presence of mantle plumes (Buchan and Ernst, 2019; Ernst et al., 2019). Volcanic summit eruptions of central volcanoes might be accompanied by magma migration through radial and circumferential dikes that may erupt on the Martian surface similarly to terrestrial volcanic systems. In periods when the magma pressure in the chamber could not be sufficient to feed the summit caldera, magmas likely migrate via smaller, alternate pathways to the surface using dikes that form small volcanic edifices, emplaced at lower elevations compared to the summit caldera. These eruptions reveal younger ages than the last activity on the summit caldera of the nearby central volcano. On Earth, the collapse of the summit volcano caldera may also activate shallow plumbing systems (Roman and Lundgren, 2021) and result in magma migration through radial and circumferential dikes that are mainly controlled by the tensile stress field imposed by unloading (Corbi et al., 2015).

In some cases, the radial dike swarms on Earth are older than the circular dike swarms (Koch and Manga, 1996; Krassilnikov and Head, 2003) or form simultaneously due to multiple pulses of diking (Buchan and Ernst, 2019). Our results, however, suggest that the radial and circumferential dikes were active simultaneously during the last 200 My. We hypothesize that an active superplume may be emplaced beneath the entire Tharsis (Zhong, 2009; Lagain et al., 2021) with mantle plumes developed under each of the major volcanoes that are responsible for the volcanic activity both within the summit caldera of the central volcano and adjacent distributed-style volcanoes (Fig. 10). Recently, Lagain et al. (2021) inferred that Amazonian-age volcanic activity in Tharsis (from at least 2.4 Gyr until at least 330 Myr ago) is sourced by a stable deep-seated mantle superplume embracing individual mantle plumes that might be still active and provide magma source for central volcanoes and distributed volcanism (Fig. 10). This agrees with the hypothesis presented by Breuer and Moore (2015) who explained the extensive long-standing volcanism within Tharsis by stable and long-standing plumes having a higher temperature than the average mantle. On Earth, such a superplume model has been already proposed to explain lateral changes in S-waves velocity beneath South Africa (45°S, 55°E) extending upward from the core-mantle boundary (Ni and Helmberger, 2003). In this case, small-scale plumes extend towards the surface from the top of the large-scale and more stable superplume. The presence of separate mantle plumes under each central volcano, for example beneath Olympus Mons, Alba Mons, and three Tharsis Montes, is further supported by the elevated edifices of central volcanoes compared to the entire Tharsis dome. Mantle plumes under the Tharsis volcanoes may generate temporally active magma chambers that sourced caldera-forming eruptions, finally leading to the caldera collapse (Mouginis-Mark and Wilson, 2019).

On Earth, the two most common dike types, radial and circumferential, form in different stress conditions (Chadwick and Dieterich, 1995; Acocella and Neri, 2009; Galland et al., 2014). Galland et al. (2014) experimentally modeled that the formation of radial and circumferential dikes is governed by the geometry of the magma source (size and depth) and viscous stresses due to magma flow and strength of the country rock. In addition, the distribution of compressive and tensile stresses in the vicinity of the terrestrial magma chamber may significantly affect the magma movements depending on volcano edifice size (height and diameter) (Gonnermann and Taisne, 2015). On one hand, the radial dikes are likely formed when the magmatic underplate is seated relatively deep compared to magma chamber size, or when the magma influx (or viscosity) is low. On the other hand, circumferential dikes occur when the magma source is emplaced shallow, relative to its lateral extent, or when the magma influx (or viscosity) is high (Galland et al., 2014). If this is true for Mars, most radial dikes have likely migrated from the relatively small and short-living magma chambers located within the crust, whereas circumferential dikes have likely originated from the broadly-extended magmatic underplates at the crust-mantle boundary (Fig. 10). In addition, according to Buchan and Ernst (2019), Mars models of magma emplacement indicate a crustal stress distribution that is favorable for the formation of circumferential fractures within the crust. Those fractures could be broadly used by ascending magma. Therefore, our results when combined with data on mechanical rock properties and the regional stress regime in Tharsis, may provide improved constraints on the mechanism of the magma emplacement.

However, considering the spatial distribution of volcanic edifices together with their summit alignments, we inferred that each magmatic plumbing system might be different. For example, we demonstrated that volcanic clusters nearby the Olympus Mons, Pavonis Mons, and Ascraeus Mons are most likely supplied by radial and circumferential dikes (Figs. 5 and 9), while magmas supplying the volcanoes linked to Alba Mons and Arsia Mons clusters are transported only via radial dikes. These volcano clusters extend up to ~1200 km from the summit calderas of the central volcanoes (Fig. 5). Mouginis-Mark and Wilson (2019) inferred that intrusions of lateral dikes to radial distances >2000 km are linked to the formation of the individual calderas at Olympus Mons. Richardson et al. (2021) highlighted that vents of Olympus Mons, Arsia Mons, and Ascraeus Mons clusters exhibit radially aligned orientations with respect to each central volcano. However, in this study, these orientations are less clear for Tharsis Montes. Based on our measurements, we suppose that the Arsia, Pavonis, and Ascraeus dike swarms might overlap with each other as a similar pattern has been observed for terrestrial systems (e.g., Pilanesberg Complex in South Africa; de Kock et al., 2019).

Our evidence for young volcanic activity is supported by the newest observation of the seismic *InSight* mission, which suggests the presence of a liquid Martian core. The liquid core may generate the convection within the Martian mantle resulting in the formation of mantle plumes that source surface volcanism and tectonic activity (Stähler et al., 2021). Considering our model of the origin of distributed volcanism around the central Tharsis volcanoes, we found volcano-tectonic evidence indicating that one magmatic plumbing system controls one central volcano and its adjacent distributed volcanoes.

5.4. Recent volcanic reservoirs beneath the major Tharsis volcanoes

To date, only several studies modeled the ages of the latest volcanic activity of low shields on Mars, either by crater counting of individual volcanoes (Brož, 2010; Hauber et al., 2011; Christoph and Garry, 2017) or by crater counting across volcanic plains (Brož and Hauber, 2012). The twelve Tharsis major volcanoes have been previously dated using the crater counting method by Neukum et al. (2004), Werner (2009), Robbins et al. (2011), and Ciazela et al. (2019). The five largest volcanoes in Tharsis (Olympus Mons, Alba Mons, Arsia Mons, Pavonis Mons, and Ascraeus Mons) were active over the last 250 Ma, within their summit calderas and show similar ages obtained by different studies with an exception of Alba Mons (Fig. 8). The age of the latest volcanic activity for the Alba Mons summit caldera ranges between 450 ± 100 Ma (Robbins et al., 2011) and 133 ± 42 Ma (Ciazela et al., 2019). In addition, the obtained model ages of the major volcanoes match the ages of adjacent volcanic edifices (Fig. 8), which are <200 Ma in most cases, except for the edifices within the Arsia Mons summit caldera and Arsia's northeastern flank. According to Robbins et al. (2011), the latest activity of the Olympus Mons caldera took place 140 ± 20 Ma. Other studies indicate even younger age that is ~100 Ma (Werner, 2009) or 64 ± 26 Ma (Ciazela et al., 2019). Our ages of distributed volcanism in the Olympus Mons subprovince are in line with previously published data for the summit caldera activity of Olympus (Fig. 8). We found that distributed volcanism occurred mainly between 140 ± 40 Ma and 27 ± 6 Ma.

Analogical observations are made in the other Tharsis subprovinces. For example, Alba Mons summit caldera activity is dated between ~180 Ma (Werner, 2009) and 133 ± 42 Ma (Ciazela et al., 2019). Our ages of the volcanic landforms to the south of Alba Mons range from 160 ± 31 Ma to 59 ± 13 Ma. The volcanic edifices within the Arsia Mons caldera reveal ages between 296 ± 36 Ma and 148 ± 37 Ma, whereas the latest summit caldera activity of Arsia Mons was dated to 130–125 Ma (Neukum et al., 2004; Werner, 2009; Robbins et al., 2011; Ciazela et al., 2019). Considering the volcanic activity of Pavonis Mons, Ciazela et al. (2019) and Robbins et al. (2011) showed an age between 140 and 130 Ma. For distributed volcanoes adjacent to Pavonis Mons, we determined the ages ranging from 147 ± 25 Ma to 55 ± 6 Ma. The last summit caldera activity of Ascraeus Mons has been estimated to occur between ~200 Ma (Robbins et al., 2011; Ciazela et al., 2019) and ~ 100 Ma (Neukum et al., 2004; Werner, 2009). In this study, we distinguished various smaller subprovinces adjacent to Ascraeus Mons, and the latest volcanic activity within these subprovinces ranges from 180 ± 10 Ma to 50 ± 15 Ma.

Considering the oldest volcano activity recorded in this study by volcanoes located in the vicinity of Uranius Mons, we obtained the ages of 1400 + 330/−260 Ma and 990 ± 280 Ma. These ages are also in accordance with the latest activity at the summit caldera of Uranius Mons (1020 ± 140; Ciazela et al., 2019). In general, the obtained ages of the distinguished subprovinces match the ages of summit caldera activity of the adjacent central volcano (Fig. 8).

In this study, small volcanic edifices exhibit similar ages (mostly <200 Ma) throughout the entire study area. Although the mapping of the volcanic vents and landforms indicates that distributed volcanism has occurred unevenly in Tharsis, concentrating on the southern sides of major edifices (e.g., Olympus Mons, Tharsis Montes), our results indicate common volcanic activity that occurred at a similar time in Tharsis, especially within the distinguished volcano clusters. The relatively recent volcanic activity (<200 Ma) adjacent to the major Tharsis volcanoes has been previously pointed out by Brož (2010) and Hauber et al. (2011) (Fig. 8), who suggested the prolonged distributed volcanism adjacent to the central volcanoes. Brož (2010) determined surface ages of 44 lava flows in the vicinity of major Tharsis volcanoes that range between 215 and 44 Ma. His results support our observations of distributed volcanism in Tharsis emplaced in the last 200 Myr (for more details see Table 2 and Fig. 7). These results were further supported by Hauber et al. (2011), who found the youngest volcanic activity adjacent to central volcanoes (see Fig. 3 in Hauber et al. (2011)). Therefore, our ages are in line with the previous works and we inferred that each volcanic subprovince related to a central volcano might have been supplied by a separate magmatic system (Fig. 10) as revealed by the difference in ages between the subprovinces (Figs. 7–8).

The concentrated distribution of volcanoes into clusters, together with their ages, indicate that the southeastern region of Olympus Mons and Tharsis Montes or southern flanks of Alba Mons are privileged Tharsis regions for magma migration during the last 200 Ma. Based on analyses of summit caldera complexes of Martian volcanoes, Wilson and Head (1994) suggested that the magma migration from the mantle into crustal chambers is episodic. In addition, Neukum et al. (2004) inferred that summit calderas (including Arsia Mons, Ascraeus Mons, and Olympus Mons) have undergone repeated volcanic activity during the last billion years with the most recent activity registered around 200–100 Ma. Therefore, the distributed volcanoes could have also been sourced in pulses during the last 200 Myr what is expressed by volcanic clusters of similar age determined in this study (see Section 4.2 and Fig. 7). In addition, the youngest lava flows in Tharsis were recorded on the lower flanks of Olympus Mons (~2.4 Ma) indicating that volcanism might be still active (Neukum et al., 2004).

Lagain et al. (2021) revealed the link between the depleted olivine-phyric shergottites launched 1.1 Ma and the Tharsis dome, suggesting that Amazonian-age volcanic activity (from at least 2.4 Gyr until at least 330 Myr ago) is most likely sourced by the stable deep-seated mantle superplume that might be continuously active and also constitute the source for distributed volcanism (Fig. 10). In contrast, Bleacher et al. (2007) proposed an alternative hypothesis assuming that small volcanic edifices adjacent to the Tharsis Montes can be fed by magmas migrating through the Martian crust from the mantle source zones. A similar interpretation to that of Bleacher et al. has been proposed by Richardson et al. (2021), who inferred the link between Tharsis Montes and their distributed volcanism. They hypothesized the presence of a widespread magma source at the base of the crust to the east and beneath the Tharsis Montes. They also suggested that distributed volcanism can be fed by the ascending dikes without any focusing through the Martian crust, except volcanoes emplaced on the rift apron lavas of Tharsis Montes that were supplied by focused magma along fractured pathways, forming radially orientated vents near each central volcano. The common occurrence of distributed volcanism beyond the central volcanoes together with their summit alignments and ages suggest the magma migration through radial or circumferential dikes sourced by deep-seated magmatic underplates (Fig. 10). We suppose that mantle plume activity results in the formation of temporary active magma chambers within the Martian crust, especially beneath the large volcanoes active during the Late Amazonian that fed some of the adjacent distributed volcanoes. However, many distributed volcanoes can be sourced by vertically ascending dikes (radial and circumferential) from the underplating magma source zones (Fig. 10). Except for Tharsis Montes, we confirmed the young volcanic activity in the vicinity of Olympus Mons (down to 27 ± 6 Ma) and Alba Mons (<70 Ma). Considering that volcanism on Mars has been active for four billion years, the volcanic activity related to major Tharsis volcanoes is rather dormant than extinct. When magma production is not sufficient to supply the high central volcanoes, magmas may still migrate through radial or circumferential dikes suppling distributed volcanism.

In Tharsis Montes, Robbins et al. (2011) observed a decreasing trend in summit calderas ages, from the northernmost Ascraeus Mons (250 Ma) to southwestern Pavonis Mons (130 Ma) and Arsia Mons (~130 Ma). They suggested that the volcanoes were fed by a branching plume dying out southwards. Bleacher et al. (2007) proposed an opposite theory that these volcanoes were sourced by a single mantle plume migrating towards the north. However, we found the oldest volcanic edifices within the Arsia Mons caldera (296–148 Ma) and on the northeastern flanks of Arsia (205–177 Ma). On the other hand, lava flows that originated from the southern lava apron of Arsia Mons show an apparent peak age of 150 Ma (Tesson et al., 2020). The previously mentioned ages related to the Arsia Mons activity are in accordance with the age derivation results (from 73 ± 36 Ma to 313 ± 110 Ma) obtained by Richardson et al. (2017). The authors modeled the ages of lava flows within the Arsia Mons caldera and inferred that volcanism likely began between 300 and 200 Ma with the most intense activity ~150 Ma and a smaller secondary pulse ~100 Ma. Then, the volcanism greatly waned ~90 Ma due to the larger-scale diminishing of volcanic activity at Arsia Mons related to the emplacement of lava flows on the volcano flanks (Richardson et al., 2017). Although modeling of the recurrence rate of volcanism for Arsia caldera suggests that volcanic eruptions might have been waning longer to cease ~10 Ma (Richardson et al., 2017), none of the recently published papers revealed ages younger than ~70 Ma. Towards the north direction, a large number of small volcanoes of Pavonis Mons are from 147 to 55 Ma old. The northernmost-located Ascraeus Mons is accompanied by three clusters of volcanic edifices showing the decreasing age, the eastern (180–88 Ma), northwestern (111–92 Ma), and southern (173–50 Ma). These results seem to contradict the aforementioned hypothesis of Robbins et al. (2011) and Bleacher et al. (2007) and suggest that each central volcano was supplied by a separate plume with a separate magmatic system.

In addition, our results for the volcanic edifices of the Ceraunius Fossae are contrary to the tectonostratigraphic units retrieved from

Tanaka et al. (2014). Tanaka et al. (2014) classified Alba Mons as Amazonian, whereas the volcanic plains to the south as mostly Hesperian-Amazonian. However, our results suggest that the volcanoes in the Ceraunius Fossae to the south area are also likely Late Amazonian (160–70 Ma). These results match earlier observations of Christoph and Garry (2017), who analyzed the Ceraunius Fossae low shields and inferred two separate volcanic events dated to 200 ± 30 Ma and 170 ± 20 Ma using the crater age model of Hartmann (2005). Brož (2010) also determined the low shield ages and obtained yet lower values of 137–57 Ma. All these results indicate young (<200 Ma) volcanic activity in the Ceraunius Fossae region.

Many volcanic edifices, such as those near Uranius Mons, had not been previously dated. Here, the volcanic cluster emplaced adjacent to the Uranius Mons reveals an age of ~1 Ga and might be related to the Tempe Terra volcanic structures that show ages mostly between 800 and 400 Ma (Hauber et al., 2011). These observations indicate that the volcanic cluster associated with Uranius Mons is even older than the Tempe Terra volcanism. Although there is clear evidence that <250 Ma volcanism in the Tharsis region is associated with the major volcanoes, an older volcanic Uranius Mons cluster (~1 Ga) matching the latest activity in the summit caldera of Uranius Mons, suggests that distributed volcanism related to major volcanoes was likely active throughout the Amazonian.

In contrast to similar ages of various subprovinces in Tharsis observed by Hauber et al. (2011) and Richardson et al. (2021), our study revealed the age differences between various subprovinces (Figs. 7 and 8). The distributed volcanoes show various age ranges for each subprovince: Olympus Mons (135–43 Ma), Tharsis Montes (296–55 Ma), Alba Mons (421–59 Ma), and Uranius Mons (1400–990 Ma; for more details, see Table 3). Syria Planum likely represents a completely different magmatic province. Volcanic activity in Syria Planum has begun >4 Ga (Baptista et al., 2008; Hauber et al., 2011; Xiao et al., 2012) with the main volcanic phase between the Hesperian and Early Amazonian period (Baptista et al., 2008; Richardson et al., 2012). Hauber et al. (2011) shows also younger ages with most of the volcanic edifices they dated being formed between 1600 and 800 Ma and a few even ~300 Ma. Altogether, however, the ages (4000–300 Ma; most of the ages >800 Ma; Hauber et al., 2011) indicate that the magmatic processes leading to the formation of volcanic edifices in Syria Planum cannot be associated with the Late Amazonian activity of the Tharsis volcanoes.

6. Conclusions

The spatial distribution, the orientation of volcano summit craters and central fissure vents coupled with the surface age determinations of volcanic edifices within Tharsis allowed us to reconstruct the magmatic plumbing system of the Tharsis volcanic province in the Late Amazonian period (<250 Ma), and reveal the spatial-temporal relationship between volcanic edifices and major volcanoes. This geological and morphological evidence prompts us to present the following conclusions and interpretations:

1. The major Tharsis volcanoes on Mars are associated with hundreds of smaller volcanic edifices situated mainly beside the main edifice of the nearby central volcano. Using spatial distribution, the orientation of volcano summit craters, and central fissure vents together with surface age determination, we classified volcanic landforms into subprovinces supplied by distinct and separated magmatic plumbing systems. We observe both young (<250 Ma) distributed volcanism associated with large low shield volcanoes such as Olympus Mons, Tharsis Montes, and Alba Mons, and much older (~1 Ga) distributed volcanism found in the vicinity of Uranius Mons.
2. Recently or currently active magmatic plumbing systems may be present below Olympus Mons, Tharsis Montes, and perhaps south of Alba Mons. Summit calderas of the major volcanoes and accompanying distributed volcanic landforms were likely controlled by central magmatic reservoirs sourced by individual mantle plumes located beneath central Tharsis volcanoes. Magmas ascend from mantle plume regions to magmatic underplate lenses emplaced at the base of the Martian crust or/and crustal magma chambers located beneath central volcanoes. Then, the magmas may migrate to the subsurface levels via radial and circumferential dikes, either from magmatic underplate or crustal magma chambers.
3. The volcanic edifices have the same age or are younger than the summit calderas of their central volcanoes suggesting their temporal affinity. Eruptions in volcanic edifices could thus extend into magma waning periods when magma supply is high enough to sustain summit eruptions. This similarity in model ages indicates the prolonged volcanic activity in Tharsis suggesting that major Tharsis volcanoes are not extinct but perhaps currently dormant and might be reactivated in the future. This observation is also consistent with the newest seismic data from the *InSight* mission, which suggests the presence of a liquid Martian core (Stähler et al., 2021).

Declaration of Competing Interest

The authors declare that they have no known competing financial interests or personal relationships that could have appeared to influence the work reported in this paper.

Acknowledgements

We thank editor E. Rampe, J. Richardson, and an anonymous reviewer for their thorough and insightful comments. We also acknowledge A. Muszyński and K. Stattegger from the Adam Mickiewicz University as well as D. Mège and P.-A. Tesson from the Space Research Centre Polish Academy of Sciences for reading the manuscript or engaging in discussions. The rose diagrams were plotted using Stereonet 10.2 (http://www.geo.cornell.edu/geology/faculty/RWA/programs/stereonet.html; available 30.09.2021). This research is funded by the European Funds Smart Growth (PO WER) project no. POWR.03.02.00-00-I027/17 held by the Adam Mickiewicz University in Poznan. J. Ciazela and M. Ciazela are supported by the National Science Centre Poland (OPUS-19 project no. 2020/37/B/ST10/01420). A. Lagain is supported by the Australian Government, Curtin University, and the Government of Western Australia through the Australian Research Council (DP210100336).

Appendix A. Supplementary data

Supplementary data to this article can be found online at https://doi.org/10.1016/j.icarus.2022.115151.

References

Acocella, V., Neri, M., 2009. Dike propagation in volcanic edifices: overview and possible developments. Tectonophysics 471, 67–77. https://doi.org/10.1016/j.tecto.2008.10.002.

Baptista, A.R., Mangold, N., Ansan, V., Baratoux, D., Lognonné, P., Alves, E.I., Williams, D.A., Bleacher, J.E., Masson, P., Neukum, G., 2008. A swarm of small shield volcanoes on Syria Planum. Mars. J. Geophys. Res. 113, 1–19. https://doi.org/10.1029/2007JE002945.

Baratoux, D., Toplis, M.J., Monnereau, M., Sautter, V., 2013. The Petrological Expression of Early Mars Volcanism, 118, pp. 59–64. https://doi.org/10.1029/2012JE004234.

Beuthe, M., Le Maistre, S., Rosenblatt, P., Pätzold, M., Dehant, V., 2012. Density and lithospheric thickness of the Tharsis Province from MEX MaRS and MRO gravity data. J. Geophys. Res. Planets 117, 1–32. https://doi.org/10.1029/2011JE003976.

Bleacher, J.E., Greeley, R., Williams, D.A., Cave, S.R., Neukum, G., 2007. Trends in effusive style at the Tharsis Montes, Mars, and implications for the development of the Tharsis province. J. Geophys. Res. Planets 112, 1–15. https://doi.org/10.1029/2006JE002873.

Bleacher, J.E., Glaze, L.S., Greeley, R., Hauber, E., Baloga, S.M., Sakimoto, S.E.H., Williams, D.A., Glotch, T.D., 2009. Spatial and alignment analyses for a field of small volcanic vents south of Pavonis Mons and implications for the Tharsis province. Mars. J. Volcanol. Geotherm. Res. 185, 96–102. https://doi.org/10.1016/j.jvolgeores.2009.04.008.

Bleacher, J.E., Richardson, J.A., Richardson, P.W., Glaze, L.S., Baloga, S.M., Greeley, R., Hauber, E., Lillis, R.J., 2010. Updates to the catalog of Tharsis Province small volcanic vents, Mars. In: 41st Annual Lunar and Planetary Science Conference, p. 1615.

Bouley, S., Baratoux, D., Matsuyama, I., Forget, F., Séjourné, A., Turbet, M., Costard, F., 2016. Late Tharsis formation and implications for early Mars. Nature 531, 344–347. https://doi.org/10.1038/nature17171.

Bouley, S., Baratoux, D., Paulien, N., Missenard, Y., Saint-Bézar, B., 2018. The revised tectonic history of Tharsis. Earth Planet. Sci. Lett. 488, 126–133. https://doi.org/10.1016/j.epsl.2018.02.019.

Breuer, D., Moore, W.B., 2015. Dynamics and Thermal History of the Terrestrial Planets, the Moon, and Io. In: Schubert, G. (Ed.), Treatise on Geophysics. Elsevier, pp. 255–305. https://doi.org/10.1016/B978-0-444-53802-4.00173-1.

Breuer, D., Spohn, T., 2003. Early plate tectonics versus single-plate tectonics on Mars: evidence from magnetic field history and crust evolution. J. Geophys. Res. E Planets 108. https://doi.org/10.1029/2002je001999, 8–1.

Brož, P., 2010. Plains Volcanism in Tharsis Region on Mars: Ages and Rheology of Eruption Products. Charles University in Prague.

Brož, P., Hauber, E., 2012. A unique volcanic field in Tharsis, Mars: pyroclastic cones as evidence for explosive eruptions. Icarus 218, 88–99. https://doi.org/10.1016/j.icarus.2011.11.030.

Brož, P., Hauber, E., 2013. Hydrovolcanic tuff rings and cones as indicators for phreatomagmatic explosive eruptions on Mars. J. Geophys. Res. E Planets 118, 1656–1675. https://doi.org/10.1002/jgre.20120.

Brož, P., Čadek, O., Hauber, E., Rossi, A.P., 2015. Scoria cones on Mars: detailed investigation of morphometry based on high-resolution digital elevation models. J. Geophys. Res. Planets 120, 1512–1527. https://doi.org/10.1002/2015JE004873.

Brož, P., Bernhardt, H., Conway, S.J., Parekh, R., 2021. An overview of explosive volcanism on Mars. J. Volcanol. Geotherm. Res. 409 https://doi.org/10.1016/j.jvolgeores.2020.107125.

Buchan, K.L., Ernst, R.E., 2018. A giant circumferential dyke swarm associated with the high Arctic large Igneous Province (HALIP). Gondwana Res. 58, 39–57. https://doi.org/10.1016/j.gr.2018.02.006.

Buchan, K.L., Ernst, R.E., 2019. Giant Circumferential Dyke Swarms: Catalogue and Characteristics. In: Srivastava, R.K., Ernst, R.E., Peng, P. (Eds.), Dyke Swarms of the World: A Modern Perspective. Springer Geology, pp. 1–44. https://doi.org/10.1007/978-981-13-1666-1_1.

Carr, M.J., Pontier, N.K., 1981. Evolution of a young parasitic cone towards a mature central vent; Izalco and Santa Ana volcanoes in El Salvador, Central America. J. Volcanol. Geotherm. Res. 11, 277–292. https://doi.org/10.1016/0377-0273(81)90027-5.

Chadwick, W.W., Dieterich, J.H., 1995. Mechanical modeling of circumferential and radial dike intrusion on Galapagos volcanoes. J. Volcanol. Geotherm. Res. 66, 37–52. https://doi.org/10.1016/0377-0273(94)00060-T.

Christensen, P.R., McSween, H.Y., Bandfield, J.L., Ruff, S.W., Rogers, A.D., Hamilton, V. E., Gorelick, N., Wyatt, M.B., Jakosky, B.M., Kieffer, H.H., Malin, M.C., Moersch, J. E., 2005. Evidence for magmatic evolution and diversity on Mars from infrared observations. Nature 436, 504–509. https://doi.org/10.1038/nature03639.

Christoph, J.M., Garry, W.B., 2017. Spatial and temporal relationships among low shield volcanoes in the Ceraunius fossae region of Tharsis: The last gasp of Martian volcanism. In: 48th Annual Lunar and Planetary Science Conference, p. 2798.

Ciazela, J., Mege, D., Pieterek, B., Ciazela, M., Gurgurewicz, J., Lagain, A., Tesson, P.-A., 2019. Largest Tharsis volcanoes keep growing and mark >4-Ga-lasting martian hot spots. In: 50th Annual Lunar and Planetary Science Conference, p. 1364.

Clinton, J.F., Ceylan, S., van Driel, M., Giardini, D., Stähler, S.C., Böse, M., Charalambous, C., Dahmen, N.L., Horleston, A., Kawamura, T., Khan, A., Orhand-Mainsant, G., Scholz, J.R., Euchner, F., Banerdt, W.B., Lognonné, P., Banfield, D., Beucler, E., Garcia, R.F., Kedar, S., Panning, M.P., Perrin, C., Pike, W.T., Smrekar, S. E., Spiga, A., Stott, A.E., 2021. The Marsquake catalogue from InSight, sols 0–478. Phys. Earth Planet. Inter. 310 https://doi.org/10.1016/j.pepi.2020.106595.

Connor, C.B., Conway, F.M., Sigurdsson, H., 2000. Basaltic volcanic fields. Encycl. volcanoes 331–343.

Connor, C.B., Connor, L., Germa, A., Richardson, J., Bebbington, M., Gallant, E., Saballos, A., 2019. How to use kernel density estimation as a diagnostic and forecasting tool for distributed volcanic vents. Stat. Volcanol. 4, 1–25. https://doi.org/10.5038/2163-338x.4.3.

Corazzato, C., Tibaldi, A., 2006. Fracture control on type, morphology and distribution of parasitic volcanic cones: an example from Mt. Etna, Italy. J. Volcanol. Geotherm. Res. 158, 177–194. https://doi.org/10.1016/j.jvolgeores.2006.04.018.

Corbi, F., Rivalta, E., Pinel, V., Maccaferri, F., Bagnardi, M., Acocella, V., 2015. How caldera collapse shapes the shallow emplacement and transfer of magma in active volcanoes. Earth Planet. Sci. Lett. 431, 287–293. https://doi.org/10.1016/j.epsl.2015.09.028.

Crumpler, L.S., Aubele, J.C., 1978. Structural evolution of Arsia Mons, Pavonis Mons, and Ascreus Mons: Tharsis region of Mars. Icarus 34, 496–511. https://doi.org/10.1016/0019-1035(78)90041-6.

de Kock, M.O., Gumsley, A.P., Klausen, M.B., Söderlund, U., Djeutchou, C., 2019. The Precambrian Mafic Magmatic Record, Including Large Igneous Provinces of the Kalahari Craton and Its Constituents: A Paleogeographic Review. In: Srivastava, R.K., Ernst, R.E., Peng, P. (Eds.), Dyke Swarms of the World: A Modern Perspective. Springer Geology, pp. 155–214.

Dickson, J.L., Kerber, L.A., Fassett, C.I., Ehlmann, B.L., 2018. A global, blended CTX mosaic of Mars with vectorized seam mapping: A new mosaicking pipeline using principles of non-destructive image editing. In: 49th Lunar and Planetary Science Conference.

Edwards, C.S., Nowicki, K.J., Christensen, P.R., Hill, J., Gorelick, N., Murray, K., 2011. Mosaicking of global planetary image datasets: 1. Techniques and data processing for thermal emission imaging system (THEMIS) multi-spectral data. J. Geophys. Res. E Planets 116, 1–21. https://doi.org/10.1029/2010JE003755.

Ernst, R.E., Liikane, D.A., Jowitt, S.M., Buchan, K.L., Blanchard, J.A., 2019. A new plumbing system framework for mantle plume-related continental large igneous provinces and their mafic-ultramafic intrusions. J. Volcanol. Geotherm. Res. 384, 75–84. https://doi.org/10.1016/j.jvolgeores.2019.07.007.

Fassett, C.I., 2016. Analysis ofimpact crater populations and the geochronology of planetary surfaces in the inner solar system. J. Geophys. Res. Planets 121, 1900–1926. https://doi.org/10.1002/2016JE005094.

Fergason, R.L., Hare, T.M., Laura, J., 2018. HRSC and MOLA Blended Digital Elevation Model at 200m v2. [WWW Document]. Astrogeology PDS Annex. U.S. Geol. Surv. URL. http://bit.ly/HRSC_MOLA_Blend_v0.

Galland, A., Burchardt, S., Hallot, E., Mourgues, R., Bulois, C., 2014. Dynamics of dikes versus cone sheets in volcanic systems. J. Geophys. Res. Solid Earth 119, 3076–3095. https://doi.org/10.1002/2014JB011059.

Genova, A., Goossens, S., Lemoine, F.G., Mazarico, E., Neumann, G.A., Smith, D.E., Zuber, M.T., 2016. Seasonal and static gravity field of Mars from MGS, Mars odyssey and MRO radio science. Icarus 272, 228–245. https://doi.org/10.1016/j.icarus.2016.02.050.

Gonnermann, H., Taisne, B., 2015. Magma Transport. In: Dikes, in: Sigurdsson, H. (Ed.), Encyclopedia of Volcanoes. Elsevier Inc., pp. 215–224

Greeley, R., 1982. The Snake River plain, Idaho: representative of a new category of volcanism. J. Geophys. Res. 87, 2705–2712. https://doi.org/10.1029/JB087iB04p02705.

Grott, M., Breuer, D., 2010. On the spatial variability of the martian elastic lithosphere thickness: evidence for mantle plumes? J. Geophys. Res. 115, 1–16. https://doi.org/10.1029/2009JE003456.

Hartmann, W.K., 2005. Martian Cratering 8: Isochron Refinement and the Chronology of Mars, 174, pp. 294–320. https://doi.org/10.1016/j.icarus.2004.11.023.

Hartmann, W.K., Neukum, G., 2001. Cratering chronology and the evolution of Mars. Space Sci. Rev. 96, 165–194. https://doi.org/10.1023/A:1011945222010.

Hauber, E., Bleacher, J., Gwinner, K., Williams, D., Greeley, R., 2009. The topography and morphology of low shields and associated landforms of plains volcanism in the Tharsis region of Mars. J. Volcanol. Geotherm. Res. 185, 69–95. https://doi.org/10.1016/j.jvolgeores.2009.04.015.

Hauber, E., Brož, P., Jagert, F., Jodowski, P., Platz, T., 2011. Very recent and wide-spread basaltic volcanism on Mars. Geophys. Res. Lett. 38, 1–5. https://doi.org/10.1029/2011GL047310.

Hauck, S.A., Phillips, R.J., 2002. Thermal and crustal evolution of Mars. J. Geophys. Res. Planets 107. https://doi.org/10.1029/2001je001801, 6–1.

Hjartardóttir, Á.R., Einarsson, P., Bramham, E., Wright, T.J., 2012. The Krafla fissure swarm, Iceland, and its formation by rifting events. Bull. Volcanol. 74, 2139–2153. https://doi.org/10.1007/s00445-012-0659-0.

Horvath, D.G., Moitra, P., Hamilton, C.W., Craddock, R.A., Andrews-Hanna, J.C., 2021. Evidence for geologically recent explosive volcanism in Elysium. Icarus 365, 114499. https://doi.org/10.1016/j.icarus.2021.114499.

Hughes, S.S., Sakimoto, S.E.H., Gregg, T.K.P., Brady, S.M., 2005. Petrological evidence for multiple chemically evolved magma batches and implications for plains volcanism on earth and Mars. In: 36th Annual Lunar and Planetary Science Conference.

Ivanov, B.A., 2001. Mars/moon cratering rate ratio estimates. Space Sci. Rev. 96, 87–104. https://doi.org/10.1023/A:1011941121102.

Johnson, C.L., Phillips, R.J., 2005. Evolution of the Tharsis region of Mars: insights from magnetic field observations. Earth Planet. Sci. Lett. 230, 241–254. https://doi.org/10.1016/j.epsl.2004.10.038.

Khan, A., Ceylan, S., van Driel, M., Giardini, D., Lognonné, P., Samuel, H., Schmerr, N.C., Stähler, S.C., Duran, A.C., Huang, Q., Kim, D., Broquet, A., Charalambous, C., Clinton, J.F., Davis, P.M., Drilleau, M., Karakostas, F., Lekic, V., McLennan, S.M., Maguire, R.R., Michaut, C., Panning, M.P., Pike, W.T., Pinot, B., Plasman, M., Scholz, J.-R., Widmer-Schnidrig, R., Spohn, T., Smrekar, S.E., Banerdt, W.B., 2021. Upper mantle structure of Mars from InSight seismic data. Science (80) 373 (434). https://doi.org/10.1126/science.abf2966. LP – 438.

Kiefer, W.S., 2003. Melting in the martian mantle: Shergottite formation and implications for present-day mantle convection on Mars. Meteorit. Planet. Sci. 38, 1815–1832. https://doi.org/10.1111/j.1945-5100.2003.tb00017.x.

Kiefer, W.S., Li, Q., 2009. Mantle convection controls the observed lateral variations in lithospheric thickness on present-day Mars. Geophys. Res. Lett. 36, 1–5. https://doi.org/10.1029/2009GL039827.

Kneissl, T., Van Gasselt, S., Neukum, G., 2011. Map-projection-independent crater size-frequency determination in GIS environments - new software tool for ArcGIS. Planet. Space Sci. 59, 1243–1254. https://doi.org/10.1016/j.pss.2010.03.015.

Koch, D.M., Manga, M., 1996. Neutrally buoyant diapirs: a model for Venus coronae. Geophys. Res. Lett. 23, 225–228. https://doi.org/10.1029/95GL03776.

Koulakov, I., Abkadyrov, I., Al Arifi, N., Deev, E., Droznina, S., Gordeev, E.I., Jakovlev, A., El Khrepy, S., Kulakov, R.I., Kugaenko, Y., Novgorodova, A., Senyukov, S., Shapiro, N., Stupina, T., West, M., 2017. Three different types of plumbing system beneath the neighboring active volcanoes of Tolbachik, Bezymianny, and Klyuchevskoy in Kamchatka. J. Geophys. Res. Solid Earth 122, 3852–3874. https://doi.org/10.1002/2017JB014082.

Krassilnikov, A.S., Head, J.W., 2003. Novae on Venus: geology, classification, and evolution. J. Geophys. Res. Planets 108. https://doi.org/10.1029/2002je001983.

Kremer, C.H., Mustard, J.F., Bramble, M.S., 2019. A widespread olivine-rich ash deposit on Mars. Geology 47, 677–681. https://doi.org/10.1130/G45563.1.

Krishnan, V., Kumar, P.S., 2021. Evidence for long-lived middle to late amazonian volcanism, tectonics, and recent boulder fall activities in the Northern Tharsis Region, Mars. In: 52th Annual Lunar and Planetary Science Conference, p. 1855.

Lagain, A., Bouley, S., Baratoux, D., Costard, F., Wieczorek, M., 2020. Impact cratering rate consistency test from ages of layered ejecta on Mars. Planet. Space Sci. 180, 104755 https://doi.org/10.1016/j.pss.2019.104755.

Lagain, A., Benedix, G.K., Servis, K., Baratoux, D., Doucet, L.S., 2021. The Tharsis mantle source of depleted shergottites revealed by 90 million impact craters. Nat. Commun. 12, 6352. https://doi.org/10.1038/s41467-021-26648-3.

Le Corvec, N., Spörli, K.B., Rowland, J., Lindsay, J., 2013. Spatial distribution and alignments of volcanic centers: clues to the formation of monogenetic volcanic fields. Earth-Science Rev. 124, 96–114. https://doi.org/10.1016/j.earscirev.2013.05.005.

Magee, C., Ernst, R.E., Muirhead, J., Phillips, T., Jackson, C.A.-L., 2019. Magma transport pathways in large igneous provinces: Lessons from combining field observations and seismic reflection data. In: Srivastava, R.K., Ernst, R.E., Peng, P. (Eds.), Dyke Swarms of the World: A Modern Perspective. Springer Geology, Singapore, pp. 45–85.

Mangold, N., Loizeau, D., Poulet, F., Ansan, V., Baratoux, D., LeMouelic, S., Bardintzeff, J.M., Platevoet, B., Toplis, M., Pinet, P., Masson, P., Bibring, J.P., Gondet, B., Langevin, Y., Neukum, G., 2010. Mineralogy of recent volcanic plains in the Tharsis region, Mars, and implications for platy-ridged flow composition. Earth Planet. Sci. Lett. 294, 440–450. https://doi.org/10.1016/j.epsl.2009.07.036.

McEwen, A.S., Preblich, B.S., Turtle, E.P., Artemieva, N.A., Golombek, M.P., Hurst, M., Kirk, R.L., Burr, D.M., Christensen, P.R., 2005. The rayed crater Zunil and interpretations of small impact craters on Mars. Icarus 176, 351–381. https://doi.org/10.1016/j.icarus.2005.02.009.

Michael, G.G., Neukum, G., 2010. Planetary surface dating from crater size – frequency distribution measurements : partial resurfacing events and statistical age uncertainty. Earth Planet. Sci. Lett. 294, 223–229. https://doi.org/10.1016/j.epsl.2009.12.041.

Michael, G.G., Platz, T., Kneissl, T., Schmedemann, N., 2012. Planetary surface dating from crater size-frequency distribution measurements: spatial randomness and clustering. Icarus 218, 169–177. https://doi.org/10.1016/j.icarus.2011.11.033.

Michael, G.G., Kneissl, T., Neesemann, A., 2016. Planetary Surface Dating from Crater size-frequency Distribution Measurements: Poisson Timing Analysis, 277, pp. 279–285. https://doi.org/10.1016/j.icarus.2016.05.019.

Montési, L.G.J., 2001. Concentric dikes on the flanks of Pavonis Mons: implications for the evolution of martian shield volcanoes and mantle plumes. Spec. Pap. Geol. Soc. Am. 352, 165–181. https://doi.org/10.1130/0-8137-2352-3.165.

Morris, R.V., Vaniman, D.T., Blake, D.F., Gellert, R., Chipera, S.J., Rampe, E.B., Ming, D. W., Morrison, S.M., Downs, R.T., Treiman, A.H., Yen, A.S., Grotzinger, J.P., Achilles, C.N., Bristow, T.F., Crisp, J.A., Marais, D.J.D., Farmer, J.D., Fendrich, K.V., Frydenvang, J., Graff, T.G., Morookian, J.M., Stolper, E.M., Schwenzer, S.P., 2016. Silicic volcanism on Mars evidenced by tridymite in high-SiO2 sedimentary rock at Gale crater. Proc. Natl. Acad. Sci. U. S. A. 113, 7071–7076. https://doi.org/10.1073/pnas.1607098113.

Mouginis-Mark, P.J., Christensen, P.R., 2005. New observations of volcanic features on Mars from the THEMIS instrument. J. Geophys. Res. 110, 1–17. https://doi.org/10.1029/2005JE002421.

Mouginis-Mark, P.J., Wilson, L., 2019. Late-stage intrusive activity at Olympus Mons, Mars: summit inflation and giant dike formation. Icarus 319, 459–469. https://doi.org/10.1016/j.icarus.2018.09.038.

Nakamura, K., 1977. Volcanoes as possible indicators of tectonic stress orientation - principle and proposal. J. Volcanol. Geotherm. Res. 2, 1–16. https://doi.org/10.1016/0377-0273(77)90012-9.

Németh, K., Kereszturi, G., 2015. Monogenetic volcanism: personal views and discussion. Int. J. Earth Sci. 104, 2131–2146. https://doi.org/10.1007/s00531-015-1243-6.

Neukum, G., Jaumann, R., Hoffmann, H., Hauber, E., Head, J.W., Basilevsky, A.T., Ivanov, B.A., Werner, S.C., Van Gasselt, S., Murray, J.B., McCord, T., 2004. Recent and episodic volcanic and glacial activity on Mars revealed by the high resolution stereo camera. Nature 432, 971–979. https://doi.org/10.1038/nature03231.

Ni, S., Helmberger, D.V., 2003. Seismological constraints on the south African superplume: could be the oldest distinct structure on earth. Earth Planet. Sci. Lett. 206, 119–131. https://doi.org/10.1016/S0012-821X(02)01072-5.

Peters, S.I., Christensen, P.R., 2017. Flank vents and graben as indicators of late Amazonian volcanotectonic activity on Olympus Mons. J. Geophys. Res. Planets 122, 501–523. https://doi.org/10.1002/2016JE005108.

Phillips, R.J., Zuber, M.T., Solomon, S.C., Golombek, M.P., Jakosky, B.M., Banerdt, W.B., Smith, D.E., Williams, R.M.E., Hynek, B.M., Aharonson, O., Hauck, S.A., 2001. Ancient geodynamics and global-scale hydrology on mars. Science 80 (291), 2587–2591. https://doi.org/10.1126/science.1058701.

Pieterek, B., Ciazela, J., Mège, D., Tesson, P.-A., Ciazela, M., Gurgurewicz, J., Lagain, A., Muszyński, A., 2019. Parasitic cones in the Tharsis volcanic province on Mars: Implications for its recent magmatic plumbing system. In: 50th Annual Lunar and Planetary Science Conference, p. 1369.

Pieterek, B., Laban, M., Ciążela, J., Muszyński, A., 2022a. Explosive volcanism in Noctis fossae on Mars. Icarus 375, 114851. https://doi.org/10.1016/j.icarus.2021.114851.

Pieterek, B., Laban, M., Ciążela, J., Muszyński, A., 2022b. Widespread explosive volcanism in Noctis fossae on Mars. In: 53rd Annual Lunar and Planetray Science Conference, p. 1375.

Platz, T., Michael, G., 2011. Eruption history of the Elysium Volcanic Province. Mars. Earth Planet. Sci. Lett. 312, 140–151. https://doi.org/10.1016/j.epsl.2011.10.001.

Plesa, A.C., Padovan, S., Tosi, N., Breuer, D., Grott, M., Wieczorek, M.A., Spohn, T., Smrekar, S.E., Banerdt, W.B., 2018. The thermal state and interior structure of Mars. Geophys. Res. Lett. 45, 12,198–12,209. https://doi.org/10.1029/2018GL080728.

Richardson, J.A., Bleacher, J.E., Glaze, L.S., 2012. The volcanic history of Syria Planum. Mars. J. Volcanol. Geotherm. Res. 252, 1–13. https://doi.org/10.1016/j.jvolgeores.2012.11.007.

Richardson, J.A., Wilson, J.A., Connor, C.B., Bleacher, J.E., Kiyosugi, K., 2017. Recurrence rate and magma effusion rate for the latest volcanism on Arsia Mons. Mars. Earth Planet. Sci. Lett. 458, 170–178. https://doi.org/10.1016/j.epsl.2016.10.040.

Richardson, J.A., Bleacher, J.E., Connor, C.B., Glaze, L.S., 2020. Tharis Volcanic Vents Enhanced Database. https://doi.org/10.5281/zenodo.4275144.

Richardson, J.A., Bleacher, J.E., Connor, C.B., Glaze, L.S., 2021. Small volcanic vents of the Tharsis Volcanic Province. Mars. J. Geophys. Res. Planets 126. https://doi.org/10.1029/2020JE006620.

Robbins, S.J., Di Achille, G., Hynek, B.M., 2011. The volcanic history of Mars: high-resolution crater-based studies of the calderas of 20 volcanoes. Icarus 211, 1179–1203. https://doi.org/10.1016/j.icarus.2010.11.012.

Roman, A., Lundgren, P., 2021. Dynamics of large effusive eruptions driven by caldera collapse. Nature 592, 392–396. https://doi.org/10.1038/s41586-021-03414-5.

Sakimoto, S.E.H., Mitchell, D., Riedel, S.J., Taylor, K., 2002. Small shield volcanoes on Mars: Global geometric properties and model implications for regional Varations in eruptive styles. In: 33rd Annual Lunar and Planetary Science Conference, p. 1717.

Scanlon, K.E., Head, J.W., Marchant, D.R., 2015. Remnant buried ice in the equatorial regions of Mars: morphological indicators associated with the Arsia Mons tropical mountain glacier deposits. Planet. Space Sci. 111, 144–154. https://doi.org/10.1016/j.pss.2015.03.024.

Schumacher, S., Breuer, D., 2007. An alternative mechanism for recent volcanism on Mars. Geophys. Res. Lett. 34, 1–5. https://doi.org/10.1029/2007GL030083.

Stähler, S.C., Khan, A., Bruce Banerdt, W., Lognonné, P., Giardini, D., Ceylan, S., Drilleau, M., 2021. Seismic detection of the martian core. Science (80) 373, 443–448. https://doi.org/10.1126/science.abi7730.

Tanaka, K.L., Robbins, S.J., Fortezzo, C.M., Skinner, J.A., Hare, T.M., 2014. The digital global geologic map of Mars: chronostratigraphic ages, topographic and crater morphologic characteristics, and updated resurfacing history. Planet. Space Sci. 95, 11–24. https://doi.org/10.1016/j.pss.2013.03.006.

Taylor, G.J., Martel, L.M.V., Karunatillake, S., Gasnault, O., Boynton, W.V., 2010. Mapping Mars geochemically. Geology 38, 183–186. https://doi.org/10.1130/G30470.1.

Tenzer, R., Eshagh, M., Jin, S., 2015. Martian sub-crustal stress from gravity and topographic models. Earth Planet. Sci. Lett. 425, 84–92. https://doi.org/10.1016/j.epsl.2015.05.049.

Tesson, P., Mège, D., Lagain, A., Gurgurewicz, J., 2020. Late Amazonian lateral lava flows coeval with caldera eruptions at Arsia Mons. In: Europlanet Science Congress (Pp. EPSC2020-710).

Thordarson, T., Self, S., 1993. The Laki (Skaftár Fires) and Grímsvötn eruptions in 1783–1785. Bull. Volcanol. 55, 233–263. https://doi.org/10.1007/BF00624353.

Weizman, A., Stevenson, D.J., Prialnik, D., Podolak, M., 2001. Modeling the volcanism on Mars. Icarus 150, 195–205. https://doi.org/10.1006/icar.2000.6572.

Werner, S.C., 2009. The global martian volcanic evolutionary history. Icarus 201, 44–68. https://doi.org/10.1016/j.icarus.2008.12.019.

Wieczorek, M.A., Zuber, M.T., 2004. Thickness of the Martian crust : Improved Constraints from Geoid-to-topography Ratios, 109, pp. 1–16. https://doi.org/10.1029/2003JE002153.

Williams, J.-P., 2018. Modification of the Martian surface by impact cratering. In: Soare, R.J., Conway, S.J., Clifford, S.M. (Eds.), Dynamic Mars. Elsevier, pp. 361–386. https://doi.org/10.1016/B978-0-12-813018-6.00012-1.

Wilson, L., Head, J.W., 1994. Review and analysis and of volcanic eruption to theory relationships landforms. Rev. Geophys. 32, 221–263. https://doi.org/10.1029/94RG01113.

Wood, C.A., 1978. Morphometric evolution of composite volcanoes. Geophys. Res. Lett. 5, 5–7. https://doi.org/10.1029/GL005i006p00437.

Wood, C.A., 1979. Monogenetic volcanoes of the terrestial planets. In: 10th Annual Lunar and Planetary Science Conference, pp. 2815–2840.

Wood, C.A., 1980. Morphometric evolution of cinder cones. J. Volcanol. Geotherm. Res. 7, 387–413. https://doi.org/10.1016/0377-0273(80)90040-2.

Wray, J.J., Hansen, S.T., Dufek, J., Swayze, G.A., Murchie, S.L., Seelos, F.P., Skok, J.R., Irwin, R.P., Ghiorso, M.S., 2013. Prolonged magmatic activity on Mars inferred from the detection of felsic rocks. Nat. Geosci. 6, 1013–1017. https://doi.org/10.1038/ngeo1994.

Xiao, L., Huang, J., Christensen, P.R., Greeley, R., Williams, D.A., Zhao, J., He, Q., 2012. Ancient volcanism and its implication for thermal evolution of Mars. Earth Planet. Sci. Lett. 323–324, 9–18. https://doi.org/10.1016/j.epsl.2012.01.027.

Yokoyama, I., 2015. Eruption patterns of parasitic volcanoes. Ann. Geophys. 58 https://doi.org/10.4401/ag-6557.

Zhong, S., 2009. Migration of Tharsis volcanism on Mars caused by differential rotation of the lithosphere. Nat. Geosci. 2, 19–23. https://doi.org/10.1038/ngeo392.

Zhong, S., Roberts, J.H., 2003. On the support of the Tharsis rise on Mars. Earth Planet. Sci. Lett. 214, 1–9. https://doi.org/10.1016/S0012-821X(03)00384-4.

Zimbelman, J.R., 2000. Volcanism on Mars. In: Sigurdsson, H. (Ed.), Encyclopedia of Volcanoes. Academic Press, San Diego, pp. 771–783.

Zuber, M.T., 2000. Internal structure and early thermal evolution of Mars from Mars global surveyor topography and gravity internal structure and early thermal evolution of Mars from Mars global surveyor topography and gravity. Science 80). 287, 1788–1793. https://doi.org/10.1126/science.287.5459.1788.

Zuber, M.T., 2001. The crust and mantle of Mars. Nature 412, 220–227. https://doi.org/10.1038/35084163.

SUPPLEMENTARY MATERIAL

Figures S1-S98

Late Amazonian dike-fed distributed volcanism in the Tharsis volcanic province on Mars

Bartosz Pieterek[1*], Jakub Ciazela[2], Anthony Lagain[3], Marta Ciazela[2]

[1]Institute of Geology, Adam Mickiewicz University, ul. Bogumiła Krygowskiego 12, 60-680 Poznań, Poland, e-mail:
[2]Institute of Geological Sciences, Polish Academy of Sciences, ul. Podwale 75, 50-449 Wrocław, Poland
[3]Space Science and Technology Centre, School of Earth and Planetary Sciences, Curtin University, Perth, Western Australia, Australia

E-mail: barpie@amu.edu.pl; phone: +48 693 290 465

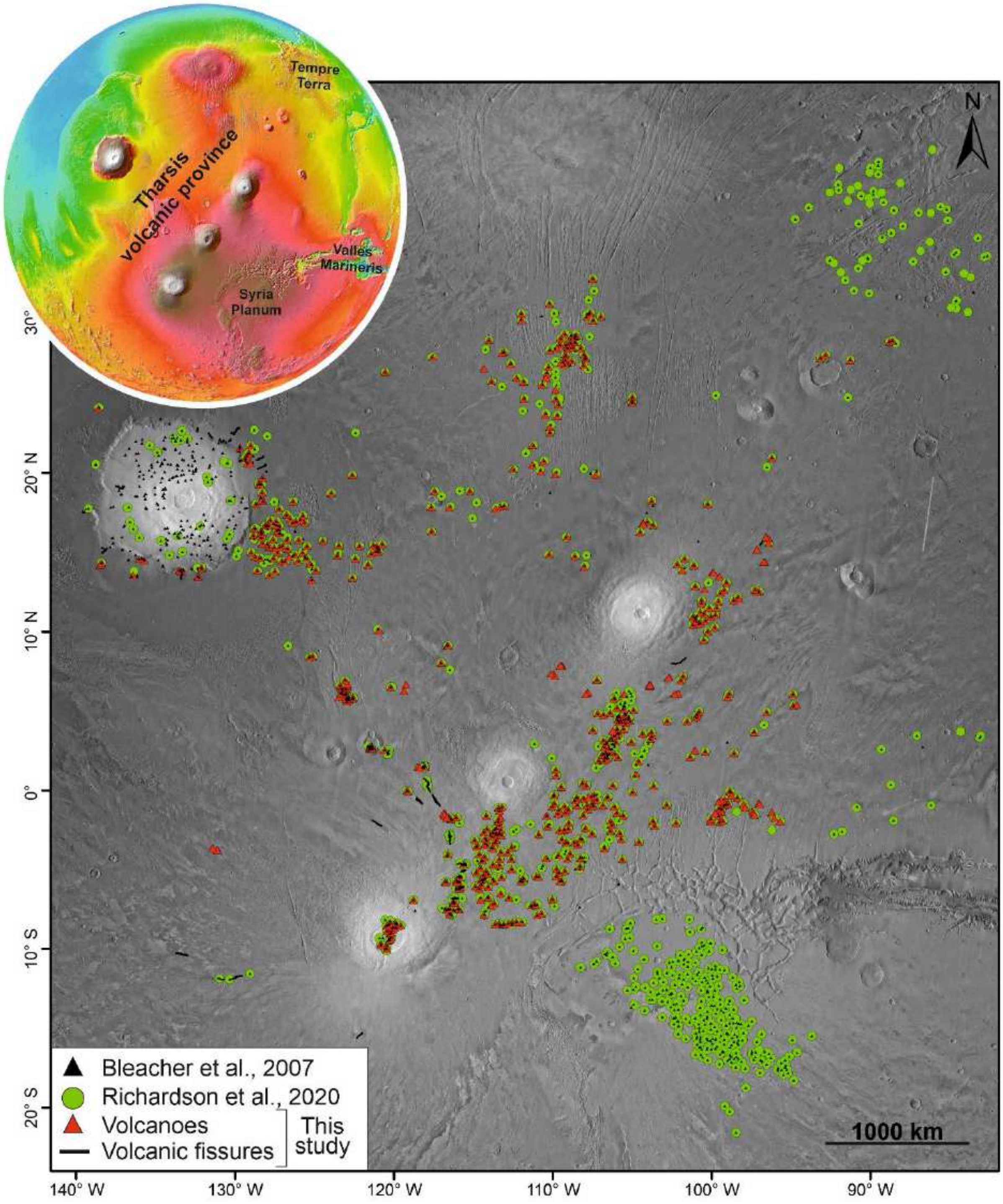

Fig. S1 Comparison of the cataloged volcanic vents and landforms mapped by Bleacher et al. (2007), Richardson et al. (2020, 2021), and this study for the Tharsis region on Mars. In this study, we did not include the Tempe Terra and Syria Planum regions due to their significantly older ages of the latest volcanic activity determined for these regions (Hauber et al., 2011). Some of the volcanic vents mapped by Richardson et al. (2021), especially in the vicinity of Arsia Mons, have been classified as volcanic fissure segments (black lines) that comprise several individual cones with overlapping flanks. Background image: MGS MOLA–MEX HRSC Blended DEM Global 200 m v2 (Fergason et al., 2018) and THEMIS-IR Day Global Mosaic 100 m (Edwards et al., 2011). The Mars globe in the inset indicates the position of the Tharsis province with respect to the Valles Marineris and is based on the digital elevation model (DEM) from MOLA/MGS (128 pixels/degree).

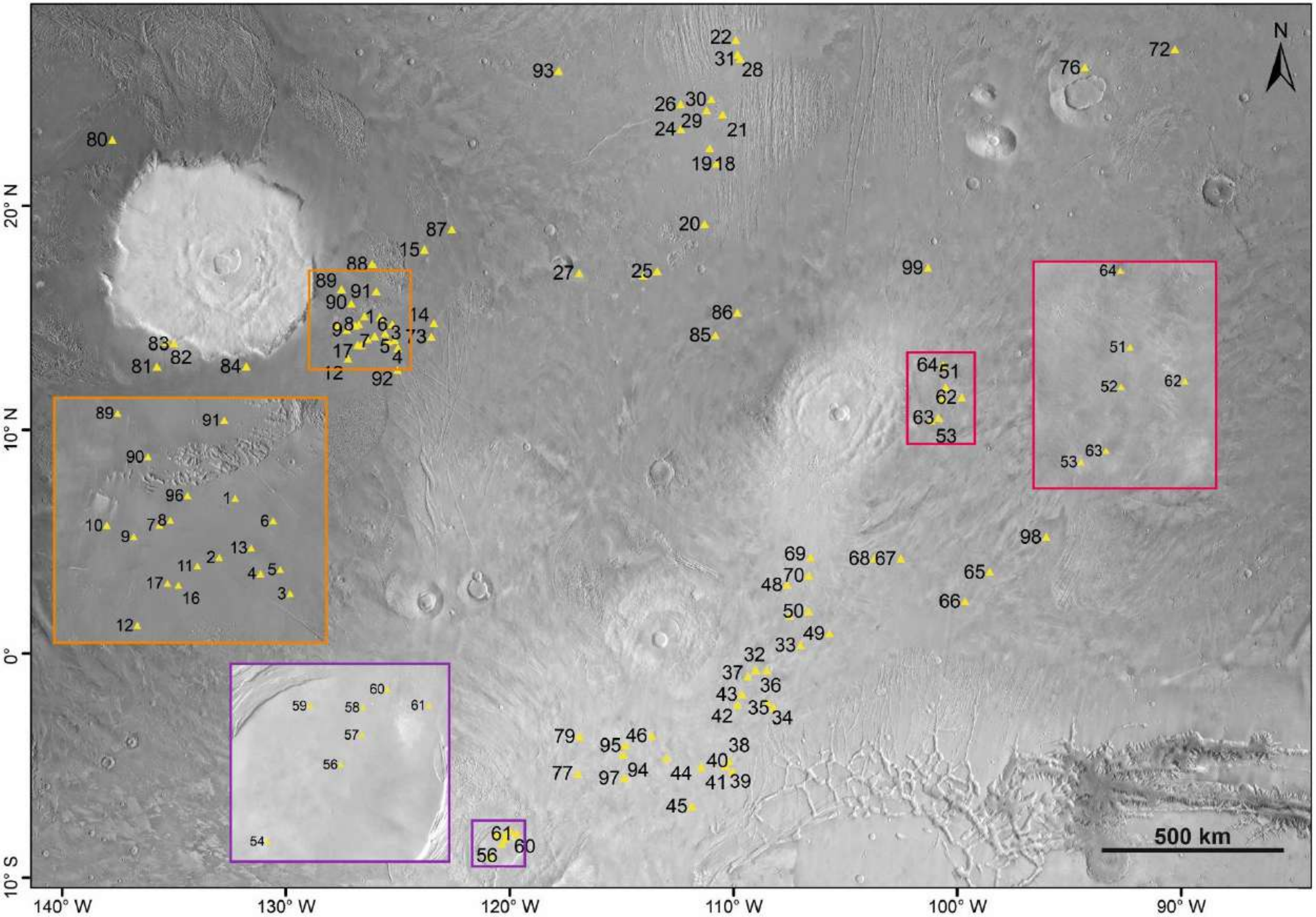

Fig. S2 The Tharsis region with 94 dated landforms (yellow triangles). The numbers adjacent to the symbols are referred to Table 2 and Figs. S3–S96. Background image: MGS MOLA–MEX HRSC Blended DEM Global 200 m v2 (Fergason et al., 2018) and THEMIS-IR Day Global Mosaic 100 m (Edwards et al., 2011).

Fig. S3-S96 Crater Size-Frequency Distributions (CSFD) and absolute model ages (± is 1σ as age uncertainty based on the number of craters fitted) for the surfaces of the volcano edifices located within the distinguished in this study subprovinces (for more details see Table 2). In all cases, the Poisson fitting technique developed by Michael et al., (2016) was used to derive an age using the Hartmann (2005) production and chronology functions. N(1) represents the cratering density of craters >1 km in diameter. The upper panels summarize the results of randomness analysis using the (inverted) standard deviation of the adjacent area (SDAA) parameter (Michael et al., 2012). Values within the gray shaded field (−3 to +3) are characterized by random distribution non-affected by secondary craters. Inserts show the impact craters distribution. The reader is referred to the Supplementary Data 3 attached to this manuscript for the visualization of the details (Randomness Analysis).

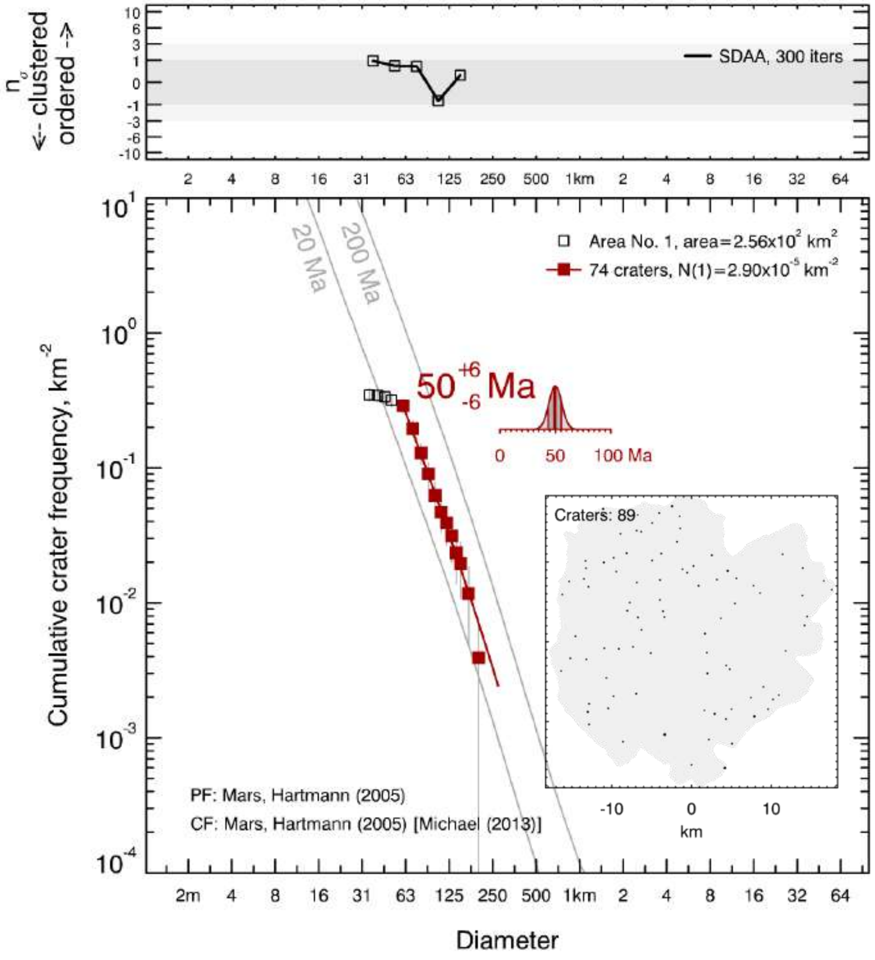

Fig. S3 CSFD and absolute model age for the surface of the Volcanic Edifice no. 1 emplaced within the Olympus Mons subprovince (for more details see Table 2).

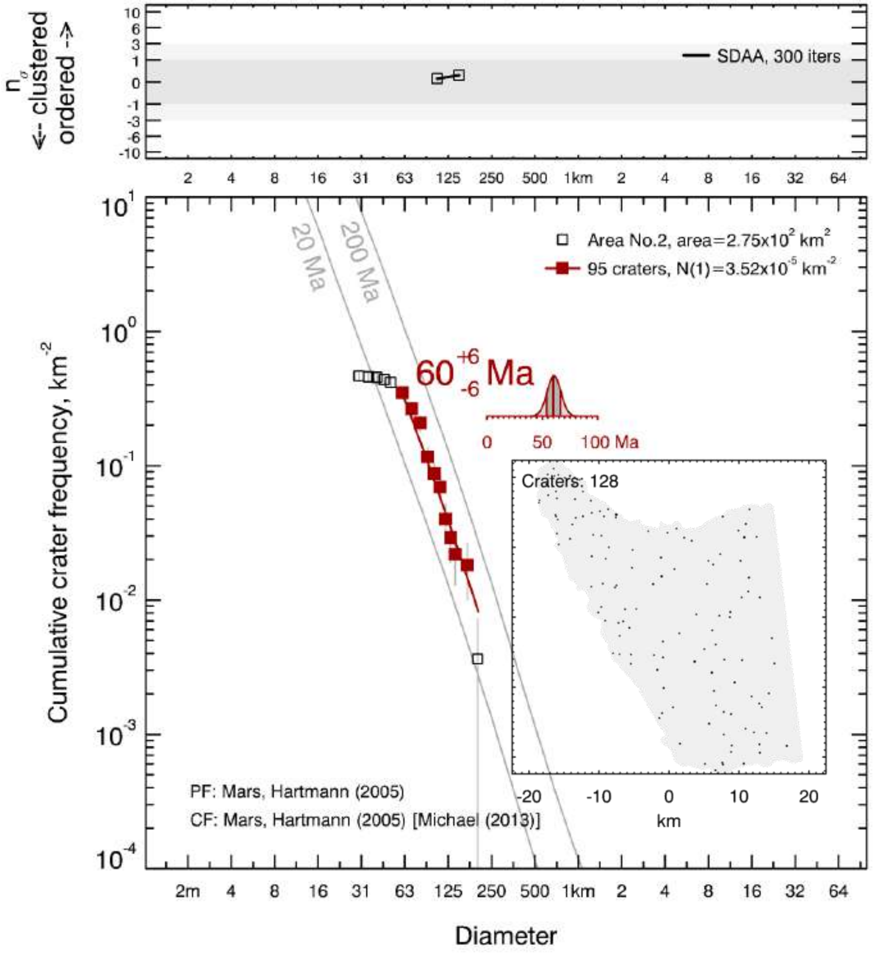

Fig. S4 CSFD and absolute model age for the surface of the Volcanic Edifice no. 2 emplaced within the Olympus Mons subprovince (for more details see Table 2).

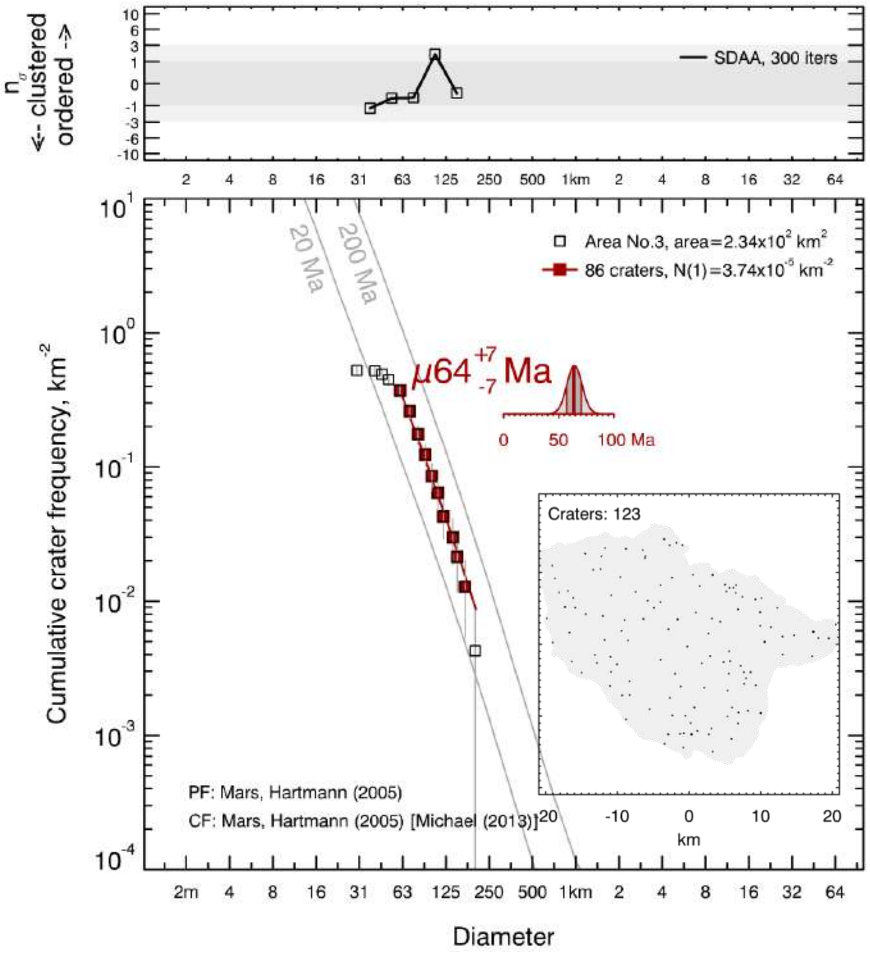

Fig. S5 CSFD and absolute model age for the surface of the Volcanic Edifice no. 3 emplaced within the Olympus Mons subprovince (for more details see Table 2).

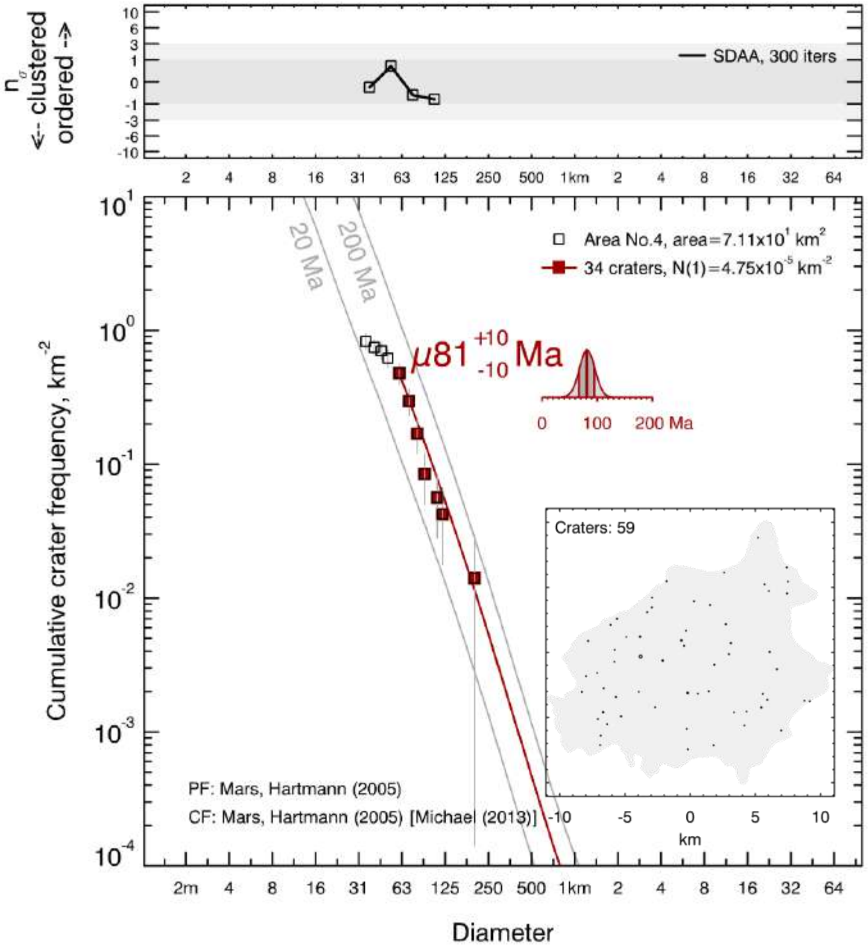

Fig. S6 CSFD and absolute model age for the surface of the Volcanic Edifice no. 4 emplaced within the Olympus Mons subprovince (for more details see Table 2).

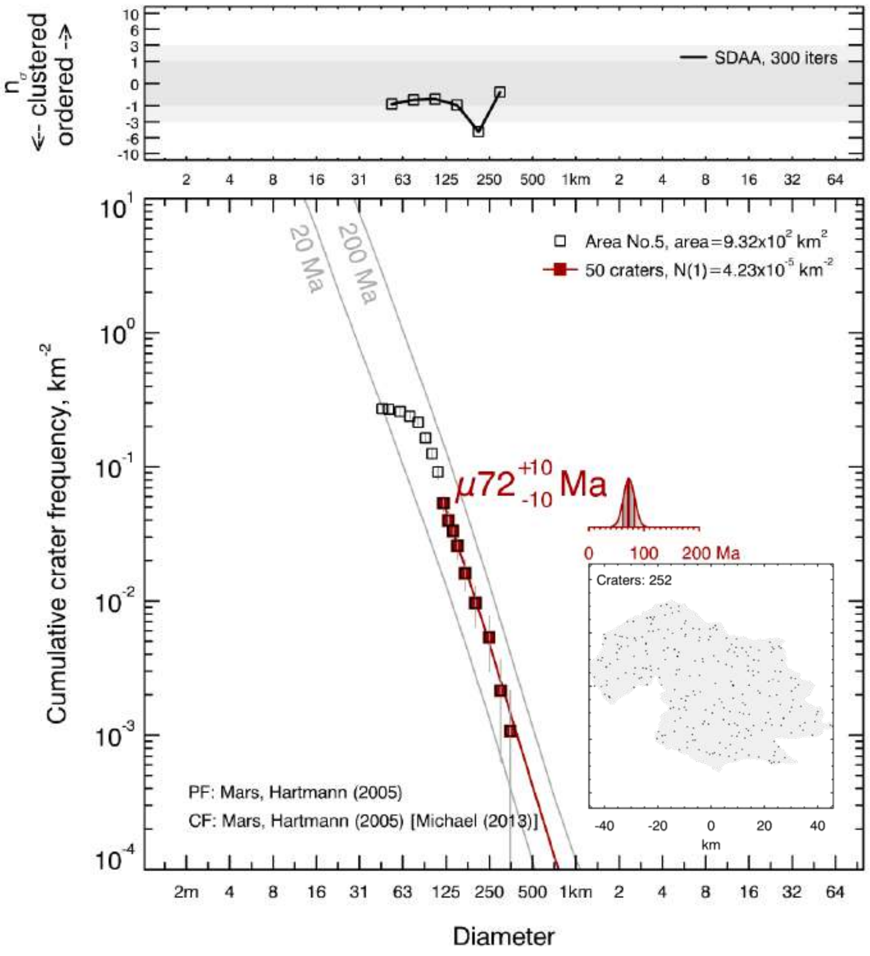

Fig. S7 CSFD and absolute model age for the surface of the Volcanic Edifice no. 5 emplaced within the Olympus Mons subprovince (for more details see Table 2).

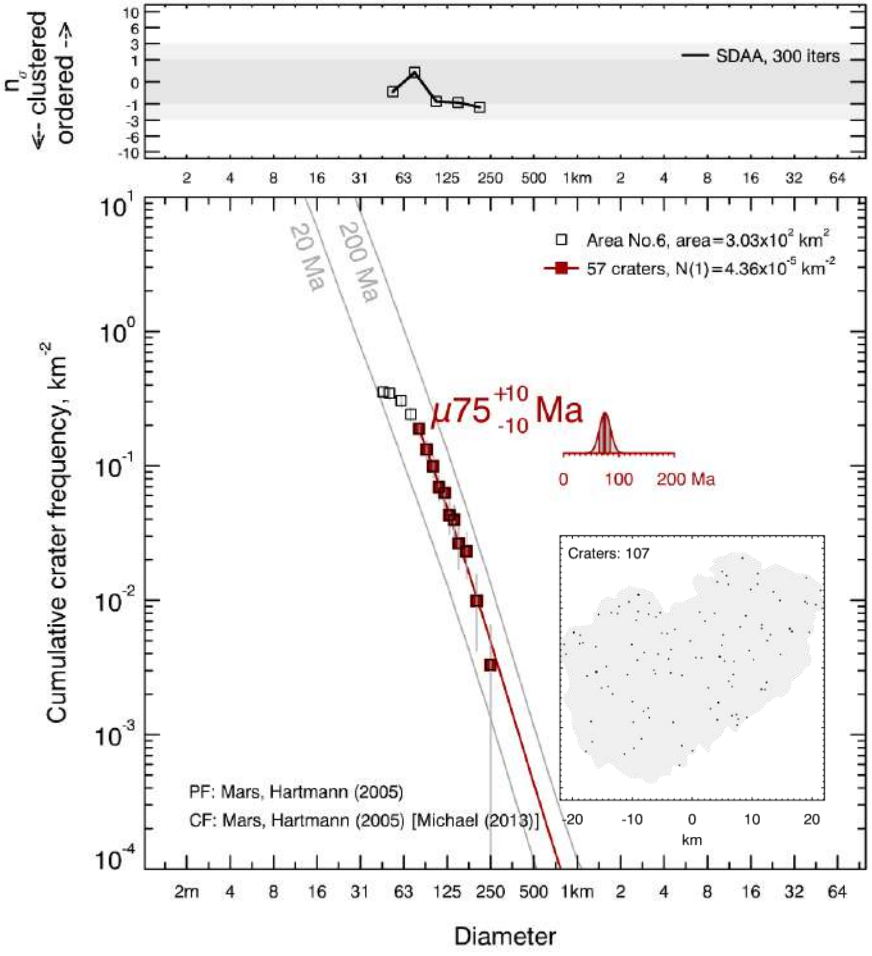

Fig. S8 CSFD and absolute model age for the surface of the Volcanic Edifice no. 6 emplaced within the Olympus Mons subprovince (for more details see Table 2).

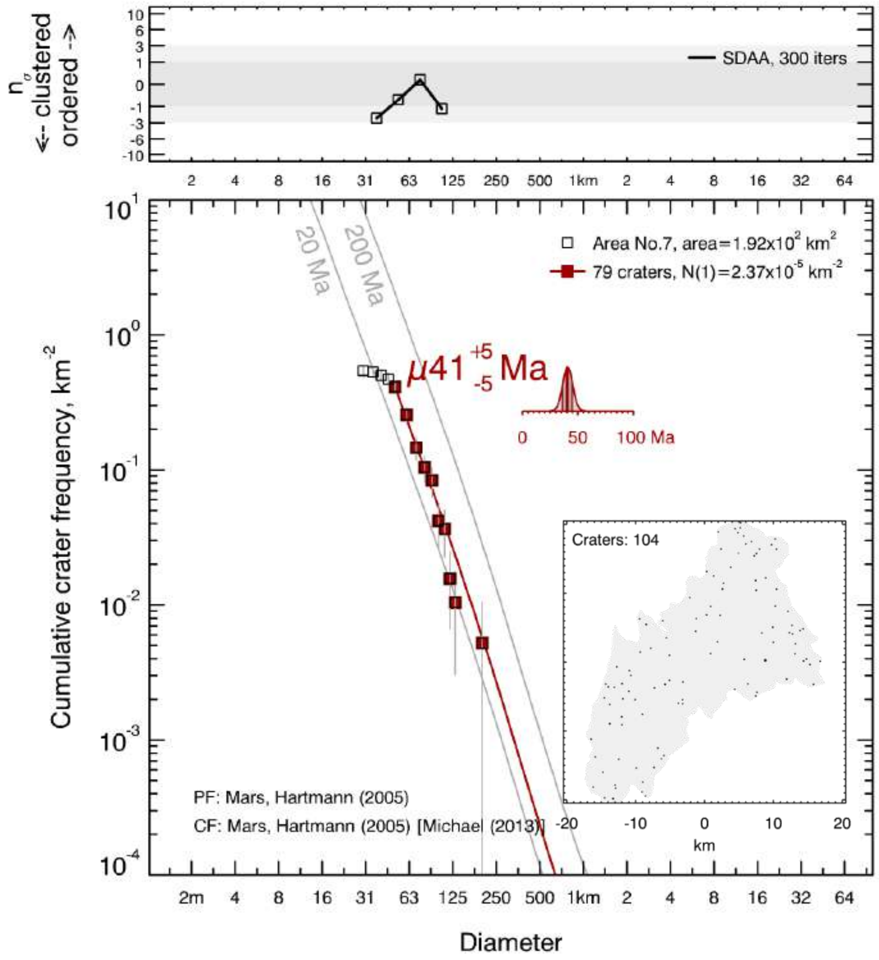

Fig. S9 CSFD and absolute model age for the surface of the Volcanic Edifice no. 7 emplaced within the Olympus Mons subprovince (for more details see Table 2).

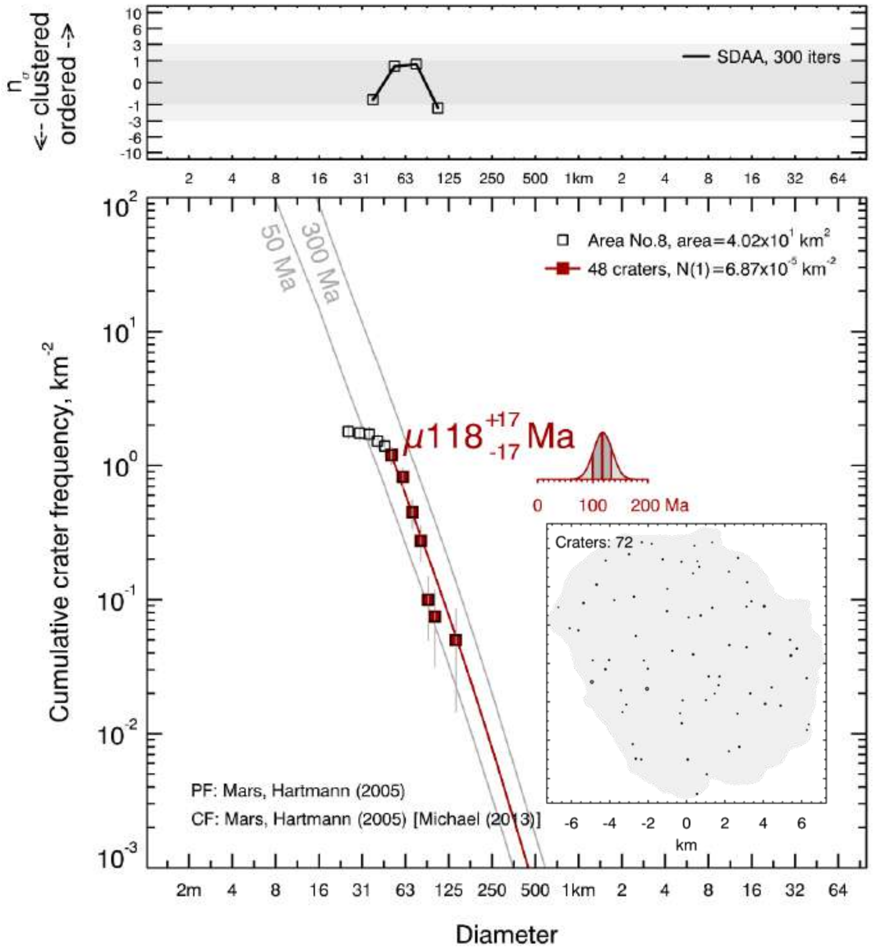

Fig. S10 CSFD and absolute model age for the surface of the Volcanic Edifice no. 8 emplaced within the Olympus Mons subprovince (for more details see Table 2).

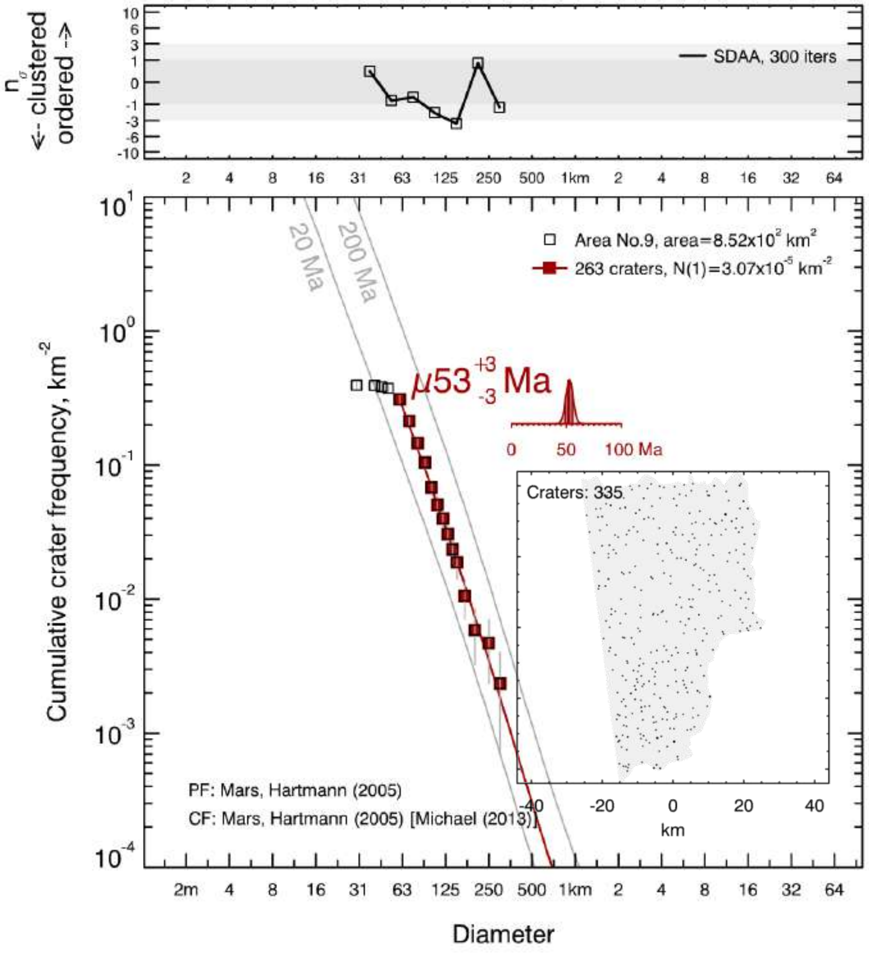

Fig. S11 CSFD and absolute model age for the surface of the Volcanic Edifice no. 9 emplaced within the Olympus Mons subprovince (for more details see Table 2).

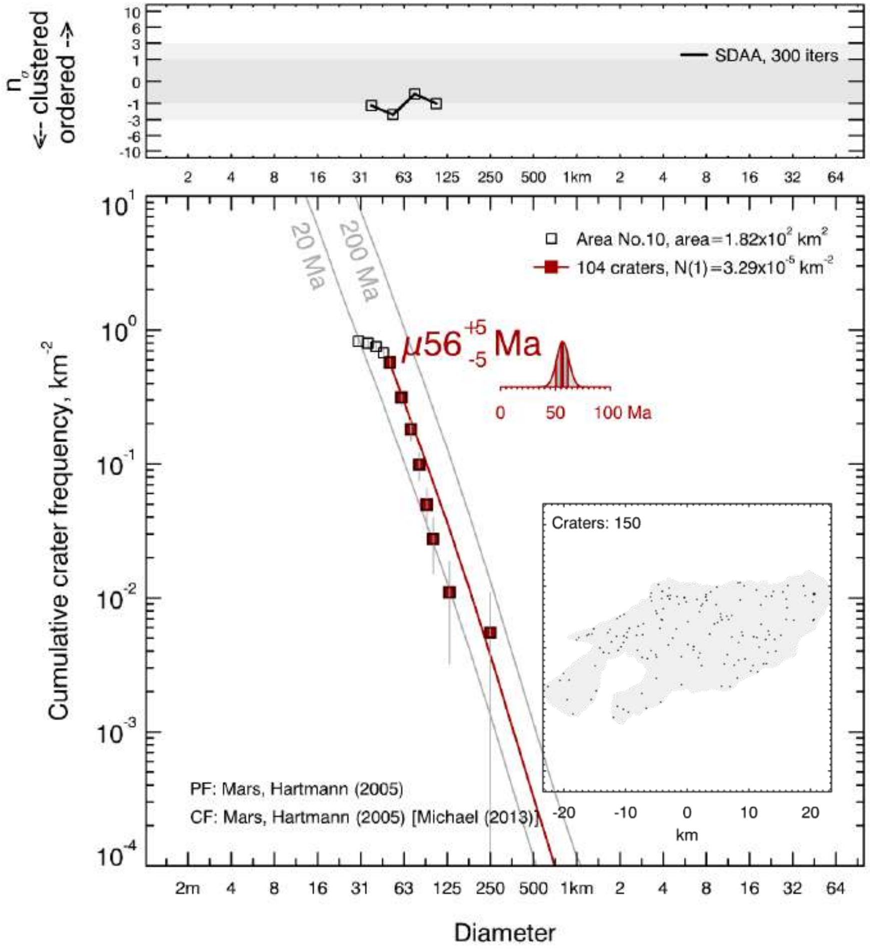

Fig. S12 CSFD and absolute model age for the surface of the Volcanic Edifice no. 10 emplaced within the Olympus Mons subprovince (for more details see Table 2).

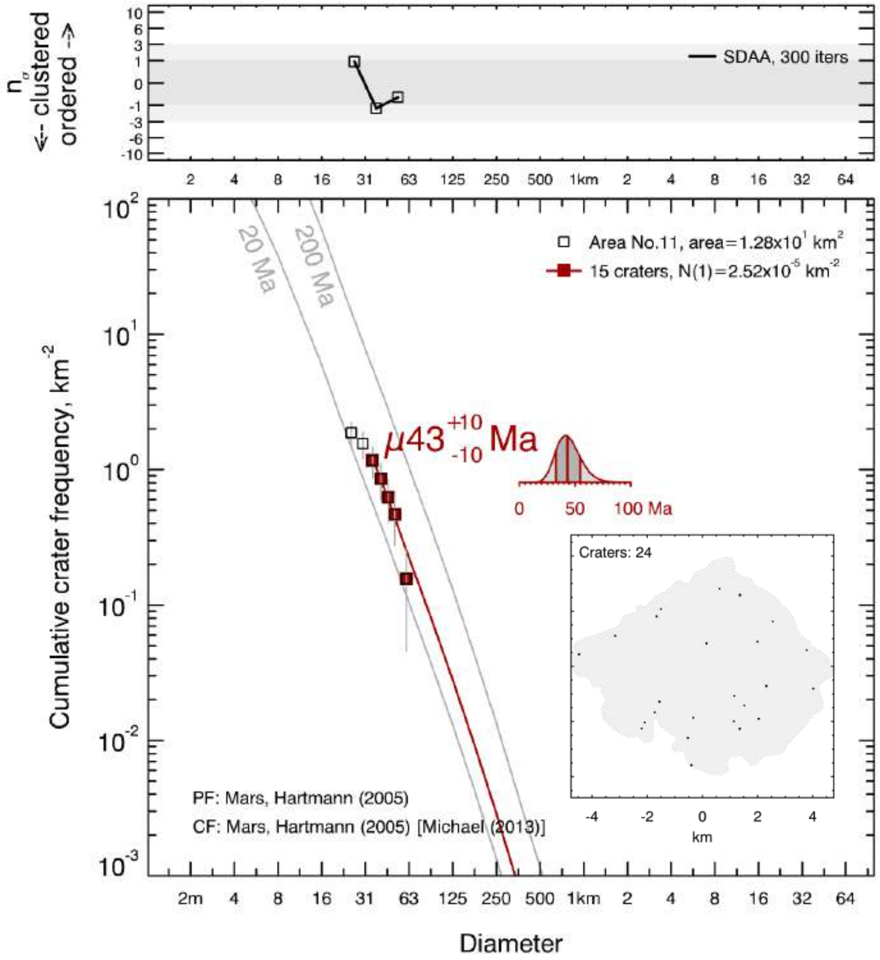

Fig. S13 CSFD and absolute model age for the surface of the Volcanic Edifice no. 11 emplaced within the Olympus Mons subprovince (for more details see Table 2).

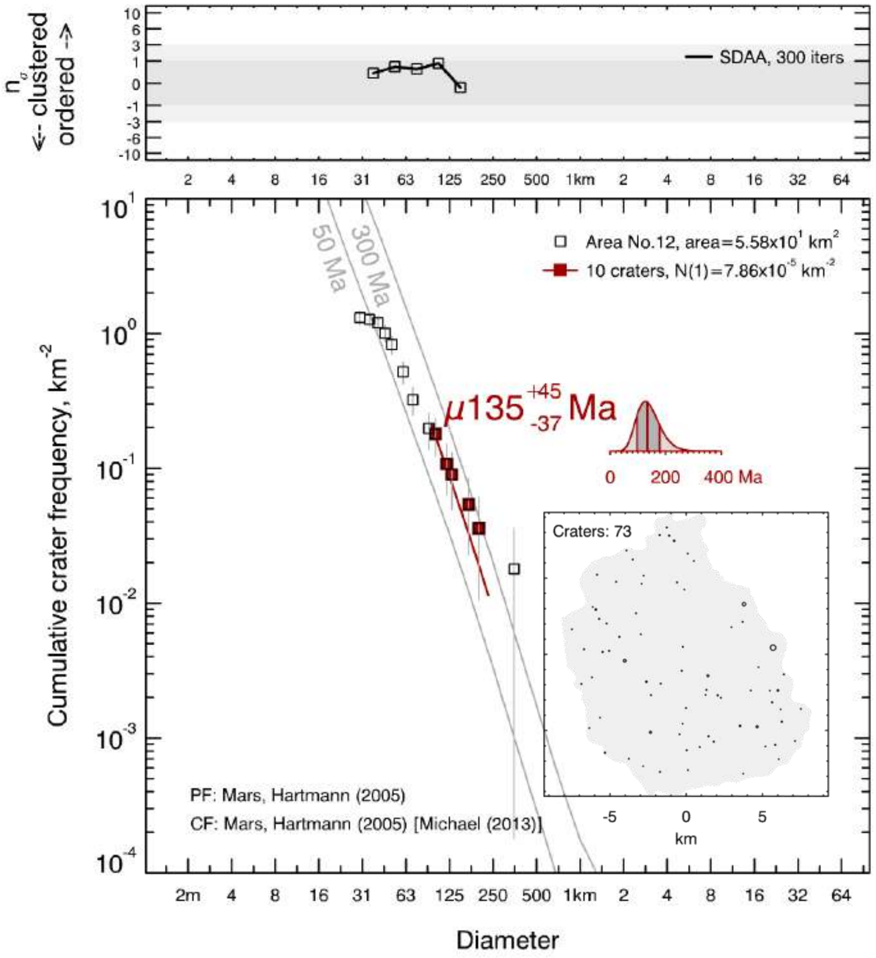

Fig. S14 CSFD and absolute model age for the surface of the Volcanic Edifice no. 12 emplaced within the Olympus Mons subprovince (for more details see Table 2).

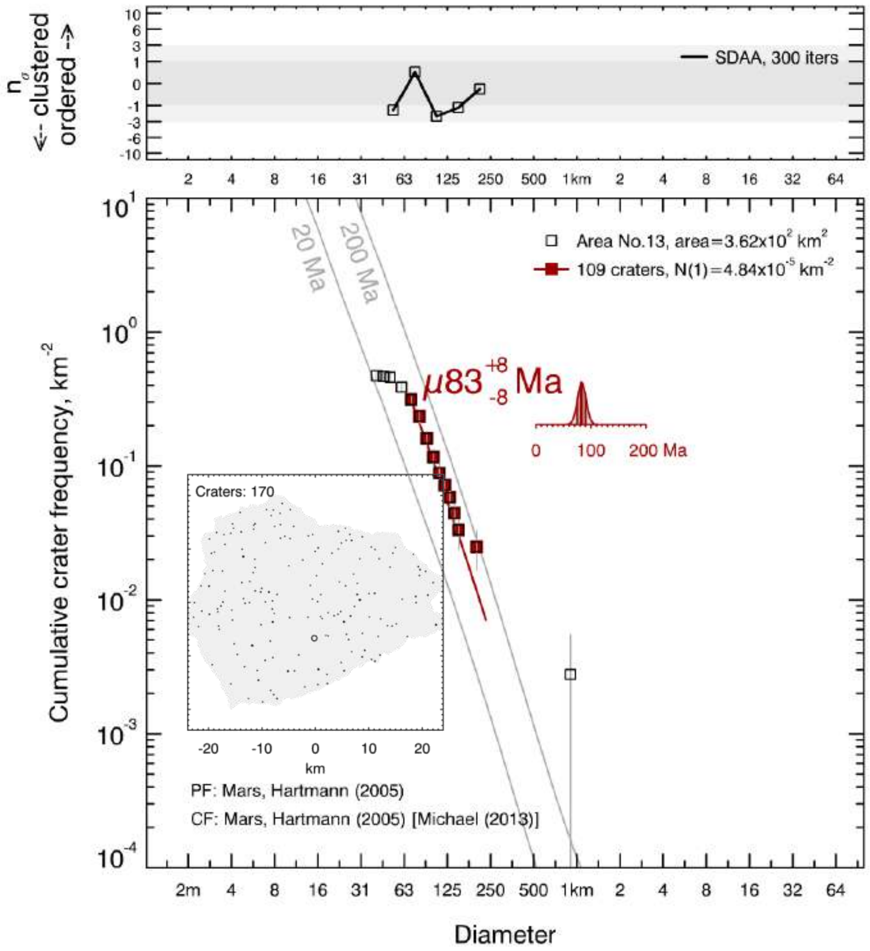

Fig. S15 CSFD and absolute model age for the surface of the Volcanic Edifice no. 13 emplaced within the Olympus Mons subprovince (for more details see Table 2).

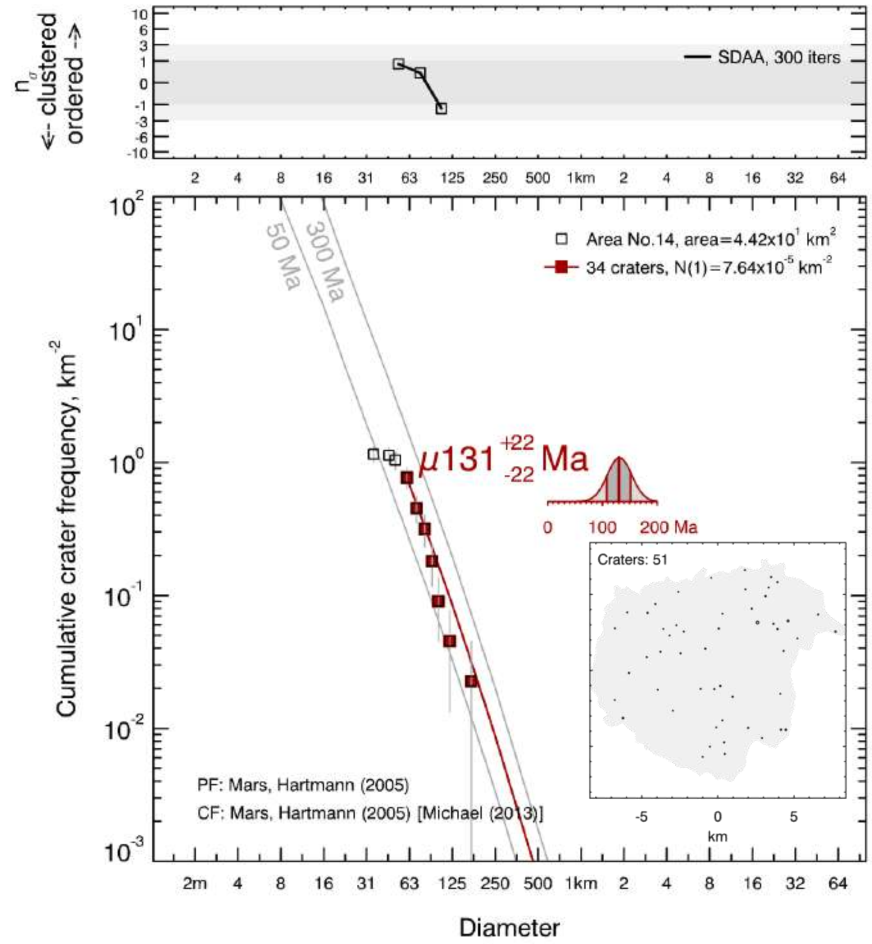

Fig. S16 CSFD and absolute model age for the surface of the Volcanic Edifice no. 14 emplaced within the Olympus Mons subprovince (for more details see Table 2).

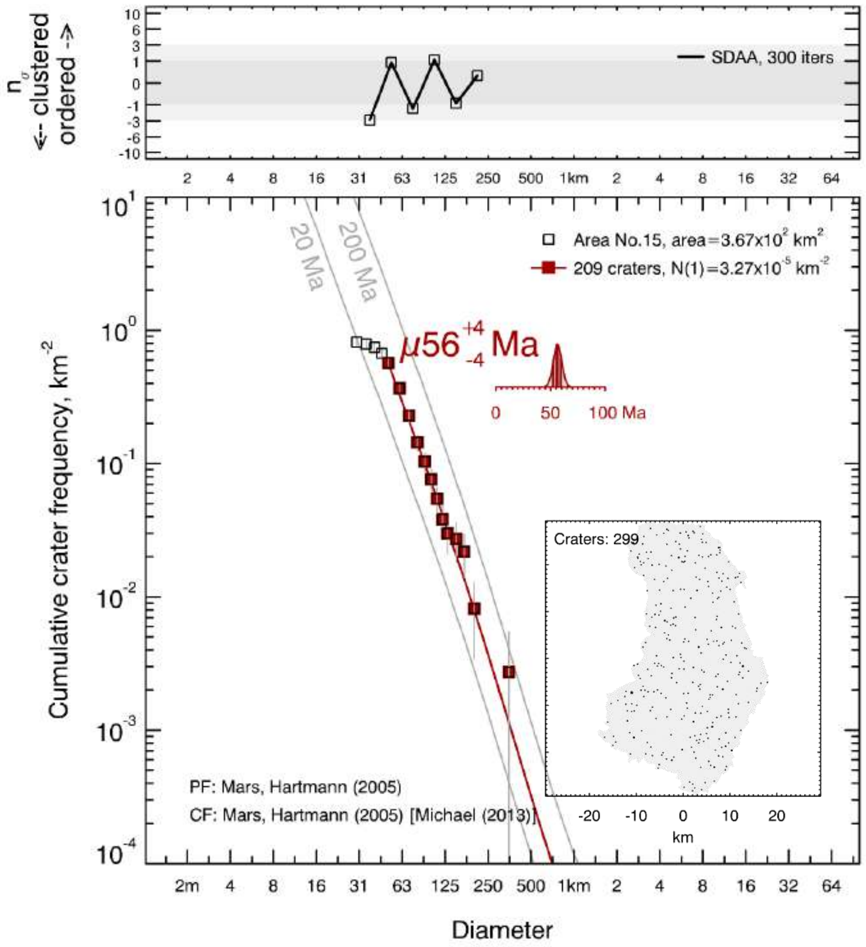

Fig. S17 CSFD and absolute model age for the surface of the Volcanic Edifice no. 15 emplaced within the Olympus Mons subprovince (for more details see Table 2).

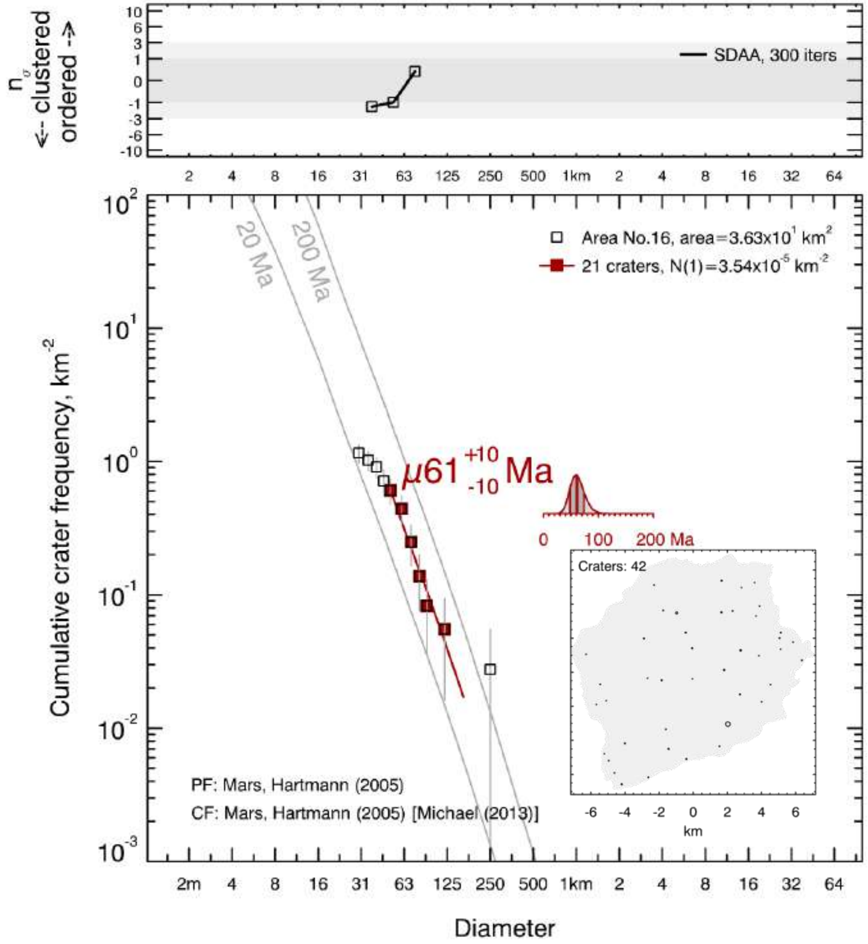

Fig. S18 CSFD and absolute model age for the surface of the Volcanic Edifice no. 16 emplaced within the Olympus Mons subprovince (for more details see Table 2).

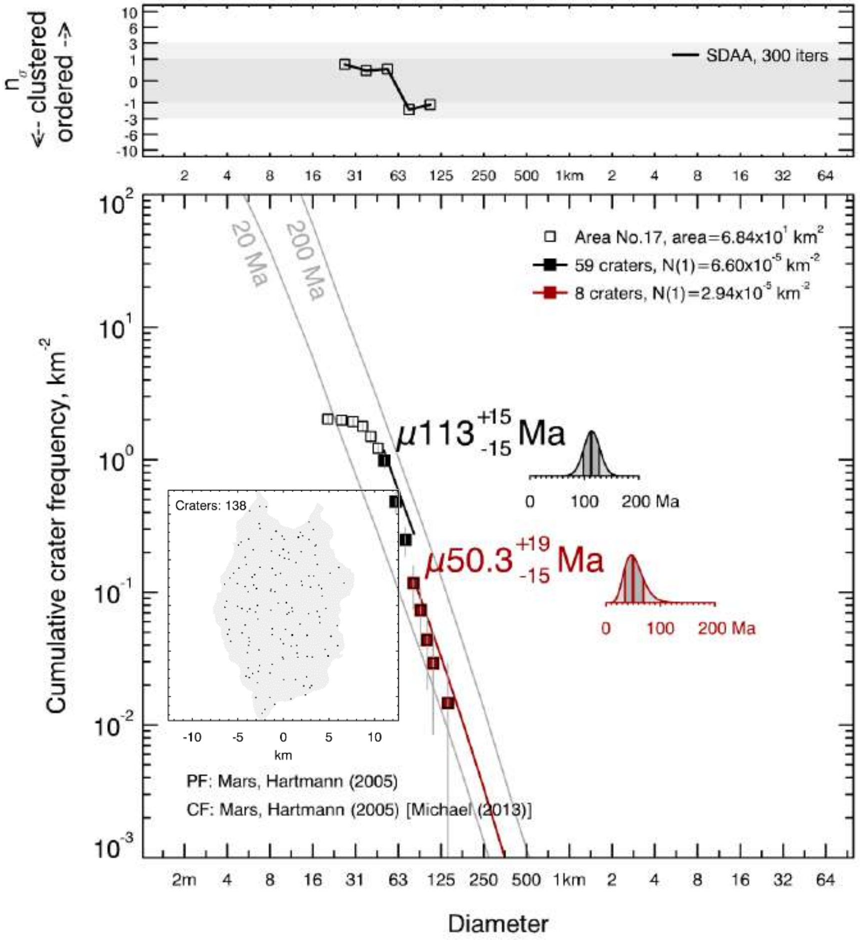

Fig. S19 CSFD and absolute model age for the surface of the Volcanic Edifice no. 17 emplaced within the Olympus Mons subprovince (for more details see Table 2). We considered impact craters of smaller (50–80 m; black) and larger (>80 m; red) diameter.

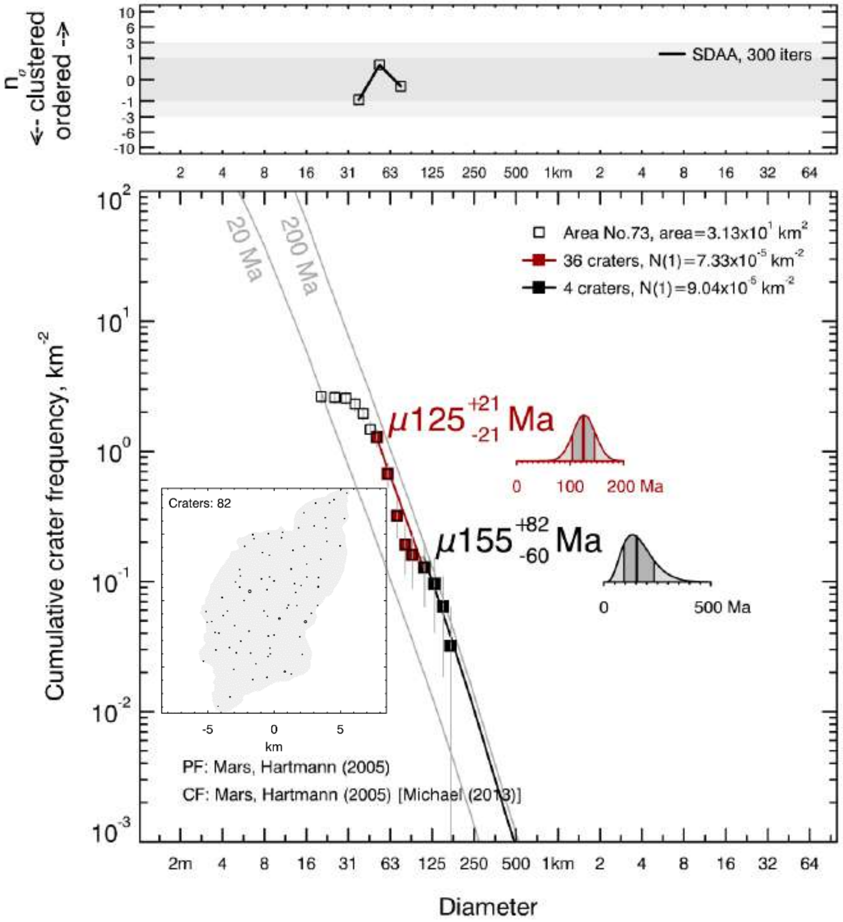

Fig. S20 CSFD and absolute model age for the surface of the Volcanic Edifice no. 73 emplaced within the Olympus Mons subprovince (for more details see Table 2). We considered impact craters of smaller (50–110 m; red) and larger (>110 m; black) diameter.

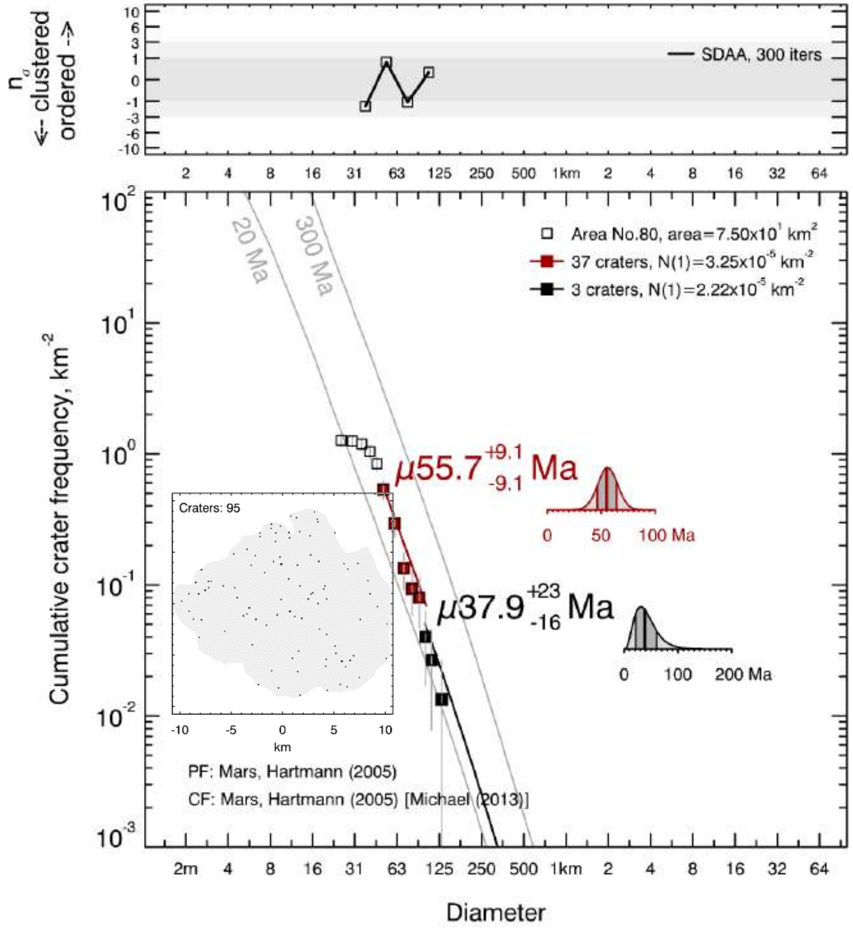

Fig. S21 CSFD and absolute model age for the surface of the Volcanic Edifice no. 80 emplaced within the Olympus Mons subprovince (for more details see Table 2). We considered impact craters of smaller (50–100 m; red) and larger (>100 m; black) diameter.

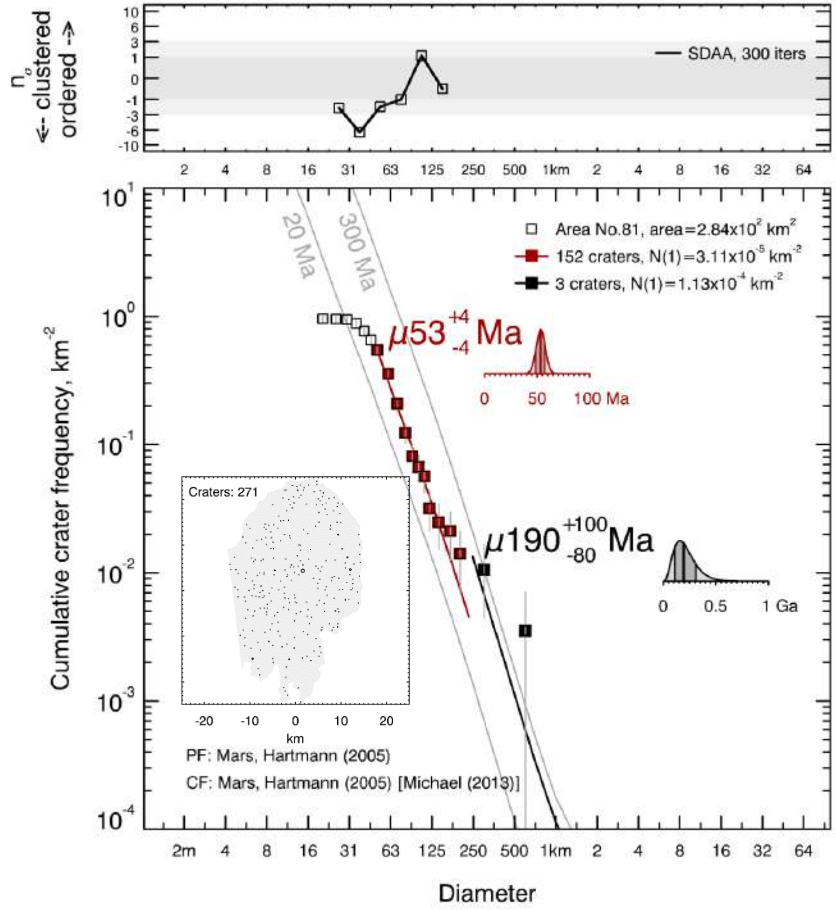

Fig. S22 CSFD and absolute model age for the surface of the Volcanic Edifice no. 81 emplaced within the Olympus Mons subprovince (for more details see Table 2). We considered impact craters of smaller (50–250 m; red) and larger (>250 m; black) diameter.

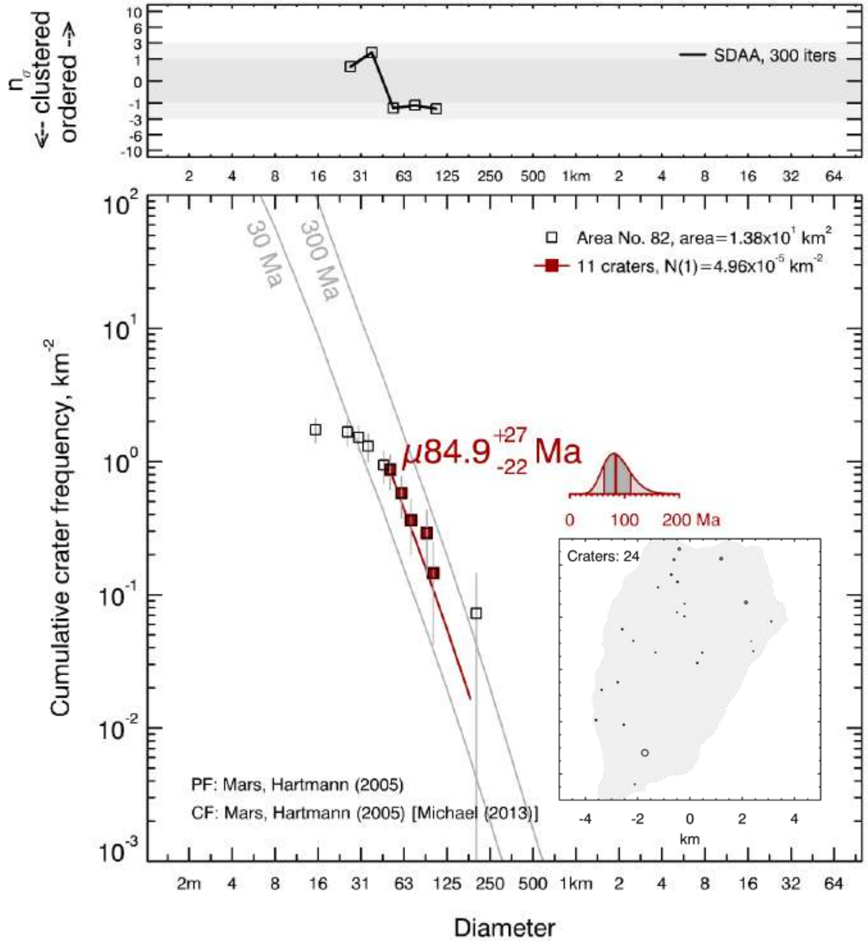

Fig. S23 CSFD and absolute model age for the surface of the Volcanic Edifice no. 82 emplaced within the Olympus Mons subprovince (for more details see Table 2).

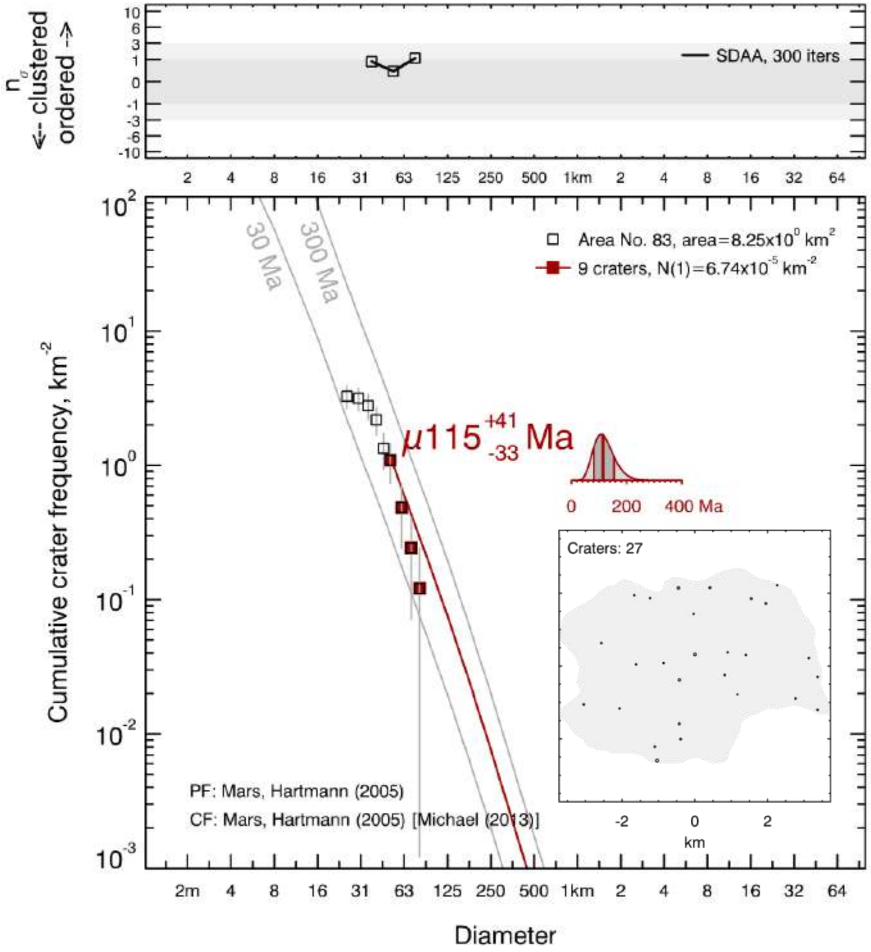

Fig. S24 CSFD and absolute model age for the surface of the Volcanic Edifice no. 83 emplaced within the Olympus Mons subprovince (for more details see Table 2).

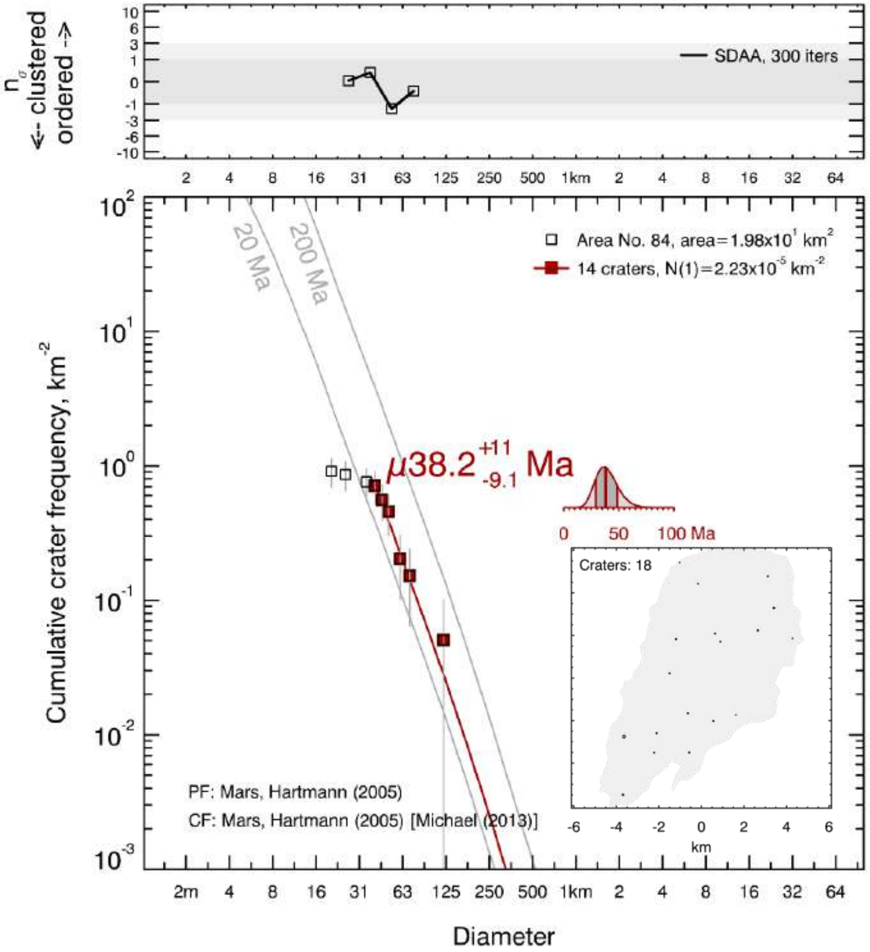

Fig. S25 CSFD and absolute model age for the surface of the Volcanic Edifice no. 84 emplaced within the Olympus Mons subprovince (for more details see Table 2).

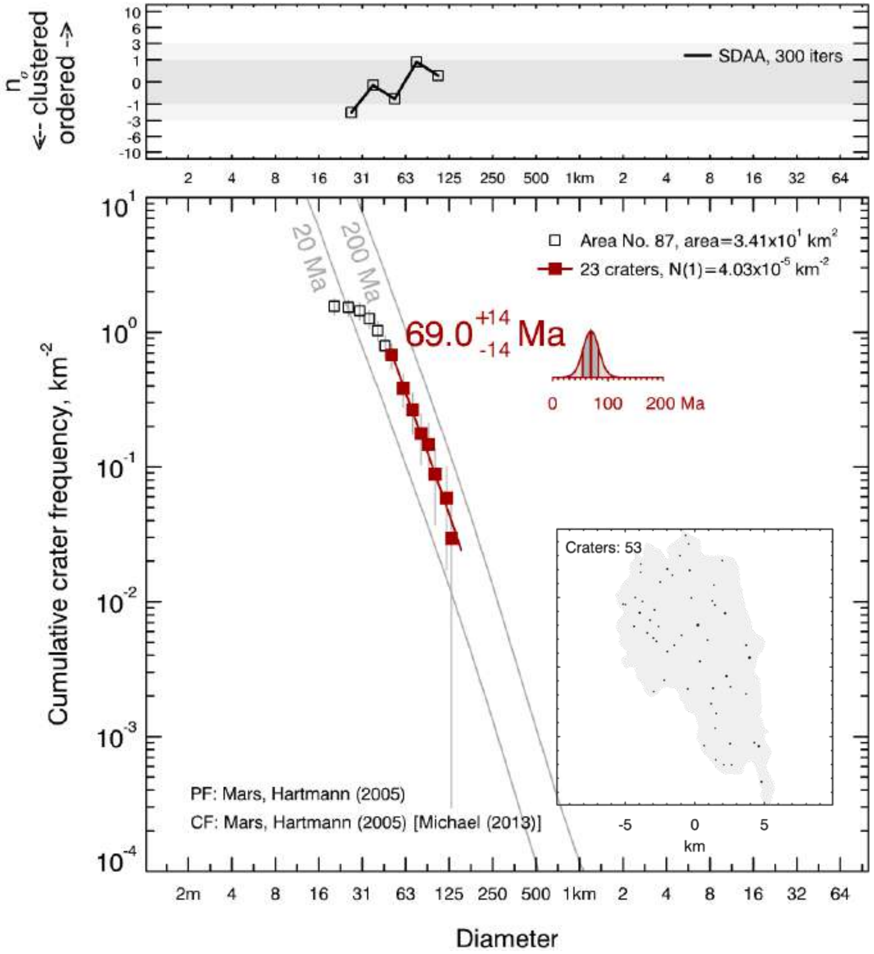

Fig. S26 CSFD and absolute model age for the surface of the Volcanic Edifice no. 87 emplaced within the Olympus Mons subprovince (for more details see Table 2).

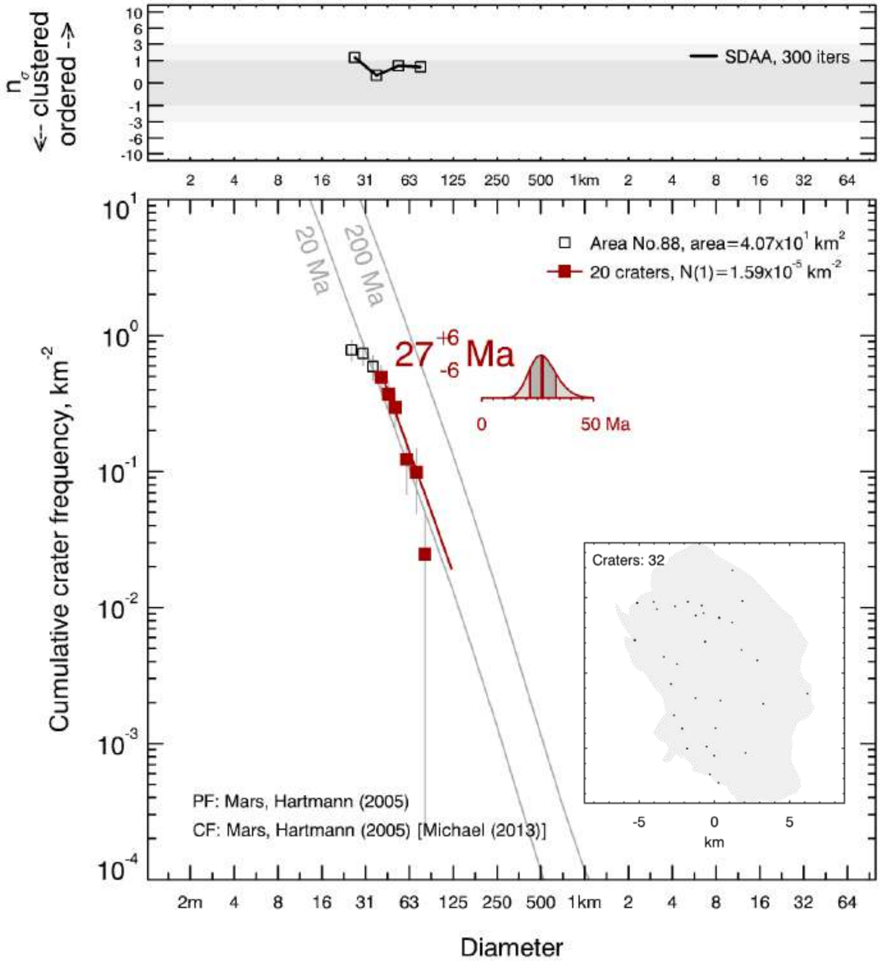

Fig. S27 CSFD and absolute model age for the surface of the Volcanic Edifice no. 88 emplaced within the Olympus Mons subprovince (for more details see Table 2).

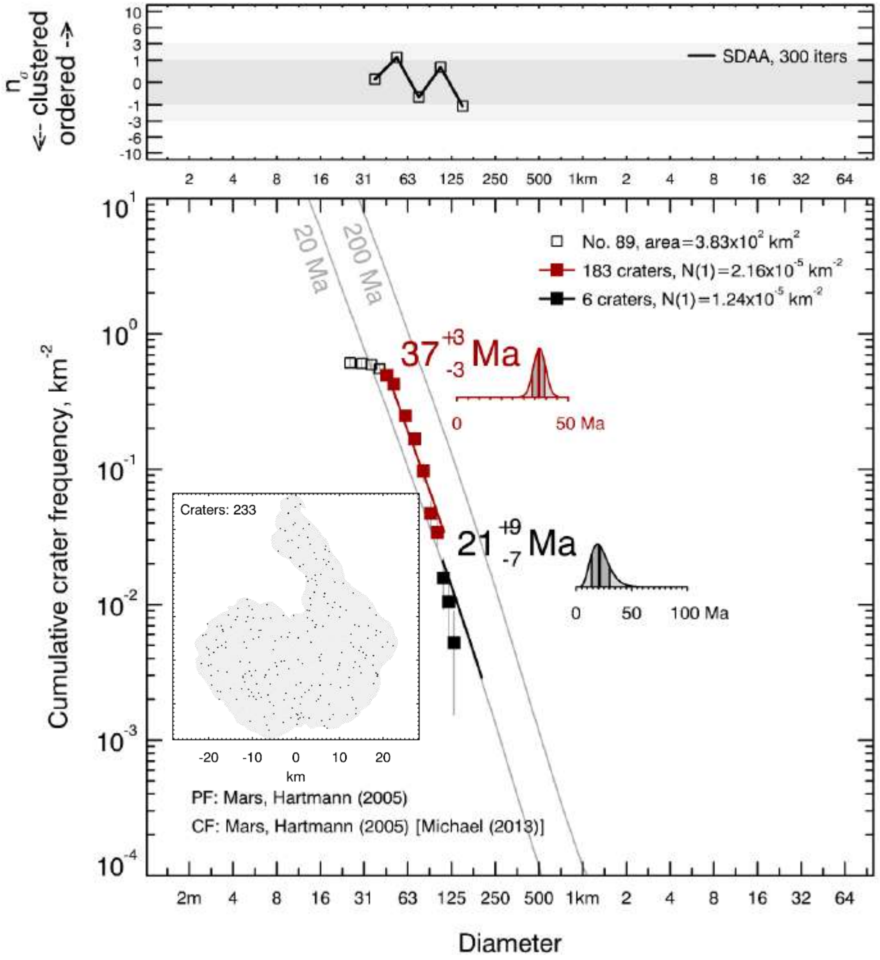

Fig. S28 CSFD and absolute model age for the surface of the Volcanic Edifice no. 89 emplaced within the Olympus Mons subprovince (for more details see Table 2). We considered impact craters of smaller (45–110 m; red) and larger (>110 m; black) diameter.

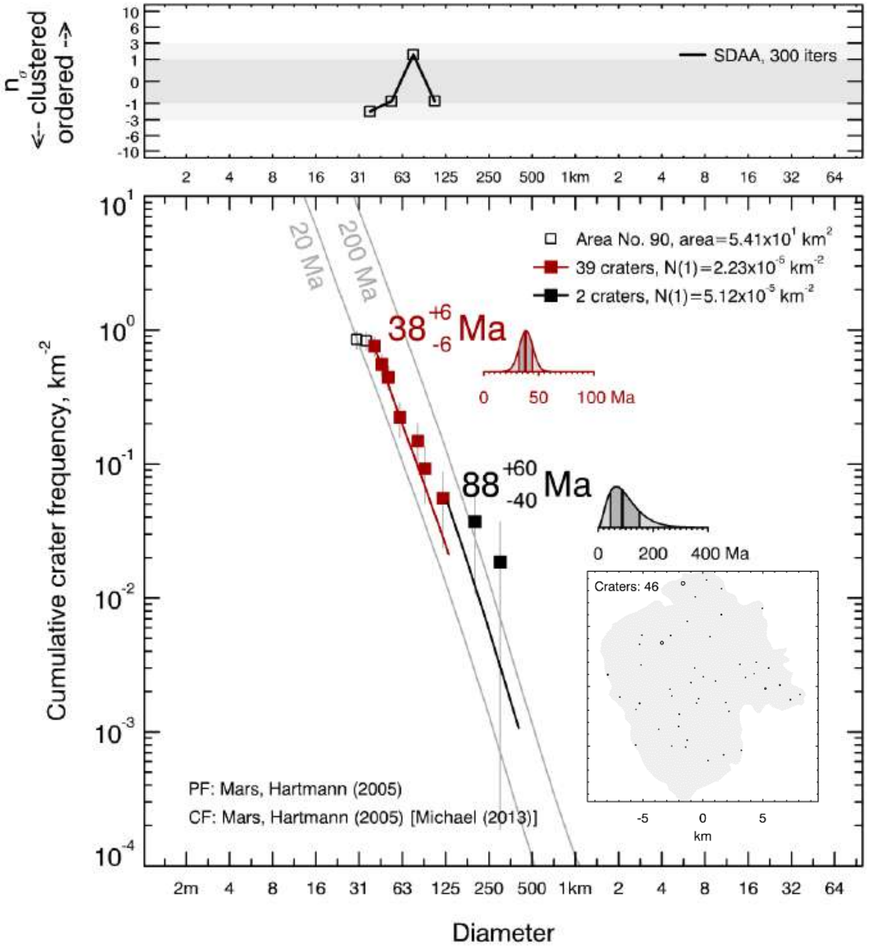

Fig. S29 CSFD and absolute model age for the surface of the Volcanic Edifice no. 90 emplaced within the Olympus Mons subprovince (for more details see Table 2). We considered impact craters of smaller (40–130 m; red) and larger (>130 m; black) diameter.

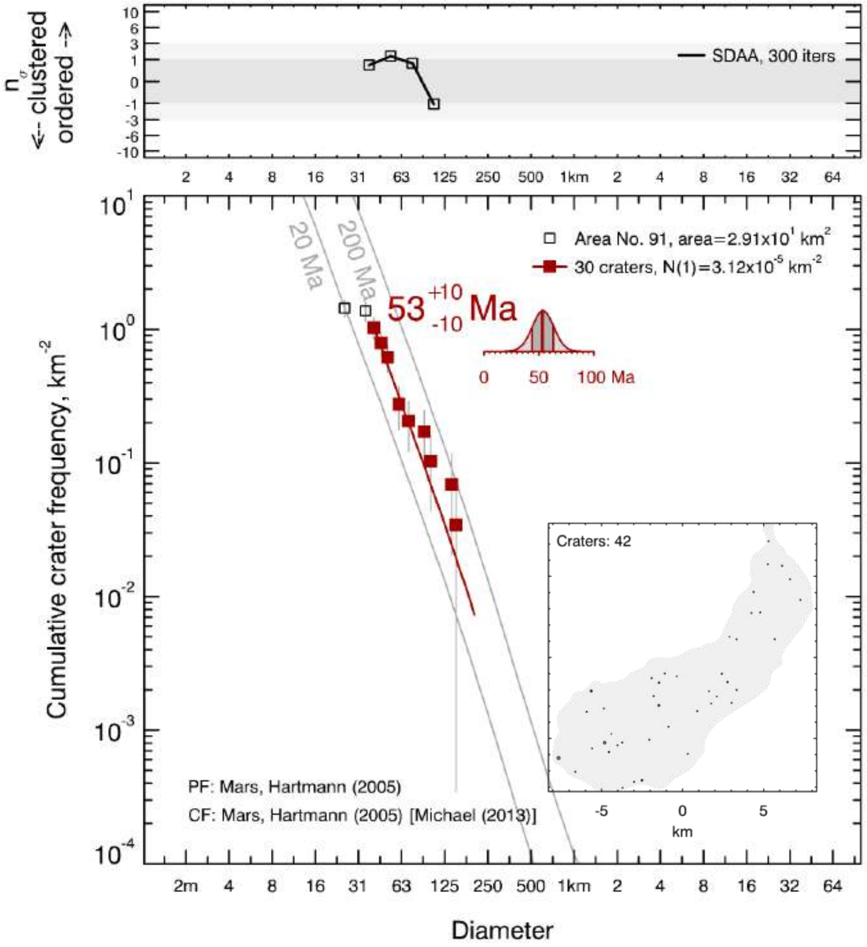

Fig. S30 CSFD and absolute model age for the surface of the Volcanic Edifice no. 91 emplaced within the Olympus Mons subprovince (for more details see Table 2).

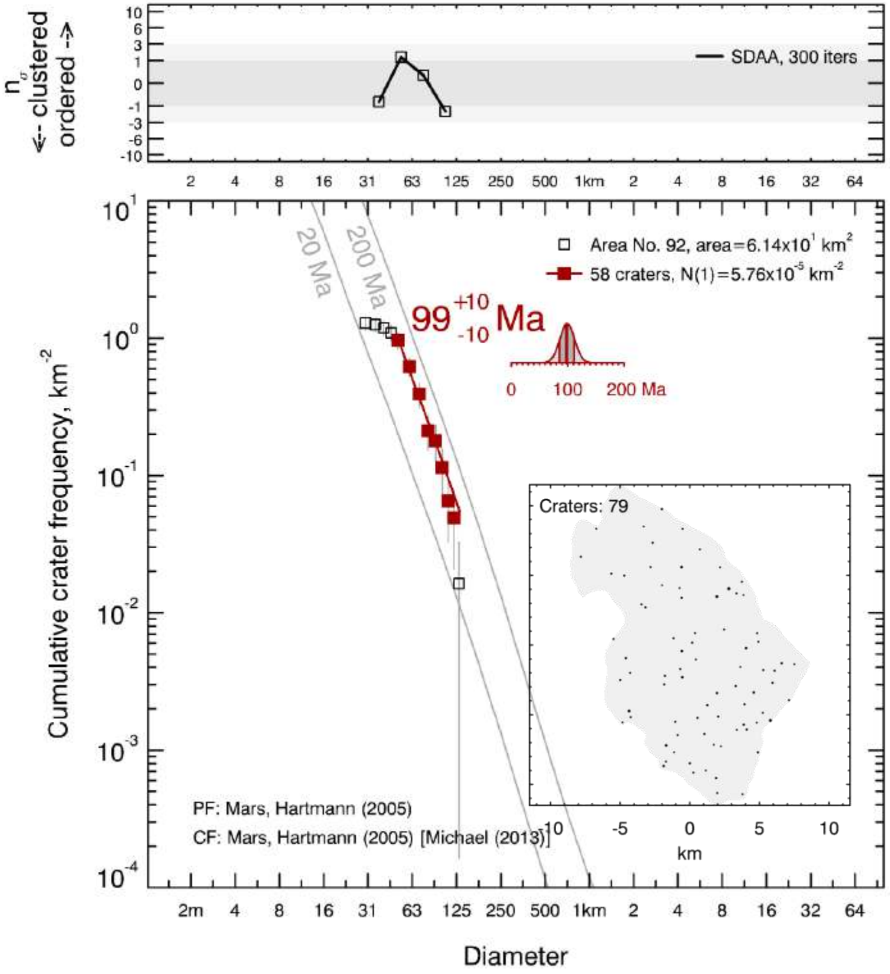

Fig. S31 CSFD and absolute model age for the surface of the Volcanic Edifice no. 92 emplaced within the Olympus Mons subprovince (for more details see Table 2).

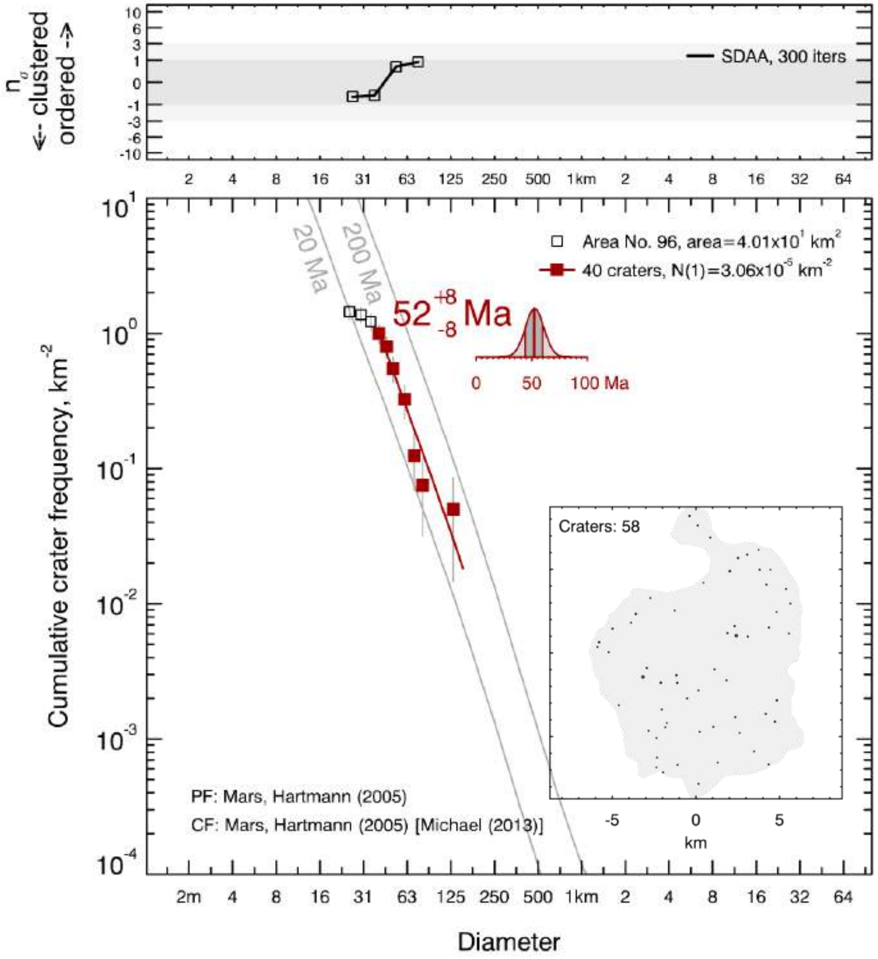

Fig. S32 CSFD and absolute model age for the surface of the Volcanic Edifice no. 96 emplaced within the Olympus Mons subprovince (for more details see Table 2).

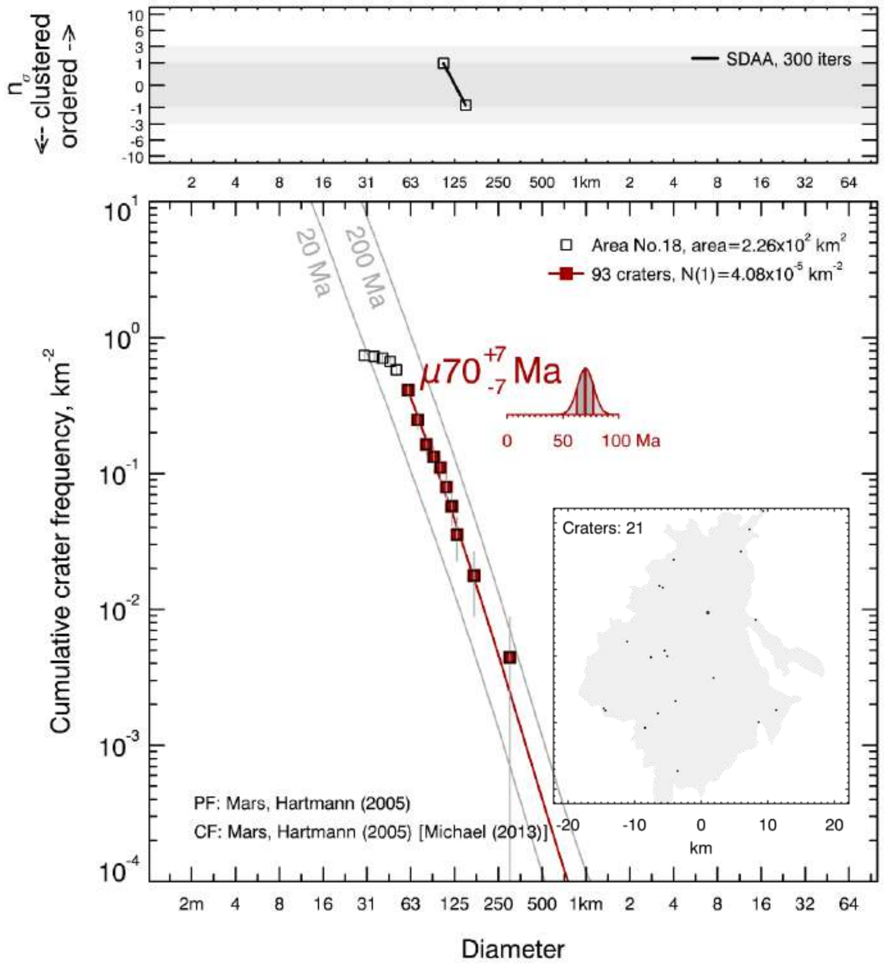

Fig. S33 CSFD and absolute model age for the surface of the Volcanic Edifice no. 18 emplaced within the Alba Mons subprovince (for more details see Table 2).

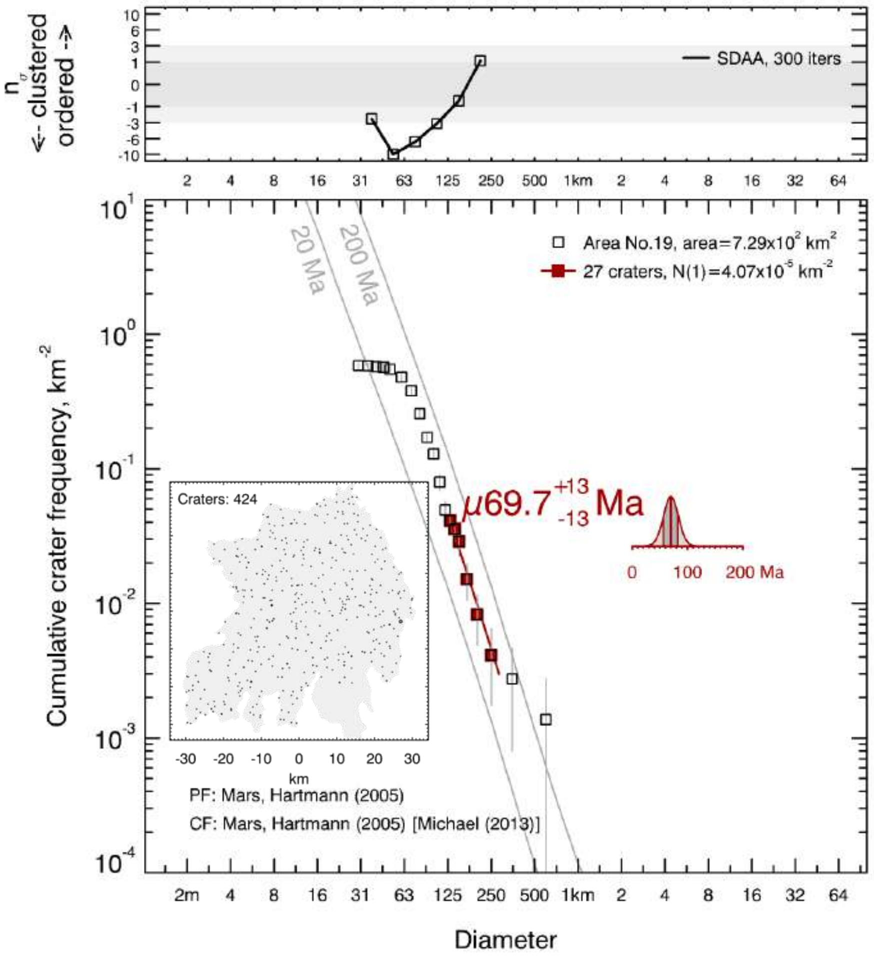

Fig. S34 CSFD and absolute model age for the surface of the Volcanic Edifice no. 19 emplaced within the Alba Mons subprovince (for more details see Table 2).

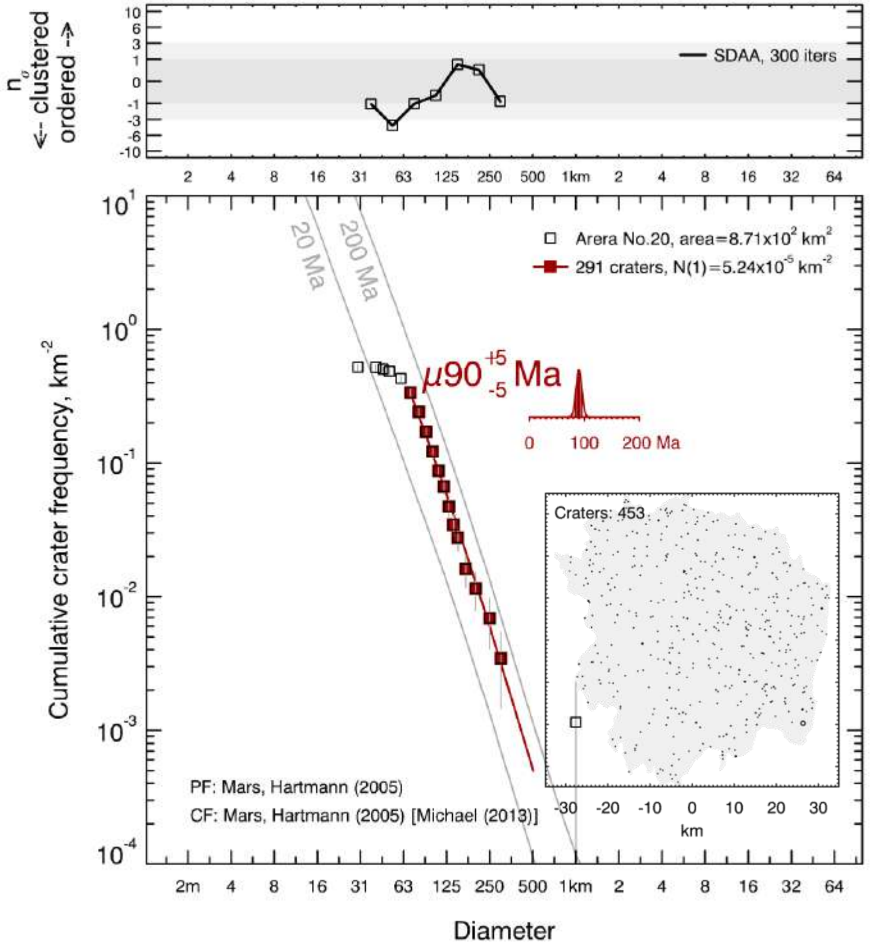

Fig. S35 CSFD and absolute model age for the surface of the Volcanic Edifice no. 20 emplaced within the Alba Mons subprovince (for more details see Table 2).

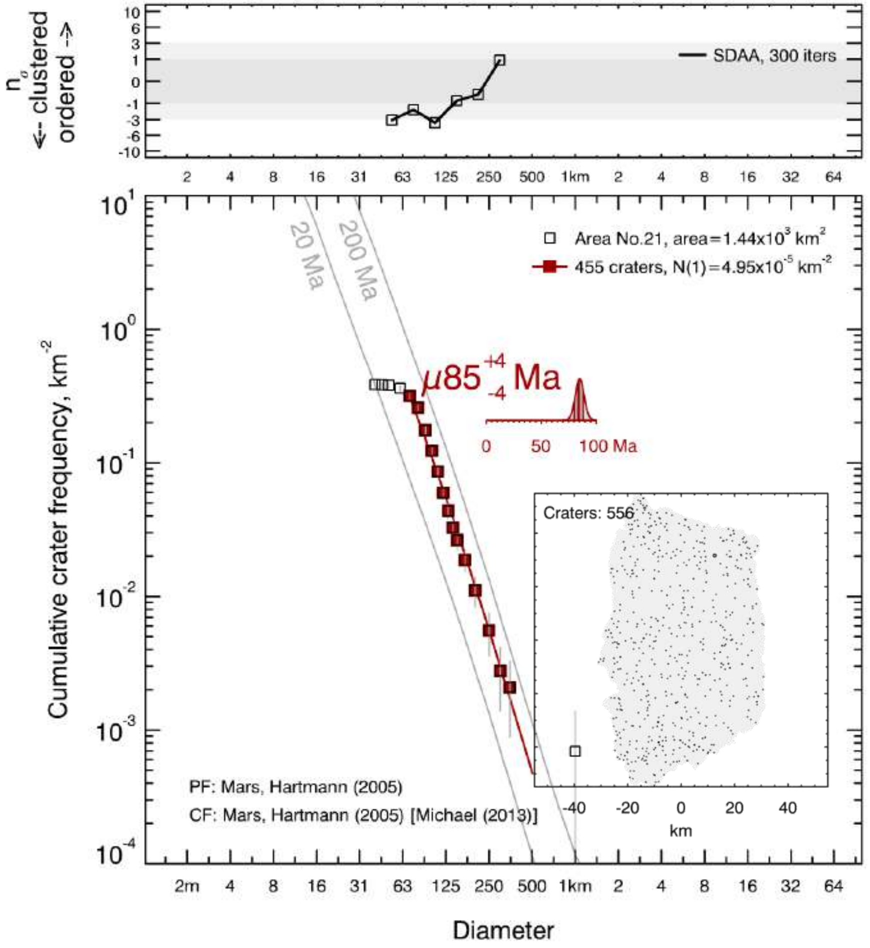

Fig. S36 CSFD and absolute model age for the surface of the Volcanic Edifice no. 21 emplaced within the Alba Mons subprovince (for more details see Table 2).

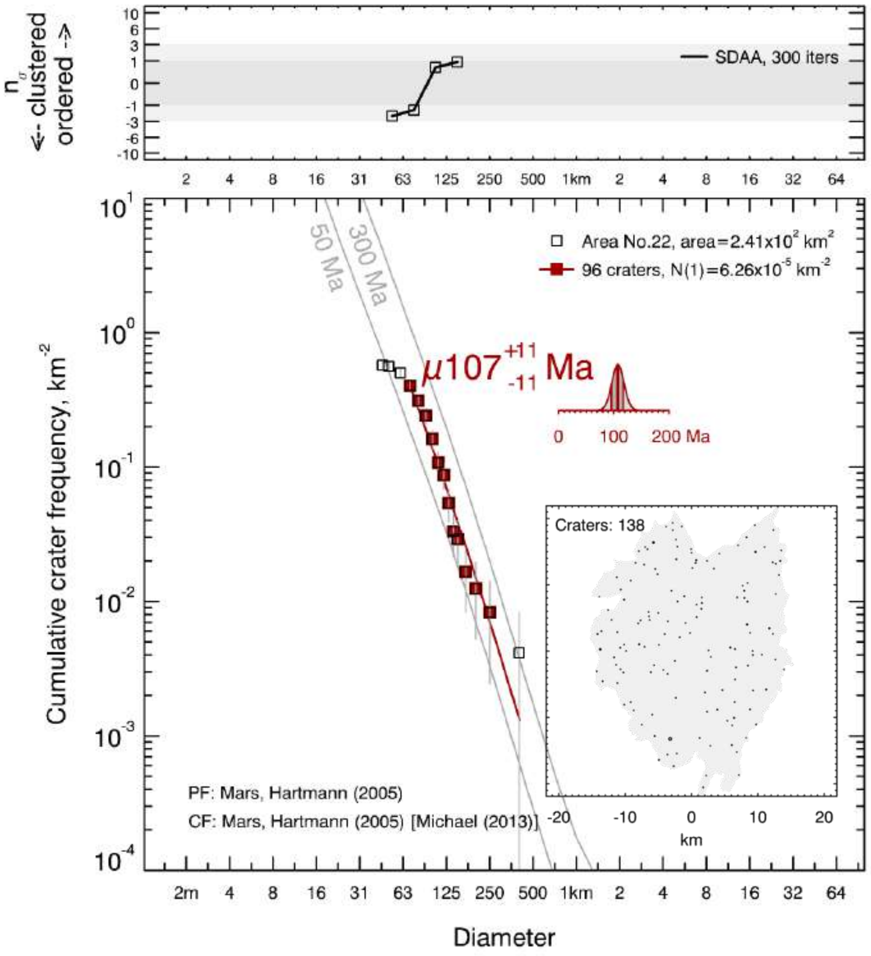

Fig. S37 CSFD and absolute model age for the surface of the Volcanic Edifice no. 22 emplaced within the Alba Mons subprovince (for more details see Table 2).

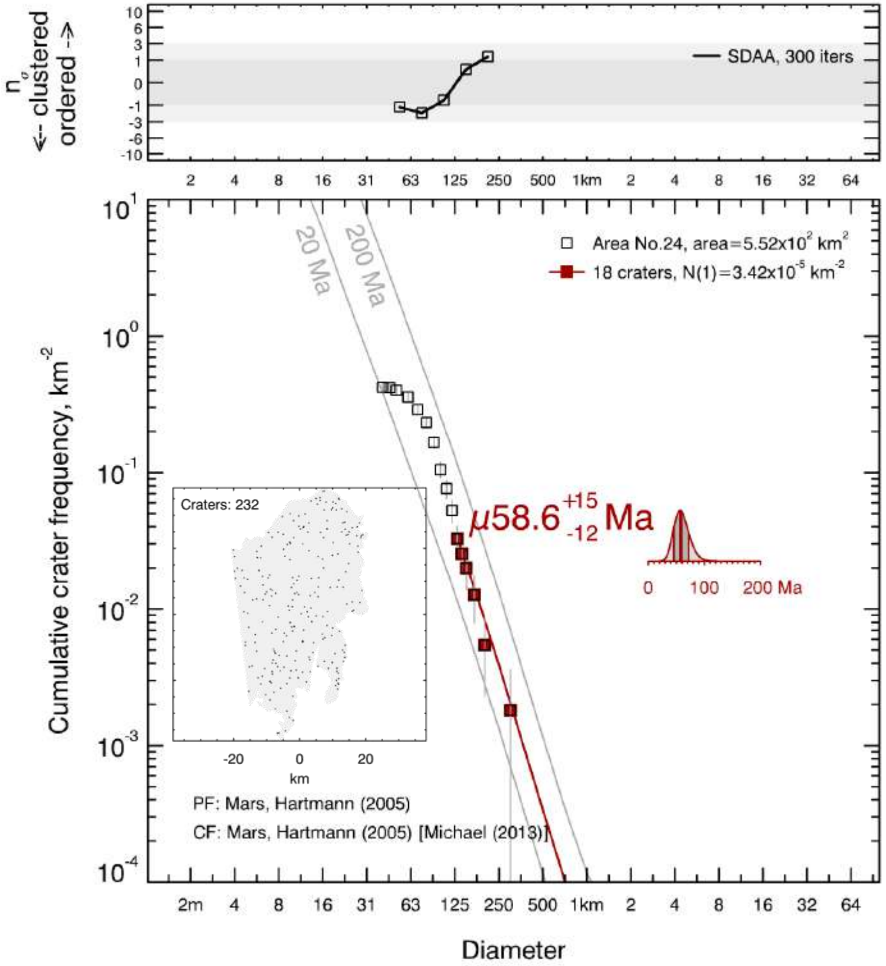

Fig. S38 CSFD and absolute model age for the surface of the Volcanic Edifice no. 24 emplaced within the Alba Mons subprovince (for more details see Table 2).

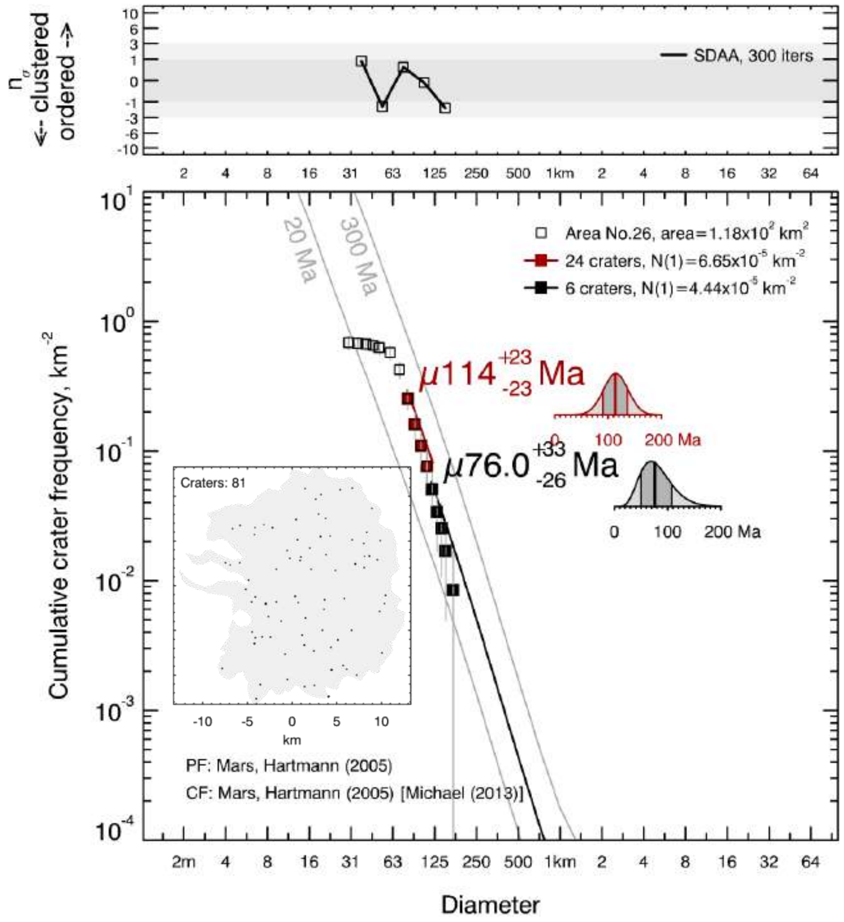

Fig. S39 CSFD and absolute model age for the surface of the Volcanic Edifice no. 26 emplaced within the Alba Mons subprovince (for more details see Table 2). We considered impact craters of smaller (80–120 m; red) and larger (>120 m; black) diameter.

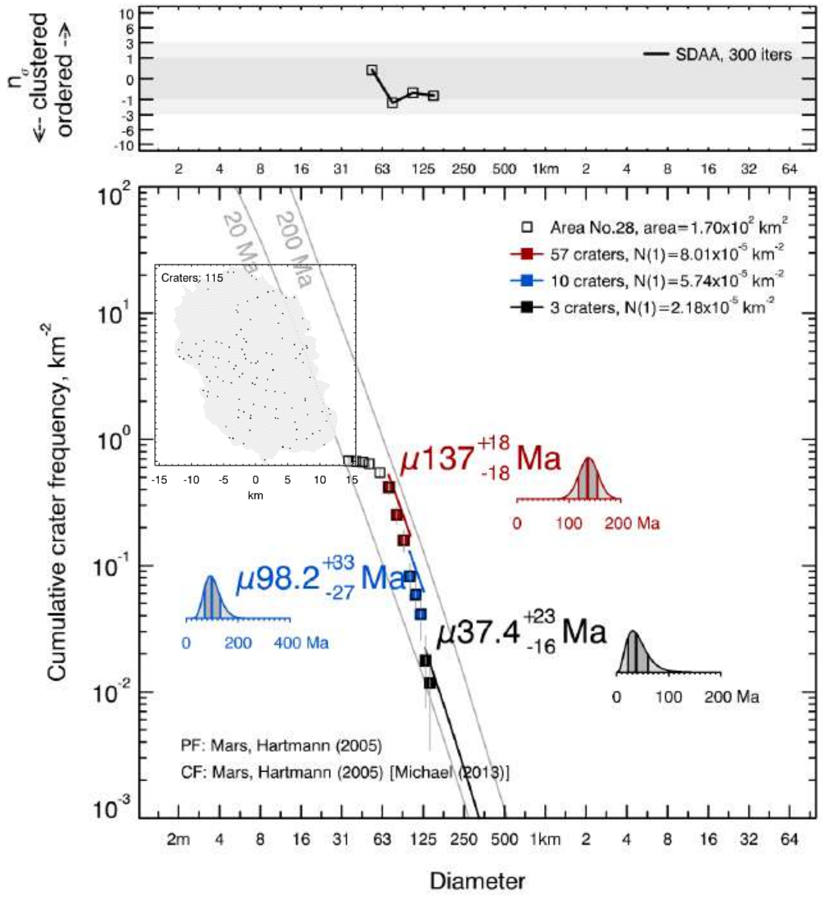

Fig. S40 CSFD and absolute model age for the surface of the Volcanic Edifice no. 28 emplaced within the Alba Mons subprovince (for more details see Table 2). We considered impact craters of small (>70 m; red), medium- (>100 m; blue), and large (>120 m; black) diameter.

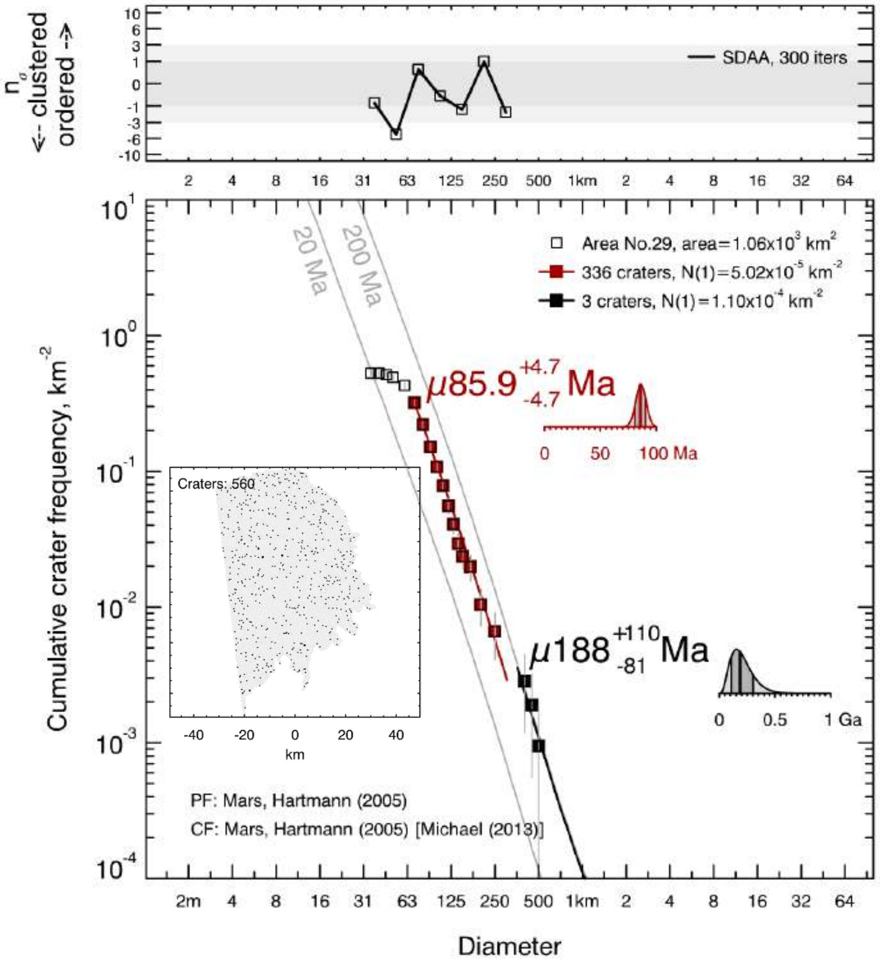

Fig. S41 CSFD and absolute model age for the surface of the Volcanic Edifice no. 29 emplaced within the Alba Mons subprovince (for more details see Table 2). We considered impact craters of smaller (80–120 m; red) and larger (>120 m; black) diameter.

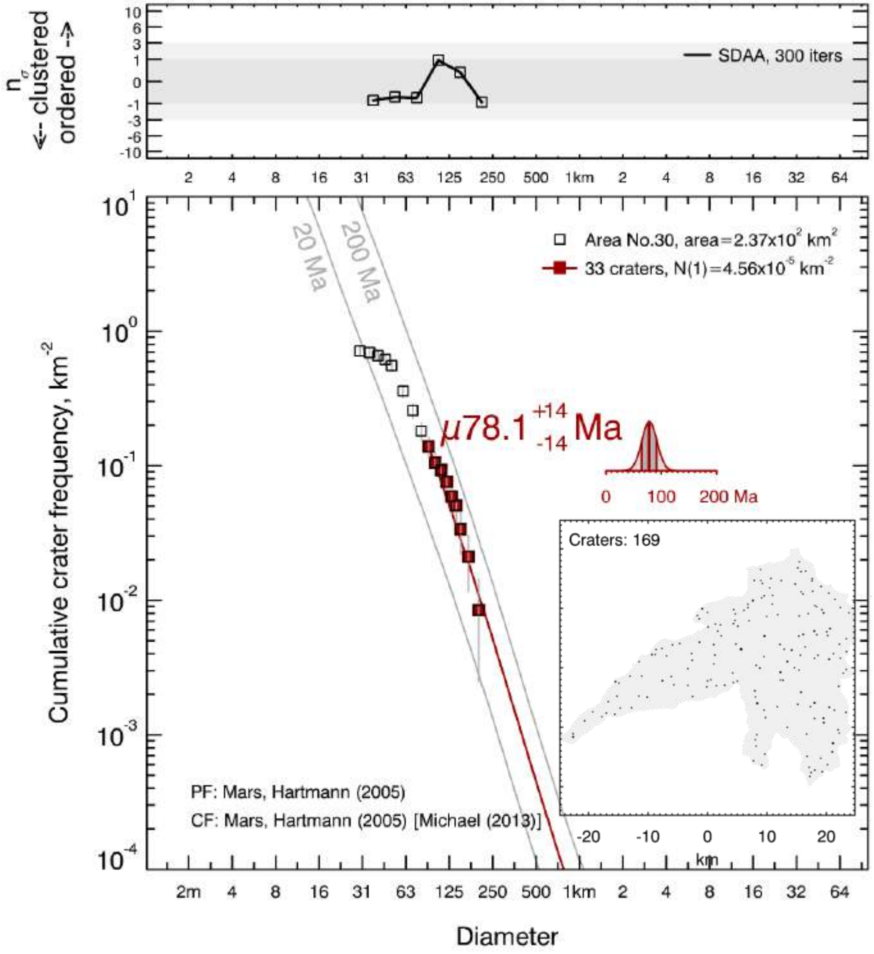

Fig. S42 CSFD and absolute model age for the surface of the Volcanic Edifice no. 30 emplaced within the Alba Mons subprovince (for more details see Table 2).

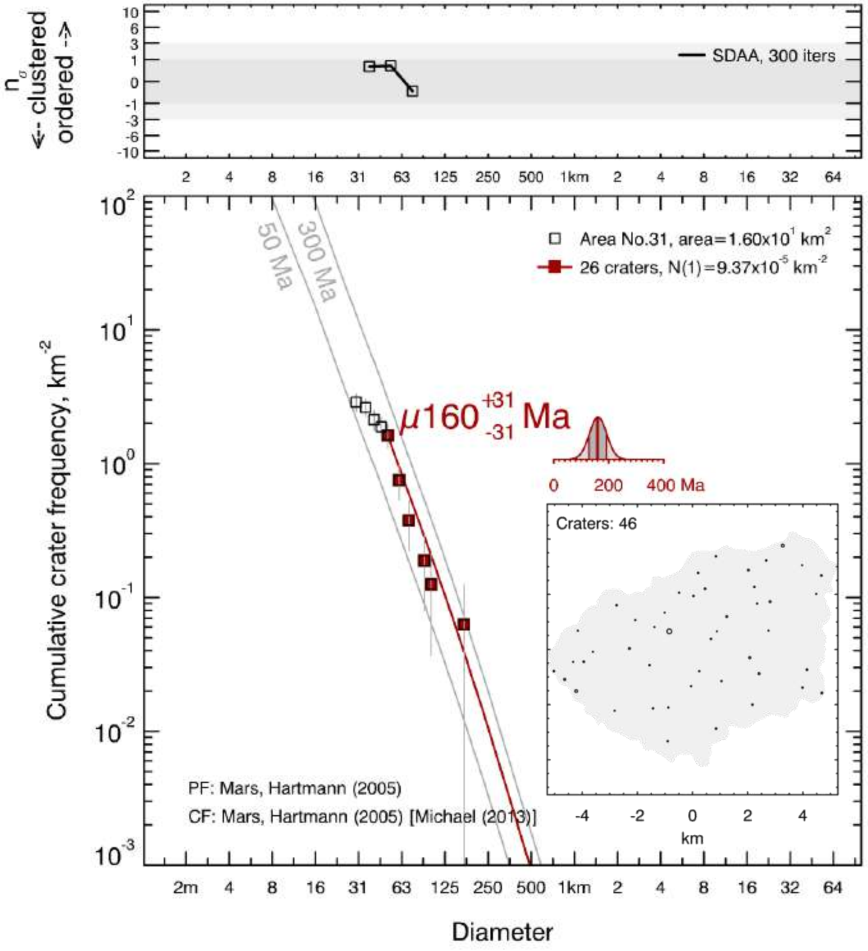

Fig. S43 CSFD and absolute model age for the surface of the Volcanic Edifice no. 31 emplaced within the Alba Mons subprovince (for more details see Table 2).

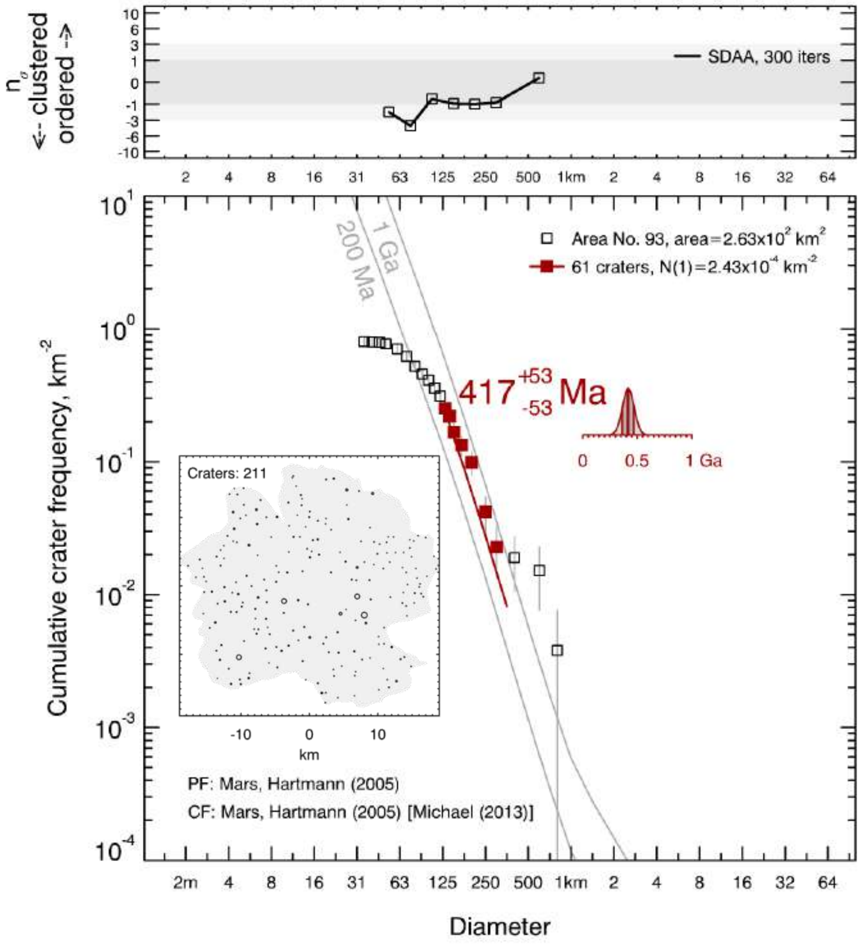

Fig. S44 CSFD and absolute model age for the surface of the Volcanic Edifice no. 93 emplaced within the Alba Mons subprovince (for more details see Table 2).

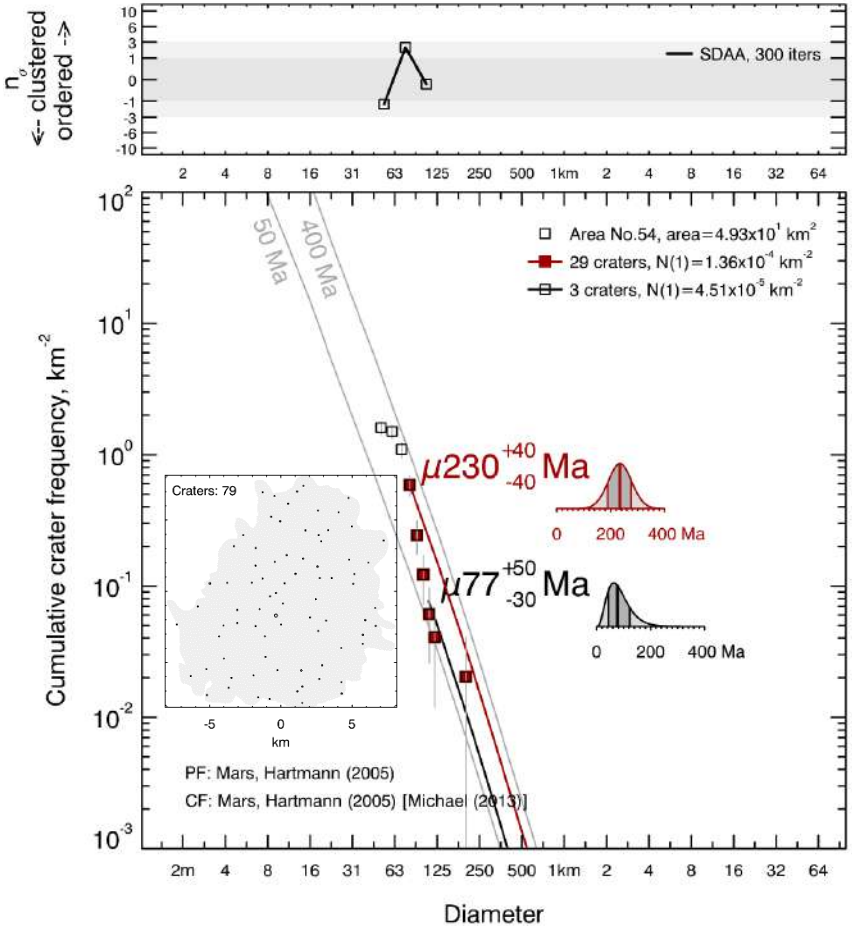

Fig. S45 CSFD and absolute model age for the surface of the Volcanic Edifice no. 54 emplaced within the Arsia Mons subprovince (for more details see Table 2). We considered impact craters of smaller (>80 m; red) and larger (>110 m; black) diameter.

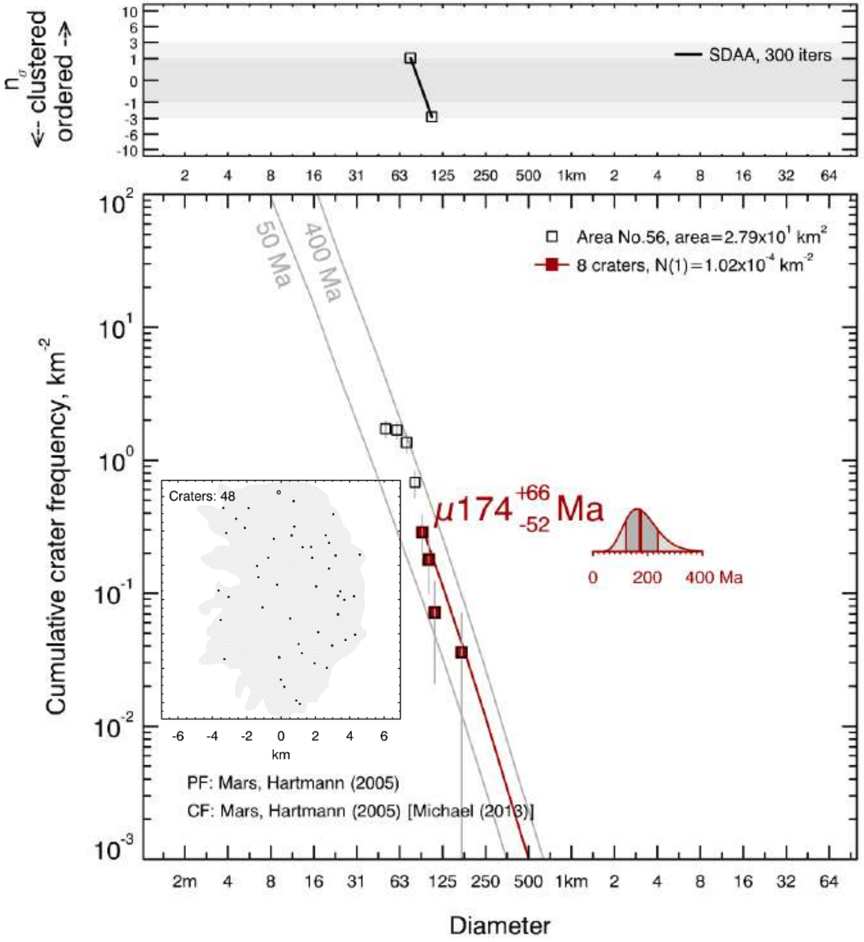

Fig. S46 CSFD and absolute model age for the surface of the Volcanic Edifice no. 56 emplaced within the Arsia Mons subprovince (for more details see Table 2).

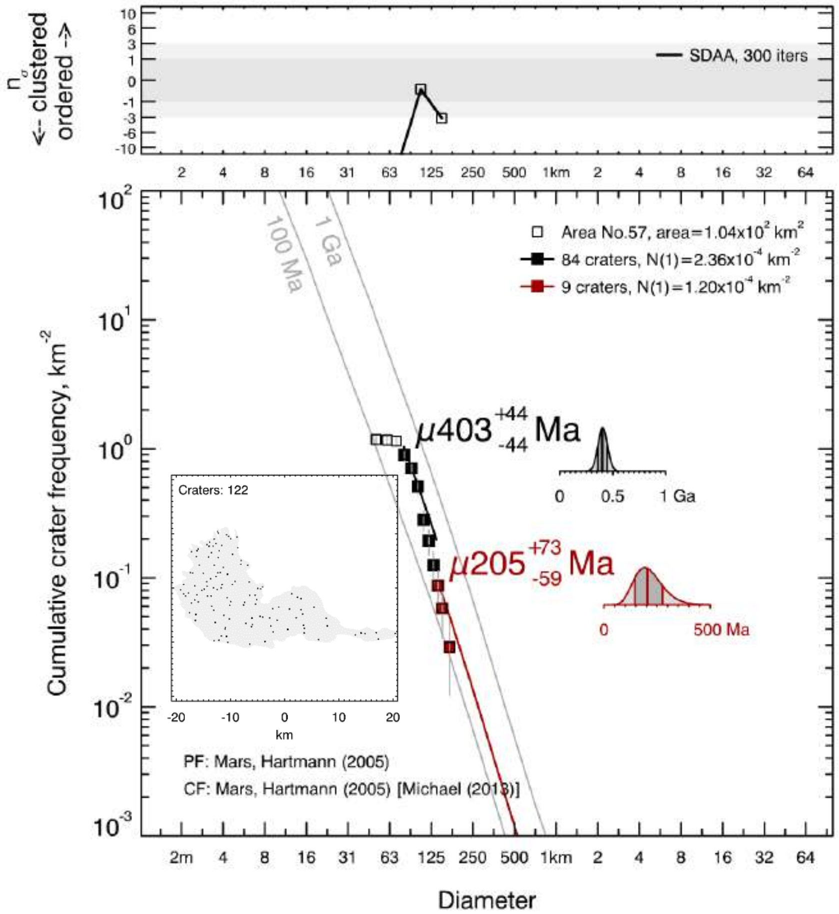

Fig. S47 CSFD and absolute model age for the surface of the Volcanic Edifice no. 57 emplaced within the Arsia Mons subprovince (for more details see Table 2). We considered impact craters of smaller (80-140 m; black) and larger (>140 m; red) diameter.

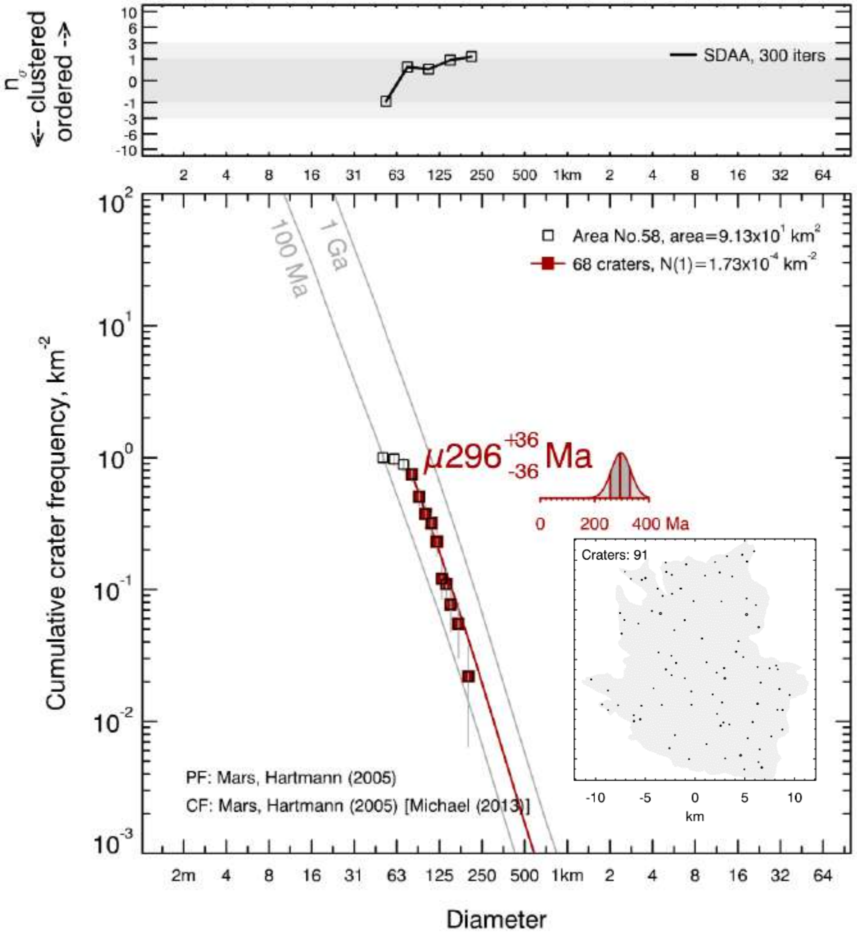

Fig. S48 CSFD and absolute model age for the surface of the Volcanic Edifice no. 58 emplaced within the Arsia Mons subprovince (for more details see Table 2).

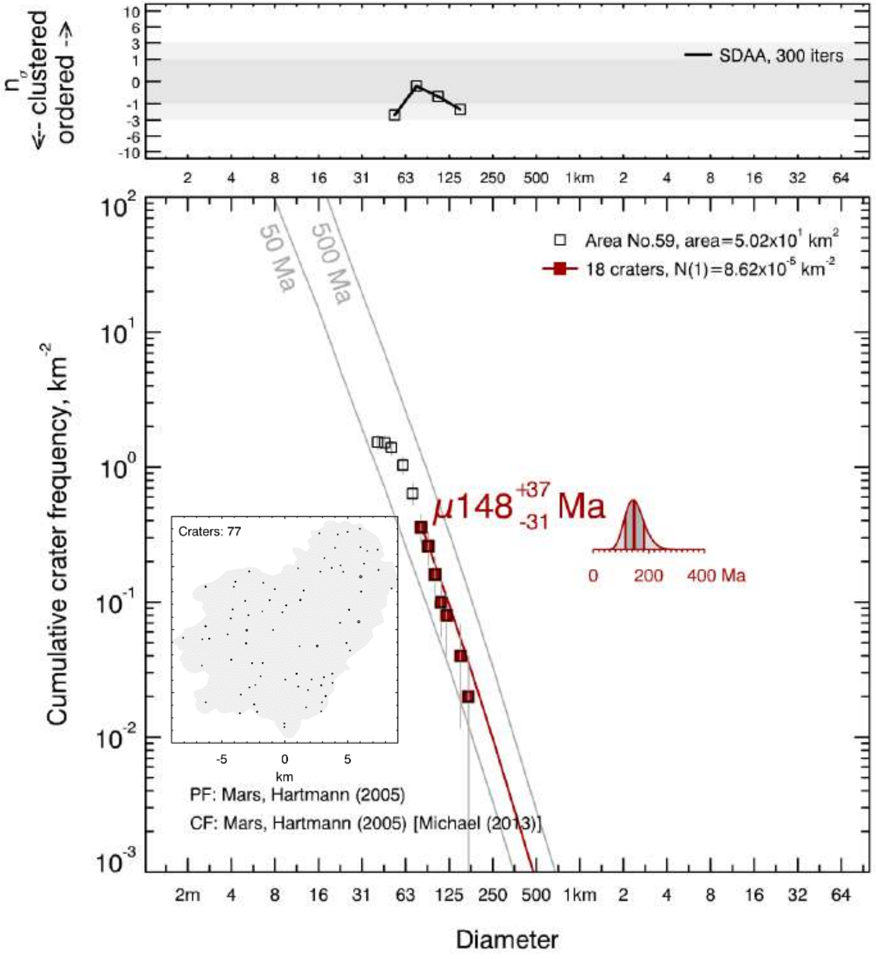

Fig. S49 CSFD and absolute model age for the surface of the Volcanic Edifice no. 59 emplaced within the Arsia Mons subprovince (for more details see Table 2).

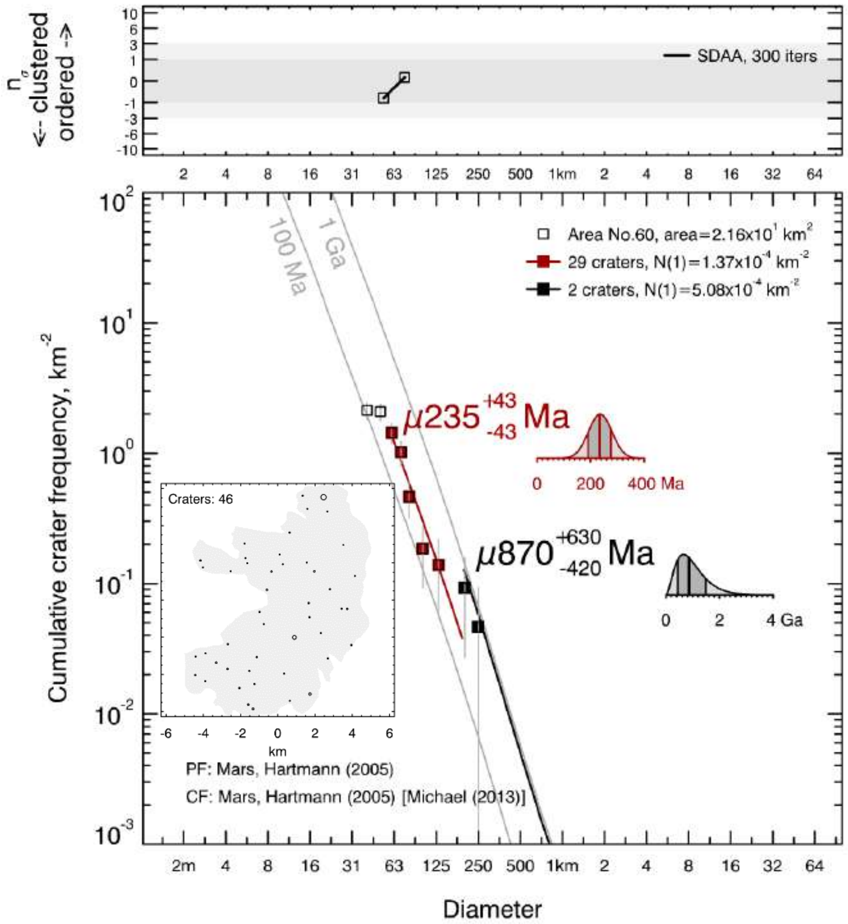

Fig. S50 CSFD and absolute model age for the surface of the Volcanic Edifice no. 60 emplaced within the Arsia Mons subprovince (for more details see Table 2). We considered impact craters of smaller (60-200 m; black) and larger (>200 m; red) diameter.

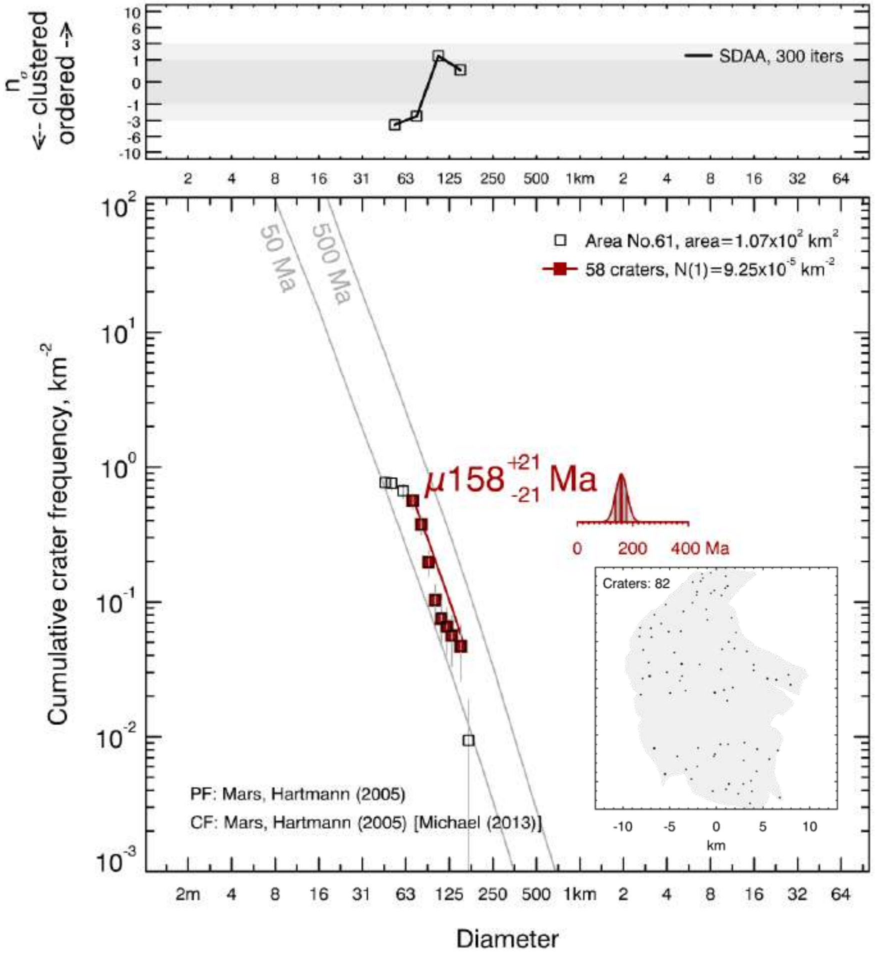

Fig. S51 CSFD and absolute model age for the surface of the Volcanic Edifice no. 61 emplaced within the Arsia Mons subprovince (for more details see Table 2).

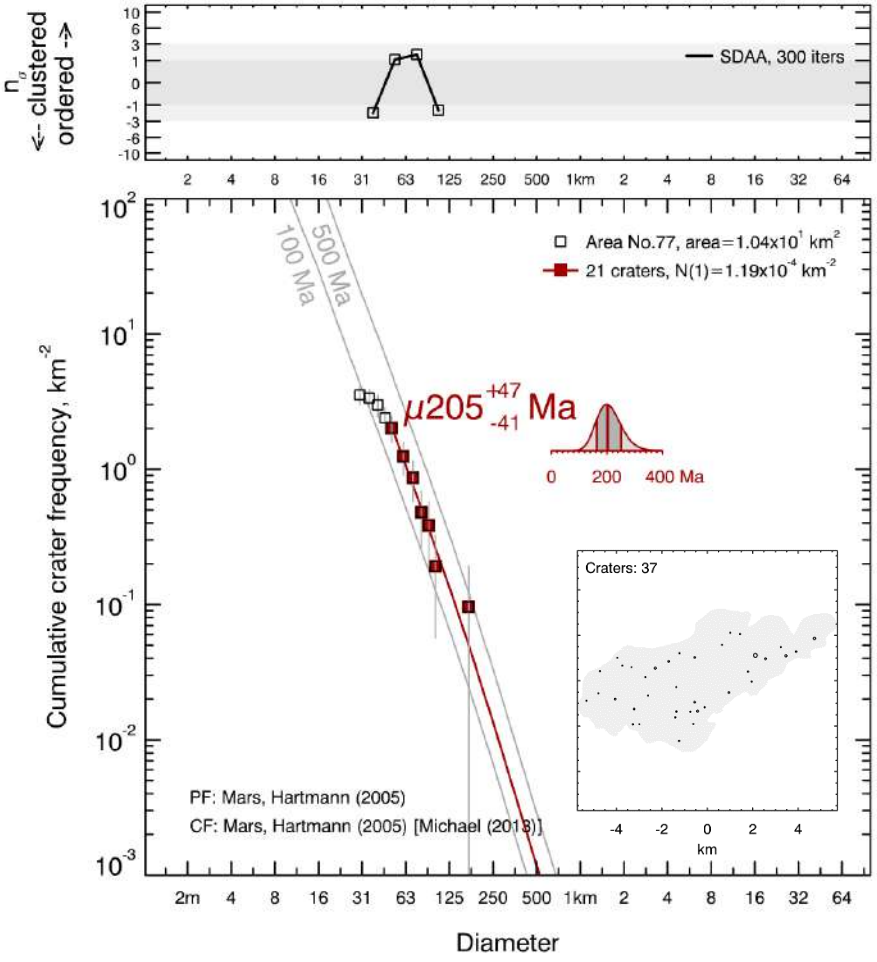

Fig. S52 CSFD and absolute model age for the surface of the Volcanic Edifice no. 77 emplaced within the Arsia Mons subprovince (for more details see Table 2).

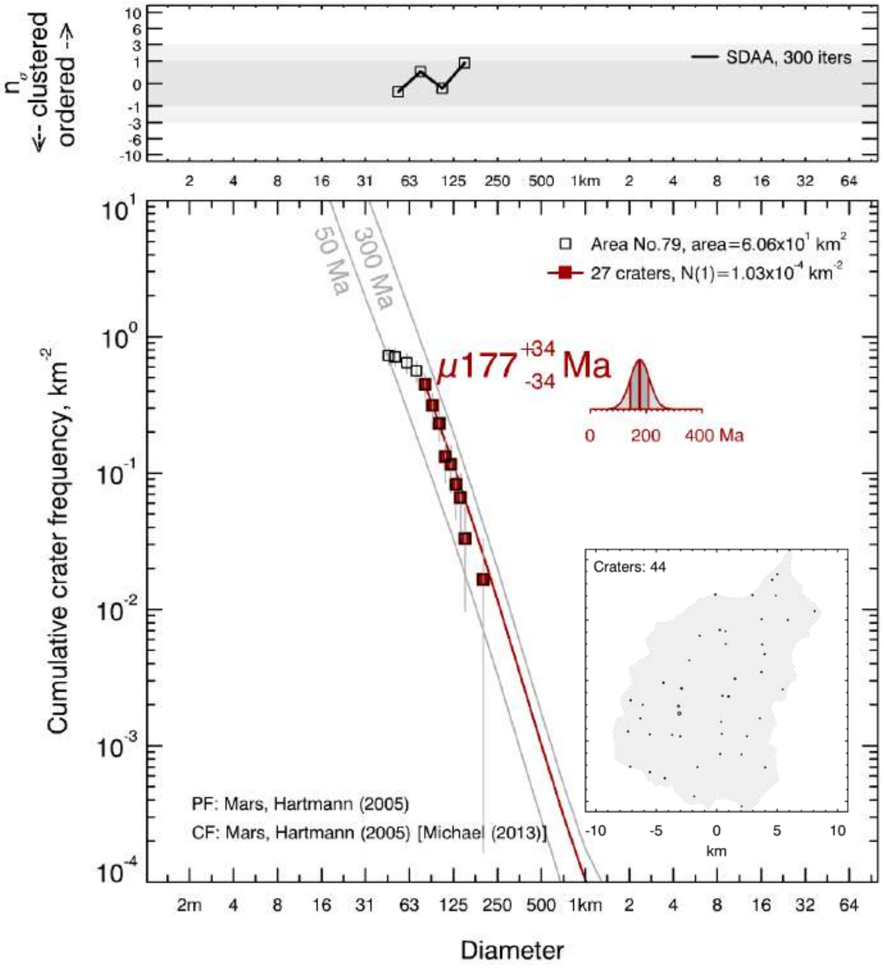

Fig. S53 CSFD and absolute model age for the surface of the Volcanic Edifice no. 79 emplaced within the Arsia Mons subprovince (for more details see Table 2).

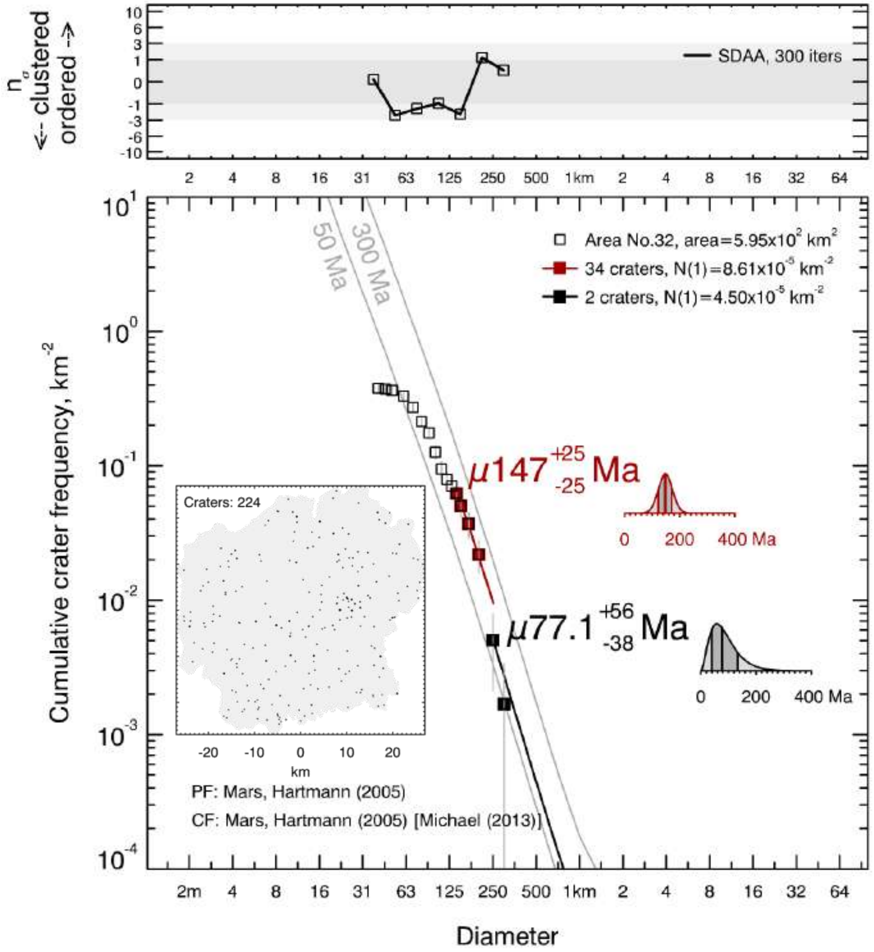

Fig. S54 CSFD and absolute model age for the surface of the Volcanic Edifice no. 32 emplaced within the Pavonis Mons subprovince (for more details see Table 2). We considered impact craters of smaller (140-260 m; red) and larger (>260 m; black) diameter.

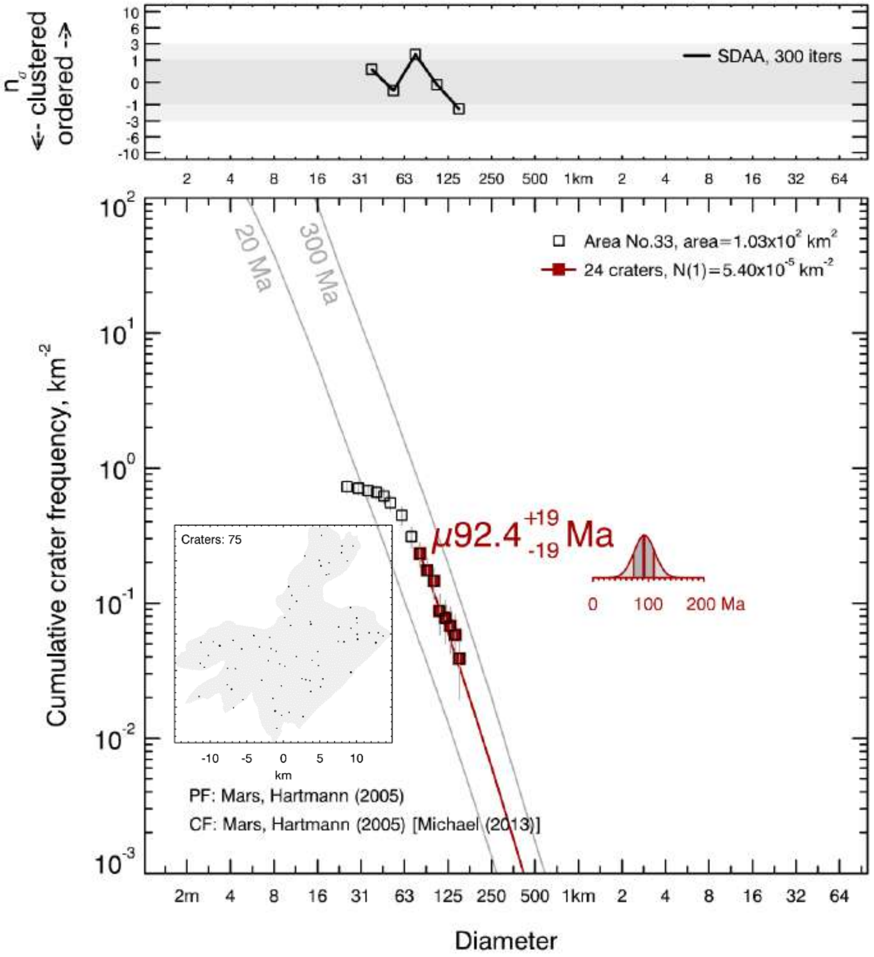

Fig. S55 CSFD and absolute model age for the surface of the Volcanic Edifice no. 33 emplaced within the Pavonis Mons subprovince (for more details see Table 2).

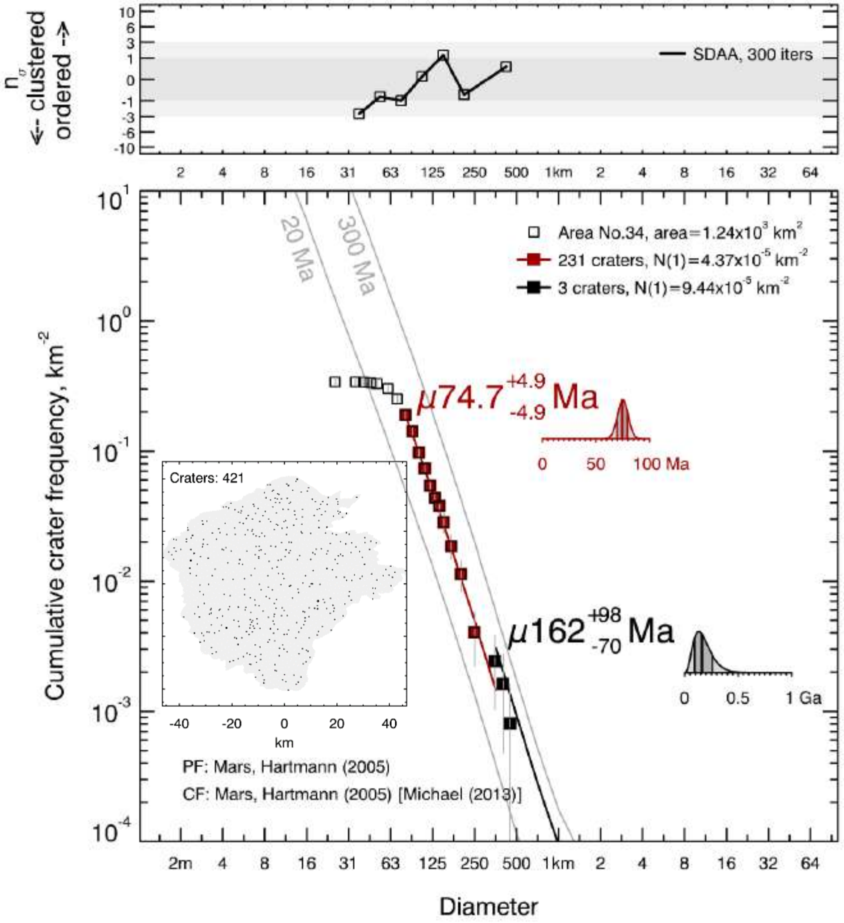

Fig. S56 CSFD and absolute model age for the surface of the Volcanic Edifice no. 34 emplaced within the Pavonis Mons subprovince (for more details see Table 2). We considered impact craters of smaller (80-360 m; red) and larger (>360 m; black) diameter.

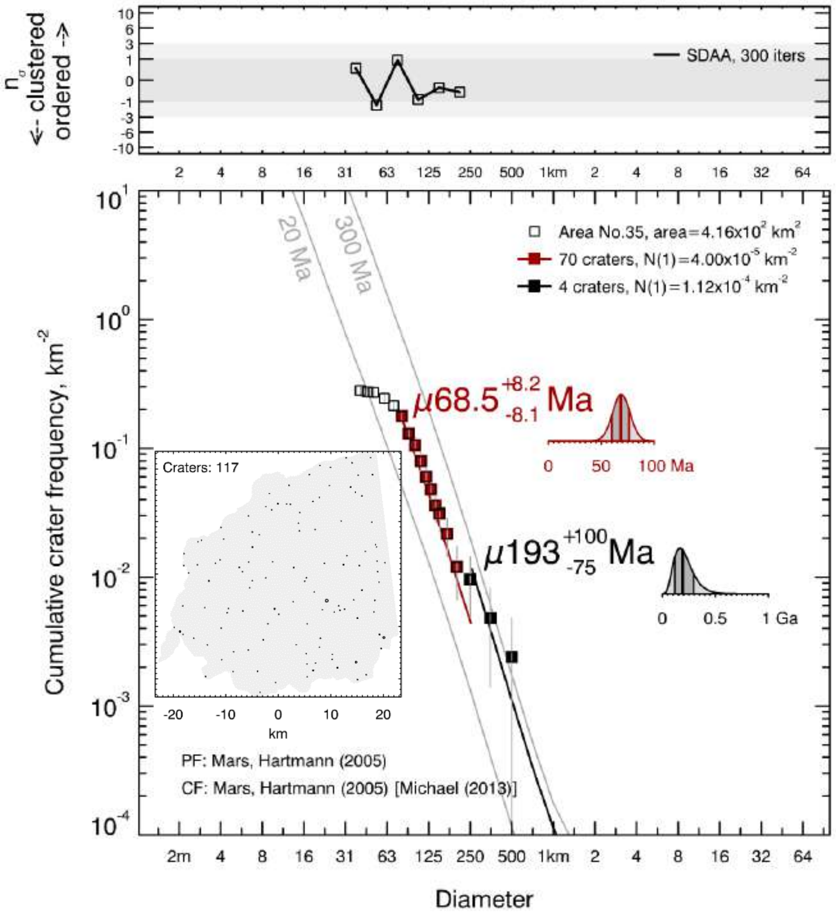

Fig. S57 CSFD and absolute model age for the surface of the Volcanic Edifice no. 35 emplaced within the Pavonis Mons subprovince (for more details see Table 2). We considered impact craters of smaller (80-260 m; red) and larger (>260 m; black) diameter.

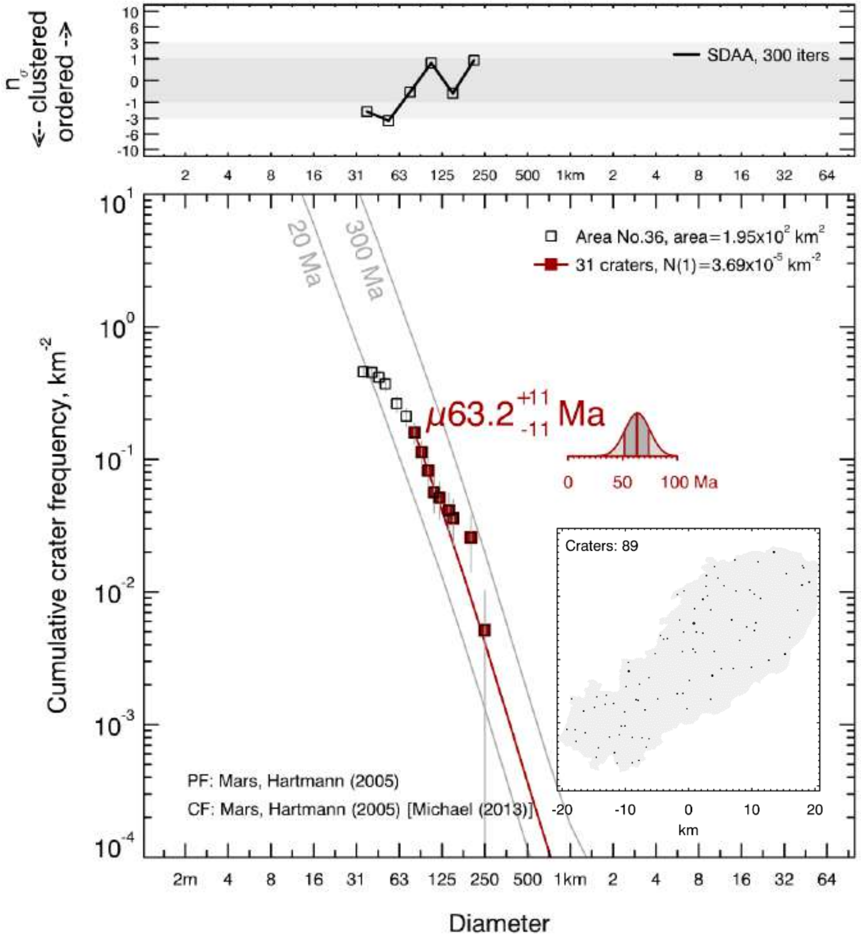

Fig. S58 CSFD and absolute model age for the surface of the Volcanic Edifice no. 36 emplaced within the Pavonis Mons subprovince (for more details see Table 2).

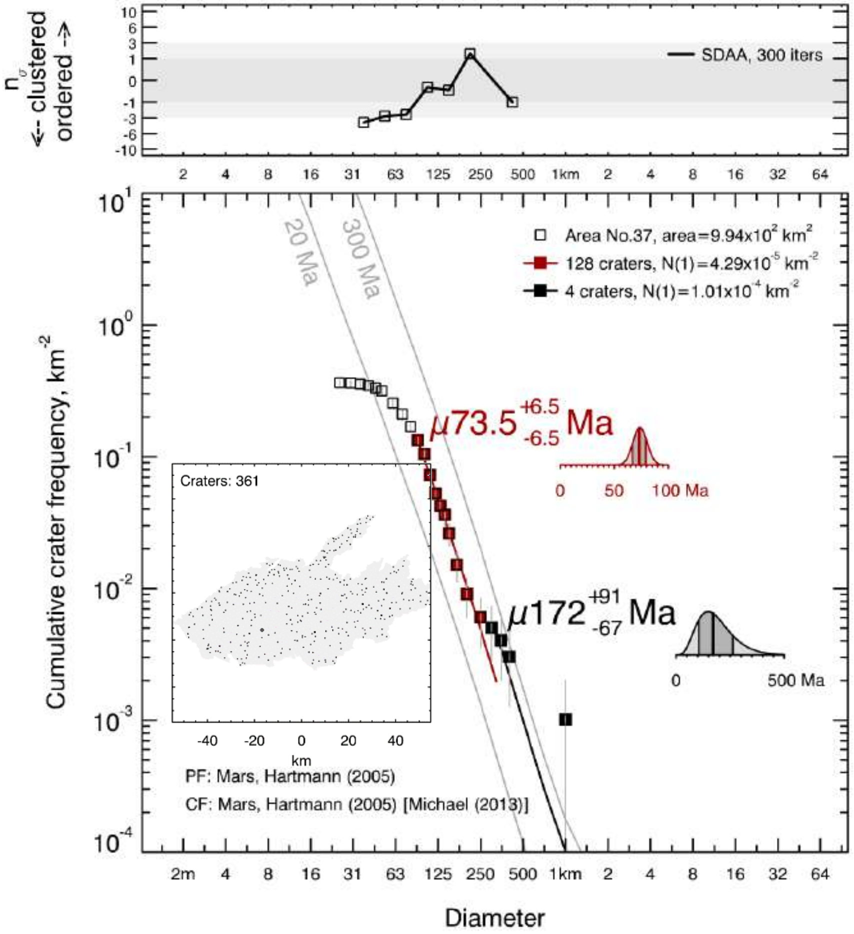

Fig. S59 CSFD and absolute model age for the surface of the Volcanic Edifice no. 37 emplaced within the Pavonis Mons subprovince (for more details see Table 2). We considered impact craters of smaller (90-320 m; red) and larger (>320 m; black) diameter.

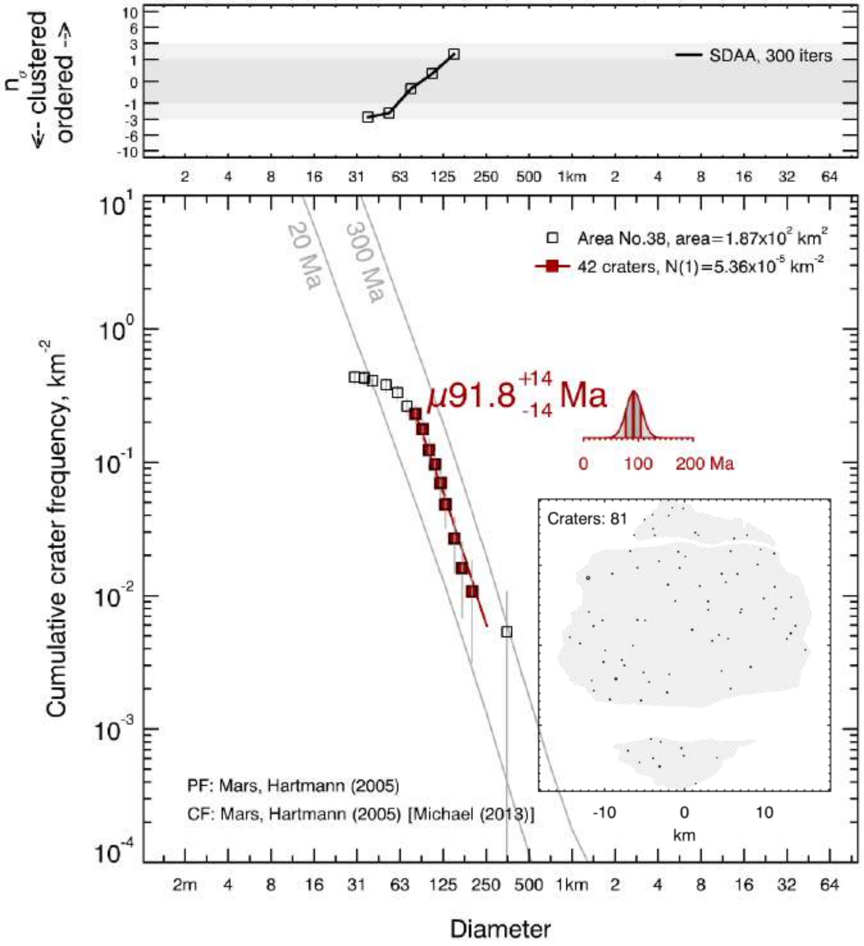

Fig. S60 CSFD and absolute model age for the surface of the Volcanic Edifice no. 38 emplaced within the Pavonis Mons subprovince (for more details see Table 2).

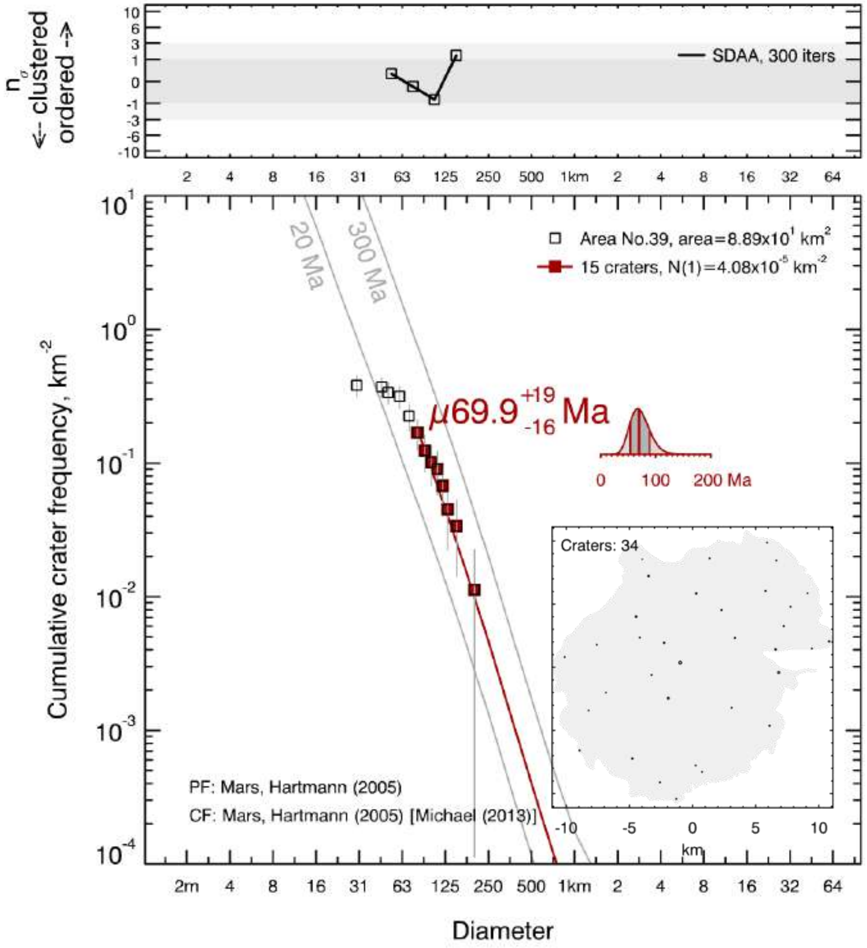

Fig. S61 CSFD and absolute model age for the surface of the Volcanic Edifice no. 39 emplaced within the Pavonis Mons subprovince (for more details see Table 2).

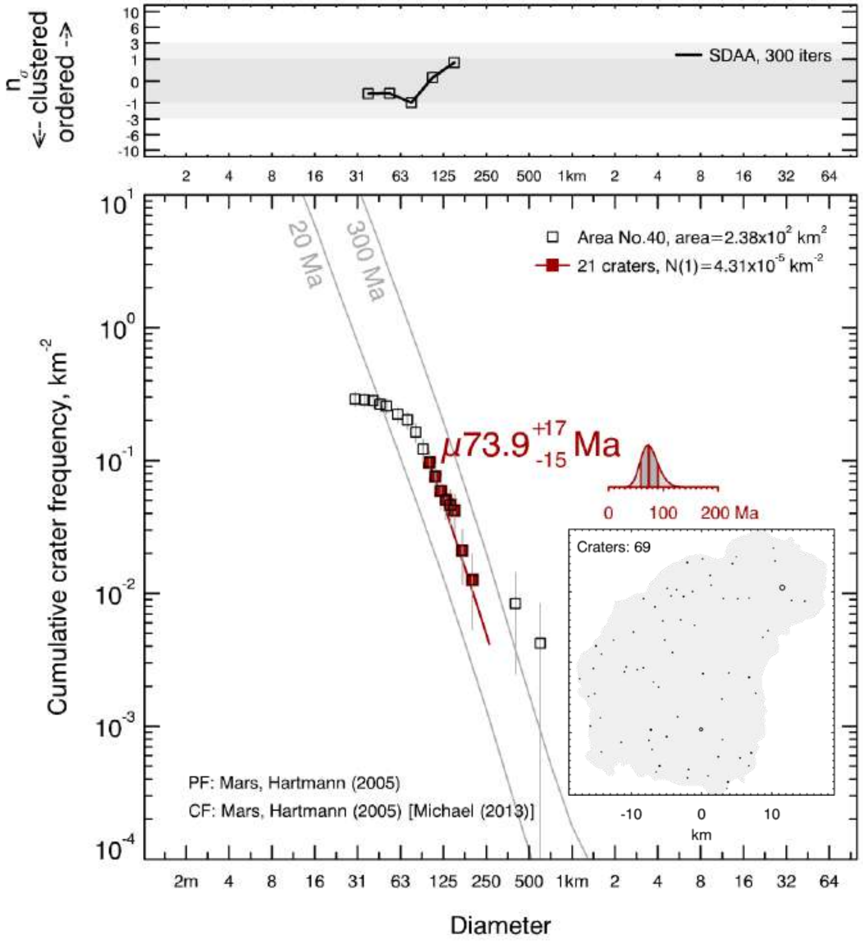

Fig. S62 CSFD and absolute model age for the surface of the Volcanic Edifice no. 40 emplaced within the Pavonis Mons subprovince (for more details see Table 2).

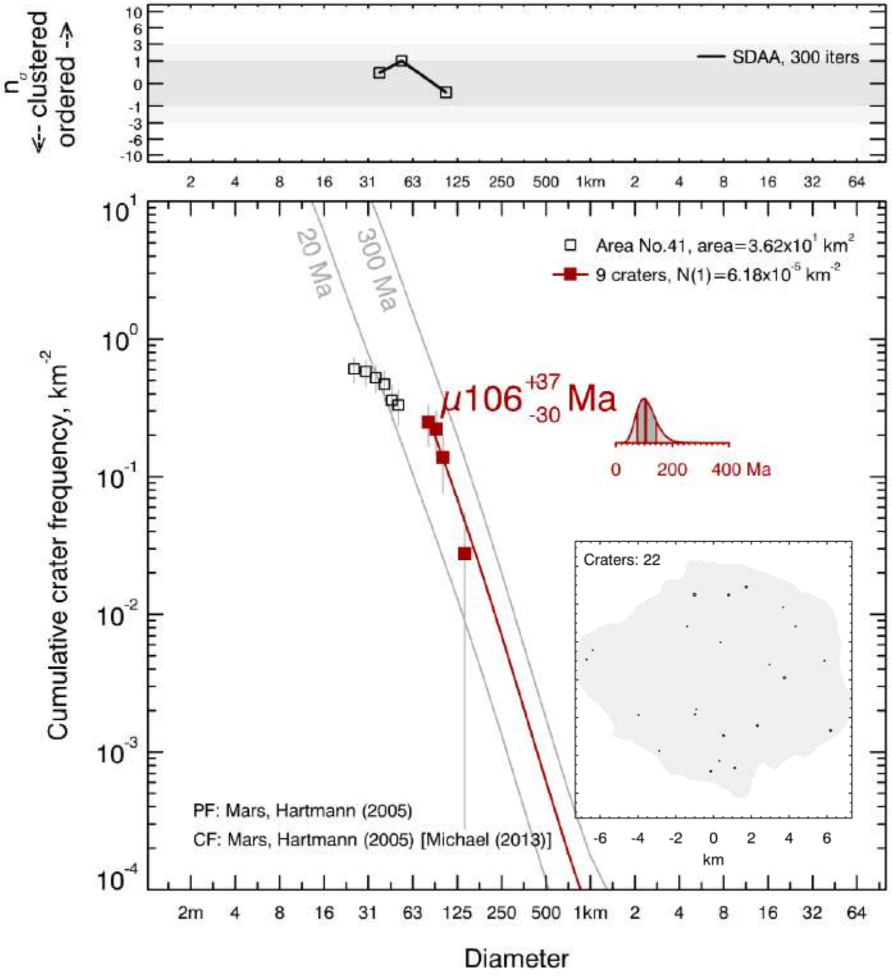

Fig. S63 CSFD and absolute model age for the surface of the Volcanic Edifice no. 41 emplaced within the Pavonis Mons subprovince (for more details see Table 2).

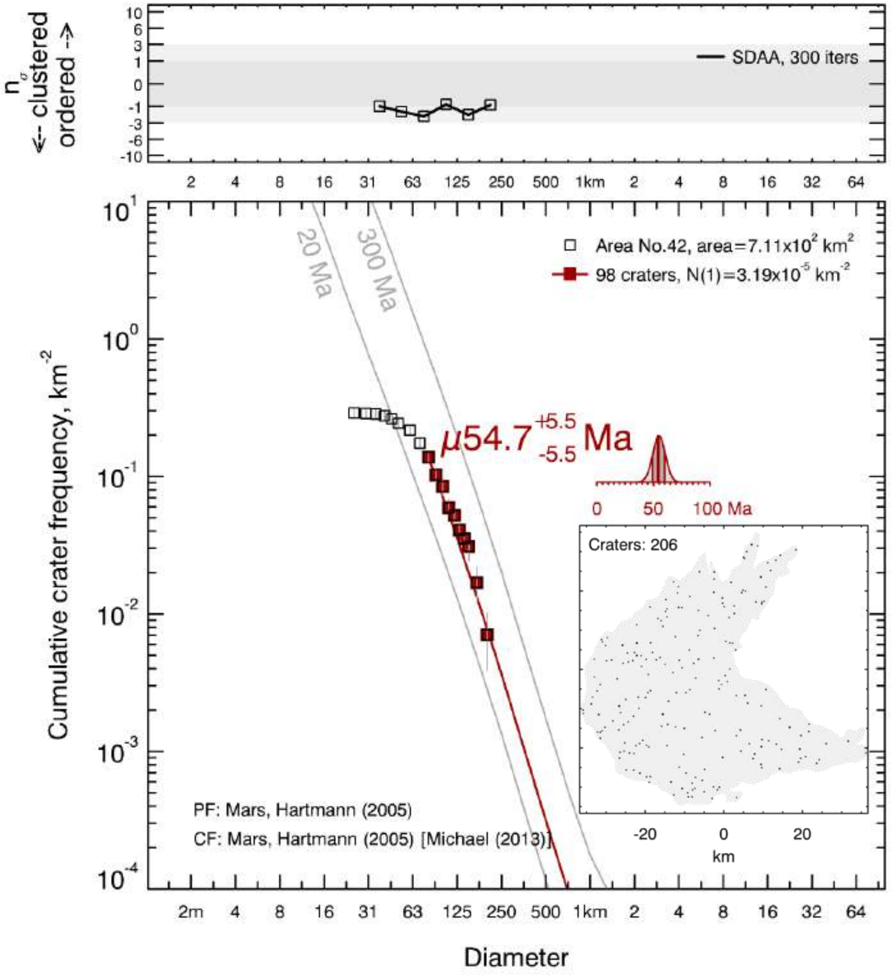

Fig. S64 CSFD and absolute model age for the surface of the Volcanic Edifice no. 42 emplaced within the Pavonis Mons subprovince (for more details see Table 2).

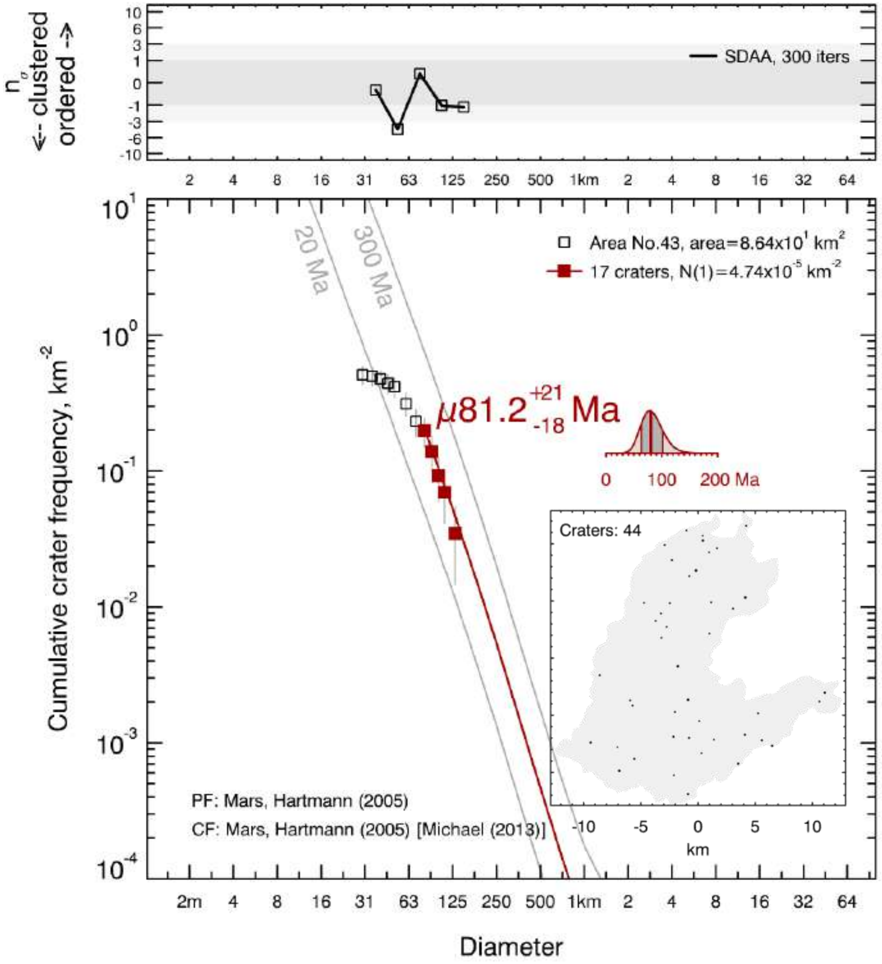

Fig. S65 CSFD and absolute model age for the surface of the Volcanic Edifice no. 43 emplaced within the Pavonis Mons subprovince (for more details see Table 2).

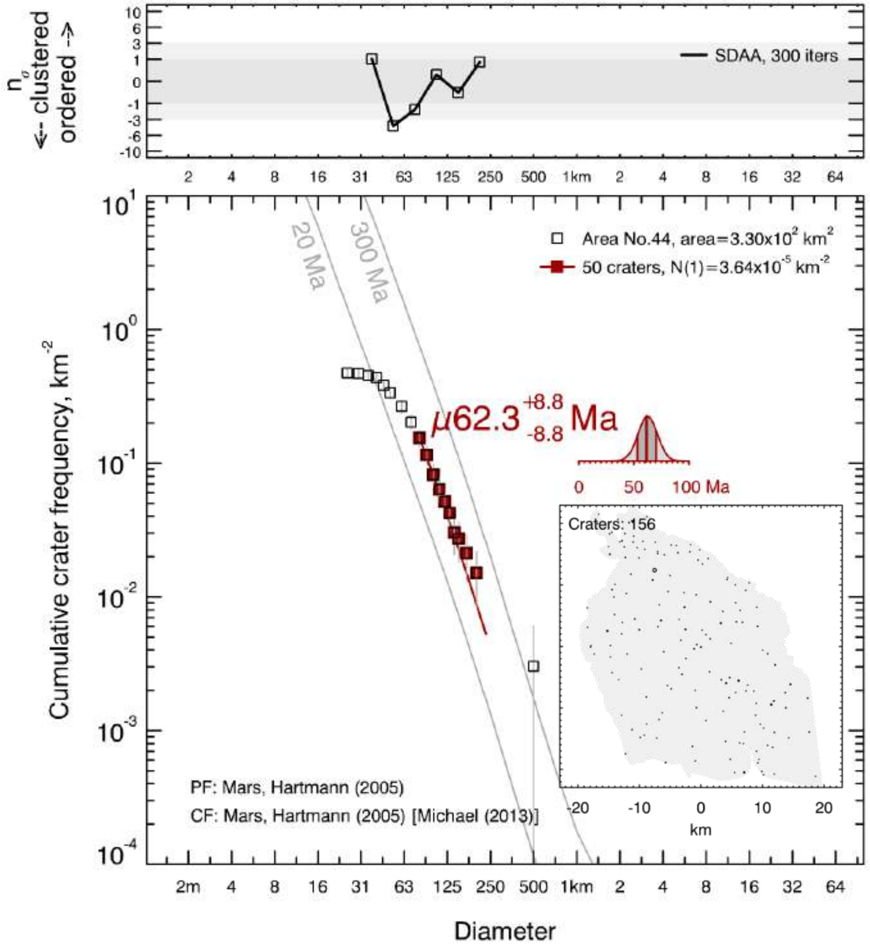

Fig. S66 CSFD and absolute model age for the surface of the Volcanic Edifice no. 44 emplaced within the Pavonis Mons subprovince (for more details see Table 2).

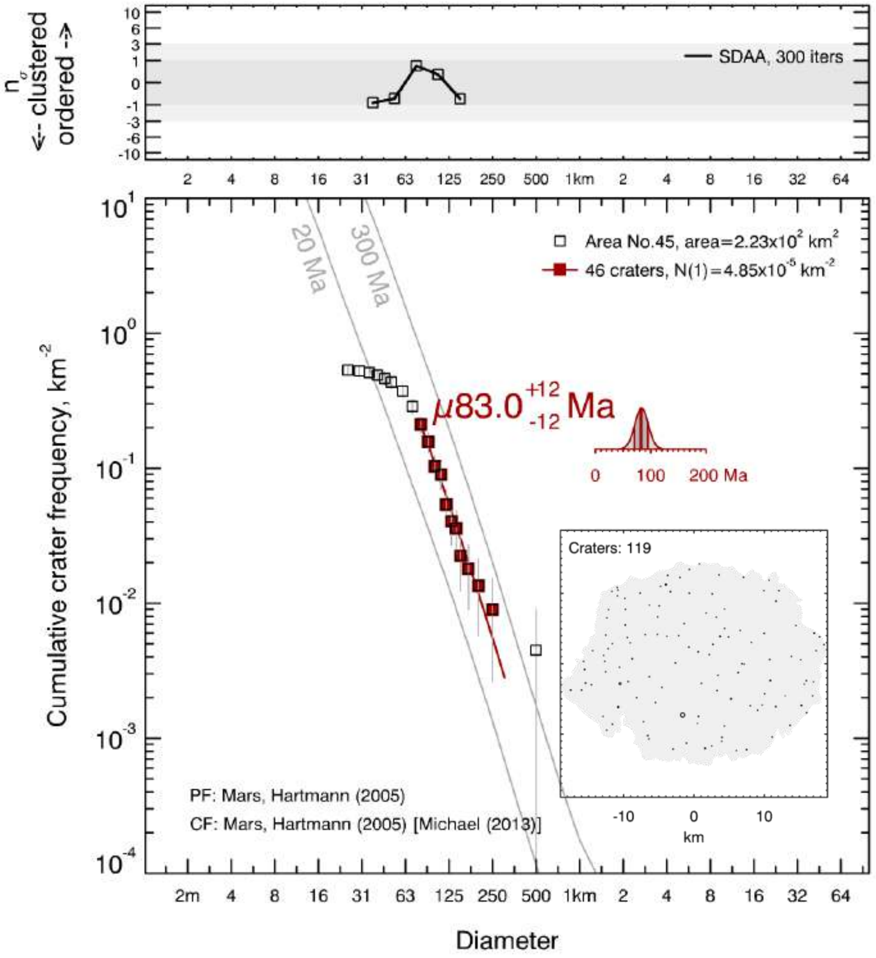

Fig. S67 CSFD and absolute model age for the surface of the Volcanic Edifice no. 45 emplaced within the Pavonis Mons subprovince (for more details see Table 2).

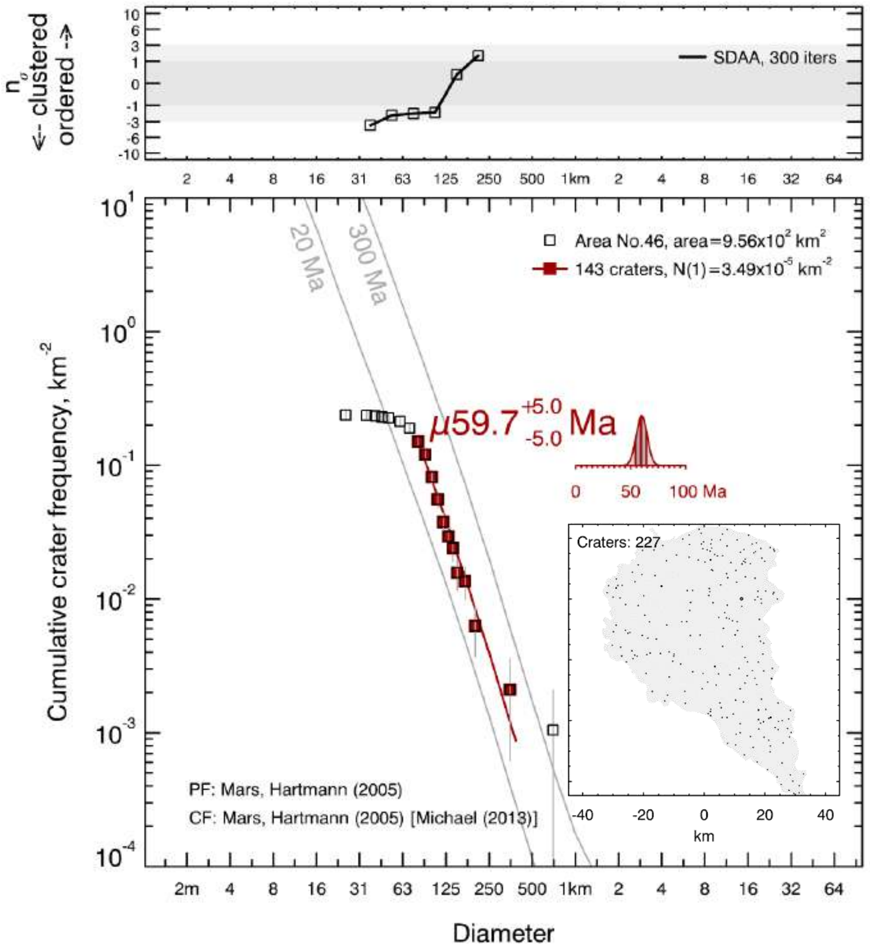

Fig. S68 CSFD and absolute model age for the surface of the Volcanic Edifice no. 46 emplaced within the Pavonis Mons subprovince (for more details see Table 2).

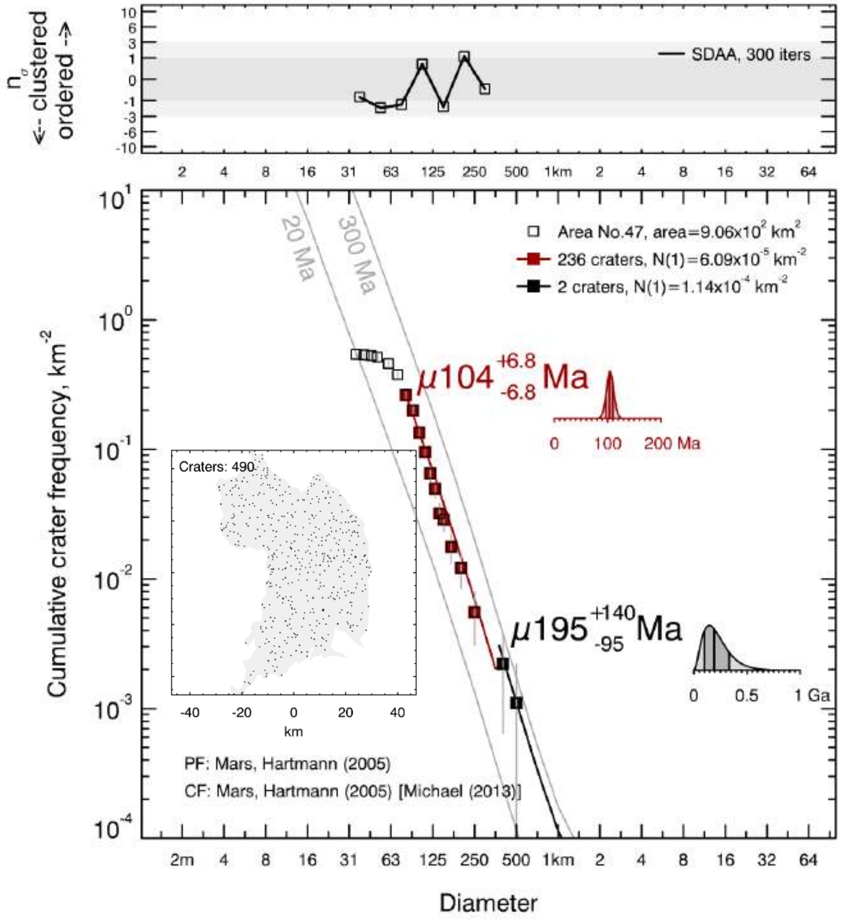

Fig. S69 CSFD and absolute model age for the surface of the Volcanic Edifice no. 47 emplaced within the Pavonis Mons subprovince (for more details see Table 2). We considered impact craters of smaller (80-380 m; red) and larger (>380 m; black) diameter.

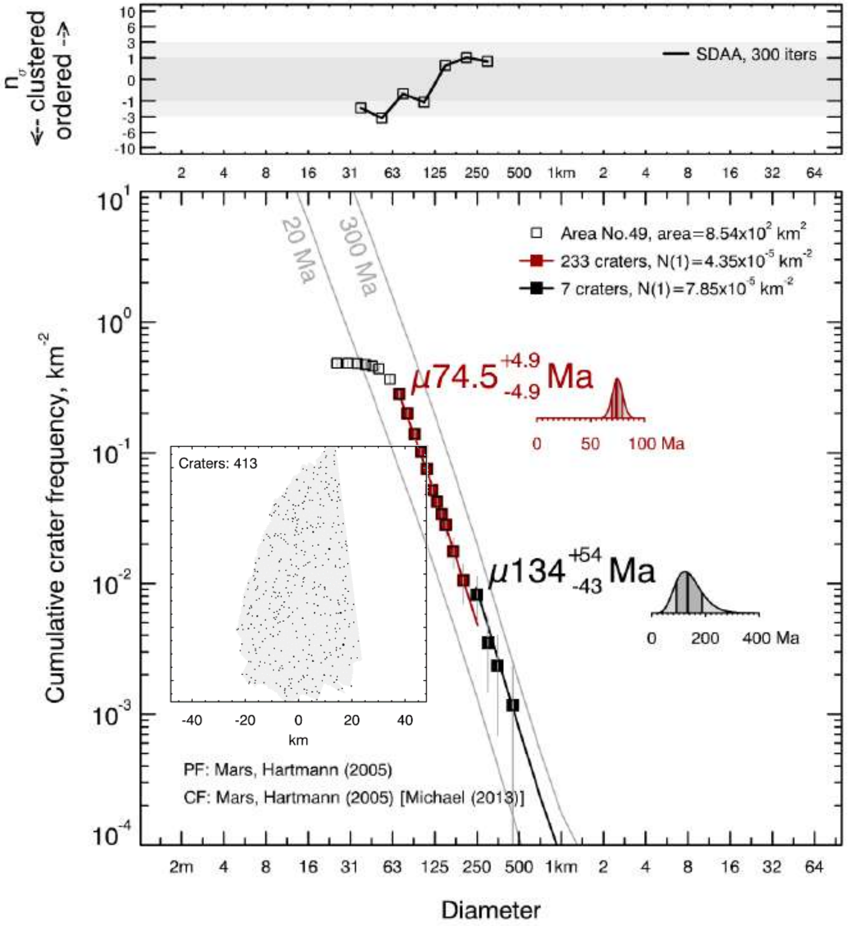

Fig. S70 CSFD and absolute model age for the surface of the Volcanic Edifice no. 49 emplaced within the Pavonis Mons subprovince (for more details see Table 2). We considered impact craters of smaller (70-260 m; red) and larger (>260 m; black) diameter.

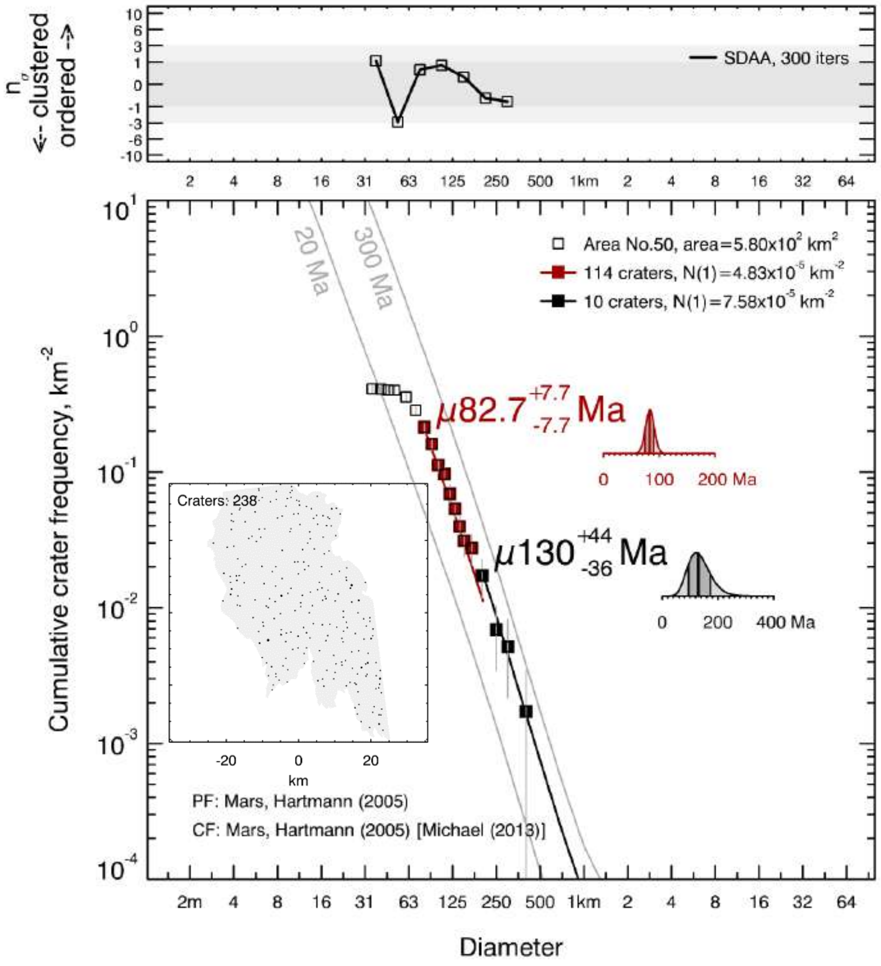

Fig. S71 CSFD and absolute model age for the surface of the Volcanic Edifice no. 50 emplaced within the Pavonis Mons subprovince (for more details see Table 2). We considered impact craters of smaller (80-200 m; red) and larger (>200 m; black) diameter.

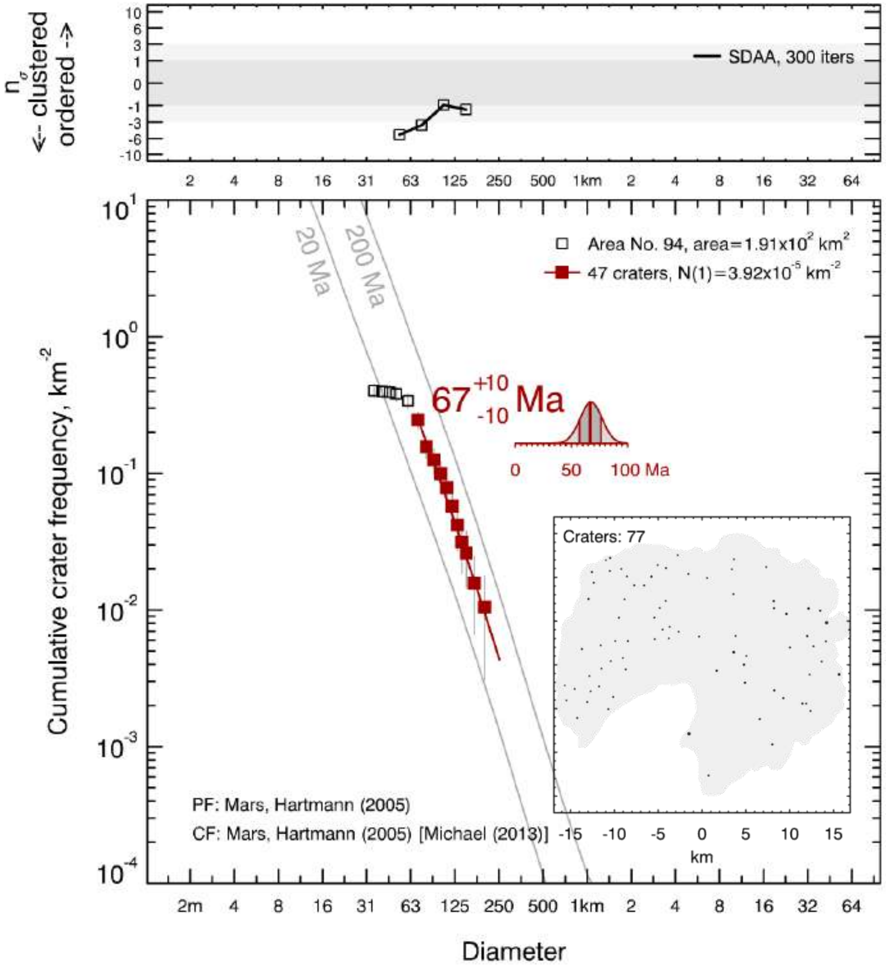

Fig. S72 CSFD and absolute model age for the surface of the Volcanic Edifice no. 94 emplaced within the Pavonis Mons subprovince (for more details see Table 2).

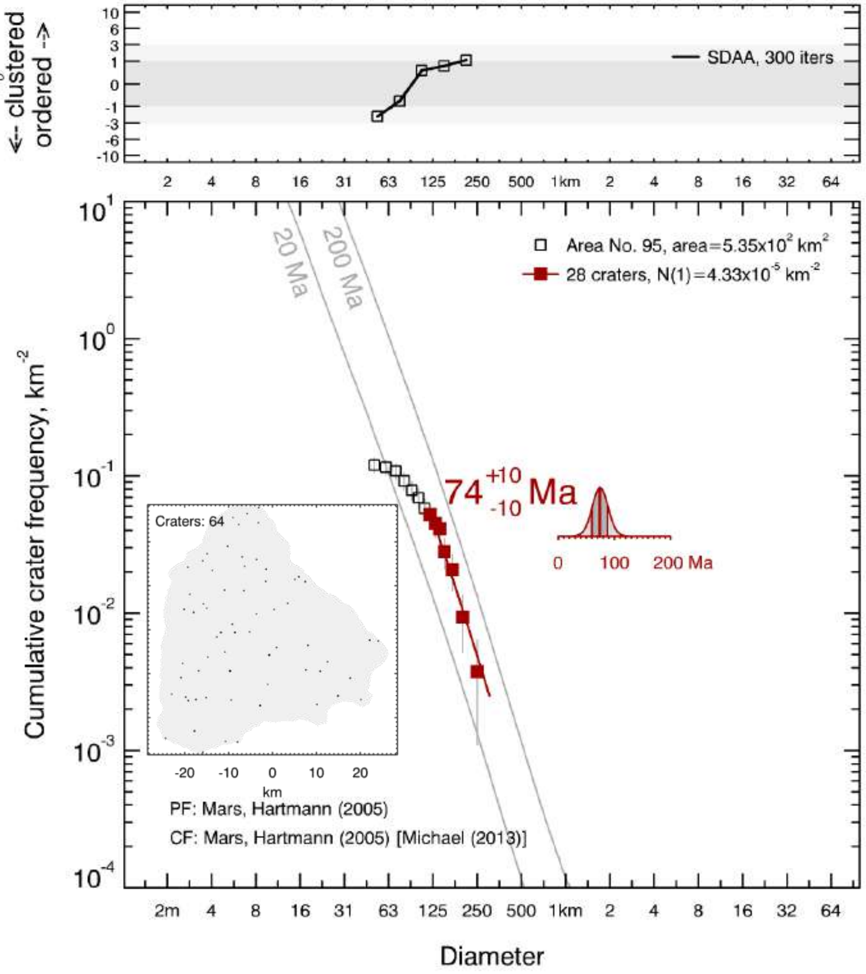

Fig. S73 CSFD and absolute model age for the surface of the Volcanic Edifice no. 95 emplaced within the Pavonis Mons subprovince (for more details see Table 2).

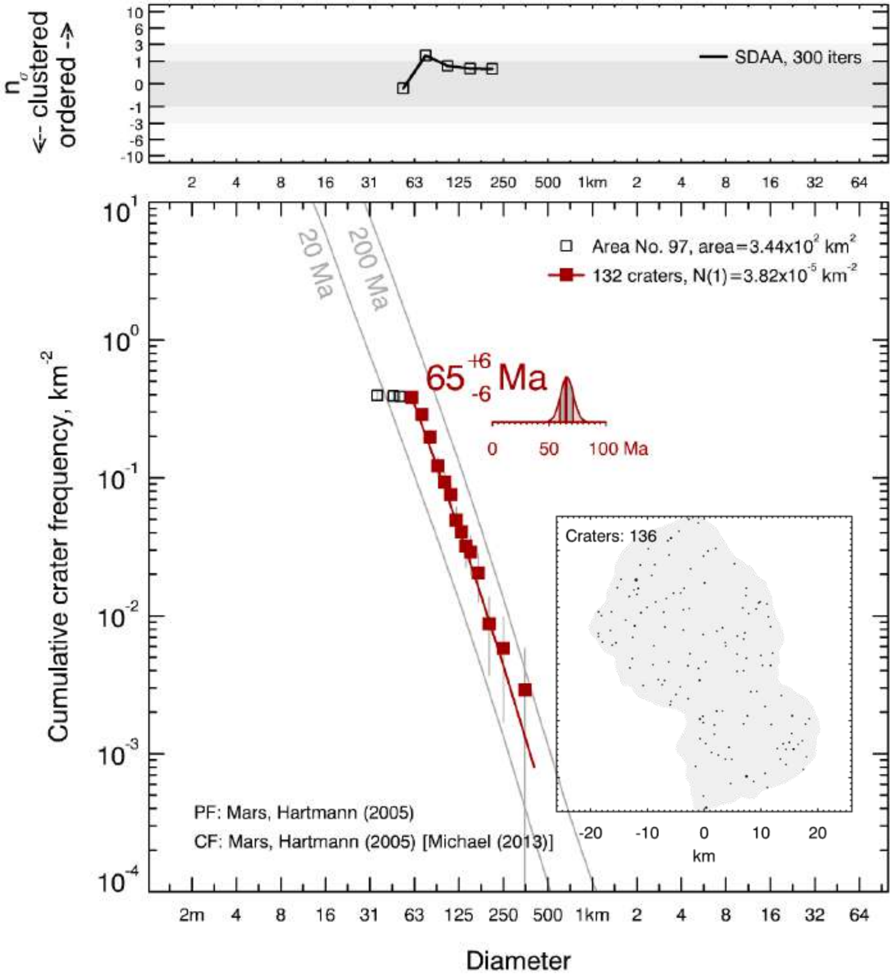

Fig. S74 CSFD and absolute model age for the surface of the Volcanic Edifice no. 97 emplaced within the Pavonis Mons subprovince (for more details see Table 2).

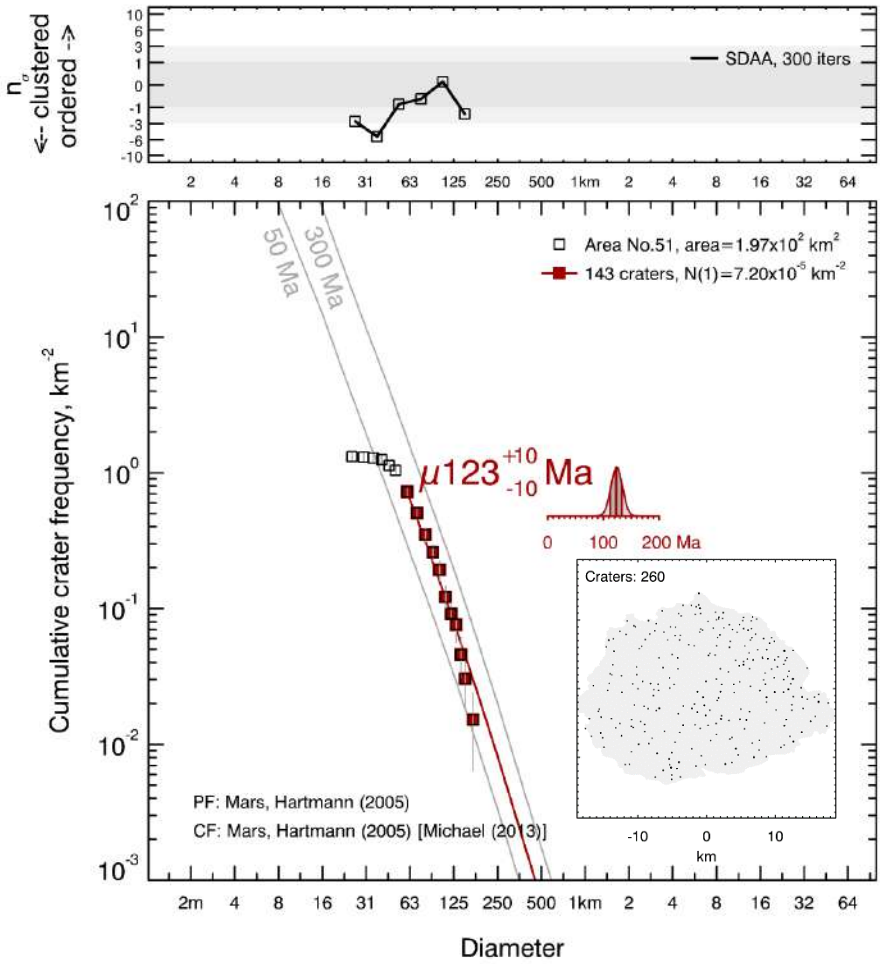

Fig. S75 CSFD and absolute model age for the surface of the Volcanic Edifice no. 51 emplaced within the eastern Ascraeus Mons subprovince (for more details see Table 2).

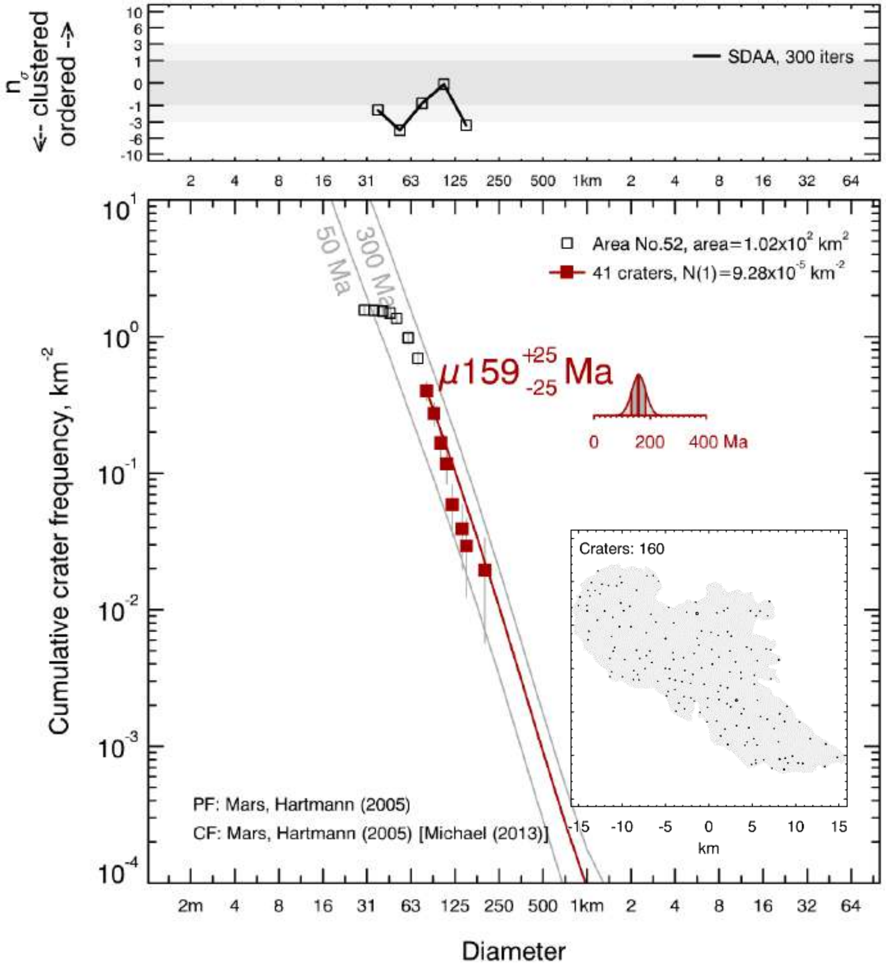

Fig. S76 CSFD and absolute model age for the surface of the Volcanic Edifice no. 52 emplaced within the eastern Ascraeus Mons subprovince (for more details see Table 2).

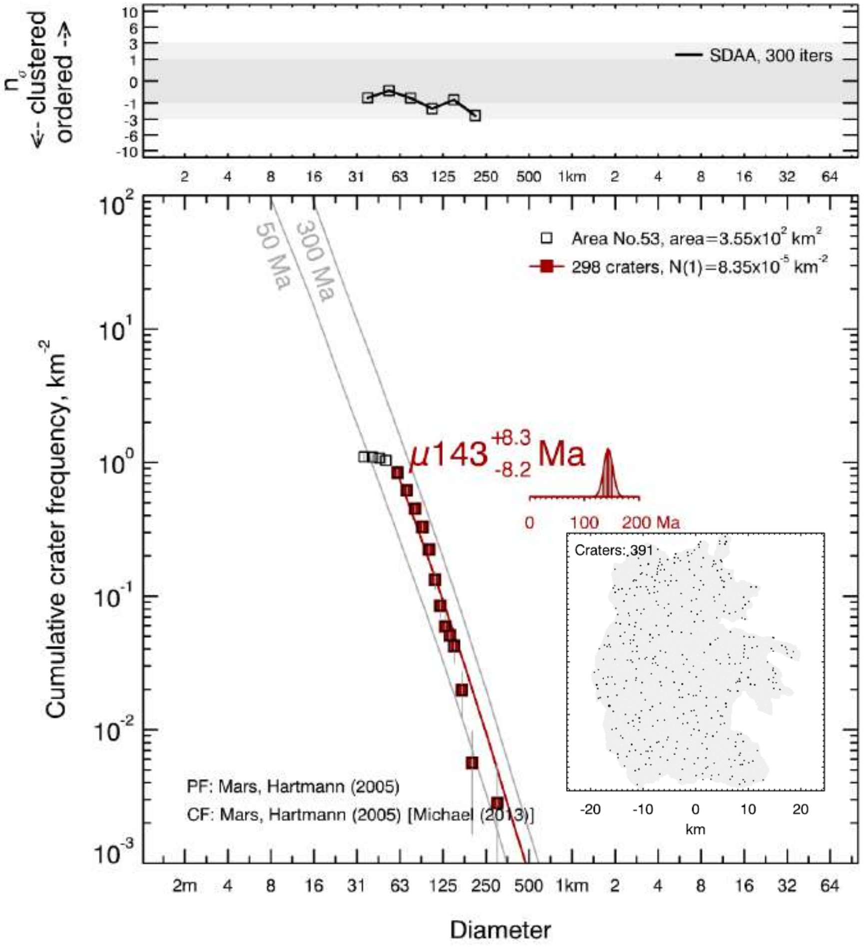

Fig. S77 CSFD and absolute model age for the surface of the Volcanic Edifice no. 53 emplaced within the eastern Ascraeus Mons subprovince (for more details see Table 2).

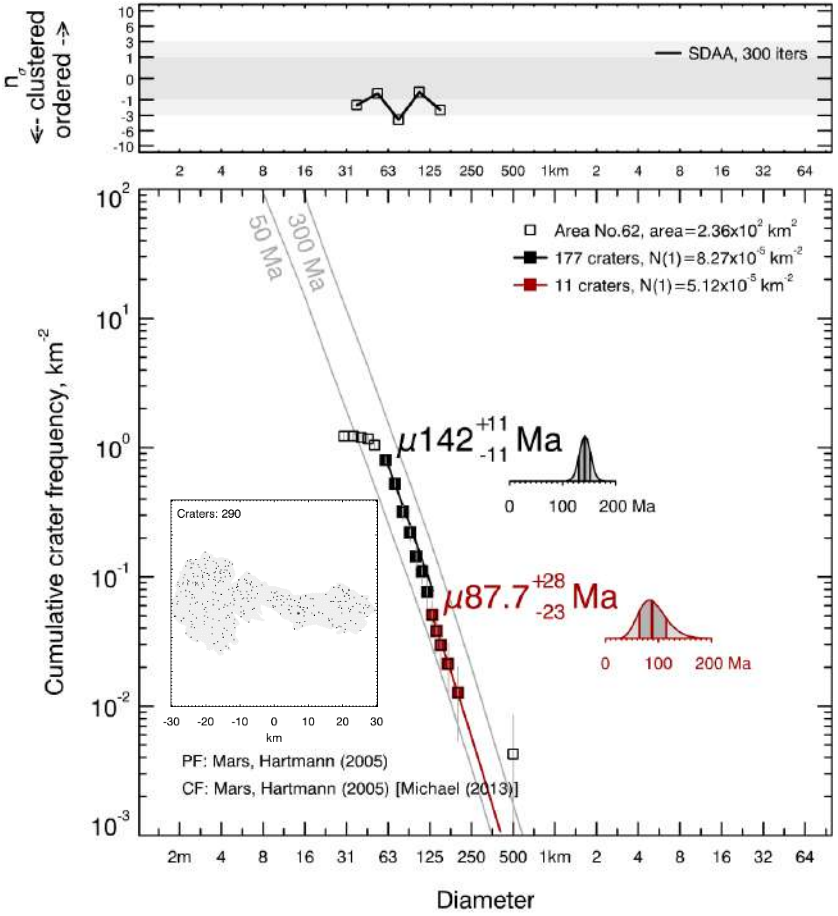

Fig. S78 CSFD and absolute model age for the surface of the Volcanic Edifice no. 62 emplaced within the eastern Ascraeus Mons subprovince (for more details see Table 2). We considered impact craters of smaller (60-130 m; black) and larger (>130 m; red) diameter.

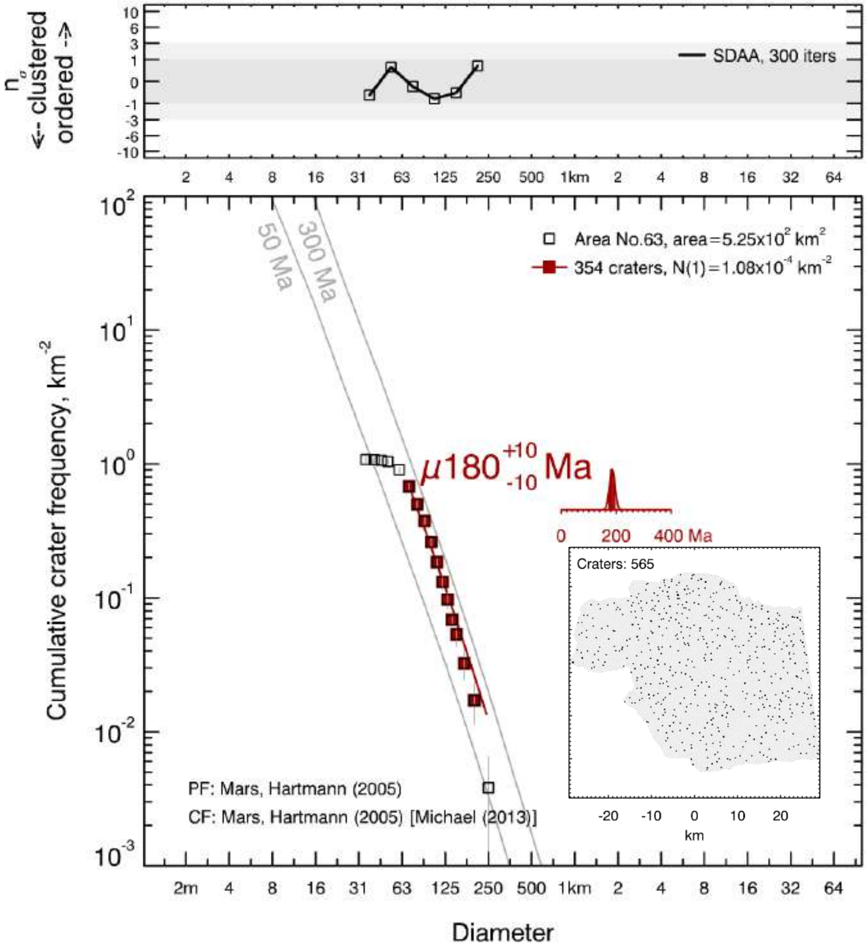

Fig. S79 CSFD and absolute model age for the surface of the Volcanic Edifice no. 63 emplaced within the eastern Ascraeus Mons subprovince (for more details see Table 2).

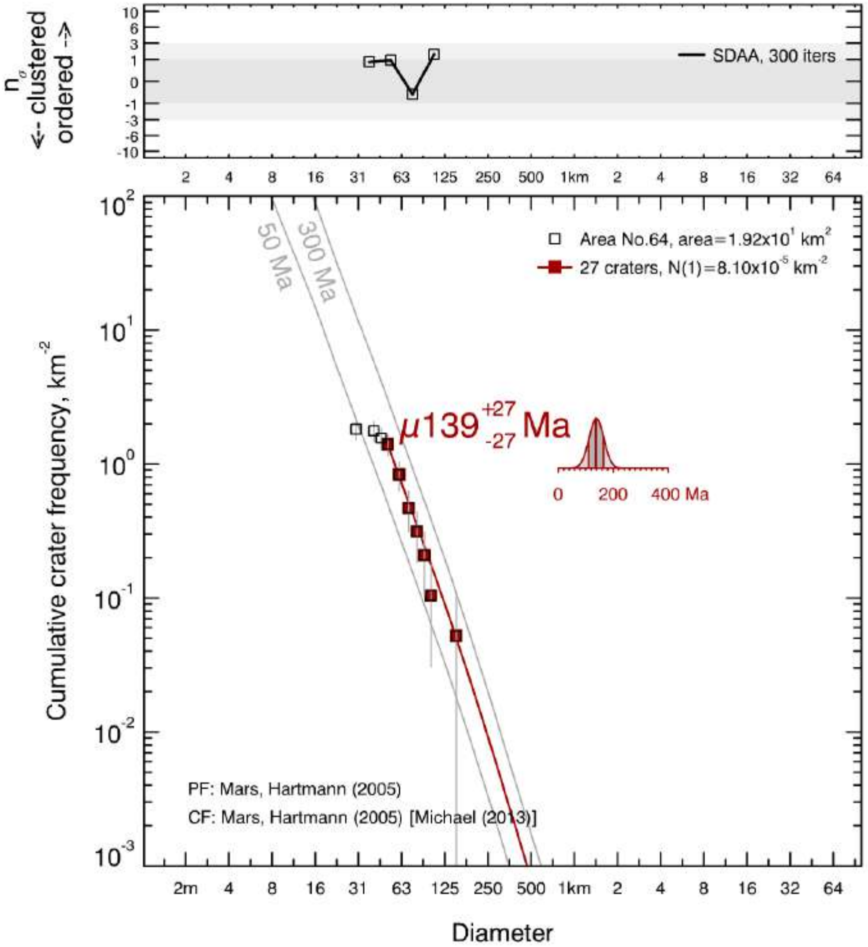

Fig. S80 CSFD and absolute model age for the surface of the Volcanic Edifice no. 64 emplaced within the eastern Ascraeus Mons subprovince (for more details see Table 2).

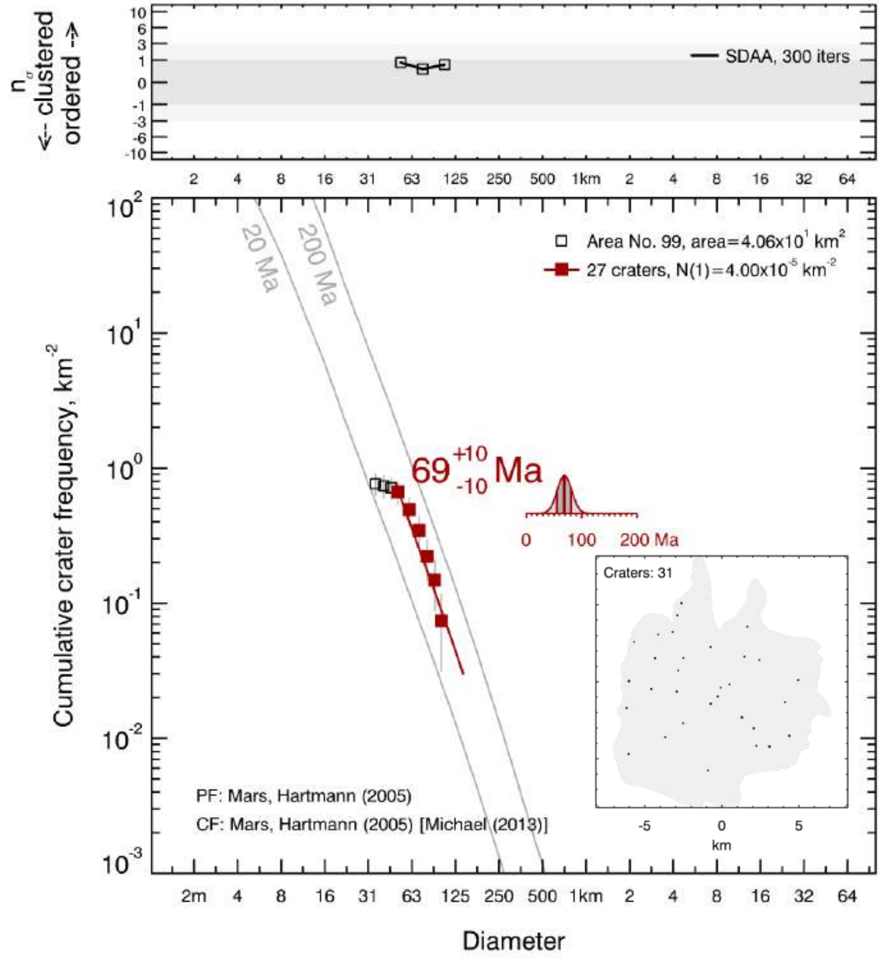

Fig. S81 CSFD and absolute model age for the surface of the Volcanic Edifice no. 99 emplaced within the eastern Ascraeus Mons subprovince (for more details see Table 2).

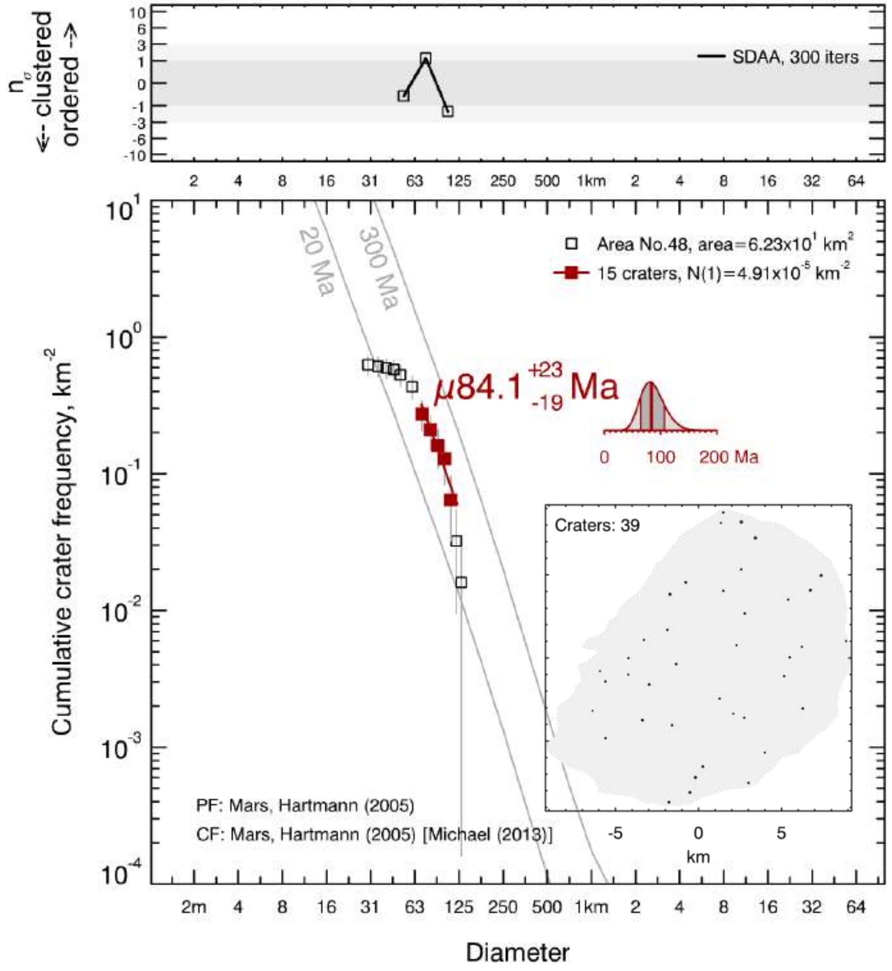

Fig. S82 CSFD and absolute model age for the surface of the Volcanic Edifice no. 48 emplaced within the southern Ascraeus Mons subprovince (for more details see

Table 2).

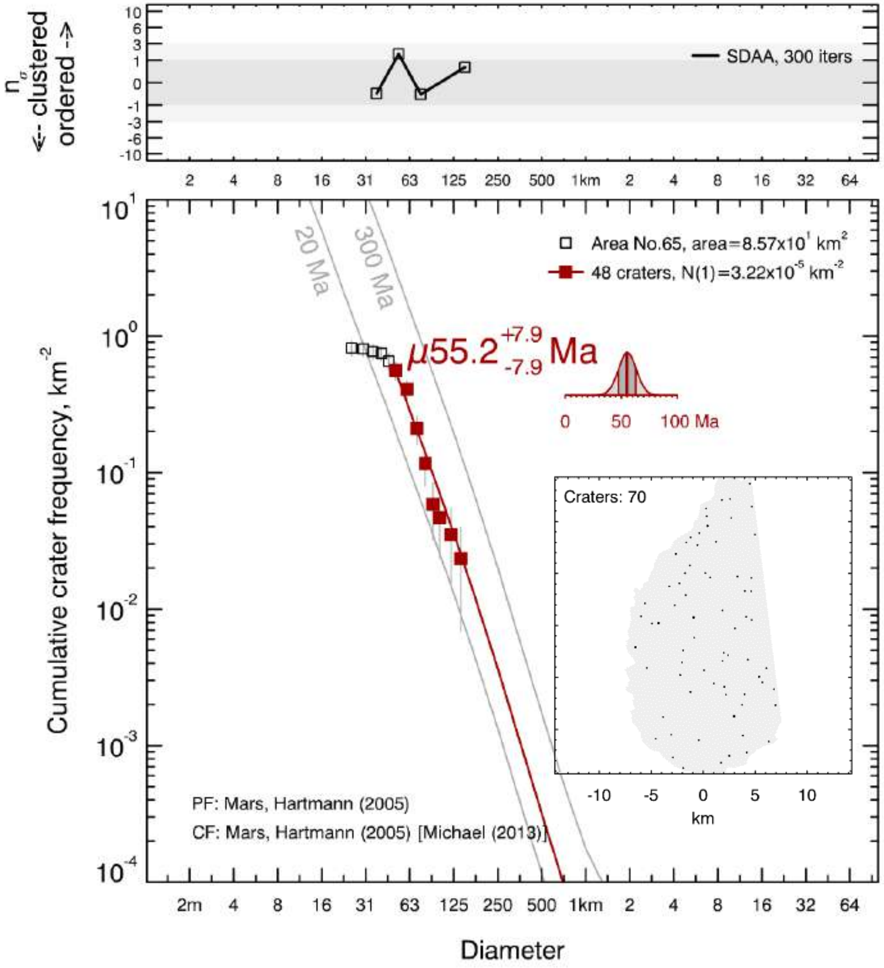

Fig. S83 CSFD and absolute model age for the surface of the Volcanic Edifice no. 65 emplaced within the southern Ascraeus Mons subprovince (for more details see Table 2).

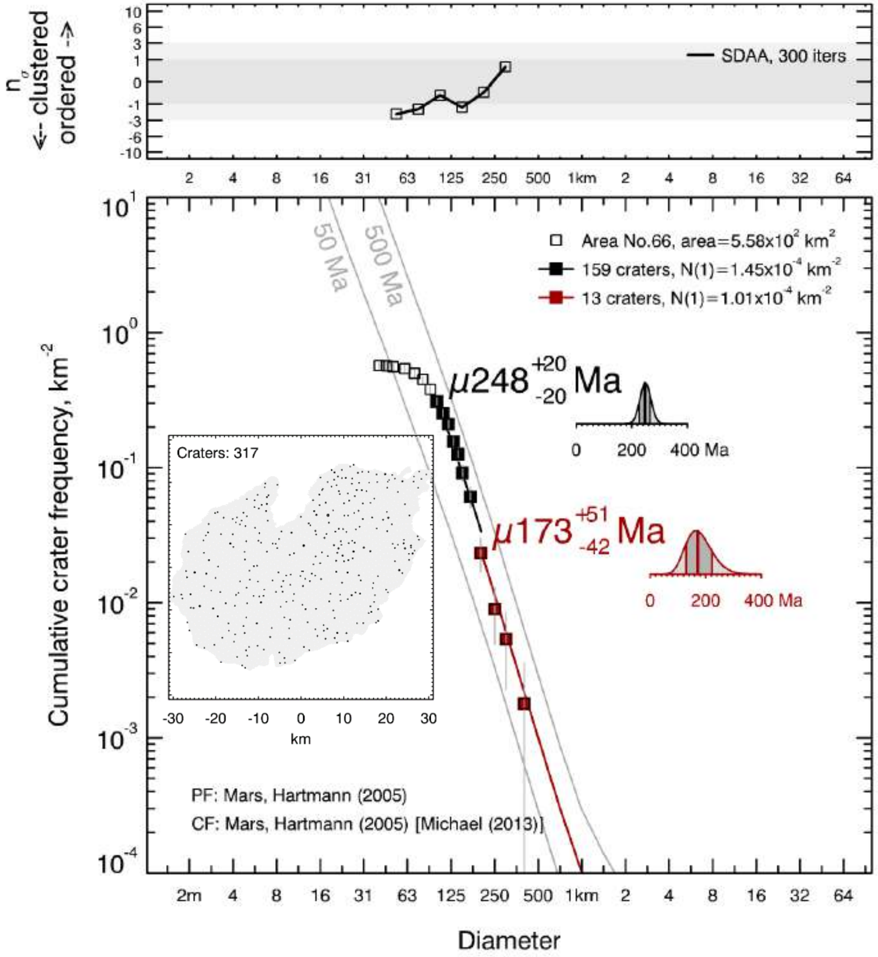

Fig. S84 CSFD and absolute model age for the surface of the Volcanic Edifice no. 66 emplaced within the southern Ascraeus Mons subprovince (for more details see Table 2). We considered impact craters of smaller (100-200 m; black) and larger (>200 m; red) diameter.

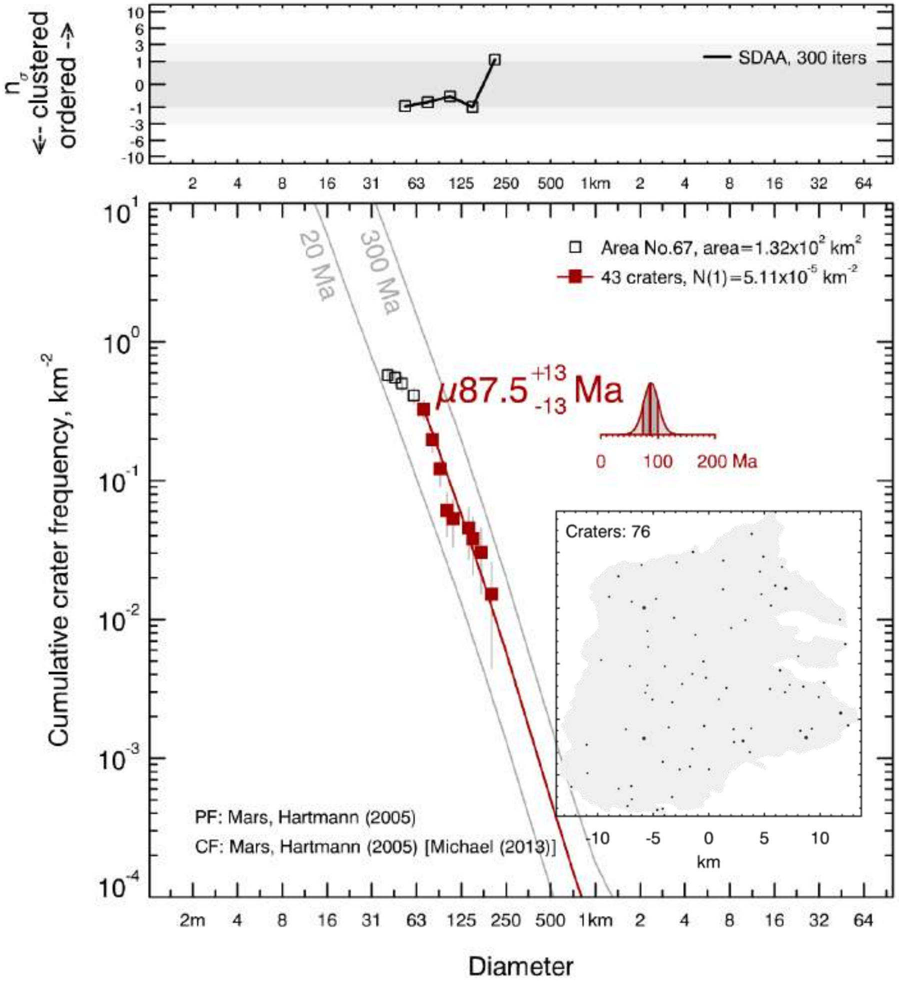

Fig. S85 CSFD and absolute model age for the surface of the Volcanic Edifice no. 67 emplaced within the southern Ascraeus Mons subprovince (for more details see Table 2).

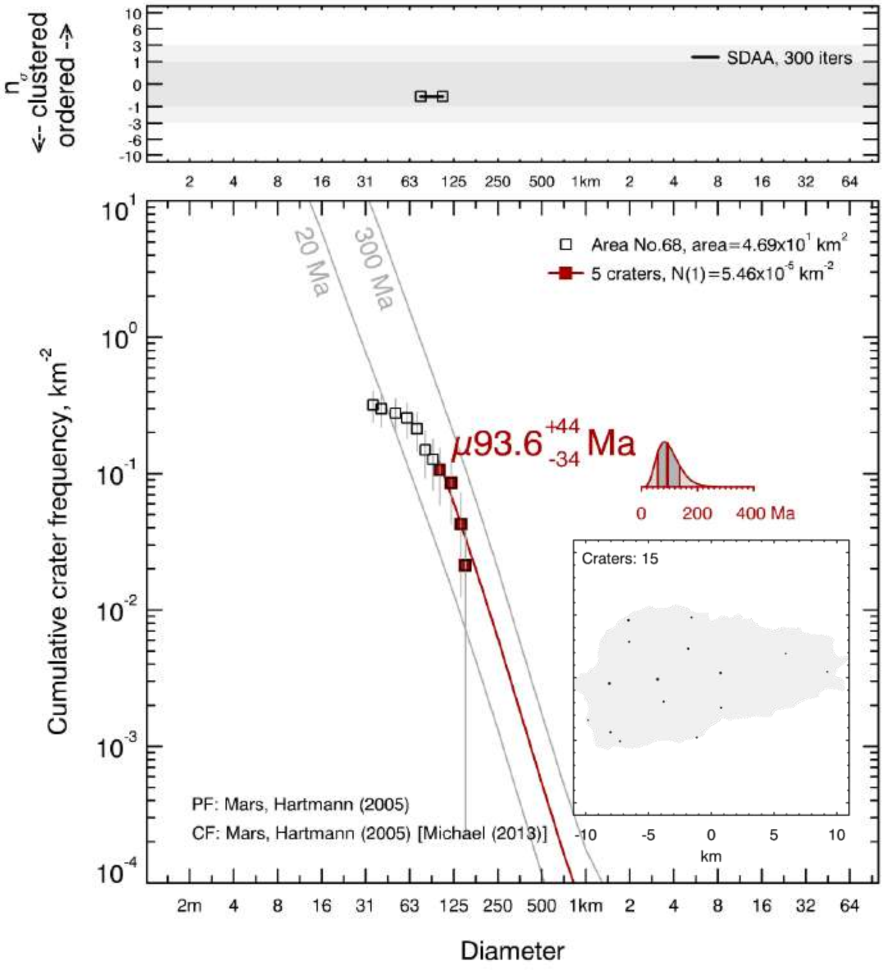

Fig. S86 CSFD and absolute model age for the surface of the Volcanic Edifice no. 68 emplaced within the southern Ascraeus Mons subprovince (for more details see

Table 2).

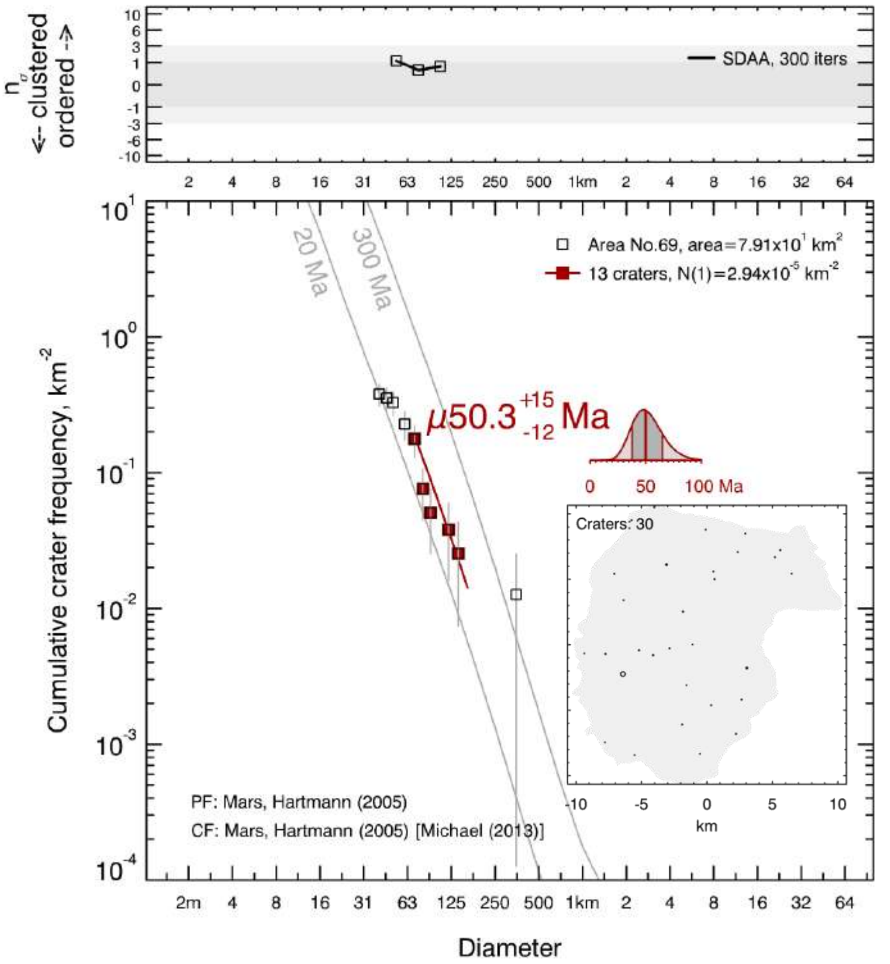

Fig. S87 CSFD and absolute model age for the surface of the Volcanic Edifice no. 69 emplaced within the southern Ascraeus Mons subprovince (for more details see

Table 2).

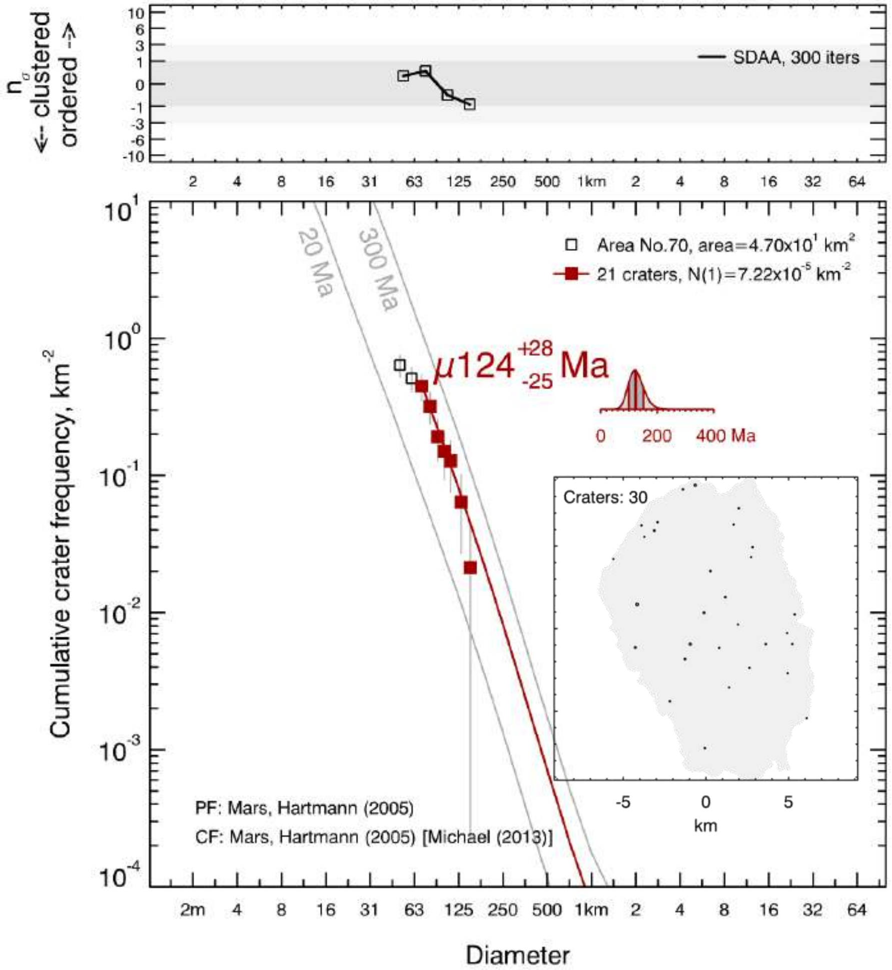

Fig. S88 CSFD and absolute model age for the surface of the Volcanic Edifice no. 70 emplaced within the southern Ascraeus Mons subprovince (for more details see Table 2).

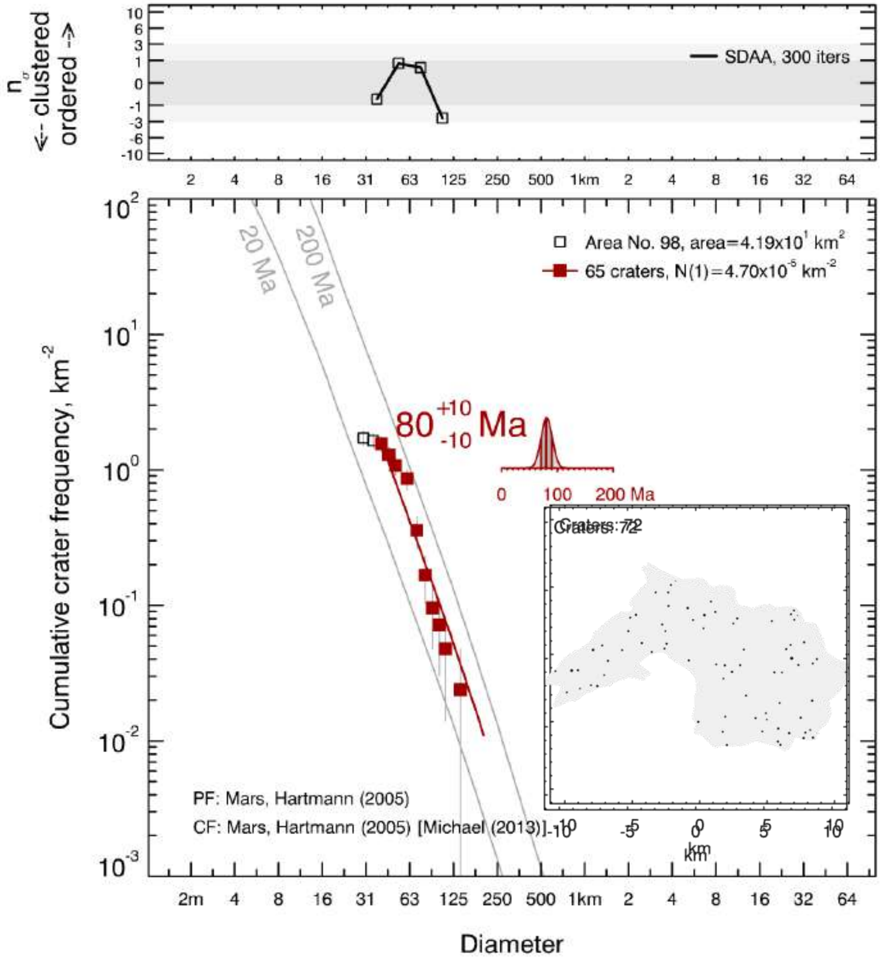

Fig. S89 CSFD and absolute model age for the surface of the Volcanic Edifice no. 98 emplaced within the southern Ascraeus Mons subprovince (for more details see Table 2).

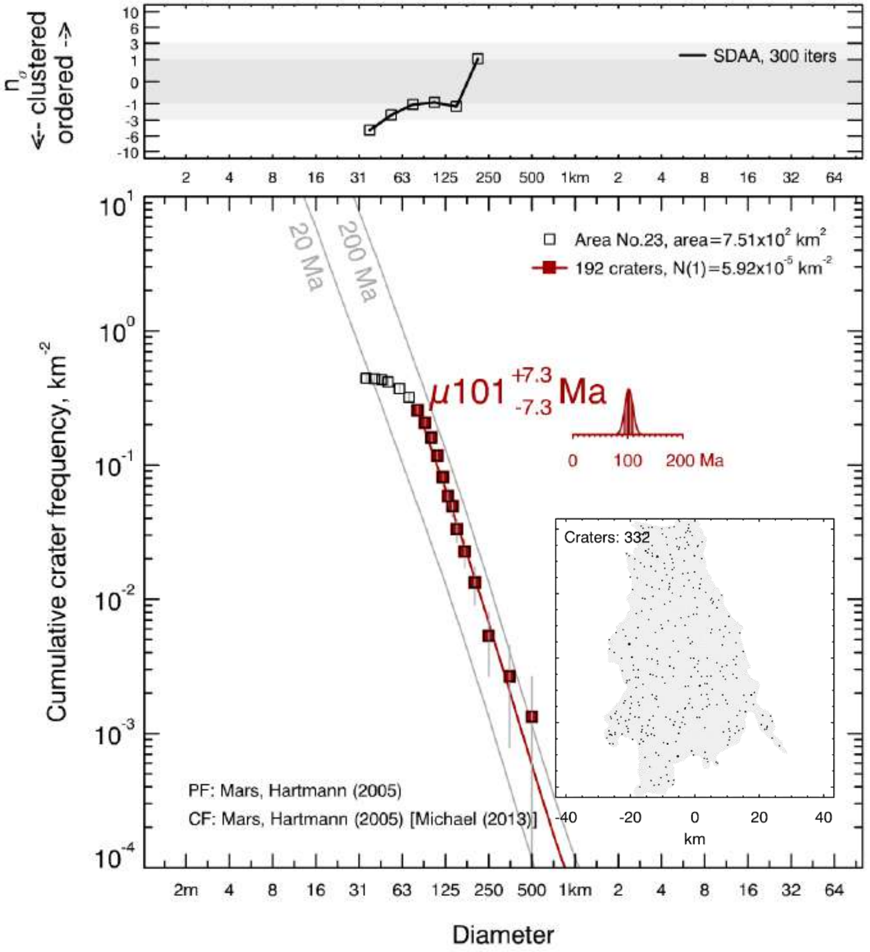

Fig. S90 CSFD and absolute model age for the surface of the Volcanic Edifice no. 23 emplaced within the northwestern Ascraeus Mons subprovince (for more details see Table 2).

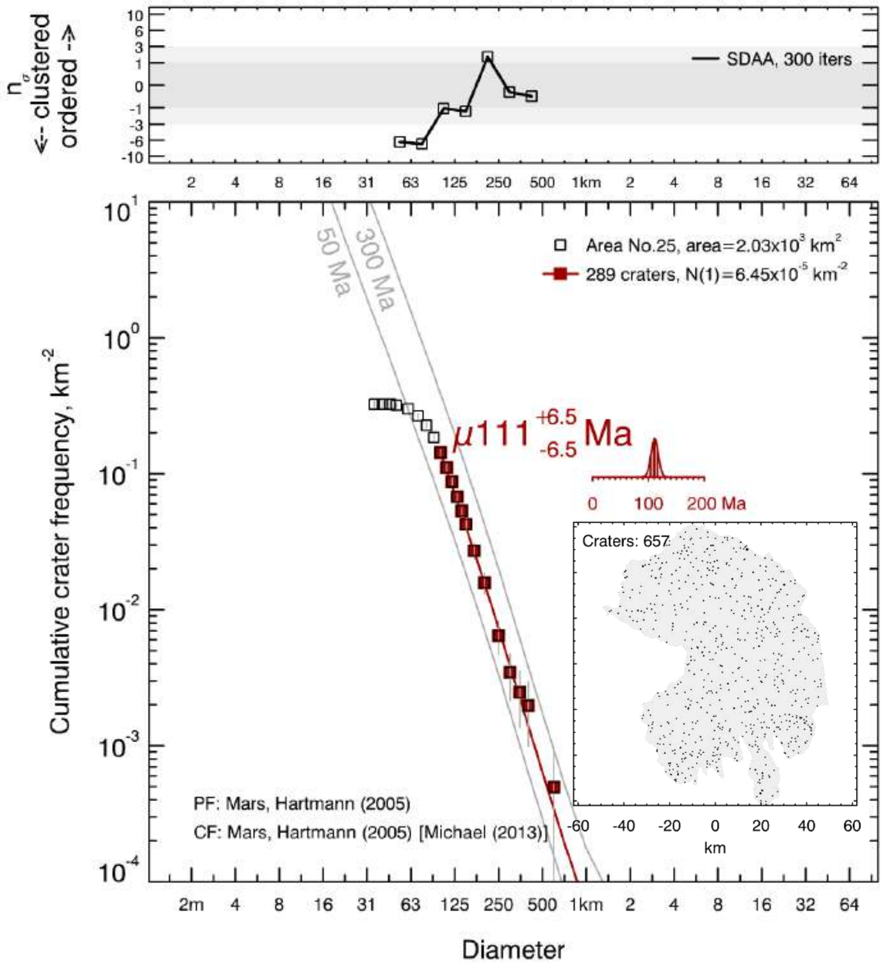

Fig. S91 CSFD and absolute model age for the surface of the Volcanic Edifice no. 25 emplaced within the northwestern Ascraeus Mons subprovince (for more details see Table 2).

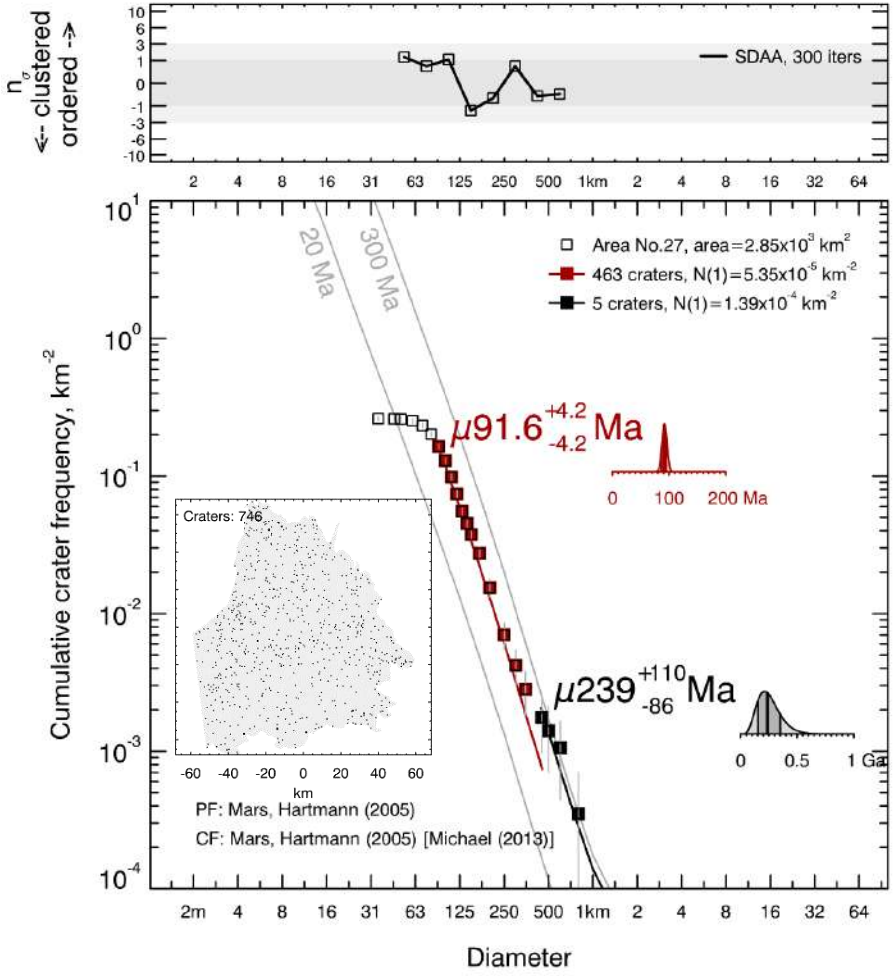

Fig. S92 CSFD and absolute model age for the surface of the Volcanic Edifice no. 27 emplaced within the northwestern Ascraeus Mons subprovince (for more details see Table 2). We considered impact craters of smaller (90-450 m; red) and larger (>450 m; black) diameter.

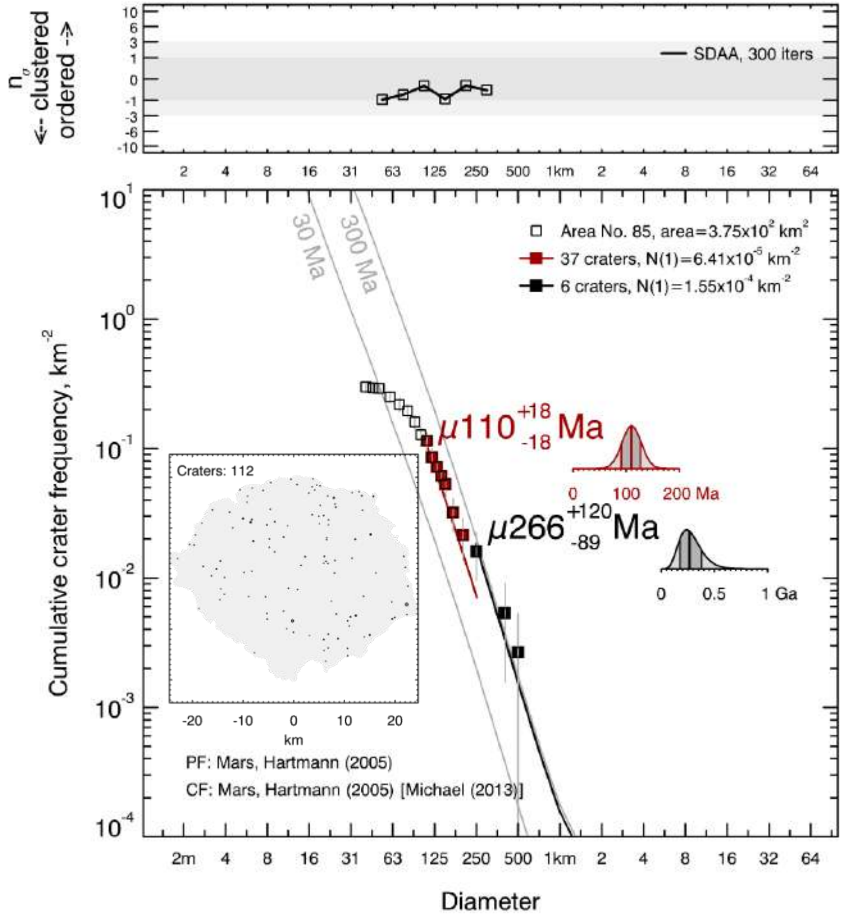

Fig. S93 CSFD and absolute model age for the surface of the Volcanic Edifice no. 85 emplaced within the northwestern Ascraeus Mons subprovince (for more details see Table 2). We considered impact craters of smaller (100-250 m; red) and larger (>250 m; black) diameter.

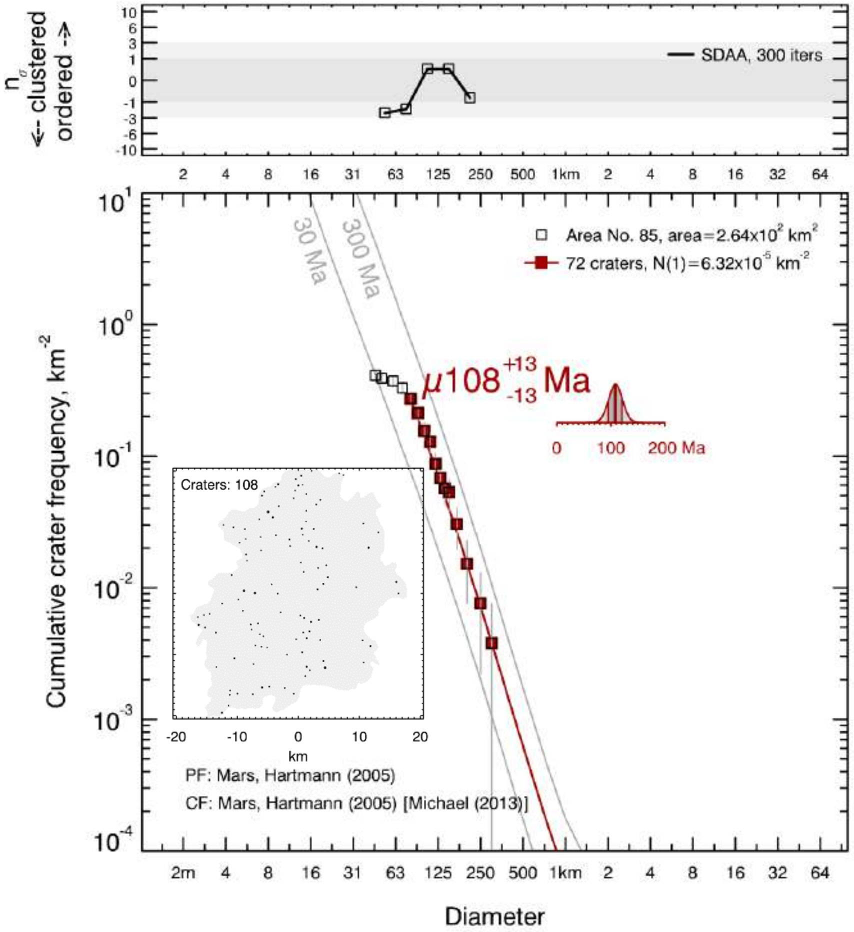

Fig. S94 CSFD and absolute model age for the surface of the Volcanic Edifice no. 86 emplaced within the northwestern Ascraeus Mons subprovince (for more details see Table 2).

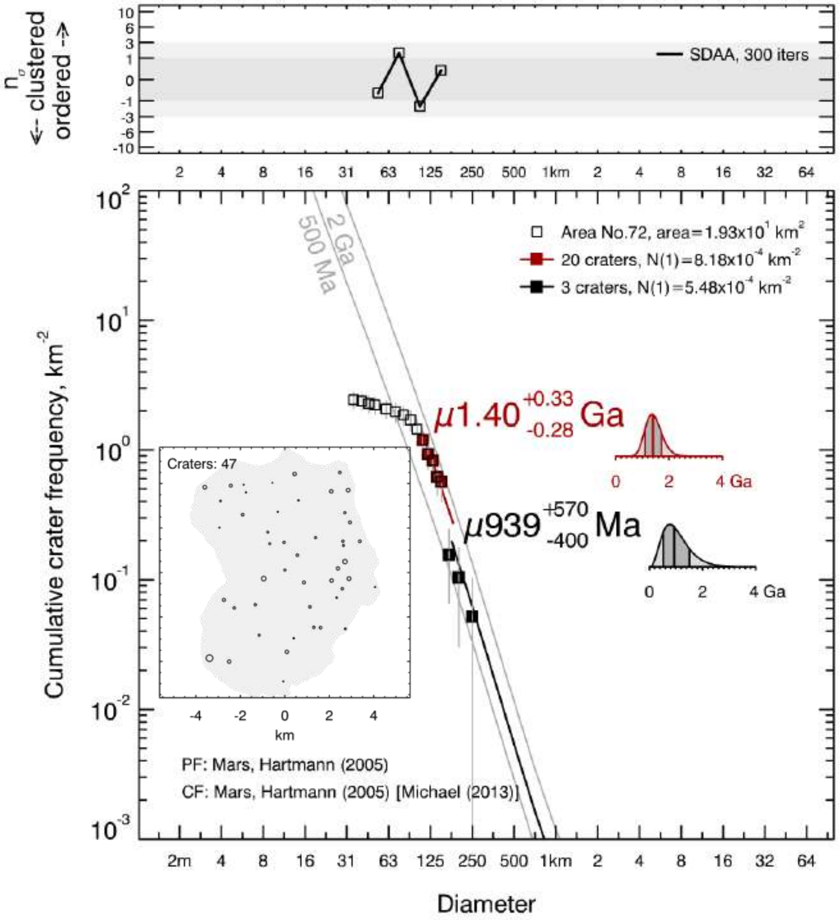

Fig. S95 CSFD and absolute model age for the surface of the Volcanic Edifice no. 72 emplaced within the Uranius Mons subprovince (for more details see Table 2). We considered impact craters of smaller (110-180 m; red) and larger (>180 m; black) diameter. For further investigations, we used older age because the younger one is based on 3 craters only.

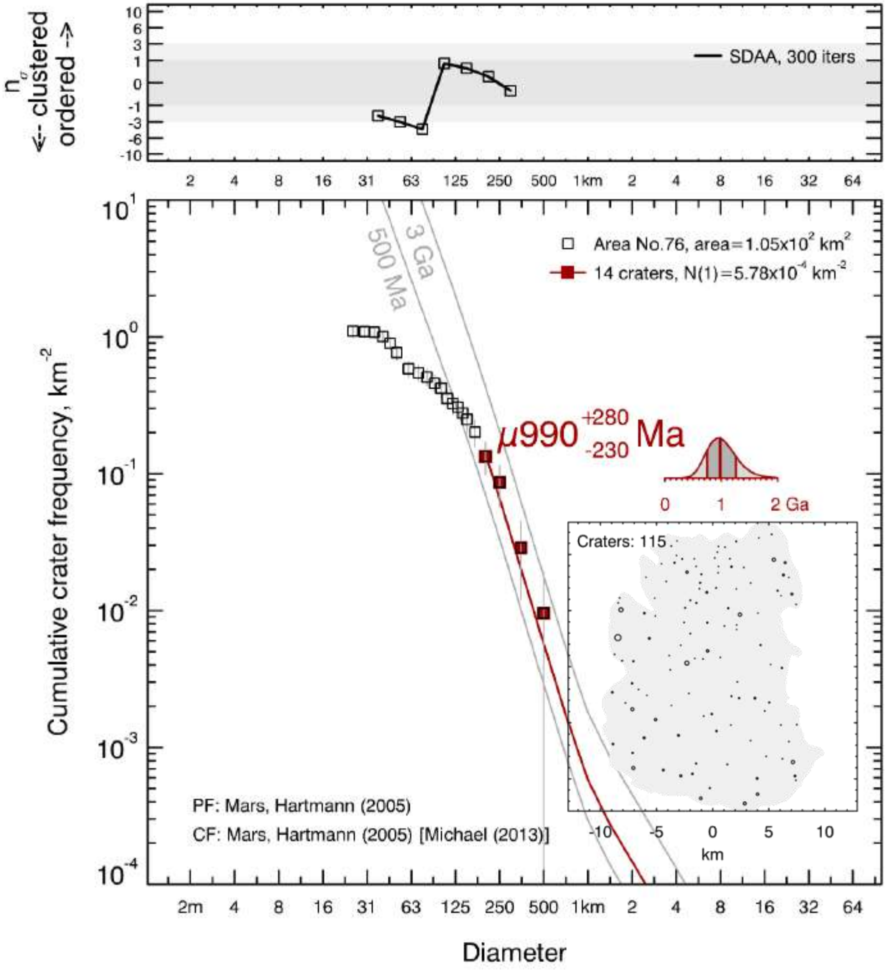

Fig. S96 CSFD and absolute model age for the surface of the Volcanic Edifice no. 76 emplaced within the Uranius Mons subprovince (for more details see Table 2).

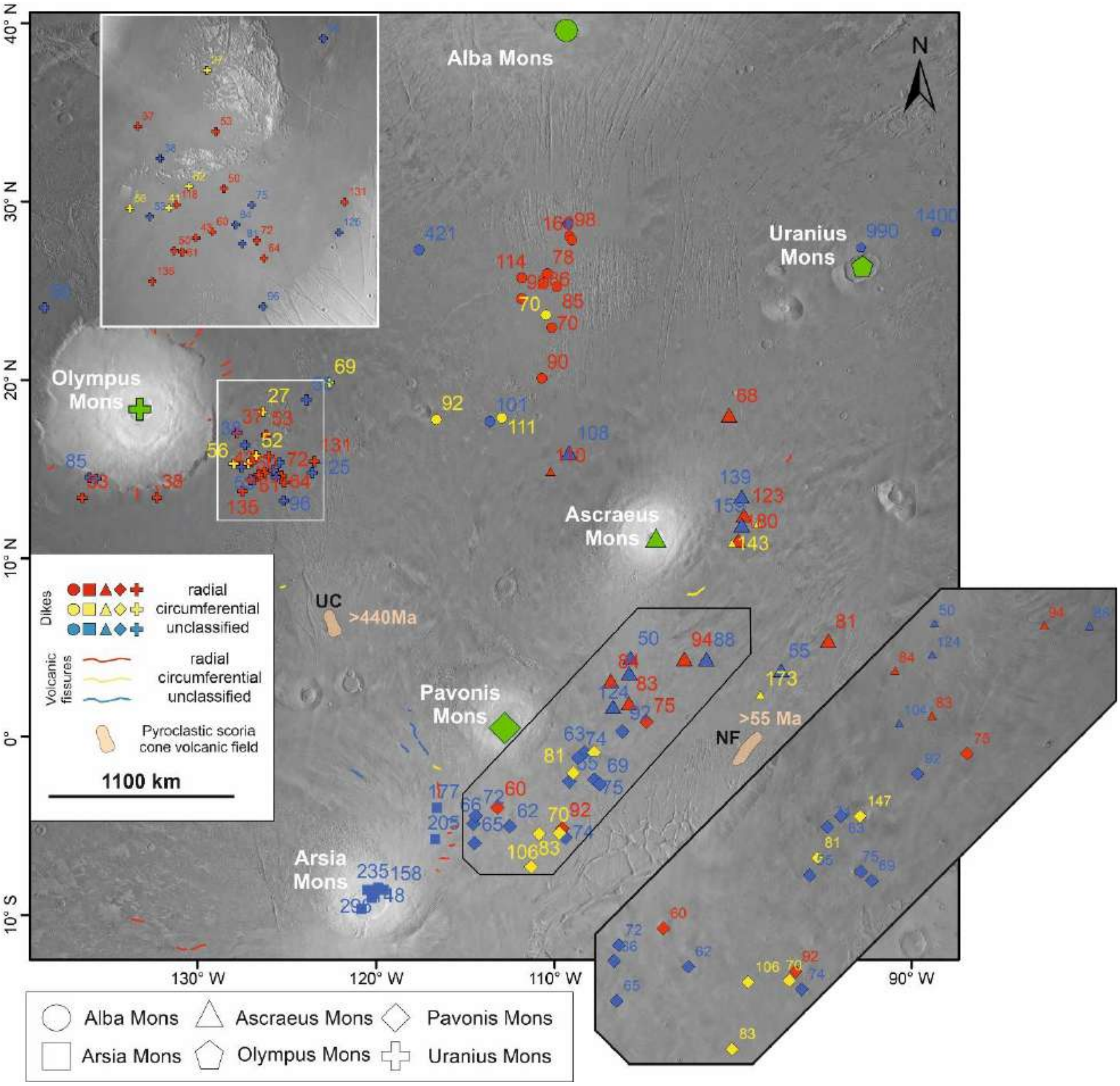

Fig. S97 Modelled ages of interpreted radial and circumferential dikes around the central Tharsis volcanoes. Ulysses Colles (UC) and Noctis Fossae (NF) are explosive volcanic fields and the ages of the latest possible volcanic activity are reported (Brož and Hauber, 2012; Pieterek et al., 2022).

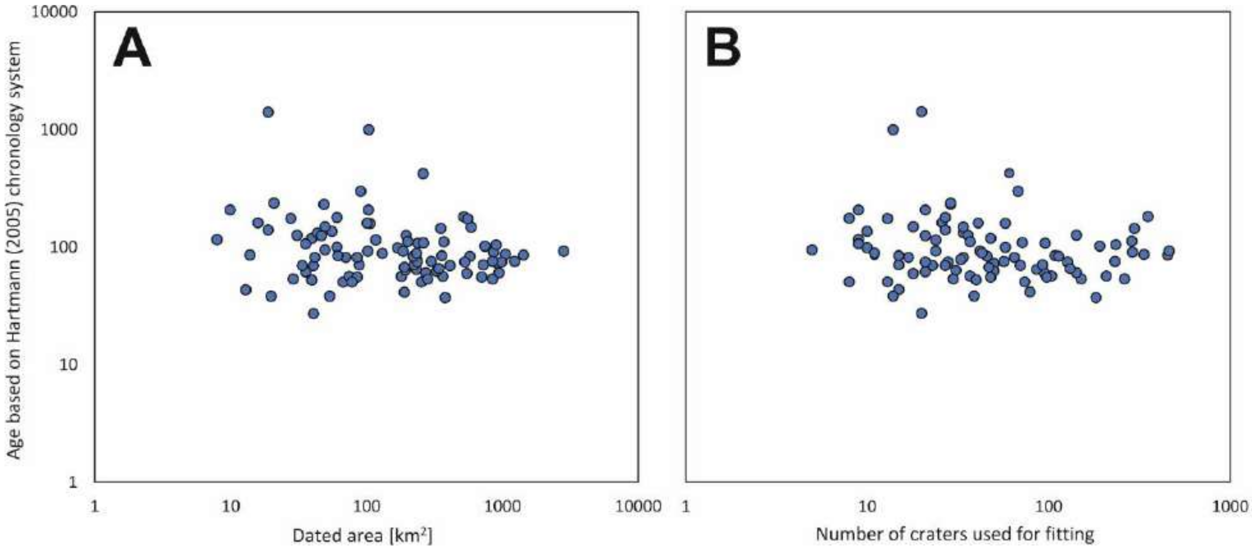

Fig. S98 Histograms of obtained ages based on Hartmann (2005) chronology system and dated area sizes (A) and number of craters used for fitting the isochrons (B)

REFERENCES

Bleacher, J.E., Greeley, R., Williams, D.A., Cave, S.R., Neukum, G., 2007. Trends in effusive style at the Tharsis Montes, Mars, and implications for the development of the Tharsis province. J. Geophys. Res. Planets 112, 1–15. https://doi.org/10.1029/2006JE002873

Brož, P., Hauber, E., 2012. A unique volcanic field in Tharsis, Mars: Pyroclastic cones as evidence for explosive eruptions. Icarus 218, 88–99. https://doi.org/10.1016/j.icarus.2011.11.030

Edwards, C.S., Nowicki, K.J., Christensen, P.R., Hill, J., Gorelick, N., Murray, K., 2011. Mosaicking of global planetary image datasets: 1. Techniques and data processing for Thermal Emission Imaging System (THEMIS) multi-spectral data. J. Geophys. Res. E Planets 116, 1–21. https://doi.org/10.1029/2010JE003755

Fergason, R.L., Hare, T.M., Laura, J., 2018. HRSC and MOLA Blended Digital Elevation Model at 200m v2. [WWW Document]. Astrogeology PDS Annex. U.S. Geol. Surv. URL http://bit.ly/HRSC_MOLA_Blend_v0

Hartmann, W.K., 2005. Martian cratering 8: Isochron refinement and the chronology of Mars 174, 294–320. https://doi.org/10.1016/j.icarus.2004.11.023

Hauber, E., Brož, P., Jagert, F., Jodowski, P., Platz, T., 2011. Very recent and wide-spread basaltic volcanism on Mars. Geophys. Res. Lett. 38, 1–5. https://doi.org/10.1029/2011GL047310

Michael, G.G., Kneissl, T., Neesemann, A., 2016. Planetary surface dating from crater size-frequency distribution measurements: Poisson timing analysis 277, 279–285. https://doi.org/10.1016/j.icarus.2016.05.019

Michael, G.G., Platz, T., Kneissl, T., Schmedemann, N., 2012. Planetary surface dating from crater size-frequency distribution measurements: Spatial randomness and clustering. Icarus 218, 169–177. https://doi.org/10.1016/j.icarus.2011.11.033

Pieterek, B., Laban, M., Ciążela, J., Muszyński, A., 2022. Explosive volcanism in Noctis Fossae on Mars. Icarus 375, 114851. https://doi.org/doi.org/10.1016/j.icarus.2021.114851

Richardson, J.A., Bleacher, J.E., Connor, C.B., Glaze, L.S., 2020. Tharis volcanic vents enhanced database. https://doi.org/doi: 10.5281/zenodo.4275144

Richardson, J.A., Bleacher, J.E., Connor, C.B., Glaze, L.S., 2021. Small Volcanic Vents of the Tharsis Volcanic Province, Mars. J. Geophys. Res. Planets 126. https://doi.org/10.1029/2020JE006620

Publikacja 2

Pieterek, B., Laban, M., Ciazela, J., Muszyński, A. (2022). Explosive volcanism in Noctis Fossae region on Mars. *Icarus, vol. 375, 114851.* https://doi.org/10.1016/j.icarus.2021.114851 (IF$_{2022}$ = **3.657**, pkt. MEiN = **140**)

Icarus 375 (2022) 114851

Contents lists available at ScienceDirect

Icarus

journal homepage: www.elsevier.com/locate/icarus

Research Paper

Explosive volcanism in Noctis Fossae on Mars

B. Pieterek [a,*], M. Laban [b], J. Ciążela [b], A. Muszyński [a]

[a] Institute of Geology, Adam Mickiewicz University, ul. Bogumila Krygowskiego 12, 61–680 Poznan, Poland
[b] Institute of Geological Sciences, Polish Academy of Sciences, Research Centre in Wrocław, Podwale 75, 50–449 Wroclaw, Poland

ARTICLE INFO

Keywords:
Mars
Noctis Fossae
Explosive volcanism
Volcanic cones
Tharsis Volcanic Province

ABSTRACT

Based on theoretical considerations, basaltic volcanism of explosive character should be common on Mars. Although the record of explosive volcanic fields on Mars continues to grow, many unexplored volcanic fields remain. In this research, we identified a group of 25 volcanic cones and associated lava flows emplaced in the Noctis Fossae region on Mars. To analyze this volcanic field, we used images from the Context Camera (CTX) and High Resolution Imaging Science Experiment (HiRISE) of *Mars Reconnaissance Orbiter* (MRO). We interpreted those volcanic cones and their geological history by (1) analyzing their spatial distribution, (2) determining the morphometric parameters, (3) measuring orientations of their summit alignments, and (4) dating these cones along with surrounding lava flows. The identified cones are characterized by various states of preservation from almost fully eroded vent relicts to well-preserved edifices of conical shapes accompanied by short-distance lava flows. Morphological data suggest that the whole set of identified cones likely represent explosive scoria cones. Using the crater count dating method coupled with the structural relationship between the lava flows and volcanic cones, we found that the southern and central cones likely formed >300 Ma, while the northernmost cones between 200 and 50 Ma. These results suggest long-lived volcanism in the studied area active until the latest Amazonian period. In addition, to the present state of knowledge, these cones represent the youngest explosive volcanism in Tharsis and support other findings of young explosive-origin features on Mars. This might shed new light on the magmatic plumbing system of the Tharsis region, although magma sources from Syria Planum, or less likely Valles Marineris, are not excluded. Such magmas of explosive nature are probably rich in volatiles, which might derive from water and/or hydroxyl bearing minerals' or subsurface permafrost deposits. In addition, these magmas might be associated with intensive hydrothermal activity in the region.

1. Introduction

As the number of the Martian surface images kept growing in the initial years of space exploration, most of the conducted research were focused on interpreting landforms that are dominant on Mars. These were large-scale geological structures such as volcanoes including the largest volcano in the Solar system, Olympus Mons (Hodges and Moore, 1979; Greeley and Spudis, 1981; Morris, 1982), and other volcanoes of Tharsis (Carr, 1974; Wise et al., 1979; Plescia and Saunders, 1982; Wilhelms and Squyres, 1984) with associated extensive lava flows (Moore and Ackerman, 1989; Wadge and Lopes, 1991), as well as enormous tectono-structural landforms such as Valles Marineris and Noctis Labyrinthus (Masson, 1977; Schonfeld, 1979; Lucchitta, 1990). Insufficient image quality caused that only a few theoretical predictions on the explosive volcanism were done (Wood, 1979; Wilson and Head, 1994). Recently, however, thanks to the growing availability of high-resolution images and high-quality elevation data, explosive volcanoes and related forms have been broadly studied (Meresse et al., 2008; Williams et al., 2009, 2015; Brož and Hauber, 2012; Huang and Xiao, 2014; Brož et al., 2015, 2017; Horvath et al., 2021; Krishnan and Kumar, 2021; Moitra et al., 2021). These include scoria cones (Brož et al., 2015), tholi (Plescia, 2000), forms of hydrovolcanic activity such as tuff rings and tuff cones (Brož and Hauber, 2013), pseudocraters (Greeley and Fagents, 2001), and a wide spectrum of pyroclastic deposits (Brož et al., 2021 and references therein). These landforms have been present throughout the history of the planet, although their activity was not continuous (Brož et al., 2021). According to Wilson and Head (1994), explosive eruptions should have been common on Mars although the availability of evidence documenting volcanic fields of explosive volcanism is still sparse. Even though major differences between terrestrial and Martian scoria cones have been identified (Dehn and Sheridan, 1990; Wilson and Head, 1994; Brož et al., 2015), there is still a

---

[*] Corresponding author.
E-mail address: barpie@amu.edu.pl (B. Pieterek).

https://doi.org/10.1016/j.icarus.2021.114851
Received 15 September 2021; Received in revised form 20 November 2021; Accepted 6 December 2021

need for searching new explosive volcanic fields on Mars to extend the current state of knowledge.

In the last decades, explosive volcanism has become an important topic in studies on the Martian magmatic system (Wilson and Head, 1994; Harrison and Chapman, 2008; Brož et al., 2014, 2015, 2017, 2021). Scoria cones have been identified especially within the major volcanic provinces such as Tharsis (Brož and Hauber, 2012; Brož et al., 2015) and major tectonic structures such as Valles Marineris (Brož et al., 2017). The Martian scoria cones differ from their terrestrial counterparts due to different environmental factors. Reduced gravity and lower atmospheric pressure cause the cones to become significantly wider and lower with gentler slopes (Wilson and Head, 1994; Brož et al., 2015). In Tharsis, Brož and Hauber (2012) documented a unique volcanic field of pyroclastic cones together with associated lava flows suggesting that Amazonian explosive volcanism might be more common on Mars than it was previously thought. In their view, extensive effusive volcanism in Tharsis during Amazonian could have buried many explosive volcanic fields. Brož et al. (2015) provided detailed morphological characteristics of Martian scoria cones in three other regions on Mars, i.e., Ulysses Colles in Tharsis, Hydraotes Colles in the Oxia Palus quadrangle, and Coprates Chasma in Valles Marineris that can be used by other authors to identify similar landforms, consistent with the explosive type of activity elsewhere on Mars. Overall, to summarize the recent state of knowledge on the occurrence of the explosive volcanism on Mars, Brož et al. (2021) published an overview study suggesting that explosive volcanism is less common on Mars than evidence for effusive activity and both eruption styles have occurred unevenly in time and space.

Several studies (i.e., Greeley and Crown, 1990; Crown and Greeley, 1993; Robbins et al., 2011; Baratoux et al., 2013; Kremer et al., 2019) pointed a significant change in the morphology of the investigated structural units such as Tyrrhena Patera, Hadriaca Patera, or Hellas Region indicating a transition between the explosive and effusive volcanism on Mars between the upper Hesperian and lower Amazonian periods. The change of the eruptive style may be caused by depletion of the volatile content in the magmas, as Mars was continuously releasing the volatiles through the volcanic activity with no volatile recycling known from the plate tectonic system on Earth (Crown and Greeley, 1993; Brož et al., 2021 and references therein).

Based on the Earth studies, it is known that the proportions of suspended solids and/or exsolved fluid phases and dissolved volatiles such as H_2O, CO_2, and F may influence volcanic explosivity (Giordano et al., 2008 and references therein). Magma differentiation and change of its composition may also play an important role in the eruptive styles (Cassidy et al., 2018). Lesher and Spera (2015) showed that the viscosity of magma increases dramatically with the increasing silica content and decreasing temperature of magma. Thus, felsic magma (SiO2-rich) is more explosive than mafic magma of basaltic composition. Both on Earth and Mars, these parameters may control whether eruptions are effusive or explosive (Brož and Hauber, 2012; Brož et al., 2021). The association of explosive-origin volcanic cones with silica-rich deposits (Skok et al., 2010; Brož et al., 2017) may indicate that enhanced volatile content or subsurface interaction of magma with H_2O resulted in more energetic and viscous eruptions triggering hydrothermal activity (Brož et al., 2017).

Mapping and identification of scoria cones on the Martian surface appear crucial to characterize explosive-style volcanism and reconstruct the magmatic plumbing system of Martian volcanic provinces. Currently, using high-resolution data, we can retrieve precise morphological parameters of studied cones and also determine the age of volcanic activity. In 2017, Brož et al. (2017) documented an unnamed volcanic cone situated on the northern edge of Noctis Labyrinthus (Noctis Fossae) and implied its explosive origin. To verify this hypothesis, we performed a detailed study of volcanic cones located in the Noctis Fossae region. Our study of the unnamed volcanic field that we call here Noctis Fossae volcanic field will shed more light on understanding the volcanism within Tharsis. As the number of studies that analyzed and interpreted Martian scoria cones remains low, this study provides new important morphological and chronological data of such a type of volcanism on Mars. This is the second documented field characterizing explosive volcanism in the Tharsis region and the first insight suggesting a different eruption style from the commonly plain-style volcanism in the Noctis Fossae area (Mangold et al., 2010).

2. Geological setting

Due to the low gravity on Mars (Wilson and Head, 1994), its volcanic provinces are far larger than those on Earth. Two of the largest volcanic Amazonian provinces, Tharsis and Elysium (Werner, 2009; Baratoux et al., 2011) are formed by large shield volcanoes accompanied by lava flows. According to Wilson and Head (2007), who studied deposits of tephra, explosive basaltic volcanism has likely played a significant role in Mars' endogenic processes. Based on modeling, these tephra deposits likely originated from explosive volcanic eruptions that could have involved large amounts of magma and entrained water.

Tharsis is a volcano-tectonic province that extends to 4500–5000 km latitudinally across Mars (Carr, 2007; Richardson et al., 2012) and hosts large shield volcanoes including giant volcanoes such as three volcanoes of Tharsis Montes (Fig. 1). Tharsis bulge is a unique example of extraterrestrial superplume volcanism (Dohm et al., 2007). The formation process began with intense volcanism in the mid-Noachian period through hotspot activity and continued by multiple episodes of large mantle upwellings (Mège and Masson, 1996; Wilson and Head, 2002; Anderson et al., 2004) to decline with time (Dohm et al., 2007). Due to compressional stress, Tharsis presents various volcano-tectonic structures: grabens underlain by dikes, faults, and ridges (Mège and Masson, 1996), as well as landforms of plain-style basaltic volcanism (Hauber et al., 2009). Dating models derived from Tharsis' low shield volcanoes show ages ranging from <100 Ma to 200 Ma (Hauber et al., 2011). In contrast, the only volcanic field of pyroclastic cones in Tharsis was identified and mapped by Brož and Hauber (2012), with well-preserved cones formed between ~440 Ma and ~1530 Ma.

The Tharsis province in its southeastern part includes the Syria Planum (Tanaka et al., 2014). Syria Planum hosts at least 263 shield volcanoes with diameters up to tens of kilometers located in the northern part of Syria Planum (Baptista et al., 2008; Xiao et al., 2012; Richardson et al., 2021). Syria Planum experienced chronologically from Early to Late Hesperian: (1) graben formation, (2) volcanic eruptions and lava flows over the entire region, and (3) deformation of lava flows and creations of new faults, troughs, and grabens, and finally (4) younger volcanic activity (Baptista et al., 2008). The volcanism in Syria Planum has begun in the Noachian period (Xiao et al., 2012) and continued until the Early Amazonian (Baptista et al., 2008; Hauber et al., 2011). Richardson et al. (2012) mapped and analyzed a field of small volcanoes within Syria Planum that was previously identified by Baptista et al. (2008), and indicate mostly continuous volcanism lasting no longer than ~900 Myr from the Early Hesperian (3.6–3.4 Ga) to Early Amazonian (2.7–2.5 Ga).

Noctis Fossae is located in the eastern part of the Tharsis Volcanic Province (0°–4°S; 255–265°W), between Tharsis Montes and Syria Planum (Fig. 1). According to Tanaka et al. (2014), the studied volcanic field is located within the northernmost sector of Noctis Labyrinthus at the contact of two main volcanic units (Fig. 1): Late Hesperian fossae region (lHv) and Amazonia-Hesperian (AHv) lava flows that originated from the Tharsis Montes eruptions (Witbeck et al., 1991). However, Mangold et al. (2010) found lava plains in two canyons of Noctis Labyrinthus that have been formed ~50–100 Ma. The southern part of the studied region is mostly dominated by NNE-trending faults forming scarps of fossaes that suggest an extensional component (Bistacchi et al., 2004) (Figs. 1 and 2). These tectonic features are likely related to a single transtensional event that occurred in Noachian (Bistacchi et al., 2004). We observed a set of 25 volcanic edifices distributed within an area of 100 × 150 km, including 2 cones at the Amazonian lava flows

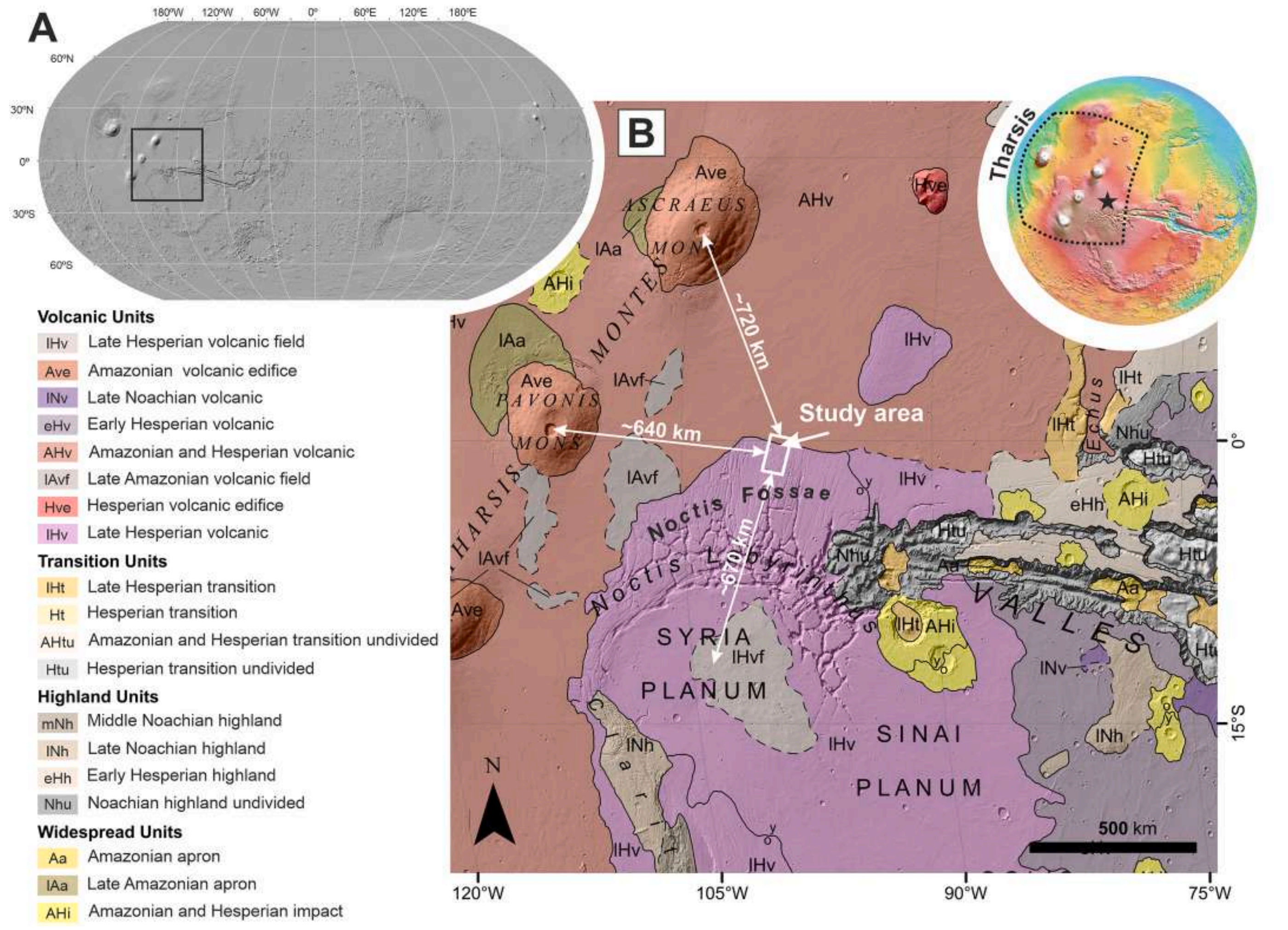

Fig. 1. Location of the Noctis Fossae region on Mars. (A) MOLA shaded relief basemap adapted from Tanaka et al. (2014) with the location of the south-eastern part of the Tharsis Volcanic Province. (B) Fragment of the regional geologic map provided by Tanaka et al. (2014). The study area includes the boundary between two main volcanic units: Amazonia-Hesperian (AHv) and Late Hesperian (lHv). In addition, Noctis Fossae is surrounded by three major volcano-tectonic structures such as Tharsis Montes volcanoes on the northern and western, Syria Planum on the south, and Valles Marineris on the east. The insert shows the location of Tharsis with the marker indicating the location of the study area on the topographic map of Mars.

that likely originated from Tharsis Montes (the northernmost part; N01-02) and 23 cones at the late Hesperian-age part of Noctis Labyrinthus (the central and southern part; N03-25) (Fig. 2).

3. Data and methods

To map, describe, and date the landforms in Noctis Fossae, we used the ArcMap software on a set of images from 1) the Mars Orbiter Laser Altimeter (MOLA) of the *Mars Global Surveyor* (MGS) and the High-Resolution Stereo Camera (HRSC) of the *Mars Express* (MEX) (spatial resolution of ~200 m/pixel), 2) the Thermal Emission Imaging System (THEMIS; Christensen et al., 2004) of the *Mars Odyssey* (MO) (~100 m/pixel), 3) the Context Camera (CTX; Malin et al., 2007) of the *Mars Reconnaissance Orbiter* (MRO) (6 m/pixel), and 4) the High Resolution Imaging Experiment (HiRISE; McEwen et al., 2007) of MRO (~52 cm/pixel) (for more details see Table 1). The combination of the THEMIS and CTX images is well suited to identify the distribution of conical forms resembling volcanoes over the studied region and also on the entire Mars. Using available imagery data for this region together with the current literature dataset of the morphological characteristics of the volcanic cones on Mars, we investigated these structures to determine their origin.

Based on the Grosse et al. (2012) methodology, we assessed basic morphological parameters for terrestrial pyroclastic cones including area of the volcano edifice basement (A_{CO}), basal width (W_{CO}), area of summit crater (A_{CR}), summit crater width (W_{CR}), basal volcano height (H_{CO}), the height of the summit crater (H_{CR}), the absolute height of the volcano (H), and flank slope angles of the cones. Due to differences in morphology and the current state of cones preservation, not all of the measurements were obtained. These morphological parameters of the studied cones such as height, volume, slope inclinations, as well as basal and summit diameters (Table 2 and 3) were determined using ArcMap software tools combined with version 2 of a blend of a Digital Elevation Model (DEM) data derived from the MOLA and HRSC images (Fergason et al., 2018). In addition, some of these parameters (e.g., basal and summit diameters) have been also measured using the CTX mosaic basemap and compared with results obtained from ArcMap measurements (Table 2 and 3). Summit alignments of the identified structures were mapped using the ArcMap software and statistical analysis was conducted using the Stereonet software. To provide a detailed slope analysis of individual volcanic cones, we used DEM derived from CTX pair-images. To achieve this, we used the Martian surface data processing information system called MarsSI (Mars System of Information) being a web Geographical Information System aimed to process Martian orbital data (Quantin-Nataf et al., 2018). To characterize the preservation state of the edifices, we have classified them using a five-point

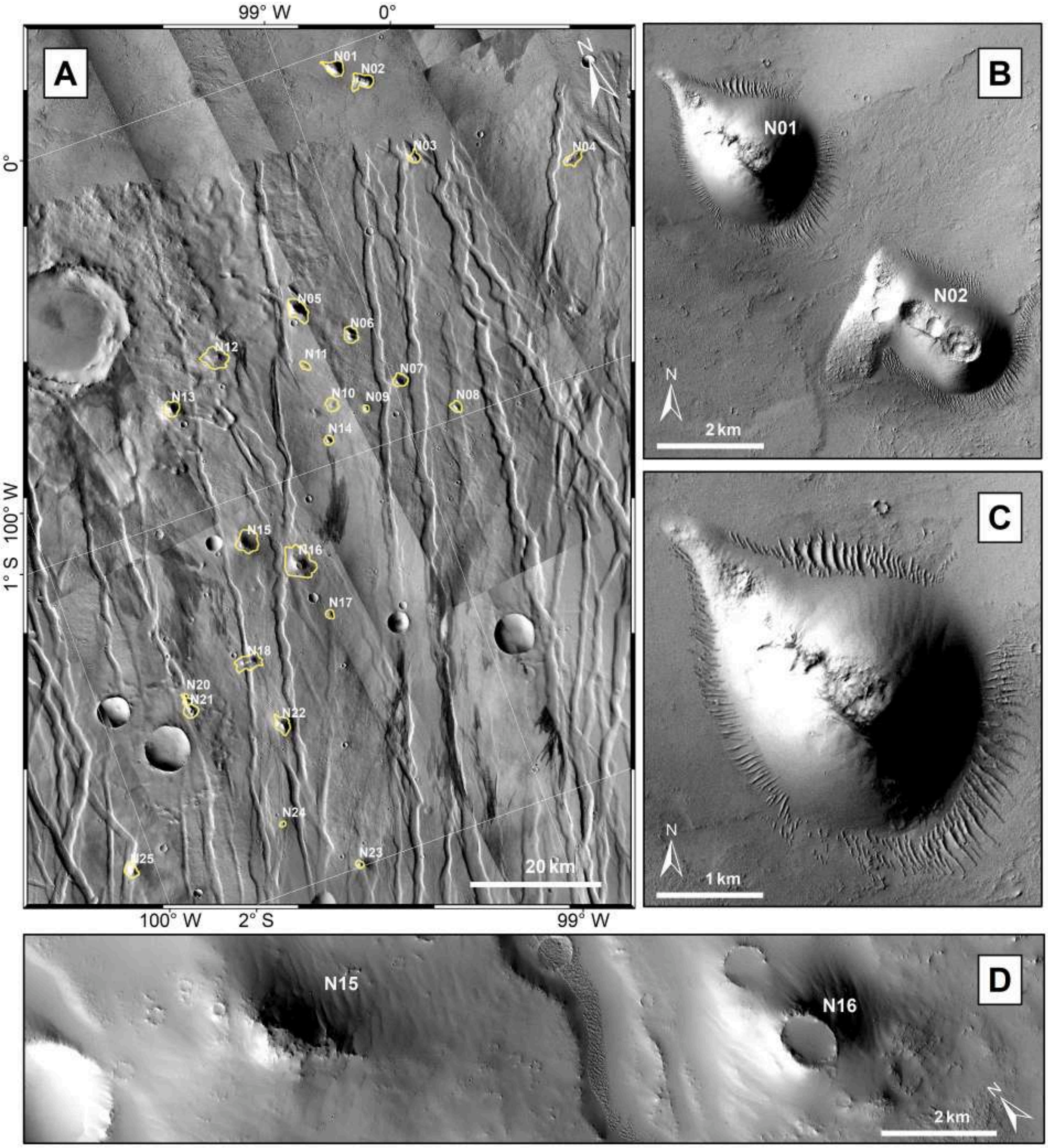

Fig. 2. (A) General CTX mosaic basemap of Noctis Fossae showing the distribution of 25 volcanic cones identified in this study. (B) The CTX image of the best-preserved volcanic cones N01 and N02 surrounded by lava flows, then covered by dunes that are prominent around the volcano basements. These cones are characterized by the isometric shape and high-angle slopes that are most likely covered by pyroclastic material or dust and have not been significantly affected by any erosional processes. The N02 volcanic cone shows a lava flow originating from its summit caldera. CTX image F04_037508_1798_XN_00S098W. (C) Close up the HiRISE image of the N01 volcanic cone showing N-trending elongation of the edifice likely indicating the direction of the subsurface dike. HiRISE image ESP_037508_1800. (D) The CTX image of volcanic cones N15 and N16 is separated by fossae. These cones with well-identified summit craters are characterized by eroded slopes covered with dust. In addition, cone N15 are elongated showing the probable direction of the subsurface dike that supplied the volcanic activity. CTX image B03_010885_1782_XI_01S099W. The details of the used images are presented in Table 1.

preservation scale based on cones shape, height, and summit carter (for more details see Table 2).

To provide the age of the volcano formation, we have applied the crater counting method to determine the surface age of three volcanic cones using HiRISE images, nine lava flows, and an impact crater using CTX images. For crater counting, we used the ArcGIS extension CraterTools2.1 (Kneissl et al., 2011). Crater statistics and derivation of crater model ages, including errors, were carried out with CraterStats II (Michael and Neukum, 2010) by applying the Neukum−Ivanov (2001) production function and Hartmann and Neukum's chronology system (Hartmann and Neukum, 2001) with Poisson timing analysis and Bayesian inference, expressing the ages as a likelihood function with an intrinsic uncertainty (Michael et al., 2016). In addition, we compared our results with three other chronology systems by Ivanov (2001), Hartmann (2005, Michael, 2013), as well as Hartmann and Daubar (2017) (Table 4).

Table 1
Table of the CTX and HiRISE images used in this study (pixel resolution, imaging time, and illumination geometry).

Image ID	Image type	Scaled pixel width	Image time	Center latitude	Center longitude	Subsolar azimuth	Incidence angle	Phase angle
B09_013008_1770_XN_03S099W	CTX	5.28 m	2009–05–06	3.01°S	260.33°	156.53°	50.14°	46.13°
D09_030770_1810_XN_01N100W	CTX	5.34 m	2013–02–18	1.05°N	259.57°	151.16°	48.61°	48.65°
G15_023913_1804_XN_00N100W	CTX	5.33 m	2011–09–02	0.55°N	259.3°	182.04°	33.47°	33.46°
B19_016898_1805_XN_00N100W	CTX	5.35 m	2010–03–05	0.54°N	259.99°	215.65°	49.8°	47.32°
F03_036796_1827_XN_02N100W	CTX	5.41 m	2014–06–02	2.74°N	260.02°	204.94°	54.78°	50.39°
G15_024269_1780_XN_02S099W	CTX	5.3 m	2011–09–30	2.03°S	260.96°	196.07°	35.86°	36.73°
G10_022146_1800_XN_00S099W	CTX	5.3 m	2011–04–18	0.03°	260.92°	150.59°	45.75°	46.89°
F04_037508_1798_XN_00S098W	CTX	5.36 m	2014–07–28	0.26°S	261.15°	193.19°	55.99°	60.16°
G19_025614_1772_XN_02S099W	CTX	5.26 m	2012–01–13	2.92°S	260.89°	218.12°	49.35°	50.53°
B03_010885_1782_XI_01S099W	CTX	5.33 m	2008–11–21	1.84°S	260.47°	197.8°	57.02°	57.33°
P20_008683_1754_XN_04S099W	CTX	5.41 m	2008–06–03	4.66°S	260.24°	221.57°	56.05°	62.01°
G17_024691_1766_XN_03S100W	CTX	5.29 m	2011–11–02	3.49°S	259.86°	207.04°	40.52°	41.06°
B05_011452_1764_XN_03S099W	CTX	5.27 m	2009–01–04	3.67°S	260.7°	186.53°	57.54°	57.53°
P12_005611_1760_XN_04S098W	CTX	5.26 m	2007–10–07	4.05°S	261.51°	168.71°	34.25°	34.27°
G05_020089_1795_XN_00S099W	CTX	5.34 m	2010–11–08	0.5°S	260.46°	188.6°	54.65°	57.7°
G06_020445_1791_XN_00S098W	CTX	5.31 m	2010–12–06	0.98°S	261.1°	180.61°	55°	55°
P21_009395_1784_XI_01S100W	CTX	5.35 m	2008–07–28	1.68°S	259.94°	218.21°	56.65°	54.19°
G23_027025_1765_XN_03S100W	CTX	5.4 m	2012–05–02	3.57°S	259.58°	220.52°	55.02°	61.35°
F03_036862_1792_XN_00S100W	CTX	5.66 m	2014–06–07	0.77°S	259.14°	205.94°	56.77°	44.15°
D20_035174_1824_XN_02N099W	CTX	5.38 m	2014–01–27	2.48°N	260.73°	217.65°	51.73°	54.82°
ESP_037508_1800	HiRISE	52.4 cm	2014–07–28	0.04°S	261.13°	12.5°	56°	60.2°
PSP_010318_1800	HiRISE	52.8 cm	2008–10–08	0.11°S	261.20°	26.3°	57°	49.5°
ESP_013364_1780	HiRISE	52.5 cm	2009–06–02	1.83°S	259.95°	332.2°	46°	51.9°

The minimum crater sizes we used for fitting the isochrons for volcanic cones are 10–15 m if based on the HiRISE images and for lava flows are 50–300 m if based on the CTX images (Table 4). There is still ongoing discussion about the minimum crater sizes usable for dating. Some craters <300 m in diameter might be secondary and should be not taken into account (e.g., McEwen et al., 2005; Werner, 2009; Lagain et al., 2021). However, the availability of high resolution data allowed to conduct of more detailed studies on the regional scale using much smaller craters (<50 m). Such diameters of impact craters have been successfully used by Brož (2010) and Hauber et al. (2011) who used craters >30 m for isochrons fitting based on CTX images to date lava flows in Tharsis. Currently, Lagain et al. (2021) inferred that spatial resolution of CTX imagery allows identifying impact craters as small as 25 m. In addition, Horvath et al. (2021) used crater diameters of ≥2 m for all craters and ≥ 3 m for the bright ejecta craters using the HiRISE imagery system.

The degree of clustering was measured at various crater diameter bins by applying the Randomness Analysis tool (Michael et al., 2012) to evaluate potential contamination with secondary craters. The inversed standard deviation of the adjacent area (SDAA) was determined for each bin size using root-2 bin spacing. This technique divides the count areas into a number of subareas equal to the number of craters in the area of the same bin size, separated by boundaries defined by mid-distances between the craters. Higher clustering of craters within the defined subarea sizes results in a higher standard deviation value (Michael et al., 2012; Williams, 2018). The non-random diameter ranges are excluded from the measurements. The SDAA values close to 0 indicate a fully random distribution according to a set of 300 Monte Carlo simulations for a crater set of a given area. Each simulation assumes that subareas are randomly scattered with a number and size of craters equivalent to those observed in a given diameter bin, and the clustering measure is computed. After 300 iterations, a histogram is built up describing the relative probability of each range of obtained values (Michael et al., 2012).

4. Results

4.1. Distribution and characteristics of volcanic cones

The 25 studied cones create a group aligned in an SW-NE direction, with the main clustering of the edifices in the central part of the studied area (Fig. 2A). Based on their location, we have classified the volcanic constructs into two provinces: 1) the northern (cones N01 and N02) emplaced on the Amazonian-Hesperian volcanic unit and 2) the south-central (cones N03–25) emplaced on the Late Hesperian volcanic unit. In general, cones located in the southcentral part of the volcanic field appear to be more eroded (an average preservation state of 3.2) than the northern cones (1.0), which seem to be pristine (Table 2). The northern cones are characterized by well-preserved morphological features such as conical shape, steep flank slopes, and distinct summit craters. For some of the southern cones, we did not observe typical features of pyroclastic cones due to their high erosion (Fig. S1). In some cases, when the state of degradation of the cone is high, we found elongated edifices mostly composed of hard rocks with a little amount of dust on their slopes that may be interpreted as relics of solidified dikes on the surface that likely fed these volcanoes (Figs. 2D and S1E—F).

In general, we demonstrated that the shapes, heights, and volumes of the investigated cones are variable (Fig. 3). They include circular (e.g., N06, N15, N16,), ellipsoidal (e.g., N04 and N18), and also irregular forms (e.g., N03, N12; Fig. S1). The better preserved a cone is, the more parameters of morphological features are possible to measure. In addition, the two northern cones (N01 and N02; Fig. 2) are most likely associated with lobate, short-distance lava flows erupting and affecting the northern flanks of cones.

We found that our study area is locally covered by dust, which is especially prominent in the vicinity of volcanic edifices (Fig. 2). Moreover, some volcanoes in the northern and central parts of the field are surrounded by groups of dunes (Figs. 2B-C and S1D). In addition, the northeastern part of the studied volcanic field is affected by the >18-km-diameter impact crater whose ejecta covered an area ranging from 10 to 15 km away from the rim of the crater (Fig. 2A). Our detailed mapping indicated that at least two volcanic cones (N12 and N13) located 12 and 14 km away from the impact crater rim (Fig. 2A) could have been covered and partially modified by ejecta deposits that were spread out on the Martian surface (Fig. S1 B—C). Another ejecta material of a 7-km-diameter impact crater affected cones N20 and N21 (Fig. 2A) that are located up to 5 km away from the crater rim.

4.2. Morphological parameters

Using the MOLA DEM, we found that most of the cones are characterized by an absolute height <100 m (17 cones) with an average value

Table 2

The morphometric parameters of the volcanic cones in the Noctis Fossae study area, based on the MGS MOLA - MEX HRSC Blended Global 200 m and CTX DEMs.

ID	X coordinates[a]	Y coordinates[a]	DEM	A_{CO} [km^2]	W_{CO} [km]	A_{CR} [km^2]	W_{CR} [km]	H_{CO} [km]	H_{CR} [km]	H [km]	W_{CO}/W_{CR}	W_{CR}/W_{CO}	H/W_{CR}	slope max. [^{0}][b]	avg. slope [^{0}][b]	volume [km^3][c]	scale of preservation[d]
N01	98° 51′ 53.684″ W	0° 2′ 44.742″ S	M	5.40	3.14	0.31	0.64	4.43	4.64	0.21	4.87	0.21	0.33	13.41	7.24	0.689	1
			C					4.38	4.71	0.33			0.51	51.60	13.92	1.055	
N02	98° 48′ 38.777″ W	0° 6′ 7.885″ S	M	6.02	3.52	0.79	1.34	4.39	4.51	0.12	2.63	0.38	0.09	7.49	3.89	0.593	1
			C					4.37	4.57	0.20			0.15	29.90	9.13	0.958	
N03	98° 45′ 0.135″ W	0° 19′ 55.106″ S	M	2.28	2.06	0.31	0.65	4.48	4.59	0.12	3.16	0.32	0.18	7.41	2.21	0.186	3
N04	98° 21′ 59.373″ W	0° 28′ 28.794″ S	M	4.18	2.97	0.35	1.10	4.54	4.62	0.08	2.71	0.37	0.07	4.07	2.35	0.282	3
N05	99° 9′ 59.673″ W	0° 35′ 58.848″ S	M	7.82	3.61	0.21	0.52	4.98	5.24	0.27	6.90	0.15	0.52	13.55	6.63	1.084	1/2
N06	99° 3′ 35.852″ W	0° 42′ 19.139″ S	M	4.27	2.48	0.43	0.76	5.04	5.11	0.07	3.27	0.31	0.10	2.02	1.44	0.165	2/3
N07	98° 58′ 50.445″ W	0° 51′ 30.763″ S	M	3.47	2.27	peak	–	5.15	5.20	0.05	–	–	–	4.25	1.39	0.065	4
N08	98° 52′ 3.732″ W	0° 58′ 18.577″ S	M	2.31	1.90	0.08	0.37	5.18	5.24	0.05	5.18	0.19	0.14	2.38	1.31	0.059	3
N09	99° 5′ 17.019″ W	0° 53′ 48.451″ S	M	0.74	1.00	0.03	0.21	5.27	–	–	4.81	0.21	–	–	–	–	3
N10	99° 10′ 0.925″ W	0° 51′ 27.484″ S	M	3.19	2.18	0.11	0.38	5.23	5.26	0.03	5.69	0.18	0.09	1.94	0.95	0.051	3
N11	99° 11′ 52.831″ W	0° 44′ 23.454″ S	M	1.48	1.51	0.06	0.30	5.14	5.17	0.03	5.10	0.20	–	1.67	0.91	0.024	4
N12	99° 24′ 31.682″ W	0° 38′ 33.880″ S	M	9.61	4.16	peak	–	5.10	5.22	0.11	–	–	–	4.12	2.58	0.515	4
N13	99° 33′ 27.948″ W	0° 43′ 35.153″ S	M	4.24	2.49	peak	–	5.23	5.32	0.09	–	–	–	6.15	2.70	0.152	2
N14	99° 12′ 23.117″ W	0° 56′ 26.545″ S	M	1.64	1.48	peak	–	5.32	5.35	0.03	–	–	–	2.07	1.05	0.017	3
N15	99° 29′ 29.833″ W	1° 06′ 51.017″ S	M	9.09	3.67	0.11	0.42	5.60	5.97	0.37	8.79	0.11	0.88	15.33	7.21	1.455	2
N16	99° 23′ 8.499″ W	1° 12′ 33.916″ S	M	18.03	5.68	0.67	0.94	5.52	5.92	0.40	6.03	0.17	0.43	12.49	5.50	4.054	1/2
N17	99° 21′ 22.930″ W	1° 21′ 45.409″ S	M	1.40	1.38	peak	–	5.76	–	–	–	–	–	–	–	–	5
N18	99° 35′ 46.177″ W	1° 24′ 25.939″ S	M	7.62	3.98	peak	–	5.65	5.70	0.05	–	–	–	1.82	0.82	0.203	4
N19	99° 46′ 45.903″ W	1° 25′ 58.200″ S	M	0.57	0.89	peak	–	5.60	5.62	0.02	–	–	–	1.30	0.66	0.003	4
N20	99° 46′ 43.629″ W	1° 26′ 53.777″ S	M	1.23	1.30	peak	–	5.61	5.63	0.02	–	–	–	1.81	0.81	0.010	3
N21	99° 46′ 42.191″ W	1° 28′ 27.813″ S	M	3.49	2.18	0.29	0.62	5.61	5.67	0.07	3.52	0.28	0.11	3.77	1.69	0.117	2
N22	99° 34′ 7.642″ W	1° 35′ 15.063″ S	M	4.79	2.95	0.02	0.19	5.82	5.96	0.15	15.88	0.06	0.81	6.87	4.34	0.363	1/2
N23	99° 30′ 17.279″ W	1° 59′ 35.405″ S	M	1.16	1.27	0.02	0.19	6.14	6.20	0.07	6.81	0.15	0.36	5.00	2.74	0.033	2
N24	99° 39′ 18.826″ W	1° 49′ 42.678″ S	M	0.54	0.87	peak	–	5.95	5.99	0.04	–	–	–	3.76	1.78	0.007	4
N25	100° 3′ 45.956″ W	1° 48′ 24.760″ S	M	3.48	2.28	peak	–	5.81	5.90	0.09	–	–	–	5.40	2.71	0.118	4

C – CTX DEM; M – MOLA DEM; A_{CO} – the area of the volcano edifice basement; W_{CO} – the basal width of the volcanic edifice (assuming the circular shape of the edifice, we have calculated W_{CO} parameter converting perimeter using ArcMap software); A_{CR} – the area of the volcano summit crater ('peak' means that summit crater is unidentifiable for the selected cone); W_{CR} – the summit crater width measured the same as W_{CR} using perimeter from ArcMap software; H_{CO} – the absolute basal volcano height; H_{CR} – the absolute height of the summit crater; H – the relative height of the volcano cone (the difference between H_{CR} and H_{CO}).

[a] X and Y coordinates are based on the Geographic Coordinate System Mars2000;

[b] Slope analysis have been conducted based on the MGS MOLA - MEX HRSC Blended DEM Global 200 m for the entire volcanic fields and CTX DEM stereo pairs for the northernmost N01 and N02 cones;

[c] Volume has been measured using the equation for frustum;

[d] Scale of volcano preservation: 1– intact; 2 – slopes and summit crater preserved; 3 – volcano cone eroded (slopes or summit crater are difficult to identify); 4 – mostly eroded; 5 – eroded.

Table 3
Areas and diameters of the cones basement and summit crater along with volcano volumes obtained by various methods.

Volcano ID	A_{CO} [km^2]	W_{CO} [km]	A_{CR} [km^2]	W_{CR} [km]	Volume[a] [km^3]	Volume[b] [km^3]	Difference in volume[c] [%]
N01	6.15	2.80	0.31	0.63	0.560	0.689	−20.7
N02	6.33	2.84	0.92	1.08	0.386	0.593	−42.2
N03	2.49	1.78	0.30	0.62	0.144	0.186	−25.6
N04	4.75	2.46	0.79	1.00	0.202	0.282	−33.3
N05	8.34	3.26	0.20	0.50	0.893	1.084	−19.3
N06	3.87	2.22	0.38	0.70	0.133	0.165	−21.3
N07	3.40	2.08	peak	–	0.054	0.065	−17.4
N08	2.54	1.80	0.08	0.32	0.052	0.059	−12.8
N09	0.72	0.96	0.03	0.20	0.004	0.003	14.7
N10	3.14	2.00	0.10	0.36	0.043	0.051	−16.5
N11	1.63	1.44	0.26	0.58	0.017	0.019	−9.9
N12	10.06	3.58	peak	–	0.382	0.515	−29.6
N13	4.01	2.26	peak	–	0.126	0.152	−19.1
N14	1.58	1.42	peak	–	0.016	0.017	−8.5
N15	8.76	3.34	peak	–	1.071	1.350	−23.0
N16	19.00	4.92	0.69	0.94	3.126	4.054	−25.9
N17	1.41	1.34	peak	–	0.002	0.002	−6.4
N18	7.45	3.08	peak	–	0.122	0.203	−50.0
N19	0.55	0.84	peak	–	0.003	0.003	−10.5
N20	1.21	1.24	peak	–	0.009	0.010	−9.1
N21	3.53	2.12	0.26	0.58	0.109	0.117	−6.8
N22	5.06	2.54	0.03	0.20	0.275	0.363	−27.8
N23	1.13	1.20	0.03	0.18	0.030	0.033	−10.9
N24	0.53	0.82	peak	–	0.006	0.007	−11.8
N25	3.66	2.16	peak	–	0.106	0.118	−10.8

[a] volume calculated applying the formula for frustum using data obtained by multiple measurements of diameter (minimum 6) of each identified volcano basal area and the summit crater.

[b] volume presented in Table 2 (see notes).

[c] the ratio of the absolute difference to the average of the two volumes.

of 103 m and a maximum height of 402 m (Fig. 3A and Table 2). These cones show volumes ranging from <0.1 to 4.1 km^3 with an average of 0.4 km^3 (Fig. 3B and Table 2 and 3). Considering the morphological parameters of the cones, we found that these parameters are strictly related to the state of preservation (Table 2). The best-preserved cones located in the northern part of the volcanic field (e.g., N01, N02, and N05) and central part (e.g., N15 and N16; Fig. 2) exhibited the highest values of morphological parameters, including volumes, basal widths, areas, and absolute heights. The basal areas of cones range from 0.5 to 18.0 km^2 and correlate with the increasing volume of cones (Fig. 3C). Basal diameters range from 0.9 to 5.7 km with an average value of 2.5 km (Fig. 3D).

Among 25 studied cones, 15 exhibit circular or elongated summit craters, which prevail in the northern and central parts of the volcanic field. Their summit crater widths, measured perpendicular to the long axis of the volcano basement, range between 0.2 and 1.3 km (Fig. 3E). The southern cones are eroded and we did not detect any summit craters (Fig. 2).

To analyze the topography of the volcanic field, we used two DEM datasets, MOLA for the entire volcanic field and CTX stereo pair images available for the northernmost N01 and N02 cones. The study area in the Noctis Fossae region is elevated up to 6.2 km in the southernmost part and lowers down to 4.2 km towards the north (Fig. 4A). Based on the MOLA DEM, the average slope angles for most of the identified cones are >1° with a maximum of 15.3° (for N15). The identified cones in the studied area are well visible on the slope map (Fig. 4B). The gentlest slopes are typically those highly eroded (Table 2). Steeper flanks are observed for the best-preserved cones (N01 and N02) with averages of 13.9° for N01 and 9.1° for N02 (Fig. 4D; Table 2). The slope values on CTX stereo pair DEM are ~1.6 times larger than those for MOLA DEM. This seems to be related to the discrepancies between MOLA DEM and CTX DEM values. Comparing heights for the two northernmost cones (N01 and N02), we observed that the heights obtained from the stereo pair DEM of CTX are ~0.6 times larger than those for MOLA (i.e., N01 shows a high of 336 and 210 m for CTX and MOLA DEMs, respectively).

4.3. *Age dating*

To provide a constrain on the temporal evolution of the studied volcanic field, we have determined the crater retention ages of three individual cones (N01, N02, and N25) for which the HiRISE images were available (Figs. 2 and 7). These surfaces exhibit young ages of the flanks ranging from ~2.4 to ~12.6 Ma (for more detail see Fig. 8). However, the dated slopes seem to be covered by a thin layer of dust suggested also by dunes at the foot of the volcanoes. We supposed that the dust layer resurfaced studied areas, and thus, lowers the modeled ages. To further constrain the age of volcanism we have dated 9 lava flows and 1 impact crater (Figs. 7–8 and S2). The northernmost lava flows (LA01-LA06) reveal relatively young ages ranging from 51 ± 9 to 131 ± 22 Ma (Fig. 7), while the southern lava flows (LA07-LA09) spreading over the fossae show ages of 191 ± 27 to 279 ± 52 Ma with one exceptionally old of ~2 Ga (LA09) (Figs. 7–8 and S3).

In addition, to estimate the minimum age of the formation of cones in the central part of the field we used the stratigraphic relationship between the cones (N12 and N13) and ejecta deposits. We have dated the surface of the impact crater (IC01) located on the late Noachian volcanic unit (Figs. 1 and 2; Tanaka et al., 2014) that shows an age of 297 ± 43 Ma indicating that volcanic cones in the central part of Noctis Fossae most likely were formed before the impact (~300 Ma). There is an age discrepancy between the northernmost lava flows (Amazonian and Hesperian unit) and the proper fossae region (late Noachian volcanic unit; Figs. 1 and 2). This age boundary is also reflected by the morphology of the studied terrains with the northern part appearing intensively resurfaced by lava flows and the rougher southern region composed of fossae devoid of fresh lava flows (Fig. 2A). In addition, we found that the northernmost ejected material from the impact crater was buried under late Amazonian lava flows (Fig. 2A). The northernmost cones (N01 and N02), were most likely emplaced on the lava flow (LA01) that exhibit the age of 126 + 30;-26 Ma, while the lava flow of LA03 surrounds the cone N01 indicating the minimum age when these cones must have been formed of 51 ± 9 Ma (Fig. S2).

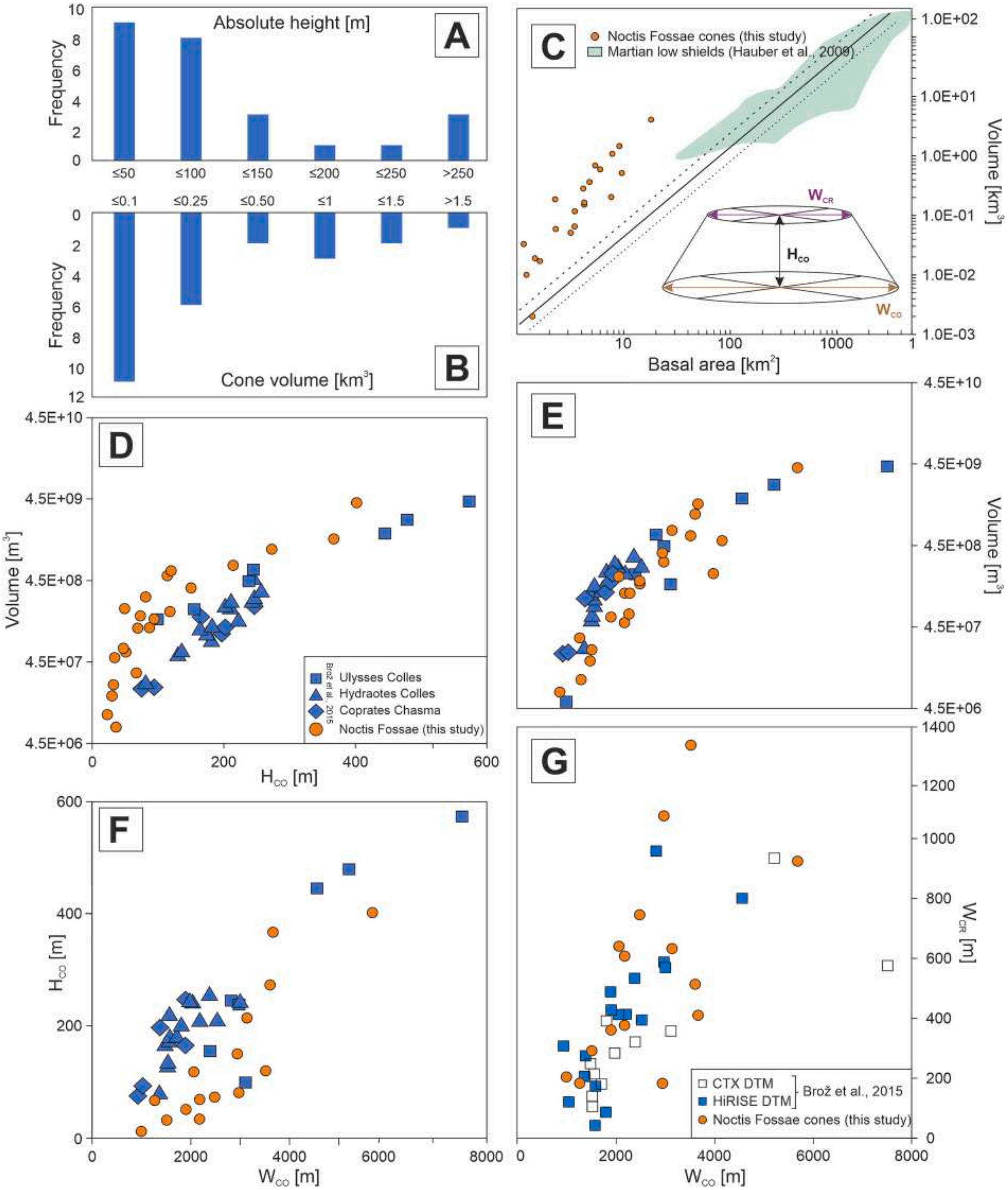

Fig. 3. Histograms of cone heights (H_{CO}) (A) and volumes (B) in the Noctis Fossae region. Our Noctis Fossae cones compared to low-shield volcanoes analyzed in the Tharsis Volcanic Province (Hauber et al., 2009) (C) as well explosive-origin volcanic cones from Ulysses Colles, Hydraotes Colles, and Coprates Chasma volcanic fields (Brož et al., 2015) (D-G). W_{CO} - basal diameter; W_{CR} - summit crater diameter.

5. Discussion

5.1. Explosive origin of the Noctis Fossae volcanic cones

In the Noctis Fossae region, we identified at least 25 volcanic cones showing various states of preservation. However, most of them exhibit morphological parameters similar to other scoria cones on Mars i.e., Ulysses Colles, Hydraotes Colles, and Coprates Chasma (Fig. 3D-G). Due to differences in atmospheric and physical conditions on Mars, Martian volcanic scoria cones differ from their terrestrial counterparts (Wilson and Head, 1994; Parfitt and Wilson, 2008; Brož and Hauber, 2012, 2013; Brož et al., 2014, 2015, 2021) (Fig. 5). On Earth, scoria cones are the most numerous volcanic features (Wood, 1979, Wood, 1980; Martin and Németh, 2006). The Earth scoria cones often form small, truncated conical edifices associated with short and viscous lava flows that are mostly composed of basaltic scoria material and tephra particles. Brož et al. (2015) highlighted differences in the morphological parameters and evolution of scoria cones on Earth and Mars. On Mars, the ejected

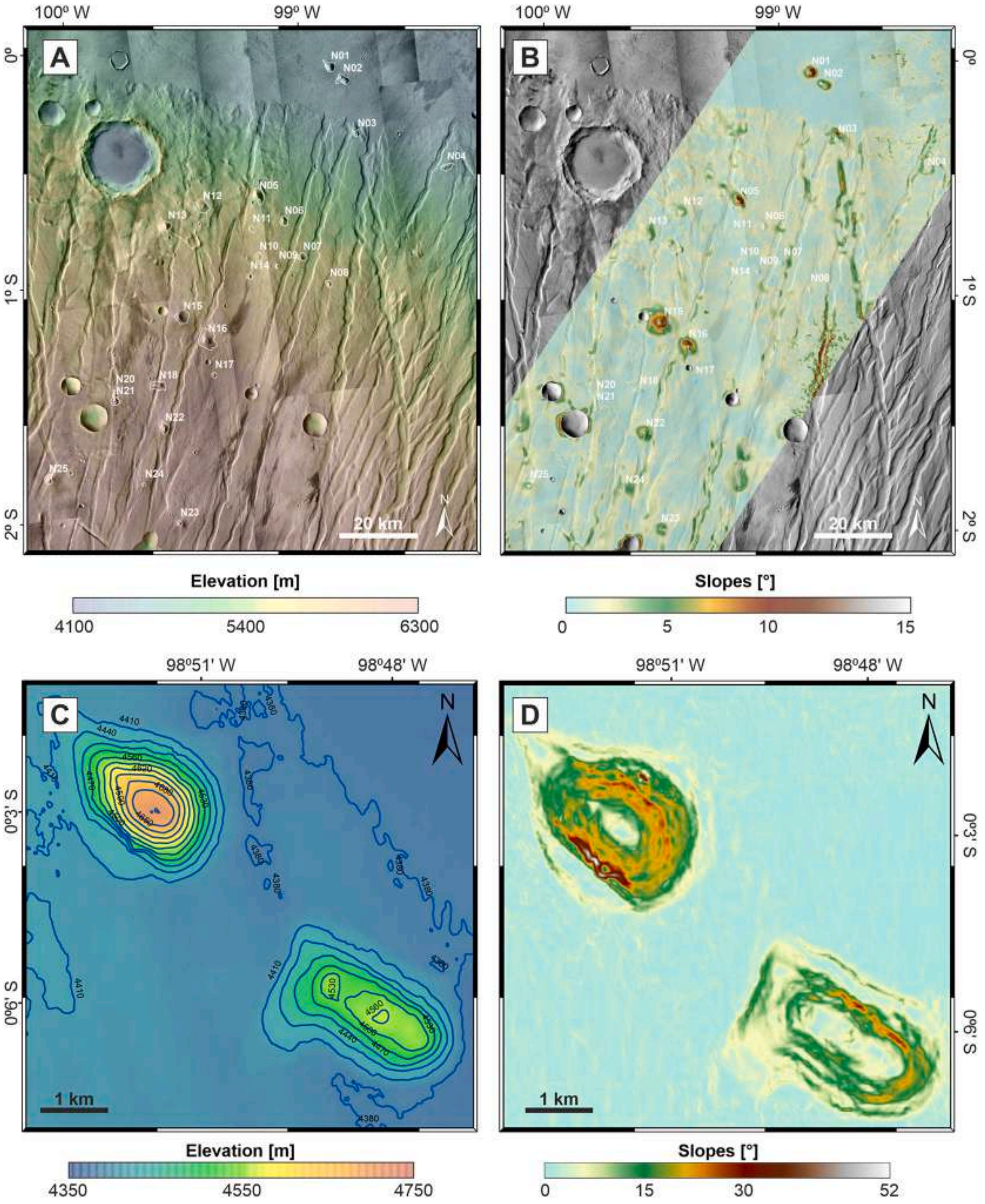

Fig. 4. Elevation (A) and slope (B) maps provided for the set of 25 investigated volcanic cones. Both maps are based on the MGS MOLA - MEX HRSC Blended digital elevation model (DEM) Global 200 m_v2. C—D) Elevation and slope maps of the best-preserved cones, N01 (left) and N02 (right) obtained from a DEM based on stereo pair CTX imagery.

material during eruption might be transported over much greater distances (even 20 times; Brož et al., 2015) than on Earth forming larger volcanic cones in plan with gentler slopes (never exceeding angle of repose of ~30^{0}; Kleinhans et al., 2011). Currently, there is no evidence for the presence of an explosive-origin volcano that might further grow by the continuation of eruptions after it reaches the angle of repose (~30^{0}).

Theoretical models predict significant morphological differences between scoria cones on Earth and Mars (Wilson and Head, 1994). It was previously highlighted that Martian scoria cones should have larger basal diameters and lower heights (Wilson and Head, 1994; Parfitt and Wilson, 2008). In addition, Dehn and Sheridan (1990) predicted that scoria cones on Mars should have 2–3 times larger basal diameters than their terrestrial counterparts. According to Wood (1979b) and Hasenaka and Carmichael (1985), the average basal diameter of terrestrial scoria cones is ranging from 0.8 to 1.0 km. This value is further supported by other studies of Fornaciai et al. (2012) and Zaidi and Mukhopadhyay (2015) who obtained values between 0.8 and 1.3 km. In Noctis Fossae, the investigated cones are larger at the basement, ranging from ~0.9 to 5.7 km in diameter with an average value of ~2.3 km (Table 2). These results are consistent with Ulysses Colles, investigated by Brož and Hauber (2012), which exhibit basal widths between 1 and 4 km in diameter (2.3 km on average). In addition, the basal diameters of Noctis Fossae volcanic field seem to be larger compared to Hydraotes Colles (1.3–3.0 km with an average value of 1.9 km) and Coprates Chasma (0.9–1.9 km with an average of 1.5 km; Brož et al., 2015). Our basal diameters in Noctis Fossae show an average ~ 2.6 larger than for the typical scoria cones on Earth. Such a difference has been previously

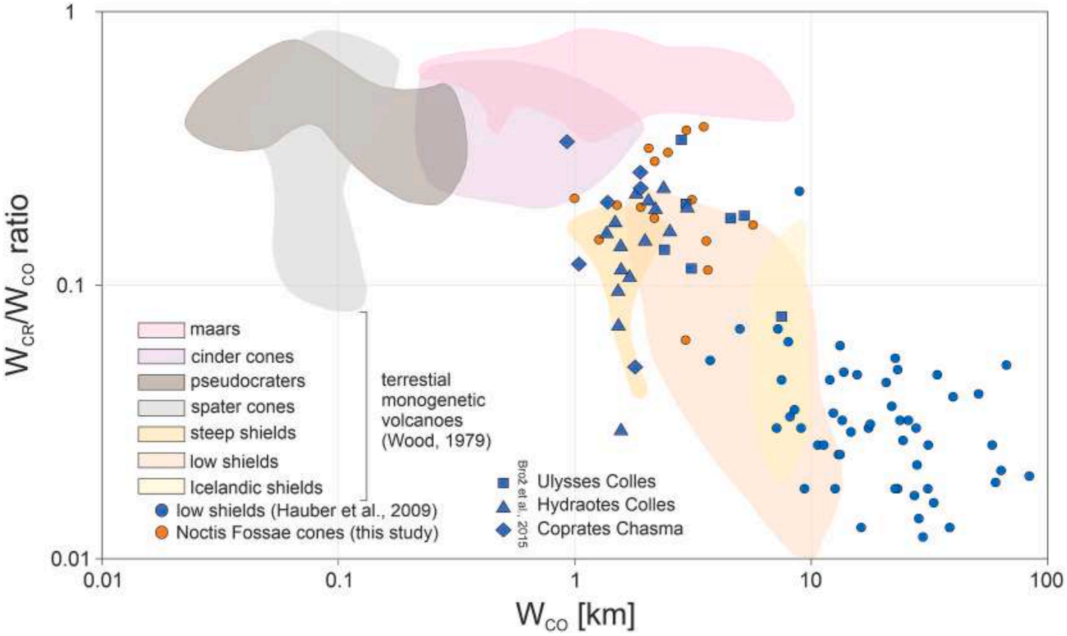

Fig. 5. Morphological parameters such as basal diameter (W_{CO}) and summit crater diameter versus basal diameter ratio (W_{CR}/W_{CO}) between the Noctis Fossae compared to explosive-origin cones from other volcanic fields (Brož et al., 2015), as well as low-shield cones studied in Tharsis Volcanic Province (Hauber et al., 2009). In addition, the volcanic fields for terrestrial monogenetic volcanoes of various origins (Wood, 1979) have been included. The Noctis Fossae cones are clustered showing morphological characteristics differing from the Tharsis low-shield volcanoes. Both types of Martian cones such as scoria cones and low-shield are slightly shifted towards larger basal diameters with respect to their terrestrial counterparts due to the reduced gravity and lower atmospheric pressure on Mars (Wilson and Head, 1994).

highlighted by Brož and Hauber (2012) and Brož et al., 2015 (Figs. 3 and 5). In Noctis Fossae, 15 of 25 cones exhibit summit craters consisting of an individual (e.g., N01, N15) or multiple (e.g., N02) vents whose diameters range from ~0.2 to 1.3 km with an average value of 0.6 km. The remaining 10 cones are characterized by central peaks (Table 2). Scoria cones from Ulysses Colles, Hydraotes Colles, and Coprates Chasma display the average diameter of summit craters of 0.6, 0.3, and 0.3 km, respectively, which are consistent with our results.

Dehn and Sheridan (1990) suggested that the Martian scoria cones should be >100 m in height and exhibit well-developed central summit craters. On Earth, the absolute heights of scoria cones, from the basal to the summit, range between 80 and 170 m (Fornaciai et al., 2012; Zaidi and Mukhopadhyay, 2015). However, Brož and Hauber (2012) demonstrated that Ulysses Colles' volcanoes are from 60 to 650 m high (230 m on average), while scoria cones from Hydraotes Colles and Coprates Chasma show lower heights up to 260 m (Fig. 3C and F). In this study, volcano heights range from 20 to 400 m (for cones N09 and N17, we have determined only the basal volcano heights). In addition, we found that the cones with low heights (<100 m) are typically highly eroded (state of preservation ranging from 3 to 5; for more details see Table 2).

In 2014, Brož and Hauber (2012) highlighted that the volumes of scoria cones on Mars are by one or two orders of magnitude larger than on Earth, for which the average volume is 0.046 km^3 (Brož et al., 2015 and references therein). The scoria cones from other volcanic fields of explosive-origin on Mars displayed similar volumes as in the Noctis Fossae volcanic field. We calculated volumes of the studied cones that range from 0.002 to 4.054 km^3 (Table 2 and 3, Fig. 3E). The studied volcanic field is characterized by the largest number of cones <0.1 km^3, moderate number 0.1–0.25 km^3, and only a few cones >0.25 km^3 (Fig. 3B). Comparing different volcanic fields of explosive origin on Mars, Brož et al. (2015) found that morphological parameters differ between the analyzed volcanic fields. The cones within the Ulysses Colles volcanic field form the largest edifices (maximum values of W_{CO}, W_{CR}, and H are 7.50 km, 0.95 km, and 0.57 km) while other fields such as Hydraotes Colles in Xanthe Terra (maximum values of W_{CO}, W_{CR}, and H are 3.00 km, 0.57 km, and 0.26 km) and Coprates Chasma within Valles Marineris (maximum values of W_{CO}, W_{CR}, and H are 1.90 km, 0.49 km, and 0.25 km) are characterized by smaller cones (Fig. 3). According to Brož and Hauber (2012), the larger sizes of the analyzed cones in the Ulysses Colles volcanic field may result from the extension-controlled eruptions in the Ulysses Fossae region. We found that the largest cones described in Noctis Fossae exhibit values of W_{CO} (5.68 km), W_{CR} (1.34 km), and H (0.40 km) (Table 2) comparable to Ulysses Colles' cones in Tharsis. This similarity indicates that in general explosive volcanism in Tharsis might have been more voluminous than in other geological regions on Mars, for example in Valles Marineris.

Several morphological parameters are applied to distinguish among different types of monogenetic volcanoes such as spatter cones, pseudocraters, and scoria cones (Fig. 5). We determined the W_{CR}/W_{CO} and H/W_{CO} ratios commonly used in terrestrial and planetary science to distinguish different geological landforms (e.g., Dapremont and Wray, 2021; Dóniz and Romero, 2011; Pérez-López et al., 2011) (Figs. 3 and 5). For the terrestrial volcanoes, the W_{CR}/W_{CO} ratio mostly ranges from 0.32 to 0.40 (Porter, 1972; Wood, 1980; Zaidi and Mukhopadhyay, 2015), but varies among different volcanic fields. Fornaciai et al. (2012) obtained the average W_{CR}/W_{CO} values ranging from 0.24 (Cima volcanic field, US-California) to 0.43 (Pinacate volcanic field, Mexico). In addition, Zaidi and Mukhopadhyay (2015) determined the average W_{CR}/W_{CO} of 0.32 for the volcanic fields (i.e., Rahat, Hadan) in Western Saudi Arabia. In contrast, Brož et al. (2015) demonstrated generally lower W_{CR}/W_{CO} for Martian scoria cones between 0.05 and 0.34 with an average value of 0.17. These values are in line with our Noctis Fossae cones ranging from 0.06 to 0.19 with an average value of 0.17 (Table 2 and Fig. 5).

In addition, we calculated that H/W_{CO} ranged from 0.01 to 0.11 with an average value of 0.04 smaller than the averages of 0.07 for Ulysses Colles, 0.10 for Hydraotes Colles, and 0.17 for Coprates Chasma (Brož et al. (2015). However, they used the high-resolution DEMs of CTX and HiRISE images that exhibit more precise data of absolute height compared to MOLA DEM, as was previously highlighted by Brož et al. (2015). On Earth, in some cases, H/W_{CO} exhibits similar values as those on Mars, ranging from 0.11 to 0.16 (Fornaciai et al., 2012; Zaidi and Mukhopadhyay, 2015). Yet this ratio also is in some cases much smaller. For example, 0.02 to 0.10 was demonstrated by Kereszturi and Németh (2012) for the eroded Pliocene scoria cones situated at the Bakony–Balaton Highland Volcanic Field in Hungary.

The Noctis Fossae cones exhibit low-angle slopes ranging between 1 and 15° based on the MOLA DEM (Table 2). However, using the CTX DEM, we found that the northernmost cones show much steeper slopes compared to MOLA results. These results indicate an average slope angle value of ~30^0 (Table 2). In addition, based on the CTX DEM, the N01 cone locally exhibit an extremely high value of 52^0 (Fig. 4D) being inconsistent with the cones' shape on the CTX image (Fig. 2C) suggesting a conversion error. As these MOLA values seem to be very low, especially compared to other results obtained for Martian scoria cones (Brož and Hauber, 2012; Brož et al., 2015), we should consider inaccuracy related to the low-resolution data. Slopes of the cones investigated by Brož et al. (2015) for the volcanic field on Mars (Ulysses Colles and Hydraotes Colles and Coprates Chasma) exhibited maximum values of 34° with average angles for individual cones ranging from 7° to 25°.

In addition, using imagery data, we observed that the Noctis Fossae volcanic field is locally covered by the dust mantling, especially in the vicinity of the volcanic cones and inside the fossaes (Figs. 2 B—C and S1). Brož and Hauber (2012) based on the HiRISE imagery inferred that the entire area of Ulysses Colles volcanic field is thickly mantled by dust. The volcanic cones in Hydraotes Colles are also associated with dunes that surround the edifices (see Fig. 5 in Brož et al., 2015). The origin of the aeolian material might be related to the explosive volcanic activity, as previously pointed by Edgett (1997), but it is more likely owned to the erosion of widespread regional and local volcanic rocks. Keszthelyi et al. (2008) suggest that the Martian pyroclastic deposits commonly occur in Tharsis, for example in areas of Biblis Patera, in the vicinity of Arsia Mons (Edgett, 1997) or on the flanks of Alba Mons (Mouginis-Mark et al., 1988). In addition, Edgett and Lancaster (1993) suggested that Martian dunes may be composed of volcanic mafic material as suggested by *Viking* lander results resembling the composition of terrestrial cinder cones (Toulmin et al., 1977). Recently, these hypotheses were supported by remote (Johnson et al., 2018) and *in situ* (Rampe et al., 2018) measurements of mineral composition (abundant olivine and pyroxene and minor amount of plagioclase) of actively transported sand inside the Gale crater.

The two northernmost Noctis Fossae volcanic cones were likely affected by the associated flow-like structures similar to terrestrial lava flows of explosive volcanoes. Such short-distance lava flows are characterized by a rough surface compared to lavas originating from the low-shield volcanoes within the Tharsis Volcanic Province (Bleacher et al., 2009; Hauber et al., 2009). Thus, it appears that the Noctis Fossae cones were most likely formed by the relatively viscous magmas. The association between the cones and viscous lava flows suggests a similarity with terrestrial pyroclastic cones such as scoria cones (Strong and Wolff, 2003; Favalli et al., 2009) or spatter cones (Fodor and Németh, 2015). However, spatter cones are small, few meters wide and several meters high, with flanks steeper than the typical angle of repose. As Brož and Hauber (2012), we also exclude the interpretation of pseudocraters origin, because these landforms exhibit different morphological characteristics (much smaller basal diameters between 30 and 180 m for cones in Amazonis Planitia (Greeley and Fagents, 2001) and large conical summit craters achieving to 40–50% of basal width (Frey et al., 1979; Lanagan et al., 2001; Fagents and Thordarson, 2009; Hamilton et al., 2011; Noguchi and Kurita, 2015). Moreover, pseudocraters have no connection with the underground magma sources, thus their formation is likely related to the magma-water(ice) interaction (Baloga et al., 2007; Fagents and Thordarson, 2009). The spatter cone origin is also unlikely for the Noctis Fossae cones due to the significantly larger basal diameters and volumes of the Noctis Fossae cones than for the terrestrial spatter cones (basal diameter ~ 80 m and volume of 0.06×10^6 m^3; Fodor and Németh, 2015; Moufti et al., 2013; Wood, 1979). Thus, considering all morphological data and their comparison to both terrestrial (Fig. 5) and Martian counterparts (Fig. 3), we believe that the cones in the Noctis Fossae volcanic field represent pyroclastic scoria cones suggesting the explosive style of the volcanic eruption.

5.2. *Spatial distribution and age-dating*

On Earth, cone or summit fissure alignments are most likely controlled by the local or regional tectonic stress manifested on the surface by fault and rift zones (Bonali and Corazzato, 2011). The spatial distribution of the Noctis Fossae cones also suggests a control by the tectonic structures of the Noctis Fossae region. The Noctis Fossae is an extensional zone characterized by NNE-trending faults (N015E) that commonly form grabens (fossaes) within the study area (Bistacchi et al., 2004). The initial tectonic stress in the Noctis Fossae region was probably further slightly modified to ~N050W by a lateral component of displacement (Bistacchi et al., 2004). The cones' summit alignments were most likely already formed in that modified (WNW) stress regime as they exhibit orientations of ~N015W (Fig. 6). Based on the detailed mapping, we can observe that individual cones together with their summit craters are aligned one after the other revealing the same direction. For example, the clusters of cones N05–N08 and N15–N17 are aligned along a trend of ~N030W, while cones N20–N22 exhibit a trend of ~N015W suggesting that each cluster might have been supplied by individual dikes originated from the same magma source (Fig. 6). Magma that supplied these cones may have migrated through dikes and manifested on the surface by explosive eruptions forming volcanic edifices. This interpretation is supported by the remnants of dike conduits that were found in the studied volcanic field (Fig. 2). In the case when the pressure of ascending magma is smaller than the regional tectonic stress, high-angle fault (70–90°) provide channels for magma migration (Kereszturi and Németh, 2012). Brož and Hauber (2012) in the Ulysses Colles volcanic field demonstrated that the spatial distribution of cones was likely controlled by the local system of grabens and faults. They highlighted that subsurface magma migration expressed by volcanic eruptions on the surface was possible due to the extensional stress regime. The lower gravity on Mars might result in the increasing width of the dikes by a factor of two and higher effusion rates by a factor of five compared to the terrestrial dike systems (Wilson and Head, 1994). Thus, magma reservoirs may be even emplaced 4 times deeper and magmas can migrate on larger distances compared to the terrestrial analogs (Wilson and Head, 1994).

According to Tanaka et al. (2014), the Noctis Fossae cones are located on two different in age geologic units revealing various states of erosion depending on the location. On Earth, the degradational evolution of the pyroclastic cones depends mainly on the amount of time (Hooper and Sheridan, 1998). The more eroded the cones are, the more time they had been exposed to erosion. This process can be expressed by modifications of the primary morphological features such as lowered maximum and average slope angles and lowered H/W_{CO} (Dohrenwend et al., 1986; Bemis and Ferencz, 2017). We think the less eroded northern cones (Table 2) may be younger than those in the central and southern parts of the Noctis volcanic field. To verify this hypothesis, we have determined the surface age of 3 volcanic cones within both geological units (Table 4 and Figs. 7–8). However, we found that they are covered by mantling dust, and thus, these results do not represent the age of volcanic activity but most likely the age of resurfacing. Assuming the explosive origin of the Noctis Fossae volcanic field, we suppose that these cones are composed of loose, fine-grained material deposited in layers (Meresse et al., 2008; Brož et al., 2015). On Earth, scoria cones are made of fine grains that can be easily transported by exogenous processes, and thus, these volcanic structures are prone to erosion (Hickson et al., 2013).

To further constrain the age of the volcanic field, we determined the

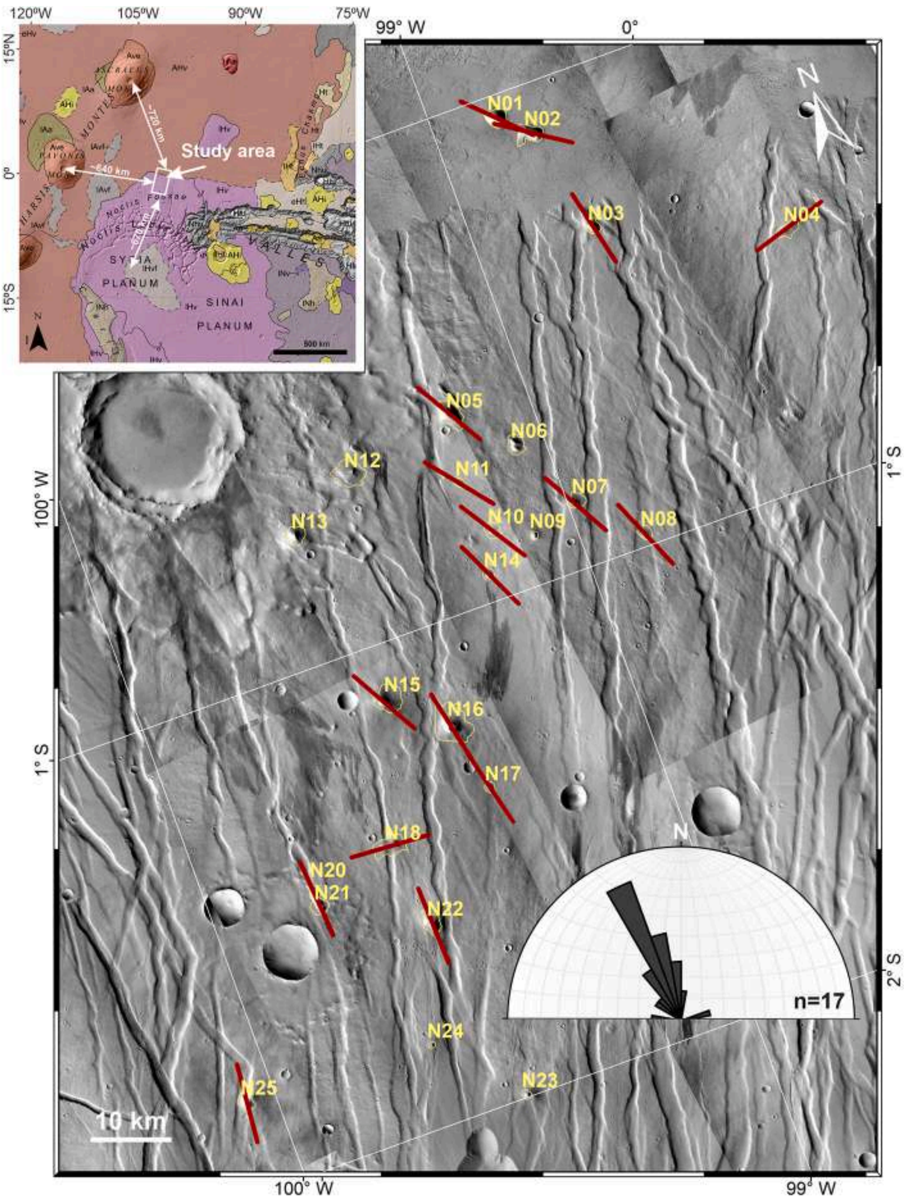

Fig. 6. The tectono-structural map of the Noctis Fossae study area showing orientations of 17 summit crater alignments. The rose diagram presents the summary spatial arrangement of this structure and indicates potential orientations of the possible feeding dikes in the NNW-SSE-trending directions. The left top insert shows the distances of the Noctis Fossae volcanic field to Tharsis Montes volcanoes and Syria Planum. (For interpretation of the references to colour in this figure legend, the reader is referred to the web version of this article.)

Table 4
Comparison of obtained surface determination ages using various chronology systems. We have used HiRISE and CTX images for volcanic cones and lava aprons, respectively. The ages from Neukum−Ivanov (2001) system have been chosen for further consideration.

ID		Chronology system								Min. crater size (m)	Area [km^2]
		Neukum−Ivanov (2001)		Ivanov (2001)		Hartmann (2005)		Hartmann & Daubar (2016)			
Volcanic cones	N01	2.4	+0.8;−0.7	2.9	+1;−0.8	5.5	+2;−1.6	5.4	+1.9;−1.4	15	5.3
	N02	12.6	+6.7;−4.9	14.8	+7.9;−5.8	15.7	+6.3; −5.0	12.9	+5.2;−4.1	10	0.5
	N25	8.2	±1.3	9.7	±1.6	18.6	±3.0	18.3	±2.9	15	6.2
	IC01[1]	297	±43	351	±51	417	±60	417	±60	100	87.4
Lava flows	LA01	126	+30;−26	148	+36;−31	201	+48;−42	201	+48;−42	60	16.7
	LA02	51	±9	60	±11	84	±15	84	±15	50	36.4
	LA03	131	±22	154	±26	194	±33	194	±33	80	69.6
	LA04	85	±15	100	±18	140	±25	140	±25	50	22.6
	LA05	53	+13;−11	63	+15;−13	88	+21;−18	88	+21;−18	50	22.1
	LA06	60	±8	70	±9	95	±12	95	±12	60	111.0
	LA07	191	±27	226	±32	268	±38	268	±38	100	142.0
	LA08	279	±52	329	±61	391	±72	391	±72	100	57.5
	LA09	1970	+490;−440	2280	±490	2080	+500;−460	2080	+500;−460	300	225.0

±, +, and − represent 1SD as defined in the Method section. The minimum crater size is the same for all chronology systems.

[1] IC01[1] dated area is a central part of an impact crater located in the western part of the studied area.

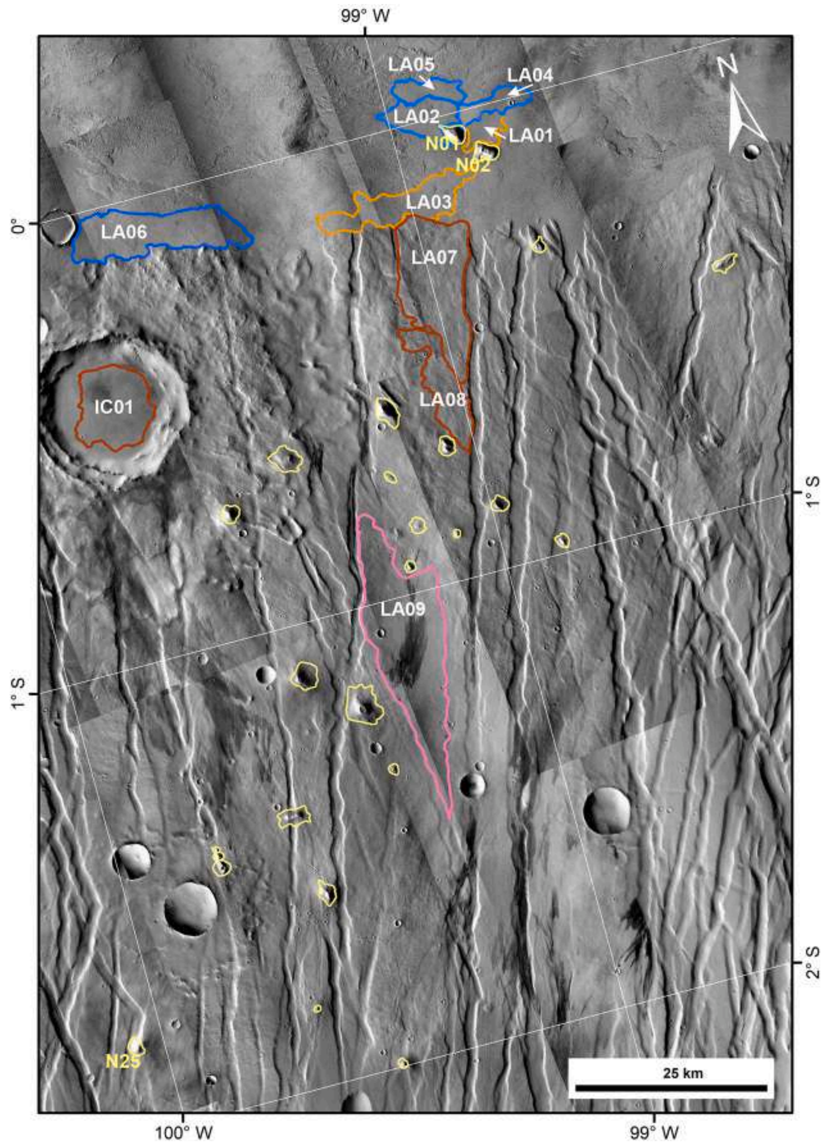

Fig. 7. The Noctis Fossae volcanic field with 25 identified volcanic cones. Three of them (N01, N02, and N25) and ten surface areas (LA01–09 and IC01) were dated using HiRISE and CTX images. The boundaries of lava flows dated in this study have been marked by the blue, orange, brown, and rose lines that correspond to the age ranges: <100, 101–150, 151–500, and > 500 Ma, respectively (see Table 4 and Fig. 4 for exact ages). (For interpretation of the references to colour in this figure legend, the reader is referred to the web version of this article.)

age of the lava flows (LA01-LA06) formed in the vicinity of the northernmost N01 and N02 cones (see Section 4.3, Fig. 7). Based on the relative stratigraphic relationships between the cones and the surrounding lava plains (Fig. 7), we concluded that the northernmost cones were most likely emplaced between 130 and 50 Ma (Fig. S2) being in line with the stratigraphic-geological unit (Amazonian and Hesperian volcanic unit; Fig. 1) of Tanaka et al. (2014). In addition, the northwestern section of the study area is affected by the >18-km large impact crater whose ejecta covered at least two volcanic cones suggesting that volcanic cones situated in the central and southern part of the volcanic field were emplaced before the impact at 297 ± 43 Ma (IC01; Figs. 7–8 and S1). Similar to our study, Brož and Hauber (2012) were not able to determine the precise age of the Ulysses Colles volcanic field formation but suggested the extended time for the formation of the cone bracketing between the older (~1.5 Ga) and younger (~0.4 Ga) surface units. In addition, they highlighted that the number of cones might have been larger, but most of them could be currently eroded as could be also the case for our study. They also pointed that the number of cones in the volcanic field does not correspond with its longevity, suggesting possible long-lived activity of the Ulysses Colles. In addition, Brož et al. (2015) found a volcanic field with possible scoria and tuff cones in the Coprates Chasma in the Valles Marineris. The associated lava flows are dated between 0.4 and 0.2 Ga. The spatial distribution of the cones suggests they formed along subsurface faults used by ascending magma. Brož et al. (2021) suggested that explosive volcanic fields have been forming through the entire Amazonian period and although explosive volcanism is unevenly distributed in time and space our results support their view. Explosive volcanism may still occur on Mars with volcanic-origin deposits such as those found by Horvath et al. (2021) formed between 53 ± 7 and 210 ± 12 ka around a segment of the Cerberus Fossae fissure system in Elysium Planitia.

5.3. Magma source for the Noctis Fossae volcanic field

The volcanic field of Noctis Fossae is located between three major tectono-volcanic structures: Valles Marineris, Syria Planum, and Tharsis Montes (Fig. 1, Table 5) which represent different stratigraphic units (Tanaka et al., 2014). To provide constraints which of them could be the magma source for the Noctis Fossae volcanic field, we analyzed spatial distribution of the studied volcanic cones, their summit crater alignments, and ages in comparison to those from the three stratigraphic units.

Although the canyon system of Valles Marineris may still be seismotectonically active (Kumar et al., 2019), there is little evidence

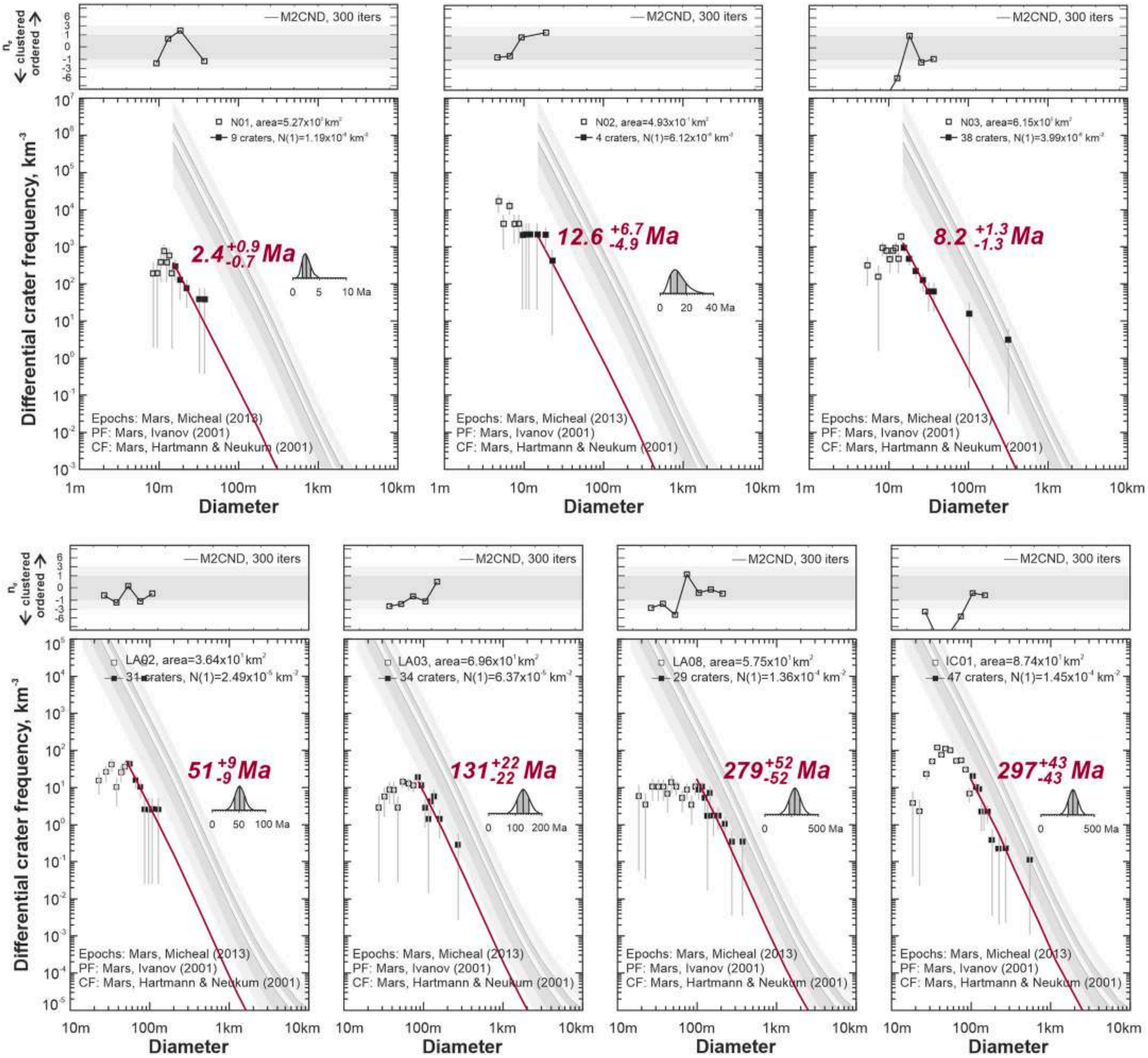

Fig. 8. Absolute model ages for three volcanoes (N01, N02, and N03) based on HiRISE images and other surface units, lava flows, and impact crater (LA02, LA03, LA08, and IC01) based on CTX images. The LA02, LA03, and LA08 represent areas on which the volcanic field was emplaced. The cumulative crater curves indicate absolute model ages of ~51, ~131, and ~ 279 Ma, respectively. We suppose that all lava flows are most likely older than identified volcanoes. The central part (IC01) of the 18.5-km-large impact crater constrains the youngest possible of the volcanic field formation because the ejecta likely covered the N12 and N13 volcanoes (for details see Fig. 7). The upper panels are summaries of their randomness analyses using the (inversed) standard deviation of the adjacent area (SDAA) parameter (see Section 3).

indicating a common occurrence of volcanic activity younger <200 Ma. In 2017, Brož et al. (2017) mapped a large set of small volcanic cones on the floor of the Coprates Chasma (Table 5) and interpreted them as scoria cones of the Late Amazonian ages (400–200 Ma). The volcano-tectonic evolution of the Valles Marineris suggests that this system has been long-lived from the Noachian to the Late Amazonian (Kumar et al., 2019), which is in line with our ages of the Noctis Fossae lava flows. Mège et al. (2017) found the highest dike concentration in the eastern part of Coprates Chasma and Ophir Chasma, which may suggest the direction of the preferred paths of the magma migration. The orientations of these dikes are N100E for Valles Marineris and N081E for eastern Coprates Chasma and matched those in Syria Planum dike swarm trend (Mège and Masson, 1996). These dikes may have propagated from the Syria Planum as interpreted by Mège and Masson (1996). These observations imply that most of the dikes emplaced in the Valles Marineris are not supplied by magma chambers underneath the Valles Marineris but rather from external magma sources related to the mantle plumes such as one in Syria Planum. Thus, Valles Marineris is unlikely a potential magma source for volcanic activity in Noctis Fossae.

Syria Planum formation started in the Noachian and lasted until the Early Hesperian due to extensional, graben-related tectonic activity (Tanaka and Davis, 1988; Baptista et al., 2008). To the north of Syria Planum, in Noctis Labyrinthus, Bistacchi et al. (2004) documented NNE–SSW (N015E) faults extending towards Noctis Fossae. We

Table 5
Summary characteristics of the tectono-volcanic provinces considered in this study as potential magma sources for the Noctis Fossae volcanism.

Province		Distance (km)	Dikes orientations	Youngest age (Ma)	T-V activity	Explosive volcanism
Valles Marineris		∼600	N100E[1]	400–200[3]	+	Coprates Chasma[3]
Tharsis Montes	Ascraeus Mons	∼720	N040E[2]	<200[4]	+	Ulysses Colles[5]
	Pavonis Mons	∼640	N040E[2]	<200[4]	+	
Syria Planum		∼670	N320E[2]	1600–200[4]	+	Not found

T-V – tectono-volcanic activity.
[1] (Mège et al., 2017).
[2] (Richardson et al., 2021).
[3] (Brož et al., 2017).
[4] (Hauber et al., 2011).
[5] (Brož and Hauber, 2012).

demonstrated that summit craters of volcanic cones in Noctis Fossae are aligned along the northwestern direction (N015W on average; Fig. 6). These orientations are slightly different compared to the initial stress regime in Noctis Labyrinthus and Syria Planum (N015E), probably due to the lateral component of displacement (see Section 5.2). In general, the same trend has been found by Richardson et al. (2021) for low-shield volcanic constructs within the Syria Planum (N040W). Hence, the summit alignments orientations might suggest a common magma source for Syria Planum and Noctis Fossae volcanoes controlled by the same tectonic regime. However, the ages of volcanoes are much different. The Syria Planum hosts hundreds of small volcanic cones forming at a timespan of billion years (Hauber et al., 2011; Richardson et al., 2012; Xiao et al., 2012). Xiao et al. (2012) interpreted most of these features as shield volcanoes formed during the Early Noachian (>4.0 Ga) with declining volcanism lasting to <3.5 Ga. However, Hauber et al. (2011) demonstrated that volcanic cones in Syria Planum exhibit various ages ranging from >1.6 Ga to ∼0.2 Ga. Richardson et al. (2012) distinguished three volcanic episodes, without any clear hiatus that span ∼900 Ma, beginning in the early Hesperian and ending in the Early Amazonian. In any case, these ages are largely inconsistent with the Noctis Fossae ages, spanning from ∼2000–300 Ma in the southern part to 126–55 Ma in the northernmost of the volcanic field. Thus, Syria Planum also seems to be unlikely a supplying region for the volcanism in Noctis Fossae.

The Tharsis bulge was likely formed by long-standing mantle plumes that lead to the formation of magma chambers and subsequent dike swarm activity (Kiefer, 2003; Plesa et al., 2018). This mantle plume tectonics subsequently formed a system of grabens radially emplaced around the Tharsis (Mège and Masson, 1996). In the southern part of Tharsis, there are three Tharsis Montes volcanoes such as Arsia Mons, Pavonis Mons, and Ascraeus Mons. Pavonis Mons and Ascraeus Mons are accompanied by several dozens of small volcanic cones and vents mainly representing widespread effusive plain-style volcanism, mostly on the southern and southeastern sides of the main edifices (Bleacher et al., 2007; Hauber et al., 2009; Richardson et al., 2021). Richardson et al. (2021) inferred that that within the most recent 500 Ma, deep-seated magma was present below the eastern flanks of the Tharsis Montes and that some of this magma erupted and built hundreds of small volcanoes in this region. Although the orientations of the Noctis Fossae summit alignments are not consistent with the general tectonic trends for Tharsis Montes vents (Richardson et al., 2021) (Table 5), the northwestern direction in Noctis Fossae could be subordinated to the radial dikes derived from the Ascraeus Mons or Pavonis Mons that control the aforementioned volcanoes. Therefore, the deep-seated magma reservoir of Tharsis Montes could be a possible magma source for the explosive volcanism in Noctis Fossae.

Although the difference between the eruptive style in the study area (explosive) and in the small volcanoes on the southeastern flanks of Tharsis Montes (effusive) is obvious, there is no straightforward explanation. The morphological observations of volcanic cones and association with the short-distance lava flows suggest relatively high viscosity of magma compared to typically low viscosity, plain-style lava flows of Tharsis (Hauber et al., 2011). However, due to the dust mantling of Noctis Fossae, there are no spectral insights on the composition of the magma. In general, the volcanism in Noctis Fossae is likely long-lived and lasted several hundred million years similar to what was previously highlighted by other authors for volcanic fields within Tharsis (Brož and Hauber, 2012; Krishnan and Kumar, 2021; Richardson et al., 2021). Using our spatio-temporal data together with the current state of knowledge, we suppose that the magma has migrated in dikes from the deep-seated magma reservoir related to the Tharsis Montes volcanism and then has accumulated forming a magma chamber beneath Noctis Fossae. The magma stagnated in a magma chamber beneath the Noctis Fossae might have differentiated to more silicic composition, stratified based on volatile content, assimilated volatiles-rich minerals of the hydrated crust (Scheller et al., 2021), and/or react with the groundwater resulting in explosive-style eruptions. However, to fully understand the origin of the explosive volcanism in Noctis Fossae and other volcanic fields on Mars, higher-resolution imagery, and mineralogical spectral data, or in situ data from rovers would be needed.

6. Conclusions

In this study, we found a cluster of 25 cones in Noctis Fossae belonging to the Tharsis Volcanic Province and interpreted them as a volcanic cone field associated with lava flows. The cones resemble terrestrial scoria cones and exhibit typical features expected for Martian scoria cones implying an explosive type of eruption. Various state of preservation among the cones suggests long-lived volcanism in the Noctis Fossae region. The formation of southern cones probably predates ∼300 Ma while the northern cones were likely formed between 126 and 55 Ma. The spatial arrangement of cones together with measurements of their summit orientation suggests that the Noctis Fossae volcanic field is controlled by the regional tectonic trends. The clusters of cones together with their summit crater alignments are mainly orientated along the N015W direction suggesting that initial tectonic stress (N015E) was slightly modified in time. The entire volcanic activity postdates the faulting because volcanic cones were also mapped inside and on the walls of the fossae. To date, the Noctis Fossae volcanic field is the youngest and the second documented scoria cones field within Tharsis.

Considering the potential magma source centers for the Noctis Fossae volcanic field, we analyzed three major structures in the vicinity of Noctis Fossae such as Valles Marineris, Syria Planum, and Tharsis Montes. None of the three tectono-volcanic regions discussed above can be excluded as a magma center for Noctis Fossae, however, most of the data (spatial distribution, summit crater orientations, cone ages) suggest that magmas were most likely derived by the system of dikes from the deep-seated magma reservoir emplaced beneath the Tharsis Montes region. This magma might have been accumulated in a magma chamber beneath Noctis Fossae to evolve to volatile-rich or more silicic (felsic) magma what could have resulted in an explosive eruption.

The identification of a new explosive volcanic field in Noctis Fossae provides evidence for the physiological diversity of Martian volcanism. These observations support recent hypotheses that explosive volcanism was more common in Tharsis than previously thought and indicate a need to further search for young volcanic fields of explosive origin on Mars. The still-growing morphological datasets of Martian scoria cones will help in more extensive mapping of these structures in the future. The detection of explosive-origin volcanic fields in dust-free areas may also enable the detection of hydrothermal mineral deposits (cf., Skok et al., 2010; Brož et al., 2017).

Declaration of Competing Interest

None.

Acknowledgments

This research is carried out within the framework of the European Funds Smart Growth (PO WER) project no. POWR.03.02.00−00−I027/17 held by the Adam Mickiewicz University in Poznan and the National Science Centre of Poland project OPUS19 no. 2020/37/B/ST10/01420 to J. Ciazela. Data have been processed with the MarsSI (marssi.univ-lyon1.fr) application founded by the European Union's Seventh Framework Program (FP7/2007-2013) (ERC Grant Agreement No. 280168). We thank W. Szczuciński for his thorough and insightful comments.

Appendix A. Supplementary data

Supplementary data to this article can be found online at https://doi.org/10.1016/j.icarus.2021.114851.

References

Anderson, R.C., Dohm, J.M., Haldemann, A.F.C., Hare, T.M., Baker, V.R., 2004. Tectonic histories between Alba Patera and Syria Planum, Mars. Icarus 171, 31–38. https://doi.org/10.1016/j.icarus.2004.04.018.

Baloga, S.M., Glaze, L.S., Bruno, B.C., 2007. Nearest-neighbor analysis of small features on Mars: applications to tumuli and rootless cones. J. Geophys. Res. 112, 1–17. https://doi.org/10.1029/2005JE002652.

Baptista, A.R., Mangold, N., Ansan, V., Baratoux, D., Lognonné, P., Alves, E.I., Williams, D.A., Bleacher, J.E., Masson, P., Neukum, G., 2008. A swarm of small shield volcanoes on Syria Planum. Mars. J. Geophys. Res. 113, 1–19. https://doi.org/10.1029/2007JE002945.

Baratoux, D., Toplis, M.J., Monnereau, M., Gasnault, O., 2011. Thermal history of Mars inferred from orbital geochemistry of volcanic provinces. Nature 472, 338–341. https://doi.org/10.1038/nature09903.

Baratoux, D., Toplis, M.J., Monnereau, M., Sautter, V., 2013. The petrological expression of early Mars volcanism, 118, pp. 59–64. https://doi.org/10.1029/2012JE004234.

Bemis, K.G., Ferencz, M., 2017. Morphometric analysis of scoria cones: the potential for inferring process from shape. Geol. Soc. Spec. Publ. 446, 61–100. https://doi.org/10.1144/SP446.9.

Bistacchi, N., Massironi, M., Baggio, P., 2004. Large-scale fault kinematic analysis in Noctis Labyrinthus (Mars). Planet. Space Sci. 52, 215–222. https://doi.org/10.1016/j.pss.2003.08.015.

Bleacher, J.E., Greeley, R., Williams, D.A., Cave, S.R., Neukum, G., 2007. Trends in effusive style at the Tharsis Montes, Mars, and implications for the development of the Tharsis province. J. Geophys. Res. Planets 112, 1–15. https://doi.org/10.1029/2006JE002873.

Bleacher, J.E., Glaze, L.S., Greeley, R., Hauber, E., Baloga, S.M., Sakimoto, S.E.H., Williams, D.A., Glotch, T.D., 2009. Spatial and alignment analyses for a field of small volcanic vents south of Pavonis Mons and implications for the Tharsis province. Mars. J. Volcanol. Geotherm. Res. 185, 96–102. https://doi.org/10.1016/j.jvolgeores.2009.04.008.

Bonali, F.L., Corazzato, C., 2011. Identifying rift zones on volcanoes: an example from La Réunion island, Indian Ocean. Bull. Volcanol. 73, 347–366. https://doi.org/10.1007/s00445-010-0416-1.

Brož, P., 2010. Plains Volcanism in Tharsis Region on Mars: Ages and Rheology of Eruption Products. Charles University in Prague.

Brož, P., Hauber, E., 2012. A unique volcanic field in Tharsis, Mars: pyroclastic cones as evidence for explosive eruptions. Icarus 218, 88–99. https://doi.org/10.1016/j.icarus.2011.11.030.

Brož, P., Hauber, E., 2013. Hydrovolcanic tuff rings and cones as indicators for phreatomagmatic explosive eruptions on Mars. J. Geophys. Res. Planets 118, 1656–1675. https://doi.org/10.1002/jgre.20120.

Brož, P., Čadek, O., Hauber, E., Rossi, A.P., 2014. Shape of scoria cones on Mars: insights from numerical modeling of ballistic pathways. Earth Planet. Sci. Lett. 406, 14–23. https://doi.org/10.1016/j.epsl.2014.09.002.

Brož, P., Čadek, O., Hauber, E., Rossi, A.P., 2015. Scoria cones on Mars: detailed investigation of morphometry based on high-resolution digital elevation models Petr. J. Geophys. Res. Planets 120, 1512–1527. https://doi.org/10.1002/2014JE004759.Received.

Brož, P., Hauber, E., Wray, J.J., Michael, G., 2017. Amazonian volcanism inside Valles Marineris on Mars. Earth Planet. Sci. Lett. 473, 122–130. https://doi.org/10.1016/j.epsl.2017.06.003.

Brož, P., Bernhardt, H., Conway, S.J., Parekh, R., 2021. An overview of explosive volcanism on Mars. J. Volcanol. Geotherm. Res. 409 https://doi.org/10.1016/j.jvolgeores.2020.107125.

Carr, M.H., 1974. Tectonism and volcanism of the Tharsis Region of Mars. J. Geophys. Res. 79, 3943–3949. https://doi.org/10.1029/JB079i026p03943.

Carr, M.H., 2007. The Surface of Mars. Cambridge University Press. https://doi.org/10.1017/CBO9780511536007.

Cassidy, M., Manga, M., Cashman, K., Bachmann, O., 2018. Controls on explosive-effusive volcanic eruption styles. Nat. Commun. 9 https://doi.org/10.1038/s41467-018-05293-3.

Christensen, P.R., Jakosky, B.M., Kieffer, H.H., Malin, M.C., McSween, H.Y., Nealson, K., Mehall, G.L., Silverman, S.H., Ferry, S., Caplinger, M., Ravine, M., 2004. The thermal emission imaging system (THEMIS) for the Mars 2001 odyssey mission. Space Sci. Rev. 110, 85–130. https://doi.org/10.1023/b:spac.0000021008.16305.94.

Crown, D.A., Greeley, R., 1993. Volcanic geology of Hadriaca Patera and the eastern Hellas region of Mars. J. Geophys. Res. 98, 3431–3451.

Dapremont, A.M., Wray, J.J., 2021. Igneous or mud volcanism on Mars? The case study of Hephaestus Fossae. J. Geophys. Res. Planets 126. https://doi.org/10.1029/2020JE006390.

Dehn, J., Sheridan, M.F., 1990. Cinder cones on the Earth, Moon, Mars, and Venus: a computer model. Lunar Planet. Sci. Conf. 270.

Dohm, J.M., Baker, V.R., Maruyama, S., Anderson, R.C., 2007. Traits and evolution of the Tharsis Superplume, Mars. Superplumes: Beyond Plate Tectonics. 523–536. https://doi.org/10.1007/978-1-4020-5750-2_17.

Dohrenwend, J.C., Survey, U.S.G., Road, M., Park, M., 1986. Degradation of quaternary cinder cones in the Cima volcanic field, Mojave Desert. California. Geol. Soc. Am. Bull. 97, 421–428. https://doi.org/10.1130/0016-7606(1986)97<421:DOQCCI>2.0.CO;2.

Dóniz, J., Romero, C., 2011. Gully erosion on cinder cones of Tenerife (Canary Islands, Spain). Phys. Geogr. 32, 139–160. https://doi.org/10.2747/0272-3646.32.2.139.

Edgett, K.S., 1997. Aeolian dune fields among volcanic landforms in a hyper-arid, desert environment: evidence of past explosive volcanism in the Tharsis region. Mars. Lunar Planet. Sci. Conf. 321.

Edgett, K.S., Lancaster, N., 1993. Volcaniclastic aeolian dunes: terrestrial examples and application to martian sands. J. Arid Environ. 25, 271–297. https://doi.org/10.1006/jare.1993.1061.

Fagents, S.A., Thordarson, T., 2009. Rootless volcanic cones in Iceland and on Mars. Geology of Mars 151–177. https://doi.org/10.1017/cbo9780511536014.007.

Favalli, M., Karátson, D., Mazzarini, F., Pareschi, M.T., Boschi, E., 2009. Morphometry of scoria cones located on a volcano flank: a case study from Mt. Etna (Italy), based on high-resolution LiDAR data. J. Volcanol. Geotherm. Res. 186, 320–330. https://doi.org/10.1016/j.jvolgeores.2009.07.011.

Fergason, R.L., Hare, T.M., Laura, J., 2018. HRSC and MOLA blended digital elevation model at 200m v2. [WWW document]. Astrogeology PDS annex. U.S. Geol. Surv. URL. http://bit.ly/HRSC_MOLA_Blend_v0.

Fodor, E., Németh, K., 2015. In: Spatter cone, in: Hargitai, H., Kereszturi, Á. (Ed.), Encyclopedia of Planetary Landforms. Springer, London, pp. 2028–2034. https://doi.org/10.1007/978-1-4614-3134-3.

Fornaciai, A., Favalli, M., Karátson, D., Tarquini, S., Boschi, E., 2012. Morphometry of scoria cones, and their relation to geodynamic setting: a DEM-based analysis. J. Volcanol. Geotherm. Res. 217–218, 56–72. https://doi.org/10.1016/j.jvolgeores.2011.12.012.

Frey, H., Lowry, B.L., Chase, S.A., 1979. Pseudocraters on Mars. J. Geophys. Res. 84, 8075. https://doi.org/10.1029/jb084ib14p08075.

Giordano, D., Russell, J.K., Dingwell, D.B., 2008. Viscosity of magmatic liquids: a model. Earth Planet. Sci. Lett. 271, 123–134. https://doi.org/10.1016/j.epsl.2008.03.038.

Greeley, R., Crown, D.A., 1990. Volcanic geology of Tyrrhena Patera. Mars. J. Geophys. Res. 95, 7133–7149. https://doi.org/10.1029/JB095iB05p07133.

Greeley, R., Fagents, S.A., 2001. Icelandic pseudocraters as analogs to some volcanic cones on Mars. J. Geophys. Res. E Planets 106, 20527–20546. https://doi.org/10.1029/2000JE001378.

Greeley, R., Spudis, D., 1981. Volcanism on Mars. Rev. Geophys. Sp. Phys. 19, 13–41.

Grosse, P., van Wyk De Vries, B., Euillades, P.A., Kervyn, M., Petrinovic, I.A., 2012. Systematic morphometric characterization of volcanic edifices using digital elevation models. Geomorphology 136, 114–131. https://doi.org/10.1016/j.geomorph.2011.06.001.

Hamilton, C.W., Fagents, S.A., Thordarson, T., 2011. Lava-ground ice interactions in Elysium Planitia, Mars: geomorphological and geospatial analysis of the Tartarus Colles cone groups. J. Geophys. Res. E Planets 116, 1–26. https://doi.org/10.1029/2010JE003657.

Harrison, K.P., Chapman, M.G., 2008. Evidence for ponding and catastrophic floods in central Valles Marineris, Mars. Icarus 198, 351–364. https://doi.org/10.1016/j.icarus.2008.08.003.

Hartmann, W.K., 2005. Martian Cratering 8: Isochron Refinement and the Chronology of Mars, 174, pp. 294–320. https://doi.org/10.1016/j.icarus.2004.11.023.

Hartmann, W.K., Daubar, I.J., 2017. Martian cratering 11. Utilizing decameter scale crater populations to study Martian history. Meteorit. Planet. Sci. 52, 493–510. https://doi.org/10.1111/maps.12807.

Hartmann, W.K., Neukum, G., 2001. Cratering choronology and the evolution of Mars. Space Sci. Rev. 96, 165–194. https://doi.org/10.1023/A:1011945222010.

Hasenaka, T., Carmichael, I.S.E., 1985. The cinder cones of Michoacán-Guanajuato, Central Mexico: their age, volume and distribution, and magma discharge rate. J. Volcanol. Geotherm. Res. 25, 105–124. https://doi.org/10.1016/0377-0273(85)90007-1.

Hauber, E., Bleacher, J., Gwinner, K., Williams, D., Greeley, R., 2009. The topography and morphology of low shields and associated landforms of plains volcanism in the Tharsis region of Mars. J. Volcanol. Geotherm. Res. 185, 69–95. https://doi.org/10.1016/j.jvolgeores.2009.04.015.

Hauber, E., Brož, P., Jagert, F., Jodowski, P., Platz, T., 2011. Very recent and wide-spread basaltic volcanism on Mars. Geophys. Res. Lett. 38, 1–5. https://doi.org/10.1029/2011GL047310.

Hickson, C., Spurgeon, T., Tilling, R., Adam, P., 2013. Factors influencing volcanic hazards and the morphology of volcanic landforms. In: Treatise on Geomorphology. Elsevier Ltd., pp. 219–242. https://doi.org/10.1016/B978-0-12-374739-6.00360-2

Hodges, C.A., Moore, H.J., 1979. The subglacial birth of Olympus Mons and its aureoles. J. Geophys. Res. 84, 8061–8073. https://doi.org/10.1029/JB084iB14p08061.

Hooper, D.M., Sheridan, M.F., 1998. Computer-simulation models of scoria cone degradation. J. Volcanol. Geotherm. Res. 83, 241–267. https://doi.org/10.1016/S0377-0273(98)00031-6.

Horvath, D.G., Moitra, P., Hamilton, C.W., Craddock, R.A., Andrews-hanna, J.C., 2021. Evidence for geologically recent explosive volcanism in Elysium. Icarus 365, 114499. https://doi.org/10.1016/j.icarus.2021.114499.

Huang, J., Xiao, L., 2014. Knobby terrain on ancient volcanoes as an indication of dominant early explosive volcanism on Mars. Geophys. Res. Lett. 41, 7019–7024. https://doi.org/10.1002/2014GL061779.Received.

Ivanov, B.A., 2001. Mars/moon cratering rate ratio estimates. Space Sci. Rev. 96, 87–104. https://doi.org/10.1023/A:1011941121102.

Johnson, J.R., Bell, J.F., Bender, S., Cloutis, E., Ehlmann, B., Fraeman, A., Gasnault, O., Maurice, S., Pinet, P., Thompson, L., Wellington, D., Wiens, R.C., 2018. Bagnold dunes campaign phase 2: visible/near-infrared reflectance spectroscopy of longitudinal Ripple Sands. Geophys. Res. Lett. 45, 9480–9487. https://doi.org/10.1029/2018GL079025.

Kereszturi, G., Németh, K., 2012. Structural and morphometric irregularities of eroded Pliocene scoria cones at the Bakony-Balaton Highland volcanic field, Hungary. Geomorphology 136, 45–58. https://doi.org/10.1016/j.geomorph.2011.08.005.

Keszthelyi, L., Jaeger, W., McEwen, A., Tornabene, L., Beyer, R.A., Dundas, C., Milazzo, M., 2008. High resolution imaging science experiment (HiRISE) images of volcanic terrains from the first 6 months of the Mars reconnaissance orbiter primary science phase. J. Geophys. Res. E Planets 113, 1–25. https://doi.org/10.1029/2007JE002968.

Kiefer, W.S., 2003. Melting in the martian mantle: Shergottite formation and implications for present-day mantle convection on Mars. Meteorit. Planet. Sci. 38, 1815–1832. https://doi.org/10.1111/j.1945-5100.2003.tb00017.x.

Kleinhans, M.G., Markies, H., De Vet, S.J., In't Veld, A.C., Postema, F.N., 2011. Static and dynamic angles of repose in loose granular materials under reduced gravity. J. Geophys. Res. E Planets 116, 1–13. https://doi.org/10.1029/2011JE003865.

Kneissl, T.A., Van Gasselt, S., Neukum, G., 2011. Map-projection-independent crater size-frequency determination in GIS environments — new software tool for ArcGIS. Planet. Space Sci. 59, 1243–1254. https://doi.org/10.1016/j.pss.2010.03.015.

Kremer, C.H., Mustard, J.F., Bramble, M.S., 2019. A widespread olivine-rich ash deposit on Mars. Geology 47, 677–681. https://doi.org/10.1130/G45563.1.

Krishnan, M.V., Kumar, P.S., 2021. Evidence for long-lived middle to late amazonian volcanism, tectonics and recent boulder fall. Lunar Planet. Sci. Conf. 1855.

Kumar, S.P., Krishna, N., Prasanna Lakshmi, K.J., Raghukanth, S.T.G., Dhabu, A., Platz, T., 2019. Recent seismicity in Valles Marineris, Mars: insights from young faults, landslides, boulder falls and possible mud volcanoes. Earth Planet. Sci. Lett. 505, 51–64. https://doi.org/10.1016/j.epsl.2018.10.008.

Lagain, A., Benedix, G.K., Servis, K., Baratoux, D., Doucet, L.S., 2021. The Tharsis mantle source of depleted shergottites revealed by 90 million impact craters. Nat. Commun. 12, 6352. https://doi.org/10.1038/s41467-021-26648-3.

Lanagan, P.D., McEwen, A.S., Keszthelyi, L.P., Thordarson, T., 2001. Rootless cones on Mars indicating the presence of shallow equatorial ground ice in recent times. Geophys. Res. Lett. 28, 2365–2367. https://doi.org/10.1029/2001GL012932.

Lesher, C.E., Spera, F.J., 2015. Thermodynamic and transport properties of silicate melts and magma. In: Sigurdsson, H., Houghton, B., Rymer, H., Stix, J., McNutt, S. (Eds.), Encyclopedia of Volcanoes. Elsevier, pp. 113–141.

Lucchitta, B.K., 1990. Young volcanic deposits in the Valles Marineris, Mars? Icarus 86, 476–509. https://doi.org/10.1016/0019-1035(90)90230-7.

Malin, M.C., Bell, J.F., Cantor, B.A., Caplinger, M.A., Calvin, W.M., Clancy, R.T., Edgett, K.S., Edwards, L., Haberle, R.M., James, P.B., Lee, S.W., Ravine, M.A., Thomas, P.C., Wolff, M.J., 2007. Context camera investigation on board the Mars reconnaissance orbiter. J. Geophys. Res. E Planets 112, 1–25. https://doi.org/10.1029/2006JE002808.

Mangold, N., Loizeau, D., Poulet, F., Ansan, V., Baratoux, D., LeMouelic, S., Bardintzeff, J.M., Platevoet, B., Toplis, M., Pinet, P., Masson, P., Bibring, J.P., Gondet, B., Langevin, Y., Neukum, G., 2010. Mineralogy of recent volcanic plains in the Tharsis region, Mars, and implications for platy-ridged flow composition. Earth Planet. Sci. Lett. 294, 440–450. https://doi.org/10.1016/j.epsl.2009.07.036.

Martin, U., Németh, K., 2006. How Strombolian is a "Strombolian" scoria cone? Some irregularities in scoria cone architecture from the Transmexican Volcanic Belt, near Volcán Ceburoco, (Mexico) and Al Haruj (Libya). J. Volcanol. Geotherm. Res. 155, 104–118. https://doi.org/10.1016/j.jvolgeores.2006.02.012.

Masson, P., 1977. Structure pattern analysis of the Noctis Labyrinthus-Valles Marineris regions of Mars. Icarus 62, 49–62. https://doi.org/10.1016/0019-1035(77)90120-8.

McEwen, A.S., Preblich, B.S., Turtle, E.P., Artemieva, N.A., Golombek, M.P., Hurst, M., Kirk, R.L., Burr, D.M., Christensen, P.R., 2005. The rayed crater Zunil and interpretations of small impact craters on Mars. Icarus 176, 351–381. https://doi.org/10.1016/j.icarus.2005.02.009.

McEwen, A.S., Eliason, E.M., Bergstrom, J.W., Bridges, N.T., Hansen, C.J., Delamere, W. A., Grant, J.A., Gulick, V.C., Herkenhoff, K.E., Keszthelyi, L., Kirk, R.L., Mellon, M.T., Squyres, S.W., Thomas, N., Weitz, C.M., 2007. Mars reconnaissance Orbiter's high resolution imaging science experiment (HiRISE). J. Geophys. Res. 112, 1–40. https://doi.org/10.1029/2005JE002605.

Mège, D., Masson, P., 1996. A plume tectonics model for the Tharsis province. Mars. Planet. Space Sci. 44, 1499–1546. https://doi.org/10.1016/S0032-0633(96)00113-4.

Mège, D., Gurgurewicz, J., Bourgeois, O., 2017. Deep dyke exposures in northern Valles Marineris highlight the significance of erosion in chasma genesis. European Planetary Science Congress. 5–6.

Meresse, S., Costard, F., Mangold, N., Masson, P., Neukum, G., 2008. Formation and evolution of the chaotic terrains by subsidence and magmatism: Hydraotes Chaos, Mars. Icarus 194, 487–500. https://doi.org/10.1016/j.icarus.2007.10.023.

Michael, G.G., 2013. Planetary surface dating from crater size – frequency distribution measurements : multiple resurfacing episodes and differential isochron fitting. Icarus 226, 885–890. https://doi.org/10.1016/j.icarus.2013.07.004.

Michael, G.G., Neukum, G., 2010. Planetary surface dating from crater size – frequency distribution measurements : partial resurfacing events and statistical age uncertainty. Earth Planet. Sci. Lett. 294, 223–229. https://doi.org/10.1016/j.epsl.2009.12.041.

Michael, G.G., Platz, T., Kneissl, T., Schmedemann, N., 2012. Planetary surface dating from crater size-frequency distribution measurements: spatial randomness and clustering. Icarus 218, 169–177. https://doi.org/10.1016/j.icarus.2011.11.033.

Michael, G.G., Walter, S.H.G., Kneissl, T., Zuschneid, W., Gross, C., Mcguire, P.C., Dumke, A., Schreiner, B., Van Gasselt, S., Gwinner, K., Jaumann, R., 2016. Systematic processing of Mars express HRSC panchromatic and colour image mosaics : image equalisation using an external brightness reference. Planet. Space Sci. 121, 18–26. https://doi.org/10.1016/j.pss.2015.12.002.

Moitra, P., Horvath, D.G., Andrews-Hanna, J.C., 2021. Investigating the roles of magmatic volatiles, ground ice and impact-triggering on a very recent and highly explosive volcanic eruption on Mars. Earth Planet. Sci. Lett. 567 https://doi.org/10.1016/j.epsl.2021.116986.

Moore, H.J., Ackerman, J.A., 1989. Martian and terrestrial lava flows. Lunar and Planetary Science Conference. 711–712.

Morris, C., 1982. Aureole deposits of the Martian volcano Olympus Mons. J. Geophys. Res. 87, 1164–1178.

Moufti, M.R., Németh, K., Murcia, H., Lindsay, J.M., El-Masry, N., 2013. Geosite of a steep lava spatter cone of the 1256 AD, Al Madinah eruption, Kingdom of Saudi Arabia. Cent. Eur. J. Geosci. 5, 189–195. https://doi.org/10.2478/s13533-012-0123-x.

Mouginis-Mark, P.J., Wilson, L., Zimbelman, J.R., 1988. Polygenic eruptions on Alba Patera. Mars. Bull. Volcanol. 50, 361–379. https://doi.org/10.1007/BF01050636.

Noguchi, R., Kurita, K., 2015. Unique characteristics of cones in central Elysium Planitia. Mars. Planet. Space Sci. 111, 44–54. https://doi.org/10.1016/j.pss.2015.03.007.

Parfitt, L., Wilson, L., 2008. Fundamentals of physical volcanology. Blackwell Science Ltd, Oxford. https://doi.org/10.1007/s00445-010-0352-0.

Pérez-López, R., Legrand, D., Garduño-Monroy, V.H., Rodríguez-Pascua, M.A., Giner-Robles, J.L., 2011. Scaling laws of the size-distribution of monogenetic volcanoes within the Michoacán-Guanajuato volcanic field (Mexico). J. Volcanol. Geotherm. Res. 201, 65–72. https://doi.org/10.1016/j.jvolgeores.2010.09.006.

Plesa, A.C., Padovan, S., Tosi, N., Breuer, D., Grott, M., Wieczorek, M.A., Spohn, T., Smrekar, S.E., Banerdt, W.B., 2018. The thermal state and interior structure of Mars. Geophys. Res. Lett. 45 https://doi.org/10.1029/2018GL080728, 12,198-12,209.

Plescia, J.B., 2000. Geology of the Uranius group volcanic constructs : Uranius Patera, Ceraunius Tholus, and Uranius Tholus, 396, pp. 376–396. https://doi.org/10.1006/icar.1999.6259.

Plescia, J.B., Saunders, R.S., 1982. Tectonic history of the Tharsis region. Mars. J. Geophys. Res. 87, 9775. https://doi.org/10.1029/jb087ib12p09775.

Porter, S.C., 1972. Distribution, morphology, and size frequency of cinder cones on Mauna kea Volcano. Hawaii. Geol. Soc. Am. Bull. 83, 3607–3612. https://doi.org/10.1130/0016-7606(1972)83.

Quantin-Nataf, C., Lozac, L., Thollot, P., Loizeau, D., Bultel, B., Fernando, J., Allemand, P., Dubuffet, F., Poulet, F., Ody, A., Clenet, H., Leyrat, C., Harrisson, S., 2018. MarsSI: Martian surface data processing information system. Planet. Space Sci. 150, 157–170. https://doi.org/10.1016/j.pss.2017.09.014.

Rampe, E.B., Lapotre, M.G.A., Bristow, T.F., Arvidson, R.E., Morris, R.V., Achilles, C.N., Weitz, C., Blake, D.F., Ming, D.W., Morrison, S.M., Vaniman, D.T., Chipera, S.J., Downs, R.T., Grotzinger, J.P., Hazen, R.M., Peretyazhko, T.S., Sutter, B., Tu, V., Yen, A.S., Horgan, B., Castle, N., Craig, P.I., Des Marais, D.J., Farmer, J., Gellert, R., McAdam, A.C., Morookian, J.M., Sarrazin, P.C., Treiman, A.H., 2018. Sand mineralogy within the Bagnold dunes, gale crater, as observed in situ and from orbit. Geophys. Res. Lett. 45, 9488–9497. https://doi.org/10.1029/2018GL079073.

Richardson, J.A., Bleacher, J.E., Glaze, L.S., 2012. The volcanic history of Syria Planum. Mars. J. Volcanol. Geotherm. Res. 252, 1–13. https://doi.org/10.1016/j.jvolgeores.2012.11.007.

Richardson, J.A., Bleacher, J.E., Connor, C.B., Glaze, L.S., 2021. Small volcanic vents of the Tharsis Volcanic Province. Mars. J. Geophys. Res. Planets 126. https://doi.org/10.1029/2020JE006620.

Robbins, S.J., Di Achille, G., Hynek, B.M., 2011. The volcanic history of Mars: high-resolution crater-based studies of the calderas of 20 volcanoes. Icarus 211, 1179–1203. https://doi.org/10.1016/j.icarus.2010.11.012.

Scheller, E.L., Ehlmann, B.L., Hu, R., Adams, D.J., Yung, Y.L., 2021. Long-term drying of Mars by sequestration of ocean-scale volumes of water in the crust. Science (80-.) 372, 56–62. https://doi.org/10.1126/science.abc7717.

Schonfeld, E., 1979. Origin of Valles Marineris. Lunar Planet. Sci. Conf. 3031–3038.

Skok, J.R., Mustard, J.F., Ehlmann, B.L., Milliken, R.E., Murchie, S.L., 2010. Silica deposits in the Nili Patera caldera on the Syrtis Major volcanic complex on Mars. Nat. Geosci. 3, 838–841. https://doi.org/10.1038/ngeo990.

Strong, M., Wolff, J., 2003. Compositional variations within scoria cones. Geology 31, 143–146. https://doi.org/10.1130/0091-7613(2003)031<0143:CVWSC>2.0.CO;2.

Tanaka, K.L., Davis, P.A., 1988. Tectonic history of the Syria Planum province of Mars. J. Geophys. Res. 93, 893–917. https://doi.org/10.1029/jb093ib12p14893.

Tanaka, K.L., Robbins, S.J., Fortezzo, C.M., Skinner, J.A., Hare, T.M., 2014. The digital global geologic map of Mars: chronostratigraphic ages, topographic and crater morphologic characteristics, and updated resurfacing history. Planet. Space Sci. 95, 11–24. https://doi.org/10.1016/j.pss.2013.03.006.

Toulmin, P., Baird, A.K., Clark, B.C., Keil, K., Rose, H.J., Christian, R.P., Evans, P.H., Kelliher, W.C., 1977. Geochemical and mineralogical interpretation of the Viking inorganic chemical results. J. Geophys. Res. 82, 4625–4634.

Wadge, G., Lopes, R.M.C., 1991. The lobes of lava flows on earth and Olympus Mons, Mars. Bull. Volcanol. 54, 10–24. https://doi.org/10.1007/BF00278203.

Werner, S.C., 2009. The global martian volcanic evolutionary history. Icarus 201, 44–68. https://doi.org/10.1016/j.icarus.2008.12.019.

Wilhelms, D.E., Squyres, S.W., 1984. The Martian hemispheric dichotomy may be due to a giant impact. Nature 309, 138–140. https://doi.org/10.1038/309138a0.

Williams, J.-P., 2018. Modification of the Martian surface by impact cratering. In: Soare, R.J., Conway, S.J., Clifford, S.M. (Eds.), Dynamic Mars. Elsevier, pp. 361–386. https://doi.org/10.1016/B978-0-12-813018-6.00012-1.

Williams, D.A., Greeley, R., Fergason, R.L., Kuzmin, R., Mccord, T.B., Pinet, P., Combe, J., Head, J.W., Xiao, L., Manfredi, L., Baratoux, D., Plaut, J.J., Raitala, J., Neukum, G., Team, H.C, 2009. The Circum-Hellas Volcanic Province, Mars: overview. Planet. Space Sci. 57, 895–916. https://doi.org/10.1016/j.pss.2008.08.010.

Williams, N.R., James, F.B., Christensen, P.R., Farmer, J.D., 2015. Evidence for an explosive origin of central pit craters on Mars. Icarus 252, 175–185. https://doi.org/10.1016/j.icarus.2014.12.005.

Wilson, L., Head, J.W., 1994. Mars: review and analysis of volcanic erupiton theory and relationships to observed landforms. Rev. Geophys. 32, 221–263. https://doi.org/10.1029/94RG01113.

Wilson, L., Head, J.W., 2002. Tharsis-radial graben systems as the surface manifestation of plume-related dike intrusion complexes: models and implications. J. Geophys. Res. 107 https://doi.org/10.1029/2001JE001593.

Wilson, L., Head, J.W., 2007. Explosive volcanic eruptions on Mars: tephra and accretionary lapilli formation, dispersal and recognition in the geologic record. J. Volcanol. Geotherm. Res. 163, 83–97. https://doi.org/10.1016/j.jvolgeores.2007.03.007.

Wise, D.U., Golombek, M.P., McGill, G.E., 1979. Tharsis Province of Mars: geologic sequence, geometry, and a deformation mechanism. Icarus 38, 456–472. https://doi.org/10.1016/0019-1035(79)90200-8.

Witbeck, N.E., Tanaka, K.L., Scott, D.H., 1991. Geologic map of the Valles Marineris region, Mars. U.S Geol. Surv. https://doi.org/10.3133/i2010.

Wood, C.A., 1979. Monogenetic volcanoes of the terrestrial planets. In: Lunar and Planetary Science Conference, pp. 2815–2840.

Wood, C.A., 1980. Morphometric evolution of cinder cones. J. Volcanol. Geotherm. Res. 7, 387–413. https://doi.org/10.1016/0377-0273(80)90040-2.

Xiao, L., Huang, J., Christensen, P.R., Greeley, R., Williams, D.A., Zhao, J., He, Q., 2012. Ancient volcanism and its implication for thermal evolution of Mars. Earth Planet. Sci. Lett. 323–324, 9–18. https://doi.org/10.1016/j.epsl.2012.01.027.

Zaidi, F.K., Mukhopadhyay, M., 2015. Morphometric analysis of the scoria cones and drainage pattern for the Quaternary and older volcanic fields in parts of the large Igneous Province (LIP), Saudi Arabia. J. African Earth Sci. 110, 1–13. https://doi.org/10.1016/j.jafrearsci.2015.06.010.

SUPPLEMENTARY MATERIAL

Explosive volcanism in Noctis Fossae on Mars

B. Pieterek[1], M. Laban[2], J. Ciążela[2], A. Muszyński[1]

[1] Institute of Geology, Adam Mickiewicz University, ul. Bogumila Krygowskiego 12, 61−680 Poznan, Poland
[2] Institute of Geological Sciences, Polish Academy of Sciences, Research Centre in Wrocław, Podwale 75, 50–449 Wroclaw, Poland

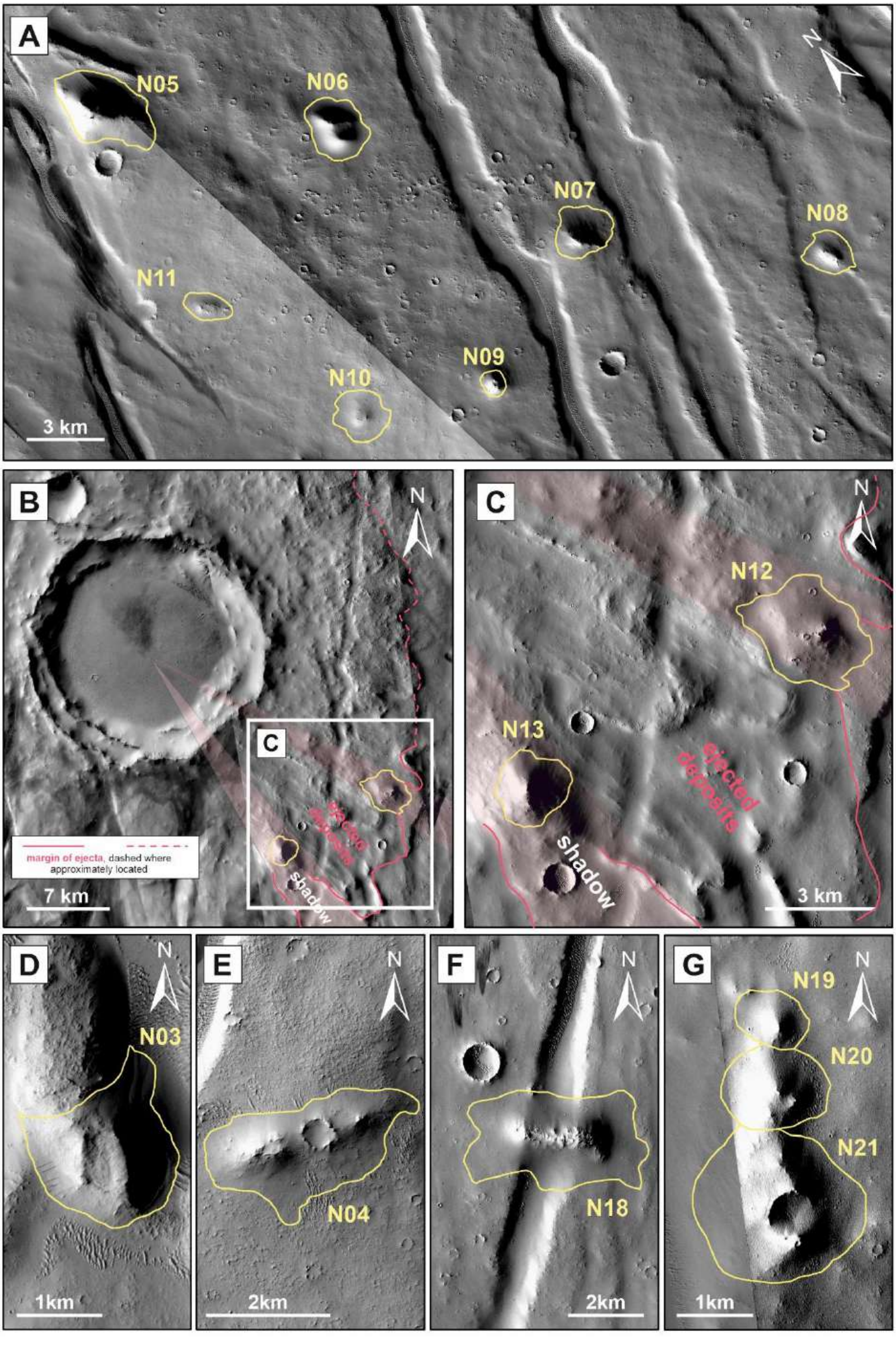
A
N
N05
N06
N07
N08
N11
N09
N10
3 km
B
N
C
ejected deposits
shadow
margin of ejecta, dashed where approximately located
7 km
C
N
N12
N13
ejected deposits
shadow
3 km
D
N
N03
1km
E
N
N04
2km
F
N
N18
2km
G
N
N19
N20
N21
1km

Fig. S1 Examples of scoria cones identified in the southern and central part of the Noctis Fossae volcanic field. **(A)** The cluster of scoria cones located in the central part of the field that presents various states of degradation and sizes (for more details see Table 2). CTX images G06_020445_1791_XN_00S098W and G15_024269_1780_XN_02S099W. **(B & C)** The 18-km-large impact crater in the central part of the studied area whose ejecta likely affected two cones (N12 and N13) indicating that scoria cones emplaced within the fossae region had been formed before ~300 Ma (Table 4). Analyzing the ejected deposits, we found that behind the cones N12 and N13 there is no ejecta suggesting that cones constituted morphological obstacles that likely stopped the ejected material during impact. CTX images G05_020089_1795_XN_00S099W and B19_016898_1805_XN_00N100W **(D-G)** Examples of the identified cones within fossae's part of the Noctis Fossae volcanic field. Except typical conical shapes with high-angle slopes and well detectable summit craters (D&G), we found highly eroded cones showing elongated shapes with outcropping hard rocks (E–F) that likely constitute relicts of dikes that fed these volcanoes. For these figures, we used CTX images including: **(D)** F04_037508_1798_XN_00S098W, **(E)** B20_017399_1773_XN_02S098W, **(F)** B03_010885_1782_XI_01S099W, and **(G)** B03_010885_1782_XI_01S099W, B09_013008_1770_XN_03S099W.

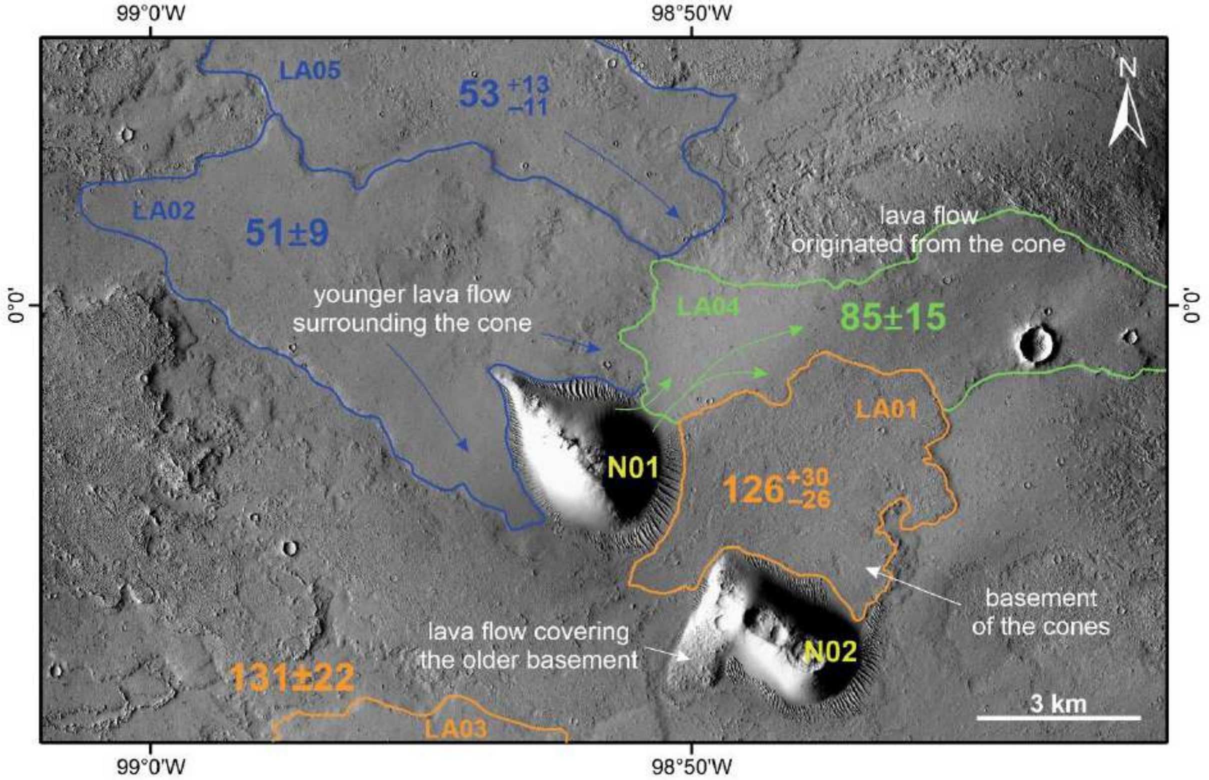

Fig. S2 The stratigraphic relationship between the lava flows and the northernmost volcanic cones (N01 and N02). The lava flows (orange) that show the oldest ages of ~126 Ma and ~131 Ma likely constituted the basement for the formation of the cones. Then, the old basement was covered by younger lava flow (green) likely originated from the cone's volcanic activity (based on the structural relationship confirmed by dating). In the last ~50 Ma, these cones were likely surrounded by the youngest lava flows (blue) derived from the northwest direction. All ages are in My. CTX image F04_037508_1798_XN_00S098W.

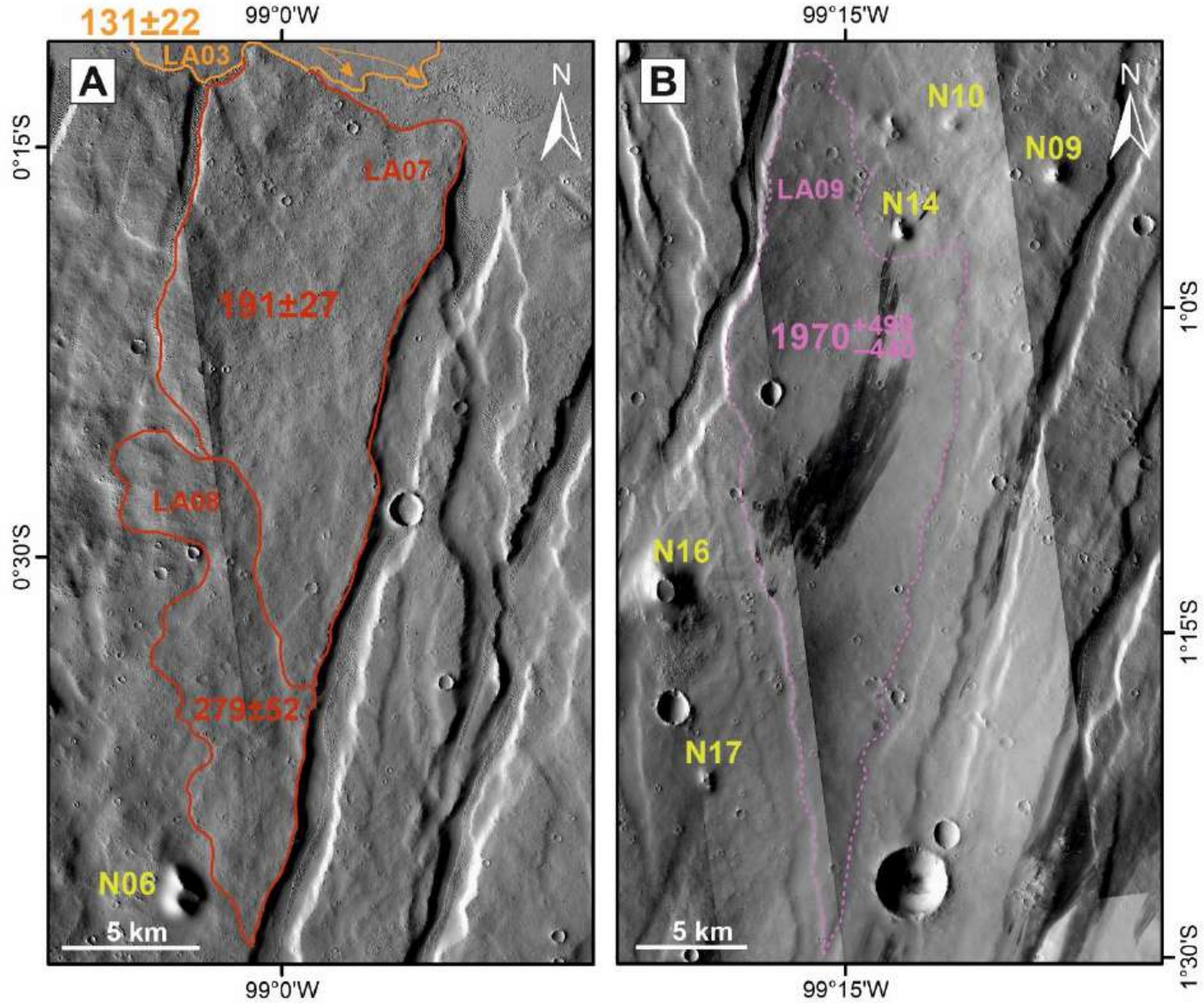

Fig. S3 The lava flows dated in the older fossae region of the Noctis Fossae volcanic field using CTX images. The boundaries of lava flows dated in this study have been distinguished based on the geometry of the lava flows expressed in their morphological features. Lava flows LA07 and LA08 located in the northernmost part of the fossae **(A)** revealed younger ages (Late Amazonian) compared to the lava flow (LA09) located to the southern part **(B)** of the studied volcanic field.

Publikacja 3

Ciążela, J., Bakala, J., Kowalinski, M., Płocieniak, S., Zalewska, N., **Pieterek, B.,** Mrozek, T., Ciążela, M., Paslawski, G., Steslicki, M., Szaforz, Z., Barylak, J., Kuzaj, M., Maturilli, A., Helbert, J., Muszyński, A., Rataj, M., Gburek, S., Józefowicz, M., Marciniak, D. (2022). Concept and design of Martian far-IR ORE Spectrometer (MIRORES). *Remote Sensing, 14, 2799.* https://doi.org/10.3390/rs14122799 (IF_{2022} = **5.349,** pkt. MEiN **= 100**)

remote sensing

MDPI

Article

Concept and Design of Martian Far-IR ORE Spectrometer (MIRORES)

Jakub Ciazela [1], Jaroslaw Bakala [2], Miroslaw Kowalinski [2,*], Stefan Plocieniak [2], Natalia Zalewska [2], Bartosz Pieterek [3], Tomasz Mrozek [2], Marta Ciazela [1], Grzegorz Paslawski [1], Marek Steslicki [2], Zaneta Szaforz [2], Jaromir Barylak [2], Mateusz Kuzaj [4], Alessandro Maturilli [5], Joern Helbert [5], Andrzej Muszynski [3], Miroslaw Rataj [2], Szymon Gburek [2], Mateusz Jozefowicz [6] and Dariusz Marciniak [1]

[1] Research Centre in Wrocław, Institute of Geological Sciences, Polish Academy of Sciences, Podwale 75, 50-449 Wrocław, Poland; j.ciazela@twarda.pan.pl (J.C.); mc@cbk.pan.wroc.pl (M.C.); g.paslawski@twarda.pan.pl (G.P.); dariusz.marciniak@twarda.pan.pl (D.M.)

[2] Space Research Centre, Polish Academy of Sciences, ul. Bartycka 18A, 00-716 Warsaw, Poland; jb@cbk.pan.wroc.pl (J.B.); sp@cbk.pan.wroc.pl (S.P.); natalia@cbk.waw.pl (N.Z.); tmrozek@cbk.pan.wroc.pl (T.M.); sm@cbk.pan.wroc.pl (M.S.); zs@cbk.pan.wroc.pl (Z.S.); jbarylak@cbk.pan.wroc.pl (J.B.); rataj@cbk.waw.pl (M.R.); sg@cbk.pan.wroc.pl (S.G.)

[3] Institute of Geology, Adam Mickiewicz University, ul. Bogumiła Krygowskiego 12, 61-680 Poznań, Poland; barpie@amu.edu.pl (B.P.); anmu@amu.edu.pl (A.M.)

[4] Faculty of Fundamental Problems of Technology, Wroclaw University of Science and Technology, Wybrzeże Stanisława Wyspiańskiego 27, 50-370 Wrocław, Poland; 236777@student.pwr.edu.pl

[5] Institut für Planetenforschung, Deutsches Zentrum für Luft- und Raumfahrt (DLR), Rutherfordstrasse 2, D-12489 Berlin, Germany; alessandro.maturilli@dlr.de (A.M.); joern.helbert@dlr.de (J.H.)

[6] European Space Foundation, Grodzka 42/1, 31-044 Kraków, Poland; m.jozefowicz@spacefdn.com

* Correspondence: mk@cbk.pan.wroc.pl

Citation: Ciazela, J.; Bakala, J.; Kowalinski, M.; Plocieniak, S.; Zalewska, N.; Pieterek, B.; Mrozek, T.; Ciazela, M.; Paslawski, G.; Steslicki, M.; et al. Concept and Design of Martian Far-IR ORE Spectrometer (MIRORES). *Remote Sens.* **2022**, *14*, 2799. https://doi.org/10.3390/rs14122799

Academic Editor: Louis Scuderi

Received: 28 April 2022
Accepted: 29 May 2022
Published: 10 June 2022

Abstract: Sulfide ores are a major source of noble (Au, Ag, and Pt) and base (Cu, Pb, Zn, Sn, Co, Ni, etc.) metals and will, therefore, be vital for the self-sustainment of future Mars colonies. Martian meteorites are rich in sulfides, which is reflected in recent findings for surface Martian rocks analyzed by the Spirit and Curiosity rovers. However, the only high-resolution (18 m/pixel) infrared (IR) spectrometer orbiting Mars, the Compact Reconnaissance Imaging Spectrometer for Mars (CRISM), onboard the Mars Reconnaissance Orbiter (MRO), is not well-suited for detecting sulfides on the Martian surface. Spectral interference with silicates impedes sulfide detection in the 0.4–3.9 μm CRISM range. In contrast, at least three common hydrothermal sulfides on Earth and Mars (pyrite, chalcopyrite, marcasite) have prominent absorption peaks in a narrow far-IR (FIR) wavelength range of 23–28 μm. Identifying the global distribution and chemical composition of sulfide ore deposits would help in choosing useful targets for future Mars exploration missions. Therefore, we have designed a new instrument suitable for measuring sulfides in the FIR range called the Martian far-IR Ore Spectrometer (MIRORES). MIRORES will measure radiation in six narrow bands (~0.3 μm in width), including three bands centered on the sulfide absorption bands (23.2, 24.3 and 27.6 μm), two reference bands (21.5 and 26.1) and one band for clinopyroxene interference (29.0 μm). Focusing on sulfides only will make it possible to adapt the instrument size (32 × 32 × 42 cm) and mass (<10 kg) to common microsatellite requirements. The biggest challenges related to this design are: (1) the small field of view conditioned by the high resolution required for such a study (<20 m/pixel), which, in limited space, can only be achieved by the use of the Cassegrain optical system; and (2) a relatively stable measurement temperature to maintain radiometric accuracy and enable precise calibration.

Keywords: sulfides; ore minerals; Mars; microsatellite; far-infrared spectroscopy

1. Introduction

In 2001, the European Space Agency (ESA) created the Aurora program aiming at a human mission to Mars in 2033 [1]. Despite a seven-year delay in the implementation of this program, ESA has successfully launched the first of two preparatory flagship missions (Exobiology on Mars (ExoMars)) and started activities related to the second mission (Mars Sample Return (MSR)). The MSR mission should be directly followed by the human mission and is intended to be a concerted effort of all humanity, organized together with NASA, the Japan Aerospace Exploration Agency (JAXA), the Indian Space Research Organization (ISRO), and the Russian Roscosmos [2,3].

Among the four strategic resources envisaged during the human stage of Solar System exploration, after water and propellants, ESA has listed base metals (e.g., Fe, Ti, Cu) and noble metals (e.g., platinum group elements, Au, Ag) [4]. Some chalcophile and siderophile metals are expected to be vital for the future colonization of Mars, and those used as conductors in electronic devices such as Cu, Ag, and Au, will be especially important. The key metals will have to be extracted in situ as flights between Earth and Mars are feasible only in a narrow time window of 50–150 days before Mars and Earth are in opposition, which only occurs every two years. Chalcophile and siderophile metals are hosted mostly in sulfides and oxides, and occasionally in platinum-group metal (PGM) minerals and native metals, which are all major sources of most noble metals (Au, Ag, Pt, and Pd) and base metals (Fe, Ti, V, Cr, Cu, Pb, Zn, Sn, Co, Ni, etc.) on Earth [5]. Among these, sulfides are the most important group of ore minerals [6] and are especially crucial for Cu, Ag, and Au.

Despite the lack of direct evidence, sulfide ore deposits are predicted to be present on Mars [7–10]. Rover data along with geochemical modeling suggest the presence of pyrite (FeS_2: cubic crystal system), marcasite (FeS_2: orthorhombic crystal system), and pyrrhotite ($Fe_{1\text{-}x}S$) at the Martian surface [11–13]. Furthermore, studies of Martian meteorites [14,15] show that the Martian crust is significantly enriched in chalcophile (sulfide-loving) elements compared to the Martian mantle. Martian meteorites host a variety of magmatic and hydrothermal sulfides [16–18], matching those from the sulfide ores on Earth.

To date, however, it has been difficult to localize ore-forming minerals on Mars based on the available remote-sensing instruments such as the Compact Reconnaissance Imaging Spectrometer for Mars (CRISM; operating in a wavelength range of 0.4–3.9 µm), launched in 2005 on the Mars Reconnaissance Orbiter (MRO); the Observatoire pour la Minéralogie, l'Eau, les Glaces et l'Activité (OMEGA; 0.4–5.1 µm) and the Planetary Fourier Spectrometer (PFS; 1.3–45 µm), launched on Mars Express (MEX) in 200; or the Thermal Emission Spectrometer (TES; 0.3–2.9 and 6–50 µm), launched on Mars Global Surveyor in 1996. The mineral spectra of CRISM/MRO allow for a thorough mineral interpretation of investigated areas with a resolution of ~18 m/pixel, being one order of magnitude higher than the resolution of ~300 m/pixel provided previously by OMEGA/MEX [19]. However, although major sulfides have been found by rovers on the Mars surface, and their spectra are available through the USA Geological Survey (USGS) spectral library (https://speclab.cr.usgs.gov/spectral-lib.html, accessed on 27 April 2022), the weak spectral features of sulfides in the near-infrared (NIR) and interference with silicates impede sulfide detection in the NIR range available from CRISM. For example, pyrite exhibits only a broad shoulder just beyond 1 µm which, in addition, interferes with a similar shoulder displayed by clinopyroxene (Figure 1) [20]. This is crucial, as clinopyroxene is one of the several most abundant minerals on the Mars surface [21,22].

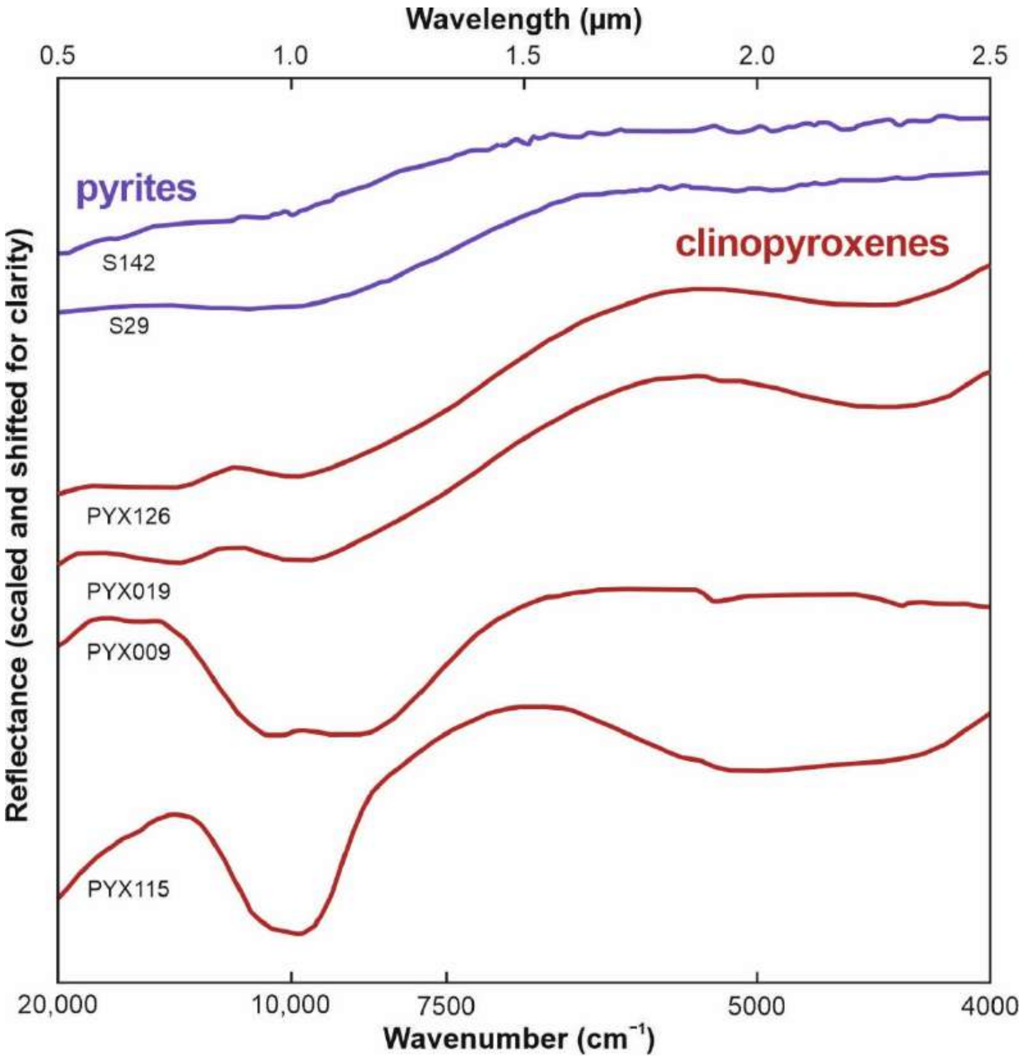

Figure 1. Near-infrared (NIR) spectra of pyrites S142 and S29 compared to those of clinopyroxenes PYX126, PYX019, PYX009 and PYX115, which are all described by Horgan et al. [20]. Note the lack of distinct spectral features in pyrites and their similarity to the NIR spectra of some clinopyroxenes. Considering the low pyrite abundances compared to those of clinopyroxene, pyrite is difficult to observe in the NIR range. The y axis has no numerical scale as the plots are shifted for clarity.

By contrast, the three most common hydrothermal sulfides on Earth and Mars (i.e., pyrite, chalcopyrite, and marcasite) possess prominent absorption bands in a narrow wavelength range of 23–28 μm [23–26]. The case is similar for pyrrhotite, troilite, and pentlandite [24], which are the most common magmatic sulfides in the Martian meteorites [27,28], even if they are less common in the context of large ore deposits. Importantly, the far-infrared (FIR) spectral features of the abovementioned sulfides have no significant interferences with rock-forming minerals in contrast to the currently available NIR range. The NIR spectral features of sulfides are lost in the spectral features of ubiquitous silicates including orthopyroxene, clinopyroxene, olivine, and plagioclase. Quartz may also occur locally on Mars [29] and trigonal quartz shows one of its minor peaks at 401 cm^{-1} (24.9 μm) [30], close to the pyrite peak, which is, however, beyond the measured pyrite band at 409–414 cm^{-1} (24.15–24.45 μm).

Although the PFS/MEX and TES/MGS cover the FIR spectral range, their spatial resolution of ~10 km and ~3 km, respectively, are not sufficient to search for ore deposits (Figure 2), which normally cover much smaller areas (up to hundreds of meters). Therefore, we designed a relatively inexpensive and simple Martian far-IR ORE Spectrometer

(MIRORES) based on pyroelectric detectors measuring six narrow (~0.3 µm) spectral bands obtained with diffraction grating, including three main bands centered at 23.2 µm (431 cm^{-1}), 24.3 µm (411.5 cm^{-1}), and 27.6 µm (362 cm^{-1}), two reference bands centered at 21.5 µm (465 cm^{-1}) and 26.1 µm (383 cm^{-1}), as well as one band for the interference with clinopyroxene at 29.0 µm (345 cm^{-1}). Measuring only six bands minimizes the required instrument dimensions to microsatellite size (32 × 32 × 42 cm) and mass (<10 kg). Although infrared spectroscopy methods have traditionally focused on the Earth atmospheric windows (3–5 µm and 8–14 µm), in recent years there has been increasing interest in longer wavelengths stimulated by space applications [31]. The largest challenge related to our design is, however, the small field of view conditioned by the high resolution we require (<20 m/pixel), which, in limited space, can only be achieved by the use of the Cassegrain optical system. Although it is being prepared for a Martian mission, our instrument may be adapted to measure sulfide ores on the Moon or large asteroids.

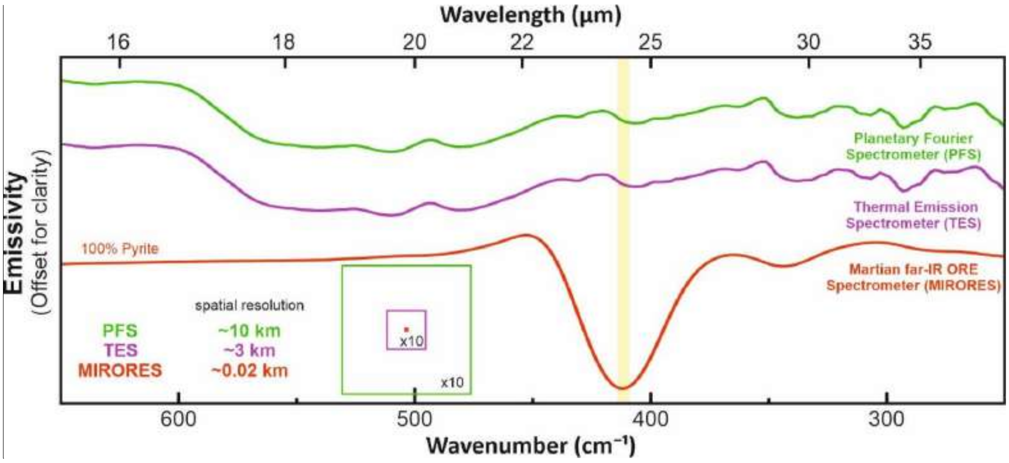

Figure 2. Simulation of observed emissivity spectra from 20 m × 20 m field covered by pyrite and surrounded by infinite area of basalts with shergottitic composition (see Section 3) as recorded by the Planetary Fourier Spectrometer (PFS), Thermal Emission Spectrometer (TES), and our MIRORES spectrometer. The simulations show that the orebodies similar in size to those on Earth would be impossible to detect with the far-IR spectrometers currently orbiting Mars due to the low spatial resolution of the spectrometers (see the bottom left corner of the figure).

2. Spectral Ranges and Interferences

The instrument will measure the FIR spectra of the Martian surface with the key detectors collecting signals from three narrow bands between 23 and 28 µm, where pyrite (24.3 µm = 412 cm^{-1}), marcasite (23.2 µm = 431 cm^{-1} on the slope), and chalcopyrite (27.6 µm = 362 cm^{-1}) show their main absorption lines. Three additional side detectors collect reference signals from narrow bands centered at 21.5, 26.1 and 29.0 µm (465, 383 and 345 cm^{-1}), where sulfides show no spectral features. However, the radiance received by the detectors depends on many factors, including solar geometry and slope inclination, which need to be normalized. This can be overcome by applying the band ratios of the signals received from the main detectors to the reference signals interpolated from the reference detectors. This will reduce the solar geometry and topographic effects on the remotely sensed data and is widely applied in ore prospecting with Landsat 8 and ASTER spectral bands on Earth [32]. Measurements in the FIR spectral range have two major advantages: (1) limited atmospheric interferences (Figures 3 and 4), and (2) strong absorption features of sulfides (Figure 5A) compared to common silicates (Figure 5B).

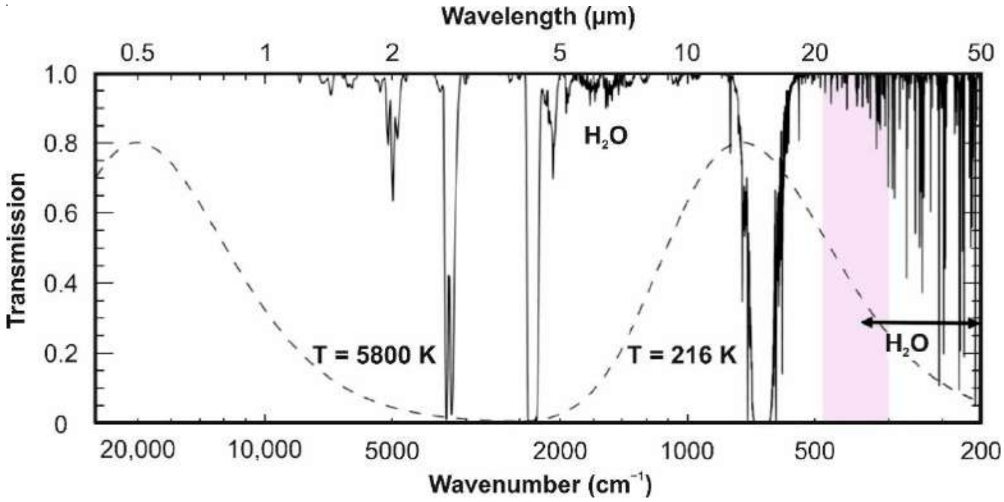

Figure 3. Synthetic infrared transmission spectrum for the atmosphere of Mars (clear of dust and aerosols), calculated assuming temperature structure and composition from the COSPAR Reference Atmosphere for Mars. The dashed lines show blackbody emission curves for temperatures of 5800 and 216 K, representative of the Sun and the Martian surface, respectively. Note the excellent atmospheric transmission in our target range of 21–30 µm (pink field). Modified from [33]. © IOP Publishing. Reproduced with permission. All rights reserved.

The Martian atmosphere is composed of CO_2 (96 vol.%), N_2 (1.9 vol.%), Ar (1.9 vol.%), and trace amounts of other gases including O_2, H_2O, and O_3 [33]. CO_2 shows a strong vibration–rotation absorption band centered around 15 µm (Figure 3), in which surface measurements on Mars are impossible, but pure CO_2 absorbs relatively little beyond that band. H_2O, which is a strong absorber on Earth typically containing ~40 kg·m^{-2} in the atmospheric column, is scarce on Mars with only 0.01–0.1 kg·m^{-2}. Although H_2O is not an issue in our target range of 23–28 µm, it may become a significant absorber at >30 µm (Figure 3) and selected lines <30 µm (Figure 4). On the whole, however, the transmittance of the Martian atmosphere in the FIR range is significantly higher than that of the Earth atmosphere (Figure 3). This is not the case only when larger amounts of dust are present in the Martian atmosphere during seasonal dust storms, which could then hinder our measurements. In normal conditions, dust opacity is only ~0.1 [34] and the absorption features of dust are weak in our target spectral range of 20–30 µm [35].

Considering the second advantage, the spectral features of sulfides in the FIR range are much stronger than the spectral features of any of the common Martian silicates known from the most abundant Martian meteorites, i.e., shergottites; that is, olivines, clinopyroxenes, orthopyroxenes, and plagioclase (Figures 4 and 5) [21]. This is a major advantage compared to the NIR range, where sulfides are nearly indistinguishable from pyroxenes (Figure 1). Sulfates, which are also ubiquitous on the surface of Mars, especially in water-rich environments [22,36,37], do not interfere with sulfides either (Figures 5C and 6B). Akaganeite, however, shows a peak centered at 414 cm^{-1} (24.2 µm) [38], which is close to pyrite (see Supplementary Figure S1A in Supplementary Material 1). Yet this is a rare mineral believed to form on Earth and Mars as an alteration of pyrrhotite [39]. The Curiosity rover detected akaganeite (as a minor component, <1.7 wt.%) only in samples where pyrrhotites (also minor, ~1 wt.%) were present, suggesting a genetic link between the two phases [13]. Therefore, the presence of akaganeite even increases our chances of finding sulfide mineralization. The case for some arsenides may be similar; for example, mimetite (418 cm^{-1} = 23.9 µm) [38], which occurs most of all in oxidation zones of metallic ores [40]. Hematite, which is also an ore mineral but is probably more common than sulfides on Mars [41], has its peak at 467 cm^{-1} (21.4 µm), far from the sulfide peaks (Supplementary Figure S1A). K-rich alkali feldspars, common in granites on Earth, such as microcline with a peak at 413 cm^{-1} (24.2 µm), would be more problematic for sulfide detection (see

Supplementary Figure S1C in Supplementary Material 1). These, however, even if not weathered to clay minerals, are associated with felsic silica-rich evolved magmas, which are rare in the recent history of Mars [41,42]. Among common secondary silicates, the only mineral interfering with sulfides may be prehnite (see Supplementary Figure S1B in Supplementary Material 1), which occurs on Mars [43–46]. Prehnite shows a weak absorption peak centered at 420 cm^{-1} (23.8 μm) near the pyrite peak and, therefore, larger amounts of prehnite could mimic a signal of smaller amounts of pyrite. For larger sulfide concentrations (>20%), to which MIRORES is dedicated, its potential interference with pyrite is nearly negligible. Similar could be the case for carbonates, which may constitute up to 2–5 wt.% of martian dust [47]. Magnesium-bearing carbonates, magnesite and dolomite, show very broad but relatively weak absorption features overlapping sulfides. In addition, these features are so broad that they extend to the reference detectors and therefore are easily distinguishable from sulfides (Figure 6C).

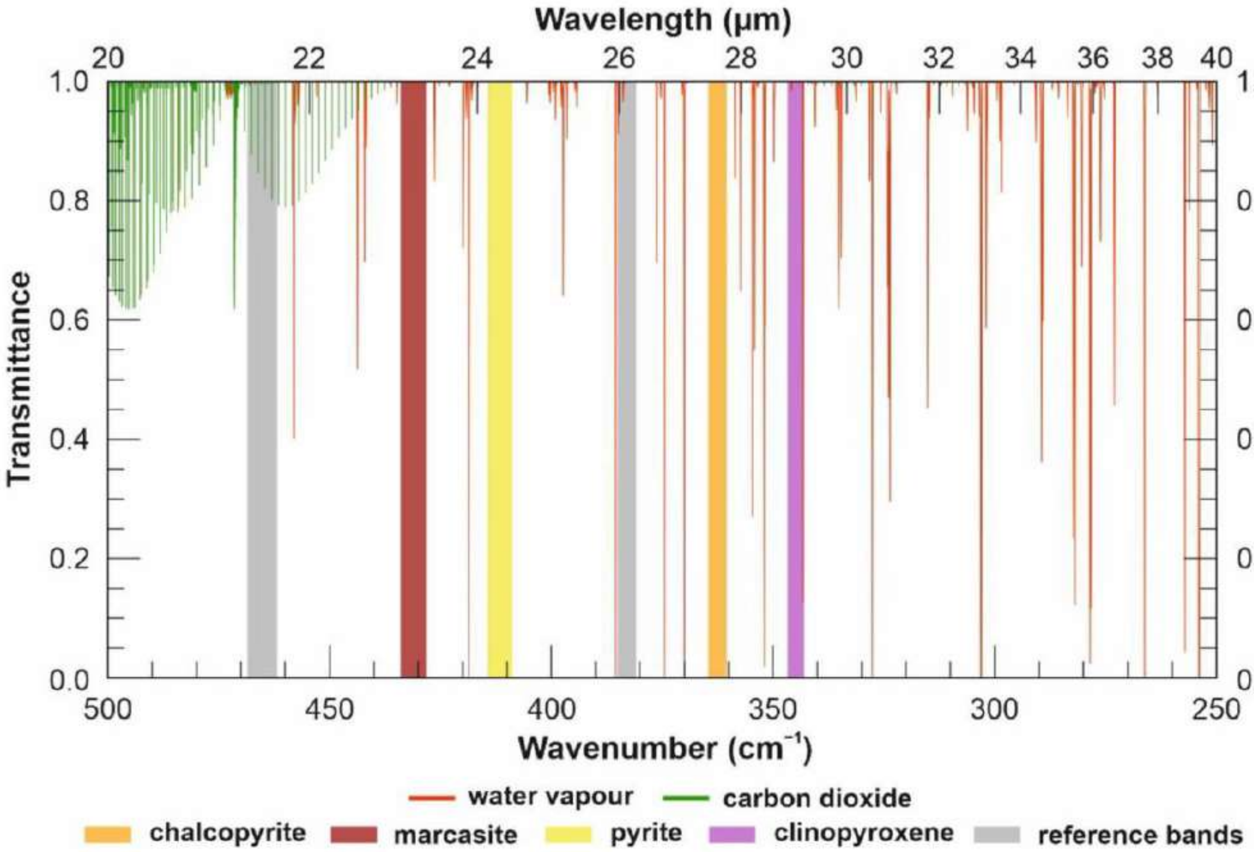

Figure 4. Exact positions of H_2O (red) and CO_2 (green) lines in the wavelength range covered by MIRORES. The values of H_2O and CO_2 absorption coefficients are from the HITRAN database [48], and details of the applied model are in Supplementary Material 2 (IDL script).

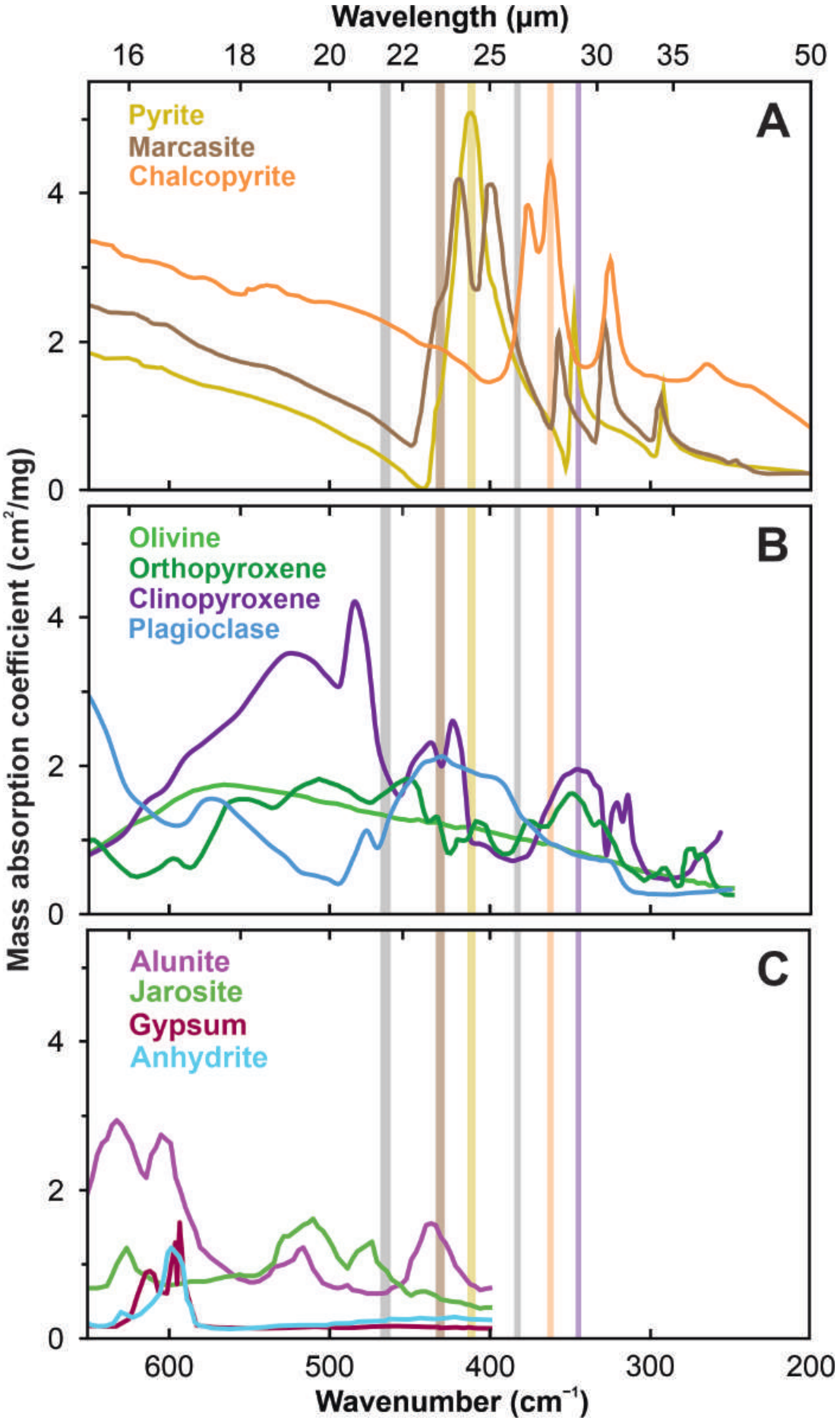

Figure 5. Mass absorption coefficients of possible Martian (**A**) sulfides [23], (**B**) silicates [49–51], and (**C**) sulfates [52–54] measured at room temperature. Literature data for the sulfates and silicates are unavailable for <400 cm^{-1} (>25 μm) and <250 cm^{-1} (>40 μm), respectively. The mass absorption coefficients of sulfates were calculated from reported transmittances, sample masses, and KBr pellet cross-sectional areas according to the method presented by Brusentsova et al. [23]. The spectral ranges of the six detectors are marked with rectangles: orange (360–364 cm^{-1} = 27.45−27.75 μm: chalcopyrite), yellow (409–414 cm^{-1} = 24.15−24.45 μm: pyrite), brown (428–434 cm^{-1} = 23.05−23.35 μm: marcasite), gray (381–385 cm^{-1} = 25.95−26.25 μm and 462–468 cm^{-1} = 21.35−21.65 μm: reference bands), and purple (343–347 cm^{-1} = 28.85−29.15 μm: clinopyroxene).

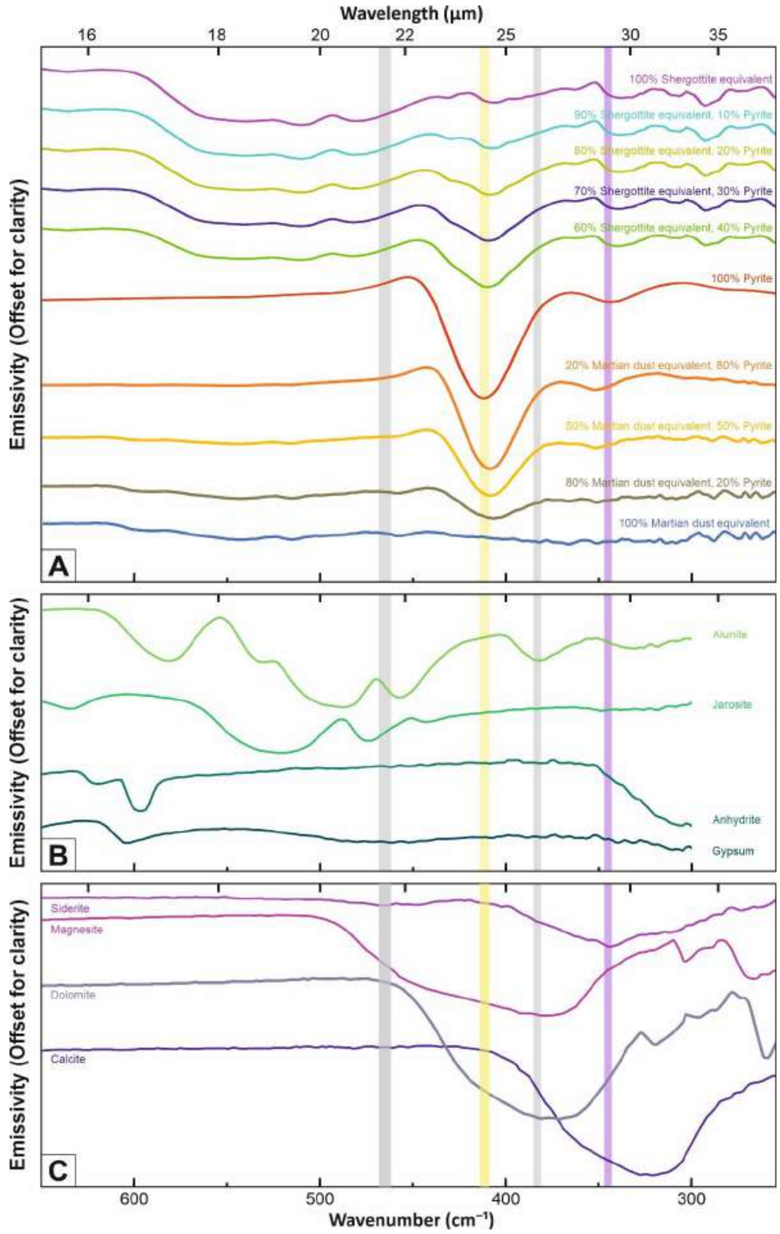

Figure 6. (**A**) presents the emissivity of the Navajún (La Rioja, Spain) pyrite [55], (**B**) equivalents of olivine-phyric shergottites, and (**C**) their various mixtures. The composition of olivine-phyric shergottite equivalents is the same as in the text of Section 3 but normalized from 92% to 100%. The mineral composition of Martian dust is close to JSC Mars-1A (volcanic ash altered at low temperature) proposed by Kölbl et al. [56]: 64% plagioclase (labradorite), 12% olivine (fayalite), 10% magnetite, 9% pyroxene (diopside), and 5% hematite. The input spectra of olivine (fayalite), plagioclase (labradorite), orthopyroxene (bronzite), clinopyroxene (diopside), magnetite, and hematite were collected from the ASU Spectral Library, and was measured by us at the German Aerospace Centre (DLR) in conditions similar to those applied for the ASU measurements: grain dimensions of 710–1000 μm and a surface temperature of 80 °C, but a pressure of 0.7 mbar instead of a nitrogen atmosphere. Emissivity was calibrated against a blackbody measured at the same temperature as the sample. The simulations of various pyrite and shergottite mixtures were performed using the PFSLook software [57]. The spectral ranges of four of the six detectors are marked with the rectangles: yellow (409–414 cm^{-1} = 24.15−24.45 μm: pyrite), grey (381–385 cm^{-1} = 25.95−26.25 μm and 462–468 cm^{-1} = 21.35−21.65 μm: reference bands), and purple (343–347 cm^{-1} = 28.85−29.15 μm: clinopyroxene). Note that the pyrite absorption band becomes visible (under the reference level in grey) when the pyrite content is at least ~20%.

3. Simulated Mass Absorption Coefficients for Various Mineral Mixtures

Large monomineralic fields either on Mars or on Earth are rare and are especially rare for ore minerals. Ore minerals are usually disseminated in host rocks, and emitted spectra would represent a mixture of ore minerals (Figure 5A) and rock-forming minerals (Figure 5B). Whereas the most common ore mineral on Mars is most likely pyrite [11–13,41,58–60], basalts are the most common rocks found by orbiters and in Martian meteorites. To date, >200 distinct meteorites have been classified as samples from Mars. Most of them belong to the SNC clan, which is an abbreviation of shergottites, nakhlites, and chassignites. By far the most abundant of them, shergottites, represent various types of basalts or similar mafic rocks and include three types: most-evolved basaltic, intermediate olivine-phyric, and most-primitive poikilitic. All three types are composed of four minerals in >95 vol.%, i.e., olivine, orthopyroxene, clinopyroxene, and plagioclase, whereas the remaining minerals, including oxides and sulfides, are accessory minerals. The intermediate-type olivine-phyric shergottite is composed of olivine (7–17 vol.%), orthopyroxene (1.5–7.0 vol.%), clinopyroxene (55–65 vol.%), and plagioclase (14–18 vol.%) [21].

Using the linear mixing method, we simulated various mixtures of pyrite and olivine-phyric shergottites (1:9, 2:8, 3:7, 4:6 surface ratios) to determine what would be the minimum amount of pyrite needed to detect it from orbit. Linear mixing of spectra is widely used in various fields of science, from remote sensing through to medicine and biology [61,62]. It has been well-established that thermal infrared spectra of surfaces composed of multiple minerals may be modeled by using linear combinations of each mineral spectrum weighted by the areal fraction of the surface measured [63–65]. Comparison of results obtained by linear mixing and radiative transfer algorithms have shown a good agreement between the two [66,67]. Therefore, emissivities (Figure 6) or mass absorption coefficients measured or incorporated from spectral libraries for single minerals can be combined into the spectrum of a surface using linear mixing. Minerals and their proportions, here, are selected based on the predicted composition of Martian rocks such as basalt and its varieties [68]. For the linear mixing of emissivities (Figure 6), we used the C++-based PFSLook program described by Zalewska and colleagues [57,69]. For mass absorption coefficients (Figure 6), we used our Matlab-based code (see Supplementary Material 3).

We found that fields containing 10–20% pyrite could be detected by the proposed method (Figures 6 and 7). In MIRORES's field of view of 16.5 m × 19.9 m, which makes about ~330 m^2, 33–66 m^2 covered by pyrite will be needed to detect it from orbit. This should allow the detection of not only volcanic-hosted massive sulfide (VMS) deposits but also their stockworks. For example, the Rio Tinto VMS deposits in the Iberian Pyrite Belt contain two large orebodies with massive pyrite, San Dionisio (~600 m × 130 m = 78,000 m^2) and Filon Sur (~1100 m × 50 m = 55,000 m^2), but also larger pyrite stockworks around the Salomon and Argamasilla sites (640 m × 280 m = 179,200 m^2) defined as containing >20% S [70]. This S amount is an equivalent of 23–37 vol.% pyrite, given that pyrite contains 53% S, and has a density of 5.0 g/cm^3, whereas the density of other minerals is between 3–5 g/cm^3. This is considerably more than the 10–20 vol.% needed to detect with MIRORES. Although plate tectonics is currently absent on Mars, it was likely present in the early history of Mars [71,72]. The plate tectonics ceased then but the largest volcanic province, Tharsis, displayed prolonged tectonic activity that was only slowly declining during the Amazonian [73,74]. Therefore, hydrothermal alteration and associated ore deposits are anticipated in the vicinity of volcanic cones, fractures, and degassing structures [75,76]. The largest hydrothermal seafloor deposits documented so far on Mars are 400-m-thick and contain abundant jarosite inferred to form from the oxidation weathering of iron sulfides in the Eridania Basin [77]. The iron sulfides likely formed in a deep-water (500–1500 m) hydrothermal setting. The Eridania basin occurs within some of the most ancient terrains on Mars, where striking evidence for remnant magnetism might suggest an early phase of crustal spreading [77].

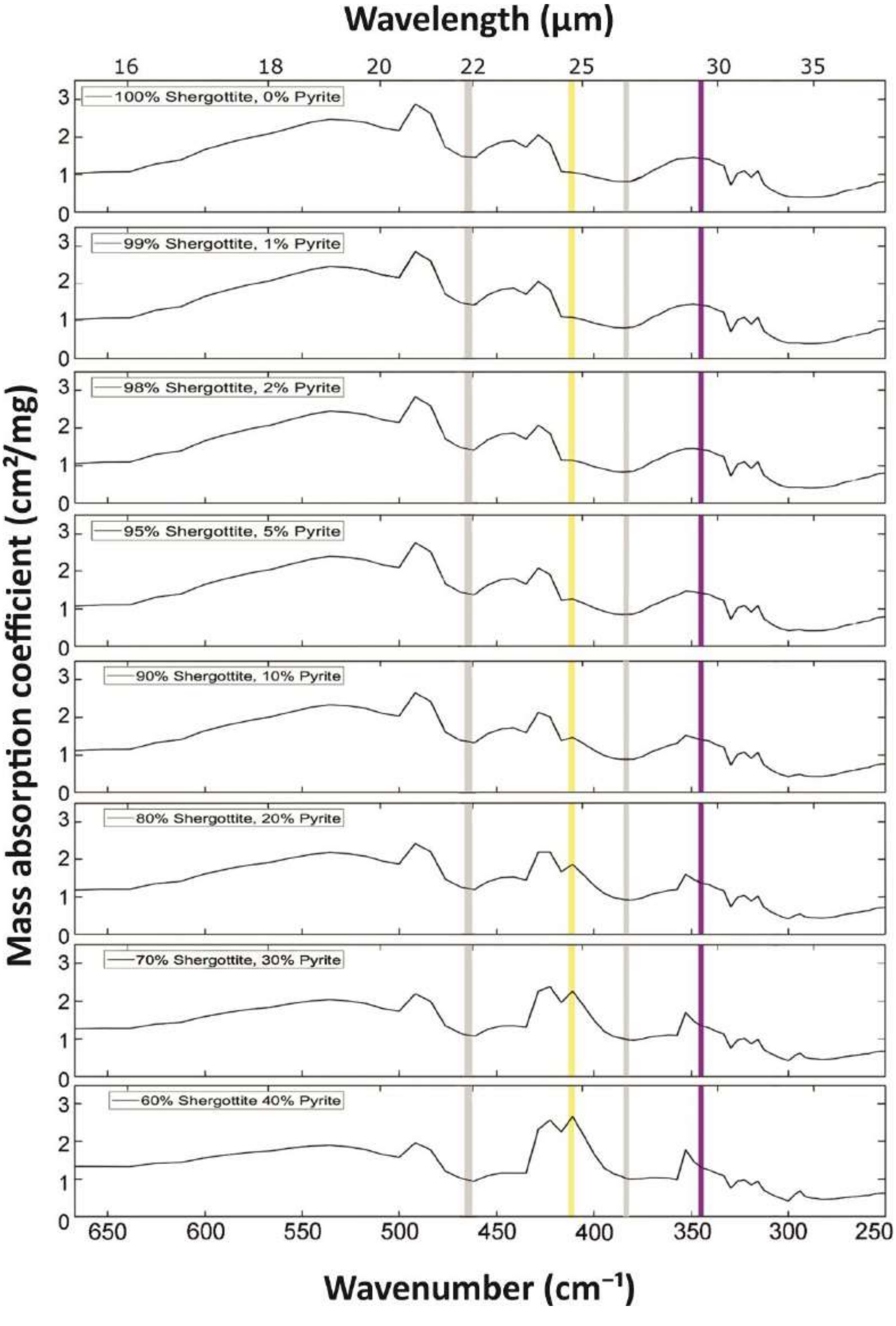

Figure 7. Mass absorption coefficients that we simulated for surfaces composed of various proportions of pyrite and olivine-phyric shergottites. The composition of olivine-phyric shergottites was the same as in the text of Section 3 but normalized from 92% to 100%. The input spectra were derived from Figure 5. The spectral ranges of four of six detectors are marked with rectangles: yellow (409–414 cm^{-1} = 24.15−24.45 μm: pyrite), grey (381–385 cm^{-1} = 25.95−26.25 μm and 462–468 cm^{-1} = 21.35−21.65 μm: reference bands), and purple (343–347 cm^{-1} = 28.85−29.15 μm: clinopyroxene). There is partial interference between pyrite and the secondary clinopyroxene peak on the right (at ~421 cm^{-1} = 23.8 μm, cf. Figure 5), becoming significant when pyrite is <10%. The signal from this interference was taken out using Equation (1). The mineral mixtures were calculated using the Matlab script in Supplementary Material 3.

In impact-related craters >10 km, hydrothermal deposits [78] such as the lenses of massive pyrite may also be large enough to be detected using MIRORES. Large-scale impact-related ore mineralization, although more likely for Mars [10], is also known from several impact craters on Earth such as the Sudbury basin in Canada [79] or the Witwatersrand Supergroup in South Africa [80]. In the Sudbury basin, sulfide ores composed of massive pyrite, such as one located at the Fraser epidote zone, are up to 270 m × 40 m = 10,800 m^2 large [81]. Even larger and also detectable by MIRORES are the local ores of massive chalcopyrite (230 m × 240 m = 55,200 m^2) situated in the West part of the McCreedy East deposit [82]. Note, however, that both the Rio Tinto VMS and impact-related Sudbury deposits contain one of the greatest known concentrations of massive sulfides on Earth [70], so only large or relatively large mineralization can be detected using the MIRORES instrument on Mars.

On Mars, the Gusev, Gale, and other meteorite crater walls are suitable for the remote detection of ore minerals. In the Gusev crater, pyrite and marcasite have been detected by the Mössbauer spectrometer of the Spirit rover, and pyrrhotite was inferred from geochemical constraints [12]. In addition, pyrrhotite was found in two drill powders from the Gale crater analyzed by the Curiosity X-ray diffractometer [13]. These outcrops are not covered by a thin layer of sediments, which could otherwise hinder our measurements, as could potentially larger amounts of dust in the Martian atmosphere during seasonal dust storms. Hydrothermal minerals are preferentially found at crater rims representing products of local impact-induced hydrothermal circulation [10,78]. Other extensive outcrops of hydrothermal deposits are expected to occur in volcanic provinces, where hard rocks are exposed along caldera walls, volcano slopes, and fissures, as demonstrated by Skok et al. [75] and Broz [83] using the CRISM/MRO instrument.

4. General Design

We propose a relatively inexpensive, simple instrument (Figures 8 and 9) measuring only a limited 21–30 μm range of the FIR spectrum, where strong absorption peaks are displayed by most sulfides, including pyrite at 24.3 μm and chalcopyrite at 27.6 μm (Figure 5). In addition, marcasite, with the same chemical composition as pyrite (both FeS_2) but a different crystallographic structure, shows two absorption bands centered close to pyrite (at 25.0 μm and 23.8 μm) and is therefore measured on the short-wave slope of the latter one at 23.2 μm. As well as these three bands, we will measure two bands at 21.5 μm and 26.1 μm for reference (grey bands in Figure 5), which will allow us to interpolate the background level of radiance varying as a function of incidence angle, emission angle, atmospheric H_2O, surface properties, and other factors. Lastly, a special reference detector at 29.0 μm (purple bands in Figure 6) will make it possible to remove partial interference on pyrite from the secondary peak of clinopyroxene at ~24.0 μm by using the following formula:

$$Py_{24.3_{Cpx}} = \frac{Cpx_{29.0} - R_{26.1}}{4} \tag{1}$$

where $Py_{24.3_{Cpx}}$ is the contribution of the secondary peak of clinopyroxene to the absorption peak at the pyrite (Py) detector, $Cpx_{29.0}$ is the signal from the detector monitoring the intensity of the clinopyroxene (Cpx) signal, and $R_{26.1}$ is the signal from the reference detector at 26.1 μm. Here, 0.7 is the ratio between the absorption peak amplitude at the peak of clinopyroxene at 29.0 μm and the absorption peak amplitude of a part of the clinopyroxene ~23.8 μm peak within the pyrite detector. The equation is free of any assumption on the modal content of clinopyroxene on the surface. We only operate on the ratio between the two absorption features of clinopyroxene, which should be relatively constant independent of the clinopyroxene content.

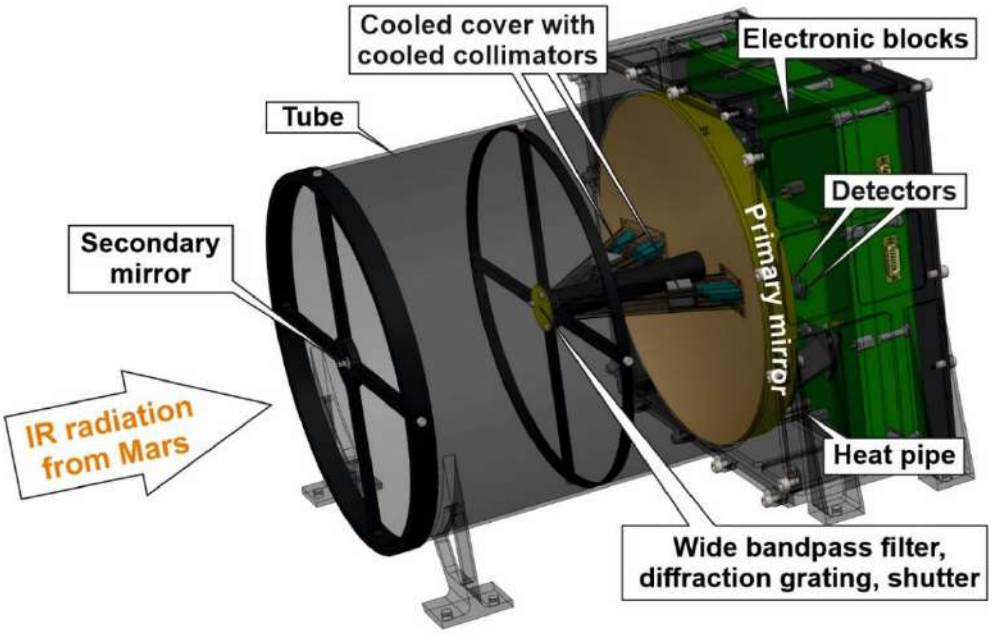

Figure 8. Simplified 3D scheme of the MIRORES instrument. The size of the instrument is 42 × 32 × 32 cm. The spectrometer has seven detectors, two of which are visible on the scheme.

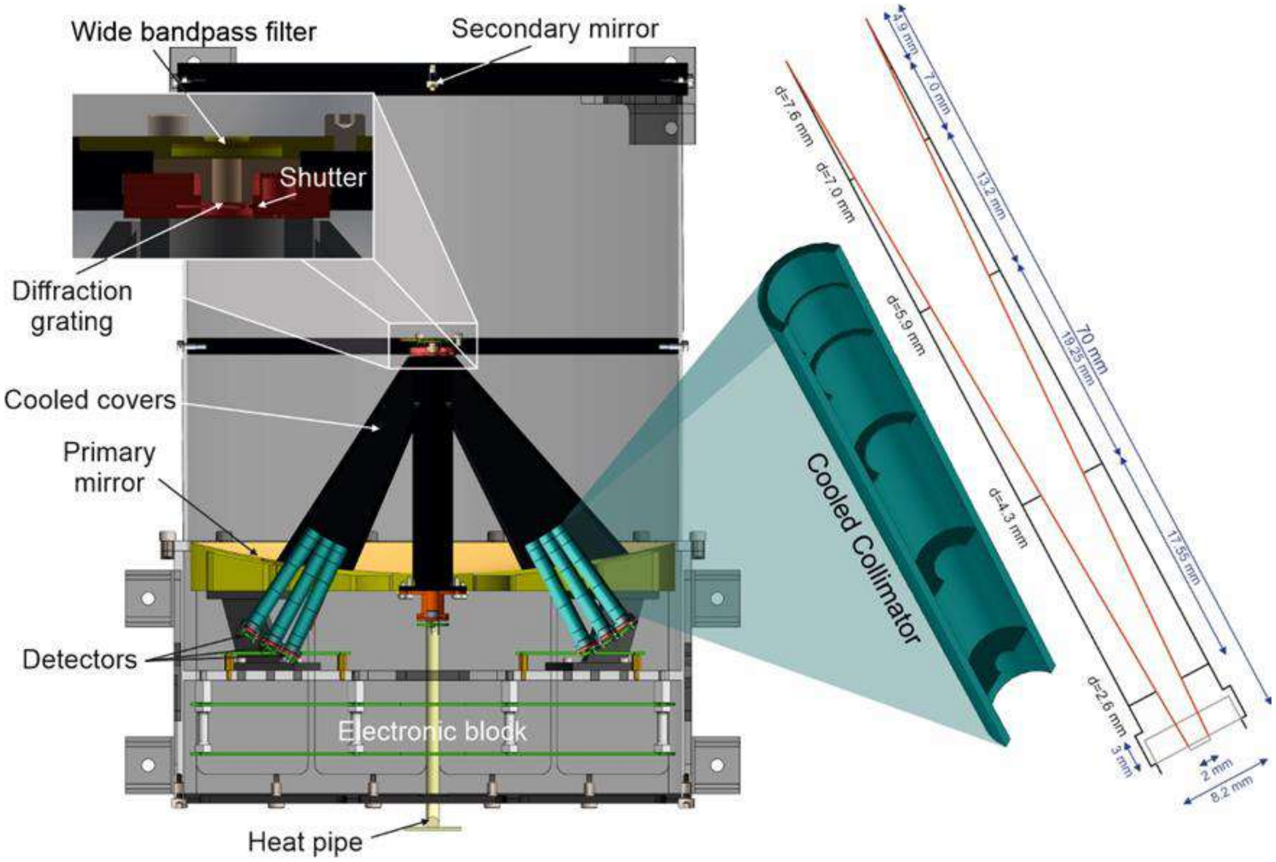

Figure 9. Simplified cross section of the MIRORES instrument. The size of the instrument is 42 × 32 × 32 cm. The six main detectors are placed behind the six turquoise collimators, the optical design of which is depicted on the left. The zoom on the right shows the position of the shutter behind the diffraction grating. The wide bandpass filter transmits radiation in the 21–30 μm range.

Measurements in only six bands allow the instrument dimensions to be 42 × 32 × 32 cm and the instrument mass to be <10 kg (Figures 8 and 9). The instrument optics are based on two mirrors (primary and secondary) set up in a typical Cassegrain system. The primary mirror with a diameter of 300 mm reflects the radiation into the smaller secondary mirror with a diameter of 4.1 mm located at a distance of 300 mm. Then, all radiation reflected from the secondary mirror is directed to the wide bandpass filter (20−33 μm) and a diffraction grating. Here, the broadband beam is split into six quasi-monochromatic beams, which are refracted and fall into the set of six pyroelectric detectors (three for target minerals, two for reference, and one for the clinopyroxene interference). The detectors are mounted on a copper plate to facilitate heat dissipation. Heat dissipation is reinforced by a temperature stabilization system. The radiation stream transmitted by the device's optical system is digitized by a front-end electronics (FEE) system and sent to an onboard computer.

The key components of the instrument, the primary and secondary mirrors, will be connected to the satellite through heat pipes. Assuming that the mirrors are shielded from direct solar radiation by the satellite body, they receive only from 22 W (Mars blackbody radiation) to 32 W (blackbody radiation + reflected radiation from the Sun), so the heat pipes need to expel on average 27 W to maintain a constant temperature. In the assumed model, Mars has a temperature of 193 K at night, the solar flux is 715 W/m^2, the satellite temperature is 273 K, the space temperature is 4 K, and the electronic power dissipates up to 10 W.

5. Optical System

The optical system is composed of a primary mirror, a secondary mirror, a filter, a diffraction grating, and collimators for each detector (Figure 9). The primary mirror has a diameter of 300 mm and is made of alumina. The secondary mirror is formed by a gold-covered steel sphere; which is a bearing ball with a diameter of 4.1 mm easily available on the market, manufactured, for example, by FŁT Polska Sp. Z.o.o. The distance between the primary and secondary mirrors is 300 mm (Figure 10). The effective focal length of the telescope is 30.3 m, the detector window diameter is 2 mm, and the assumed satellite altitude is 250 km. The field of view in a static position can thus be calculated as 0.002 m through 30.3 m times 250,000 m, which makes 16.5 m. Given that the satellite will move during the 1 ms measurement with an orbital speed of 3430 m/s, the shift related to the satellite position change is 3.4 m. Therefore, the length of the field of view along the satellite path will be 19.9 m, so the field of view can be reported as 16.5 m × 19.9 m (328.4 m^2). This field resolution should correspond to an angular resolution of $6.6 \cdot 10^{-5}$ radians, which equals 13.6 arcsecs. This translates to an F-number of 101 (see also Supplementary Figure S2 in Supplementary Material 1). This value, although high, is sufficient for our spectrometer measuring just one spectrum at a given time. Therefore, this amount of light is sufficient to obtain proper results above the noise level.

The light reflected from the secondary mirror goes through the wide bandpass multilayer interference temperature-invariant filter (Figure 9) made of chemical vapor deposition diamond. Thanks to pre-coating with amorphous hydrogenated diamond-like carbon (DLC) and coating with multilayers of ZnSe and PbTe, the filter can cut off the visible, as well as near-, and mid-infrared radiation (<20 μm), as well as radiation >33 μm [84]. The filtered light, including the useful spectral range (21–30 μm), then goes through the transmission diffraction grating with a pitch of 50 μm made of aluminum frame and 25-micrometer-thick copper wire. These parameters allow us to obtain a spectral resolution of ~0.3 μm. For example, the spectral resolution for the 21.5 μm detector is 0.31 μm, calculated as 21.5 μm through 70 (number of active slits, 20 active slits/1 mm).

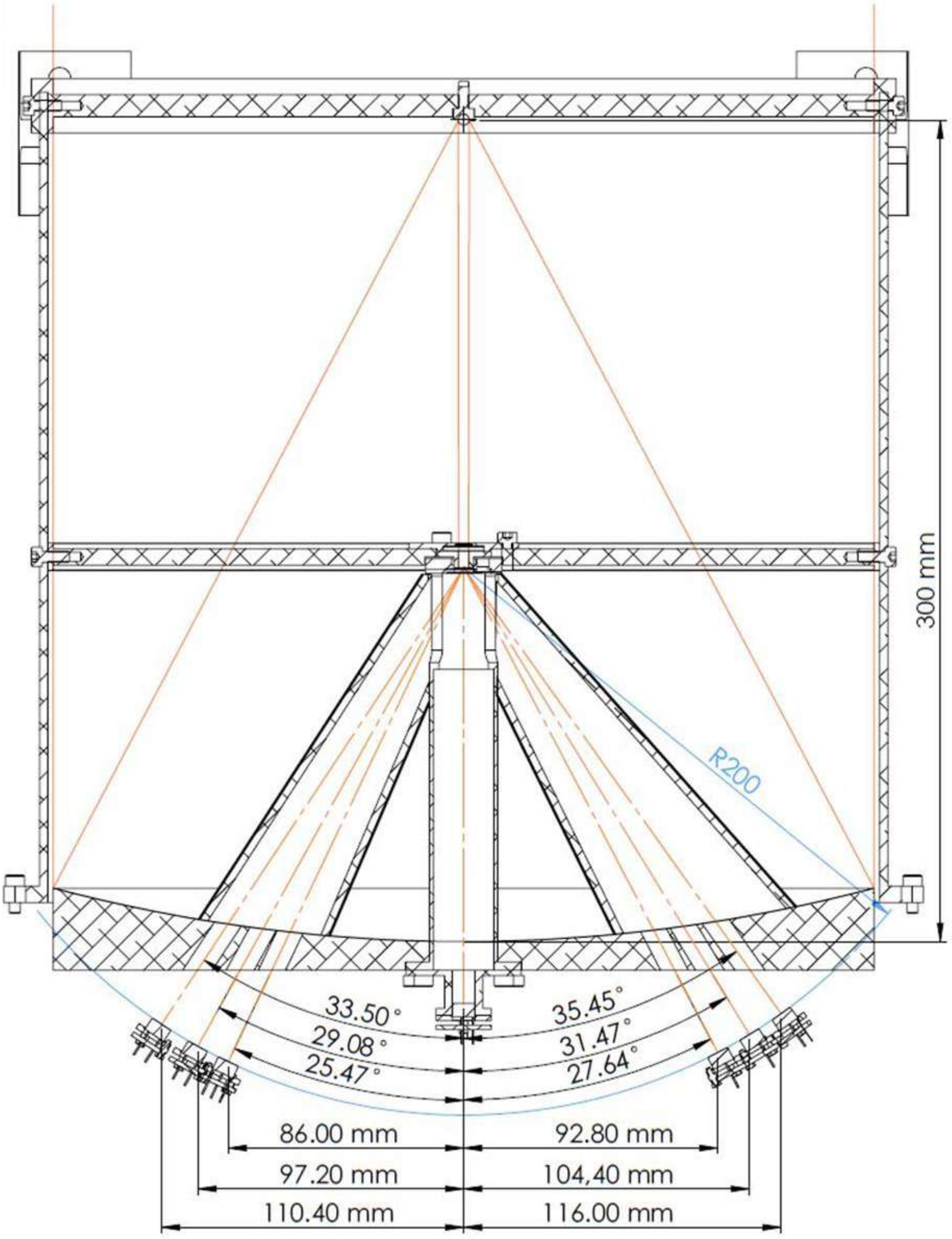

Figure 10. The optical system of the MIRORES instrument with the primary mirror at the bottom, and the secondary mirror at the top. Orange solid lines: incident radiation; orange dash–dotted lines: refracted radiation. R200 is the distance between the detectors and diffraction grating (200 mm). The thin blue curve marks this distance of 200 mm from the diffraction grating, and all the detectors are situated along this theoretical curve.

The distance from the diffraction grating to each detector is 200 mm. The light passing through the diffraction grating is refracted with an angle (θ) that can be calculated from the following formula Equation (2):

$$\lambda = \frac{p \times \sin\theta}{n} \tag{2}$$

where λ is the refracted wavelength, p is the pitch of the diffraction grating, and n is the refraction order. In our case, the refraction order is always 1 as wavelengths of <20 μm, distinguished by higher radiation levels, are filtered out. The radiation in the third order, which is always cut off by the filter, would be nine times weaker. The radiation in the second order would be four times weaker but the even orders are neutralized in this optical geometry.

The positions of the three main detectors and three reference detectors (Figure 10) are calculated from the refraction angle and the distance between detectors and diffraction grating (200 mm). These positions are + 116.00 mm ($Cpx_{29.0}$), + 104.40 mm ($R_{26.1}$), + 92.80 mm (marcasite at 23.2 μm − $Mrc_{23.2}$), −86.00 mm ($R_{21.5}$), −97.20 mm ($Py_{24.3}$), and −110.40 mm (chalcopyrite at 27.6 μm − $Ccp_{27.6}$) from the optical axis (Figure 8). All detectors register radiation from the same area of Mars. The non-refracted portion of radiation travels straight to the seventh detector located at position 0 (Figure 10). This detector registers the broadband non-refracted radiation >20 μm to monitor the brightness of the Martian surface. In the optical axis, the sizes of the light beams on the detectors are 3.4 mm, which are a bit larger than the size of the detector apertures (2 mm) but smaller than the size of the Airy disc (corresponding to the first minimum of the Airy pattern). The quality of the beam is relatively insensitive to potential change in the position of the focal plane (see Supplementary Figure S3 in Supplementary Material 1). Predicted mechanical deformation due to estimated temperature changes (Supplementary Figure S4 in Supplementary Material 1) should not affect the quality of the optical system (Supplementary Figure S2 in Supplementary Material 1). The full ray-tracing analysis and tolerance analysis are included in Supplementary Material 1 (Supplementary Figures S2 and S5, respectively). The light paths in the section between the diffraction grating and detectors are surrounded by the PA 2200 powdered polyamide cover to protect the detectors against potential stray light (Figure 8).

The position of the detectors may change slightly after future tests and calibrations, but this will not be significant. For example, pyrite, which is the most important in our set of minerals, is planned to be measured at 411.5 cm^{-1} (24.3 μm) following the values reported in our emissivity measurements (Figure 6); however, Brusentova et al. [23] indicated 412 cm^{-1} (24.3 μm) and Farmer [30] reported 415 cm^{-1} (24.1 μm). These values are further supported by other numerous studies [24–26] with the one exception of Lennie and Vaughan [85], who reported 425 cm^{-1} (23.5 μm). The purpose of that study was, however, related to the phase transition between pyrite and marcasite, and its spectroscopy results were only intended to identify phases. Therefore, the authors needed only qualitative or semiquantitative spectral features of the minerals with no need for high accuracy of the measurements. More problematic could be the fact that the wavenumber of spectral features increases with decreasing temperatures, which, according to Farmer [30], is ~0.1 $cm^{-1}/°C$ for some bonds such as O–H. This rate is, however, at least one order of magnitude lower for most Fe–S bonds crucial for sulfide detection [23].

6. Detection System

The detection system consists of six infrared-sensitive optoelectronic components based on the L3100 × 2020 detectors provided by Laser Components GMBH (Figure 11). These are pyroelectric detectors operating with a single voltage supply (VCC). The detector specific sensitivity (D *) expressed in Jones units is ~9×10^{8} $cmHz^{1/2}/W$ at 10 Hz. The signal to noise ratio is >2 (for 1 ms). The output signal after digitalization in FEE is 16 bits (Supplementary Materials 4 and 5) and the required data rate volume is the basic standard of 115,000 b/s assuming that one measurement lasts 1 ms and measurement occurs every

5.59 ms. The collected signal can also be temporarily stored on an onboard computer mounted in the electronic blocks (Figure 8).

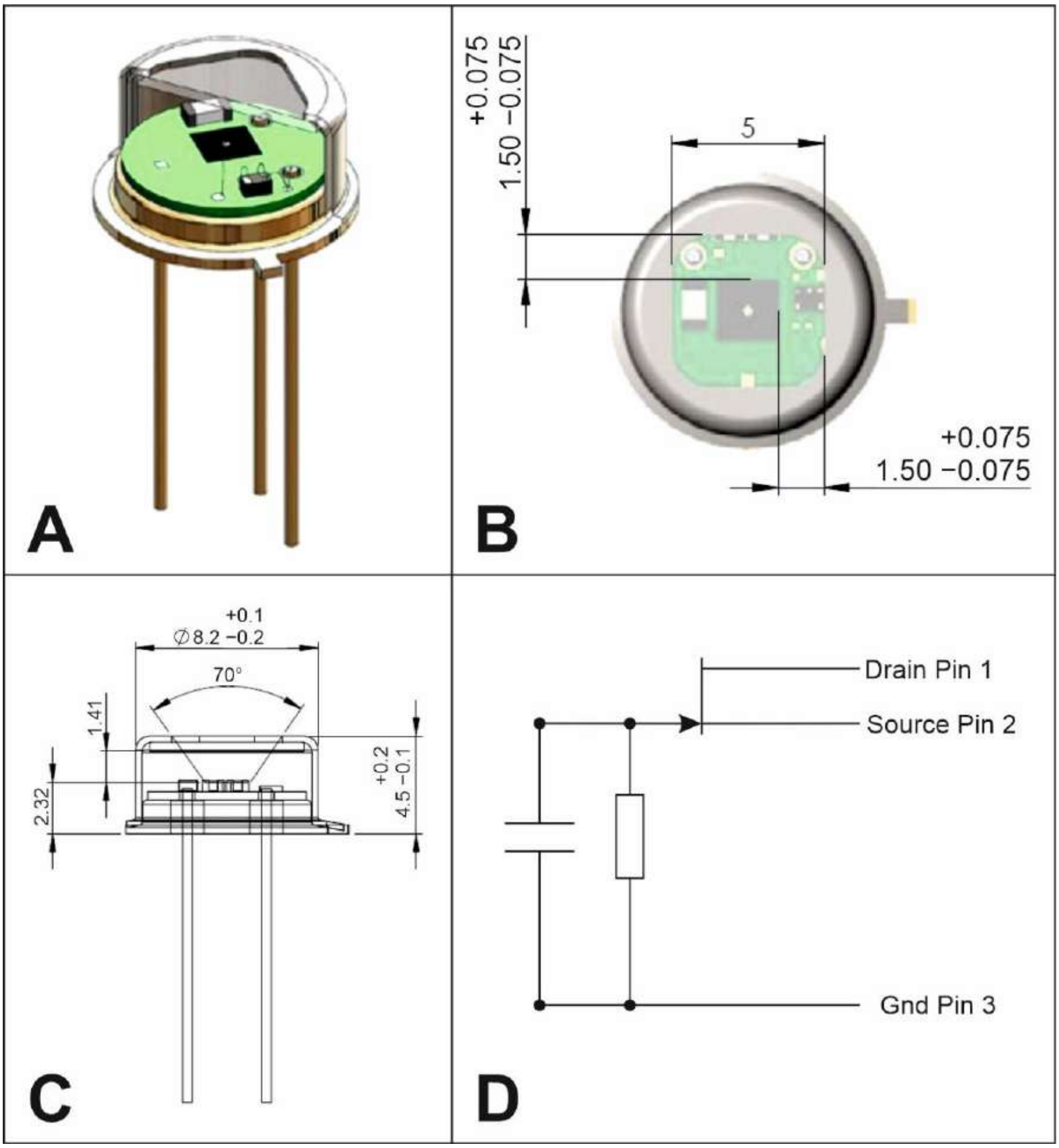

Figure 11. (**A**) Three-dimensional cross section of pyroelectric detector L3100 × 2020, followed by its horizontal (**B**) and vertical (**C**) cross sections. All reported distances are in mm. (**D**) Circuit diagram of the detector.

As pyroelectric detectors are sensitive only to modulated radiation, we mounted a shutter behind the wide bandpass filter and the diffraction grating (Figure 9). The detectors show high transmission (>60%) of the far-infrared radiation (>15 µm) and low transmission (0–40%) of the mid- and near-infrared (<15 µm). The detector has a built-in high-density polyethylene (HDPE) filter. To protect the detectors, we also need additional filters to cut out more radiation <20 µm, including potentially damaging UV radiation. Although one such filter for the incoming radiation is located in front of the diffraction grating, additional filters are needed in front of each detector to eliminate thermal radiation from all the components placed between the primary filter and the detectors, such as the primary mirror or collimators.

For the Mars temperature of 293 K and surface emissivity of 1, we obtain a heat of $2.45 \cdot 10^{-9}$ W at the detector (calculated for the pyrite detector receiving radiation from 24.15−24.45 μm) assuming no loss of signal on the filters and diffraction grating. In reality, our wideband pass filter, which is not cooled, transmits only ~85% radiation at this band, and the cooled narrowband filter passes 90% of the radiation. Considering that another 50% of radiation is lost on the diffraction grating and 7% is lost on around the detector due to the difference between the area of the beam (diameter of 3.5 mm), and aperture of the detector (square 2 × 2 mm) assuming Gaussian distribution of radiation intensity within the beam, the entire loss is 100% – (90% × 85% × 50% × 93%) = 64%. Therefore, the true signal is $0.82 \cdot 10^{-9}$ W. This, after amplification of 10,000 V/W, becomes 8.2 μV. The noise is calculated based on radiation from parts of collimators directly visible from a detector (40 mm^2 translating to 1 mm^2 when considering the angle between the collimator and detector planes) and their temperature (50 K). Given that each detector is shielded with a narrow bandpass filter, which is 23.4−25.2 μm for the pyrite detector, we obtain a value of $0.58 \cdot 10^{-9}$ W and $0.52 \cdot 10^{-9}$ W considering the filter transmission of 90%, which becomes 5.2 μV after signal amplification. With 8.2 μV obtained for the signal and 5.2 μV obtained for the noise, the calculated signal to noise ratio is 1.6. One cooling system that can be potentially applied to cool the detectors and parts of collimators (the 40 mm^2) in view of the detectors, to stabilize the instrument background and simplify the in-flight radiometric calibration, is used by Rigopoulou et al. [86]. The rest of collimator and the cover (Figure 8) are cooled to 190 K with a Peltier system and heatpipe.

For radiance calibration, we will observe two sources at known temperatures, deep space and an external plate mounted on the satellite. Deep space is characterized by a constant temperature and will be measured at least twice per orbit. The plate will be measured every 10 min and will have variable but known temperatures that can be measured continously with an expected accuracy of 0.1 K.

7. Conclusions

At least three common hydrothermal sulfides on Earth and Mars (pyrite, chalcopyrite, marcasite) have prominent absorption peaks in a narrow far-IR (FIR) wavelength range of 23–28 μm. The spectral features of sulfides in the FIR range are much stronger than the spectral features of any of the common Martian minerals, including olivines, clinopyroxenes, orthopyroxenes, plagioclase, major sulfates and major carbonates. Our simulations indicated that fields containing 10–20% pyrite could be detected from orbit in the far-IR range. However, ore deposits including massive pyrite are relatively small, maximally up to hundreds of meters by hundreds of meters. Therefore, although the existing instruments PFS/MEX and TES/MGS cover the FIR spectral range, their spatial resolutions of ~10 km and ~3 km, respectively, are not sufficient to search for ore deposits.

Therefore, we designed a new instrument with a resolution that allows detecting ore deposits. This was achieved by the use of the Cassegrain optical system. The field of view of 16.5 × 19.9 m makes it possible to detect areas covered by 33–66 m^2 of pyrite on a surface of ~330 m^2, creating possibilities for detecting large and moderate-size orebodies and probably also their stockworks. The instrument should be integrated into a satellite launched to Mars, such as that planned by the Polish mission to Mars consortium or a larger mission between 2026 and 2030, the Earth Return Orbiter of ESA in 2026/28 or the Mars Sample Return mission (HX-2) of the China National Space Administration (CNSA) in 2028/30. Prototype creation was started in 2021 and prototype testing is scheduled for 2022–2024.

Supplementary Materials: The following supporting information can be downloaded at: https://www.mdpi.com/article/10.3390/rs14122799/s1. References [23,87–91] are cited in the supplementary materials.

Author Contributions: Conceptualization, J.C., J.B. (Jaroslaw Bakala), M.K. (Miroslaw Kowalinski), S.P., M.C., J.B. (Jaromir Barylak) and M.R.; Investigation, N.Z., G.P., M.S., J.B. (Jaromir Barylak), M.K. (Mateusz Kuzaj), A.M. (Alessandro Maturilli) and J.H.; Methodology, J.C., J.B. (Jaroslaw Bakala), M.K. (Miroslaw Kowalinski), S.P., N.Z., G.P., A.M. (Alessandro Maturilli) and J.H.; Project administration, M.J.; Resources, N.Z.; Software, S.P., N.Z. and M.S.; Supervision, J.C. and M.K. (Miroslaw Kowalinski); Visualization, J.B. (Jaroslaw Bakala), M.K. (Miroslaw Kowalinski), N.Z., B.P., M.C., G.P., M.S. and M.K. (Mateusz Kuzaj); Writing — original draft, J.C., M.K. (Miroslaw Kowalinski), S.P. and N.Z.; Writing — review & editing, J.C., J.B. (Jaroslaw Bakala), M.K. (Miroslaw Kow-alinski), S.P., N.Z., B.P., T.M., M.C., M.S., Z.S., A.M. (Andrzej Muszynski), S.G., M.J. and D.M. All authors have read and agreed to the published version of the manuscript.

Funding: The work was funded by the NCN project no. 2020/37/B/ST10/01420 to J. Ciazela, the European Space Agency (ESA) Space Resources project no. ESA AO/1-10824/21/NL/RA, and the European Funds Smart Growth (PO WER) project no. POWR.03.02.00-00-I027/17.

Data Availability Statement: Supplementary Materials 1–5 are available online.

Conflicts of Interest: The authors declare no conflict of interest.

References

1. Messina, P.; Vennemann, D. The European space exploration programme: Current status of ESA's plans for Moon and Mars exploration. *Acta Astronaut.* **2005**, *57*, 156–160. [CrossRef] [PubMed]
2. International Space Exploration Coordination Group. *The Global Exploration Roadmap*; National Aeronautics and Space Administration: Washington, DC, USA, 2013.
3. International Space Exploration Coordination Group. *The Global Exploration Roadmap*; National Aeronautics and Space Administration: Washington, DC, USA, 2018.
4. European Space Agency (ESA). ESA Space Resources Strategy. Available online: https://sci.esa.int/documents/34161/35992/1567260390250-ESA_Space_Resources_Strategy.pdf (accessed on 22 May 2019).
5. U.S. Geological Survey. *Mineral Commodity Summaries*; Online; U.S. Geological Survey: Washington, DC, USA, 2016.
6. Vaughan, D.J.; Corkhill, C.L. Mineralogy of sulfides. *Elements* **2017**, *13*, 81–87. [CrossRef]
7. King, P.L.; McSween, J.Y. Effects of H_2O, pH, and oxidation state on the stability of Fe minerals on Mars. *J. Geophys. Res. E Planets* **2005**, *110*, 113. [CrossRef]
8. King, P.L.; McLennan, S.M. Sulfur on Mars. *Elements* **2010**, *6*, 107–112. [CrossRef]
9. Pirajno, F.; van Kranendonk, M.J. Review of hydrothermal processes and systems on Earth and implications for Martian analogues. *Aust. J. Earth Sci.* **2005**, *52*, 329–351. [CrossRef]
10. West, M.D.; Clarke, J.D.A. Potential martian mineral resources: Mechanisms and terrestrial analogues. *Planet. Space Sci.* **2010**, *58*, 574–582. [CrossRef]
11. Squyres, S.W.; Aharonson, O.; Clark, B.C.; Cohen, B.A.; Crumpler, L.; De Souza, P.A.; Farrand, W.H.; Gellert, R.; Grant, J.; Grotzinger, J.P.; et al. Pyroclastic activity at home plate in Gusev crater, Mars. *Science* **2007**, *316*, 738–742. [CrossRef]
12. Morris, R.V.; Klingelhöfer, G.; Schröer, C.; Fleischer, I.; Ming, D.W.; Yen, A.S.; Gellert, R.; Arvidson, R.E.; Rodionov, D.S.; Crumpler, L.S.; et al. Iron mineralogy and aqueous alteration from Husband Hill through Home Plate at Gusev Crater, Mars: Results from the Mössbauer instrument on the Spirit Mars Exploration Rover. *J. Geophys. Res. E Planets* **2008**, *113*, E12S42. [CrossRef]
13. Vaniman, D.T.; Bish, D.L.; Ming, D.W.; Bristow, T.F.; Morris, R.V.; Blake, D.F. Mineralogy of a Mudstone at Bay, Yellowknife Crater, Gale. *Science* **2014**, *343*, 1–9. [CrossRef]
14. Wang, Z.; Becker, H. Chalcophile elements in Martian meteorites indicate low sulfur content in the Martian interior and a volatile element-depleted late veneer. *Earth Planet. Sci. Lett.* **2017**, *463*, 56–68. [CrossRef]
15. Wang, Z.; Becker, H. Silver contents and Cu/Ag ratios in Martian meteorites and the implications for planetary differentiation. *Geochim. Cosmochim. Acta* **2017**, *216*, 96–114. [CrossRef]
16. Baumgartner, R.J.; Fiorentini, M.L.; Lorand, J.P.; Baratoux, D.; Zaccarini, F.; Ferrière, L.; Prašek, M.K.; Sener, K. The role of sulfides in the fractionation of highly siderophile and chalcophile elements during the formation of martian shergottite meteorites. *Geochim. Cosmochim. Acta* **2017**, *210*, 1–24. [CrossRef]
17. Lorand, J.P.; Pont, S.; Chevrier, V.; Luguet, A.; Zanda, B.; Hewins, R. Petrogenesis of martian sulfides in the Chassigny meteorite. *Am. Mineral.* **2018**, *103*, 872–885. [CrossRef]
18. Franz, H.B.; Kim, S.T.; Farquhar, J.; Day, J.M.D.; Economos, R.C.; McKeegan, K.D.; Schmitt, A.K.; Irving, A.J.; Hoek, J.; Iii, J.D. Isotopic links between atmospheric chemistry and the deep sulphur cycle on Mars. *Nature* **2014**, *508*, 364–368. [CrossRef]
19. Bibring, J.-P.; Soufflot, A.; Berthe, M.; All, E. OMEGA: Observatoire pour la Mineralogie, l'Eau, les Glaces et l'Activite. *Mars Express Sci. Payload* **2004**, *1240*, 37–49.
20. Horgan, B.H.N.; Cloutis, E.A.; Mann, P.; Bell, J.F. Near-infrared spectra of ferrous mineral mixtures and methods for their identification in planetary surface spectra. *Icarus* **2014**, *234*, 132–154. [CrossRef]

21. Taylor, L.A.; Nazarov, M.A.; Shearer, C.K.; McSween, H.Y.; Cahili, J.; Neal, C.R.; Ivanova, M.A.; Barsukova, L.D.; Lentz, R.C.; Clayton, R.N.; et al. Martian meteorite Dhofar 019: A new shergottite. *Meteorit. Planet. Sci.* **2002**, *37*, 1107–1128. [CrossRef]
22. Bibring, J.P.; Langevin, Y.; Mustard, J.F.; Poulet, F.; Arvidson, R.; Gendrin, A.; Gondet, B.; Mangold, N.; Pinet, P.; Forget, F.; et al. Global mineralogical and aqueous Mars history derived from OMEGA/Mars express data. *Science* **2006**, *312*, 400–404. [CrossRef]
23. Brusentsova, T.; Peale, R.E.; Maukonen, D.; Figueiredo, P.; Harlow, G.E.; Ebel, D.S.; Nissinboim, A.; Sherman, K.; Lisse, C.M. Laboratory far-infrared spectroscopy of terrestrial sulphides to support analysis of cosmic dust spectra. *Mon. Not. R. Astron. Soc.* **2012**, *420*, 2569–2579. [CrossRef]
24. Hony, S.; Bouwman, J.; Keller, L.P.; Waters, L.B.F.M. The detection of iron sulfides in Planetary Nebulae. *Astron. Astrophys.* **2003**, *393*, L103–L106. [CrossRef]
25. Dyar, M.D.; Holden, P.; Bishop, J.L.; Lane, M.D. Spectroscopic Characterization of hydrothermal sulfide chimneys at the Juan de Fuca Ridge. *Lunar Planet. Sci. Conf.* **2009**, *40*, 2221.
26. Nian-Xin, M.; Ye-Xiao, H.; Wei, L.; Hong-Juan, Y.; Xue-Chu, S. Far-infrared spectra of naturally occuring FeS2 (Pyrite). *Acta Phys. Sin.* **1993**, *42*, 1712–1718. [CrossRef]
27. Lorand, J.P.; Chevrier, V.; Sautter, V. Sulfide mineralogy and redox conditions in some shergottites. *Meteorit. Planet. Sci.* **2005**, *40*, 1257–1272. [CrossRef]
28. Gattacceca, J.; Hewins, R.H.; Lorand, J.P.; Rochette, P.; Lagroix, F.; Cournède, C.; Uehara, M.; Pont, S.; Sautter, V.; Scorzelli, R.B.; et al. Opaque minerals, magnetic properties, and paleomagnetism of the Tissint Martian meteorite. *Meteorit. Planet. Sci.* **2013**, *48*, 1919–1936. [CrossRef]
29. Smith, M.R.; Bandfield, J.L. Geology of quartz and hydrated silica-bearing deposits near Antoniadi Crater, Mars. *J. Geophys. Res. Planets* **2012**, *117*, 34. [CrossRef]
30. Farmer, V.C. *Infrared Spectra of Minerals*; Mineralogical Society: London, UK, 1974.
31. Rogalski, A. Next decade in infrared detectors. In Proceedings of the Electro-Optical and Infrared Systems: Technology and Applications XIV. International Society for Optics and Photonics, Warsaw, Poland, 9 October 2017; Volume XIV, p. 104330L. [CrossRef]
32. Safari, M.; Maghsoudi, A.; Pour, A.B. Application of Landsat-8 and ASTER satellite remote sensing data for porphyry copper exploration: A case study from Shahr-e-Babak, Kerman, south of Iran. *Geocarto Int.* **2018**, *33*, 1186–1201. [CrossRef]
33. Read, P.L.; Lewis, S.R.; Mulholland, D.P. The physics of Martian weather and climate: A review. *Rep. Prog. Phys.* **2015**, *78*, 125901. [CrossRef]
34. Montabone, L.; Forget, F.; Millour, E.; Wilson, R.J.; Lewis, S.R.; Cantor, B.; Kass, D.; Kleinböhl, A.; Lemmon, M.T.; Smith, M.D.; et al. Eight-year climatology of dust optical depth on Mars. *Icarus* **2015**, *251*, 65–95. [CrossRef]
35. Bandfield, J.L. Global mineral distributions on Mars. *J. Geophys. Res.* **2002**, *107*, 5042. [CrossRef]
36. Farrand, W.H.; Glotch, T.D.; Rice, J.W.; Hurowitz, J.A.; Swayze, G.A. Discovery of jarosite within the Mawrth Vallis region of Mars: Implications for the geologic history of the region. *Icarus* **2009**, *204*, 478–488. [CrossRef]
37. Zalewska, N. Hellas Planitia as a potential site of sedimentary minerals. *Planet. Space Sci.* **2013**, *78*, 25–32. [CrossRef]
38. Chukanov, N.V.; Chervonnyi, A.D. *Infrared Spectroscopy of Minerals and Related Compounds*; Springer: Cham, Switzerland, 2016; ISBN 3319253492.
39. Carter, J.; Viviano-Beck, C.; Loizeau, D.; Bishop, J.; Le Deit, L. Orbital detection and implications of akaganéite on Mars. *Icarus* **2015**, *253*, 296–310. [CrossRef]
40. Bajda, T. Solubility of mimetite Pb5(AsO4)3Cl at 555C. *Environ. Chem.* **2010**, *7*, 268–278. [CrossRef]
41. Ehlmann, B.L.; Edwards, C.S. Mineralogy of the Martian Surface. *Annu. Rev. Earth Planet. Sci.* **2014**, *42*, 291–315. [CrossRef]
42. Cousin, A.; Sautter, V.; Payré, V.; Forni, O.; Mangold, N.; Gasnault, O.; Le Deit, L.; Johnson, J.; Maurice, S.; Salvatore, M.; et al. Classification of igneous rocks analyzed by ChemCam at Gale crater, Mars. *Icarus* **2017**, *288*, 265–283. [CrossRef]
43. Xue, Y.; Yang, Y.; Yu, L. Mineral composition of the Martian Gale and Nili Fossae regions from Mars Reconnaissance Orbiter CRISM images. *Planet. Space Sci.* **2018**, *163*, 97–105. [CrossRef]
44. Singh, P.; Sarkar, R.; Porwal, A. Orbital remote sensing of impact-induced hydrothermal systems on Mars. *Ore Geol. Rev.* **2019**, *108*, 101–111. [CrossRef]
45. Mancarella, F.; Fonti, S.; Alemanno, G.; Orofino, V.; Blanco, A. Aqueous alteration detection in Tikhonravov crater, Mars. *Planet. Space Sci.* **2018**, *152*, 165–175. [CrossRef]
46. Lin, H.; Zhang, X. Retrieving the hydrous minerals on Mars by sparse unmixing and the Hapke model using MRO/CRISM data. *Icarus* **2017**, *288*, 160–171. [CrossRef]
47. Bandfield, J.L.; Glotch, T.D.; Christensen, P.R. Spectroscopic identification of carbonate minerals in the martian dust. *Science* **2003**, *301*, 1084–1087. [CrossRef]
48. Rothman, L.S.; Gordon, I.E.; Babikov, Y.; Barbe, A.; Benner, D.C.; Bernath, P.F.; Birk, M.; Bizzocchi, L.; Boudon, V.; Brown, L.R.; et al. The HITRAN2012 molecular spectroscopic database. *J. Quant. Spectrosc. Radiat. Transf. HITRAN2012 Mol. Spectrosc. Database* **2013**, *130*, 4–50. [CrossRef]
49. Gielen, C.; Van Winckel, H.; Min, M.; Waters, L.; Evans, T.L. SPITZER survey of dust grain processing in stable discs around binary post-AGB stars. *Astron. Astrophys.* **2008**, *490*, 725–735. [CrossRef]
50. Koike, C.; Tsuchiyama, A.; Shibai, H.; Suto, H.; Tanabé, T.; Chihara, H.; Sogawa, H.; Mouri, H.; Okada, K. Absorption spectra of Mg-rich Mg-Fe and Ca pyroxenes in the mid- and far-infrared regions. *Astron. Astrophys.* **2000**, *363*, 1115–1122.

51. Chihara, H.; Koike, C. Infrared absorption spectra of plagioclase feldspar: Dependencies of composition and temperature. *Planet. Space Sci.* **2017**, *149*, 94–99. [CrossRef]
52. Bishop, J.; Murad, E. The visible and infrared spectral properties of jarosite and alunite. *Am. Mineral.* **2005**, *90*, 1100–1107. [CrossRef]
53. Bishop, J.L.; Lane, M.D.; Dyar, M.D.; King, S.J.; Brown, A.J.; Swayze, G.A. Spectral properties of Ca-sulfates: Gypsum, bassanite, and anhydrite. *Am. Mineral.* **2014**, *99*, 2105–2115. [CrossRef]
54. Bhattacharya, S.; Mitra, S.; Gupta, S.; Jain, N.; Chauhan, P.; Parthasarathy, G. Jarosite occurrence in the Deccan Volcanic Province of Kachchh, western India: Spectroscopic studies on a Martian analog locality. *J. Geophys. Res.* **2016**, *121*, 402–431. [CrossRef]
55. Calvo, M.; Sevillano, E. Pyrite crystals from Soria and La Rioja provinces, Spain. *Mineral. Mag.* **1989**, *20*, 451–456.
56. Kölbl, D.; Pignitter, M.; Somoza, V.; Schimak, M.P.; Strbak, O.; Blazevic, A.; Milojevic, T. Exploring fingerprints of the extreme thermoacidophile Metallosphaera sedula grown on synthetic martian regolith materials as the sole energy sources. *Front. Microbiol.* **2017**, *8*, 1918. [CrossRef]
57. Zalewska, N.E.; Mroczkowska-Szerszeń, M.; Fritz, J.; Błęcka, M. Modeling of surface spectra with and without dust from Martian infrared data: New aspects. *Aircr. Eng. Aerosp. Technol.* **2019**, *91*, 333–345. [CrossRef]
58. Zolotov, M.Y.; Shock, E.L. Formation of jarosite-bearing deposits through aqueous oxidation of pyrite at Meridiani Planum, Mars. *Geophys. Res. Lett.* **2005**, *32*, 90. [CrossRef]
59. Schwenzer, S.P.; Abramov, O.; Allen, C.C.; Bridges, J.C.; Clifford, S.M.; Filiberto, J.; Kring, D.A.; Lasue, J.; McGovern, P.J.; Newsom, H.E.; et al. Gale Crater: Formation and post-impact hydrous environments. *Planet. Space Sci.* **2012**, *70*, 84–95. [CrossRef]
60. Yen, A.S.; Morris, R.V.; Clark, B.C.; Gellert, R.; Knudson, A.T.; Squyres, S.; Mittlefehldt, D.W.; Ming, D.W.; Arvidson, R.; McCoy, T.; et al. Hydrothermal processes at Gusev Crater: An evaluation of Paso Robles class soils. *J. Geophys. Res. E Planets* **2008**, *113*, 108. [CrossRef]
61. De Angelis, S.; Manzari, P.; De Sanctis, M.C.; Altieri, F.; Carli, C.; Agrosì, G. Application of spectral linear mixing to rock slabs analyses at various scales using Ma_Miss BreadBoard instrument. *Planet. Space Sci.* **2017**, *144*, 1–15. [CrossRef]
62. Shi, C.; Wang, L. Incorporating spatial information in spectral unmixing: A review. *Remote Sens. Environ.* **2014**, *149*, 70–87. [CrossRef]
63. Ramsey, M.S.; Christensen, P.R. Mineral abundance determination: Quantitative deconvolution of thermal emission spectra. *J. Geophys. Res. Solid Earth* **1998**, *103*, 577–596. [CrossRef]
64. Lyon, R. Analysis of rocks by spectral infrared emission (8 to 25 microns). *Econ. Geol.* **1965**, *60*, 715–736. [CrossRef]
65. Thomson, J.L.; Salisbury, J.W. The Mid-Infrared Reflectance of Mineral Mixtures (7–14/m). *Remote Sens. Environ.* **1993**, *13*, 1–13. [CrossRef]
66. Smith, M.D.; Bandfield, J.L.; Christensen, P.R. Separation of atmospheric and surface spectral features in Mars Global Surveyor Thermal Emission Spectrometer (TES) spectra. *J. Geophys. Res.* **2000**, *105*, 9589. [CrossRef]
67. Christensen, P.R.; Bandfield, J.L.; Smith, M.D.; Hamilton, V.E.; Clark, R.N. Identification of a basaltic component on the Martian surface from Thermal Emission Spectrometer data spectra of Mars during the initial aerobraking and science-phasing. *J. Geophys. Res. Plants* **2000**, *105*, 9609–9621. [CrossRef]
68. Bishop, J.L.; Michalski, J.R.; Carter, J. *Remote Detection of Clay Minerals*, 1st ed.; Elsevier Ltd.: Amsterdam, The Netherlands, 2017; Volume 8, ISBN 9780081003558.
69. Zalewska, N. Modeling of Sprectra With and Without Dust from Martian Surface Based on Infrared Data. *Trans. Inst. Aviat.* **2016**, *245*, 287–308. [CrossRef]
70. Martin-Izard, A.; Arias, D.; Arias, M.; Gumiel, P.; Sanderson, D.J.; Castañon, C.; Lavandeira, A.; Sanchez, J. A new 3D geological model and interpretation of structural evolution of the world-class Rio Tinto VMS deposit, Iberian Pyrite Belt (Spain). *Ore Geol. Rev.* **2015**, *71*, 457–476. [CrossRef]
71. Connerney, J.E.P.; Acuña, M.H.; Ness, N.F.; Kletetschka, G.; Mitchell, D.L.; Lin, R.P.; Reme, H. Tectonic implications of Mars crustal magnetism. *Proc. Natl. Acad. Sci. USA* **2005**, *102*, 14970–14975. [CrossRef] [PubMed]
72. Lenardic, A.; Nimmo, F.; Moresi, L. Growth of the hemispheric dichotomy and the cessation of plate tectonics on Mars. *J. Geophys. Res. E Planets* **2004**, *109*, 53. [CrossRef]
73. Bouley, S.; Baratoux, D.; Paulien, N.; Missenard, Y.; Saint-Bézar, B. The revised tectonic history of Tharsis. *Earth Planet. Sci. Lett.* **2018**, *488*, 126–133. [CrossRef]
74. Mège, D.; Masson, P. A plume tectonics model for the Tharsis province, Mars. *Planet. Space Sci.* **1996**, *44*, 1499–1546. [CrossRef]
75. Skok, J.R.; Mustard, J.F.; Ehlmann, B.L.; Milliken, R.E.; Murchie, S.L. Silica deposits in the Nili Patera caldera on the Syrtis Major volcanic complex on Mars. *Nat. Geosci.* **2010**, *3*, 838–841. [CrossRef]
76. Schulze-Makuch, D.; Dohm, J.M.; Fan, C.; Fairén, A.G.; Rodriguez, J.A.P.; Baker, V.R.; Fink, W. Exploration of hydrothermal targets on Mars. *Icarus* **2007**, *189*, 308–324. [CrossRef]
77. Michalski, J.R.; Dobrea, E.Z.N.; Niles, P.B.; Cuadros, J. Ancient hydrothermal seafloor deposits in Eridania basin on Mars. *Nat. Commun.* **2017**, *8*, 15978. [CrossRef]
78. Osinski, G.R.; Tornabene, L.L.; Banerjee, N.R.; Cockell, C.S.; Flemming, R.; Izawa, M.R.M.; Mccutcheon, J.; Parnell, J.; Preston, L.J.; Pickersgill, A.E.; et al. Impact-generated hydrothermal systems on Earth and Mars. *Icarus* **2013**, *224*, 347–363. [CrossRef]

79. Dare, S.A.S.; Barnes, S.J.; Prichard, H.M. The distribution of platinum group elements (PGE) and other chalcophile elements among sulfides from the Creighton Ni-Cu-PGE sulfide deposit, Sudbury, Canada, and the origin of palladium in pentlandite. *Miner. Depos.* **2010**, *45*, 765–793. [CrossRef]
80. Frimmel, H.E. Detrital origin of hydrothermal Witwatersrand goldÐa review. *Terra Nova* **1997**, *9*, 192–197. [CrossRef]
81. Li, C.; Naldrett, A.J. A numerical model for the compositional variations of Sudbury sulfide ores and its application to exploration. *Economic* **1994**, *89*, 1599–1607. [CrossRef]
82. Dare, S.A.S.; Barnes, S.J.; Prichard, H.M.; Fisher, P.C. Chalcophile and platinum-group element (PGE) concentrations in the sulfide minerals from the McCreedy East deposit, Sudbury, Canada, and the origin of PGE in pyrite. *Miner. Depos.* **2011**, *46*, 381–407. [CrossRef]
83. Brož, P.; Hauber, E.; Wray, J.J.; Michael, G. Amazonian volcanism inside Valles Marineris on Mars. *Earth Planet. Sci. Lett.* **2017**, *473*, 122–130. [CrossRef]
84. Hawkins, G.J.; Sherwood, R.E.; Djotni, K.; Threadgold, T.M. Cooled optical filters for Q -band infrared astronomy (15–40 µm). *Adv. Opt. Mech. Technol. Telesc. Instrum. II* **2016**, *9912*, 991235. [CrossRef]
85. Lennie, A.R.; Vaughan, D.J. Kinetics of the marcasite-pyrite transformation: An infrared spectroscopic study. *Am. Mineral.* **1992**, *77*, 1166–1171.
86. Rigopoulou, D.; Pearson, C.; Ellison, B.; Wiedner, M.; Okada, V.O.; Tan, B.K.; Garcia-Bernete, I.; Gerin, M.; Yassin, G.; Caux, E.; et al. The far-infrared spectroscopic surveyor (FIRSS). *Exp. Astron.* **2021**, *51*, 699–728. [CrossRef]
87. Kendix, E.; Moscardi, G.; Mazzeo, R.; Baraldi, P.; Prati, S.; Joseph, E.; Capelli, S. Far infrared and Raman spectroscopy analysis of inorganic pigments. *J. Raman Spectrosc.* **2008**, *39*, 1104–1112. [CrossRef]
88. Murad, E.; Bishop, J.L. The infrared spectrum of synthetic akaganeite, β-FeOOH. *Am. Mineral.* **2000**, *85*, 716–721. [CrossRef]
89. Salisbury, J.W.; Walter, L.S.; Vergo, N. Availability of a library of infrared (2.1–25.0 µm) mineral spectra. *Am. Mineral.* **1989**, *74*, 938–939.
90. Stimson, M.; O'Donnell, M. The Infrared and Ultraviolet Absorption Spectra of Cytosine and Isocytosine in the Solid State. *J. Am. Chem. Soc.* **1952**, *74*, 1805–1808. [CrossRef]
91. Salisbury, J.W.; Walter, L.S.; Vergo, N. Mid-infrared (2.1–25 um) spectra of minerals: First edition. *USGS Open-File Rep.* **1987**, 390.

SUPPLEMENTARY MATERIAL 1

Concept and design of Martian far-IR ORE Spectrometer (MIRORES)

J. Ciazela[1], J. Bakala[2], M. Kowalinski[2*], S. Plocieniak[2], N. Zalewska[2], B. Pieterek[3], T. Mrozek[2], M. Ciazela[1], G. Paslawski[1], M. Steslicki[2], Z. Szaforz[2], J. Barylak[2], M. Kuzaj[4], A. Maturilli[5], J. Helbert[5], A. Muszynski[3], M. Rataj[2], S. Gburek[2], M. Jozefowicz[6], and D. Marciniak[1]

[1]Institute of Geological Sciences, Polish Academy of Sciences, Research Centre in Wrocław, Podwale 75, 50-449 Wrocław, Poland
[2]Space Research Centre, Polish Academy of Sciences, ul. Bartycka 18A, 00-716 Warsaw, Poland
[3]Institute of Geology, Adam Mickiewicz University, ul. Bogumiła Krygowskiego 12, 61-680 Poznań, Poland
[4]Wroclaw University of Science and Technology, Wybrzeże Stanisława Wyspiańskiego 27, 50-370 Wrocław, Poland
[5]Institut für Planetenforschung, Deutsches Zentrum für Luft- und Raumfahrt (DLR), Rutherfordstrasse 2, D-12489 Berlin, Germany
[6]European Space Foundation, Grodzka 42/1, 31 044 Kraków, Poland
*Correspondence: mk@cbk.pan.wroc.pl

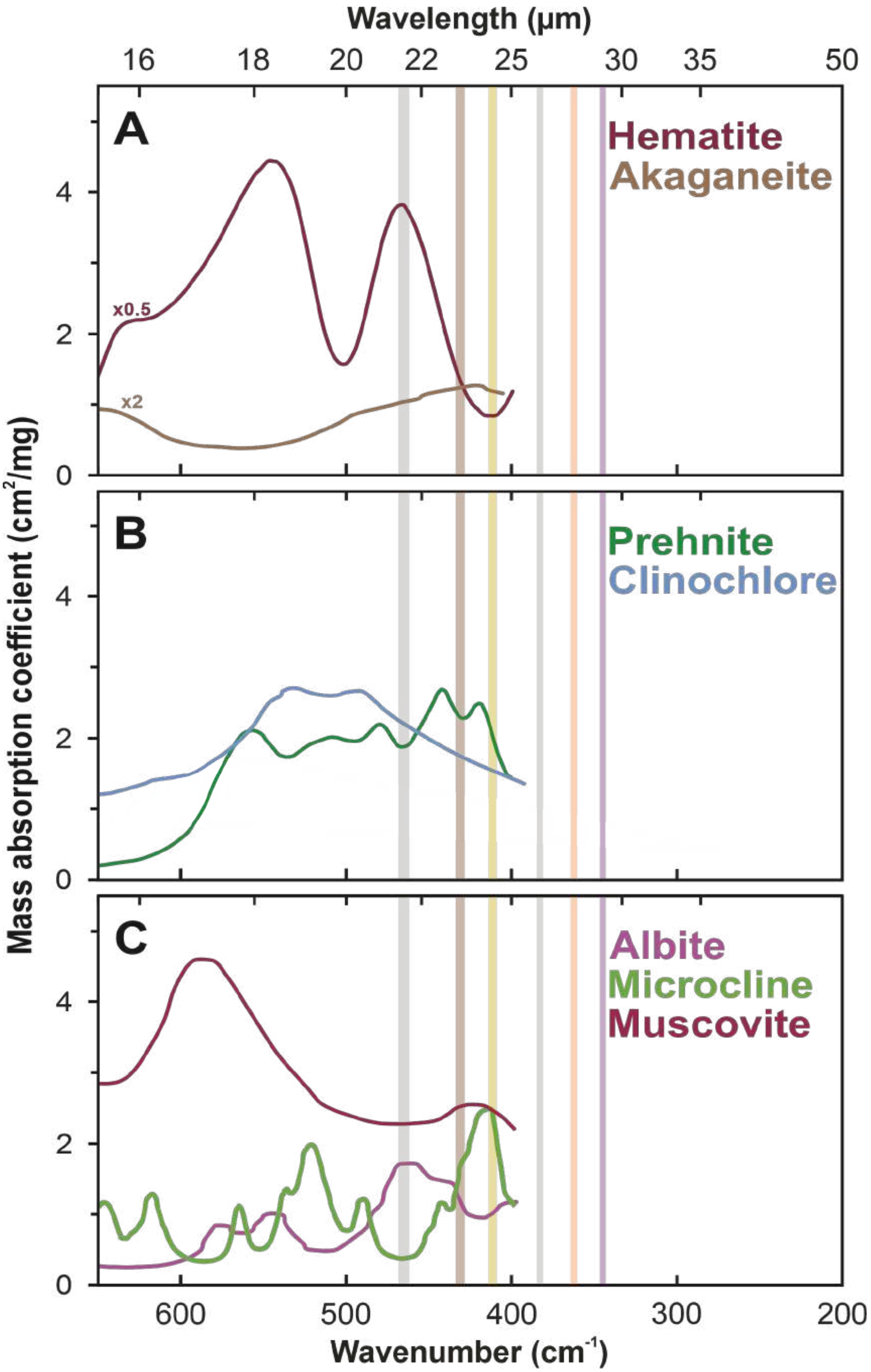
Wavelength (μm)
16
18
20
22
25
30
35
50
A
Hematite
Akaganeite
x0.5
x2
B
Prehnite
Clinochlore
C
Albite
Microcline
Muscovite
0
2
4
Mass absorption coefficient (cm²/mg)
600
500
400
300
200
Wavenumber (cm⁻¹)

Figure S1. Mass absorption coefficients of key Martian minerals with similar characteristic to sulfides classified into **(A)** oxides [1–3,4 and JHU spectral library (https://speclib.jpl.nasa.gov/documents/jhu_desc)], **(B)** secondary rock-forming minerals [3,4,5 and JHU spectral library (https://speclib.jpl.nasa.gov/documents/jhu_desc)], and **(C)** rarer primary rock-forming minerals on Mars [5]. The spectral ranges of the six detectors are marked with rectangles: orange (360–364 cm^{-1} = 27.45–27.75 µm: chalcopyrite), yellow (409–414 cm^{-1} = 24.15−24.45 µm: pyrite), brown (428–434 cm^{-1} = 23.05–23.35 µm: marcasite), gray (381–385 cm^{-1} = 25.95–26.25 µm and 462–468 cm^{-1} = 21.35–21.65 µm: reference bands), and purple (343–347 cm^{-1} = 28.85–29.15 µm: clinopyroxene).

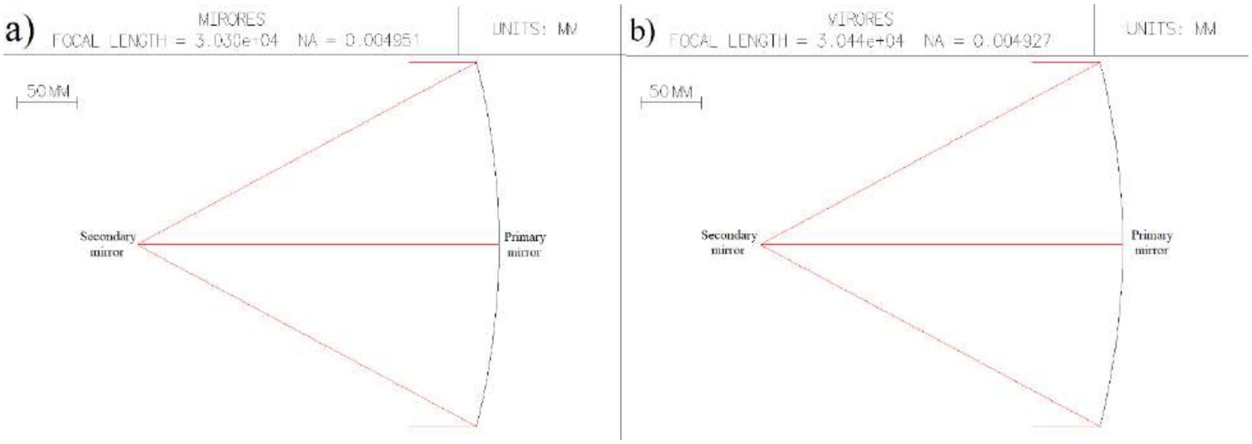

Figure S2. Ray tracing analysis corresponding to **(a)** the case with no distance shift and **(b)** to the case with a shift related the thermal expansion of both mirrors and related change in the distance between them depicted on Figure S3.D (see also the figure caption) when assumed that material will expand equally to back and front. The two images are nearly indistinguishable. The difference between the two focal lengths ($3.030 \cdot 10^4$ in **a** and $3.044 \cdot 10^4$ in **b**) is only 14 cm (0.46 rel.%). This would change the field of view by only 9 cm. NA is numerical aperture of the system and is nearly the same for **(a)** and **(b)**. The. F-number calculated as 1/(2NA) is thus 101. The analysis has been prepared in the OSLO software.

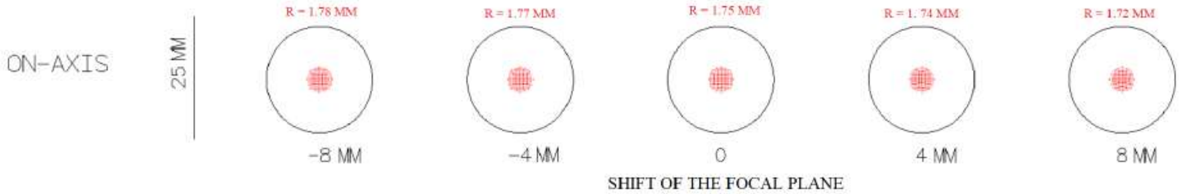

Figure S3. Optical quality of the beam in the optical axis (0, 0) when the detector is located exactly in the focal plane and when shifted by various distances. A shift from the focal by 8 mm implies the beam size is changed by 0.03 mm. The ~22 mm large black circumference represents the size of the Airy disc (corresponding to the first minimum of the Airy pattern).

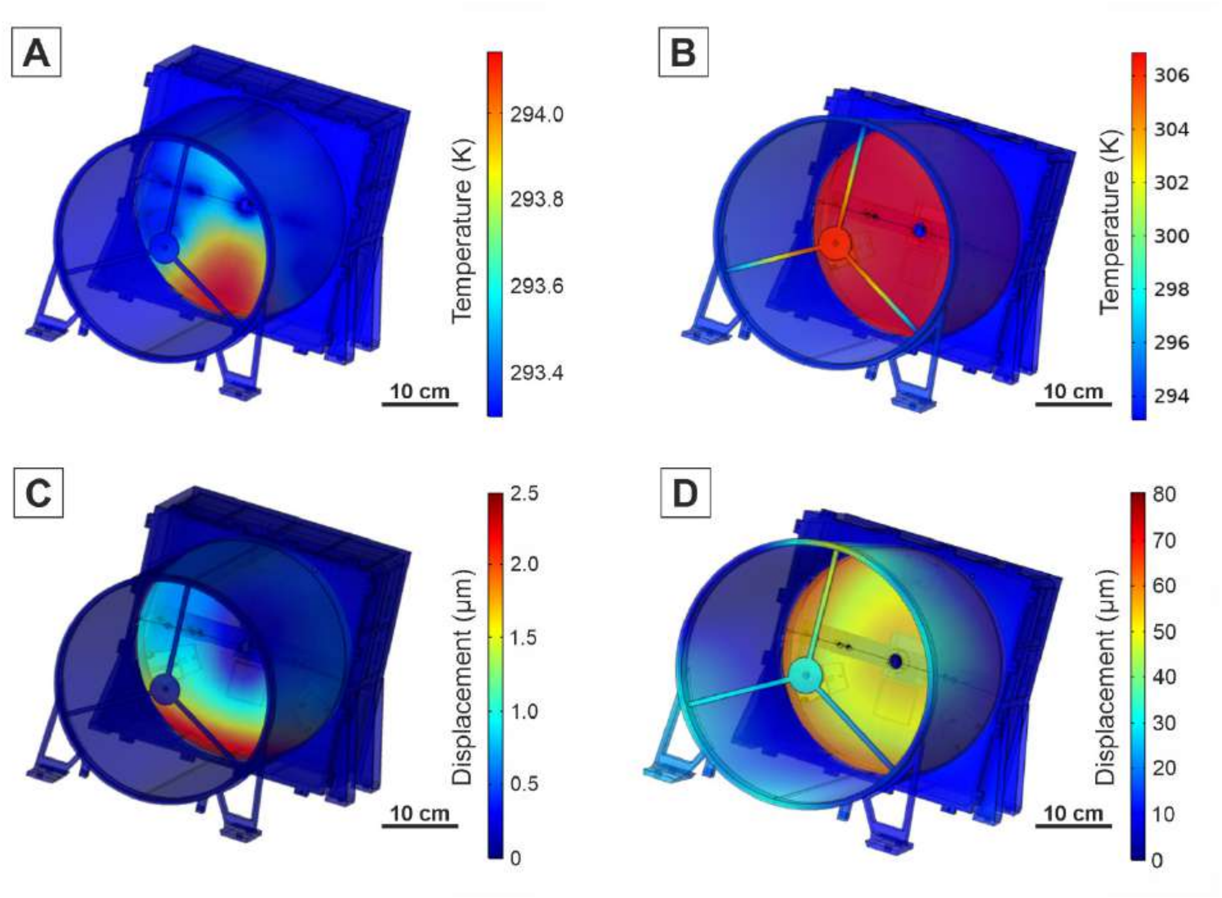

Figure S4. Thermal (A, B) and thermo-mechanical (C, D) analysis showing how changes in thermal environment induce mechanical displacement that can affect the optical performances. The assumed heat sources are 372 W/m^2 are blackbody radiation from the surface of Mars (assumed surface temperature was 293 K) and 94 W/m^2 from the reflected radiation of the Sun (assumed Mars albedo was 0.17). The instrument is assumed to operate in nadir geometry and to be shielded from direct solar radiation by the satellite shield. In simulations B and D, in which the maximum temperature reaches 307 K, it was assumed that only the electronics box has a fixed temperature of 293.15 K (20.00°C). In the remaining elements, the heat flux is dissipated by thermal conductivity. In simulations A + C, in which the temperature of the instrument is close to 293.15 K, it was assumed that the electronics box and all mechanical elements had a temperature of 293.15 K. During the construction of the device, the power flow should be adapted to how much heat could be received by the satellite but the simulations show that we should aim at achieving parameters depicted in models A + C. In the optimal scenario (A + C) thickness differences are ~1 μm, which is negligible for the optical system. However, even in the worse scenario (B + D), relative displacement between external part and internal part of the aluminium-made primary mirror (resulting in changing mirror's curvature) is ~10 μm. and the distance between primary and secondary mirror is shortened by 25 μm, which do not affect yet the focal length that is still 30 m. The focal length starts to change beyond this limit, and is estimated to be 41 m for displacements of 15 μm within the primary mirror, and 60 m for 20 μm.

a)

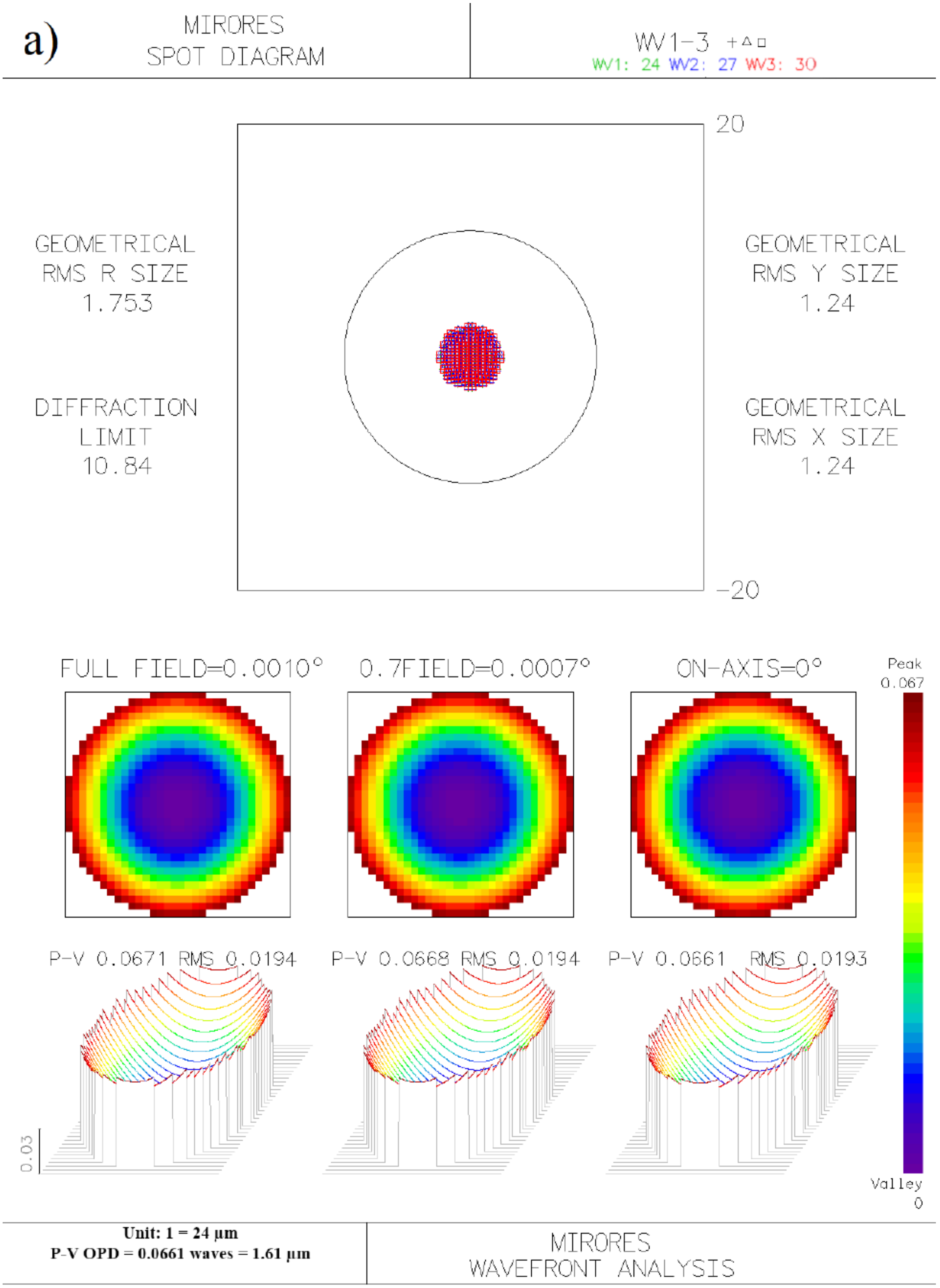

Unit: 1 = 24 µm
P-V OPD = 0.0661 waves = 1.61 µm

b)

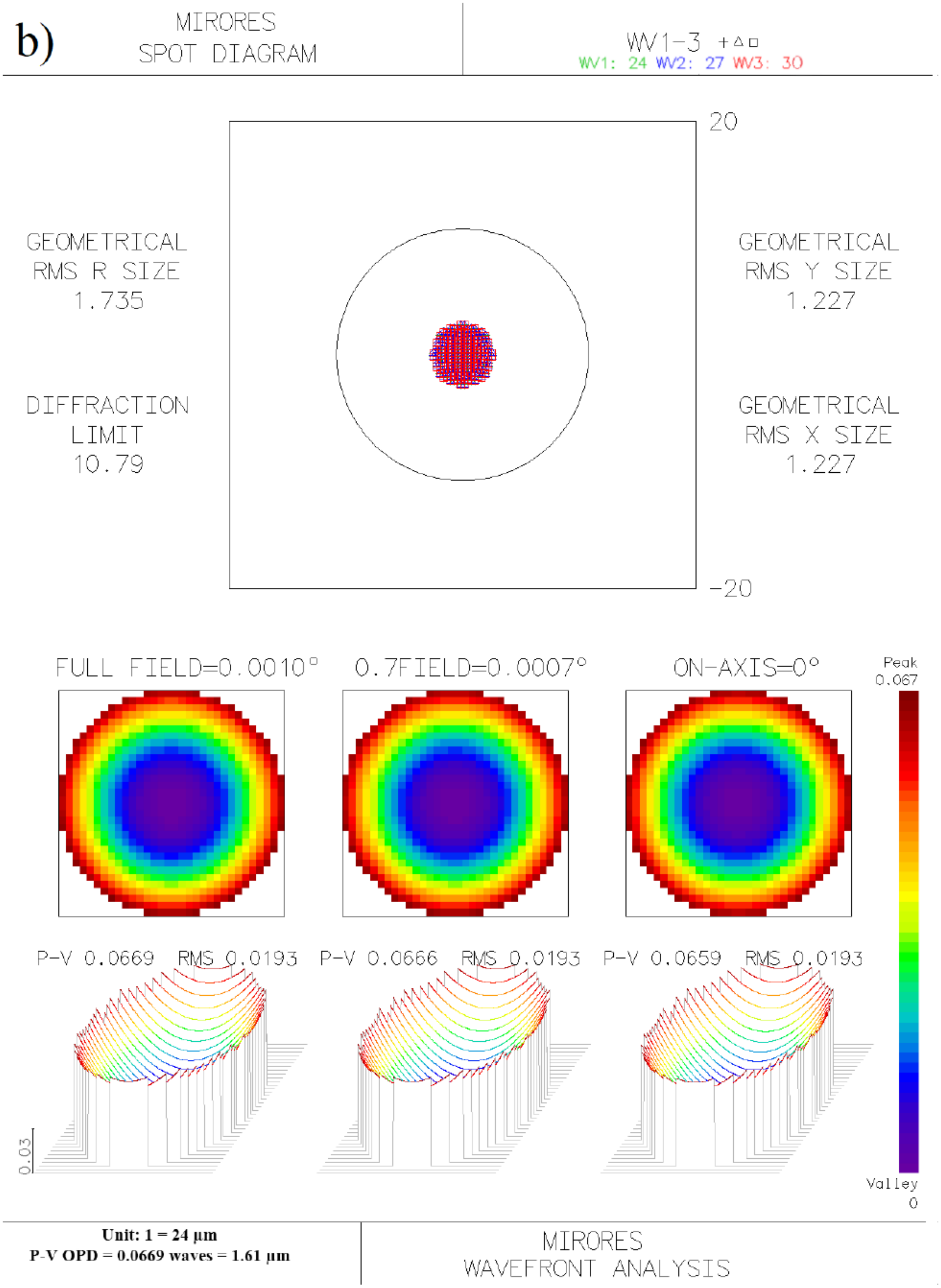
MIRORES
SPOT DIAGRAM
WV1-3 + △ □
WV1: 24 WV2: 27 WV3: 30
20
-20
GEOMETRICAL
RMS R SIZE
1.735
DIFFRACTION
LIMIT
10.79
GEOMETRICAL
RMS Y SIZE
1.227
GEOMETRICAL
RMS X SIZE
1.227
FULL FIELD=0.0010°
0.7FIELD=0.0007°
ON-AXIS=0°
Peak
0.067
Valley
0
P-V 0.0669 RMS 0.0193
P-V 0.0666 RMS 0.0193
P-V 0.0659 RMS 0.0193
0.03
Unit: 1 = 24 µm
P-V OPD = 0.0669 waves = 1.61 µm
MIRORES
WAVEFRONT ANALYSIS

Figure S5. Tolerance analysis corresponding to **(a)** the case with no distance shift and **(b)** to the case with shift due to thermal expansion. The upper panels show the optical quality of the beam in the optical axis (0,0) (~1.7 mm in radius) as compared to the size of the Airy disc (corresponding to the first minimum of the Airy pattern) (~10.8 mm in radius). Only 0.05 mm change of diffraction limit and 0.02 mm change of spot size are visible between panels (a) and (b), which leads to a conclusion that the resolution will remain optimal during measurements. The lower panels show changes in wavefront for slight deviations (0.0010° and 0.0007°) from the optical axis. WV 1-3 are wavelengths (24 μm, 27 μm, and 30 μm) with corresponding symbols (cross, square, triangle) visible in spot diagram used for calculating spot size. RMS is random mean square, which estimates the uncertainty of computation. P-V is optical path difference (OPD) between peak (P) and valley (V) of the wavefront spot expressed in wavelength units (1 = 24 μm).

References:

1. Kendix, E.; Moscardi, G.; Mazzeo, R.; Baraldi, P.; Prati, S.; Joseph, E.; Capelli, S. Far infrared and Raman spectroscopy analysis of inorganic pigments. *J. Raman Spectrosc.* **2008**, *39*, 1104–1112, doi:10.1002/jrs.1956.
2. Murad, E.; Bishop, J.L. The infrared spectrum of synthetic akaganeite, β-FeOOH. *Am. Mineral.* **2000**, *85*, 716–721, doi:10.2138/am-2000-5-609.
3. Salisbury, J.W.; Walter, L.S.; Vergo, N. Availability of a library of infrared (2.1-25.0 μm) mineral spectra. *Am. Mineral.* **1989**, *74*, 938–939.
4. Stimson, M.; O'Donnell, M. The Infrared and Ultraviolet Absorption Spectra of Cytosine and Isocytosine in the Solid State. *J. Am. Chem. Soc.* **1952**, *74*, 1805–1808, doi:10.1143/JPSJ.28.1051.
5. Salisbury, J.W.; Walter, L.S.; Vergo, N. Mid-infrared (2.1-25 um) spectra of minerals: First edition. *USGS Open-File Rep.* **1987**, 390.
6. Brusentsova, T.; Peale, R.E.; Maukonen, D.; Figueiredo, P.; Harlow, G.E.; Ebel, D.S.; Nissinboim, A.; Sherman, K.; Lisse, C.M. Laboratory far-infrared spectroscopy of terrestrial sulphides to support analysis of cosmic dust spectra. *Mon. Not. R. Astron. Soc.* **2012**, *420*, 2569–2579, doi:10.1111/j.1365-2966.2011.20228.x.